frontiers | Research Topics

Pharmacokinetic-pharmacodynamic model of drugs and their pharmacokinetic differences between normal and disease states

Edited by
Zipeng Gong, Ling Ye, Guo Ma, Kaustubh Kulkarni and Yan-Fang Xian

Published in
Frontiers in Pharmacology

ISSN 1664-8714
ISBN 978-2-8325-5319-0
DOI 10.3389/978-2-8325-5319-0

About Frontiers

Frontiers is more than just an open access publisher of scholarly articles: it is a pioneering approach to the world of academia, radically improving the way scholarly research is managed. The grand vision of Frontiers is a world where all people have an equal opportunity to seek, share and generate knowledge. Frontiers provides immediate and permanent online open access to all its publications, but this alone is not enough to realize our grand goals.

Frontiers journal series

The Frontiers journal series is a multi-tier and interdisciplinary set of open-access, online journals, promising a paradigm shift from the current review, selection and dissemination processes in academic publishing. All Frontiers journals are driven by researchers for researchers; therefore, they constitute a service to the scholarly community. At the same time, the *Frontiers journal series* operates on a revolutionary invention, the tiered publishing system, initially addressing specific communities of scholars, and gradually climbing up to broader public understanding, thus serving the interests of the lay society, too.

Dedication to quality

Each Frontiers article is a landmark of the highest quality, thanks to genuinely collaborative interactions between authors and review editors, who include some of the world's best academicians. Research must be certified by peers before entering a stream of knowledge that may eventually reach the public - and shape society; therefore, Frontiers only applies the most rigorous and unbiased reviews. Frontiers revolutionizes research publishing by freely delivering the most outstanding research, evaluated with no bias from both the academic and social point of view. By applying the most advanced information technologies, Frontiers is catapulting scholarly publishing into a new generation.

What are Frontiers Research Topics?

Frontiers Research Topics are very popular trademarks of the *Frontiers journals series*: they are collections of at least ten articles, all centered on a particular subject. With their unique mix of varied contributions from Original Research to Review Articles, Frontiers Research Topics unify the most influential researchers, the latest key findings and historical advances in a hot research area.

Find out more on how to host your own Frontiers Research Topic or contribute to one as an author by contacting the Frontiers editorial office: frontiersin.org/about/contact

Pharmacokinetic-pharmacodynamic model of drugs and their pharmacokinetic differences between normal and disease states

Topic editors

Zipeng Gong — Guizhou Medical University, China
Ling Ye — Southern Medical University, China
Guo Ma — Fudan University, China
Kaustubh Kulkarni — Blueprint Medicines, United States
Yan-Fang Xian — The Chinese University of Hong Kong, China

Citation

Gong, Z., Ye, L., Ma, G., Kulkarni, K., Xian, Y.-F., eds. (2024). *Pharmacokinetic-pharmacodynamic model of drugs and their pharmacokinetic differences between normal and disease states*. Lausanne: Frontiers Media SA. doi: 10.3389/978-2-8325-5319-0

Table of contents

frontiers | Frontiers in Pharmacology

TYPE Editorial
PUBLISHED 05 August 2024
DOI 10.3389/fphar.2024.1451176

OPEN ACCESS

EDITED AND REVIEWED BY
Xin Wang,
East China Normal University, China

*CORRESPONDENCE
Zipeng Gong,
gzp4012607@126.com

RECEIVED 18 June 2024
ACCEPTED 27 June 2024
PUBLISHED 05 August 2024

CITATION
Gong Z, Chen R, Ye L, Ma G, Xian Y and Kulkarni K (2024), Editorial: Pharmacokinetic-pharmacodynamic model of drugs and their pharmacokinetic differences between normal and disease states.
Front. Pharmacol. 15:1451176.
doi: 10.3389/fphar.2024.1451176

Editorial: Pharmacokinetic-pharmacodynamic model of drugs and their pharmacokinetic differences between normal and disease states

Zipeng Gong[1,2,3]*, Ruixing Chen[1], Ling Ye[4], Guo Ma[5], Yanfang Xian[6] and Kaustubh Kulkarni[7]

[1]State Key Laboratory of Functions and Applications of Medicinal Plants, Guizhou Provincial Key Laboratory of Pharmaceutics, School of Pharmacy, Guizhou Medical University, Guiyang, China, [2]Key Laboratory of Basic Pharmacology of Ministry of Education, Zunyi Medical University, Zunyi, China, [3]Guizhou Provincial Engineering Research Center for the Development and Application of Ethnic Medicine and TCM, Guizhou Medical University, Guiyang, China, [4]NMPA Key Laboratory for Research and Evaluation of Drug Metabolism, Guangdong Provincial Key Laboratory of New Drug Screening, School of Pharmaceutical Sciences, Southern Medical University, Guangzhou, China, [5]School of Pharmacy, Fudan University, Shanghai, China, [6]School of Chinese Medicine, Faculty of Medicine, The Chinese University of Hong Kong, Shatin, Hong Kong SAR, China, [7]Boundless Bio Inc, San Diego, CA, United States

KEYWORDS

normal status, disease states, metabolizing enzymes, transporters, pharmacokinetic-pharmacodynamic link model

Editorial on the Research Topic
Pharmacokinetic-pharmacodynamic model of drugs and their pharmacokinetic differences between normal and disease states

This Research Topic is part of a series with "Pharmacokinetic Differences of Drugs and Their Regulatory Mechanisms Under Dual Status Including Normal and Diseased Organism"

In the main frame of the above Research Topic, 16 contributions have been published including but not limited to pharmacokinetic comparisons between normal and disease status, the changes in the expression and function of drug-metabolizing enzymes and drug transporters in disease status and their associated regulatory mechanisms, ADME/toxicity of drugs as well as their modulation, drug-drug interactions mediated by nuclear receptors, transporters and metabolic enzymes based on the approaches and techniques of pharmacokinetics, transcriptomics and metabolomics (Gong et al., 2022). However, pharmacokinetic studies are not only essential for new drug development, but the study of pharmacokinetic-pharmacodynamic (PK-PD) models also plays a significant role in this process. The PK-PD model can uncover the intrinsic relationship between drug concentration and its effects, assisting in understanding the dynamic characteristics of the drug's action site within the body. It helps deduce the action site producing the effect and the drug concentration at that site, enabling researchers to grasp the comprehensive characteristics of the drug's pharmacokinetic and pharmacodynamic processes *in vivo* (Derendorf et al., 2000)However, preclinical pharmacokinetic data are mainly derived from healthy animals, which is unreasonable. On one hand, patients are the ultimate users of

drugs, as drugs are primarily used to treat individuals with diseases (Liang et al., 2023). On the other hand, the body's pathological state and the severity of the disease significantly impact the ADME (absorption, distribution, metabolism, and excretion) of drugs, which are crucial for determining the safety and efficacy of clinical treatments. Consequently, studying pharmacokinetics and the PK-PD model in disease states is more meaningful and relevant to clinical practice.

Considering that drugs are primarily used in the body under disease conditions, this research will not only continue to focus on the pharmacokinetic differences of drugs, including Traditional Chinese medicine, and their regulatory mechanisms under both normal and diseased states, but will also emphasize the study of drug PK-PD models based on cellular pharmacokinetics and integrated pharmacokinetics. We aim to provide references and insights for individualized, safe, and effective drug use, and for optimizing the drug evaluation system based on disease states (Gong et al., 2015).

Within the framework of this Research Topic, 14 contributions have been published, covering subjects including, but not limited to: the pharmacokinetic differences of drugs, including Traditional Chinese medicine, and their mechanisms under normal and diseased states, the study of cellular pharmacokinetics, the changes in the expression and function of drug-metabolizing enzymes and drug transporters in disease status and their related regulatory mechanisms, the research on intestinal microbiome mediated drug metabolism and its effect on drug efficacy and toxicity, ADME/toxicity of drugs as well as their regulation, drug-drug interactions mediated by nuclear receptors, transporters and metabolic enzymes based on the methods and techniques of pharmacokinetics, transcriptomics, and metabolomics, the study of drug PK-PD model based on the cellular pharmacokinetics and integrated pharmacokinetics.

Nwabufo et al. demonstrated the dysregulated expression of 25 clinically relevant drug metabolizing enzymes and membrane transporters (DMETs) in Vero E6 cells and post-mortem lung tissues of COVID-19 patients. They found that SARS-CoV-2 infection leads to DMETs dysregulation, with inflammatory cells being the main drivers of the differences in DMETs localization between COVID-19 and control lung tissues.

Nie et al. established a two-compartment population pharmacokinetics (PopPK) modelfor naloxone in adult patients undergoing general anesthesia. Compared the pharmacokinetic discrepancy of naloxone between covariates and dosage regimens in 47 patientsby Monte Carlo simulations, and the conclusion was that fixed-dose regimens were better.

Lian et al. elucidated the mechanism by which the compatible herbs in the Jin-Gu-Lian formula reduce Alangium chinense (AC)-induced neurotoxicity. The combined use of AC and the herbal extract of the Jin-Gu-Lian formula (CH) significantly reduced the plasma exposure levels of two main components of AC, and markedly downregulated the gene expression of cytochrome P450 enzymes induced by AC.

Xiong et al. developed a highly efficient method for simultaneously determining four major compounds in the Mori Cortex total flavonoid extract. Thus, they studied the pharmacokinetic differences between normal and diabetic rats after oral administration, providing a pharmacokinetic basis for the pharmacological and toxicological studies of Mori Cortex.

Nie et al. compared the pharmacokinetic differences of seven active components of Ling-Gui-Zhu-Gan decoction (LGZGD) in normal rats and rats with non-alcoholic fatty liver disease (NAFLD). They found that the expression levels of the metabolic enzyme UGT1A1 and nine transport proteins were significantly reduced in NAFLD rats, which might explain the pharmacokinetic differences between normal and NAFLD rats.

Wang et al. explored the pharmacokinetic differences caused by metabolic enzymes for six main components of Huangqi Liuyi Decoction in mice liver microsomes. The metabolism of the active components might be related to CYP2C37, CYP2C11, CYP1A2, CYP2E1, and CYP3A11.

Liu et al. investigated the toxicity and pharmacodynamic components of Asarum essential oil (AEO) using molecular distillation technology. They identified the main anti-inflammatory components as methyl eugenol, α-pinene, and β-pinene, and the main toxic components as camphor, methyl eugenol, and 3,5-dimethoxytoluene.

Zhan et al. found that the inhibitory effect of vortioxetine on CYP450 enzymes is reversible and lacks time-dependent inhibition. Additionally, they identified the types of inhibition mechanisms of vortioxetine on CYP450 enzymes in human and rat liver microsomes. This study provides important guidance for the safe clinical use of vortioxetine.

Alasmari et al. used the PBPK model to accurately simulate the pharmacokinetic differences of ceftriaxone in healthy individuals and patients with mild, moderate, and severe chronic kidney disease (CKD). Additionally, they found that dose reduction could achieve same exposure comparable to that of healthy individuals.

Ye et al. elucidated the characteristics and pharmacological effects of Glycycoumarin (GCM) through pharmacokinetic studies. They found that GCM was rapidly absorbed and converted into its conjugated metabolites with low bioavailability after administration. Additionally, it was distributed in various tissues except the brain.

Sun et al. developed a simple and efficientmethod to determine the concentration of riluzole in human plasma, which successfully applied it to the pharmacokinetic study of riluzole in Chinese patients with amyotrophic lateral sclerosis (ALS).

Tao et al. compared the PK, PD, and safety of Ciprofol in Chinese patients with normal renal function and those with impaired renal function after injection. Their investigation revealed that Ciprofol was well tolerated, providing an important guide to clinical dose adjustment.

Chen et al. found that the interaction between lacosamide and nisoldipine significantly altered the pharmacokinetic parameters of lacosamide and its metabolites *in vivo* and *in vitro*. In addition, the mechanism of nisoldipine and lacosamide metabolism was associated with mixed inhibition.

Zhu et al. studied the pharmacokinetics of 15 prototype components in the extract of Pogostemon cablin (PC) after oral administration in rats. It providing reference value for the clinical application of PC.

Therefore, given that drugs are largely taken by patients, the Research Topic focused mainly on PK-PD Model of drugs and their pharmacokinetic differences between normal and disease states, which could optimize the design of rational dosing regimens for

clinical therapeutics, and provide reference individualized safety and effective drug use.

Author contributions

ZG: Writing–original draft, Writing–review and editing. RC: Writing–original draft, Writing–review and editing. LY: Writing–original draft, Writing–review and editing. GM: Writing–original draft, Writing–review and editing. YX: Writing–original draft, Writing–review and editing. KK: Writing–original draft, Writing–review and editing.

Funding

The author(s) declare that financial support was received for the research, authorship, and/or publication of this article. This study was funded by the National Natural Science Foundation of China (Nos. 81860734, 82160789), Guiyang Science and Technology Bureau [(2021) 43-12], the Excellent Young Talents Plan of Guizhou Province [QKHPTRC-YQK(2023) 029]; Natural Science Research Foundation of Guizhou Provincial Department of Education [qianjiaoji(2023)066]; the project of Key Laboratory of Basic Pharmacology of Ministry of Education in ZunyiMedicial University [KY (2022)394]; the Excellent Young Talents Plan of Guizhou Medical University (No. 2022-104).

Acknowledgments

We would like to express our gratitude to all the authors for the valuable sharing of their findings and opinions.

Conflict of interest

Author KK is employed by Boundless Bio Inc.

The remaining authors declare that the research was conducted in the absence of any commercial or financial relationships that could be construed as a potential conflict of interest.

Publisher's note

References

Derendorf, H., Lesko, L. J., Chaikin, P., Colburn, W. A., Lee, P., Miller, R., et al. (2000). Pharmacokinetic/pharmacodynamic modeling in drug research and development. *J. Clin. Pharmacol.* 40 (12), 1399–1418. doi:10.1177/009127000004001211

Gong, Z., Chen, Y., Zhang, R., Yang, Q., and Zhu, X. (2015). Advances on pharmacokinetics of traditional Chinese medicine under disease states. *China. J. Chin. Mat. Med.* 40 (2), 169–173. doi:10.4268/cjcmm20150202

Gong, Z., Yang, Q., Wang, Y., Weng, X., Li, Y., Dong, Y., et al. (2022). Pharmacokinetic differences of wuji pill components in normal and chronic visceral hypersensitivity irritable bowel syndrome rats attributable to changes in tight junction and transporters. *Front. Pharmacol.* 13, 948678. doi:10.3389/fphar.2022.948678

Liang, Y., Liu, M., Wang, Y., Liu, L., and Gao, Y. (2023). Analyzing the material basis of anti-RSV efficacy of lonicerae japonicae flos based on the PK-PD model. *molecules* 28 (18), 6437. doi:10.3390/molecules28186437

frontiers | Frontiers in Pharmacology

TYPE Original Research
PUBLISHED 16 February 2023
DOI 10.3389/fphar.2023.1133982

OPEN ACCESS

EDITED BY
Ling Ye,
Southern Medical University, China

REVIEWED BY
Lei An,
Beijing Technology and Business University, China
Meng Qin,
Beijing University of Chemical Technology, China

*CORRESPONDENCE
Bo Peng,
bpeng@icmm.ac.cn
Ying Chen,
ychen@icmm.ac.cn

†These authors have contributed equally to this work

SPECIALTY SECTION
This article was submitted to Drug Metabolism and Transport, a section of the journal Frontiers in Pharmacology

RECEIVED 29 December 2022
ACCEPTED 07 February 2023
PUBLISHED 16 February 2023

CITATION
Lian D, Chen T, Yan L, Hou H, Gao S, Hu Q, Zhang G, Li H, Song L, Gao Y, Pu Y, Chen Y and Peng B (2023), Protective effect of compatible herbs in Jin-Gu-Lian formula against *Alangium chinense*-induced neurotoxicity *via* oxidative stress, neurotransmitter metabolisms, and pharmacokinetics.
Front. Pharmacol. 14:1133982.
doi: 10.3389/fphar.2023.1133982

Protective effect of compatible herbs in Jin-Gu-Lian formula against *Alangium chinense*-induced neurotoxicity *via* oxidative stress, neurotransmitter metabolisms, and pharmacokinetics

Dongyin Lian[1†], Tengfei Chen[1†], Lihua Yan[1], Hongping Hou[1], Shuangrong Gao[1], Qin Hu[2], Guangping Zhang[1], Han Li[1], Ling Song[1], Yunhang Gao[1], Yunxi Pu[3], Ying Chen[1*] and Bo Peng[1*]

[1]Institute of Chinese Materia Medica, China Academy of Chinese Medical Sciences, Beijing, China, [2]College of Life Sciences and Bio-Engineering, Beijing University of Technology, Beijing, China, [3]College of Letters and Science, University of California, Santa Barbara, CA, United States

Background: *A. chinense* frequently used in Miao medicine to treat rheumatic diseases. However, as a famous toxic herb, *Alangium chinense* and its representative components exhibit ineluctable neurotoxicity, thus creating significant challenges for clinical application. The combined application with compatible herbs in Jin-Gu-Lian formula attenuates such neurotoxicity according to the compatible principle of traditional Chinese medicines.

Purpose: We aimed to investigate the detoxification of the compatible herbs in Jin-Gu-Lian formula on *A. chinense*-induced neurotoxicity and investigate its mechanism.

Methods: Neurobehavioral and pathohistological analysis were used to determine the neurotoxicity in rats administered with *A. chinense* extract (AC), extract of compatible herbs in Jin-Gu-Lian formula (CH) and combination of AC with CH for 14 days. The mechanism underlying the reduction of toxicity by combination with CH was assessed by enzyme-linked immunosorbent assays, spectrophotometric assays, liquid chromatography tandem-mass spectrometry and real-time reverse transcription-quantitative polymerase chain reaction.

Results: Compatible herbs attenuated the AC-induced neurotoxicity as evidenced by increased locomotor activity, enhanced grip strength, the decreased frequency of AC-induced morphological damage in neurons, as well as a reduction of neuron-specific enolase (NSE) and neurofilament light chain (NEFL) levels. The combination of AC and CH ameliorated AC-induced oxidative damage by modulating the activities of superoxide dismutase (SOD) and glutathione peroxidase (GSH-Px), and total antioxidant capacity (T-AOC). AC treatment significantly reduced the levels of monoamine and acetylcholine neurotransmitters in the brains of rats, including acetylcholine (Ach), dopamine (DA), 3,4-dihydroxyphenylacetic acid (DOPAC), homovanillic acid (HVA), norepinephrine (NE), and serotonin (5-HT). Combined AC and CH treatment

regulated the abnormal concentrations and metabolisms of neurotransmitters. Pharmacokinetic studies showed that the co-administration of AC and CH significantly decreased plasma exposure levels of two main components of AC, as evidenced by the reduction of maximum plasma concentration (C_{max}), area under the plasma concentration-time curve (AUC) compared to AC. In addition, the AC-induced downregulation in mRNA expression of cytochrome P450 enzymes was significantly reduced in response to combined AC and CH treatment.

Conclusion: Compatible herbs in Jin-Gu-Lian formula alleviated the neurotoxicity induced by *A. chinense* by ameliorating oxidative damage, preventing abnormality of neurotransmitters and modulating pharmacokinetics.

KEYWORDS

***Alangium chinense*, neurotoxicity, pharmacokinetics, cytochrome P450, oxidative stress, neurotransmitters**

1 Introduction

Alangium chinense (Lour.) Harms (also known as Ba Jiao Feng) is derived from the *Alangium* genus of the Alangiaceae family and is widely distributed in the southwest of China (Hu et al., 2020). *Alangium chinense*, a routine and important Miao medicine in ethnomedicine, is used at a high frequency of more than 100 in 842 Miao medical formulas collected from relevant Miao medicine books, including Chinese Miao Medicine, Chinese Materia Medica of Miao Medicinal Volume, Medico-Miao and other Miao ethnic medicine books (Li et al., 2017). The properties and effects of *A. chinense* are described as dispelling pathogenic wind and eliminating dampness, relaxing tendon and freeing meridians, dispersing blood stasis and detumescence, as well as relieving pain. In traditional clinical treatment, *A. chinense* was used in combination with other herbal materials in many widely used folk prescriptions as a remedy for rheumatic diseases (Zheng et al., 2022), acroanesthesia and fractures, including Jin Gu Lian (JGL) capsules, Feng Shi Ding tablets and Xiao Bi Ling mixture (Meng et al., 2021). Previous experimental studies reported that *A. chinense* and its representative active components (such as anabasine and salicin) relieved arthritis, exhibited anti-inflammatory activity and ameliorated rheumatoid arthritis. These abilities are associated with the attenuated expression of proinflammatory cytokines, the inhibition of NF-κB signaling, the improvement of oxidative stress pathways and the relaxation of skeletal and smooth muscle (Zhang et al., 2013; Zhai et al., 2018; Hu et al., 2020).

Alangium chinense was documented as a famous toxic herb in traditional Chinese medicine (TCM). Although the therapeutic actions of *A. chinense* have been reported in both clinics and experiments, its clinical application is limited due to its obvious adverse effects on the central nervous system, lungs, liver and smooth muscles (Hu et al., 2020; Meng et al., 2021). Previous clinical studies reported that the oral administration of more than 40 g of *A. chinense* led to severe neurotoxicity, including dizziness, convulsions, muscle weakness and respiratory depression (Zhang et al., 2008). According to the *Dictionary of Chinese Materia Medica*, the 50% lethal dose (LD_{50}) of *A. chinense* water extract in mice after intraperitoneal injection was 9.98 g/kg (Zhao et al., 2006). In one study, an intravenous injection of 1.25 g/kg and 4 g/kg *A chinense* water extract resulted in significant toxicity, including respiratory paralysis and muscle weakness in rabbits and beagles, respectively (Zhang et al., 2019). After exposure to intravenous total alkaloids of *A. chinense*, the minimal dose for muscle relaxation and the minimal lethal dose in rabbits were respectively found to be 2.47 mg/kg and 5.65 mg/kg (Zhao et al., 2006). Another study reported that neurotoxicity and hepatoxicity were observed in rabbits following the intravenous administration of total alkaloids of *A. chinense* at a repeated dose of 1.9 mg/kg for 15 days (Zhao et al., 2006). Anabasine, a bioactive chemical, is known as the primary constituent responsible for the therapeutic actions and adverse effects of *A. chinense* (Hu et al., 2020; Meng et al., 2021). Following the intravenous administration of anabasine, the minimal doses for muscle relaxation and respiratory paralysis in rabbits were 1.18 mg/kg and 1.47 mg/kg (Zhao et al., 2006).

Collectively, the above results suggest that *A. chinense* and its active component have narrow therapeutic windows, thus creating a significant challenge for clinical application. Compatibility is an essential aspect of TCM medication. According to the compatibility principle of TCM, the combination of toxic herbs with other herbal medicines can generate the expected therapeutic actions but with lower adverse effects (Steven and Yi, 2021; Xiang et al., 2021). Many researchers have reported that the combined application of compatible herbs in various herbal formulations can weaken or eliminate the toxicity of the poisonous TCM based on well-designed toxic evaluations performed both *in vivo* and *in vitro* (Zhang et al., 2018). Jin Gu Lian prescription consists of a total of five types of herbs: *A. chinense* (Lour.) Harms (Cornaceae; Alangii Radix; Ba Jiao Feng in Chinese), *Gaultheria leucocarpa var. yunnanensis* (Franch.) T. Z. Hsu and R. C. Fang (Ericaceae; Gaultheriae Herba; Tou Gu Xiang in Chinese), *Heptapleurum leucanthum* (R.Vig.) Y. F. Deng (Araliaceae; Schefflerae Leucanthae Caulis seu Folium; Han Tao Ye in Chinese), *Sargentodoxa cuneata* (Oliv.) Rehder and E. H. Wilson (Lardizabalaceae; Sargentodoxae Caulis; Da Xue Teng in Chinese), and *Psammosilene tunicoides* W. C. Wu and C. Y. Wu (Caryophyllaceae; Psammosilenes Radix; Jin Tie Suo in Chinese). Previous research investigated the pharmacokinetic characteristics of a representative formula JGL and its core drug pair (*A. chinense and Sargentodoxa cuneate*). These results demonstrated that combination of the core drug pair with other herbs in JGL decreased the absorption and avoided the accumulation of anabasine by reducing maximum plasma concentration (C_{max})

TABLE 1 The five herbal medicines of Jin-Gu-Lian formula.

Chinese name	Binomial synonym	Scientific name	Family	Origin	Batch number
Ba Jiao Feng	Alangii Radix	*Alangium chinense* (Lour.) Harms	Cornaceae	Henan	YL-17720220302
Tou Gu Xiang	Gaultheriae Herba	*Gaultheria leucocarpa* var. *yunnanensis* (Franch.) T.Z.Hsu and R.C.Fang	Ericaceae	Guizhou	YL-1720220201
Han Tao Ye	Schefflerae Leucanthae Caulis seu Folium	*Heptapleurum leucanthum* (R.Vig.) Y.F.Deng	Araliaceae	Guangdong	YL-1762022070
Da Xue Teng	Sargentodoxae Caulis	*Sargentodoxa cuneata* (Oliv.) Rehder and E.H.Wilson	Lardizabalaceae	Anhui	JYC-20220206
Jin Tie Suo	Psammosilenes Radix	*Psammosilene tunicoides* W.C.Wu and C.Y.Wu	Caryophyllaceae	Yunnan	YL-17820220304

and apparent volume of distribution ($V_{z/F}$), which might reduce the possibility of toxicity of anabasine (Zheng et al., 2022). However, the effects of a compatible approach on the neurotoxicity induced by *A. chinense* has yet to be investigated.

In this study, we aimed to investigate the rationality of the compatible application of *A. chinense* with other herbal medicines in JGL formula in terms of attenuation of toxicity. This study was designed to reveal the effect of compatible herbs in JGL on the attenuation of neurotoxicity induced by *A. chinense* and investigate its mechanism by evaluating the amelioration of oxidative damages, the regulation of neurotoxic biomarkers, the alteration of neurotransmitter levels, and modulation of the pharmacokinetic characteristics of active components in *A. chinense*.

2 Materials and methods

2.1 Drugs and reagents

2.1.1 Crude drugs and extraction

All crude drugs were supplied by Guizhou Yibai Pharmaceutical Co., Ltd. The voucher specimens are deposited in the Laboratory of Quality Control for Traditional Chinese Medicine in the Institute of Chinese Materia Medica, China Academy of Chinese Medical Sciences, and were identified by Professor Lihua Yan from the institute according to the standard of Chinese pharmacopoeia (2020) and the standard of TCM materials and Ethnic medicinal materials in Guizhou Province (2019). Detailed information was shown in Table 1.

The dried roots of *A. chinense* (Lour.) Harms (Ba Jiao Feng) were soaked and extracted with boiling water (1:10, 1:8 and then 1:8 w/v) for 2 h following filtration with 150 μm strainer. The extraction step was repeated thrice. The merged mixtures were concentrated under the vacuum freeze dryer to prepare powder and the yield of powder was 5.30% (w/w). The preparation of compatible herbs of JGL consisted of 30% *G. leucocarpa var. yunnanensis* (Franch.) T. Z. Hsu and R. C. Fang (Tou Gu Xiang), 35% *H. leucanthum* (R.Vig.) Y. F. Deng (Han Tao Ye), 30% *S. cuneata* (Oliv.) Rehder and E. H. Wilson (Da Xue Teng), 5% *P. tunicoides* W. C. Wu and C. Y. Wu (Jin Tie Suo). These compatible herbs were prepared through the same procedure and the yield was 5.64% (w/w). The powder of *A. chinense* extract (AC) and the extract of compatible herbs (CH) was analyzed by ultra-performance liquid chromatography-quadrupole-time-of-flight tandem mass (UPLC-Q-TOF-MS) analysis. Anabasine and venoterpine were quantified in AC and the combination of AC and CH. The content of anabasine and venoterpine in AC was 249.2 ± 2.2 μg/g and 2.1 ± 0.0 μg/g, respectively. The content of anabasine and venoterpine in the combination of AC and CH was 175.0 ± 0.9 μg/g and 1.4 ± 0.0 μg/g respectively.

The UPLC-Q-TOF-MS analysis was performed on a Waters ACQUITY UPLC H-Class system with a Waters UPLC BEH C_{18} column (2.1 mm × 100 mm, 1.7 μm). Briefly, the powder of AC or CH was dissolved in water (1:20, w/v), placed in an ultrasonic bath for 30 min, and centrifuged for 5 min at 10,000 rpm. The supernatant was filtered through a 0.22 μm filter membrane for subsequent UPLC-MS analysis. Linear gradient elution with mobile phases of phase A containing the aqueous phases of 0.1% formic acid and phase B containing acetonitrile was applied (0–12 min, 5%–55% B; 12–15 min, 55%–95% B) at a flow rate of 0.3 mL/min. The column was maintained at 35°C and the injection volume was 1 μL. MS analysis was carried out on a Q-TOF high-resolution mass spectrometer (Xevo G2-S; Waters) with an ESI Source. The MS conditions were capillary voltage: 2.2 kV (ESI+), 2.0 kV (ESI-); drying gas (N_2) flow rate: 600 L/h; drying gas temperature: 400°C; cone voltage: 40 V; ion source temperature: 120°C; scanning mode: positive and negative ion switching scanning; scan range: 100.0–1500.0 m/z; collision voltage: 20–50 eV. Data analysis was performed using MassLynx 4.1 software (Waters).

2.1.2 Reagents and chemicals

DL-anabasine (ANA, lot no: C10954677, purity: 97.0%) was obtained from Shanghai Macklin Biochemical Co., Ltd. (Shanghai, China). Venoterpine (VEN, lot no: X31O11L129589, purity: 98.0%) was purchased from Shanghai Yuanye Bio-Technology Co., Ltd. (Shanghai, China). Nicotine (NIC, lot no: V-942900-NU1, purity: 100.0%) was obtained from CFW Laboratories Inc. (Walnut, United States) as internal standard (IS). Chromatographic methanol and acetonitrile were provided by Merck (Darmstadt, Germany), and chromatographic formic acid was provided by ROE SCIENTIFIC (Newark, United States). Other reagents were commercially available and were analytically and chromatographically pure.

2.2 Animals, drug administration, and sample collection

All animals were obtained from Beijing Vital Laboratory Animal Technology (Beijing, China) and maintained in a specific pathogen-free laboratory of the Institute of Chinese Materia Medica, China Academy of Chinese Medical Sciences (Beijing, China) under

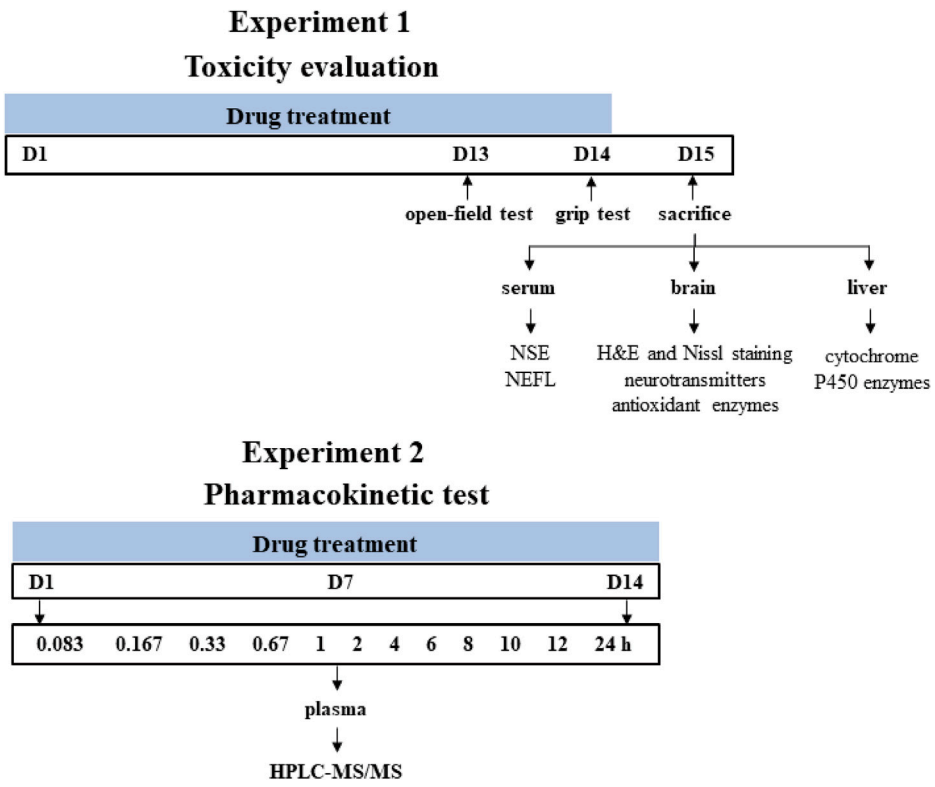

FIGURE 1
Schematic diagram of the experiment design. Time points represent the days of drug treatment.

controlled conditions (25°C ± 1°C, 45% relative humidity and a 12 h light/dark cycle). The study protocol was approved by the Institutional Animal Ethical and Welfare Committee (Approval Number: 2021B094, 2021B196). All animal procedures were in accordance with Institutional Animal Care and Use Committee guidelines. A schematic study diagram is shown in Figure 1. The detailed designs of animal experiments were shown as follows.

2.2.1 Experiment 1 (toxicity evaluation)

Male Sprague-Dawley rats (200 ± 20 g) were randomly divided into four groups with eight rats in each group and orally gavaged with the distilled water (control group), *A. chinense* extract (AC group, equivalent to 30 g/kg of crude drugs), extract of compatible herbs of JGL (CH group, equivalent to 30 g/kg of crude drugs), combination of AC with CH (AC/CH group, equivalent to 30 g/kg of crude drugs of *A. chinense* herbs and 30 g/kg of crude drugs of compatible herbs) once-daily for 14 days. One hour after administration on the 13th day (Day 13), the locomotor activity of rats was measured using the open-field test. One hour after the last administration (Day 14), grip force of rats was measured by grip test. On Day 15, rats were anesthetized with pentobarbital sodium (48 mg/kg, i.p.). The blood, brain and liver were collected for further analysis.

2.2.2 Experiment 2 (pharmacokinetic study)

Male Sprague-Dawley rats (220 ± 20 g) were randomly divided into two groups with five rats in each group and orally gavaged with continuous administration (once-daily for 14 days) of *A. chinense* extract (AC, equivalent to 30 g/kg of crude drugs) and continuous administration (once-daily for 14 days) of combination of AC and CH (equivalent to 30 g/kg of crude drugs of *A. chinense* herbs and 30 g/kg of crude drugs of compatible herbs). All rats were fasted (free access to water) for at least 12 h prior to first and last drug administration. Rats were anesthetized with isoflurane for about 30 s and then blood samples were collected at different time after the first and last administration for the two groups. All rats were euthanized with carbon dioxide after the experiment.

2.3 Behavioral test

The open field test and grip test were undertaken to investigate the neurobehavioral disorders of rats.

2.3.1 Open-field test

The locomotor activity of animal was measured using the open-field test. After administration for 13 days, rats were placed in a black square chamber (100 cm length × 100 cm width × 50 cm height) and allowed to explore freely for 5 min. The spontaneous movements of rats were recorded by a video camera and analyzed by SMART Video Tracking System V3.0 (Panlab, United States). The parameters recorded included total distance traveled, number of rearing (animal's double forelimbs leave the ground at the same time, or the two forelimbs are placed on the wall of the cage), total movement time and total rest time.

2.3.2 Grip test

The grip strength meter (YLS-13A, Jinan Yiyan technology development Co. Ltd, China) was used to assess the forelimb grip strength of rats according to manufacturer instruction. After 14 days, rats were gently placed on the grid plate and allowed to grip the metal bars with their front paws. The rats were pulled by the tail slowly. The maximal grip force during the process of steady grasping until losing strength was measured in grams. Each rat was tested thrice.

2.4 Histological and pathological assessment

Rats were anesthetized with pentobarbital sodium (48 mg/kg, i.p.). The brain was collected and the left part of brain was fixed in 4% paraformaldehyde in PBS and embedded in paraffin. After locating inferior colliculi, optic chiasma and hypothalamus, the brain was cut transversely to different sections. 4 μm thick slices were cut and stained with hematoxylin and eosin (H&E staining) and toluidine blue (Nissl staining).

2.5 ELISA for neuron-specific enolase (NSE) and neurofilament light chain (NEFL) levels

Rats were anesthetized with pentobarbital sodium (48 mg/kg, i.p.). Blood was collected from the abdominal aorta. Serum was separated by centrifugation at 3500 × g for 20 min at room temperature. The levels of NSE and NEFL in serum were measured by rat ELISA kits according to the manufacture instructions (Cusabio, China). The OD was measured at 450/650 nm.

2.6 Antioxidant enzymes analysis of brain

After killing the anesthetized rats, brains were collected rapidly, frozen in liquid nitrogen and stored at −80°C until use. The brains were homogenized in nine volumes of 0.9% NaCl with two metal beads at a speed of 60 Hz for 30 s and centrifuged (3500 rpm/min) at 4°C for 15 min. The supernatant was collected. Superoxide dismutase (SOD), glutathione peroxidase (GSH-Px) activities and total antioxidant capacity (T-AOC) were determined using commercial assay kits (Nanjing Jiancheng Bioengineering Institute, China) according to the manufacturer instructions.

2.7 LC-MS/MS for neurotransmitter level in the brain

Monoamine and acetylcholine neurotransmitters were analyzed as reported previously with slight modification (Wang L. S. et al., 2019). Briefly, brain tissue was precisely weighed and homogenized in distilled water at a final concentration of 5 g/mL 50 μL brain homogenate was mixed with 10 μL trifluoroacetic acid under the fume hood to precipitate protein. The mixture was centrifuged at 20,000 *g* for 15 min at 4°C. The supernatant was collected for analyzing acetylcholine (Ach), dopamine (DA), 3,4-dihydroxyphenylacetic acid (DOPAC), homovanillic acid (HVA), norepinephrine (NE), and serotonin (5-HT) in the LC-MS/MS system (Agilent, United States).

2.8 Pharmacokinetic test

2.8.1 Plasma sample preparation

Blood samples (no more than 150 μL) were collected from the eye venous plexus into tubes containing heparin sodium at 5, 10, 20, 40 min, and 1, 2, 4, 6, 8, 10, 12, 24 h after first and last administration. Plasma was obtained by centrifugation at 12,000 rpm for 3 min at 4 C and stored at −80 C until analysis.

All plasma samples were prepared *via* protein precipitation. An aliquot of 50 μL plasma sample was spiked with 400 μL of dichloromethane containing 10 ng/mL of NIC. After vortexed for 1 min and ultrasound for 1 min, the suspension was centrifuged at 14,000 rpm for 5 min at 4 C. 350 μL of lower solution was transferred to a new tube, and was centrifuged and concentrated at 1,700 rpm and 45 C to dryness. The residue was redissolved in 100 μL of methanol followed by a 1 min vortex and a 2 min ultrasound. The supernatant was injected into the ExionLC high-performance liquid chromatography tandem with a Qtrap 5500 mass spectrometer (HPLC-MS/MS, AB SCIEX, Toronto, Canada) system for analysis after centrifuging at 14,000 rpm for 5 min at 4°C.

2.8.2 HPLC-MS/MS analytical conditions

The concentration of analytes in rat plasma samples was determined by HPLC-MS/MS method. In previous study, an UPLC-MS/MS method was established for simultaneous determination of salidroside, anabasine, chlorogenic acid, and protocatechuic acid in rat plasma and compared the pharmacokinetic properties of two groups of rats after being orally administrated with Jin-Gu-Lian formula and its core drug pair, respectively (Zheng et al., 2022). In our study, it was necessary to investigate the plasma concentrations of anabasine and venoterpine in plasma at the toxic dose, which was higher than that use in Zheng's study. Therefore, we established an HPLC-MS/MS method for simultaneous determination of the two compounents in plasma of rats, and carried out methodological verification including dilution reliability (detailed information in Supplementary Materials).

The Phenomenex Kinetex C_{18} 100 A LC Column (100 mm × 3 mm, 2.6 μm) was used at a temperature of 40 C. The autosampler temperature was 6 C. After 5 μL injection, mobile phase A (water with 0.05% formic acid) and B (methanol) were used for elution at a flow rate of 0.3 mL/min according to the following procedure: 0–1.0 min, 95% A; 1.0–2.0 min, 95%–5% A; 2.0–3.0 min, 5% A; 3.0–3.1 min, 5%–95% A; 3.1–5.0 min, 95% A.

Multiple reaction monitoring (MRM) scans were used to detect the analytes and IS in the positive ion mode of the electrospray ionization (ESI) source. The ion spray voltage was maintained at 5500 V and curtain gas pressure was maintained at 35 psi. The collision gas was set to six psi and the turbo spray temperature was maintained at 500°C. The nebulizer gas (gas 1) and heater gas (gas 2) were both set at 45 psi, using nitrogen. The precursor/product pairs

of ANA, VEN, and IS were *m/z* 163.0→118.1, m/*z* 150.1→132.1, and *m/z* 163.2→130.1, respectively. The declustering potentials (DP) of ANA, VEN, and IS were 74.0, 78.0, and 70.1 V, respectively. The collision energies (CE) for ANA, VEN, and IS were 30.0, 27.0, and 27.2 V, respectively. The dwell time and collision exit potential (CXP) for all compounds were 100 ms and 13 V, respectively.

2.9 Analysis of the mRNA levels of cytochrome P450 in the liver

After killing the anesthetized rats, livers were collected, frozen in liquid nitrogen and store in −80°C until use. Total RNA in liver tissues was isolated by the RNA Easy Fast Tissue/Cell Kit (Tiagen, China). Complementary (c)DNA was prepared from 500 ng RNA using the EasyScript® First-Strand cDNA Synthesis SuperMix Kit (TransGen Biotech, China). cDNA was subjected to RT-qPCR to quantify gene expression using PerfectStart Green qPCR SuperMix (TransGen Biotech, China). The primer pairs (Invitrogen, Thermo Fisher Scientific, United States) used for analyses are listed in Supplementary Table S1. Beta-actin was normalized for the amounts of cDNA. Relative expression of target genes was calculated using the $2^{-\Delta\Delta CT}$ method.

2.10 Statistical analysis

Data acquisition and analysis for the concentration of ANA and VEN were conducted using the Analyst 1.7 software (AB SCIEX, Toronto, Canada). Pharmacokinetic parameters of ANA and VEN were calculated using a non-compartment model with the MaS Studio 1.5.2.14 stable software (Shanghai BioGuider Medicinal Technology Co., Ltd, Shanghai, China).

Data were expressed as mean ± standard deviation. Statistical analyses were performed using GraphPad Prism 8.0 software (La Jolla, CA, United States). All data involving toxicity were analyzed using one-way ANOVA followed by a Tukey's (SOD, GSH-Px, Ach, 5-HT, HVA, open-field test) or Dunnett's T3 *post hoc* test (NEFL, NE, DA), or Kruskal-Wallis test followed by a Dunn's *post hoc* test for multiple comparisons (NSE, T-AOC, DOPAC, grip force). The statistical differences involving pharmacokinetic study were performed by independent t-tests. In each case, *p*-value of <0.05 was considered statistically significant.

3 Results

3.1 Component analysis of AC and CH extracts by UPLC-Q-TOF-MS

UPLC-Q-TOF-MS analysis was performed to identify the constituents of AC and CH extracts. Firstly, literature on the chemical composition of JGL formula have been carefully reviewed and concluded. In this study, the chemical formulae of all compounds were based on high-precision excimer $[M + H]^+$, $[M + Na]^+$ or $[M-H]^-$ with a mass error of 10 ppm and a partial isotopic abundance. Then, the most rational structures were analyzed and identified by searching chemical databases such as Pubchem (https://pubchem.ncbi.nlm.nih.gov/) and Massbank (http://www.massbank.jp). For the isomers, preference would be given to the structures previously reported from the five herbs of JGL formula. Finally, 16 compounds of AC and 44 compounds of CH were confirmed further by fragment ions, retention times, and literature comparison (Table 2; Table 3). The base peak intensity (BPI) chromatograms of AC and CH in negative and positive ionization modes were shown in Figure 2. The chemical structures of the main constitutions found in AC and CH were shown in Figure 3.

3.2 Behavioral changes in rats

The neurotoxic effects were evaluated by detecting neurobehavioral disorders using the open field test and grip test. In the open field test (Table 4), AC treatment significantly inhibited locomotor activity when compared to the control rat, as evidenced by the reduced total distance traveled, the total movement time, the number of rearing and the increased total rest time. This effect was partially prevented by treatment with a combination of AC and CH ($p < 0.05$). Similar results were observed in the grip test. As shown in Table 4, the mean forelimb grip strength in AC-treated rats (918.2 ± 50.3 g) was markedly lower than that of control rats (1206.0 ± 107.0 g) ($p < 0.01$). Rats administered with a combination of AC and CH had significantly increased grip strength (1192.0 ± 55.5 g) when compared to only AC-treated rats ($p < 0.01$). These results suggested that the compatible herbs of JGL could mitigate the neurobehavioral abnormalities induced by *A. chinense.*

3.3 Neuronal morphology of the rat brain

Morphological changes in brain tissues were detected by H&E and Nissl staining. As shown in Figure 4, the structure of neurons in control rats was normal with regular, round or oval nuclei and nucleoli, and clear Nissl bodies in the cytoplasm. After treatment with AC, there was clear cellular damage in the ventral striatum, as evidenced by neuronal eosinophilic degeneration, nucleus pycnosis, karyorrhexis, neuronal necrosis, reduced Nissl bodies and scattered arrangement. Compared to only AC treatment, except slight neuronal eosinophilic degeneration, we almost did not observe these aforementioned morphological properties in the brain of rats treated with AC and CH.

3.4 Serum levels of neurotoxicity biomarkers

Given that CH can ameliorate AC-induced neurobehavioral disorders in rats, we investigated the effects of AC in absence or presence of CH on neurotoxic biomarkers. As shown in Figure 5A, compared with control rats, AC only treatment significantly increased the serum levels of NSE and NEFL ($p < 0.05$, $p < 0.01$). Compared with AC-treated rats, the combined AC and CH treatment resulted in a significant reduction of NSE and NEFL levels ($p < 0.05$).

3.5 Oxidative stress biomarkers in rat brains

Oxidative damage has been reported to be an essential mechanism of neurotoxicity. Here, we investigated the levels

TABLE 2 The identification of constituents of the *Alangium chinense* extract (AC) by UPLC-Q-TOF-MS.

Peak no.	Name	Formula	Exact m/z	Observed m/z	MS^2 ions	RT (min)	PPM	Extracting ions	References
1	Venoterpine	$C_9H_{11}NO$	149.0841	150.0911	108.0440	2.05	−5.3	$[M + H]^+$	Zhu et al. (1996)
2	Gallic acid	$C_7H_6O_5$	170.0215	169.0132	125.0235	2.29	−3.0	$[M-H]^-$	Yue (2016)
3	Anabasine	$C_{10}H_{14}N_2$	162.1157	163.1236	146.0959, 134.0964, 120.0814	2.52	0.6	$[M + H]^+$	Wei et al. (2020)
4	Glucosyringic acid	$C_{15}H_{20}O_{10}$	360.1056	359.0971	197.0497, 153.0166	3.53	−1.9	$[M-H]^-$	Yue (2016)
5	Salicin	$C_{13}H_{18}O_7$	286.1053	285.0977	191.2886, 123.0449, 121.0283	3.84	1.1	$[M-H]^-$	Yue (2016)
6	Loganic acid	$C_{16}H_{24}O_{10}$	376.1370	375.1286	213.0753, 169.0128, 113.0235	4.15	−1.3	$[M-H]^-$	Yue (2016)
7	Tachioside	$C_{13}H_{18}O_8$	302.1002	301.0925	161.0457, 140.0412, 139.0833, 124.0141	4.61	0.7	$[M-H]^-$	Yue (2016)
8	(+)-Lyoniresinol 3a-O-β-D-glucopyranoside	$C_{28}H_{38}O_{13}$	582.2312	605.2210	249.1133, 267.1234, 268.1270	4.73	0.0	$[M + Na]^+$	Yue (2016)
9	7-O-β-Glucopyranosylsalicin	$C_{19}H_{28}O_{12}$	448.1581	447.1496	285.0017, 123.0069	5.18	−1.6	$[M-H]^-$	Zhang et al. (2009)
10	(7S,8R)-Urolignoside	$C_{26}H_{34}O_{11}$	522.2101	545.2000	249.1131	5.19	0.2	$[M + Na]^+$	Yue (2016)
11	(11S)-6-Hydroxy-5-(11-hydroxypropan-12-yl)-3,8-dimethyl-2H-chromen-2-one	$C_{14}H_{16}O_4$	248.1049	249.1130	191.1123, 163.0776	5.23	1.2	$[M + H]^+$	Zhang et al. (2015)
12	Chinenionside A	$C_{24}H_{38}O_{11}$	502.2414	525.2323	371.2097, 209.1543	5.47	2.1	$[M + Na]^+$	Yue (2016)
13	Henryoside	$C_{26}H_{32}O_{15}$	584.1741	583.1697	153.0178, 135.0073, 297.0623, 315.0142, 345.0106	5.91	5.8	$[M-H]^-$	Yue (2016)
14	Mansonone H	$C_{15}H_{14}O_4$	258.0892	259.0970	231.1022, 230.0578, 215.0708	8.86	0.0	$[M + H]^+$	Zhang et al. (2013)
15	Mansonone E	$C_{15}H_{14}O_3$	242.0943	243.1024	199.0748, 115.0554	10.33	1.2	$[M + H]^+$	Zhang et al. (2013)
16	Lacinilene C	$C_{15}H_{18}O_3$	246.1256	247.1334	219.1387, 201.1290	11.54	0.0	$[M + H]^+$	Zhang et al. (2013)

of antioxidants in brain tissues (Figure 5B). AC treatment considerably reduced the activity of SOD, GSH-Px and T-AOC in rat brains when compared to controls ($p < 0.01$), thus indicating serious oxidative damage. Compared with AC treatment, the combined AC and CH treatment significantly enhanced the activity of SOD, GSH-Px and T-AOC in rat brains ($p < 0.01$). These data suggested that the compatible herbs of JGL could reduce oxidative damage in brain induced by *A. chinense*.

3.6 Neurotransmitter levels in rat brains

Next, we determined the levels of neurotransmitters in rat brains. As shown in Figure 5C, the levels of some monoamine and acetylcholine neurotransmitters reduced significantly in brains of AC-treated rats when compared to control rats, including Ach, DA, DOPAC, HVA, NE, and 5-HT ($p < 0.05$, $p < 0.01$). Compared with AC treatment, combined AC and CH treatment led to a significant increase in all six neurotransmitters ($p < 0.05$).

TABLE 3 The identification of constituents of the extract of compatible herbs of JGL (CH) by UPLC-Q-TOF-MS.

Peak no.	Name	Formula	Exact m/z	Observed m/z	MS^2 ions	RT (min)	PPM	Extracting ions	References
1	5-Methoxysalicylic acid	$C_8H_8O_4$	168.0423	167.0344	152.0105, 108.0205	1.36	−1.8	$[M-H]^-$	Zhou et al. (2022)
2	Glucosyringic acid	$C_{15}H_{20}O_{10}$	360.1056	359.0977	197.0448, 182.0211	1.70	−0.3	$[M-H]^-$	Liu et al. (2022)
3	Syringic acid	$C_9H_{10}O_5$	198.0528	197.0446	182.0215, 166.9987, 138.0311, 123.0080	1.70	−2.0	$[M-H]^-$	Liu et al. (2022)
4	Protocatechuic acid	$C_7H_6O_4$	154.0266	153.0189	135.0432, 109.0282	1.85	0.7	$[M-H]^-$	Liu et al. (2022)
5	Catechol	$C_6H_6O_2$	110.0368	109.0288	-	1.85	−1.8	$[M-H]^-$	Zhou et al. (2022)
6	Vanillic acid	$C_8H_8O_4$	168.0423	167.0342	152.0103, 123.0480	2.12	−1.2	$[M-H]^-$	Liu et al. (2022)
7	Neochlorogenic acid	$C_{16}H_{18}O_9$	354.0951	353.0871	191.0559, 179.0345, 135.0445	2.15	−0.6	$[M-H]^-$	Wang X. et al. (2019)
8	4-Hydroxy-2,6-dimethoxyphenol-1-O-β-D-glucopyranoside	$C_{14}H_{20}O_9$	332.1107	331.1028	256.0684, 169.0497	2.25	−0.3	$[M-H]^-$	Wang X. et al. (2019)
9	3,4-Dihydroxyphenylethyl alcohol glucoside	$C_{14}H_{20}O_8$	316.1158	315.1085	135.0445	2.52	1.6	$[M-H]^-$	Liu et al. (2022)
10	Chlorogenic acid	$C_{16}H_{18}O_9$	354.0951	353.0872	191.0558, 179.0344, 161.0240, 127.0394, 109.0289	2.69	8.0	$[M-H]^-$	Liu et al. (2022)
11	Salidroside	$C_{14}H_{20}O_7$	300.1209	299.1135	179.0343, 161.0236, 137.0233, 113.0233	3.06	1.3	$[M-H]^-$	Liu et al. (2022)
12	Methyl salicylate lactoside/ methylsalicylate gentiobioside	$C_{20}H_{28}O_{13}$	476.1530	475.1453	443.1357, 281.0682, 151.0396, 137.0226	3.31	0.2	$[M-H]^-$	Wang X. et al. (2019)
13	Apocynin	$C_9H_{10}O_3$	166.0630	167.0705	149.0227, 107.0464	3.38	−1.8	$[M + H]^+$	Liu et al. (2022)
14	5-O-p-coumaroyl quinic acid	$C_{16}H_{18}O_8$	338.1002	337.0918	191.0549, 163.0389	3.43	−1.5	$[M-H]^-$	Wang X. et al. (2019)
15	Homogentisic acid	$C_8H_8O_4$	168.0423	167.0341	149.0446, 139.0397, 109.0294	3.43	−1.8	$[M-H]^-$	Zhou et al. (2022)
16	3-[3-(β-D-Glucopyranosyloxy)-2-methoxyphenyl]propanoic acid	$C_{16}H_{22}O_9$	358.1264	357.1179	269.0680, 195.0646	3.56	−2.2	$[M-H]^-$	Zhou et al. (2022)
17	Caffeic acid	$C_9H_8O_4$	180.0423	179.0338	135.0440	3.61	−3.4	$[M-H]^-$	Zhou et al. (2022)
18	4-Hydroxybenzoic acid	$C_7H_6O_3$	138.0317	137.0238	-	3.76	−0.7	$[M-H]^-$	Wang X. et al. (2019)
19	Methyl chlorogenate	$C_{17}H_{20}O_9$	368.1107	367.1031	179.0564, 161.0236, 135.0434, 134.0366	3.88	0.5	$[M-H]^-$	Liu et al. (2022)
20	Fraxin	$C_{16}H_{18}O_{10}$	370.0900	369.0823	207.0287, 192.0053	3.88	0.3	$[M-H]^-$	Zhou et al. (2022)

(Continued on following page)

TABLE 3 (*Continued*) The identification of constituents of the extract of compatible herbs of JGL (CH) by UPLC-Q-TOF-MS.

Peak no.	Name	Formula	Exact m/z	Observed m/z	MS^2 ions	RT (min)	PPM	Extracting ions	References
21	Phloridzin	$C_{21}H_{24}O_{10}$	436.1369	435.1291	273.0740	4.00	1.1	$[M-H]^-$	Zhou et al. (2022)
22	(−)-Epicatechin	$C_{15}H_{14}O_6$	290.0790	289.0712	179.0333, 165.0550, 137.0235, 125.0232	4.21	0.0	$[M-H]^-$	Liu et al. (2022)
23	(−)-5′-Methoxyisolariciresinol-2α-O-β-D-xylopyranoside	$C_{26}H_{34}O_{11}$	522.2011	521.2018	506.1494, 359.1494, 341.0912	4.22	−1.0	$[M-H]^-$	Wang X. et al. (2019)
24	Lariciresinol 4-O-glucoside	$C_{26}H_{34}O_{11}$	522.2101	521.2029	359.1494, 344.1256, 329.1039, 313.1070	4.22	−1.0	$[M-H]^-$	Zhou et al. (2022)
25	3,4-Dihydroxybenzaldehyde	$C_7H_6O_3$	138.0317	139.0394	111.0438	4.28	−0.7	$[M + H]^+$	Zhou et al. (2022)
26	Methyl 1-(hexopyranosyloxy)-7-hydroxy-7-(hydroxymethyl)-1,4a,7,7a-tetrahydrocyclopenta [c] pyran-4-carboxylate	$C_{17}H_{24}O_{11}$	404.1319	403.1247	371.0871, 327.1069, 241.0736, 223.0630, 191.0561, 179.0360, 165.0556, 139.0397	4.32	1.2	$[M-H]^-$	Zhou et al. (2022)
27	Liriodendrin	$C_{34}H_{46}O_{18}$	742.2684	741.2606	417.1549, 387.1077, 181.0499, 166.0264	4.75	0.1	$[M-H]^-$	Zhou et al. (2022)
28	(+)-Lyoniresin-4-yl-β-D-glucopyranoside	$C_{28}H_{38}O_{13}$	582.2217	581.2249	419.1671, 404.1458, 233.0809	4.79	2.6	$[M-H]^-$	Liu et al. (2022)
29	Scopoletin	$C_{10}H_8O_4$	192.0423	193.0498	165.0526, 149.0241	4.90	−1.6	$[M + H]^+$	Zhou et al. (2022)
30	Ellagic acid	$C_{14}H_6O_8$	302.0063	300.9992	283.0592, 229.0130	5.00	1.3	$[M-H]^-$	Zhou et al. (2022)
31	Rutin	$C_{27}H_{30}O_{16}$	610.1534	609.1456	300.0276, 271.0266, 255.0281, 179.0340	5.06	4.1	$[M-H]^-$	Zhou et al. (2022)
32	(+)-Lyoniresinol-2-α-O-β-L-arabinopyranoside	$C_{27}H_{36}O_{12}$	552.2207	551.2149	536.1904, 419.1715, 401.1611, 386.1366	5.16	3.6	$[M-H]^-$	Wang X. et al. (2019)
33	Gaultheroside A	$C_{27}H_{36}O_{12}$	552.2207	551.2129	389.1226	5.16	−0.2	$[M-H]^-$	Zhou et al. (2022)
34	Isochlorogenic acid B	$C_{25}H_{24}O_{12}$	516.1268	515.1198	353.0892, 191.0554, 179.0349, 173.0452, 161.0239, 135.0443	5.23	1.4	$[M-H]^-$	Zhou et al. (2022)
35	(+)-Lyoniresinol	$C_{22}H_{28}O_8$	420.1784	419.1703	404.1461, 373.1283, 389.1586	5.30	−0.7	$[M-H]^-$	Wang X. et al. (2019)
36	Calceolarioside B	$C_{23}H_{26}O_{11}$	478.1475	477.1397	315.1084, 179.0343, 161.0240, 135.0439	5.40	0.2	$[M-H]^-$	Zhou et al. (2022)

(Continued on following page)

TABLE 3 (*Continued*) **The identification of constituents of the extract of compatible herbs of JGL (CH) by UPLC-Q-TOF-MS.**

Peak no.	Name	Formula	Exact m/z	Observed m/z	MS^2 ions	RT (min)	PPM	Extracting ions	References
37	Tectoridin	$C_{22}H_{22}O_{11}$	462.1162	461.1084	315.0719	5.55	5.0	$[M-H]^-$	Zhou et al. (2022)
38	9-(2,3-dihydroxypropoxy)-9-oxononanoic acid	$C_{12}H_{22}O_6$	262.1416	261.1338	187.1004, 125.0235	5.61	1.5	$[M-H]^-$	Zhou et al. (2022)
39	Quercitrin	$C_{21}H_{20}O_{11}$	448.1006	447.0927	300.0267, 271.0249, 243.0244	5.71	0.9	$[M-H]^-$	Zhou et al. (2022)
40	Azelaic acid	$C_9H_{16}O_4$	188.1049	187.0970	143.0343	5.86	0.0	$[M-H]^-$	Zhou et al. (2022)
41	Feruloyltyramine	$C_{18}H_{19}NO_4$	313.1314	314.1390	177.0550, 145.0290, 121.0650, 117.0338	6.91	−0.6	$[M + H]^+$	Zhou et al. (2022)
42	scheffleside K	$C_{41}H_{64}O_{14}$	780.4296	779.4228	629.3684, 471.3461	10.39	1.3	$[M-H]^-$	Wang et al. (2014)
43	Asiatic acid	$C_{30}H_{48}O_5$	488.3502	487.3418	469.3308, 391.0167	11.31	−1.0	$[M-H]^-$	Liu et al. (2022)
44	Medicagenic acid	$C_{30}H_{46}O_6$	502.3294	501.3216	483.2984, 439.3230	11.86	0.8	$[M-H]^-$	Zhou et al. (2022)

3.7 Pharmacokinetics of ANA and VEN in rat

Anabasine (ANA) and venoterpine (VEN) have been reported to exhibit pharmacological effects and are the major active components in *A. chinense* (Zhu et al., 1996; Hu et al., 2020). Therefore, we selected ANA and VEN as marker compounds to detect the effect of compatible herbs in JGL on the pharmacokinetics of *A. chinense*. The chemical structures of the two analytes (ANA and VEN) and IS are shown in Figure 6A. The HPLC-MS/MS method was validated as described in Supplementary Materials and the results were shown in Supplementary Figure S1; Supplementary Tables S2–S6.

3.7.1 The pharmacokinetics of ANA and VEN in rats after single administration

The single administration of AC and the combination of AC/CH led to ANA and VEN entering the blood within 5 min (Figures 6B,D). The concentrations of ANA and VEN in plasma at different timepoints are shown in Supplementary Table S7. Table 5 shows the main pharmacokinetic parameters, as calculated by the non-compartment model.

Compared with the single administration of AC, the combined AC and CH treatment led to a significant decrease in the C_{max} (115.79 ± 20.62 ng/mL) of ANA ($p < 0.01$) and a significant increase in the mean residence time ($MRT_{0-\infty}$, 6.34 ± 1.20 h) of ANA ($p < 0.05$). The half time ($t_{1/2}$, 4.27 ± 1.11 h), area under the plasma concentration-time curve (AUC_{0-t}, 733.71 ± 133.58 ng·h/mL) and $AUC_{0-\infty}$ (763.78 ± 140.45 ng·h/mL) of ANA showed a downward trend, but there was no statistical significance due to large individual differences. There was no significant change in the t_{max} (1.53 ± 0.65 h) and MRT_{0-t} (5.43 ± 0.93 h) of ANA.

Compared with the single administration of AC, the C_{max} (2.25 AUC± 0.76 ng/mL) of VEN decreased significantly ($p < 0.01$), while the $t_{1/2}$ (3.49 ± 0.76 h), MRT_{0-t} (3.24 ± 0.49 h) and $MRT_{0-\infty}$ (3.85 ± 0.99 h) of VEN increased significantly ($p < 0.05$, $p < 0.05$, $p < 0.05$) in rats treated with the combination of AC and CH. The AUC_{0-t} (7.29 ± 2.50 ng·h/mL) and $AUC_{0-\infty}$ (7.47 ± 2.60 ng·h/mL) of VEN showed a downward trend, but there was no statistical significance due to large individual differences. There was no significant change in t_{max} (1.07 ± 0.60 h).

3.7.2 The pharmacokinetics of ANA and VEN in rats after continuous administration

We also detected the pharmacokinectics of ANA and VEN after 14 days of continuous administration with AC or a combination of AC and CH (Figures 6C,E). The plasma concentrations of ANA and VEN were shown in Supplementary Table S8. The main pharmacokinetic parameters were calculated by using the non-compartment model and were shown in Table 5.

Compared with the continuous administration of AC, the C_{max} (127.51 ± 12.09 ng/mL), AUC_{0-t} (746.93 ± 35.00 ng·h/mL) and $AUC_{0-\infty}$ (748.7 ± 36.50 ng·h/mL) of ANA was decreased significantly ($p < 0.01$, $p < 0.01$, $p < 0.01$) in rats administered continuously with a combination of AC and CH, while the $t_{1/2}$ (2.55 ± 0.61 h), t_{max} (2.00 ± 0.00 h), MRT_{0-t} (4.77 ± 0.44 h) and $MRT_{0-\infty}$ (4.83 ± 0.49 h) of ANA did not change significantly. Similar pharmacokinetic characteristics were observed in the main parameters of VEN, as evidenced by a significant decrease in C_{max} (5.67 ± 0.34 ng/mL), AUC_{0-t} (16.18 ± 2.82 ng·h/mL) and $AUC_{0-\infty}$ (16.44 ± 2.72 ng·h/mL) ($p < 0.01$, $p < 0.05$, $p < 0.05$, respectively).

3.8 mRNA expression of hepatic drug-metabolizing cytochrome P450 enzymes

Cytochrome P450 is the most important metabolic enzyme family in the liver that accounts for either metabolic

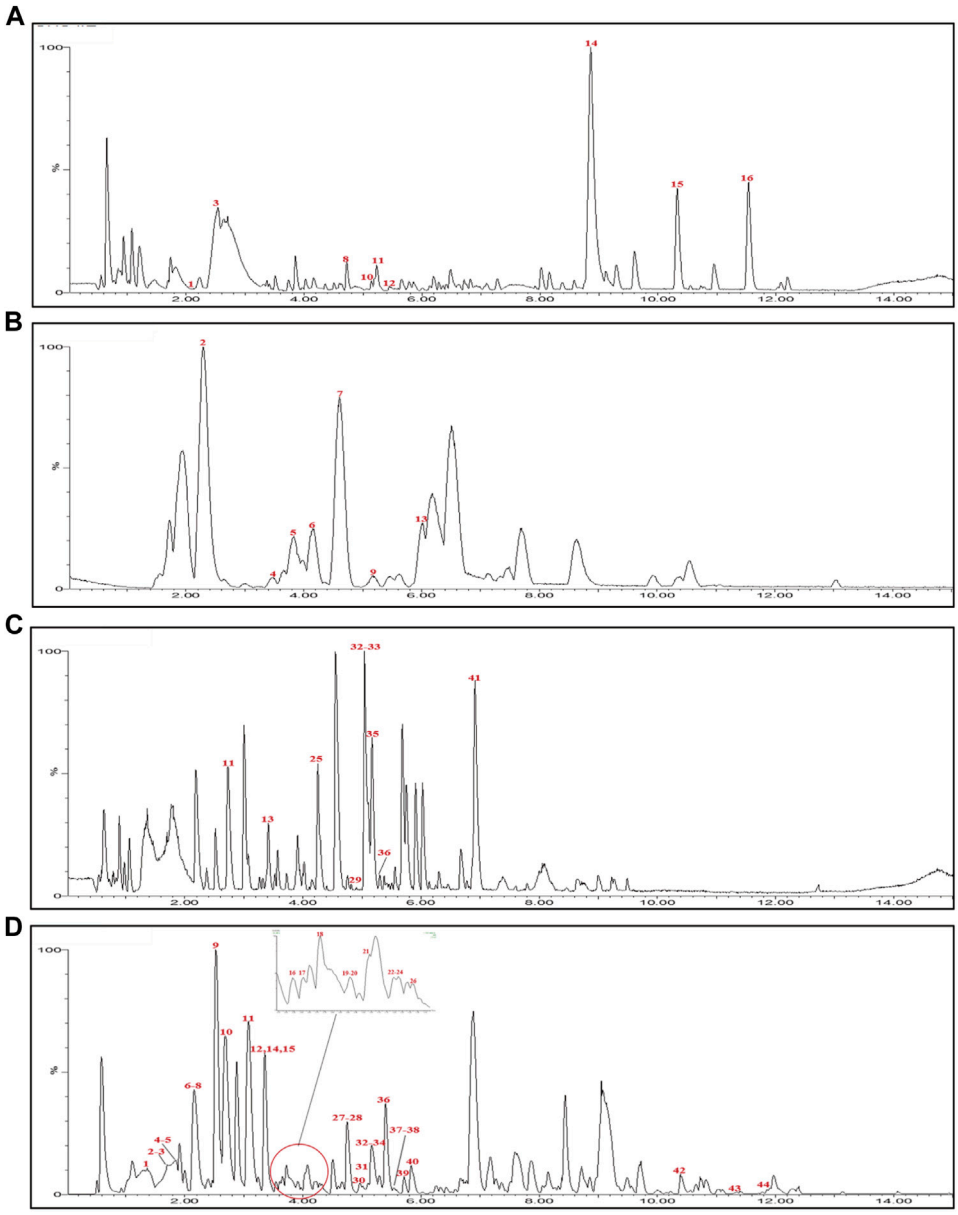

FIGURE 2
Base peak intensity (BPI) chromatograms for Alangium chinense extract (AC) and extract of compatible herbs of Jin-Gu-Lian formula (CH) by ultra-performance liquid chromatography-quadrupole-time-of-flight tandem mass (UPLC-Q-TOF-MS). **(A)** BPI chromatogram of the positive (ESI+) ionization modes for AC; **(B)** BPI chromatogram of the negative (ESI−) ionization modes for AC; **(C)** BPI chromatogram of the positive (ESI+) ionization modes for CH; **(D)** BPI chromatogram of the negative (ESI−) ionization modes for CH.

detoxification or activation in toxicity (Guengerich, 2008). They play key roles in the pharmacokinetic herb-herb interactions (Rittle and Green, 2010). Here, we analyzed the expression of P450 isozymes in rat livers by RT-qPCR. As shown in Figure 6F, AC treatment resulted in the significant downregulation of the gene expression of cytochrome P450 isozymes, including the cytochrome P450 family 1 subfamily a polypeptide 2 (*Cyp1a2*), cytochrome P450 family 3 subfamily a polypeptide 1 (*Cyp3a1*), cytochrome P450 family 2 subfamily d polypeptide 4 (*Cyp2d4*) and cytochrome P450 family 2 subfamily e polypeptide 1 (*Cyp2e1*) ($p < 0.05$; $p < 0.01$). Combined administration of AC and CH significantly reduced the downregulation of the mRNA expression of cytochrome P450 isozymes induced by AC ($p < 0.05$; $p < 0.01$).

4 Discussion

Previous studies described *A. chinense* as a 'double-edged sword'. On one hand, *A. chinense* is used as a medicine for the treatment of rheumatic arthritis, acroanesthesia, and fractures in the Miao population in China (Li et al., 2017). On the other hand, *A. chinense* is famous as a poisonous medicine that results in toxicity

10.3389/fphar.2023.1133982

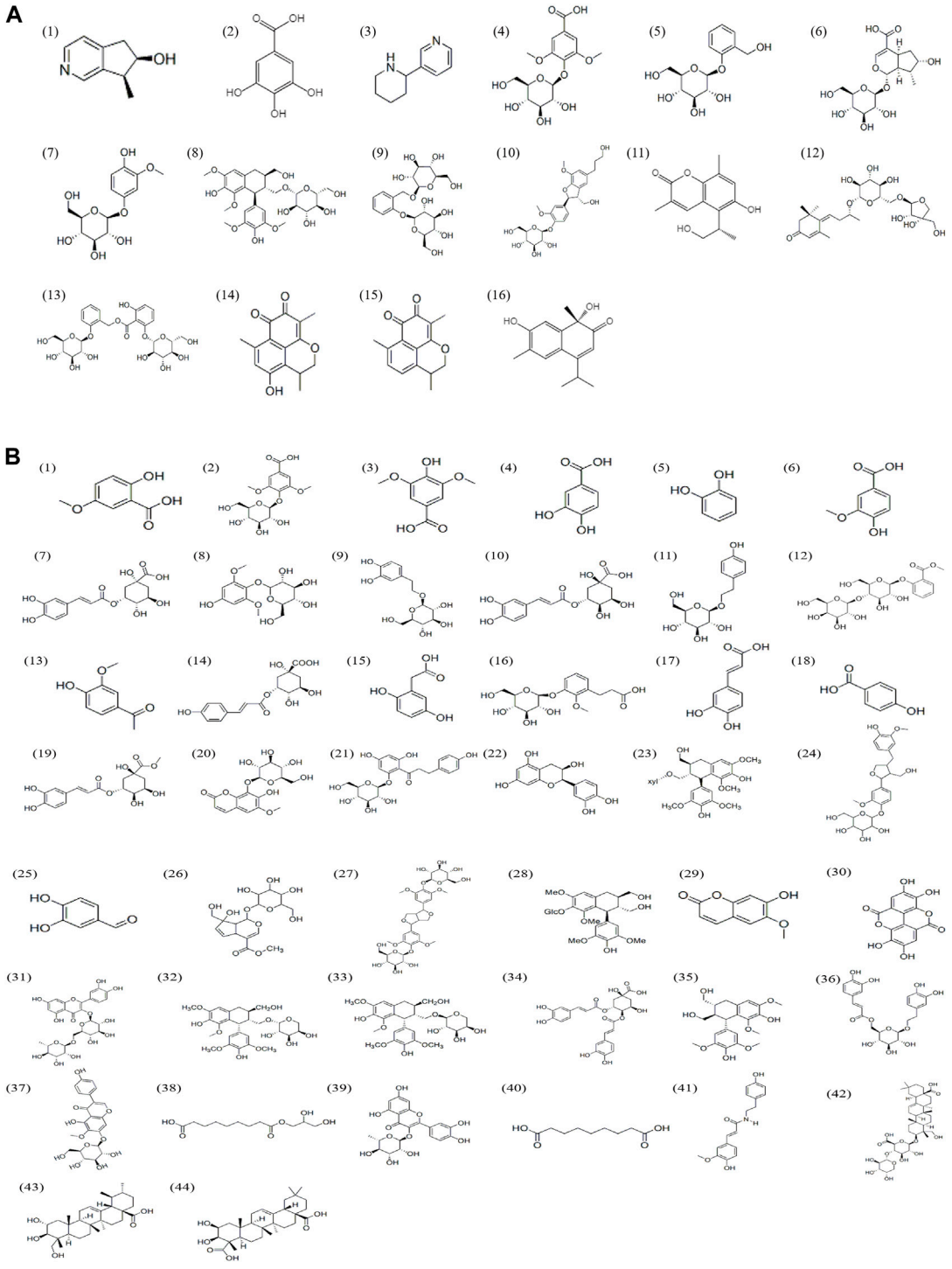

FIGURE 3
Chemical structures of compounds in the *Alangium chinense* extract **(A)** and the extract of compatible herbs of JGL **(B)**.

involving different organs, such as central nervous system (CNS), lungs, liver and smooth muscles (Hu et al., 2020; Meng et al., 2021). Clinical studies have reported that the oral administration of more than 40 g of *A. chinense* led to severe neurotoxicity, including dizziness, convulsions, muscle weakness and respiratory depression (Zhang et al., 2008). According to the compatibility principle of traditional Chinese medicine, the combination of *A. chinense* with other herbs in the JGL formula could yield the expected therapeutic effects with synergistic action when used to treat rheumatic arthritis but with no severe adverse actions. However, little is known about the effect of compatible herbs in JGL on the neurotoxicity induced by *A. chinense*. In the present

TABLE 4 Effect of *Alangium chinense* and the compatible herbs on the behavioral activity in rats.

Groups	Open-field test				Grip force(g)
	Total distance traveled (cm)	Total movement time(s)	Total rest time(s)	Number of rearing	
Control	3798.65 ± 419.15	258.69 ± 9.44	41.31 ± 9.44	29 ± 6	1206.19 ± 106.95
AC	2436.09 ± 485.58$^{\#\#}$	226.62 ± 5.87$^{\#\#}$	73.38 ± 5.87$^{\#\#}$	18 ± 6$^{\#}$	918.18 ± 50.27$^{\#\#}$
CH	3317.65 ± 786.39	245.17 ± 9.04	54.83 ± 9.04	29 ± 10	1156.34 ± 32.11
AC/CH	3354.07 ± 500.33*	250.17 ± 18.76*	49.83 ± 18.76*	31 ± 5*	1191.89 ± 55.53**

Quantitative data represent the mean ± SD, from 6–8 rats in each group. $^{\#}p < 0.05$, $^{\#\#}p < 0.01$, compared with control. $^{*}p < 0.05$, $^{**}p < 0.01$, compared with only AC treatment.

study, AC treatment resulted in neurobehavioral disorders, as evidenced by reduced locomotor activity and muscle strength. H&E and Nissl staining showed that AC treatment induced morphological changes in neurons. Previous studies reported that anabasine, the alkaloid of *A. chinense*, led to significant behavioral changes in terms of fetal movement, memory and attention (Levin et al., 2014; Green et al., 2018). In current study, the compatible herbs of JGL could ameliorate the *A. chinense*-induced neurotoxicity by reducing the frequency of induced abnormal behaviors and morphological damage in neurons.

Neuron-specific enolase (NSE) is abundant in neurons of the central nervous system (CNS) and is considered as a neurotoxic marker to assess cerebral neurodegeneration in a wide range of CNS disorders (Sahu et al., 2017). Neurofilaments are released when the axon of a neuron incurs damage. The serum levels of neurofilament light chain (NEFL) can indicate neuronal cell death in the brain and serve as a potential fluid biomarker of neurotoxicity (Sano et al., 2021). We found that AC treatment induced enhanced levels of NSE and NEFL in rat brains, thus concurring with the previous finding that excessive NSE levels are due to oxidative stress (Ciancarelli et al., 2015). The compatible herbs of JGL could reduce the overexpression of NSE and NEFL.

A diverse range of molecular mechanisms are involved in neurotoxicity. Of these, reactive oxygen species (ROS) are known to play an essential role in neuronal fate and development (Wilson et al., 2018). An imbalance between ROS production and the activity of the antioxidant system can lead to excessive ROS accumulation and oxidative stress, thus causing damage to DNA, RNA, protein and lipids (Schieber and Chandel, 2014). In neurocytes, oxidative damage can adversely affect several neuronal functions, including locomotor activity, muscle strength, memory, learning and cognition, thus contributing to developmental neurotoxicity (Spinu et al., 2019). Some antioxidants, including SOD, GSH-Px, catalase (CAT) and glutathione (GSH), can directly and indirectly remove free radicals and ameliorate developmental neurotoxicity (Nishimura et al., 2021). Sesquiterpenes and alkaloids from *A. chinense* were previously shown to exert antioxidant activities against cysteine-induced rat liver microsomal lipid peroxidation (Zhang et al., 2013). Salicin from *A. chinense* can inhibit ROS generation, reduce the levels of malondialdehyde (MDA) and increase the levels of several antioxidant enzymes, including glutathione (GSH), SOD and catalase (CAT) via the Nrf2-HO-1-ROS pathway (Zhai et al., 2018). In agreement with previous reports, we found that AC treatment gave rise to considerable oxidative damage, as evidenced by obvious reductions in the activities of SOD, GSH-Px and T-AOC. The combination of CH with AC could reduce AC-induced oxidative damage by increasing the activity of the cellular antioxidant system. These data suggest that the compatible herbs of JGL could mitigate the neurotoxicity of *A. chinense* by regulating oxidative stress-related disorders.

Neurotransmitters play important roles in the function of the nervous system and mainly include monoamines, amino acids and choline (Vogt, 2019). Neurotransmitter abnormalities are regarded as a biomarker of neurotoxicity and are responsible for numerous neurodegenerative diseases and brain injuries (Iadecola et al., 2001; Sun et al., 2018; Stradtman and Freeman, 2021; Tinkov et al., 2021). Many neurotoxicants are known to exert adverse effects in the concentration and signaling of neurotransmitters (Stradtman and Freeman, 2021; Tinkov et al., 2021). A significant reduction in the levels of monoamine neurotransmitters, including 5-HT, DA, DOPAC and NE was reported to be associated with impaired attention, locomotor dysfunction, disrupted motor coordination, and impaired learning tasks (Sun et al., 2018; Conley et al., 2020; Stradtman and Freeman, 2021). The disruption of cholinergic neurotransmission, as evidenced by upregulated AChE activity, the inhibition of choline acetyltransferase activity, cholinergic neuron death and the reduction of ACh levels is associated with oxidative damage and known to be involved in locomotor and motor deficits (Tinkov et al., 2021). Anabasine, the active component of AC, has been identified as an agonist of nAChRs with greater affinity for α7 nAChR and lower affinity for α4β2 subtypes (Levin et al., 2014). Anabasine-induced α7 nAChR activation results in the release of different transmitters, including dopamine, norepinephrine, serotonin, histamine, GABA and glutamate. These alterations can explain the effect of anabasine on behavioral changes including fetal movement, memory and attention (Levin et al., 2014; Green et al., 2018). Hsieh et al. (1993) previously reported that AC extract affected the motor activity and changed the concentration of monoamine in a rat model. Studies involving another species from the Alangium genus, *Alangium platanifolium*, showed similar effects on neurobehavioral changes as *A. chinense* (Hu et al., 2020). Zhu et al. (1996) reported that *A. platanifolium* extract interacted strongly with a number of neurotransmitters, including α2-adrenoceptor, 5HT1, 5HT2, dopamine 1, dopamine 2, $GABA_A$ and $GABA_B$ and plays a role in locomotor activity, muscle relaxant activity and analgesic activity. Our present results were in accordance with these previous literatures. The levels of neurotransmitters were illustrated in Figure 5C. AC treatment led to abnormalities in the

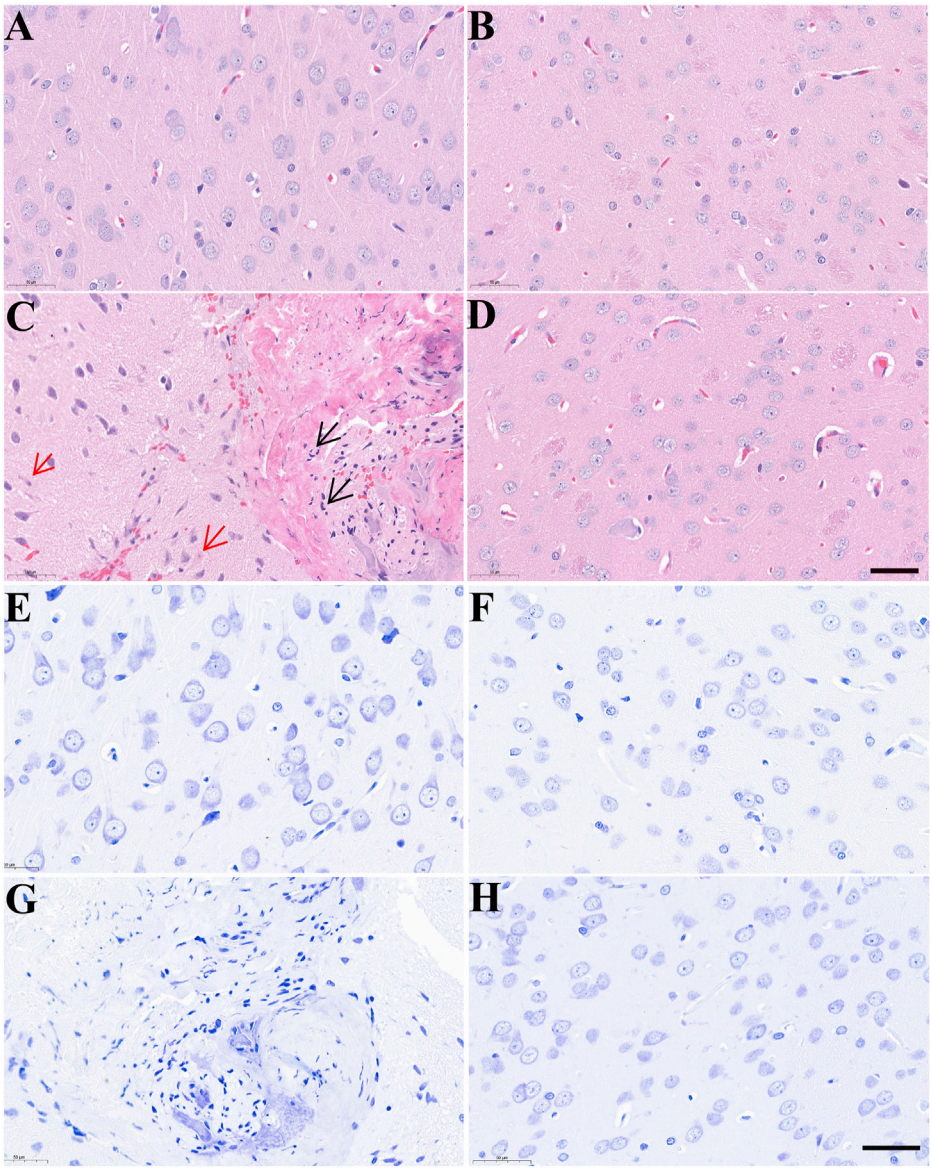

FIGURE 4
The effects of *Alangium chinense* combined with the compatible herbs of JGL on the morphological structure of neurons in the brain. Rats were orally gavaged with distilled water (control group, A and E), extract of compatible herbs of JGL (CH group, B and F), *Alangium chinense* extract (AC group, C and G), a combination of AC and CH (AC/CH group, D and H) once-daily for 14 days. Scale bar = 50 μm in H&E **(A–D)** and Nissl staining **(E–H)**. Black arrows indicated nucleus pycnosis, karyorrhexis and neuronal necrosis. Red arrows indicated neuronal eosinophilic degeneration.

concentrations and metabolism of neurotransmitters in the brain. Combined treatment with CH and AC reduced the attenuation of monoamine and acetylcholine neurotransmitter levels induced by AC. These observations suggested that the compatible herbs of JGL could regulate the abnormal concentrations and metabolisms of neurotransmitters to mitigate the neurotoxicity induced by *A. chinense*.

The combinational principle of TCM is a primary approach used to reduce the toxicity of toxic herbs by interacting with other herbal materials that cause changes in the pharmacokinetic process, decrease the exposure levels of toxic constituents or inhibit toxic metabolism (Zhang et al., 2018). The toxicity of drugs is directly related to the exposure levels of components *in vivo* and may be positively correlated (Zhang et al., 2018; Chang et al., 2020). In the present study, significant differences of pharmacokinetic profiling in rats were observed between AC treatment and the co-administration of AC and CH. Continuous administration with combination of AC and CH for 14 days demonstrated that the C_{max} of ANA reduced from 204.71 to 127.51 ng/mL, $AUC_{0\text{-}t}$ felt down from 1028.67 to 746.93 ng·h/mL and $AUC_{0\text{-}\infty}$ felt down from 1036.87 to 748.70 ng·h/mL in comparison with AC treatment. The decrease of C_{max} and AUC in response to the combined administration of AC and CH indicated lower absorption and reduced exposure level of ANA in plasma, which might bring about a lower possibility of toxicity induced by AC. Similar results were found for these pharmacokinetic parameters of ANA following the single

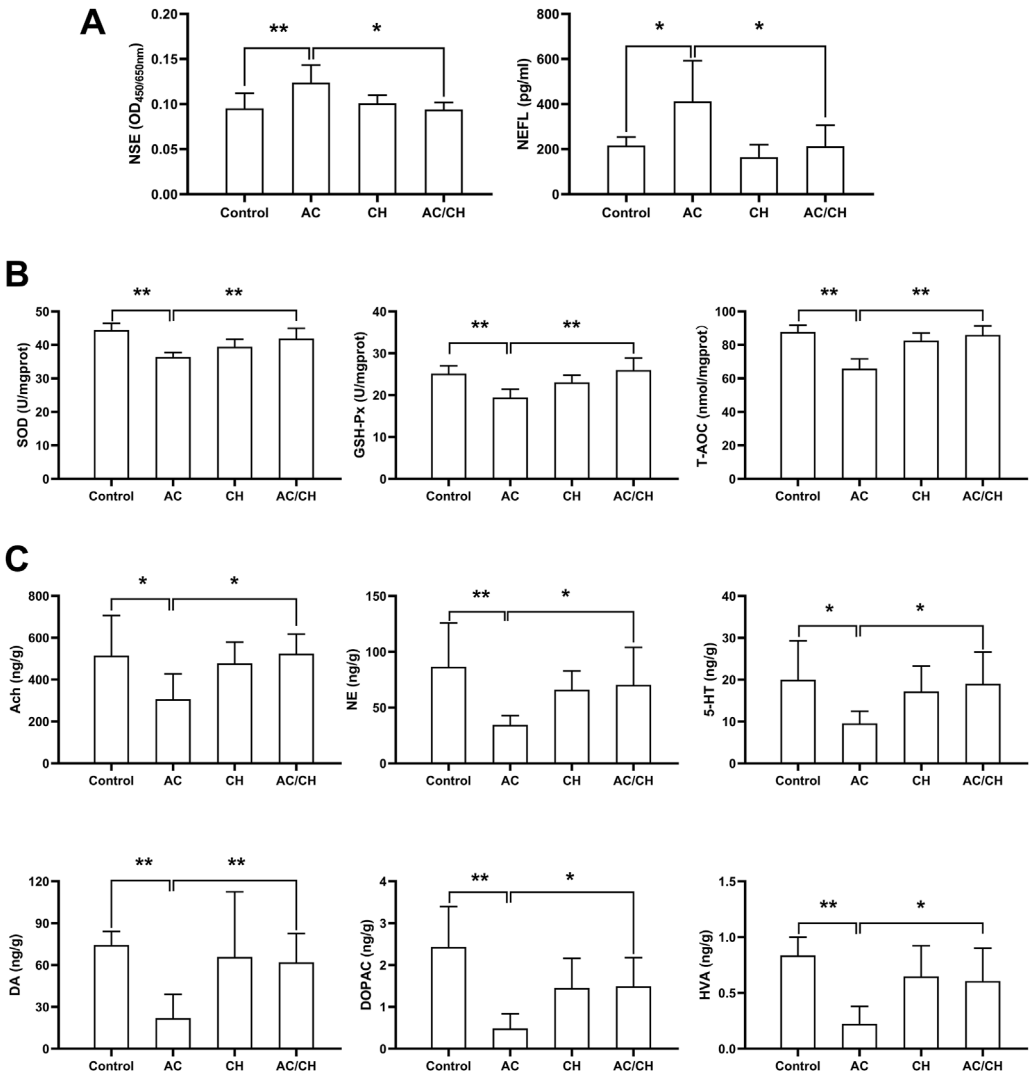

FIGURE 5
The effects of *Alangium chinense* combined with the compatible herbs of JGL on neurotoxicity biomarkers, oxidative stress and neurotransmitters. Rats were orally gavaged with distilled water (control group), *Alangium chinense* extract (AC group), extract of compatible herbs of JGL (CH group) or a combination of AC and CH (AC/CH group) once-daily for 14 days. **(A)** Serum NSE and NEFL levels were analyzed by ELISA assays. **(B)** Superoxide dismutase (SOD) activity, glutathione peroxidase (GSH-Px) activity and total antioxidant capacity (T-AOC) in brain were detected. **(C)** The levels of monoamine and acetylcholine neurotransmitters in brain were analyzed by LC-MS/MS. Quantitative data represent the mean ± SD from 6–8 rats in each group. $*p < 0.05$, $**p < 0.01$.

administration of the extracts. Additionally, single administration of AC and CH led to longer MRT of ANA than AC treatment, which suggested that the compatibility of AC with CH in JGL formula helped to prolong the retention of ANA *in vivo*. Our results went in hand with previous reports that the C_{max} and $V_{z/F}$ of ANA were significantly attenuated and the clearance rate (CL) was decreased responsible for prolonged MRT in the combination of core drug pair and other herbs in JGL formula (Zheng et al., 2022). These results suggested that the maintenance of ANA, which characterized in terms of duality of efficacy and toxicity, at an appropriated lower level with a longer retention time in plasma might contribute to its expected therapeutic actions with fewer side effects. Notably, the rats treated with combination of AC and CH in our study demonstrated significant reduction in the AUC of ANA and this result was inconsistent with previous study that the core drug pair combined with other herbs in JGL showed increased tendency in the AUC of ANA (Zheng et al., 2022). Some possible reasons for this discrepancy are (1) taking different herbal medicines as objects, that *A. chinense* for the present study and the core drug pair for the previous study, in which the active components of *S. cuneate* may decrease the absorption and slow down the metabolism of the active components (ANA) of *A. chinense* in rats, (2) different dosage of *A. chinense,* that the dose used in the previous study is lower than the toxic dose in the present study. In addition to anabasine, we also compared the pharmacokinetic properties of venoterpine (VEN), another main component of *A. chinense*, in rats administrated with AC and combination of AC and CH. The continuous treatment of herbs for 14 days led to marked reductions in the C_{max}, AUC_{0-t} and

10.3389/fphar.2023.1133982

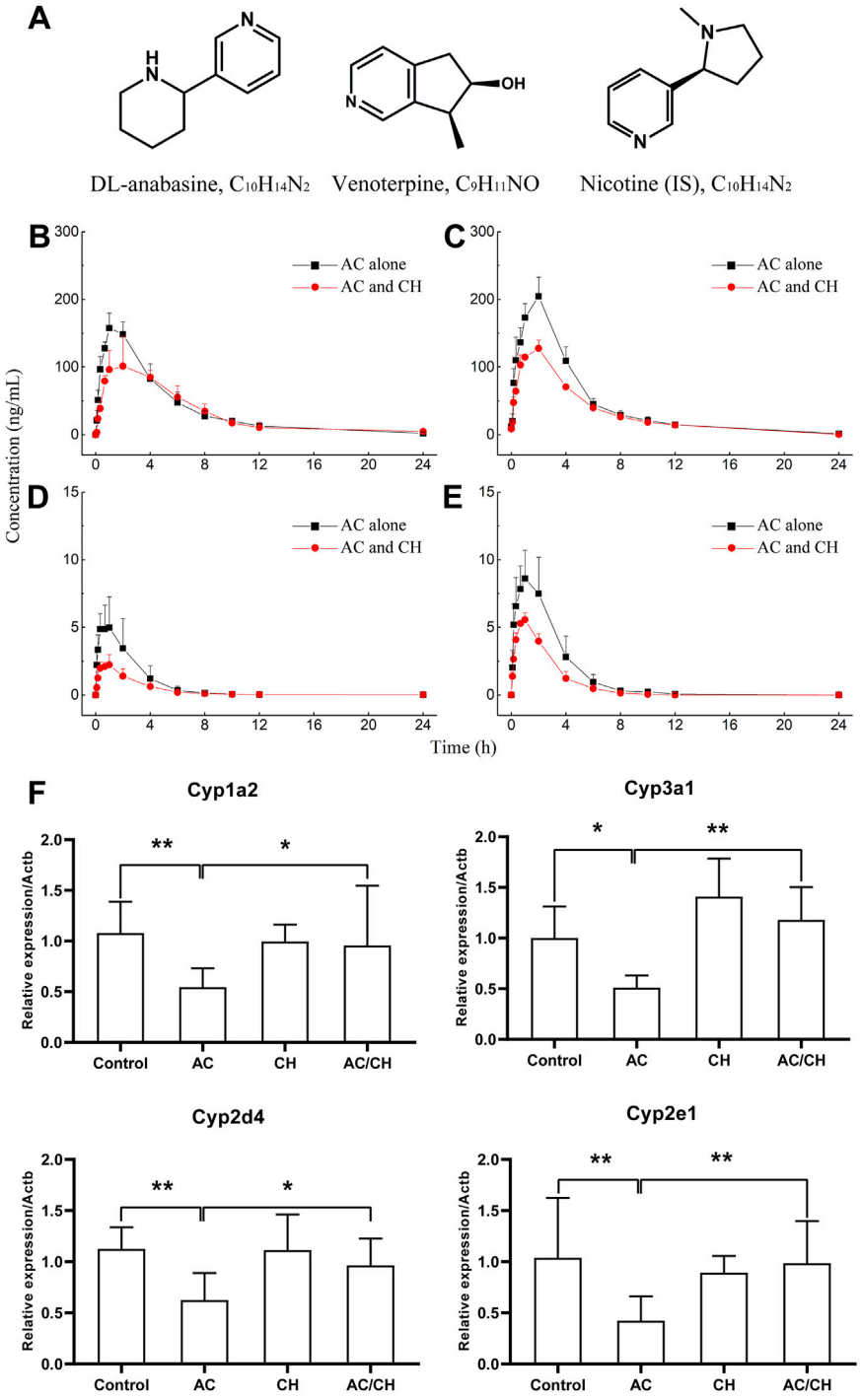

FIGURE 6
Pharmacokinetic process for the active components of *Alangium chinense* and the gene expression of hepatic cytochrome P450. **(A)** Chemical structure of DL-anabasine (ANA), venoterpin (VEN) and nicotine (IS). In a pharmacokinetic study **(B–E)**, male rats were treated with AC alone or co-administration of AC and CH once a day for 14 days. Mean rat plasma concentration-time profiles of ANA **(B)** and VEN **(D)** after single administration, ANA **(C)** and VEN **(E)** after continuous administration. Data are expressed as mean ± SD ($n = 5$). The gene expression of cytochrome P450 isozymes in liver was analyzed by RT-qPCR **(F)**. The relative expression of target genes was calculated using the $2^{-\Delta\Delta CT}$ method. The amount of each transcript was normalized to that of beta-actin. Quantitative data represent the mean ± SD of eight rats. *$p < 0.05$, **$p < 0.01$.

$AUC_{0-\infty}$ of VEN following the co-administration of AC and CH in comparison with AC alone. These results indicated that the absorption and exposure level of VEN in rats was decreased through the interaction between different medicinal materials in JGL formula, thus reducing the frequency of *A. chinense* induced toxicity.

Pharmacokinetic herb-herb interactions can be partly explained by the regulation of cytochrome P450 enzymes. Cytochrome

TABLE 5 The pharmacokinetic parameters of anabasine (ANA) and venoterpin (VEN).

Analytes	PK parameters	Single administration		14 days continuous administration	
		AC	AC and CH	AC	AC and CH
ANA	$t_{1/2}$ (h)	3.08 ± 0.73	4.27 ± 1.11	3.21 ± 0.43	2.55 ± 0.61$^{\#}$
	t_{max} (h)	1.20 ± 0.45	1.53 ± 0.65	1.80 ± 0.45	2.00 ± 0.00
	C_{max} (ng/mL)	159.62 ± 19.64	115.79 ± 20.62**	204.71 ± 28.28$^{\#}$	127.51 ± 12.09**
	AUC_{0-t} (h·ng/mL)	830.64 ± 131.28	733.71 ± 133.58	1028.67 ± 39.20$^{\#}$	746.93 ± 35.00**
	$AUC_{0-\infty}$(h·ng/mL)	852.10 ± 121.22	763.78 ± 140.45	1036.87 ± 35.91$^{\#}$	748.7 ± 36.50**
	MRT_{0-t} (h)	4.29 ± 0.87	5.43 ± 0.93	4.42 ± 0.36	4.77 ± 0.44
	$MRT_{0-\infty}$ (h)	4.72 ± 0.74	6.34 ± 1.20*	4.62 ± 0.40	4.83 ± 0.49$^{\#}$
VEN	$t_{1/2}$ (h)	2.45 ± 0.09	3.49 ± 0.76*	1.31 ± 0.26$^{\#\#}$	1.12 ± 0.22$^{\#\#}$
	t_{max} (h)	0.67 ± 0.33	1.07 ± 0.60	0.93 ± 0.15	0.93 ± 0.15
	C_{max} (ng/mL)	5.46 ± 1.80	2.25 ± 0.76**	9.08 ± 1.78$^{\#}$	5.67 ± 0.34**$^{\#\#}$
	AUC_{0-t} (h·ng/mL)	15.71 ± 8.21	7.29 ± 2.50	30.40 ± 10.73$^{\#}$	16.18 ± 2.82*$^{\#\#}$
	$AUC_{0-\infty}$(h·ng/mL)	15.76 ± 8.24	7.47 ± 2.60	30.64 ± 10.88$^{\#}$	16.44 ± 2.72*$^{\#\#}$
	MRT_{0-t} (h)	2.27 ± 0.25	3.24 ± 0.49*	2.25 ± 0.41	1.95 ± 0.39$^{\#\#}$
	$MRT_{0-\infty}$ (h)	2.34 ± 0.25	3.85 ± 0.99*	2.32 ± 0.43	2.04 ± 0.36$^{\#\#}$

Rats were treated with single administration and 14 days continuous administration of AC, combination of AC, and CH., Quantitative data were the mean ± SD of five rats. *$p < 0.05$, **$p < 0.01$, compared with only AC treatment. $^{\#}p < 0.05$, $^{\#\#}p < 0.01$, compared with single administration.

P450 enzymes are a diverse group of catalytic enzymes in the liver and can be involved in the biotransformation of approximately 75% of clinical drugs (Rittle and Green, 2010). The enzyme activity as well as the induction and inhibition of these enzymes are main parameters for drug metabolism and have been widely implicated in the toxification and detoxification processes of a variety of chemical agents (Guengerich, 2008). In theory, human *Cyp1a2, Cyp2d6, Cyp2e1*, and *Cyp3a4* correspond to rat *Cyp1a2, Cyp2d4, Cyp2e1*, and *Cyp3a1* (Ma et al., 2019). Therefore, we detected the mRNA expression levels of *Cyp1a2, Cyp2d4, Cyp2e1*, and *Cyp3a1* in the livers of rats from different treatments to explain the regulatory effect of CH on the pharmacokinetics process of AC. AC treatment significantly downregulated the expression of these CYP enzymes when compared to those of the controls. The AC-induced reduction in the expression levels of *Cyp1a2*, *Cyp2d4*, *Cyp2e1*, and *Cyp3a1* mRNA was markedly ameliorated when rats were administered with both AC and the compatible herbs of JGL. Although the specific activity of CYPs was not detected, our present results suggested that these four CYP isoforms might be associated with the mechanisms generated by combining *A. chinense* and the compatible herbs of JGL and that these effects were generated by regulatory effects in the pharmacokinetics process.

In addition to cytochrome P450 enzymes, the intestinal metabolism also plays an essential role in the absorption of orally administered drugs through the intestinal microbiota (López-Yerena et al., 2020). This dynamic intestinal absorption process is regarded as an important factor that explains the compatibility of TCM and ethnomedicines (Wang et al., 2022). A previous study demonstrated that some toxic alkaloids from TCM underwent hydroxylation, deoxygenation, demethylation, deoxidation and demethylation and ester hydrolysis through the intestinal bacteria, thus reducing their toxicity. Nicotin, an alkaloid with a similar chemical structure to anabasine and venoterpine is predominantly transported across Caco-2 cell monolayers in a unidirectional mode by pH-dependent specific transport systems in a manner that corresponds to its intestinal secretion (Fukada et al., 2002). The anti-rheumatic arthritis fraction (ARF) of *G. leucocarpa* exhibited good membrane permeability and strong intestinal absorption characteristics by virtue of active transport and passive diffusion. In addition, three main active ingredients of ARF were demonstrated to be the substrates of P-glycoprotein and may further affect the intestinal absorption characteristics of medicines and herbs (Wang et al., 2022). These previous studies suggested that the complex composition of TCM and the interaction between multiple constituents could result in different absorption levels of active components in the intestinal segments. In the present study, the single and continuous administration of AC and CH led to a reduction in the *in vivo* exposure levels of ANA and VER when compared to single AC treatment. This led us to hypothesize that the components of CH might regulate the intestinal metabolism of anabasine and venoterpine to influence their absorption characteristics. Further metabolic experiments involving anabasine and venoterpine are needed to test this hypothesis.

Collectively, the data described herein are valuable and improve our understanding of the mechanisms by which the compatible herbs of JGL can inhibit the neurotoxicity induced by *A. chinense* to some extent. However, there are some issues that need to be investigated in

future studies. Firstly, in addition to the changes in the mRNA expression levels of CYPs, we need to investigate how the compatible herbs of JGL can specifically modulate the activity of CYPs and intestinal metabolism, and then result in detoxication. Secondly, we need to identify the exact ingredients of the compatible herbs of JGL that interact with the active components of *A. chinense*, such as anabasine or other chemicals. According to the present chemical analysis, there were many different types of compounds in JGL, including alkaloids, organic acids, phenolics and saponins, which may have synergistic interactions among them. Previous works have reported that the toxicity of alkaloids in herbal medicines can be attenuated after being combined with other herbs containing saponins or organic acids. For example, the detoxification mechanisms of ginseng to aconitine was that ginsenoside Rg1 could regulate the ion channels pathway (Xu et al., 2022), accelerate the metabolism of aconitine and promote the absorption of benzoylaconine (Xu et al., 2020). Glycyrrhizic acid and liquiritigenin from *Glycyrrhiza uralensis* alleviated *Semen Strychni*-induced acute neurotoxicity through regulating high mobility group protein B1 (HMGB1) related pathway (Duan et al., 2022). Further research needs to investigate the interaction between alkaloids of AC and other chemical constituents from CH, which may attenuate the toxicity of *A. chinense* by modifying solubility, absorption or metabolism of its active alkaloids. Thirdly, transcriptomics and proteomics assays are required to unravel the possible involvement of other mediators underlying the neurotoxic action of AC when combined with other compatible herbs.

5 Conclusion

Our data demonstrate that the compatible herbs of JGL formula lead to a reduction in neurotoxicity induced by *A. chinense*. Furthermore, this combination inhibited oxidative damage, reduced the levels of neurotoxic biomarkers, regulated the abnormal levels and metabolisms of neurotransmitters, as well as modulated the pharmacokinetic processes of the active components of *A. chinense* by changing the levels of exposure to chemicals and by ameliorating the downregulation of the expression of cytochrome P450. This investigation provided experimental data for clinical application of JGL formula and its herbal compatibility.

Data availability statement

The original contributions presented in the study are included in the article/Supplementary Material, further inquiries can be directed to the corresponding author.

Ethics statement

The animal study was reviewed and approved by the Institutional Animal Ethical and Welfare Committee of Institute of Chinese Materia Medica, China Academy of Chinese Medical Sciences.

Author contributions

BP conceptualized and designed the project, supervised the study and wrote the original manuscript. DL performed experiments, collected and analyzed data and wrote the original manuscript draft. TC designed and performed pharmacokinetic experiments, collected and analyzed data and wrote the original manuscript draft. YC provided technical expertise for analyzing neurotransmitters, reviewed and edited the manuscript. HH and SG conducted the histological and pathological experiment, reviewed the manuscript. QH provided technical expertise for qPCR and analyzed data. GZ designed the behavioral study and reviewed the manuscript. LY performed the component analysis, analyzed data, edited the manuscript. HL, LS, and YG provided support in the animal study and reviewed the manuscript. YP analyzed data and reviewed the manuscript. All authors contributed to the article and approved the submitted version.

Funding

This work was supported by the National Key R&D Program of China (2018YFC1708100, 2018YFC1708105) to BP and Scientific and Technological Innovation Project of China Academy of Chinese Medical Sciences (CI 2021A04905, CI 2021A04406, CI 2021A04615) to YC, LY, and GZ.

Acknowledgments

We thank Baoqiang Dai and Lifang Wang for their help in animal care.

Conflict of interest

The authors declare that the research was conducted in the absence of any commercial or financial relationships that could be construed as a potential conflict of interest.

Publisher's note

Supplementary material

The Supplementary Material for this article can be found online at: https://www.frontiersin.org/articles/10.3389/fphar.2023.1133982/full#supplementary-material

References

Chang, R., Liu, J., Luo, Y., Huang, T., Li, Q., Wen, J., et al. (2020). Isoflavones' effects on pharmacokinetic profiles of main iridoids from Gardeniae Fructus in rats. *J. Pharm. Anal.* 10 (6), 571–580. doi:10.1016/j.jpha.2019.11.004

Ciancarelli, I., De Amicis, D., Di Massimo, C., Sandrini, G., Pistarini, C., Carolei, A., et al. (2015). Influence of intensive multifunctional neurorehabilitation on neuronal oxidative damage in patients with Huntington's disease. *Funct. Neurol.* 30 (1), 47–52.

Conley, T. E., Beaudin, S. A., Lasley, S. M., Fornal, C. A., Hartman, J., Uribe, W., et al. (2020). Early postnatal manganese exposure causes arousal dysregulation and lasting hypofunctioning of the prefrontal cortex catecholaminergic systems. *J. Neurochem.* 153 (5), 631–649. doi:10.1111/jnc.14934

Duan, X., Wen, J., Zhang, M., Wang, C., Xiang, Y., Wang, L., et al. (2022). Glycyrrhiza uralensis Fisch. and its active components mitigate Semen Strychni-induced neurotoxicity through regulating high mobility group box 1 (HMGB1) translocation. *Biomed. Pharmacother.* 149, 112884. doi:10.1016/j.biopha.2022.112884

Fukada, A., Saito, H., and Inui, K. (2002). Transport mechanisms of nicotine across the human intestinal epithelial cell line Caco-2. *J. Pharmacol. Exp. Ther.* 302 (2), 532–538. doi:10.1124/jpet.102.034629

Green, B. T., Lee, S. T., Keele, J. W., Welch, K. D., Cook, D., Pfister, J. A., et al. (2018). Complete inhibition of fetal movement in the day 40 pregnant goat model by the piperidine alkaloid anabasine but not related alkaloids. *Toxicon* 144, 61–67. doi:10.1016/j.toxicon.2018.02.007

Guengerich, F. P. (2008). Cytochrome p450 and chemical toxicology. *Chem. Res. Toxicol.* 21 (1), 70–83. doi:10.1021/tx700079z

Hsieh, M. T., Chueh, F. Y., Tsai, H. Y., Peng, W. H., and Hsieh, C. C. (1993). Effects of Alangium chinese on motor activity and the concentration of monoamines in rats. *zhong Hua Yao Xue Za Zhi* 45 (45), 447–456.

Hu, X. Y., Wei, X., Zhou, Y. Q., Liu, X. W., Li, J. X., Zhang, W., et al. (2020). Genus Alangium - a review on its traditional uses, phytochemistry and pharmacological activities. *Fitoterapia* 147, 104773. doi:10.1016/j.fitote.2020.104773

Iadecola, C., Niwa, K., Nogawa, S., Zhao, X., Nagayama, M., Araki, E., et al. (2001). Reduced susceptibility to ischemic brain injury and N-methyl-D-aspartate-mediated neurotoxicity in cyclooxygenase-2-deficient mice. *Proc. Natl. Acad. Sci. U. S. A.* 98 (3), 1294–1299. doi:10.1073/pnas.98.3.1294

Levin, E. D., Hao, I., Burke, D. A., Cauley, M., Hall, B. J., and Rezvani, A. H. (2014). Effects of tobacco smoke constituents, anabasine and anatabine, on memory and attention in female rats. *J. Psychopharmacol.* 28 (10), 915–922. doi:10.1177/0269881114543721

Li, K., Wu, D., Sun, Y. C., and Yun, X. L. (2017). An analysis of medicine rules in Miao medicine prescriptions for curing rheumatology based on association rules. *J. Chengdu Univ. TCM* 40 (3), 7–10. doi:10.13593/j.cnki.51-1501/r.2017.03.007

Liu, J. L., Ren, W., Yang, S. J., Tang, R., Mao, L. S., and Shui, P. X. (2022). Study on the effective ingredients and potential mechanism of Sargentodoxa cuneata in the treatment of cerebral infarction based on UPLC-HR-MS and network pharmacology. *Nat. Prod. Res. Dev.* 34 (03), 436–447. doi:10.16333/j.1001-6880.2022.3.011

López-Yerena, A., Vallverdú-Queralt, A., Mols, R., Augustijns, P., Lamuela-Raventós, R. M., and Escribano-Ferrer, E. (2020). Absorption and intestinal metabolic profile of oleocanthal in rats. *Pharmaceutics* 12 (2), 134. doi:10.3390/pharmaceutics12020134

Ma, Y. L., Zhao, F., Yin, J. T., Liang, C. J., Niu, X. L., Qiu, Z. H., et al. (2019). Two approaches for evaluating the effects of galangin on the activities and mRNA expression of seven CYP450. *Molecules* 24 (6), 1171. doi:10.3390/molecules24061171

Meng, Y. Y., Du, H. Z., Wang, X. B., Wan, W. R., and Chen, Z. Y. (2021). Research progress on chemical constituents and pharmacological effects of Alangium chinense (Lour.) Harms. *Stud. Trace Elem. Health* 38 (3), 40–43.

Nishimura, Y., Kanda, Y., Sone, H., and Aoyama, H. (2021). Oxidative stress as a common key event in developmental neurotoxicity. *Oxid. Med. Cell Longev.* 2021, 6685204. doi:10.1155/2021/6685204

Rittle, J., and Green, M. T. (2010). Cytochrome P450 compound I: capture, characterization, and C-H bond activation kinetics. *Science* 330 (6006), 933–937. doi:10.1126/science.1193478

Sahu, S., Nag, D. S., Swain, A., and Samaddar, D. P. (2017). Biochemical changes in the injured brain. *World J. Biol. Chem.* 8 (1), 21–31. doi:10.4331/wjbc.v8.i1.21

Sano, T., Masuda, Y., Yasuno, H., Shinozawa, T., Watanabe, T., and Kakehi, M. (2021). Blood neurofilament light chain as a potential biomarker for central and peripheral nervous toxicity in rats. *Toxicol. Sci.* 185 (1), 10–18. doi:10.1093/toxsci/kfab122

Schieber, M., and Chandel, N. S. (2014). ROS function in redox signaling and oxidative stress. *Curr. Biol.* 24 (10), R453–R462. doi:10.1016/j.cub.2014.03.034

Spinu, N., Bal-Price, A., Cronin, M. T. D., Enoch, S. J., Madden, J. C., and Worth, A. P. (2019). Development and analysis of an adverse outcome pathway network for human neurotoxicity. *Arch. Toxicol.* 93 (10), 2759–2772. doi:10.1007/s00204-019-02551-1

Steven, L. C. T., and Yi, G. X. (2021). Discussion on relevance and studies of prescription compatibility in Chinese medicine. *Chin. J. Integr. Med.* 27 (10), 788–793. doi:10.1007/s11655-020-3217-1

Stradtman, S. C., and Freeman, J. L. (2021). Mechanisms of neurotoxicity associated with exposure to the herbicide atrazine. *Toxics* 9 (9), 207. doi:10.3390/toxics9090207

Sun, L., Chen, Y., Hou, C., Sun, X., Wang, Z., Li, S., et al. (2018). Neuroprotective effect of total glycosides from paeonies against neurotoxicity induced by strychnos alkaloids related to recovering the levels of neurotransmitters and neuroendocrine hormones in rat serum and brain. *RSC Adv.* 8 (51), 29210–29219. doi:10.1039/c8ra05384g

Tinkov, A. A., Paoliello, M. M. B., Mazilina, A. N., Skalny, A. V., Martins, A. C., Voskresenskaya, O. N., et al. (2021). Molecular targets of manganese-induced neurotoxicity: A five-year update. *Int. J. Mol. Sci.* 22 (9), 4646. doi:10.3390/ijms22094646

Vogt, N. (2019). Sensing neurotransmitters. *Nat. Methods* 16 (1), 17. doi:10.1038/s41592-018-0268-8

Wang, C. Q., Wang, Y., Wang, W. J., Wang, L., and Ye, W. C. (2014). New oleanane saponins from Schefflera kwangsiensis. *Phytochem. Lett.* 10, 268–271. doi:10.1016/j.phytol.2014.10.010

Wang, X., Dong, Y., Song, R., Yu, A., Wei, J., Fan, Q., et al. (2022). Intestinal metabolism and absorption mechanism of multi-components in *Gaultheria leucocarpa* var. yunnanensis - an assessment using *in situ* and *in vitro* models, comparing gut segments in pathological with physiological conditions. *J. Ethnopharmacol* 286, 114844. doi:10.1016/j.jep.2021.114844

Wang, L. S., Zhang, M. D., Tao, X., Zhou, Y. F., Liu, X. M., Pan, R. L., et al. (2019). LC-MS/MS-based quantification of tryptophan metabolites and neurotransmitters in the serum and brain of mice. *J. Chromatogr. B Anal. Technol. Biomed. Life Sci.* 1112, 24–32. doi:10.1016/j.jchromb.2019.02.021

Wang, X., Li, X., Wang, R., Wang, L., Fan, S., Wang, X., et al. (2019). Human gastrointestinal metabolism of the anti-rheumatic fraction of Dianbaizhu (Gaultheria leucocarpa var. yunnanensis) *in vitro*: Elucidation of the metabolic analysis in gastric juice, intestinal juice and human intestinal bacteria by UPLC-LTQ-Orbitrap-MS(n) and HPLC-DAD. *J. Pharm. Biomed. Anal.* 175, 112791. doi:10.1016/j.jpba.2019.112791

Wei, X., Yang, J., Dai, Z., Yu, H. F., Ding, C. F., Khan, A., et al. (2020). Antitumor pyridine alkaloids hybrid with diverse units from Alangium chinense. *Tetrahedron Lett.* 61 (7), 151502. doi:10.1016/j.tetlet.2019.151502

Wilson, C., Munoz-Palma, E., and Gonzalez-Billault, C. (2018). From birth to death: A role for reactive oxygen species in neuronal development. *Semin. Cell Dev. Biol.* 80, 43–49. doi:10.1016/j.semcdb.2017.09.012

Xiang, J. Y., Chi, Y. Y., Han, J. X., Xiang, H., and Xie, Q. (2021). The toxicity and attenuation methods of toxic Chinese Materia Medica for its reasonable application: A review. *Am. J. Chin. Med.* 49 (1), 41–67. doi:10.1142/S0192415X21500038

Xu, Y., Yang, L., Liang, K., An, R., Wang, X., and Zhang, H. (2020). Pharmacokinetic effects of ginsenoside Rg1 on aconitine, benzoylaconine and aconine by UHPLC-MS/MS. *Biomed. Chromatogr.* 34 (4), e4793. doi:10.1002/bmc.4793

Xu, X., Xie, X. F., Dong, Y. H., Zhang, H. Q., and Peng, C. (2022). Ginsenoside Rg_1 reduces cardiotoxicity while increases cardiotonic effect of aconitine *in vitro*. *Chin. J. Integr. Med.* 28 (8), 693–701. doi:10.1007/s11655-022-3509-0

Yue, Y. D. (2016). *Chemical constituents and bioactivities of Swertia Bimaculata and Alangium chinense*. Wuhan: Huazhong University of Science and Technology.

Zhai, K. F., Duan, H., Khan, G. J., Xu, H., Han, F. K., Cao, W. G., et al. (2018). Salicin from Alangium chinense ameliorates rheumatoid arthritis by modulating the nrf2-HO-1-ROS pathways. *J. Agric. Food Chem.* 66 (24), 6073–6082. doi:10.1021/acs.jafc.8b02241

Zhang, C. H., Wang, D. W., Xu, X. M., Lou, X. P., and Qiu, C. W. (2008). One fatal case of the poisonous effect of Alangium chinese (Lour) Harms. *Fa Yi Xue Za Zhi* 24 (2), 155–156.

Zhang, X. H., Liu, S. S., and Xuan, L. J. (2009). Cyclopentenylglycines and other constituents from Alangium chinense. *Biochem. Syst. Ecol.* 37, 214–217. doi:10.1016/j.bse.2008.11.015

Zhang, Y., Liu, Y. B., Li, Y., Ma, S. G., Li, L., Qu, J., et al. (2013). Sesquiterpenes and alkaloids from the roots of Alangium chinense. *J. Nat. Prod.* 76 (6), 1058–1063. doi:10.1021/np4000747

Zhang, Y., Liu, Y. B., Li, Y., Li, L., Ma, S. G., Qu, J., et al. (2015). Terpenoids from the roots of Alangium chinense. *J. Asian Nat. Prod. Res.* 17, 1025–1038. doi:10.1080/10286020.2015.1082551

Zhang, Q., Li, Y., Liu, M., Duan, J., Zhou, X., and Zhu, H. (2018). Compatibility with panax notoginseng and rehmannia glutinosa alleviates the hepatotoxicity and nephrotoxicity of tripterygium wilfordii via modulating the pharmacokinetics of triptolide. *Int. J. Mol. Sci.* 19 (1), 305. doi:10.3390/ijms19010305

Zhang, Y. M., Liao, X. L., Wang, X. N., and Pang, Y. Z. (2019). Research status on pharmacological and toxicological effects of Alangium chinense. *Chin. J. Clin. Pharmacol.* 35 (19), 2476–2479.

Zhao, G. P., Dai, S., and Chen, R. S. (2006). *0049 Ba Jiao Feng Gen. Dictionary of Chinese Materia Medica 2nd version*. Shanghai: Shanghai Science and Technology Press.

Zheng, L., Zhou, T., Liu, H., Zhou, Z., Chi, M., Li, Y., et al. (2022). Pharmacokinetics study of jin-gu-lian prescription and its core drug pair (Sargentodoxa cuneata (oliv.) rehd. et W and Alangium chinense (lour.) Harms) by UPLC-MS/MS. *Molecules* 27 (13), 4025. doi:10.3390/molecules27134025

Zhou, Z. Y., Huang, Y., Xiao, J. C., Liu, H., Wang, Y. L., Gong, Z. P., et al. (2022). Chemical profiling and quantification of multiple components in Jin-Gu-Lian capsule using a multivariate data processing approach based on UHPLC-Orbitrap Exploris 240 MS and UHPLC-MS/MS. *J. Sep. Sci.* 45, 1282–1291. doi:10.1002/jssc.202100762

Zhu, M., Bowery, N. G., Greengrass, P. M., and Phillipson, J. D. (1996). Application of radioligand receptor binding assays in the search for CNS active principles from Chinese medicinal plants. *J. Ethnopharmacol.* 54 (2-3), 153–164. doi:10.1016/s0378-8741(96)01454-7

frontiers | Frontiers in Pharmacology

TYPE Original Research
PUBLISHED 01 March 2023
DOI 10.3389/fphar.2023.1148332

OPEN ACCESS

EDITED BY
Zipeng Gong,
Guizhou Medical University, China

REVIEWED BY
Rongchang Chen,
Chinese Academy of Medical Sciences and Peking Union Medical College, China
Yingfei Li,
China Academy of Chinese Medical Sciences, China
Ziqiang Li,
Second Affiliated Hospital of Tianjin University of Traditional Chinese Medicine, China

*CORRESPONDENCE
Shan Xiong,
shanxiong83@sohu.com
Jia Liu,
qq919482224@163.com
Qingqiang Yao,
yao_imm@163.com

SPECIALTY SECTION
This article was submitted to Drug Metabolism and Transport, a section of the journal Frontiers in Pharmacology

RECEIVED 20 January 2023
ACCEPTED 17 February 2023
PUBLISHED 01 March 2023

CITATION
Xiong S, Li X, Chu H, Deng Z, Sun L, Liu J, Mu Y and Yao Q (2023), Comparative pharmacokinetics of four major compounds after oral administration of Mori Cortex total flavonoid extract in normal and diabetic rats.
Front. Pharmacol. 14:1148332.
doi: 10.3389/fphar.2023.1148332

Comparative pharmacokinetics of four major compounds after oral administration of Mori Cortex total flavonoid extract in normal and diabetic rats

Shan Xiong[1]*, Xiaofan Li[2], Haiping Chu[1], Zhipeng Deng[3], Linying Sun[4], Jia Liu[1]*, Yanling Mu[1] and Qingqiang Yao[1]*

[1]School of Pharmacy and Pharmaceutical Sciences & Institute of Materia Medica, Shandong First Medical University & Shandong Academy of Medical Sciences, NHC Key Laboratory of Biotechnology Drug (Shandong Academy of Medical Sciences), Key Lab for Rare and Uncommon Diseases of Shandong Province, Jinan, China, [2]Institute of Basic Medicine, Shandong First Medical University & Shandong Academy of Medical Science, Jinan, China, [3]School of Pharmaceutical Sciences, Shandong University of Traditional Chinese Medicine, Jinan, China, [4]School of Public Health, Shandong First Medical University & Shandong Academy of Medical Science, Jinan, China

Introduction: Mori Cortex has been used in traditional Chinese Medicine as an antidiabetic agent. The aim of this study was to establish a UPLC-MS/MS method for simultaneous determination of morin, morusin, umbelliferone and mulberroside A in rat plasma and investigate the pharmacokinetics differences between normal and diabetic rats following oral administration of Mori Cortex total flavonoid extract.

Methods: Samples were pre-treated by protein precipitation and genkwanin was used as internal standard. Chromatographic separation was performed using a Hypersil GOLD C_{18} column (50 mm × 2.1 mm, 3 μm). The mobile phase consisted of acetonitrile and water (containing 0.1% formic acid) in gradient mode at a flow rate of 0.5 ml/min. The transitions of m/z 300.9→107.1, m/z 419.3→297.1, m/z 160.9→77.0, m/z 567.1→243.2 and m/z 283.1→268.2 were selected for morin, morusin, umbelliferone, mulberroside A and internal standard, respectively.

Results: The intra- and inter-day precision for analytes were less than 12.5% and the accuracy ranged from −8.1% to 3.5%. The extraction recovery was >88.5% and no obvious matrix effect was observed. The $AUC_{(0\text{-}t)}$ and C_{max} of morin were 501.3 ± 115.5 ng/mL*h and 127.8 ± 56.0 ng/mL in normal rats and 717.3 ± 117.4 ng/ml*h and 218.6 ± 33.5 ng/ml in diabetic rats. Meanwhile, the $AUC_{(0\text{-}t)}$ and C_{max} of morusin were 116.4 ± 38.2 ng/ml*h and 16.8 ± 10.1 ng/mL in normal rats and 325.0 ± 87.6 ng/mL*h and 39.2 ± 5.9 ng/ml in diabetic rats. For umbelliferone and mulberroside A, the $AUC_{(0\text{-}t)}$ and C_{max} also increased significantly in diabetic rats ($p < 0.05$).

Discussion: The validated method was successfully applied to the pharmacokinetic study in normal and diabetic rats.

Abbreviations: UPLC-MS/MS, ultra-performance liquid chromatography-tandem mass spectrometry; DM, diabetes mellitus; TCM, traditional Chinese Medicine; STZ, streptozotocin; FBG, fasting blood glucose; ESI, electrospray ionization source; MRM, multiple-reaction monitoring; QC, quality control; LLOQ, the lower limit of quantification; ULOQ, the upper limits of quantification; RSD, relative standard deviation; RE, relative error.

KEYWORDS
UPLC-MS/MS, pharmacokinetic, Mori Cortex total flavonoid extract, diabetes mellitus, rats

1 Introduction

A large number of studies have shown that long-standing serious hyperglycemia is the main cause of metabolic disorders and autoimmune disorders (Maritim et al., 2003). Diabetes mellitus (DM) is a chronic disease caused by acquired deficiency in production of insulin by the pancreas, or by the ineffectiveness of the insulin produced (Riaz, 2009). This deficiency results in increased concentrations of glucose in the blood, which in turn leads to retinopathy, nephropathy, neuropathy, coronary heart disease, cerebrovascular disease, and peripheral vascular diseases (Gregg et al., 2016; O'Brien and Corrall, 1988). The main purpose of diabetes treatment is to prevent or delay the complications by improving blood sugar control (Kooti et al., 2016). In China, traditional Chinese medicine (TCM) has been widely used in the treatment of diabetes and its complications (Tong et al., 2012). The prevention and treatment of diabetic complications by using TCM have lots of advantage including comprehensive treatment and small toxicity and side effects (Jia et al., 2003; Wang et al., 2016; Martel et al., 2017; Aras et al., 2019).

Mori Cortex, also called "Sang-Bai-Pi" in Chinese, which is derived from the root bark of Morus *alba* L. according to the China Pharmacopeia (The Committee of China Pharmacopeia, 2020). The modern pharmacological studies have shown that Mori Cortex has the active effect of antidiabetic (Ma et al., 2018), antioxidant (Ahmad et al., 2013; Abbasa et al., 2014; Bayazid et al., 2020), anti-inflammatory (Lim et al., 2013; Bayazid et al., 2020), antimicrobial (Grienke et al., 2016) and anticarcinogenic (Lim et al., 2014). It was first recorded for the antidiabetic effect of Mori Cortex in "Compendium of Materia medica". According to ancient prescriptions, the decoction of Cortex Mori (12 g) and Lycii Fructus (15 g) was used to control the blood glucose level for diabetic patients (Xiao et al., 2014). Recent studies have shown that Mori Cortex extract could lower the blood glucose and improve insulin resistance (Qi et al., 2016; Kim and Choe, 2017; Ma et al., 2018).

To the best of the authors' knowledge, there is no study focusing on the simultaneous quantification of morin, morusin, umbelliferone, and mulberroside A in rat plasma. The aim of this study was to develop an ultra-performance liquid chromatography-tandem mass spectrometry (UPLC-MS/MS) method for the simultaneous determination of morin, morusin, umbelliferone and mulberroside A, which are the main active components of Mori Cortex total flavonoid extract with higher content, in normal and diabetic rat (Liu et al., 2019). The structures of these four target analytes and IS are shown in Figure 1.

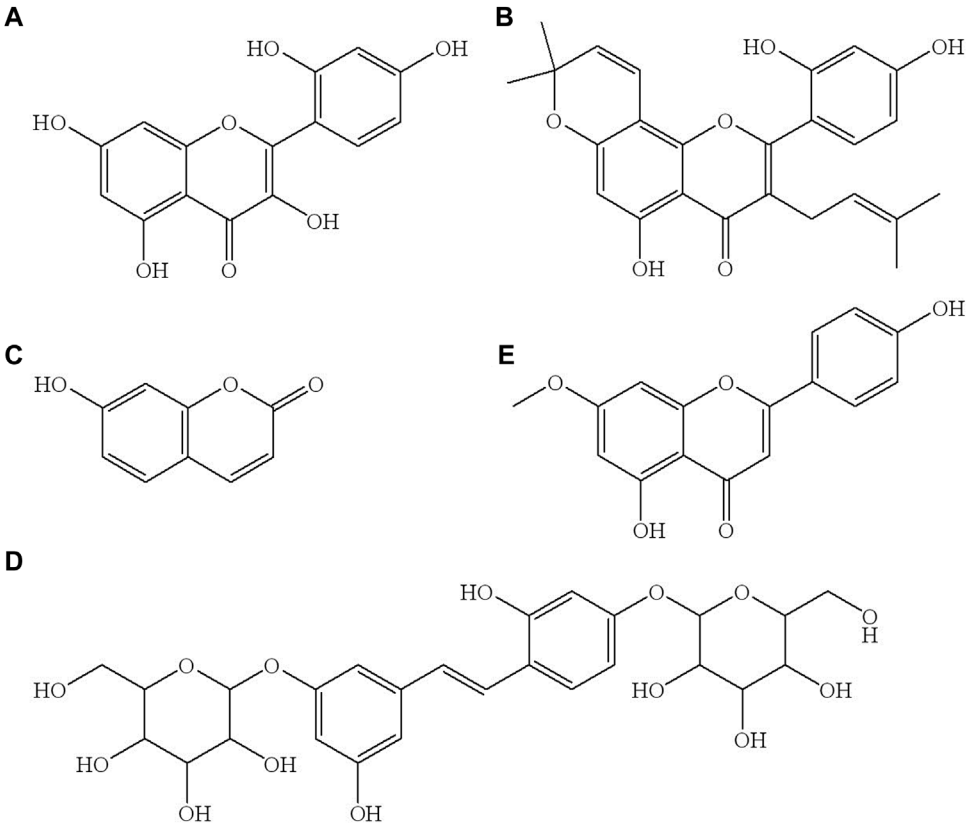

FIGURE 1
The chemical structure of morin **(A)**, morusin **(B)**, umbelliferone **(C)**, mulberroside A **(D)** and genkwain IS, **(E)**.

2 Materials and methods

2.1 Chemicals and reagents

Mori Cortex total flavonoid extract (Lot number HP20171011), morin (98% purity), morusin (98% purity), umbelliferone (98% purity) and mulberroside A (98% purity) were supplied by Baoji Herbet Bio-Tech Co. Ltd (Baoji, China). Genkwanin (internal standard (IS), 98% purity) was supplied by the National Institute for the Control of Pharmaceutical and Biological Products (Beijing, China). Propylene glycol was purchased from Nanjing Weier Pharmaceutical Co. Ltd (Nanjin, China). Streptozotocin (STZ) was purchased from Sigma (Sigma-Aldrich, St Louis, MO, United States). HPLC-grade formic acid was obtained from Tianjin Kermel Chemical Reagent Co. Ltd (Tianjin, China). HPLC-grade acetonitrile and methanol were obtained from Tedia Company (Fairfield, United States). Purified water was employed by Wahaha Co. Ltd (Hangzhou, China). All of the other chemicals were analytical grade or better.

2.2 Animals

Male Sprague-Dawley rats (7–8 weeks old, weighing 200 ± 20 g) were purchased from Jinan Pengyue Experimental Animal Breeding Co. Ltd (Jinan, China). They were housed in a room with a 12/12 h light/dark cycle and an ambient temperature of 23°C ± 3°C. All animal experiments were carried out according to the National Institute of Health Guideline for the Care and Use of Laboratory Animals, and performed by the Animal Ethics Committee of School of Pharmacy and Pharmaceutical Sciences & Institute of Materia Medica, Shandong First Medical University & Shandong Academy of Medical Sciences (2017036, Jinan, China).

The rats were given a single intraperitoneal injection with a freshly prepared solution of STZ (60 mg/kg) in 0.1 mol/L citrate buffer (pH = 4.4) to induce diabetes (Seke Etet et al., 2017; Zhang et al., 2017). After 8 weeks, the rats with fasting blood glucose (FBG) for 5–6 h exceeding 16.7 mmol/L were considered successful diabetes models. The FBG was measured from the tail vein using a One-Touch Ultra® Blood Glucose Meter (LifeScan Inc., Milpitas, United States).

2.3 Instrumentation and UPLC-MS/MS conditions

A Shimadzu Prominence UPLC (Shimadzu, United States) system coupled to an AB SCIEX™ 5500 Q-Trap® mass spectrometer (Applied Bio-systems, United States) equipped with an electrospray ionization interface operated in negative multiple reaction monitoring (MRM) mode were applied to analysis. The analytes separation was achieved *via* gradient elution of 0.1% formic acid in water (A) and acetonitrile (B) at a flow rate of 0.5 mL/min on a Thermo Hypersil Gold C_{18} column (50 mm × 2.1 mm, 3 μm; Thermo Scientific, New York, United States). The run time was 4.0 min for each analysis. The gradient elution program was used as follows: 5% B→10% B at 0–0.2 min, 10% B→70% B at 0.2–2.0 min, 70% B at 2.0–2.5 min, 70% B→5% B at 2.50–2.51 min; 5% B at 2.51–4.0 min. The temperatures of autosampler and column were set at 15°C and 40°C, respectively. The supernatant injection volume was 2 μl. The MRM conditions (source-dependent mass parameters) were defined as follows: Ion Spray Voltage, −4500 V; temperature, 550°C; curtain gas, 35.0 psi; collision gas, medium; Gas 1, 55.0 psi; Gas 2, 55.0 psi. The transitions of m/z 300.9→107.1, m/z 419.3→297.1, m/z 160.9→77.0, m/z 567.1→243.2 and m/z 283.1→268.2 were selected for morin, morusin, umbelliferone, mulberroside A and IS, respectively. The system control and data analysis were performed using AB SCIEX Analyst software (version 1.6.3).

2.4 Preparation of standard solutions, calibration standards and quality control samples

The analytes were accurately weighted and separately dissolved in methanol to yield the stock solutions with a concentration of 5 mg/mL. The stock solutions were stored at −80°C until analyzed. The stock solutions were stepwise diluted with acetonitrile to make a series of mixed working solutions at concentration levels of 20–20000 ng/ml for target analytes. In addition, the IS was dissolved in methanol and then diluted with acetonitrile to obtain a working solution of 50 ng/ml. The solution of IS was maintained at 4°C.

Calibration standards were prepared by adding 10 μl of the mixed working solutions to 190 μl blank plasma to obtain final concentrations in the range 1–1000 ng/mL for target analytes. The quality control (QC) samples were prepared separately by the same method at four concentration levels of 1 (lower limit of quantification, LLOQ), 3 (LQC), 80 (MQC) and 800 ng/ml (HQC) for the four analytes.

2.5 Sample preparation

50 μl of rat plasma was mixed with 50 μl of IS solution (50 ng/ml) in a 1.5 ml polypropylene tube and then 100 μl acetonitrile was added to precipitate protein. The mixture was vortexed for 5 min, then centrifuged at 13000 rpm for 5 min at 4°C. The supernatant was collected in an autosampler vial and 2 μl of aliquot was injected into the UPLC-MS/MS system for analysis.

2.6 Validation of UPLC-MS/MS analytical method

The selectivity, linearity range, carryover, inter- and intra-day precision and accuracy, matrix effect, recovery and stability under different storage conditions were evaluated according to the FDA Guidance for Industry Bioanalytical Method Validation (Xiong et al., 2017; Food and Drug Administration, 2018; Li et al., 2019).

The selectivity was evaluated by comparing the chromatogram of blank rat plasma from six different matrices with standard plasma samples spiked with analytes and IS. The purpose was to explore whether there was interference from endogenous substances.

TABLE 1 Optimized mass parameters for analytes and IS.

Analytes	Precursor ion (m/z)	Quantitative ion (m/z)	Qualitative ion (m/z)	Dp (V)	Ep (V)	Cxp (V)	CE (V)
Morin	300.9	107.1	125.0	−20	−15	−15	−35
Morusin	419.3	297.1	89.0	−60	−15	−43	−20
umbelliferone	160.9	77.0	105.0	−100	−15	−5	−34
mulberroside A	567.1	243.2	405.2	−200	−10	−5	−39
IS	283.1	268.2	239.9	−65	−15	−50	−32

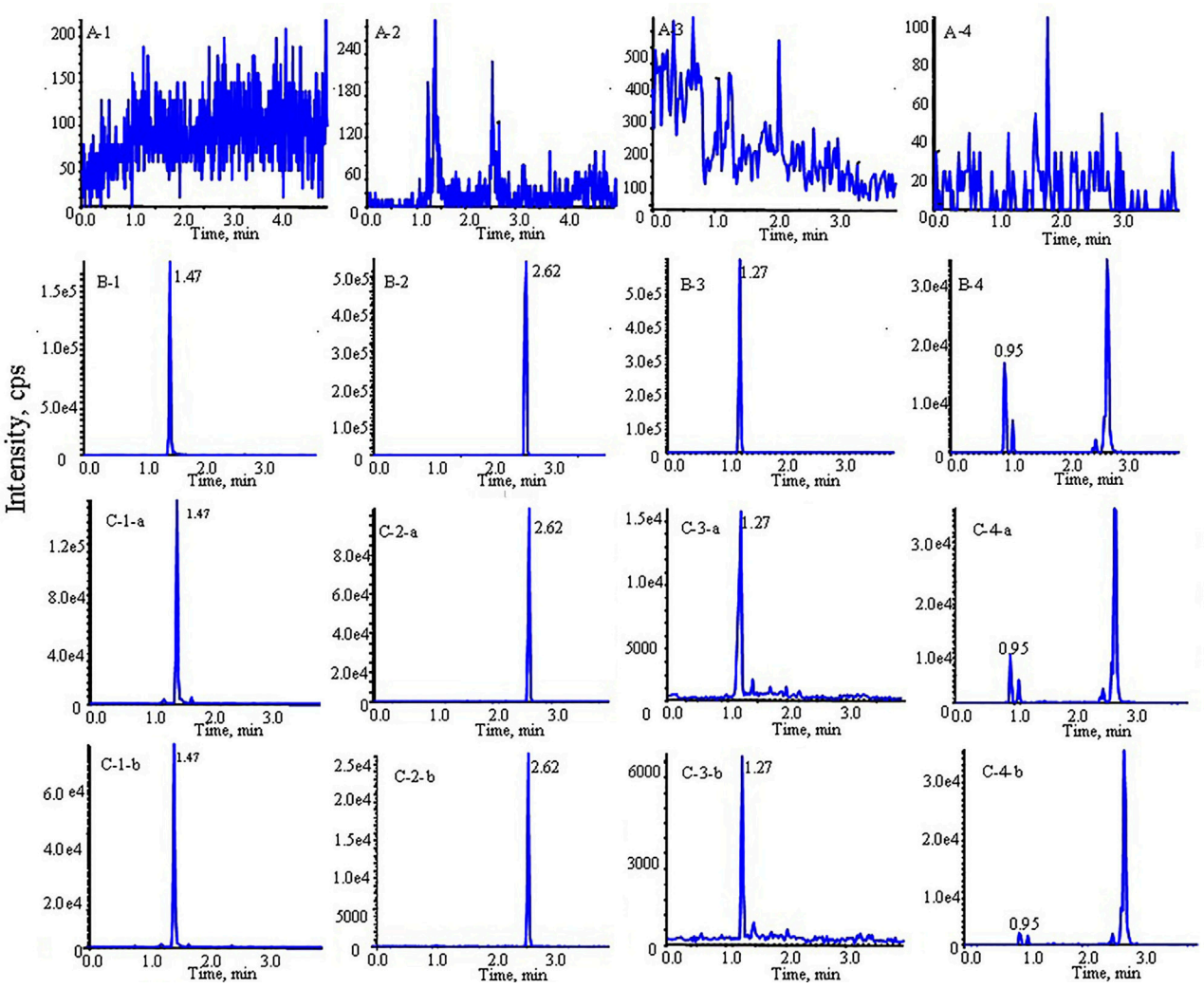

FIGURE 2
Typical multiple reaction monitoring (MRM) chromatograms of morin, morusin, umbelliferone and mulberroside A from rat plasma: **(A)** blank plasma sample; **(B)** blank plasma spiked with analytes; **(C)** rat plasma sample after oral administration of Mori Cortex total flavonoid extract (1: morin, 2: morusin, 3: umbelliferone, 4: mulberroside A; **(a)** diabetic rats, **(b)** normal rats).

The linearity for morin, morusin, umbelliferone and mulberroside A were evaluated by plotting the peak area ratios of the analytes/IS versus the concentration values of the standard plasma samples on three consecutive days (a weighted $1/X^2$ least squares linear regression). The LLOQ was determined by spiking the lowest concentration on the calibration curve with acceptable precision of less than 20% of the relative standard deviation (RSD, %) and relative error (RE, %) of ±20%. The carryover was assessed by analyzing the response of the blank plasma following the upper limits of quantification (ULOQ).

The intra- and inter-day accuracy and precision were determined by analyzing five replicates on three consecutive

TABLE 2 analytical parameters for quantification of analytes.

Analytes	Regression equation	*R*	Linear range (ng/mL)	LLOQ (ng/mL)
Morin	$y = 2.98 \times 10^{-4}x+9.24 \times 10^{-4}$	0.9967	1–1000	1
Morusin	$y = 1.22 \times 10^{-3}x+1.19 \times 10^{-3}$	0.9964	1–1000	1
umbelliferone	$y = 2.03 \times 10^{-3}x+1.51 \times 10^{-3}$	0.9978	1–1000	1
mulberroside A	$y = 8.18e^{-5}x+1.64e^{-5}$	0.9961	1–1000	1

TABLE 3 Precision and accuracy for the determination of analytes in rat plasma (n = 5).

Analytes	Spiked concentration (ng/mL)	Intra-day		Inter-day	
		Precision (RSD,%)	Accuracy (RE,%)	Precision (RSD,%)	Accuracy (RE,%)
Morin	1	5.7	−4.2	9.4	−1.9
	3	5.5	−6.3	5.4	−7.5
	40	5.7	−2.5	7.9	−6.6
	800	4.1	−0.5	5.9	−2.9
Morusin	1	9.5	3.5	12.5	−5.4
	3	2.4	−3.3	6.4	−8.1
	40	5.5	−3.9	7.6	−1.5
	800	5.0	−3.0	7.8	2.7
umbelliferone	1	5.8	−0.3	7.8	−5.6
	3	4.6	1.8	6.4	−1.4
	40	5.1	−0.7	5.8	1.6
	800	5.2	−4.1	7.6	−2.1
mulberroside A	1	8.9	−0.9	11.0	−3.2
	3	6.7	−0.5	9.0	−1.7
	40	8.5	3.1	10.4	−2.9
	800	4.7	−5.2	8.4	−2.0

days. The intra-day assessment was investigated in the 1 day and the inter-day assessment was investigated for three consecutive days. The precision was calculated in terms of RSD (%), while the accuracy was expressed as the RE (%). The RSD should be within 15% and accuracy was required to not be exceed ±15% at four QC levels.

The recovery of four target analytes were evaluated at three QC levels (LQC, MQC, and HQC) by comparing the mean peak areas of QC samples in six replicates with that of the pre-extraction blank plasma spiked with the corresponding working standard solution. The matrix effect was investigated by comparing the peak area of analytes resolved in pre-extraction matrix of blank plasma with those in the water-substituted samples. The recovery and matrix effect of the IS were assessed in the same way.

The stability of analytes in rat plasma was assessed by analyzing QC samples at low, middle and high levels (n = 5) under different storage condition including the short-term stability at room temperature for 6 h, the post-treatment stability at 15°C in autosampler for 12 h, three freeze-thaw stability, and the long-term stability at −80°C for 7 days.

2.7 Preparation of the oral solutions

The Mori Cortex total flavonoid extract (8 g) was stirred with propylene glycol (20 ml) by ultrasonic in a 50 ml volumetric flask, and then added purified water to 50 ml slowly. The contents of morin, morusin, umbelliferone and mulberroside A in the Mori Cortex total flavonoid extract were 0.1093%, 1.0050%, 0.1128% and 0.0764%, respectively.

2.8 Pharmacokinetic study

Ten male Sprague-Dawley rats were enrolled in the pharmacokinetic study: five normal rats and five diabetic rats.

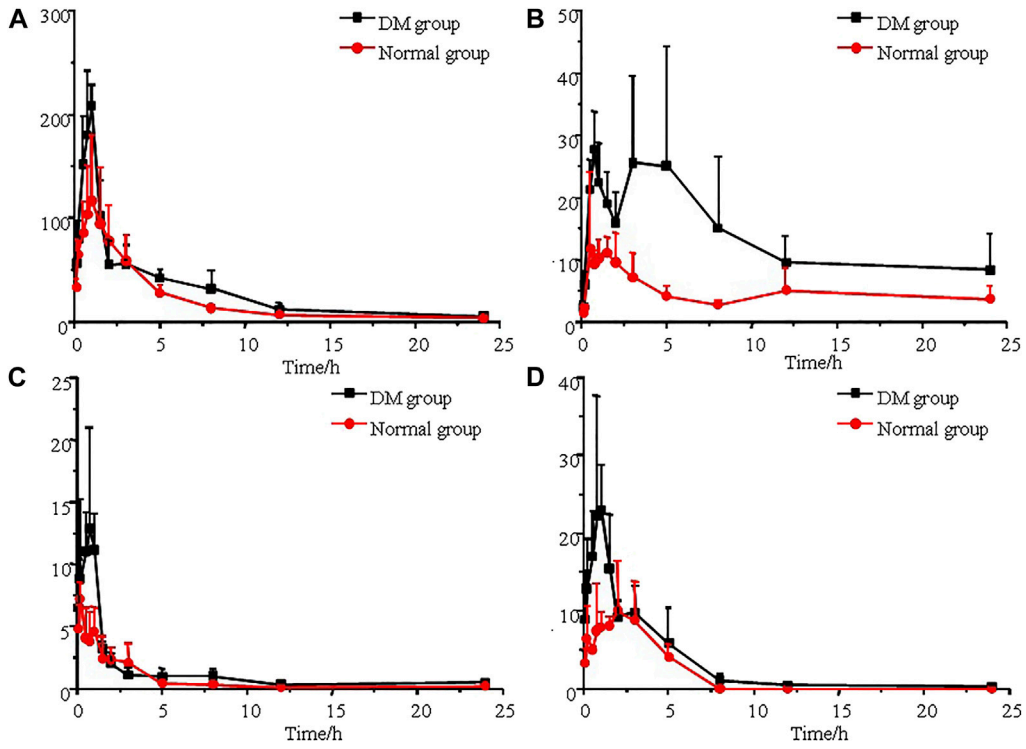

FIGURE 3
Mean plasma concentration-time curves of morin **(A)**, morusin **(B)**, umbelliferone **(C)** and mulberroside A **(D)** after oral administration of Mori Cortex total flavonoid extract (n = 5).

All of the rats were fasted for at least 12 h and had free access to drinking water before the experimental. The two groups of rats were administered Mori Cortex total flavonoid extract at the doses of 2 g/kg by oral after overnight fasting. Blood samples (150 μl) were obtained from retroorbital plexus into a heparinized tube at 0 (pre-dose), 0.083, 0.167, 0.5, 0.75, 1, 1.5, 2, 3, 5, 8, 12 and 24 h after oral administration. The collected blood samples were immediately centrifuged at 3500 rpm at 4°C for 15 min to obtain plasma fraction. The samples were frozen at −80°C until analyzed.

3 Results

3.1 Method development

Acetonitrile/methanol-water (containing 0, 0.1% formic acid and 10 mM ammonium acetate with 0.1% formic acid) being the mobile phase with gradient elution was used to evaluate UPLC separation and sensitivity in MS detection in order to obtain the good peak shape and optimal response for all the analytes. Finally, the mobile phase containing acetonitrile and 0.1% formic acid in water was selected for the separation of the four analytes and IS, and the excellent peak shape and lower background noise were also obtained.

The ESI source was operated in negative ion mode to achieve maximum response and the deprotonated precursor molecular ions $[M-H]^-$ were chosen to be monitored. The m/z 300.9→107.1 as the quantitative ion for morin was selected due to the better peak shape of LLOQ samples. For morusin, the mass transition of m/z 419.3→89.0 was not chosen for quantitative analysis because it showed interference of endogenous substances in blank plasma samples. The MS/MS spectrogram of morin, morusin, umbelliferone, mulberroside A and IS are shown in Supplementary Figure S1. The optimal mass spectrometry parameters and transitions for analytes are listed in Table 1.

3.2 Method validation

As shown in Figure 2, the retention times were 1.47, 2.62, 1.27, 0.95 and 2.05 min for morin, morusin, umbelliferone, mulberroside A and IS, respectively. No unacceptable interference was observed at the retention times.

The eight-point calibration curve was found to be linear over the concentration range of 1–1000 ng/mL for four analytes. Correlation coefficients were ≥0.99 for all analytes. The calibration curve results for four analytes are summarized in Table 2. The LLOQ values for analytes were 1 ng/mL with RSD <12.5% and RE varied from −5.6% to 3.5% (Table 3), indicating LLOQs of all analytes met the requirements. There was no carryover effect after the injection of ULOQ samples.

The intra- and inter-day precision and accuracy within the acceptance limit for the analytes are summarized in Table 3. The precision was ≤10.4% and the accuracy was within ± 8.1% for four

TABLE 4 Pharmacokinetic parameters of analytes after oral administration of Mori Cortex total flavonoid extract in normal and diabetic rats plasma (mean ± SD, n = 5).

Pharmacokinetic parameters	Unit	Morin		Morusin		Umbelliferone		Mulberroside A	
		Normal rats	Diabetic rats	Normal rats	Diabetic rats	Normal rats	Diabetic rats	Normal rats	Diabetic rats
$AUC_{(0\text{-}t)}$	ng/mL[a]h	501.3 ± 115.5	717.3 ± 117.4[a]	116.4 ± 38.2	325.0 ± 87.6[a]	16.4 ± 5.1	28.4 ± 3.6[a]	36.8 ± 14.6	75.6 ± 11.1[a]
$AUC_{(0\text{-}\infty)}$	ng/mL[a]h	511.9 ± 122.2	767.8 ± 150.8[a]	337.3 ± 150.7	569.8 ± 218.5[a]	17.6 ± 5.9	34.5 ± 9.8[a]	55.3 ± 22.9	75.9 ± 11.0[a]
MRT	h	5.1 ± 0.9	5.5 ± 1.3	10.5 ± 1.9	9.4 ± 2.2	3.9 ± 1.9	4.9 ± 1.8	2.3 ± 0.2	3.6 ± 0.7[a]
$t_{1/2z}$	h	4.4 ± 1.6	5.6 ± 2.9	4.3 ± 3.4	9.8 ± 8.8	4.6 ± 2.9	8.1 ± 5.9	2.7 ± 0.8	3.0 ± 0.9
T_{max}	h	0.9 ± 0.2	0.9 ± 0.1	1.2 ± 0.6	2.9 ± 2.1	0.3 ± 0.4	0.5 ± 0.4	1.8 ± 0.8	1.0 ± 0.3
CLz/F	L/h/kg	40.9 ± 9.5	27.1 ± 6.6[a]	68.1 ± 25.7	40.7 ± 18.9	1315.5 ± 693.1	616.3 ± 166.2	406.2 ± 209.5	267.9 ± 37.5
Vz/F	L/kg	247.8 ± 68.2	200.7 ± 76.1	3307.5 ± 1876.8	438.4 ± 261.8[a]	6969.0 ± 3405.8	6174.7 ± 3089.6	1508.6 ± 839.6	1188.7 ± 466.4
C_{max}	ng/mL	127.8 ± 56.0	218.6 ± 33.5[a]	16.8 ± 10.1	39.2 ± 5.9[a]	7.6 ± 0.7	16.8 ± 6.6[a]	13.1 ± 6.5	28.5 ± 12.3[a]

[a]$p < 0.05$ compared with normal rats.

AUC, area under the plasma concentration–time curve; *MRT*, mean residence time; $t_{1/2z}$, terminal half-life; T_{max}, time at C_{max}; *CLz*/F, clearance rate; *Vz*/F, apparent volume of distribution; C_{max}, peak concentration in plasma.

analytes. The data suggested that the analytical method was reliable and accurate.

The mean extraction recovery and matrix effect of the analytes and IS are summarized in Supplementary Table S1. The results suggested that the assay obtained high recovery and no obvious matrix effect of each analyte and IS was observed.

The stability data of four analytes are shown in Supplementary Table S2. The results proved that the storage conditions, disposal, intermittent analysis and analysis techniques were valid and reliable for the analytes in rat plasma.

3.3 Application to a pharmacokinetic comparison

The established UPLC-MS/MS method was successfully applied to the determination of morin, morusin, umbelliferone and mulberroside A in rat plasma samples collected from normal rats and diabetic rats after oral administration of Mori Cortex total flavonoid extract. The mean plasma concentration versus time plots for morin, morusin, umbelliferone and mulberroside A are shown in Figure 3. In addition, the pharmacokinetic parameters of the normal and diabetic rats were calculated by DAS software version 2.0 and compared using the independent samples t-test (a value of $p < 0.05$ was considered statistically significant). Compared with normal rats, some main pharmacokinetic parameters of all target analytes obtained from diabetic rats changed. The $AUC_{(0\text{-}t)}$ and C_{max} of morin were 501.3 ± 115.5 ng/ml*h and 127.8 ± 56.0 ng/mL in normal rats and 717.3 ± 117.4 ng/ml*h and 218.6 ± 33.5 ng/mL in diabetic rats. Additionally, the $AUC_{(0\text{-}t)}$ and C_{max} of morusin were 116.4 ± 38.2 ng/ml*h and 16.8 ± 10.1 ng/mL in normal rats and 325.0 ± 87.6 ng/mL*h and 39.2 ± 5.9 ng/mL in diabetic rats. For umbelliferone and mulberroside A, the $AUC_{(0\text{-}t)}$ were 16.4 ± 5.1 and 36.8 ± 14.6 ng/ml*h in normal rats, and 28.4 ± 3.6 and 75.6 ± 11.1 ng/ml*h in diabetic rats. Meanwhile, the C_{max} were 7.6 ± 0.7 and 13.1 ± 6.5 ng/mL in normal rats, and 16.8 ± 6.6 and 28.5 ± 12.3 ng/ml in diabetic rats. The changes were significant ($p < 0.05$). The main pharmacokinetic parameters are presented in Table 4.

4 Discussion

The current cognition regarding the effects of diabetes mellitus on the pharmacokinetics and pharmacodynamics of antidiabetic drugs remains unclear. There are only substantially less data about the effects of diabetes mellitus on these properties of drugs for human, so the data obtained from the experimental animal models has extremely referential and practical values.

In this study, as shown in Table 4, the $AUC_{(0\text{-}t)}$ of morin, morusin, umbelliferone and mulberroside A in diabetic rats were 717.3 ± 117.4, 325.0 ± 87.6, 28.4 ± 3.6 and 75.6 ± 11.1 ng/mL*h, compared with 501.3 ± 115.5, 116.4 ± 38.2, 16.4 ± 5.1 and 36.8 ± 14.6 ng/mL*h in normal rats ($p < 0.05$). Meanwhile, the $AUC_{(0\text{-}\infty)}$ of the target analytes obtained from diabetic rats were also significant increased ($p < 0.05$), compared with those obtained from the normal rats. Significant differences in maximum concentration (C_{max}; 127.8 ± 56.0 vs 218.6 ± 33.5 ng/ml for

morin, 16.8 ± 10.1 vs 39.2 ± 5.9 ng/mL for morusin, 7.6 ± 0.7 vs 16.8 ± 6.6 ng/mL for umbelliferone and 13.1 ± 6.5 vs 28.5 ± 12.3 ng/ml for mulberroside A) were observed between normal and diabetic rats ($p < 0.05$). Compared with normal rats, the *MRT* increased by 56.5% ($p < 0.05$) in the diabetic rats for mulberroside A. In addition, the *CL*z/F were decreased by 33.7%, 40.2%, 53.2% and 34.0% for morin, morusin, umbelliferone and mulberroside A in the diabetic rats, respectively. In addition, the bimodal phenomenon appeared in the mean plasma concentration-time curves of morusin in diabetic rats. Many factors would lead to the results such as the changes of gastrointestinal tract, liver and kidney function, local blood flow rate caused by diabetes. The results indicated that the pharmacokinetics of four target analytes in diabetic rats was significantly changed and the bioavailability was enhanced.

Diabetes mellitus is one of the most grievous problems threatening public health. Not only are antidiabetic drugs more widely used, but the pharmacokinetics of these antidiabetic drugs may also be changed due to the disease itself (Gwiltet al., 1991). Diabetes affects the metabolism of the three major nutrients, including protein, lipid and carbohydrate, and the systems that regulate biotransformation pathways of these nutrients also participates in the regulation of drug metabolism *in vivo* in many cases. The researches show diabetes could influence all processes of drugs in the body, such as the absorption, distribution, metabolism and excretion of drugs (Zini et al., 1990; Okabe and Hashizume, 1994; Cashion et al., 2004). For absorption, the significantly reduced in digestive tract blood flow caused by diabetes could be associated with the change of gastric pH, the prolongation of gastric emptying time and slowing of intestinal peristalsis. The differences in the absorption rate and bioavailability between normal and diabetic rats might depend on the above factors (Horowitz and Fraser, 1994; Horowitz et al., 1996). The higher level of circulating glucose in the blood would lead to non-enzymatic glycation of several proteins including albumin, which could affect the plasma protein binding rate of drugs (Day et al., 1979; Cohen et al., 2006). In addition, diabetes could affect drug metabolism due to the abnormal hepatic function caused by diabetes including non-alcohol steatohepatitis, macrovesicular steatosis, liver fibrosis/cirrhosis and focal fatty liver. It was also one of the important reasons for the changes in pharmacokinetics of the target analytes from Mori Cortex total flavonoid extract *in vivo* (Petrides et al., 1994; Wang et al., 2000). Diabetes nephropathy occurred frequently and it would influence the glomerular filtration, tubular secretion and tubular reabsorption, so the influence of excretion on the pharmacokinetics of drugs was also worthy of attention (Raine, 1995; Suzuki and Arakawa, 1995).

There were lots of factors that lead to pharmacokinetic changes in diabetes and further investigations would be required to reveal the underlying mechanisms for pharmacokinetics and pharmacodynamics of four target analytes in Mori Cortex total flavonoid extract in diabetic rats.

5 Conclusion

In summary, we have developed and validated a reliable, accurate and rapid UPLC-MS/MS method for simultaneous determination of morin, morusin, umbelliferone and mulberroside A in rat plasma. Moreover, this method was successfully applied for pharmacokinetic comparisons in normal and diabetic rats. The results would provide the pharmacokinetic rationale for the pharmacology and toxicology research of Mori Cortex.

Data availability statement

The raw data supporting the conclusion of this article will be made available by the authors, without undue reservation.

Ethics statement

The animal study was reviewed and approved by Animal Ethics Committee of School of Pharmacy and Pharmaceutical Sciences & Institute of Materia Medica, Shandong First Medical University & Shandong Academy of Medical Sciences (Jinan, China).

Author contributions

All authors listed have made a substantial, direct, and intellectual contribution to the work and approved it for publication.

Funding

This study has been financially supported by Academic Promotion Program of Shandong First Medical University (No. 2019LJ003), Innovation Project of Shandong Academy of Medical Sciences; Natural Science Foundation of Shandong Province, (No. ZR2019MH051), Medical and Health Technology Development Program of Shandong Province (No. 202011000517) and Technology Innovation Development Project of Taian City (No. 2020NS165).

Conflict of interest

The authors declare that the research was conducted in the absence of any commercial or financial relationships that could be construed as a potential conflict of interest.

Publisher's note

Supplementary material

The Supplementary Material for this article can be found online at: https://www.frontiersin.org/articles/10.3389/fphar.2023.1148332/full#supplementary-material

References

Abbasa, G. M., Abdel Bara, F. M., Barakaa, H. N., Gohara, A. A., and Lahloub, M. F. (2014). A new antioxidant stilbene and other constituents from the stem bark of Morus nigra L. *Nat. Prod. Res.* 28 (13), 952–959. doi:10.1080/14786419.2014.900770

Ahmad, A., Gupta, G., Afzal, M., Kazmi, I., and Anwar, F. (2013). Antiulcer and antioxidant activities of a new steroid from Morus alba. *Life Sci.* 92 (3), 202–210. doi:10.1016/j.lfs.2012.11.020

Aras, A., Bursal, E., Türkan, F., Tohma, H., Kılıç, Ö., Gülçin, İ., et al. (2019). Phytochemical content, antidiabetic, anticholinergic, and antioxidant activities of endemic lecokia cretica extracts. *Chem. Biodivers.* 16 (10), e1900341. doi:10.1002/cbdv.201900341

Bayazid, A. B., Kim, J. G., Park, S. H., and Lim, B. O. (2020). Antioxidant, anti-inflammatory, and antiproliferative activity of Mori cortex radicis extracts. *Nat. Prod. Commun.* 15 (1), 1934578X1989976–8. doi:10.1177/1934578x19899765

Cashion, A. K., Holmes, S. L., Hathaway, D. K., and Gaber, A. O. (2004). Gastroparesis following kidney/pancreas transplant. *Clin. Transpl.* 18 (3), 306–311. doi:10.1111/j.1399-0012.2004.00167.x

Cohen, M. P., Ziyadeh, F. N., and Chen, S. (2006). Amadori-modified glycated serum proteins and accelerated atherosclerosis in diabetes: Pathogenic and therapeutic implications. *J. Lab. Clin. Med.* 147 (5), 211–219. doi:10.1016/j.lab.2005.12.006

Day, J. F., Thorpe, S. R., and Baynes, J. W. (1979). Nonenzymatically glucosylated albumin. *in vitro* preparation and isolation from normal human serum. *J. Biol. Chem.* 254 (3), 595–597. doi:10.1016/s0021-9258(17)37845-6

Food and Drug Administration (2018). *Bioanalytical Method Validation Guidance for Industry*. Available at: https://www.fda.gov/regulatory-information/search-fda-guidance-documents/bioanalytical-method-validation-guidance-industry (accessed 28 04, 2022).

Gregg, E. W., Sattar, N., and Ali, M. K. (2016). The changing face of diabetes complications. *Lancet Diabetes Endocrinol.* 4 (6), 537–547. doi:10.1016/S2213-8587(16)30010-9

Grienke, U., Richter, M., Walther, E., Hoffmann, A., Kirchmair, J., Makarov, V., et al. (2016). Discovery of prenylated flavonoids with dual activity against influenza virus and Streptococcus pneumoniae. *Sci. Rep.* 6, 27156. doi:10.1038/srep27156

Gwilt, P. R., Nahhas, R. R., and Tracewell, W. G. (1991). The effects of diabetes mellitus on pharmacokinetics and pharmacodynamics in human. *Clin. Pharmacokinet.* 20 (6), 477–490. doi:10.2165/00003088-199120060-00004

Horowitz, M., and Fraser, R. (1994). Disordered gastric motor function in diabetes mellitus. *Diabetologia* 37 (6), 543–551. doi:10.1007/BF00403371

Horowitz, M., Wishart, J. M., Jones, K. L., and Hebbard, G. S. (1996). Gastric emptying in diabetes: An overview. *Diabet. Med.* 13 (5), S16–S22.

Jia, W., Gao, W., and Tang, L. (2003). Antidiabetic herbal drugs officially approved in China. *Phytother. Res.* 17 (10), 1127–1134. doi:10.1002/ptr.1398

Kim, K. K., and Choe, M. (2017). Antidiabetic effects of water extract and fraction of Mori cortex. *FASEB J.* 31 (S1), 798–807. doi:10.1096/fasebj.31.1_supplement.798.7

Kooti, W., Farokhipour, M., Asadzadeh, Z., Ashtary-Larky, D., and Asadi-Samani, M. (2016). The role of medicinal plants in the treatment of diabetes: A systematic review. *Electron Physician* 8 (1), 1832–1842. doi:10.19082/1832

Li, B., Lu, M., Chu, Z., Lei, S., Sun, P., Xiong, S., et al. (2019). Evaluation of pharmacokinetics, bioavailability and urinary excretion of scopolin and its metabolite scopoletin in Sprague Dawley rats by liquid chromatography–tandem mass spectrometry. *Biomed. Chromatogr.* 33 (12), e4678. doi:10.1002/bmc.4678

Lim, H. J., Jin, H. G., Woo, E. R., Lee, S. K., and Kim, H. P. (2013). The root barks of Morus alba and the flavonoid constituents inhibit airway inflammation. *J. Ethnopharmacol.* 149 (1), 169–175. doi:10.1016/j.jep.2013.06.017

Lim, S. L., Park, S. Y., Kang, S., Park, D., Kim, S. H., Um, J. Y., et al. (2014). Morusin induces cell death through inactivating STAT3 signaling in prostate cancer cells. *Am. J. Cancer. Res.* 5 (1), 289–299.

Liu, J., Mu, Y., Xiong, S., Sun, P., and Deng, Z. (2019). A UPLC-MS/MS method for comparative pharmacokinetics study of morusin and morin in normal and diabetic rats. *Biomed. Chromatogr.* 33 (7), e4516. doi:10.1002/bmc.4516

Ma, L. L., Yuan, Y. Y., Zhao, M., Zhou, X. R., Tashina, J., Wang, F. Y., et al. (2018). Mori Cortex extract ameliorates nonalcoholic fatty liver disease (NAFLD) and insulin resistance in high-fat-diet/streptozotocin-induced type 2 diabetes in rats. *Chin. J. Nat. Med.* 16 (6), 411–417. doi:10.1016/S1875-5364(18)30074-8

Maritim, A. C., Sanders, R. A., and Watkins, J. B., 3rd (2003). Diabetes, oxidative stress, and antioxidants: A review. *J. Biochem. Mol. Toxicol.* 17 (1), 24–38. doi:10.1002/jbt.10058

Martel, J., Ojcius, D. M., Chang, C. J., Lin, C. S., Lu, C. C., Ko, Y. F., et al. (2017). Anti-obesogenic and antidiabetic effects of plants and mushrooms. *Nat. Rev. Endocrinol.* 13 (3), 149–160. doi:10.1038/nrendo.2016.142

O'Brien, I. A., and Corrall, R. J. (1988). Epidemiology of diabetes and its complications. *N. Engl. J. Med.* 318 (24), 1619–1620. doi:10.1056/nejm198806163182414

Okabe, N., and Hashizume, N. (1994). Drug binding properties of glycosylated human serum albumin as measured by fluorescence and circular dichroism. *Biol. Pharm. Bull.* 17 (1), 16–21. doi:10.1248/bpb.17.16

Petrides, A. S., Vogt, C., Schulze-Berge, D., Matthews, D., and Strohmeyer, G. (1994). Pathogenesis of glucose intolerance and diabetes mellitus in cirrhosis. *Hepatology* 19 (3), 616–627. doi:10.1002/hep.1840190312

Qi, S. Z., Li, N., Tuo, Z. D., Li, J. L., Xing, S. S., Li, B. B., et al. (2016). Effects of Morus root bark extract and active constituents on blood lipids in hyperlipidemia rats. *J. Ethnopharmacol.* 180, 54–59. doi:10.1016/j.jep.2016.01.024

Raine, A. E. (1995). The rising tide of diabetic nephropathy: The warning before the flood? *Nephrol. Dial. Transpl.* 10 (4), 460–461. doi:10.1093/ndt/10.4.460

Riaz, S. (2009). Diabetes mellitus. *Sci. Res. Essays.* 44 (5), 367–373. doi:10.1007/s15006-013-0393-3

Seke Etet, P. F., Farahna, M., Satti, G. M. H., Bushara, Y. M., El-Tahir, A., Hamza, M. A., et al. (2017). Garcinia kola seeds may prevent cognitive and motor dysfunctions in a type 1 diabetes mellitus rat model partly by mitigating neuroinflammation. *J. Complement. Integr. Med.* 14 (3), 20160167. doi:10.1515/jcim-2016-0167

Suzuki, Y., and Arakawa, M. (1995). The treatment of the uraemic diabetic. Are we doing enough? A view from Japan. Fumitake gejyo and collaborate study group. *Nephrol. Dial. Transpl.* 10 (7), 47–55. doi:10.1093/ndt/10.supp7.47

The Committee of China Pharmacopeia (2020). *China Pharmacopeia, section I*. China Medical Science Press, 311.

Tong, X. L., Dong, L., Chen, L., and Zhen, Z. (2012). Treatment of diabetes using traditional Chinese medicine: Past, present and future. *Am. J. Chin. Med.* 40 (5), 877–886. doi:10.1142/S0192415X12500656

Wang, P. C., Zhao, S., Yang, B. Y., Wang, Q. H., and Kuanga, H. X. (2016). Anti-diabetic polysaccharides from natural sources: A review. *Carbohydr. Polym.* 148, 86–97. doi:10.1016/j.carbpol.2016.02.060

Wang, T., Fontenot, R. D., Soni, M. G., Bucci, T. J., and Mehendale, H. M. (2000). Enhanced hepatotoxicity and toxic outcome of thioacetamide in streptozotocin-induced diabetic rats. *Toxicol. Appl. Pharmacol.* 166 (2), 92–100. doi:10.1006/taap.2000.8952

Xiao, B. X., Wang, Q., Fan, L. Q., Kong, L. T., Guo, S. R., and Chang, Q. (2014). Pharmacokinetic mechanism of enhancement by Radix Pueraria flavonoids on the hyperglycemic effects of Cortex Mori extract in rats. *J. Ethnopharmacol.* 151 (2), 846–851. doi:10.1016/j.jep.2013.11.038

Xiong, S., Xue, M., Mu, Y., Deng, Z., Sun, P., and Zhou, R. (2017). Determination of AZD3759 in rat plasma and brain tissue by LC-MS/MS and its application in pharmacokinetic and brain distribution studies. *J. Pharm. Biomed. Anal.* 140, 362–366. doi:10.1016/j.jpba.2017.03.056

Zhang, S., Li, H., Zhang, L., Li, J., Wang, R., and Wang, M. (2017). Effects of troxerutin on cognitive deficits and glutamate cysteine ligase subunits in the hippocampus of streptozotocin-induced type 1 diabetes mellitus rats. *Brain Res.* 1657, 355–360. doi:10.1016/j.brainres.2016.12.009

Zini, R., Riant, P., Barré, J., and Tillement, J. P. (1990). Disease-induced variations in plasma protein levels: Implications for drug dosage regimens (part I). *Clin. Pharmacokinet.* 19 (2), 147–159. doi:10.2165/00003088-199019020-00004

frontiers | Frontiers in Pharmacology

TYPE Original Research
PUBLISHED 21 March 2023
DOI 10.3389/fphar.2023.1130287

OPEN ACCESS

EDITED BY
Guo Ma,
Fudan University, China

REVIEWED BY
Bhawana Rastogi,
Swami Vivekanand Subharti University, India
Mellar Pilgrim Davis,
Geisinger Health System, United States

*CORRESPONDENCE
Mingxia Wang,
mxia_wang@163.com
Li Jia,
281575038@qq.com

SPECIALTY SECTION
This article was submitted to Drug Metabolism and Transport, a section of the journal Frontiers in Pharmacology

RECEIVED 23 December 2022
ACCEPTED 10 March 2023
PUBLISHED 21 March 2023

CITATION
Nie X, Gao X, Gao J, Heng T, Zhang Y, Sun Y, Feng Z, Jia L and Wang M (2023), Population pharmacokinetics of nalbuphine in patients undergoing general anesthesia surgery.
Front. Pharmacol. 14:1130287.
doi: 10.3389/fphar.2023.1130287

Population pharmacokinetics of nalbuphine in patients undergoing general anesthesia surgery

Xuyang Nie[1], Xiaonan Gao[1], Jinglin Gao[1], Tianfang Heng[2], Yuqi Zhang[2], Yaqi Sun[1], Zhangying Feng[1], Li Jia[2]* and Mingxia Wang[1]*

[1]Department of Clinical Pharmacology, The Fourth Hospital of Hebei Medical University, Shijiazhuang, China, [2]Department of Anesthesiology, The Fourth Hospital of Hebei Medical University, Shijiazhuang, China

Purpose: The aim of this study was to build a population pharmacokinetics (PopPK) model of nalbuphine and to estimate the suitability of bodyweight or fixed dosage regimen.

Method: Adult patients who were undergoing general anesthetic surgery using nalbuphine for induction of anesthesia were included. Plasma concentrations and covariates information were analyzed by non-linear mixed-effects modeling approach. Goodness-of-fit (GOF), non-parametric bootstrap, visual predictive check (VPC) and external evaluation were applied for the final PopPK model evaluation. Monte Carlo simulation was conducted to assess impact of covariates and dosage regimens on the plasma concentration to nalbuphine.

Results: 47 patients aged 21–78 years with a body weight of 48–86 kg were included in the study. Among them, liver resection accounted for 14.8%, cholecystectomy for 12.8%, pancreatic resection for 36.2% and other surgeries for 36.2%. 353 samples from 27 patients were enrolled in model building group; 100 samples from 20 patients were enrolled in external validation group. The results of model evaluation showed that the pharmacokinetics of nalbuphine was adequately described by a two-compartment model. The hourly net fluid volume infused (HNF) was identified as a significant covariate about the intercompartmental clearance (Q) of nalbuphine with objective function value (OFV) decreasing by 9.643 ($p < 0.005$, $df = 1$). Simulation results demonstrated no need to adjust dosage based on HNF, and the biases of two dosage methods were less than 6%. The fixed dosage regimen had lower PK variability than the bodyweight regimen.

Conclusion: A two-compartment PopPK model adequately described the concentration profile of nalbuphine intravenous injection for anesthesia induction. While HNF can affect the Q of nalbuphine, the magnitude of the effect was limited. Dosage adjustment based on HNF was not recommended. Furthermore, fixed dosage regimen might be better than body weight dosage regimen.

KEYWORDS

Nalbuphine, Population pharmacokinetics, NONMEM, induced anesthesia, general anesthesia surgery

1 Introduction

Surgery is an essential component of global healthcare. In 2008, researchers found that approximately 234.2 million major operations were performed annually (Weiser et al., 2008). In clinic, patients are usually given a combination of sedatives and opioid analgesics for the induction of intravenous anesthesia before surgery. However, analgesic drugs commonly used in anesthesia induction, such as fentanyl, sufentanil and remifentanil, are often accompanied by adverse reactions such as cough, dizziness, respiratory depression and hemodynamic instability (Hirsch et al., 2015; Shuying et al., 2016).

As a semi-synthetic opioid analgesic with analgesic potency comparable to morphine, nalbuphine is primarily used to prevent and treat moderate to severe pain, including pain treatment before to surgery, following surgery, and during childbirth (Errick and Heel, 1983). Notably, unlike other opioids, nalbuphine can not only activate κ opioid receptors, but also partially antagonize μ opioid receptors (Schmidt et al., 1985). Due to this distinct hybrid agonist-antagonist opioid receptor activity, nalbuphine provides analgesia with fewer side effects. Firstly, nalbuphine has a "capping effect" on respiratory inhibition when the dose exceeds 0.3–0.5 mg/kg (Giannina et al., 1995). Secondly, after the use of nalbuphine in general anesthesia, patients were hemodynamically stable during surgery, recovered consciousness rapidly after surgery, and had a low incidence of nausea, vomiting and emergence agitation (Sear et al., 1987; Dalens et al., 2006; Chawda et al., 2010; Kubica-Cielinska and Zielinska, 2015). Additionally, nalbuphine is efficient in reducing propofol dosage and the pain associated with its injection, and in reducing the sensitivity of postoperative pain caused by high doses of remifentanil or sufentanil (He et al., 2021). Thus, nalbuphine also has been widely used in the induction and maintenance of general anesthesia.

Nalbuphine has been used clinically for more than 40 years, and its pharmacokinetics (PK) had been extensively studied in infants, children, healthy adult and elderly patients, but remain limited in patients undergoing general anesthesia surgery. Sear et al. (1987) found that nalbuphine exhibited lower total clearance (CL) and apparent volume of distribution (V_d) in anesthetized patients compared with the results obtained in awake volunteers. Similarly, our previous study (Gao et al., 2022) found that nalbuphine CL(33.42 L/h) and V_d (137.69 L) were significantly lower in patients undergoing general anesthesia than in healthy patients (CL 90.0 L/h; V_d 326.5 L) (He et al., 2021), regardless of whether the patient had liver dysfunction. However, neither of these studies analyzed the reasons for the above-mentioned results. Thus, it is necessary to further explore the factors that affect the PK of nalbuphine during general anesthesia surgery.

In addition, the choice of nalbuphine dosage regimens is also an issue worth to be discussed. Wang et al. (2022) found that the PK variability of the drug was lower for fixed-dose dosage regimens than that for weight-based dosage regimens. Previous studies had shown that weight of neonates and children is a significant factor affecting nalbuphine PK behavior (Jacqz-Aigrain et al., 2003; Bressolle et al., 2011). In China, nalbuphine is also recommended to be administered by body weight (0.2 mg/kg) for induction of anesthesia in clinic and drug package insert. However, nalbuphine is often administered at a fixed dose (10–20 mg) in many PK studies in adults (Sear et al., 1987; He et al., 2021). Thus, it also needs to be considered whether it is necessary to administer nalbuphine by weight when used for induction of anesthesia.

Population pharmacokinetics (Pop PK) analysis is a valid and scientific method for describing PK behavior and identifying sources of variability, and that plays an increasing role in clinical drug studies. Although PopPK of nalbuphine has been reported in studies from neonates to children undergoing general anesthesia and post-surgery (Bressolle et al., 2011; Pfiffner et al., 2022), adult patients undergoing general anesthesia surgery has not been included in their studies. Therefore, the purpose of this study was to analyze the factors affecting the PK of nalbuphine in adult patients undergoing general anesthesia using PopPK analysis method, and to perform dosage regimen simulations to evaluate and optimize the clinical dosing strategy for this study population.

2 Materials and methods

2.1 Study design

Participants were patients who scheduled for elective surgery at the Fourth Hospital of Hebei Medical University in 2021. Exclusion criteria were 1) allergic to nalbuphine, 2) contraindications to general anesthesia, 3) III and IV grades of intubation according to the Mallampati classification, 4) a history of asthma, chronic pain or chronic cough, 5) known or suspected cardiopulmonary, renal or metabolic disease, 6) pregnant, 7) long-term opioid medications, and 8) excessive intraoperative bleeding. A total of 47 patients were recruited in this research. Among them, twenty-seven patients who received intensive PK sampling were used for build model. The remaining 20 patients were used for external verification of PopPK model.

Before operation, all patients were routinely fasted overnight, and did not use sedative or analgesic drugs within 24 h. After entering the operating room, the electrocardiogram (ECG), heart rate (HR), saturation of pulse oximetry (SpQ2) and bispectral index (BIS) of patients were continuously monitored. Then radial artery puncture was performed under local anesthesia and was used to monitor the mean arterial pressure of patients. The left and peripheral vein were opened for drug injection and blood collection, respectively. Anesthesia induction was performed after preoxygenation 5 min with 100% oxygen. Nalbuphine (Yichang Human well Pharmaceutical, Hubei, China) 15 mg was injected over 2–3 min, followed by 0.05 mg/kg midazolam, 0.2 μg/kg sufentanil, 0.03 mg/kg etomidate, and cisatracurium 0.2 mg/kg. After tracheal intubation, anesthesia was maintained with sevoflurane and remifentanil, and intermittent injections of cis-atracurium were used to maintain inotropy.

This study was conducted in accordance with principles in the Declaration of Helsinki, and was approved by the ethics committee of the Fourth Hospital of Hebei Medical University, Shijiazhuang, China (No. 2019121). Informed consent was obtained from all participants (Gao et al., 2022).

2.2 Sampling and bioanalytical methods

Blood samples (2 mL) were drawn: before dosing and at 3, 5, 10, 15, 30 and 45 min and 1, 1.5, 2, 3, 4, 5, 6 and 12 h after nalbuphine administration for modelbuilding group; before dosing, during endotracheal intubation and at 1, 3 and 10 min after endotracheal intubation for external validation group.

The blood samples were heparinized and centrifuged, with plasma samples stored at −80°C until analysis. Plasma nalbuphine concentrations were measured using a validated ultra-performance liquid chromatography-tandem mass spectrometry (UPLC-MS/MS) method after protein precipitation with acetonitrile. The lower limit of quantitation (LLOQ) was 0.1 ng/mL. The calibration range was 0.1–500 ng/mL (Gao et al., 2022).

2.3 Population pharmacokinetic model development

Non-linear mixed effect modelling was performed by NONMEM® (version 7.5.0) interfaced by MaS studio (version 1.6.0.5) and Perl-speaks-NONMEM (PsN, version 5.2.6) toolkit. Statistical analyses and graphical visualizations of NONMEM output post-processing were carried out with RStudio (version 1.2.5033) using R software (version 4.2.1).

2.3.1 Basic structure model

Based on graphical exploratory analysis, the plasma concentrations of nalbuphine were modeled by one- and two-compartment models using first-order conditional estimation with the η–ε interaction (FOCE-I) method. Between-subject variability (BSV), as a structural pharmacokinetic parameter, was assumed to be log-normally distributed and was applied by exponential model. For estimating the residual unexplained variability (RUV), three models were tested, including proportional, additive and a combination of a proportional error model and an additive error model.

The optimal structural model selection was based upon objective function value (OFV), precision of parameter estimates and visual inspection of goodness-of-fit (GOF) plots for nested models, and Akaike's Information Criterion (AIC) for non-nested models.

2.3.2 Covariate model

The demographic statistics information, disease information and clinical laboratory measurements were collected as potential covariates. Only the covariates with missing values less than 20% of patients were included in covariate evaluation.

The correlation between covariates and covariates, covariates and PK parameters were firstly investigated using statistical and graphical method. When correlations existed between covariates (correlation coefficient > 0.7), only one of the covariates more commonly used clinically could be included in subsequent analyses to avoid multicollinearity and instability of parameter estimates. A stepwise forward inclusion and backward elimination process were then tested formally.

In forward inclusion process, covariates were added individually to the basic model one by one. Continuous covariates were tested by a linear function (Eq. 1), a power function (Eq. 2), or an exponential function (Eq. 3), while categorical covariates were assessed by Eq. 4. And the covariate would be included in the basic model if the OFV decrease more than 3.84 ($p < 0.05$, $df = 1$). All covariates that individually had a potential influence on the basic model were available after the first step of inclusion. The model with most decreasing OFV could be used as the base covariate model for subsequent analysis. Then each of potentially influencing covariates was added to the base covariate model and a decrease of OFV exceeding 6.63 was considered to be significant ($p < 0.01$, $df = 1$). A full model was constructed when all significant covariates were incorporated into the basic model. In backward elimination process, covariates from the full model were removed one at a time. An increase of OFV > 7.88 ($p < 0.005$, $df = 1$) was considered as a criterion to retain a covariate in model. The final model was formed when basic model combined with all covariates that met the above statistical criteria and had an impact over 20% on the parameter.

$$\theta_i = \theta_1 + \theta_2 \cdot \left(cov_i / cov_{median}\right) \quad (1)$$

$$\theta_i = \theta_1 \cdot \left(cov_i / cov_{median}\right)^{\theta_2} \quad (2)$$

$$\theta_i = \theta_1 \cdot \theta_2^{\left(cov_i / cov_{median}\right)} \quad (3)$$

$$\theta_i = \theta_1 \cdot \theta_2^{cov_i} \quad (4)$$

where θ_i describe the pharmacokinetic parameter value for the individual i; θ_1, and θ_2 describe the typical value of a pharmacokinetic parameter; cov_{i} and cov_{median} describe covariate values for the ith individual and the population median, respectively.

2.3.3 Model evaluation

GOF, non-parametric bootstrap and visual predictive check (VPC) were applied for internal model evaluation (Nguyen et al., 2017).

GOF plots were used to evaluated model fitness, including prediction-based diagnostic plots [observation versus population prediction (PRED), observation versus individual prediction (IPRED)] and residual-based model diagnostic plots (conditional weighted (CWRES) versus PRED, CWRES versus time). When data points were randomly distributed near y = x in the prediction-based diagnostic plots and most of the CWRES were within ± 2 in the residual-based model diagnostic plots, and the locally weighted regression (LOESS) lines did not show obvious bias, suggesting that the model well described the trend of data concentration. Note that the DV-IPRED diagnostic map can be applied as a basis for model evaluation only when the contraction value of the residual variance was less than 30%.

Non-parametric bootstrap was performed for final model with 1,000 times resampling. The median and the 2.5th and 97.5th percentiles of the PopPK parameter estimates from successfully minimized resampled datasets were compared with the final model parameter estimates. If the 95% confidence interval for each parameter contains the final model parameters and the proportion of successful model minimization (robustness rate) > 80%, the model is stable and the parameters have high confidence.

In order to adjust for differences of independent variables, a prediction corrected visual predictive check (pcVPC) method was conducted by simulating 1,000 datasets based on the final model, and used to evaluate the variability and central tendency between the observed and simulated data. The median and 5th and 95th percentiles of the prediction corrected simulated data were compared with that of the prediction corrected observed data. When the number of observations falling outside the simulation-based 90% prediction interval was less than 10%, the model could be considered to have a high prediction accuracy.

In addition, the final model was externally evaluated using the following two datasets: external evaluation dataset without observations and external evaluation dataset within the first observation of each subject. The relative prediction error (PE%), the median prediction error (MDPE), the median absolute prediction error (MAPE) and the percentage of PE% falling within the ± 20% and ± 30% were calculated to reflect accuracy and precision of the final model. The model was considered to be predictive and clinically acceptable when the standards of MDPE ≤ ± 20%, MAPE ≤ ± 30%, F_{20} ≥ 35% and F_{30} ≥ 50% were reached.

2.3.4 Simulations

2.3.4.1 The evaluation of the effect of covariates on the PK of nalbuphine

Based on the final model, a Monte Carlo simulation approach was used to evaluate the effect of different levels of covariates on the PK of nalbuphine following 15 mg or 0.2 mg/kg intravenous injection once only. The various covariates levels were set as 10th, 50th and 90th percentile of the model building population. The Monte Carlo simulation was run 1,000 times at each covariate level.

2.3.4.2 Dosage regimen simulation and statistical analysis

In this study, fixed dose regimen (15 mg) was explored in patients undergoing anesthesia surgery based on published literature (Cai et al., 2011; He et al., 2021). To assess the appropriateness of fixed dosage or bodyweight dosage strategies on the PK of nalbuphine in patients undergoing general anesthesia, two dosing regimens, 12 mg and 0.2 mg/kg, were selected for the study based on the drug instructions.

Based on the final model, PK profiles of two dose regimens were simulated for 1,000 times, respectively, applying the weight and the HNF information of 27 patients from the model-building dataset. The sampling time was set at pre-dose and 0.05, 0.08, 0.17, 0.25, 0.5, 0.75, 1, 2, 3, 4, 6, 8, 10 and 12 h after dosing. Statistical analyses were used to compare the concentration at the 0.05 h, 12 h and median operation time of fixed dosage regimen with that of bodyweight dosage regimen; Scatter plots were used to show the PK profiles of nalbuphine of two dosage regimens.

2.4 The effectiveness and safety outcomes of patients

Hemodynamic indices and sedation levels were recorded for all patients around the administration of nalbuphine, around tracheal intubation and intraoperatively; adverse effects such as respiratory depression, agitation, nausea and vomiting were recorded for patients intraoperatively and postoperatively.

3 Results

3.1 Patients and datasets

Blood samples from patients used for the model building group were collected according to the study design. Blood samples from patients used for the external validation group were collected by our anesthesiology researcher at a later stage of the model construction according to the same dosing protocol. Due to the difficulty of obtaining clinical samples and in the principle of maximizing the use of clinical sample resources, this data was obtained after communication with the anesthesiology researchers. Because of its sparse sampling sites, it was only used for external validation. In this study, a total of 458 plasma concentrations were collected from 48 patients. The concentrations of all samples except pre-dose time were more than the LLOQ. And no data were recognized as outliers. However, one subject with 5 samples was excluded due to the lack of HNF in external validation group. In total, there were 27 patients with 353 samples and 20 patients with 100 samples in model building group and external validation group, respectively.

The 47 patients enrolled were aged 21–78 years and weighed 48–86 kg. 29.8% of patients underwent lumpectomy and 70.2% underwent open surgery. Among them, liver resection accounted for 14.8%, cholecystectomy for 12.8%, pancreatic resection for 36.2% and other surgeries for 36.2%. The demographic statistics information, disease information and clinical laboratory measurements of two groups were listed in Table 1. The concentration versus time profile of building group was displayed in Figure 1.

3.2 Population pharmacokinetic model

A two-compartment model was selected as the basic structure model based on results from the model building dataset and previously published data. Compared with one-compartment model, it decreased AIC by 519.209, and had a good GOF diagnosis plot (Figure 2). The model was parameterized by CL, volume of distribution for the central compartment (V_1), intercompartmental clearance (Q) and volume of distribution for the peripheral compartment (V_2). The BSV was incorporated into all parameters using exponential model. The RUV was described by a combination of a proportional error model and an additive error model. The Population pharmacokinetic parameter estimates of nalbuphine of the basic model were shown in Table 2.

After correlation analysis, strong correlations (R > 0.7) were found between sex and height; weight and body mass index (BMI); Aspartate aminotransferase (AST), Albumin (ALB), Gamma-glutamyl transferase (GGT) and alanine aminotransferase (ALT); ALB, Globulin (GLB) and total protein (TP) (Figure 3). These strongly correlated covariates were avoided to be included in the model at the same time. During the forward inclusion process, ALT and hourly net fluid volume infused (HNF) were identified to be a significant covariate on CL and Q, respectively. However, only HNF was remained in model with OFV decreasing by 9.643 in the backward elimination process. The stepwise process of building the PopPK model of nalbuphine were shown in Table 3. Parameter estimates of the final model were shown in Table 4 and the equations were as below:

$$CL\ (L/h) = 32.9$$
$$V1\ (L) = 32.5$$
$$Q\ (L) = 245 \cdot (HNF/617.96)^{-0.58}$$
$$V2\ (L) = 83.5$$

TABLE 1 Baseline demographics characteristics and clinical laboratory measurements of patients included in the analysis.

	Model-building dataset	External validation dataset
Number of patients	27	20
Number of concentrations	353	100
Dose (mg/kg)	0.24 ± 0.04, (0.24, 0.18–0.31)	0.24 ± 0.05, (0.2, 0.18–0.32)
Age (years)	53.85 ± 16.63, (58, 21–76)	52.5 ± 13.56, (54.5, 27–78)
Height (cm)	163.96 ± 6.87, (165, 153–175)	159.85 ± 8.05, (157.5, 148–175)
Total body weight (kg)	63.32 ± 9.3, (62, 48–82)	62.25 ± 9.67, (59.5, 50.8–86)
Body mass index (kg/m^2)	23.54 ± 3, (23.23, 16.61–30.12)	24.2 ± 2.77, (23.28, 20.8–29.9)
Systolic pressure (mmHg)	138.8 ± 17.22, (138, 102–170)	135.21 ± 13.83, (138, 117–160)
Diastolic pressure (mmHg)	77.26 ± 9.27, (78, 60–92)	75 ± 10.06, (75.5, 60–92)
Heart rate (/min)	71.37 ± 14.48, (70, 50–110)	83.05 ± 9.83, (79, 70–100)
Alanine aminotransferase (U/L)	58.86 ± 69.62, (23.6, 6–260.9)	35.37 ± 52.46, (15.45, 5.5–200.9)
Aspartate aminotransferase (U/L)	42.16 ± 33.64, (24.4, 10.6–128.7)	28.4 ± 27.28, (18.75, 9.6–113.7)
Gamma-glutamyl transferase (U/L)	191.87 ± 319.87, (77.2, 8.4–1,493.2)	129.93 ± 286.12, (18, 8.4–1,219.1)
Total protein (g/L)	66.79 ± 8.67, (66.3, 50–82)	70.95 ± 5.8, (72, 58.5–78.9)
Albumin (g/L)	40.29 ± 5.63, (40.8, 29.2–50.7)	40.73 ± 5.03, (42.1, 29.5–48.1)
Globulin (g/L)	26.51 ± 4.84, (26.4, 15–35.9)	30.22 ± 3.49, (30.1, 24.1–38.8)
Total bilirubin (μmol/L)	25.83 ± 28.65, (13.18, 3.7–104.34)	26.47 ± 40.57, (10.07, 5.51–169.9)
Serum creatinine (μmol/L)	56.69 ± 14.47, (55.9, 34–90.1)	48.92 ± 15.44, (48.85, 23.6–98.9)
Creatinine clearance (mL/min)	111.19 ± 27.38, (105.14, 53.4–160.98)	130.38 ± 45.6, (124.01, 65.72–263.83)
Uric acid (μmol/L)	281.46 ± 90.59, (297.5, 124.4–463.3)	259.11 ± 80.71, (247.7, 152.1–428.9)
Hemoglobin (g/L)	123.83 ± 22.03, (124, 87–178)	119.94 ± 25.88, (122.5, 71–162)
D dimer (mg/L)	0.27 ± 0.42, (0.1, 0.02–2.02)	0.34 ± 0.63, (0.16, 0.03–2.57)
Hourly net fluid volume infused (mL/h)	617.96 ± 247.61, (563.56, 234.26–1,202.25)	634.19 ± 178.94, (610.42, 314.29–1,047.24)
Operation duration (h)	4.31 ± 1.9, (4, 0.83–8.33)	3.59 ± 1.78, (3.05, 1.27–7.85)
Female	15 (55.6%)	14 (70%)
Smoke	11 (40.7%)	2 (10%)
Drink	11 (40.7%)	1 (5%)
Tumor	21 (77.8%)	17 (85%)
Hepatobiliary disease	15 (55.6%)	7 (35%)
Hypertension	7 (25.9%)	6 (30%)
CTP-B	5 (18.5%)	4 (20%)
Laparoscopic surgery	8 (29.6%)	6 (30%)

Data were expressed as mean ± standard deviation (median, range) for continuous covariates, and number (percentage) for categorical covariates. Creatinine clearance was calculated with Cockcroft-Gault formula for male as followed: $CL_{Cr}\,(mL \cdot min^{-1}) = (140 - AGE) \times WT\,(kg) \div (S_{Cr}\,(\mu mol \cdot L^{-1}) \times 0.81)$ Creatinine clearance in female = male value × 0.85. Hourly net fluid volume infused (HNF) was calculated with the following formula:HNF = (FVI + BVI − UVO) ÷ OT where FVI, BVI, and UVO, was fluid volume infused, blood volume infused, and urine volume output during surgery, respectively. OT, was operation time. CTP-B: Number of patients with a liver function class of B according to Child-Turcotte-Pugh (CTP) classification; the others were class A.

All relative precision of the final fixed-effect parameter estimates were less than 30%, and that of the final random-effect parameter estimates were less than 50%. All shrinkages of BSV and RUV except BSV on Q (30.72%) were less than 20%. These suggested that the parameter estimates were reliable. It was worth noting that HNF as a covariate of Q has led to a decrease in BSV from 35.5% to 17.9%, indicating that 17.6% of BSV in Q was explained by HNF.

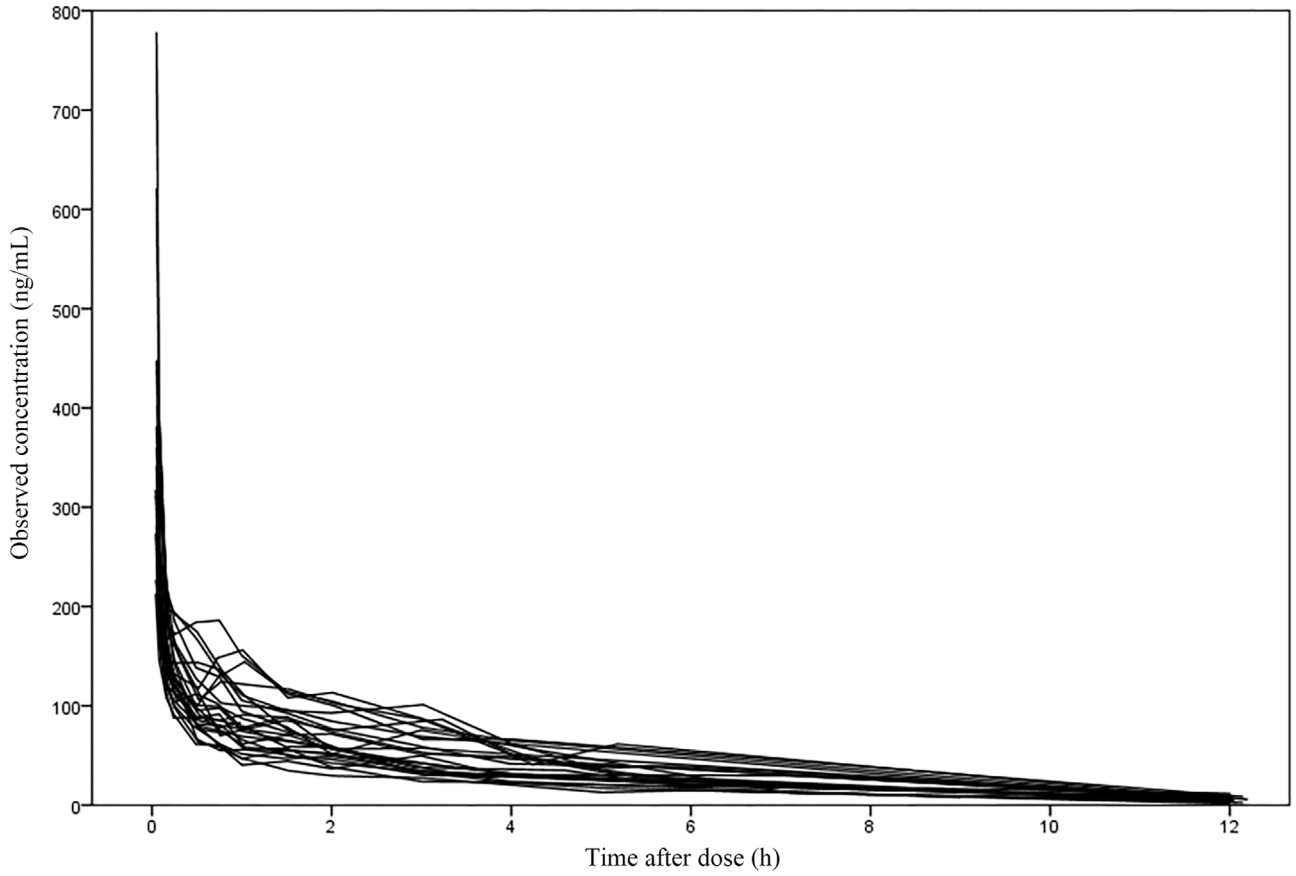

FIGURE 1
The concentration-time profile of nalbuphine in the building group (27 subjects with 353 samples).

3.3 Model evaluation

The GOF diagnostic plots of the final model was presented in Figure 4. Compared to the basic model, the fitting of IPRED vs. DV and PRED vs. DV plots were improved slightly. The CWRES in the final model was randomly distributed near CWRES = 0 and most of the CWRES were within ± 2, and did not show obvious trends with time, suggesting that the final model well described the trend of data concentration.

The bootstrap with 1,000 times resampling was used to verify the final model, and 984 times of them were successfully minimized. The biases between the final model parameter estimates and the bootstrapped median values were less than 8%. And all of the final model parameter estimates were within 95% confidence interval of the bootstrapped values (Table 4).

The pc-VPC plots was presented in Figure 5. The median, 5th and 95th percentiles of the prediction corrected observed nalbuphine concentrations largely overlapped with the 95% confidence interval of the corresponding prediction corrected predicted values from the simulation data. The final model could reasonably describe the observed data.

As shown in Table 5, the results of external validation of the final model in both scenarios met pre-defined criteria. Compared with validating using datasets with no observations, adding the first observation of each patient to the external validation dataset could reduce MDPE and MAPE by 4.05% and 9.72%, respectively, and increase F_{20} and F_{30} by 28.57% and 22.62%, respectively. The scatterplot of observed versus individual predicted concentrations of two scenarios were presented in Figure 6. All these results showed that the final model sufficiently described the PK of nalbuphine.

3.4 Simulation results

3.4.1 The evaluation of the effect of covariates on the PK of nalbuphine

According to the final PopPK model, HNF was the only significant covariate that had an effect on the PK of nalbuphine. Figure 7 showed the predicted concentration profiles for patient populations who were in the 10th, 50th, and 90th percentiles of HNF of the model building population (350.1, 563.6 and 973.4 mL/h, respectively). The simulation results revealed that HNF had limited impact on plasma concentration of nalbuphine.

3.4.2 Dosage regimen simulation and statistical analysis

The results of dosage regimen simulation were presented in Table 6. For two dosage regimens, the bias of C_{min} (0.05 h), C_{median} (4 h) and C_{max} (12 h) means were less than 6%. However, the scatterplot of the predicted concentrations versus time (0–12 h) of two dosage regimens

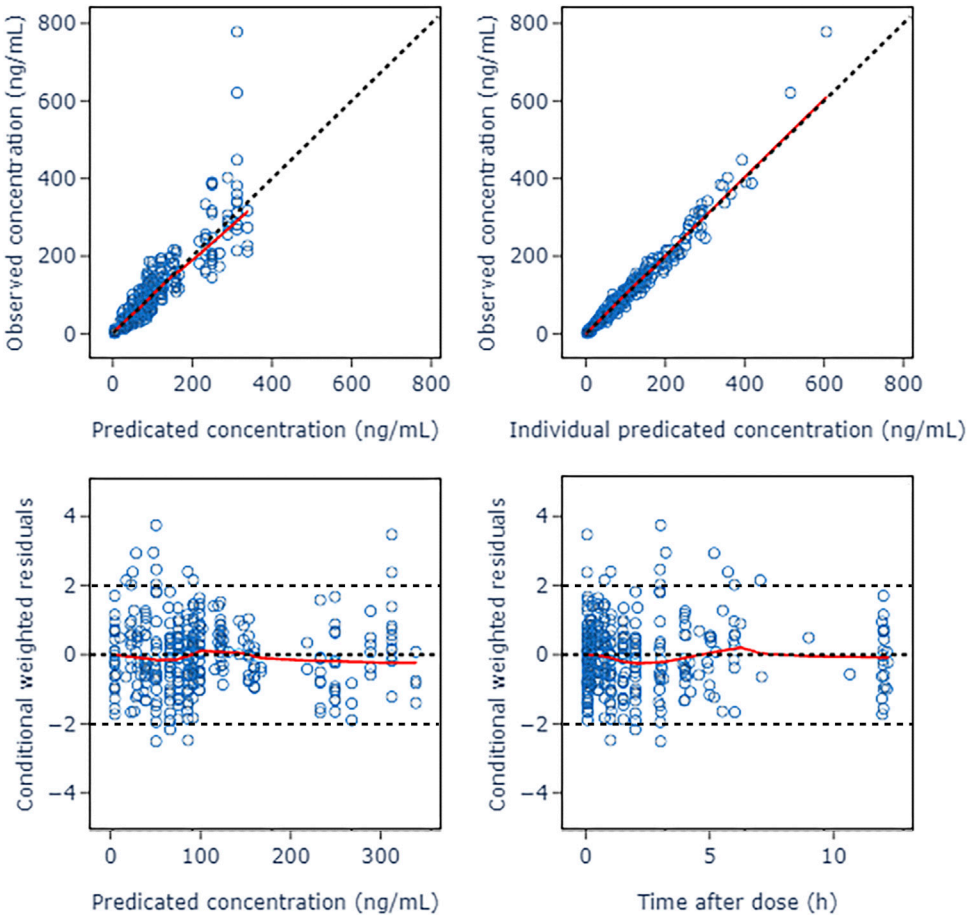

FIGURE 2
Goodness of fit plots of nalbuphine basic PopPK model. The red lines represent the locally weighted scatterplot with smoothing.

TABLE 2 Population pharmacokinetic parameter estimates of nalbuphine of the basic model.

Parameter	Estimates	RSE (%)	SHRINKSD (%)
Structural model parameter			
CL	32.9	5.5	—
V_1	31	9.9	—
Q	261	8.1	—
V_2	85.9	7.1	—
Between-subject variability			
ωCL (%CV)	27.7	12.4	4.2
ωV_1 (%CV)	38.9	24.2	17.0
ωQ (%CV)	35.5	17.2	10.9
ωV_2 (%CV)	36.5	11.7	4.5
Residual unexplained variability			
Proportional error (%CV)	13.7	8.0	13.8
Additive error (ng/mL)	2.90	20.5	13.8

RES: relative standard error; CL: total clearance (L/h); V_1: volume of distribution for the central compartment (L); Q: intercompartmental clearance (L/h); V_2: volume of distribution for the peripheral compartment (L); ω_{CL}, ω_{V1}, ω_Q and ω_{v2}: the estimates of between-subject variability of CL, V_1, Q and V_2, respectively.

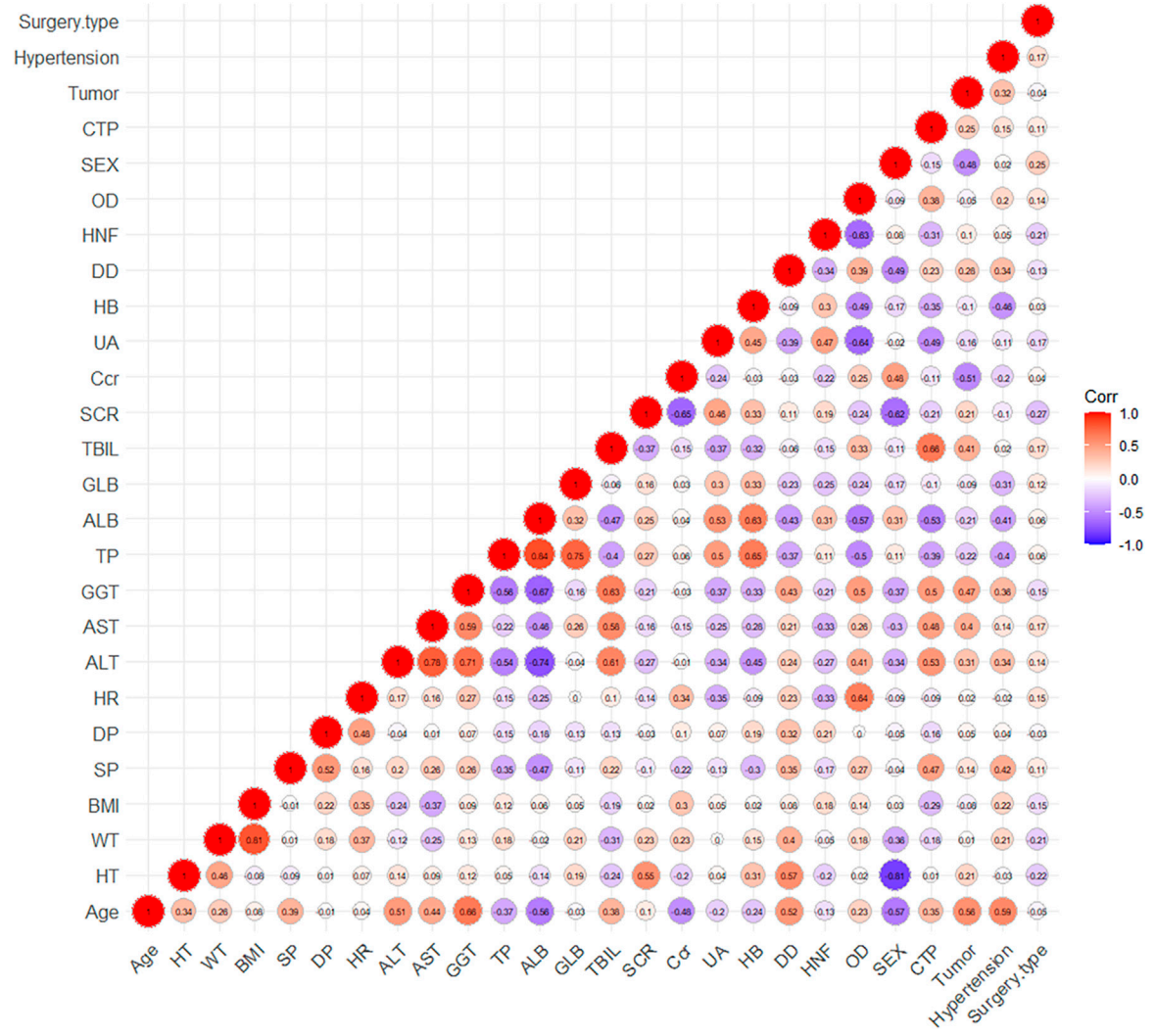

FIGURE 3
The graph of correlation between covariates.

suggested that the PK variability of the fixed dosage regimen was lower than that of the bodyweight dosage regimen (Figure 8).

3.5 The effectiveness and safety outcomes of patients

In the course of the trial, only one patient had mild cough during tracheal intubation; all patients were hemodynamically stable with good sedation levels and BIS between 40 and 65 during the operation; all patients recovered consciousness rapidly and did not become agitated during the postoperative awakening period; no patient had postoperative adverse effects such as nausea and vomiting.

4 Discussion

This study investigated the PopPK of nalbuphine in adult patients undergoing general anesthesia surgery, and analyzed the effect of a fixed dosage regimen and a body weight dosage regimen on nalbuphine distribution and metabolism.

A two-compartment model got the best description for PK profile of nalbuphine. It was consistent with the model structure of most previous studies (Jaillon et al., 1989; Bressolle et al., 2011; Pfiffner et al., 2022), except for that reported by Jacqz-Aigrain et al. (2003). The typical values of nalbuphine PK parameters from the final model were 32.9 L/h for CL, 32.5 L for V1, 245 L/h for Q and 83.5 L for V2. The results were consistent with our previous results, which were obtained using non-compartmental analysis (NCA) (Gao et al., 2022). While Bressolle et al. (2011) built a PopPK model of nalbuphine after surgery in children (1–11 years) using an allometric scaling model, and their population parameter estimates were 130 L/h/70 kg for CL, 210 L/70 kgforV1, 75.6 L/70 kg for Q and 151 L/70 kg for V2. It revealed that it may be limited to apply the model established with allometric scaling in the children population to the adult population due to the differences in the physiological status of children and adults. The PopPK model developed in this study using data from clinically adult patients could characterize the

TABLE 3 The stepwise process of building the PopPK model of nalbuphine.

Model no.	Model description	Functional expressions	OFV	ΔOFV	Compare to	*p*-value
1	Base Two-compartment model	—	2,158.168	—	—	—
Forward inclusion						
2	Add ALT on CL in model 1	a	2,150.776	−7.39	model 1	< 0.05
3	Add GGT on CL in model 1	b	2,153.271	−4.90	model 1	< 0.05
4	Add CTP on CL in model 1	c	2,153.111	−5.06	model 1	< 0.05
5	Add HR on V_1 in model 1	b	2,151.111	−7.06	model 1	< 0.05
6	Add NFI on V_1 in model 1	b	2,154.207	−3.96	model 1	< 0.05
7	Add OD on V_1 in model 1	b	2,150.612	−7.56	model 1	< 0.05
8	Add HR on Q in model 1	b	2,152.292	−5.88	model 1	< 0.05
9	Add NFI on Q in model 1	b	2,148.529	−9.64	model 1	< 0.05
10	Add OD on Q in model 1	b	2,150.299	−7.87	model 1	< 0.05
11	Add Cancer on Q in model 1	c	2,152.809	−5.36	model 1	< 0.05
12	Add WT on V_2 in model 1	b	2,154.098	−4.07	model 1	< 0.05
13	Add GGT on V_2 in model 1	b	2,151.149	−7.02	model 1	< 0.05
14	Add UA on V_2 in model 1	b	2,152.796	−5.37	model 1	< 0.05
15	Add DD on V_2 in model 1	b	2,153.374	−4.79	model 1	< 0.05
16	Add NFI on V_2 in model 1	b	2,154.225	−3.94	model 1	< 0.05
17	Add OD on V_2 in model 1	b	2,153.697	−4.47	model 1	< 0.05
18	Add CTP on V_2 in model 1	c	2,153.759	−4.41	model 1	< 0.05
19	Add ST on V_2 in model 1	c	2,154.225	−3.94	model 1	< 0.05
20	Add ALT on CL in model 9	a	2,141.133	−7.40	model 9	< 0.01
Backward elimination						
21	remove NFI on Q from model 20	—	2,150.776	9.64	model 20	< 0.005
22	remove ALT on CL from model 20	—	2,148.529	7.40	model 20	> 0.005

a: linear function; b: power function; c: exponential function.

TABLE 4 Population pharmacokinetic parameter estimates of nalbuphine in the final model and bootstrap evaluation.

Parameter	Final model			Bootstrap			Relative bias (%)
	Estimates	RSE (%)	SHRINKSD (%)	Median	2.5th-97.5th percentile		
Structural model parameter							
CL	32.9	5.47	NA	32.8	29.46	36.54	−0.30
V_1	32.5	10.25	NA	31.9	25.90	38.10	−1.85
Q	245	13.99	NA	247	216.63	297.38	0.82
V_2	83.5	7.94	NA	84.6	70.70	97.34	1.32
HNF on Q	−0.58	14.11	NA	−0.557	−0.802	−0.084	−3.97
Between-subject variability							
ωCL (%CV)	27.7	12.26	4.30	26.9	19.8	33.5	−2.89
ωV_1 (%CV)	40.1	22.92	13.10	37.4	19.8	56.4	−6.73
ωQ (%CV)	17.9	42.65	30.72	16.6	0.2	39.0	−7.26
ωV_2 (%CV)	40.8	13.84	3.18	38.5	27.2	50.7	−5.64
Residual unexplained variability							
Proportional error (%CV)	0.139	8.02	12.79	0.137	0.11	0.16	−1.44
Additive error (ng/mL)	2.88	19.81	12.79	2.9035	1.88	4.72	0.82

RES: relative standard error; CL: total clearance (L/h); V_1: volume of distribution for the central compartment (L); Q: intercompartmental clearance (L/h); V_2: volume of distribution for the peripheral compartment (L); HNF, on Q: influence of Hourly net fluid volume infused (HNF) on Q; ω_{CL}, ω_{V1}, ω_Q and ω_{v2}: the estimates of between-subject variability of CL, V_1, Q and V_2, respectively.

PK profile of nalbuphine in adults more accurately, especially for patients undergoing general anesthesia surgery. However, compared to the results obtained in healthy adults, the metabolism and distribution of nalbuphine were also significantly decreased in the population in this study. Jaillon et al. (1989) found that the CL, V1, and V2 of nalbuphine in young healthy volunteers (62–90 kg) were 1.783 L/h/kg, 1.97 L/kg and 5.45 L/kg, respectively. He et al. (2021) found that CL and V_d of nalbuphine were 90.0 L/h and 326.5 L in

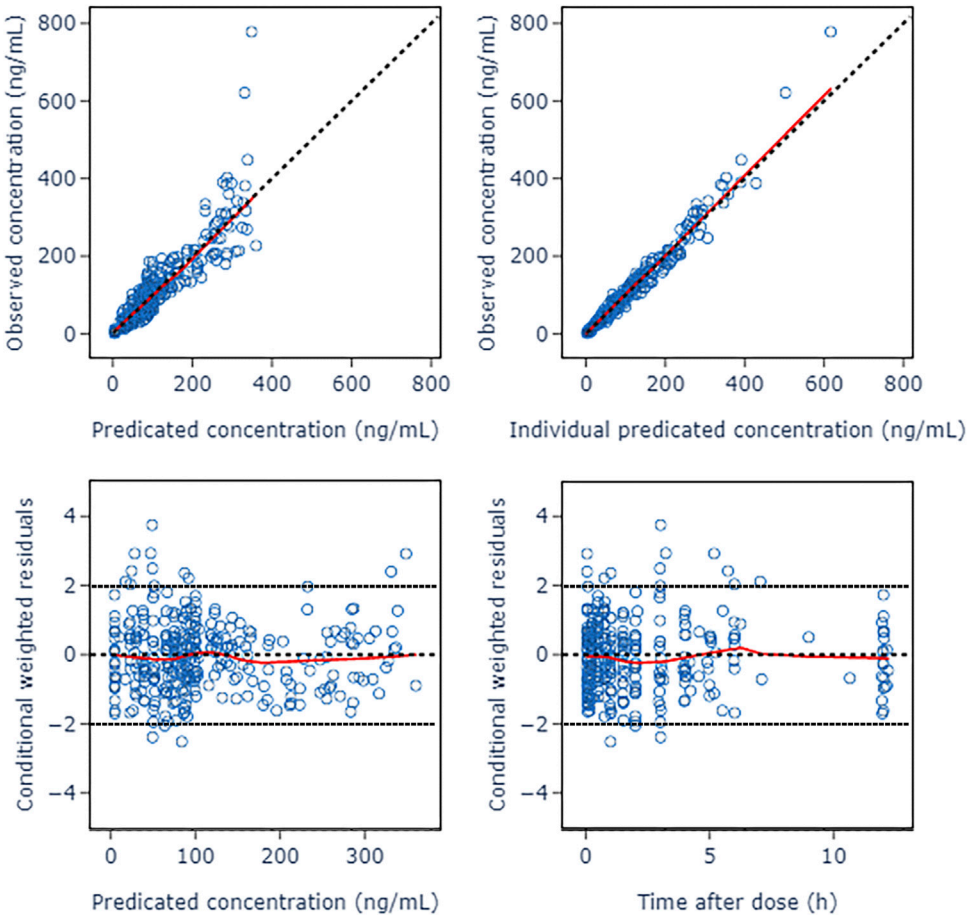

FIGURE 4
Goodness of fit plots of nalbuphine final PopPK model. The red lines represent the locally weighted scatterplot with smoothing.

healthy adults (55.2–64.2 kg) after 10 mg intravenous injection. As a result, we assumed that variations in the included population and the scenarios of nalbuphine administration were to blame for the disparities in parameters between our research.

A previous study by Sear et al. (1987) found that nalbuphine presented lower clearance (65.7 L/h) and apparent distribution volume (207.6 L) in patients undergoing general anesthesia than in conscious volunteers. There were many factors that might affect the distribution and metabolism of drugs during the operation, and it was difficult to quantify with a single influencing factor (Choi et al., 2017). Large amounts of fluid and blood transfusions during surgery could increase the volume of the systemic circulation, thereby increasing hepatic blood flow and facilitating the distribution of drugs (Eleveld et al., 2014). Conversely, anesthetic drugs and cryogenic environment could reduce the patient's heart rate and blood pressure, and slow the systemic circulation and the distribution of drugs (Mccollum and Dundee, 1986; Stowe et al., 1992). Zausig et al. (2009) found a 38% decrease in myocardial contractility after intravenous propofol. In addition, surgical stress may also cause a range of hormonal and metabolic changes (Choi et al., 2017). Therefore, the duration of surgery and intraoperative fluid volume, blood transfusion, urine volume, and HNF were chosen to be tested as factors related to surgery during the covariate screening process. And the results found that OFV was significantly reduced ($p < 0.005$) and the model was improved after introducing HNF values as a covariate for Q.

As the hepatic extraction ratio of nalbuphine was estimated to be 0.5–0.7, the influence of HNF on Q of nalbuphine revealed in the present study could be partially explained by the changes of hepatic blood flow (Jaillon et al., 1989; Bressolle et al., 2011). During surgery, fluid and blood transfusions could increase the volume of the patient's body circulation, which in turn increases hepatic blood flow. The HNF combined with information on volume of fluid infused, volume of blood transfused, volume of urine and duration of operation could reflect the degree of increase in volume of body circulation and hepatic blood flow per unit time of patients. Unexpectedly, the results in the simulations showed that the effect of HNF appeared to be limited. Therefore, clinical pre-adjustment of nalbuphine administration dose based on the level of HNF is not recommended. However, close attention should be paid to the anesthetic effect and hemodynamic changes in patients who might be or had been intraoperatively transfused with higher volumes of fluids, blood transfusions, or blood loss.

Liver is an important organ for drug metabolism and its function can directly affect the PK of drugs. Usually, the livers of adults have fully developed and have a better ability to metabolize drugs

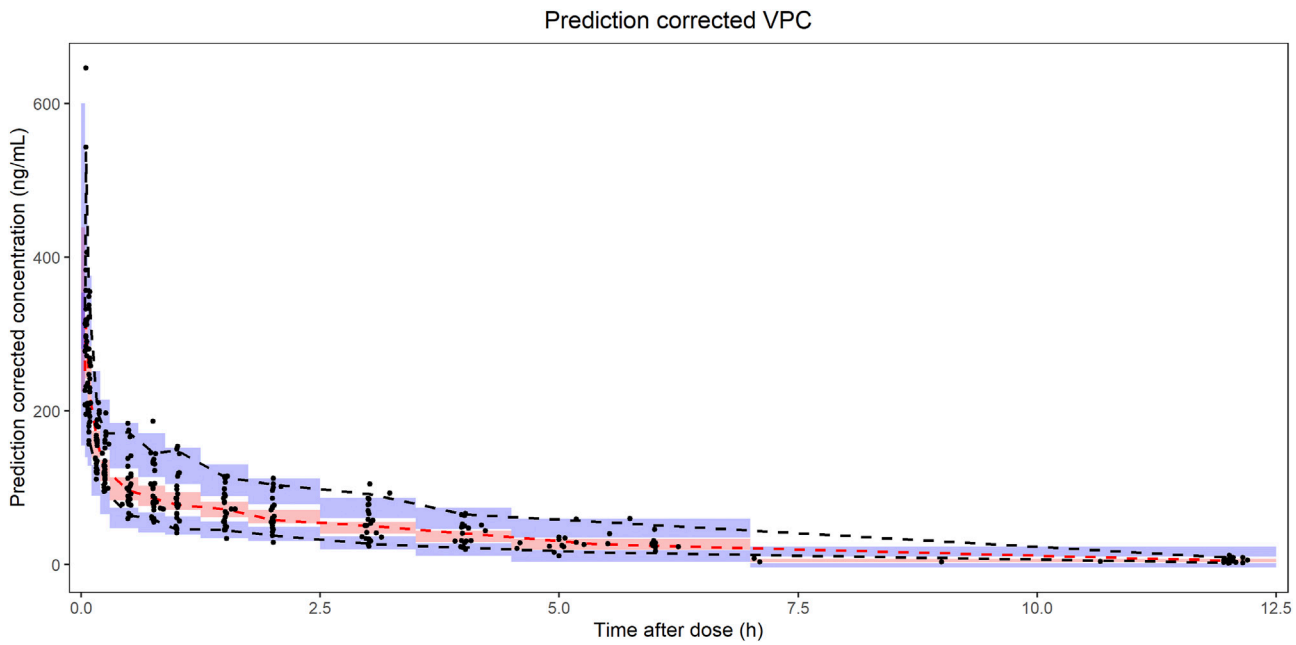

FIGURE 5
Prediction corrected visual predictive checks (pc-VPC) of nalbuphine final PopPK model. The black dots represented prediction corrected observations. The black dashed lines represented 90% interval of the prediction corrected observations. The red dashed lines represented median of the prediction corrected observations. The red shaded area represented 95% confidence interval (CI) of the median prediction. The blue shaded area represented 95% CI of the 5th and 95th prediction interval.

TABLE 5 External validate results of nalbuphine PopPK model.

Indices	Data without observations	Data within an observation
MDPE (%)	12.97	8.92
MAPE (%)	24.05	14.33
F_{20}	40.48	69.05
F_{30}	61.90	84.52

PE: prediction error of dependent variable; MDPE: median prediction errors; MAPE: median absolute prediction errors; F_{20}, F_{30}: PE% within ± 20% and 30%, respectively.

compared to infants, children and the elderly. In addition, adult patients with liver disease belong to a special population whose metabolism of drugs is different from that of healthy adults. Hepatic insufficiency could alter the drug distribution and metabolic processes by affecting drug metabolizing enzyme activity, hepatic blood flow and drug binding to plasma proteins (Gao et al., 2022). Nalbuphine is mainly metabolized in the liver mainly by cytochrome P450 enzymes (CYP450) 3A4, 2D6, 2C19 and uridine diphosphate-glucuronyl transferase (UGT) 1A3, 2B7, and clearance is mainly dependent on hepatic blood flow (Bressolle et al., 2011). Our previous NCA analysis found that the $t_{1/2}$ of nalbuphine in patients with hepatic insufficiency was prolonged with increased serum total bilirubin (TBIL) levels (Gao et al., 2022). Although 55.6% of the patients in this study had hepatobiliary disease, there were no covariates related to liver function that could be included in the final model. Notably, alanine aminotransferase (ALT) but not TBIL may have had an effect on the CL of nalbuphine in the present study. During the stepwise process, ALT had been added to the model as a covariate of CL by decreasing the model OFV value of 7.39. Unfortunately, ALT was removed from the full model according to the pre-defined criteria in the backward elimination process. We speculate that this may be due to the small sample size of patients included in this study and the fact that most patients with liver disease had ALT within 3 times the normal value and had insignificant decreases in liver function. Therefore, the effect of ALT on nalbuphine CL needs to be further studied in a larger group of patients with liver disease.

Age and weight were considered to be an important factor affecting the PK characteristics of nalbuphine (Bressolle et al., 2011). Studies in infants, healthy volunteers, and elderly patients found that the CL of nalbuphine significantly decreased with age, which was consistent with the previous univariate analysis (Jaillon et al., 1989; Bessard et al., 1997). And allometric growth models had been used to describe the distribution and metabolism of nalbuphine in infants and children (Jacqz-Aigrain et al., 2003; Bressolle et al., 2011).

However, the introduction of age did not have a significant effect on the final model in this study when building the PopPK model. Changes

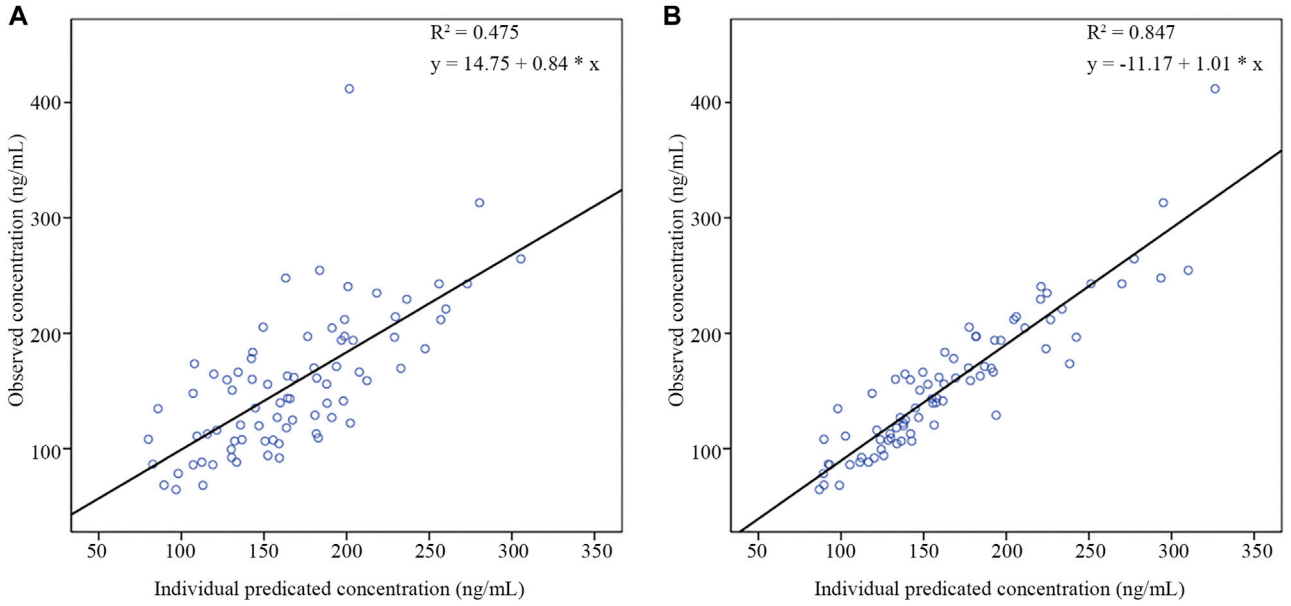

FIGURE 6
The scatter plots of external validation of the final nalbuphine model. **(A)** external evaluation dataset without observations; **(B)** external evaluation dataset within the first observation of each subject.

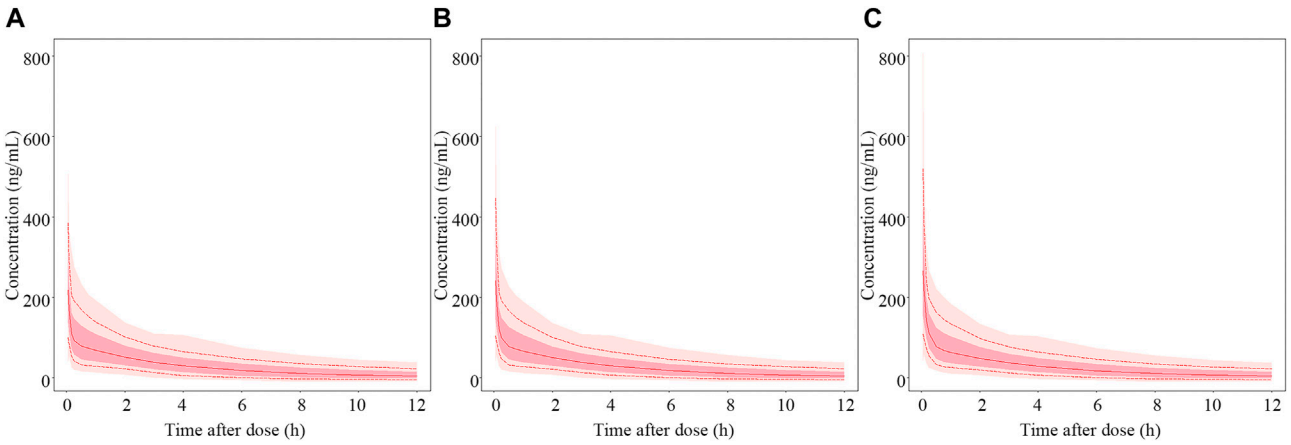

FIGURE 7
Simulated PK profiles of nalbuphine. The median hourly net fluid volume infused (HNF) of patient in the model building group was 563.6 mL/h. **(A–C)** represent PK profiles of nalbuphine at the 10th, 50th and 90th percentile of HNF levels, respectively. The solid lines represent the median values of 1,000 simulations. The whole shadow and dark shadow represent all simulations and 5% to 95% simulations of the corresponding population in each panel, respectively.

in organ weight and blood flow had been reported to be the main causes of age-related changes in hepatic clearance (Soejima et al., 2022). In present study, only adult patients undergoing general anesthesia were included, with limited effect of age on their liver weight. In addition, the changes of blood flow caused by surgery were greater than that caused by age. That might be the reason why age was not to be related to the CL of nalbuphine in this study.

In this study, fixed dose regimen (15 mg) was explored in patients undergoing anesthesia surgery based on published literature (Cai et al., 2011; He et al., 2021). During the trial, all patients were hemodynamically stable and well sedated intraoperatively, and there were no adverse effects such as irritability, nausea and vomiting in the postoperative period. Only one patient developed a mild cough during tracheal intubation. Fixed dose of nalbuphine (15 mg) in patients undergoing general anesthesia showed good efficacy and safety. However, 0.2 mg/kg dose regimen was recommended in package inserts of nalbuphine. In order to investigate the effect of body weight on the PK of nalbuphine, the established PopPK model was used to simulate the plasma concentration of nalbuphine in patients with fixed dosage regimen and bodyweight dosage regimen,

TABLE 6 Statistical analysis results of nalbuphine simulation on two dosage regimens.

Time(h)	Dosage regimen simulation	Mean	Median	Min	Max	Percentile values		Bias (%)
						25th	75th	
0.05	fixed dosing	246.75	241.84	67.76	572.04	203.51	284.82	5.46
	bodyweight dosing	260.22	251.36	62.11	700.00	206.57	306.13	
4	fixed dosing	30.14	29.65	0.46	84.77	23.50	36.19	5.58
	bodyweight dosing	31.82	30.78	0.47	96.07	23.87	38.56	
12	fixed dosing	5.06	3.99	0.00	32.90	1.71	7.39	5.55
	bodyweight dosing	5.34	4.15	0.00	36.73	1.76	7.71	

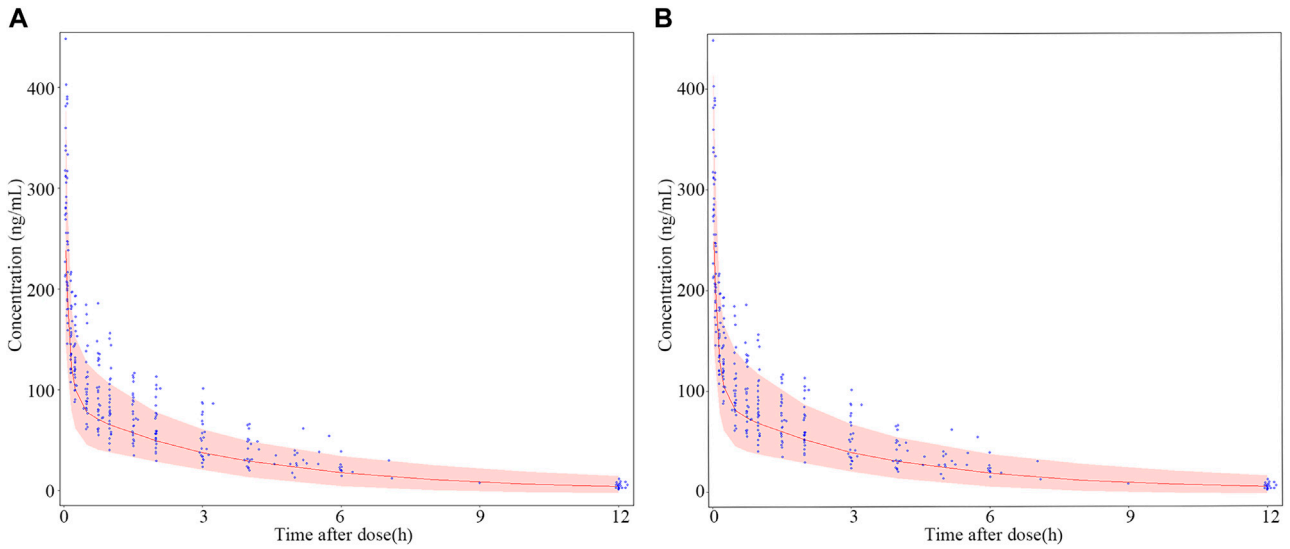

FIGURE 8
Dosage regimen simulation plots of nalbuphine. **(A)** fixed dosing regimen (12 mg); **(B)** bodyweight dosing regimen (0.2 mg/kg). The blue points were the observed concentration. The red lines represent the 50th percentiles of simulated concentrations distribution in each panel. The shadow represent 5th and 95th percentiles of simulated concentrations distributed in each panel. Two observed concentration (621 μg/mL and 778.1 μg/mL) at 0.05 h were not shown in this Figure.

respectively. Not surprisingly, the bias of the two dosage regimens met the predefined criteria (±15%) either at the beginning of dosage or at the end of the operation period or at the end stage of elimination. However, individualized dosing based on body weight did not reduce inter-patient variability in PK exposure. And fixed dosage regimen is easier to operationalize than weight dosage regimen in clinical, especially for those patients who are critically ill and unable to measure weight. Thus, we would recommend the replacement of bodyweight dosage regimen with fixed dosage regimen in adult patients undergoing general anesthesia surgery.

Several limitations in this study should be considered. First, interactions associated with concomitant drugs were not considered in modeling the PopPK of nalbuphine. Patients in our study received co-administration of nalbuphine, midazolam, sufentanil, and sevoflurane, all of which were metabolized by CYP3A4. However, considering the design of this study, it was unable to identify whether there are PK effects between nalbuphine and other medications used during operation. Second, the investigation of the effect of cancer disease on the PK of nalbuphine was arbitrary. The present study only classified whether the patient had cancer or not. More representative tumor-related indicators need to be identified and included in future analyses of nalbuphine PopPK models. Moreover, there might be some unclear biases in this PopPK model of nalbuphine due to the small size of the sample. It should be verified by more patient data in the future.

5 Conclusion

In conclusion, a PopPK model of nalbuphine for adult patients undergoing general anesthesia surgery was developed

in this study. While the Q of nalbuphine was significantly affected by the patient's HNF during surgery, the magnitude of the effect was limited, and no dosage adjustments were recommended. The body weight dosage regimen can be replaced by the fixed drug dosage regimen with low PK variability based on the final PopPK simulation.

Data availability statement

The raw data supporting the conclusion of this article will be made available by the authors, without undue reservation.

Ethics statement

The studies involving human participants were reviewed and approved by Ethical Committee of the Fourth Hospital of Hebei Medical University, Shijiazhuang, China. The patients/participants provided their written informed consent to participate in this study.

Author contributions

XN, XG, JG, ZF, LJ, and MW contributed to the conception and design of the study. XN, XG, TH, YZ, and YS contributed to data collection. XN, XG, and MW contributed to modeling process and manuscript preparation. All authors contributed to the manuscript and approved the submitted version.

Funding

This work was supported by National Science and Technology Major Project for Major New Drugs Innovation and Development 2020 in China (No. 2020ZX09201006) and Hebei Medical Science Research Project (No. 20200105).

Acknowledgments

The author, XN is thankful to the surgeons and nurses of the Department of Anesthesiology at the Fourth Hospital of Hebei Medical University for their help during the study, and all the patients that have contributed to this project.

Conflict of interest

The authors declare that the research was conducted in the absence of any commercial or financial relationships that could be construed as a potential conflict of interest.

Publisher's note

References

Bessard, G., Alibeu, J. P., Cartal, M., Nicolle, E., Serre, D. F., and Devillier, P. (1997). Pharmacokinetics of intrarectal nalbuphine in children undergoing general anaesthesia. *Fundam. Clin. Pharmacol.* 11 (2), 133–137. doi:10.1111/j.1472-8206.1997.tb00180.x

Bressolle, F., Khier, S., Rochette, A., Kinowski, J. M., Dadure, C., and Capdevila, X. (2011). Population pharmacokinetics of nalbuphine after surgery in children. *Br. J. Anaesth.* 106 (4), 558–565. doi:10.1093/bja/aer001

Cai, L. J., Zhang, J., Wang, X. M., Zhu, R. H., Yang, J., Zhang, Q. Z., et al. (2011). Validated LC-MS/MS assay for the quantitative determination of nalbuphine in human plasma and its application to a pharmacokinetic study. *Biomed. Chromatogr.* 25 (12), 1308–1314. doi:10.1002/bmc.1601

Chawda, P. M., Pareek, M. K., and Mehta, K. D. (2010). Effect of nalbuphine on haemodynamic response to orotracheal intubation. *J. Anaesth. Clin. Pharm.* 26 (4), 458–460. doi:10.4103/0970-9185.74584

Choi, B., Lee, Y., An, S., Lee, S., Lee, E., and Noh, G. (2017). Population pharmacokinetics and analgesic potency of oxycodone. *Br. J. Clin. Pharmacol.* 83 (2), 314–325. doi:10.1111/bcp.13101

Dalens, B. J., Pinard, A. M., Letourneau, D. R., Albert, N. T., and Truchon, R. J. (2006). Prevention of emergence agitation after sevoflurane anesthesia for pediatric cerebral magnetic resonance imaging by small doses of ketamine or nalbuphine administered just before discontinuing anesthesia. *Anesth. Analg.* 102 (4), 1056–1061. doi:10.1213/01.ane.0000200282.38041.1f

Eleveld, D. J., Proost, J. H., Cortínez, L. I., Absalom, A. R., and Struys, M. M. R. F. (2014). A general purpose pharmacokinetic model for propofol. *Anesth. Analgesia* 118 (6), 1221–1237. doi:10.1213/ANE.0000000000000165

Errick, J. K., and Heel, R. C. (1983). Nalbuphine. A preliminary review of its pharmacological properties and therapeutic efficacy. *Drugs* 26 (3), 191–211. doi:10.2165/00003495-198326030-00002

Gao, X. N., Nie, X. Y., Gao, J. L., Heng, T. F., Zhang, Y. Q., Hua, L., et al. (2022). Pharmacokinetic study of nalbuphine in surgical patients undergoing general anesthesia with varying degrees of liver dysfunction. *Drug Des. Devel Ther.* 16, 2383–2393. doi:10.2147/DDDT.S371596

Giannina, G., Guzman, E. R., Lai, Y. L., Lake, M. F., Cernadas, M., and Vintzileos, A. M. (1995). Comparison of the effects of meperidine and nalbuphine on intrapartum fetal heart rate tracings. *Obstet. Gynecol.* 86 (3), 441–445. doi:10.1016/0029-7844(95)00164-M

He, K., Ji, W., Zhao, H., Wei, Y., Yang, S., and Wen, Q. (2021). Pharmacokinetic comparison of nalbuphine with single injection and patient-controlled analgesia mimic method in healthy Chinese volunteers. *J. Clin. Pharm. Ther.* 46 (4), 1166–1172. doi:10.1111/jcpt.13421

Hirsch, J., Depalma, G., Tsai, T. T., Sands, L. P., and Leung, J. M. (2015). Impact of intraoperative hypotension and blood pressure fluctuations on early postoperative delirium after non-cardiac surgery. *Br. J. Anaesth.* 115 (3), 418–426. doi:10.1093/bja/aeu458

Jacqz-Aigrain, E., Debillon, T., Daoud, P., Boithias, C., Hamon, I., Rayet, I., et al. (2003). Population pharmacokinetics of nalbuphine in neonates. *Paediatr. Perinat. Drug Ther.* 5 (4), 190–198. doi:10.1185/146300903774115793

Jaillon, P., Gardin, M. E., Lecocq, B., Richard, M. O., Meignan, S., Blondel, Y., et al. (1989). Pharmacokinetics of nalbuphine in infants, young healthy volunteers, and elderly patients. *Clin. Pharmacol. Ther.* 46 (2), 226–233. doi:10.1038/clpt.1989.130

Kubica-Cielinska, A., and Zielinska, M. (2015). The use of nalbuphine in paediatric anaesthesia. *Anaesth. Intensive Ther.* 47 (3), 252–256. doi:10.5603/AIT.2015.0036

Mccollum, J. S., and Dundee, J. W. (1986). Comparison of induction characteristics of four intravenous anaesthetic agents. *Anaesthesia* 41 (10), 995–1000. doi:10.1111/j.1365-2044.1986.tb12740.x

Nguyen, T. H., Mouksassi, M. S., Holford, N., Al-Huniti, N., Freedman, I., Hooker, A. C., et al. (2017). Model evaluation of continuous data pharmacometric models: Metrics and graphics. *CPT-PHARMACOMET. Syst. Pharmacol.* 6 (2), 87–109. doi:10.1002/psp4.12161

Pfiffner, M., Berger-Olah, E., Vonbach, P., Pfister, M., and Gotta, V. (2022). Pharmacometric analysis of intranasal and intravenous nalbuphine to optimize pain management in infants. *Front. Pediatr.* 10, 837492. doi:10.3389/fped.2022.837492

Schmidt, W. K., Tam, S. W., Shotzberger, G. S., Smith, D. J., Clark, R., and Vernier, V. G. (1985). Nalbuphine. *Drug Alcohol Depend.* 14 (3-4), 339–362. doi:10.1016/0376-8716(85)90066-3

Sear, J. W., Keegan, M., and Kay, B. (1987). Disposition of nalbuphine in patients undergoing general anaesthesia. *Br. J. Anaesth.* 59 (5), 572–575. doi:10.1093/bja/59.5.572

Shuying, L., Ping, L., Juan, N., and Dong, L. (2016). Different interventions in preventing opioid-induced cough: A meta-analysis. *J. Clin. Anesth.* 34, 440–447. doi:10.1016/j.jclinane.2016.05.034

Soejima, K., Sato, H., and Hisaka, A. (2022). Age-related change in hepatic clearance inferred from multiple population pharmacokinetic studies: Comparison with renal clearance and their associations with organ weight and blood flow. *Clin. Pharmacokinet.* 61 (2), 295–305. doi:10.1007/s40262-021-01069-z

Stowe, D. F., Bosnjak, Z. J., and Kampine, J. P. (1992). Comparison of etomidate, ketamine, midazolam, propofol, and thiopental on function and metabolism of isolated hearts. *Anesth. Analg.* 74 (4), 547–558. doi:10.1213/00000539-199204000-00015

Wang, H., Wang, T., Hu, X., Deng, C., Jiang, J., Qin, H., et al. (2022). Fixed dosing of kukoamine B in sepsis patients: Results from population pharmacokinetic modelling and simulation. *Br. J. Clin. Pharmacol.* 88 (9), 4111–4120. doi:10.1111/bcp.15342

Weiser, T. G., Regenbogen, S. E., Thompson, K. D., Haynes, A. B., Lipsitz, S. R., Berry, W. R., et al. (2008). An estimation of the global volume of surgery: A modelling strategy based on available data. *Lancet* 372 (9633), 139–144. doi:10.1016/S0140-6736(08)60878-8

Zausig, Y. A., Busse, H., Lunz, D., Sinner, B., Zink, W., and Graf, B. M. (2009). Cardiac effects of induction agents in the septic rat heart. *Crit. Care*. 13 (5), R144. doi:10.1186/cc8038

frontiers | Frontiers in Pharmacology

TYPE Original Research
PUBLISHED 14 April 2023
DOI 10.3389/fphar.2023.1175896

OPEN ACCESS

EDITED BY
Ling Ye,
Southern Medical University, China

REVIEWED BY
Qisong Zhang,
Guangxi University, China
Cong Xie,
Southern Medical University, China
Zifei Qin,
First Affiliated Hospital of Zhengzhou University, China

*CORRESPONDENCE
Qun Wang,
gywq198856@163.com

†These authors have contributed equally to this work

RECEIVED 28 February 2023
ACCEPTED 06 April 2023
PUBLISHED 14 April 2023

CITATION
Wang Q, Tang T, Wu Z, Yang H, Gao Y, Zhang S, Song X and Chen X (2023), Study on the liver Drug's dominant metabolic enzymes for six effective components of the Huang qi Liuyi decoction. *Front. Pharmacol.* 14:1175896. doi: 10.3389/fphar.2023.1175896

Study on the liver Drug's dominant metabolic enzymes for six effective components of the Huang qi Liuyi decoction

Qun Wang[1*†], Tiantian Tang[1†], Zengguang Wu[1], Hong Yang[1], Yuan Gao[1,2], Shiyu Zhang[1], Xinli Song[1,2] and Xiaolan Chen[1,2]

[1]Guizhou University of Traditional Chinese Medicine, Huaxi University Town, Guiyang, China, [2]National Research Center of Miao Medicine and Engineering Technology, Huaxi University Town, Guiyang, China

Objective: To investigate the dominant metabolic enzymes of six effective components (astragaloside IV, glycyrrhizic acid, calycosin-glucuronide, formononetin, ononin, calycosin-7-O-β-D- glucoside) of Huangqi Liuyi decoction extract (HQD).

Methods: Mouse liver microsomes were prepared. The effects of specific inhibitors of CYP450 enzymes on the metabolism of six effective components of HQD were studied using liver microsomal incubation *in vitro*.

Results: The chemical inhibitors of CYP2C37 inhibit the metabolism of glycyrrhizic acid and astragaloside IV. Formononetin and astragaloside IV metabolism is inhibited by the chemical inhibitors of CYP2C11. The chemical inhibitors of CYP2E1 and CYP1A2 inhibit the metabolism of calycosin-glucuronide. Chemical CYP3A11 inhibitors prevent formononetin and glycyrrhizic acid from being metabolized. However, no inhibitor significantly affected the metabolism of ononin and calycosin-7-O-β-D-glucoside.

Conclusion: CYP2C37 may be involved in the metabolism of astragaloside IV and glycyrrhizic acid, the metabolism of astragaloside IV and formononetin may be related to CYP2C11, the metabolism of calycosin-glucuronide may be related to CYP1A2 and CYP2E1, and CYP3A11 may be involved in the metabolism of glycyrrhizic acid and formononetin. This research provides an experimental basis for exploring the pharmacokinetic differences caused by metabolic enzymes.

KEYWORDS

Huangqi Liuyi decoction, six effective components, CYP450 enzymes, liver microsomal, liver microsomal incubation *in vitro*

1 Introduction

Diabetic nephropathy (DN) is one of the most serious microvascular complications of diabetes mellitus (DM). The clinical manifestations are persistent proteinuria, edema, decreased renal function, hypertension. The majority of cases progress to end-stage renal failure. Early treatment of diabetic nephropathy is significant in improving the quality of life and survival rate (Liu et al., 2022; Liu et al., 2022). Huangqi Liuyi decoction, first published in the "Taiping Huimin and Pharmacy Bureau Fang," is composed of 60 g of *Astragali* and 10 g of *Glycyrrhizae*, and has the effect of greatly tonifying lung qi,

nourishing kidney water, and harmonizing the spleen and stomach. Huangqi Liuyi decoction has been shown to prevent islet damage, lower blood glucose and glycated hemoglobin in diabetic model mice. In addition, *Astragali* prevents the establishment of renal interstitial fibrosis and *Glycyrrhizae* can prevent diabetic nephropathy by lowering lipid, lowering glucose levels, and preventing anti-oxidative stress in the kidneys (Chen et al., 2014; Hou et al., 2017; Wen et al., 2018; Ma et al., 2019; Dai et al., 2022). Traditional Chinese medicine (TCM) involves a multi-component and multi-target approach. Therefore, the quality and preparation of TCM aren't easy to control, which hinders the in-depth research of TCM and the development of new drugs. To improve the pharmacological properties, individual ingredients from a compounded prescription are isolated and formulated according with the compatibility theory of TCM. This allows for clear pharmacological effects, relatively stable nature, and can effectively compensate for the shortcomings of traditional prescriptions whose quality is not easily controlled (Wang and Liang, 2004; Hu et al., 2016; Chen et al., 2019). Previously, our team discovered that the combination of four components extracted from Huangqi Liuyi Decoction, namely, astragalus saponin, glycyrrhizic acid, astragalus flavone, and astragalus polysaccharide (AKA HQD), improved renal fibrosis and slowed the progression of diabetic nephropathy in db/db mice (Wang et al., 2022). The study also discovered no statistical difference between the efficacy of Huangqi Liuyi decoction and HQD in mice with diabetic nephropathy (Wang et al., 2022b). According to pharmacokinetic studies, mice with diabetic nephropathy exhibited greater absorption and delayed elimination of the six effective components (astragaloside IV, glycyrrhizic acid, calycosin-glucuronide, formononetin, ononin, calycosin-7-O-β-D-glucoside) following oral administration HQD (Wang et al., 2022c).

The pathological state of the patient considerably influences drug-related processes *in vivo*, which directly relates to the drug's efficacy and side effects (Ma et al., 2021; Qian et al., 2022). The alterations in the pharmacokinetics of drug in DN may relate to the changes in the activity of a variety of CYP450 cytochrome (CYP) enzymes involved in drug absorption, metabolism, and excretion (Hu et al., 2014; Gong et al., 2015). In our preliminary research, DN induced the activity of CYP2C11 and CYP3A11. HQD inhibited the activity of CYP1A2, CYP2C37, and CYP3A11 and induced the activity of CYP2C11. Moreover, HQD induced the activity of CYP2E1 in the DN mouse and inhibited the activity of CYP2E1 in the control mouse. The activity of each CYP450 enzyme was consistent with changes in expression (Wang et al., 2022d). However, the specificity of individual CYP enzymes allows for only specific substrates to be metabolized by the enzyme. The enzyme primarily involved in the metabolism of a certain substrate is known as the dominant metabolizing enzyme. Analyzing the dominant metabolizing enzyme of a drug is essential for studying how variations in the activity and expression of the metabolizing enzyme effect the drug pharmacokinetics and to elucidate the pharmacokinetic differences in pathophysiological states. In the present research, an *in vitro* liver microsomal incubation method was adopted to study the influence of specific inhibitors of liver CYP450 enzymes on the metabolism of the six effective components (astragaloside IV, glycyrrhizic acid, calycosin-glucuronide, formononetin, ononin, calycosin-7-O-β-D- glucoside) of HQD so as to analyze the CYP enzymes that may be involved in the metabolism of each component. From the perspective of drug metabolism, we investigated the reasons for the pharmacokinetic differences of HQD during the pathological and physiological changes and the possible drug-drug interactions in clinical application. The information will help provide a theoretical basis for developing new drugs against diabetic nephropathy and the rationale for their clinical application.

2 Materials and methods

2.1 Materials and reagents

The China Institute of Food and Drug Control provided the following reference standards: astragaloside IV, glycyrrhizic acid, calycosin-glucuronide, formononetin, ononin, calycosin-7-O-β-D- glucoside, puerarin, and digoxin (purity >98.0%). Ticlopidine (693228-63-6), α-naiflavone (604-59-1), quinidine (56-54-2), fluconazole (86386-73-4), ketoconazole (65277-42-1), and clomethiazole (533-45-9) were supplied by Shanghai yuanye Bio-Technology Co., Ltd. (Shanghai, China). Nicotinamide adenine dinucleotide phosphate (NADPH, 704S082) and bicinchoninic acid protein assay kit (BCA, 20191123) were provided by Beijing Solarbio Science and Technology Co., Ltd. (Beijing, China). Merck KGaA (Germany) provided methanol and acetonitrile (HPLC grade). All remaining chemicals were of analytical grade. HQD was self-produced by the research group (Wang et al., 2022). The content of each component in HQD is shown in Table 1.

2.2 Animals

Ten-week-old db/db male mice (45 ± 5 g) and db/m mice (20 ± 2 g) were purchased from the Model Animal Research Center of Nanjing University and MOE Key Laboratory of Model Animal for Disease Study (SCXK [Su]2021–0016) and housed in polypropylene cages at a relative humidity of 60% ± 5%, constant temperature (25°C ± 1°C) and under a 12 h light/12 h dark cycle, mice were given free access to water and food. Twelve-week-old db/db mice developed nephropathy (Ponchiardi et al., 2013; Wang et al., 2022b). The animal studies were approved by the Animal Ethical Committee of Guizhou University of Traditional Chinese Medicine (the approval number is NO1702060).

2.3 Preparation of standard solutions

The following standard solutions were prepared in methanol. The concentrations of astragaloside IV, glycyrrhizic acid, calycosin-glucuronide, formononetin, calycosin-7-O-β-D-glucoside, and ononin were 0.524 mg/mL, 0.505 mg/mL, 0.509 mg/mL, 0.526 mg/mL, 0.512 mg/mL, and 0.508 mg/mL, respectively. The stock solution was diluted with phosphate-buffered saline (PBS) to prepare a series of standard solutions. All solutions were refrigerated at 4°C.

TABLE 1 Content of each component extracted from three batches of *Astragalus* and *Glycyrrhizae*.

Extraction fraction	Components	Content (%)
Extract of astragalus saponins	Astragalus saponins	72.17
	Astragaloside IV	2.72
Extract of glycyrrhizic acid	Glycyrrhizic acid	80.22
Extract of astragalus flavones	Astragalus flavones	71.58
	Calycosin-glucuronide	1.36
	Formononetin	0.33
	Calycosin-7-O-β-D-glucoside	1.71
	Ononin	0.86
Extract of astragalus polysaccharides	Astragalus polysaccharides	65.51

TABLE 2 Mass spectrum parameters of HPLC-MS/MS.

Compound	Q1	Q2	DP (Volts)	CE (Volts)	EP (Volts)	CXP (Volts)
	Mass	Mass				
Astragaloside IV	807.4	627.4	168	67	10	16
Glycyrrhizic acid	824.4	309.4	120	40	10	13
Calycosin-glucuronide	285.3	213.2	180	51	10	13
Formononetin	267.0	252.0	−108	−10	−10	−13
Calycosin-7-O-β-D-glucoside	447.1	285.2	109	29	10	13
Ononin	431.3	269.1	−120	−25	−10	−13
Digoxin	825.3	649.5	−108	−30	−10	−13
Puerarin	417.1	267.1	110	35	10	13

TABLE 3 Regression equation, linear range, and LLOQ for six components in liver microsomal samples.

Compound	Linear range (μg/mL)	Regression equation	*r*	LLOQ (μg/mL)
Astragaloside IV	0.01–5.34	$y = 0.0012x - 0.0268$	0.9994	0.01
Glycyrrhizic acid	0.01–5.09	$y = 0.0014x + 0.031$	0.9998	0.01
Calycosin-glucuronide	0.01–5.19	$y = 0.0224x + 0.1288$	0.9997	0.01
Formononetin	0.01–5.23	$y = 0.0671x - 1.1249$	0.9992	0.01
Ononin	0.01–5.07	$y = 0.069x + 0.6873$	0.9994	0.01
Calycosin-7-O-β-D-glucoside	0.01–5.05	$y = 0.0349x + 0.394$	0.9997	0.01

2.4 Preparation of specific inhibitor solutions

Specific inhibitor solutions with the following concentrations were prepared in methanol: 0.126 μg/mL α-naphthoflavone, 0.101 μg/mL ticlopidine, 0.104 μg/mL fluconazole, 0.106 μg/mL quinidine, 0.101 μg/mL clomethiazole, and 0.101 μg/mL ketoconazole. Before use, each inhibitor solution was diluted with PBS (1 mM, pH, 7.0) to prepare the required concentration and then stored at 4°C.

2.5 Preparation of mouse liver microsomes

Before the experiment, the mice were fasted for 12 h, and were euthanized after blood was taken from the eye sockets. The liver was quickly removed and perfused with pre-cooled saline through the hepatic portal vein until the liver was earthy yellow, washed three times with 1.15% KCl solution, wiped dry with filter paper, and then weighed. The liver was then cut up, homogenized with three times the volume of ethylene diamine tetraacetic acid

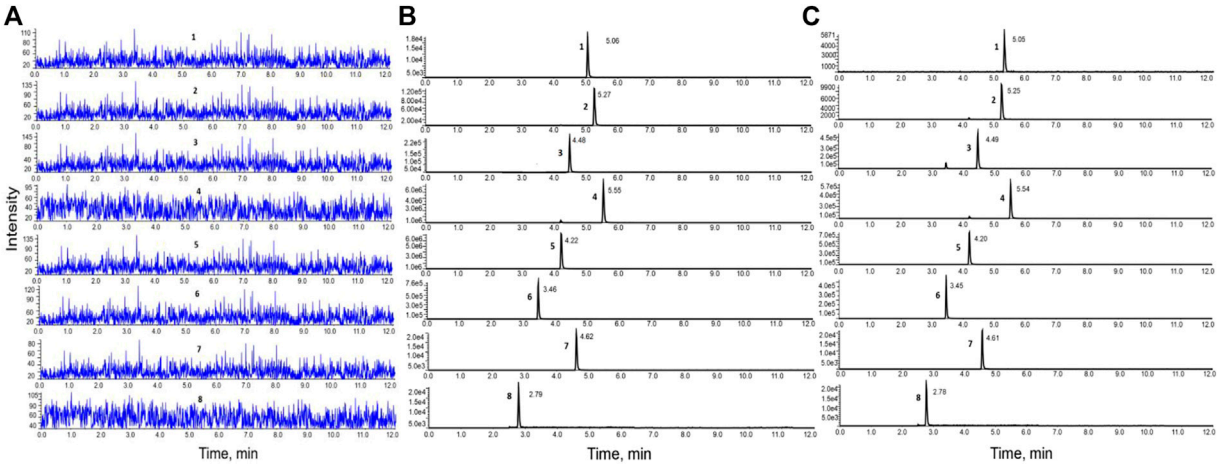

FIGURE 1
HPLC-MS/MS chromatograms of the six components. **(A)**. Blank inactivated liver microsomal sample; **(B)**. Blank inactivated liver microsomal sample mixed with the six components and internal standard; **(C)**. Samples obtained after incubation with liver microsomes.

TABLE 4 Accuracy and precision of the six components in liver microsomal samples (x ± SD, *n* = 6).

Compound	Spiked conc. (ng/mL)	Accuracy (%)	RSD (%)	Inter-day precision RSD (%)	Intra-day precision RSD (%)
Astragaloside IV	20.12	111.2 ± 5.69	5.12	4.58	4.61
	108.6	103.5 ± 5.35	5.17	7.55	2.74
	4,012.7	100.9 ± 2.78	2.75	7.78	3.31
Glycyrrhizic acid	19.54	105.4 ± 9.72	9.22	2.30	17.43
	101.7	82.15 ± 1.34	1.63	5.78	1.63
	4,092.4	109.9 ± 8.54	7.77	7.58	7.77
Calycosin-glucuronide	19.60	90.77 ± 7.57	8.34	11.55	8.53
	105.2	88.60 ± 3.08	3.48	4.78	2.61
	4,065	103.3 ± 2.92	2.83	4.91	2.64
Formononetin	19.20	104.5 ± 2.38	2.28	9.29	4.40
	107.9	106.6 ± 2.26	2.12	15.66	2.12
	4,013.8	101.8 ± 13.93	13.68	8.52	13.68
Ononin	20.78	107.5 ± 7.3	6.80	9.16	0.37
	99.46	85.84 ± 3.76	4.38	8.29	4.96
	4,034	102.6 ± 3.99	3.89	3.98	3.95
Calycosin-7-O-β-D-glucoside	20.54	109.0 ± 7.64	7.01	7.36	5.20
	101.4	85.98 ± 2.23	2.60	6.17	2.60
	4,026	102.8 ± 3.43	3.34	2.98	3.34

(EDTA) in an ice bath, and centrifuged at 4°C for 10 min at 3,000 g. The supernatant was filtered, and the filtrate was centrifuged at 4°C for 20 min at 12,000 g. The supernatant was then centrifuged at 4°C for 45 min at 100,000 g, and the precipitate was resuspended in a resuspension solution (EDTA homogenate containing 20% glycerol). The protein concentration of the microsomes was determined using the BCA protein concentration determination kit, and the microsomes were aliquoted and pre-stored at −20°C for 60 min and transferred to −80°C for storage.

TABLE 5 Matrix effects and extraction recovery of the six components in liver microsomal samples (x ± SD, *n* = 6).

Compound	Matrix effect (%)	RSD (%)	Extraction recovery (%)	RSD (%)
Astragaloside IV	90.57 ± 5.59	6.17	88.06 ± 1.10	1.25
	103.9 ± 6.33	6.09	100.7 ± 6.80	6.75
	102.2 ± 1.57	1.54	105.7 ± 1.61	1.52
Glycyrrhizic acid	90.62 ± 7.30	8.06	95.58 ± 8.87	9.28
	92.31 ± 6.75	7.31	104.1 ± 18.25	17.52
	101.5 ± 4.92	4.85	105.9 ± 10.46	9.87
Calycosin-glucuronide	94.77 ± 0.69	0.73	92.61 ± 8.26	8.92
	95.67 ± 7.55	7.89	99.77 ± 9.31	9.33
	101.3 ± 1.84	1.82	105.7 ± 6.80	6.43
Formononetin	94.79 ± 9.21	9.72	97.5 ± 7.65	7.85
	85.27 ± 2.58	3.03	99.65 ± 8.13	8.16
	95.23 ± 8.13	8.54	104.5 ± 2.58	2.47
Ononin	90.65 ± 5.10	5.63	84.09 ± 0.89	1.06
	98.84 ± 4.22	4.27	101.0 ± 3.46	3.43
	102.2 ± 3.60	3.52	105.4 ± 5.98	5.67
Calycosin-7-O-β-D-glucoside	90.8 ± 9.70	10.68	90.58 ± 3.73	4.12
	98.25 ± 1.79	1.82	92.3 ± 9.04	9.79
	103.5 ± 2.11	2.04	105.9 ± 3.65	3.45

10.3389/fphar.2023.1175896

TABLE 6 Stability of the six components in liver microsomal samples. (x ± SD, n = 6).

Compound	Spiked conc. (ng/mL)	25°C 4 h		−20°C 48 h		Three freeze–thaw cycles	
		Measured conc. (ng/mL)	RSD (%)	Measured conc. (ng/mL)	RSD (%)	Measured conc. (ng/mL)	RSD (%)
Astragaloside IV	20.12	21.46 ± 1.27	5.92	22.77 ± 2.56	11.24	21.13 ± 0.58	2.74
	108.5	109.3 ± 10.61	11.09	104.9 ± 3.58	3.41	98.03 ± 2.13	2.17
	4,012.8	4,034 ± 35.15	0.87	4,034 ± 72.45	1.80	3,902 ± 192.5	4.94
Glycyrrhizic acid	19.54	20.9 ± 2.31	11.05	20.52 ± 1.07	5.21	20.78 ± 2.95	14.19
	101.7	107.4 ± 6.62	17.93	97.94 ± 5.88	10.13	103.8 ± 1.54	17.38
	4,092	4,015 ± 219.5	5.47	4,042 ± 117.3	2.90	3,992 ± 183.4	4.59
Calycosin-glucuronide	19.60	20.59 ± 0.41	1.99	20.26 ± 0.39	1.92	20.85 ± 0.48	2.30
	105.2	97.47 ± 3	4.29	97.88 ± 1.01	1.03	99.14 ± 3.82	4.83
	4,065	4,111 ± 129.0	3.14	4,063 ± 135.3	3.33	4,104 ± 69.4	1.69
Formononetin	19.20	20.27 ± 0.11	0.54	21.10 ± 0.20	0.95	20.22 ± 0.09	0.45
	107.9	106.3 ± 0.21	1.18	107.0 ± 2.17	2.25	109.3 ± 1.78	0.94
	4,014	4,118 ± 428.3	10.40	4,033 ± 171.4	4.25	3,910 ± 110.6	2.83
Ononin	20.78	21.21 ± 1.43	6.74	20.29 ± 0.13	0.64	21.31 ± 0.32	1.50
	99.46	98.74 ± 2.44	2.47	98.51 ± 6.12	6.21	103.5 ± 2.26	2.18
	4,034	4,082 ± 121.9	2.99	4,034 ± 102.2	2.53	4,044 ± 162.4	4.02
Calycosin-7-O-β-D-glucoside	20.54	21.95 ± 1.71	7.79	20.53 ± 0.62	3.01	21.63 ± 1.13	5.11
	101.5	97.85 ± 6.11	11.09	97.13 ± 5.47	6.55	98.8 ± 2.02	9.74
	4,026	4,064 ± 84.17	2.07	4,132 ± 186.5	4.51	4,041 ± 131.2	3.25

10.3389/fphar.2023.1175896

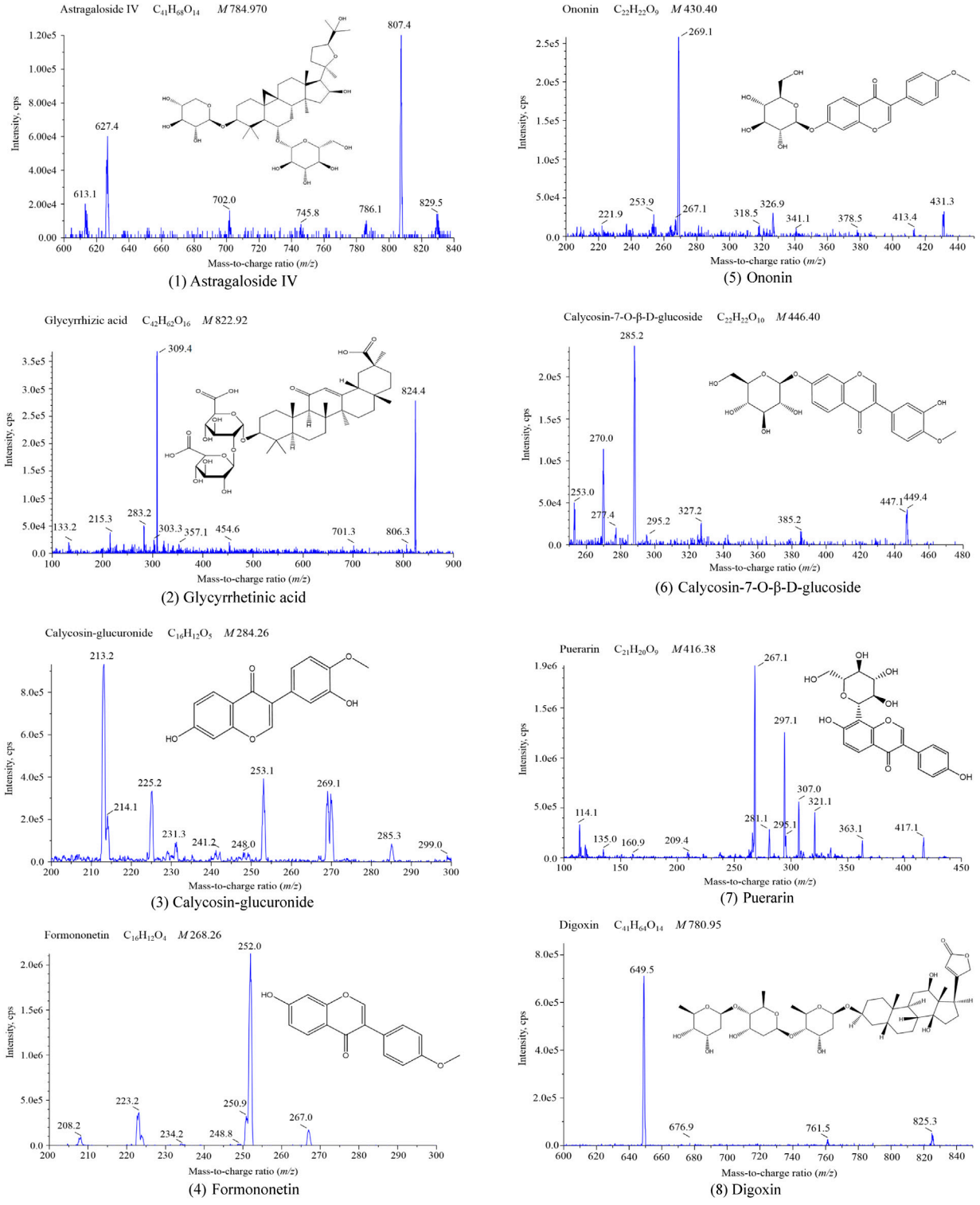

FIGURE 2
Mass spectrogram of the six components and internal standards (1) Astragaloside IV; (2) Glycyrrhetinic acid; (3) Calycosin-glucuronide; (4) Formononetin; (5) Ononin; (6) Calycosin-7-O-β-D-glucoside; (7) Puerarin; (8) Digoxin.

2.6 Liver microsomal incubation system and sample preparation

The total volume of the reaction was kept at 200 μL. The *in vitro* incubation system comprised of 50 μL liver microsomes (1 mg/mL), 50 μL specific inhibitor solution, 20 μL nicotinamide adenine dinucleotide phosphate (NADPH, 1 mmol/L), and 80 μL standard solution (100 ng/mL). The solution containing liver microsomes, specific inhibitors, and the standard solution was pre-incubated for 5 min at 37°C. NADPH, pre-incubated for 5 min at 37°C, was added

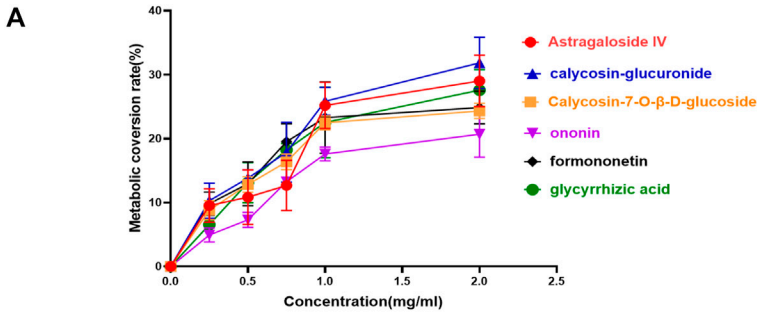

The metabolic conversion rate of each component in the liver microsomal incubation system at different protein concentrations.

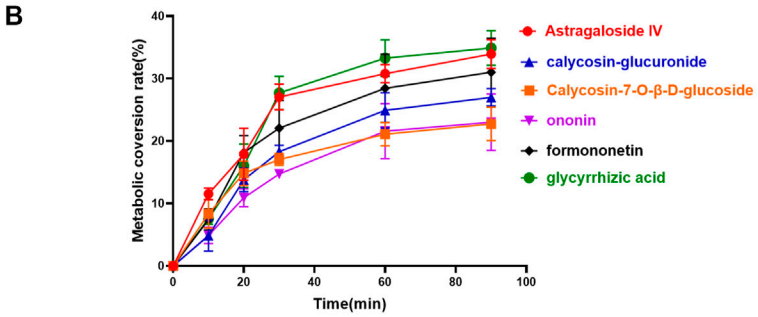

The metabolic conversion rate of each component in the liver microsomal incubation system under different reaction times.

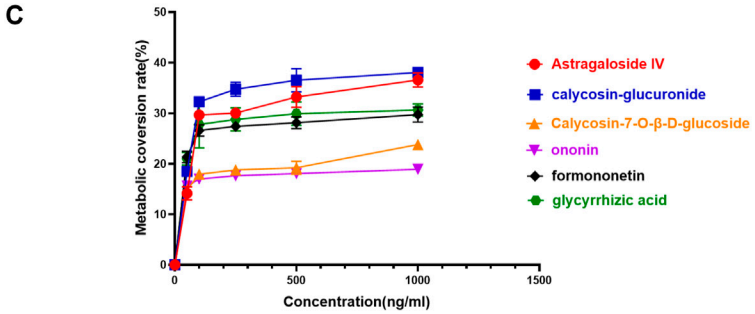

Effect of each component's concentration on its own metabolic conversion rate in the liver microsomal incubation system.

FIGURE 3
Effects of different conditions on the metabolic conversion rate of the six components in the liver microsomal incubation system. **(A)** The metabolic conversion rate of each component in the liver microsomal incubation system at different protein concentrations. **(B)** The metabolic conversion rate of each component in the liver microsomal incubation system under different reaction times. **(C)** Effect of each component's concentration on its own metabolic conversion rate in the liver microsomal incubation system.

to commence the reaction, and the solution was incubated for 60 min at 37°C on a thermostatic oscillator. At the end of the reaction, 400 L of ice-cold methanol containing the IS (the final concentrations of digoxin and puerarin were 0.745 μg/mL and 1 μg/mL, respectively) was added to terminate the reaction. The samples were vortexed for 1 min and centrifuged for 10 min (15,000 r/min). The contents of six active components in the supernatant were determined by HPLC-MS-MS. All reactions were performed in triplicate.

2.7 Preparation of quality control samples

The three concentrations of quality control samples were prepared by taking 50 μL of inactivated liver microsomes and adding 50 μL PBS solution, 80 μL mixed solution containing six components (astragaloside IV, glycyrrhizic acid, calycosin-glucuronide, formononetin, ononin, calycosin-7-O-β-D-glucoside) with low, medium, and high concentrations, 20 μL NADPH, 200 μL methanol, and 200 μL internal standard solution.

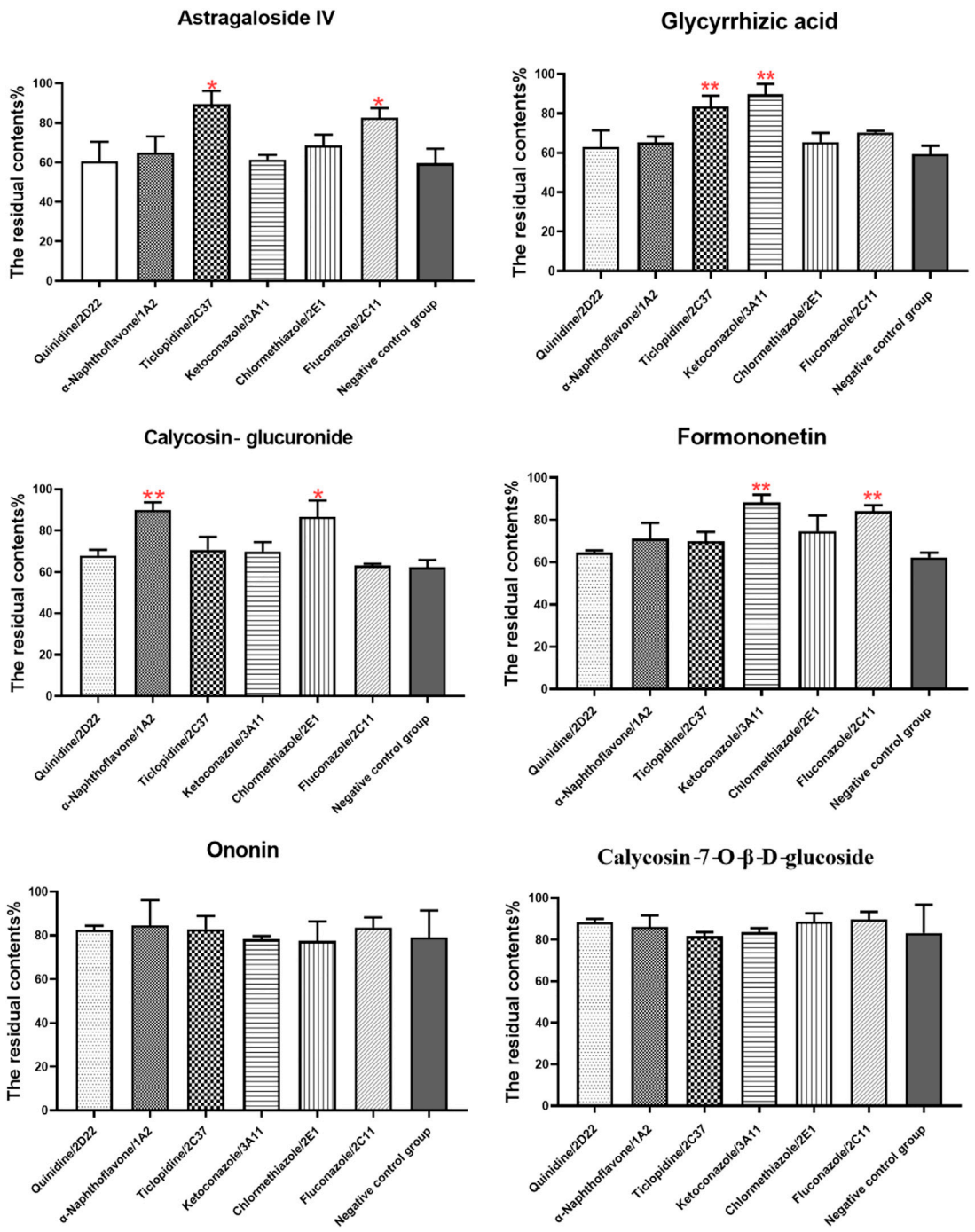

FIGURE 4
Effects of specific CYP enzyme inhibitors on the metabolism of the six components.

2.8 HPLC-MS/MS analysis

2.8.1 Conditions of HPLC-MS/MS

An Acquity HPLC system (Shimadzu Corp., Kyoto, Japan) equipped with a Q-Trap® 5,500 triple quadruple mass spectrometer (AB Sciex, Framingham, MA, United States) was utilized for HPLC-MS/MS. Multiple reaction monitoring (MRM) was employed to achieve mass spectrometric quantification. The parameters of the mass spectrometer were optimized as follows: source temperature at 600°C, nebulizer pressure at 55 psi, curtain gas at 30 psi, auxiliary gas at 55 psi, and ion spray voltage at −4.5 kV (−) or 5.5 kV (+). The mass spectrum parameters are shown in Table 2.

The liquid chromatography analyses of the six effective components were conducted using an ACEExcel2C18-AR column (100 × 2.1 mm, 2 μm, Advanced Chromatography Technologies Ltd., Aberdeen, United Kingdom) at 30°C. Analysis

was completed with a gradient elution of 0.1% formic acid (A) and acetonitrile (B). The flow rate was 0.4 mL/min. The gradient elution procedure was as follows: 0–0.6 min at 10% B, 0.6–2 min at 10%–30% B, 2–6 min at 30%–65% B, 6–8 min at 65%–90% B, 8–9 min at 90%–90% B, 9–9.1 min at 90%–10% B, and 9.1–12 min at 10% B.

2.8.2 Method validation

2.8.2.1 Specificity

Briefly, 50 μL of inactivated liver microsomes were mixed with 50 μL of mix specific inhibitor, before adding 80 μL of PBS solution, 20 μL of NADPH, and 400 μL of methanol. Subsequently, the samples were vortexed for 1 min and sonicated for 3 min. After precipitating the protein, the samples were centrifuged at 15,000 r/min for 10 min, and the supernatant was collected to obtain sample A. Next, 50 μL of inactivated liver microsomes were mixed with 50 μL of mix specific inhibitor before we added 80 μL of the mixed solution of six components (astragaloside IV, glycyrrhizic acid, calycosin-glucuronide, formononetin, ononin, calycosin-7-O-β-D-glucoside) prepared in advance, 20 μL of NADPH, 200 μL of methanol, and 200 μL of internal standard solution. The remainder of the operations were the same as those outlined above for sample A, and the supernatant was collected to obtain sample B. Another sample containing six components was incubated according to the method described in section 2.6 to obtain sample C.

2.8.2.2 Calibration curves and linearity

Briefly, 50 μL of inactivated liver microsomes were mixed with 50 μL of PBS solution, 20 μL of NADPH, 200 μL of methanol, 200 μL of internal standard solution, and then 80 μL of mixed standard solution of different concentrations was added to create a series of mixed working solutions. The samples were incubated according to the method described in section 2.6 and the supernatant was collected for determination using HPLC-MSMS. The calibration curves were drawn with the concentration (C) of each component as the horizontal coordinate X, and the ratio (A/A_i) between the peak area of each component and internal standard as the vertical coordinate Y. Linear regression analysis was conducted using the weighted least squares method to obtain the regression equation. The lowest concentration in the calibration curve was used as the lower limit of quantification (LLOQ).

2.8.2.3 Accuracy and precision

The low-, medium-, and high-concentration quality control samples were incubated according to the method described in Section 2.6. Accuracy and precision were assessed by repeated determination of six components in three concentration quality control samples six times a day for three consecutive days. The precision of the assay was computed using the relative standard deviation (RSD,%). The accuracy of the method was evaluated by the ratio of the measured concentration to the spiked concentration (%).

2.8.2.4 Extraction recovery and matrix effects

To obtain sample A, the low-, medium-, and high-concentration quality control samples were incubated according to the method described in Section 2.6 and the supernatant was collected for determination by HPLC-MS/MS. Then, 50 μL of inactivated liver microsomes were treated according to the method described in Section 2.6, with the exception of adding the six components and internal standard. Subsequently, the corresponding low, medium, and high concentrations of the six components and internal standard mixed solution were added to the supernatant to obtain sample B. The low, medium, and high concentrations of the six-component standard solution (80 μL) were mixed with the internal standard (200 μL) and the initial mobile phase (320 μL) to obtain sample C. The ratio of the peak area of sample A to sample B was defined as the extraction recovery rate, while the ratio of the peak area of sample B to sample C was defined as the matrix effect.

2.8.2.5 Stability

Low-, medium-, and high-concentrations of quality control samples were incubated according to the method described in Section 2.6. Subsequently, the quality control samples were stored at 25°C for 4 h, refrigerated for 48 h at −20°C, and underwent triple freeze-thaw cycles. The stability was evaluated by investigating the content changes of six components under different storage conditions.

2.9 Research on the dominant metabolic enzymes of six effective components of HQD

2.9.1 Optimization of protein concentration in liver microsomal incubation system

The six-component mixed standard solutions were incubated with the liver microsomal sample of different protein concentrations (0, 0.25, 0.5, 0.75, 1, 2 mg/mL) for 60 min, each with six replicates. Subsequently, samples were prepared according to the methods described in Section 2.6. The residual contents of the six effective components in each group were determined by HPLC-MS/MS to calculate the metabolic conversion rate.

2.9.2 Optimization of reaction time in liver microsomal incubation system

The mixed standard solution containing the six components was incubated with mouse liver microsomes at 37°C for different time (0, 15, 30, 45, 60, 90 min), each with six replicates. Subsequently, samples were prepared according to the methods described in Section 2.6. The residual contents of the six effective components in each group were determined by HPLC-MS/MS to calculate the metabolic conversion rate.

2.9.3 Effect of each analyte's concentration on its own metabolism

The standard solution of astragaloside IV, glycyrrhizic acid, calycosin-glucuronide, formononetin, calycosin-7-O-β-D-glucoside, and ononin was added to phosphate-buffered saline (PBS, pH 7.0) as desired for dilution to produce a series of mixed solutions (50, 100, 250, 500, 1,000 ng/mL). Each mixed solution sample was incubated with 1.0 mg/mL liver microsomes for 60 min. The residual contents of the six effective components were determined by HPLC-MS/MS to calculate the metabolic conversion rate.

2.9.4 Effects of liver CYP enzymes specific inhibitors on the metabolism of six effective components

A-naphthoflavone, quinidine, clomethiazole, ticlopidine, ketoconazole, and fluconazole were selected as specific inhibitors of CYP1A2, CYP2D22, CYP2E1, CYP2C37, CYP3A11, and CYP2C11, respectively (El-Sherbeni and El-Kadi, 2014; Xu et al., 2016). Forty-eight mice were randomly divided into eight groups of six mice each. The eight groups comprised six different specific inhibitor groups, a negative control group and a control group. For different specific inhibitor groups, mouse liver microsomes were incubated with related CYP450 enzyme specific inhibitors and mixed standard solutions. In the negative control group, mouse liver microsomes were incubated with mixed standard solution without specific inhibitors. In the control group, inactivated liver microsomes were combined with mixed standard solution without inhibitors and not incubated. After the samples were treated according to the methods described in Section 2.6, the residual level of the six effective components was determined for each group using HPLC-MS/MS. The residual contents of each component (%) = V_c/V_0*100 (where V_c is the residual amount of each group and V_0 is the content of the control group).

2.10 Statistical analysis

All data were expressed as mean ± standard deviation. SPSS 23 was used for statistical analysis between the two groups. $p \leq 0.05$ and $p \leq 0.01$ were statistically significant between the two groups.

3 Results

3.1 Method validation of HPLC-MS/MS

3.1.1 Specificity

The results demonstrated that the chromatographic peaks of the six components were well separated, with no interference between them. The retention times of astragaloside IV, glycyrrhizic acid, calycosin-glucuronide, formononetin, ononin, and calycosin-7-O-β-D-glucoside were 5.05 min, 5.25 min, 4.49 min, 5.54 min, 4.20 min, and 3.45 min, respectively (Figure 1).

3.1.2 Calibration curves and linearity

Using the concentration of the six components as the abscissa (X) and the ratio of the peak area between each component and internal standard as the ordinate (Y), the weighted least squares method was employed for linear regression calculation to obtain the regression equation. All calibration curves displayed great linearity and coefficients of correlation ranging from 0.9992 to 0.9998. The regression equation and linear range for six components in the liver microsomal samples are listed in Table 3.

3.1.3 Accuracy and precision

The inter- and intra-day precision ranged from 2.3% to 15.66% and 0.37%–17.43%, respectively. The inter- and intra-day precision and accuracy of six components in liver microsomal samples are summarized in Table 4. These results demonstrate that the method is accurate and reliable.

3.1.4 Extraction recovery and matrix effects

The mean matrix effect of the six components ranged from 90.57% ± 5.59% to 103.9% ± 6.33% with RSD <15%, and extraction recovery of the six components ranged from 88.06 ± 1.10 to 105.9 ± 10.46 with RSD <20%, which suggested that the recoveries of the six components were reliable in microsomal samples. Furthermore, there was no matrix interference. The matrix effect and extraction recovery are displayed in Table 5.

3.1.5 Stability

The result is displayed in Table 6. Our results revealed that the components are stable when stored at room temperature (approximately 25°C) for 4 h, refrigerated (−20°C) for 48 h and three freeze-thaw cycles. Therefore, the stability of samples conformed to the standard of biological sample determination. Figure 2.

3.2 Dominant metabolic enzymes of the six effective components in HQD

3.2.1 Optimization of protein concentration in liver microsomal incubation system

The results are shown in Figure 3. The metabolic conversion rate of astragaloside IV, glycyrrhizic acid, calycosin-glucuronide, formononetin, ononin, calycosin-7-O-β-D-glucoside initially increased with the increase in protein concentration. At higher concentration, the conversion rate for each analyte saturated. Therefore, for subsequent experiments, a 1 mg/mL concentration of liver microsomal protein was selected.

3.2.2 Optimization of reaction time in liver microsomal incubation system

The metabolic conversion rate of astragaloside IV, glycyrrhizic acid, calycosin-glucuronide, formononetin, ononin, calycosin-7-O-β-D-glucoside increased with time, however, saturated after 60 min (Figure 3). Thus, 60 min was selected as the incubation reaction time.

3.2.3 Effect of each analyte's concentration on its own metabolism

The metabolic conversion rates of the six components increased with the increase of their respective concentrations and plateaued after increasing to 100 ng/mL (Figure 3). Therefore, 100 ng/mL was chosen as the concentration of the six components in the incubation system of liver microsomes.

3.3 Effects of specific liver CYP enzyme inhibitors on the metabolism of six effective components

The effect of specific CYP enzyme inhibitors on the metabolism of six components was investigated (Figure 4). Compared to the control group, all components in negative control group were

metabolized obviously, indicating that the condition of liver microsomal incubation system was reasonable and feasible. The addition of specific CYP enzymes inhibitors reveals that ticlopidine, a specific inhibitor of CYP2C37, prevented the metabolism of astragaloside IV and glycyrrhizic acid. Fluconazole, a specific inhibitor of CYP2C11, prevented the metabolism of astragaloside IV and formononetin. α-naphthoflavone, a specific inhibitor of CYP1A2, prevented the metabolism of calycosin-glucuronide. Clomethiazole, a specific inhibitor of CYP2E1, prevented the metabolism of calycosin-glucuronide. Lastly, ketoconazole, a specific inhibitor of CYP3A11, prevented the metabolism of formononetin and glycyrrhizic acid. However, the metabolism of calycosin-7-O-β-D-glucoside and ononin was not affected by the addition of these CYP enzymes inhibitors. Taken together, CYP2C37 and CYP2C11 may be involved in the metabolism of astragaloside IV, while the metabolism of calycosin-glucuronide may be related to CYP1A2 and CYP2E1. Moreover, CYP3A11 and CYP2C11 may be involved in the metabolism of formononetin, and the metabolism of glycyrrhizic acid may be related to CYP3A11 and CYP2C37.

4 Discussion

The db/db mouse model derived from the C57BL/6J mice has a defective leptin receptor gene with the characteristic of spontaneous diabetes mellitus 2 development. The pathogenesis of this model is very similar to that of human type 2 diabetes mellitus. After 4 weeks of age, this mouse strain gradually develops diabetic signs such as obesity, glycosuria, hyperglycemia, and hyperlipidemia, whereas complications of diabetic nephropathy occur at 8–12 weeks of age (Ponchiardi et al., 2013; Wang et al., 2022c). A previous study by our group found that blood glucose, triglycerides, cholesterol, blood creatinine, urea nitrogen, and 24-h urinary protein were significantly higher in 12-week-old db/db mice compared to control ($p < 0.05$). Simultaneously, our previous study found that many collagen fibers (blue) were visible in the glomerular basement membrane and tubular interstitium of 12-week-old db/db mice, and significantly more than that of the control, with obvious collagen fiber deposition and obvious glomerular and tubular lesions (Wang et al., 2022d). Therefore, 12-week-old db/db mice were used as the mouse model of diabetic nephropathy and db/m mice of the same age were used as the control. To avoid the effect of disease on drug metabolizing enzymes, the liver of the control mice was used to construct an *in vitro* liver microsome incubation system.

The CYP450 family of enzymes is the most important enzyme for the oxidative metabolism of drugs in the liver and an important object of preclinical drug metabolism studies. CYPs belong to phase I drug metabolizing enzymes, of which CYP2D6, CYP1A2, CYP2C19, CYP3A4, CYP2E1, and CYP2C9 are the six most dominant subtypes. These six subtypes account for approximately 80% of the liver's total CYP450 enzymes, and 90% of drugs are metabolized by these six subtypes (Feng et al., 2019). Therefore, the six enzyme subtypes, CY2D6, CY1A2, CY2C19, CY3A4, CY2E1, and CY2C9, which have a large distribution and can metabolize numerous drugs, were selected for our investigation. Humans and mice are both mammals, and although many subtypes of CYP450 enzymes are unique to their species, they also have direct homology and similar functions. Therefore, it is possible to predict the physiological activity of different subtypes of CYP450 in humans by studying homologous subtypes in mice. Therefore, we chose to use mouse liver microsomes for metabolic studies (Martignoni et al., 2006; Li et al., 2017). Among them, mouse CYP1A2, CYP2D22, CYP3A11, CYP2E1, CYP2C11, and CYP2C37 are homologous to human CYP1A2, CYP2D6, CYP3A4, CYP2E1, CYP2C9, and CYP2C19, respectively. (Martignoni et al., 2006; Han et al., 2012; Yang et al., 2016; Weng et al., 2020). First, an *in vitro* incubation system for liver microsomes was established. According to the correspondence of CYP450 enzyme homologs between humans and mice, the related CYP450 enzyme-specific inhibitors quinidine (CYP2D22), α-naphthoflavone (CYP1A2), ticlopidine (CYP2C37), ketoconazole (CYP3A11), clomethiazole (CYP2E1) and fluconazole (CYP2C11) were added, and high-performance liquid chromatography-triple quadrupole tandem mass spectrometry (HPLC-MS/MS) was used to determine the metabolic residues of the six components (astragaloside IV, glycyrrhizic acid, calycosin-glucuronide, formononetin, ononin, calycosin-7-O-β-D-glucoside). However, the results also showed that CYP450 enzyme-specific inhibitors had no significant effect on calycosin-7-O-β-D-glucoside and ononin *in vitro*. Active ingredients bind, cleave, and metabolize intestinal flora after entering the intestine, which affects drug absorption and utilization, especially components containing glucosides such as calycosin-7-O-β-D-glucoside and ononin. Moreover, numerous drug transporters found on intestinal epithelial cells are targets for improving drug absorption and bioavailability, and calycosin-7-O- β-D-glucoside and ononin are likely metabolized by other metabolizing enzymes (Zhang et al., 2014; Wang et al., 2015).

5 Conclusion

An *in vitro* liver microsomal incubation method was adopted to study the effects of specific inhibitors of liver CYP450 enzymes on the metabolism of the six effective components so as to analyze the dominant CYP enzymes that may be involved in the metabolism of each component. Combined with the changes in enzyme activity in preliminary research, this study explored the possible reasons for the differences in pharmacokinetics of HQD under physiological and pathological states from the perspective of drug metabolism, as well as the possible drug-drug interactions caused by their clinical application. The results provide a theoretical basis for the clinical application and future development of traditional Chinese medicine.

Data availability statement

The original contributions presented in the study are included in the article/supplementary material, further inquiries can be directed to the corresponding author.

Ethics statement

The animal study was reviewed and approved by The animal studies were approved by the Animal Ethical Committee of Guizhou

University of Traditional Chinese Medicine (the approval number is NO1702060).

Author contributions

QW conceived and designed the experiments; QW and TT performed all of the experiments; ZW, HY, YG, SZ, and XC contributed to the operation of mice/materials/reagents/analysis tools; QW and TT analyzed the data; and QW and TT wrote a draft of the paper.

Funding

This research was supported by the Project of Guizhou Provincial Department of Education (No. QJHKYZ[2022]257), the Provincial Program on Scientific Research Projects of the Science and Technology Department of Guizhou Province (QKHJC-ZK[2023]YB416), and the Guizhou University of Traditional Chinese Medicine Doctoral Starting Fund ([2020]79).

Conflict of interest

The authors declare that the research was conducted in the absence of any commercial or financial relationships that could be construed as a potential conflict of interest.

Publisher's note

References

Chen, C. C., Qin, X. M., Du, G. H., and Zhou, Y. Z. (2019). The "compatible art" of effective components from traditional Chinese medicine, research on the compatibility and proportion of effective components. *Acta Pharm. Sin.* 54 (5), 808–817. doi:10.16438/j.0513-4870.2018-1119

Chen, X. Y., Huang, X. J., Du, T. L., Zeng, X. H., Yao, L., and Huang, D. E. (2014). Randomized parallel group study on the effect of Huangqiliuyi Decoction on blood sugar, insulin, glycated hemoglobin, cell morphology of diabetic rats. *J. Pract. Traditional Chin. Intern. Med.* 28 (9), 113–117. doi:10.13729/j.issn.1671-7813.2014.09.54

Dai, Y. J., Guo, M. F., Jiang, L., and Gao, L. (2022). Network pharmacology-based identification of miRNA expression of Astragalus membranaceus in the treatment of diabetic nephropathy. *Medicine* 101 (5), e28747. doi:10.1097/MD.0000000000028747

El-Sherbeni, A. A., and El-Kadi, A. O. S. (2014). Characterization of arachidonic acid metabolism by rat cytochrome P450 enzymes: The involvement of CYP1As. *Drug Metabolism Dispos.* 42 (9), 1498–1507. doi:10.1124/dmd.114.057836

Feng, X. L., Liu, Y., Sun, X., Li, A., Jiang, X. Y., etal, et al. (2019). Pharmacokinetics behaviors of l-menthol after inhalation and intravenous injection in rats and its inhibition effects on CYP450 enzymes in rat liver microsomes. *Xenobiotica* 49 (10), 1183–1191. doi:10.1080/00498254.2018.1537531

Gong, Z. P., Chen, Y., Zhang, R. J., Yang, Q., and Zhu, X. X. (2015). Advances on pharmacokinetics of traditional Chinese medicine under disease states. *China J. Chin. Materia Medica* 40 (2), 169–173. doi:10.4268/cjcmm20150202

Han, Y., Ren, B., Jing, G., Jing, G. P., Meng, X. L., Zhou, Z. Y., et al. (2012). Evaluation of impact of Herba Erigerontis injection, a Chinese herbal prescription, on rat hepatic cytochrome P450 enzymes by cocktail probe drugs. *J. Ethnopharmacol.* 139 (1), 104–109. doi:10.1016/j.jep.2011.10.019

Hou, S. Z., Zhang, T., Li, Y., Guo, F. Y., and Jin, X. (2017). Glycyrrhizic acid prevents diabetic nephropathy by activating AMPK/SIRT1/PGC-1α signaling in db/db Mice. *J. Diabetes Res.* 2017, 2865912. doi:10.1155/2017/2865912

Hu, M. Y., Liu, C., Zhang, M., Hu, L., and Liuetal, L. (2014). Alteration of cytochrome P450s activity under diabetic conditions and its impact on the development of diabetes mellitus. *J. China Pharm. Univ.* 45 (2), 153–160. doi:10.11665/j.issn.1000-5048.20140204

Hu, Y. J., Wang, Y. Q., Wang, Y. P., Wang, X. C., and Xiong, Y. (2016). Study on efficient components recognition, compatibility ideas, and quality control mode for Chinese materia medica. *Chin. Traditional Herb. Drugs* 47 (17), 2965–2971. doi:10.7501/j.issn.0253-2670.2016.17.001

Li, M. M., Zhou, T., and Xv, F. (2017). Comparisons of cytochrome P450 orthologous subtypes in human, rat and mouse. *Pharm. Care Res.* 17 (2), 81–86. doi:10.5428/pcar20170201

Liu, S. L., Li, A. D., Jiang, B., Mi, J., Nan, H. M., Bao, P., et al. (2022b). Comparison of efficacy and safety of traditional Chinese patent medicines for diabetic nephropathy, A protocol for Bayesian network meta-analysis. *Medicine* 101 (19), e29152. doi:10.1097/MD.0000000000029152

Liu, X. J., Hu, X. K., Yang, H., Gui, L. M., Cai, Z. X. R., Qi, M. S., et al. (2022a). A Review of traditional Chinese medicine on treatment of diabetic nephropathy and the involved mechanisms. *Am. J. Chin. Med.* 50, 1739–1779. doi:10.1142/S0192415X22500744

Ma, K. K., Ju, Y. H., Chen, Q. Q., Li, W. Z., Li, W. P., et al. (2019). Effect of astragaloside IV on regulation of PI3K/Akt/FoxO1 signal in kidney of type 2 diabetic nephropathy rats. *Chin. J. Exp. Traditional Med. Formulae* 25 (2), 74–81.

Ma, N. H., Zhang, Y., Sun, L. Y., Zhao, Y., and Ding, Y. (2021). Comparative Studies on Multi-Component pharmacokinetics of polygonum multiflorum thunb extract after oral administration in different rat models. *Front. Pharmacol.* 12, 655332. doi:10.3389/fphar.2021.655332

Martignoni, M., Groothuis, G. M. M., and Kanter, R. D. (2006). Species differences between mouse, rat, dog, monkey and human CYP-mediated drug metabolism, inhibition and induction. *Expert Opin. drug metabolism Toxicol.* 2 (6), 875–894. doi:10.1517/17425255.2.6.875

Ponchiardi, C., Mauer, M., Najafian, B., and etal (2013). Temporal profile of diabetic nephropathy pathologic changes. *Curr. Diabetes Rep.* 4 (13), 592–599. doi:10.1007/s11892-013-0395-7

Qian, M. Y., Gao, X., Chen, X. L., Wang, J. W., Gao, H. F., etal, et al. (2022). Metabolic characteristics and pharmacokinetic differences of Qiwei Tongbi oral liquid in rheumatoid arthritis rats. *Biomed. Chromatogr. BMC* 36 (7), e5375. doi:10.1002/bmc.5375

Wang, F. J., Fan, J. E., Pei, T. T., He, Z. E., Zhang, J. X., Ju, L., et al. (2022a). Effects of shenkang pills on early-stage diabetic nephropathy in db/db mice via inhibiting AURKB/RacGAP1/RhoA signaling pathway. *Front. Pharmacol.* 13, 781806. doi:10.3389/fphar.2022.781806

Wang, L. N., Lin, X., Shen, L., and Feng, Y. (2015). Effect of common clinical diseases on pharmacokinetics of traditional Chinese medicine. *Chin. J. Exp. Traditional Med. Formulae* 21 (18), 206–210. doi:10.13422/j.cnki.syfjx.2015180206

Wang, Q., Shi, Y., Liu, X. D., Liu, T., Li, Y. J., Song, X., et al. (2022d). Pharmacokinetic difference of six active constituents of Huangqi Liuyi decoction between control and diabetic nephropathy mouse models. *Int. J. Anal. Chem.* 2022, 1–13. doi:10.1155/2022/7602992

Wang, Q., Shi, Y., Wu, Z. G., Song, X. L., Luo, J. F., Yang, H., et al. (2022b). Effects of Huangqi Liuyi decoction in the treatment of diabetic nephropathy and tissue distribution difference of its six active constituents between normal and diabetic nephropathy mouse models. *Front. Pharmacol.* 13, 934720–20. doi:10.3389/fphar.2022.934720

Wang, Q., Wang, Y. L., Liu, W., Lu, D., Jin, Y., Tang, N., et al. (2022c). Mechanisms underlying the differences in the pharmacokinetics of six active constituents of Huangqi Liuyi Decoction between normal and diabetic nephropathy mouse models. *Evidence-Based Complementary Altern. Med.* 2022, 2481654. doi:10.1155/2022/2481654

Wang, R., and Liang, X. M. (2004). Complexity of herb formula and methodology for study as well. *Res. Pract. Chin. Med.* 18, 98–100. doi:10.3969/j.issn.1673-6427.2004.z1.030

Wen, L. M., Xu, Y. L., Zhen, L., Zhen, J. Y., and Guo, W. F. (2018). Study on the effects and mechanism of astragalus Liuyi Decoction on type 2 diabetes mellitus rats. *J. Chin. Med. Mater.* 41 (3), 699–702. doi:10.13863/j.issn1001-4454.2018.03.040

Weng, M. Z., Hu, J. B., and Lin, Y. P. (2020). The determination of metabolic pathways of reishi polysaccharide in human liver particles and the vitro inhibition of CYP450 enzymes in human livers. *Acta Microsc.* 21 (9), 378–386.

Xu, X. Q., Geng, T., Zhang, S. B., Kang, D. Y., Li, Y. J., Ding, G., et al. (2016). Inhibition of Re du ning injection on enzyme activities of rat liver microsomes using cocktail method. *Chin. Herb. Med.* 8 (3), 231–241. doi:10.1016/s1674-6384(16)60045-x

Yang, R., Ma, X. H., Guo, J. H., and Liu, W. Y. (2016). Characteristics of drug metabolic enzymes.*Chin. J. New Drugs* 25 (7), 751–759.

Zhang, W., Jiang, S., Qian, D. W., Shang, E. X., Guan, H. L., Ren, H., et al. (2014). The interaction between ononin and human intestinal bacteria. *Acta Pharm. Sin.* 49 (8), 1162–1168. doi:10.16438/j.0513-4870.2014.08.009

frontiers | Frontiers in Pharmacology

TYPE Original Research
PUBLISHED 27 April 2023
DOI 10.3389/fphar.2023.1124693

OPEN ACCESS

EDITED BY
Zipeng Gong,
Guizhou Medical University, China

REVIEWED BY
Pamela J. Weathers,
Worcester Polytechnic Institute, United States
Shuyu Zhan,
Jiaxing University, China
Sara Eyal,
Hebrew University of Jerusalem, Israel

*CORRESPONDENCE
Chukwunonso K. Nwabufo,
Chukwunonso.nwabufo@usask.ca,
Chukwunonso.nwabufo@mail.utoronto.ca

RECEIVED 15 December 2022
ACCEPTED 06 April 2023
PUBLISHED 27 April 2023

CITATION
Nwabufo CK, Hoque MT, Yip L, Khara M, Mubareka S, Pollanen MS and Bendayan R (2023), SARS-CoV-2 infection dysregulates the expression of clinically relevant drug metabolizing enzymes in Vero E6 cells and membrane transporters in human lung tissues.
Front. Pharmacol. 14:1124693.
doi: 10.3389/fphar.2023.1124693

SARS-CoV-2 infection dysregulates the expression of clinically relevant drug metabolizing enzymes in Vero E6 cells and membrane transporters in human lung tissues

Chukwunonso K. Nwabufo[1,2]*, Md. Tozammel Hoque[1], Lily Yip[3], Maliha Khara[4,5], Samira Mubareka[3,5], Michael S. Pollanen[4,5] and Reina Bendayan[1]

[1]Department of Pharmaceutical Sciences, Leslie Dan Faculty of Pharmacy, University of Toronto, Toronto, ON, Canada, [2]OneDrug, Toronto, ON, Canada, [3]Sunnybrook Research Institute, Toronto, ON, Canada, [4]Ontario Forensic Pathology Service, Toronto, ON, Canada, [5]Department of Laboratory Medicine and Pathobiology, University of Toronto, Toronto, ON, Canada

SARS-CoV-2-mediated interactions with drug metabolizing enzymes and membrane transporters (DMETs) in different tissues, especially lung, the main affected organ may limit the clinical efficacy and safety profile of promising COVID-19 drugs. Herein, we investigated whether SARS-CoV-2 infection could dysregulate the expression of 25 clinically relevant DMETs in Vero E6 cells and postmortem lung tissues from COVID-19 patients. Also, we assessed the role of 2 inflammatory and 4 regulatory proteins in modulating the dysregulation of DMETs in human lung tissues. We showed for the first time that SARS-CoV-2 infection dysregulates CYP3A4 and UGT1A1 at the mRNA level, as well as P-gp and MRP1 at the protein level, in Vero E6 cells and postmortem human lung tissues, respectively. We observed that at the cellular level, DMETs could potentially be dysregulated by SARS-CoV-2-associated inflammatory response and lung injury. We uncovered the pulmonary cellular localization of CYP1A2, CYP2C8, CYP2C9, and CYP2D6, as well as ENT1 and ENT2 in human lung tissues, and observed that the presence of inflammatory cells is the major driving force for the discrepancy in the localization of DMETs between COVID-19 and control human lung tissues. Because alveolar epithelial cells and lymphocytes are both sites of SARS-CoV-2 infection and localization of DMETs, we recommend further investigation of the pulmonary pharmacokinetic profile of current COVID-19 drug dosing regimen to improve clinical outcomes.

KEYWORDS

SARS- CoV-2, drug metabolism, drug transport, inflammatory response, Vero E6 cells, human lung tissues, drug metabolizing enzymes (DMEs), membrane transporters

Introduction

Coronavirus disease 2019 (COVID-19) has killed over 6 million people and affected more than 600 million people worldwide, making it one of the deadliest pandemics of the 21st century (World Health organization, 2022). Although several vaccines are now available to protect against severe acute respiratory syndrome coronavirus 2 (SARS-CoV-2), full protection is not guaranteed for multiple reasons including evasion of neutralizing antibody by some variants of SARS-CoV-2 (Garcia-Beltran et al., 2021; Hoffmann et al., 2021; Madhi et al., 2021), breakthrough infection (Su et al., 2016; Krammer, 2020), and delay in reaching herd immunity (Our World in Data, 2021). Therefore, there is an urgent need to develop effective antiviral drugs that will complement the existing vaccines in improving the morbidity and mortality associated with COVID-19.

Currently, there is no cure for COVID-19; however, drugs such as remdesivir, molnupiravir, and nirmatrelvir have shown great promise relative to other candidates (Cascella et al., 2022). A major determining factor for the clinical efficacy and safety of these drugs is their ability to sufficiently distribute within the host and reach optimal therapeutic concentrations at disease target sites, particularly the lung tissue, the main organ affected by SARS-CoV-2 infection (Nwabufo and Aigbogun, 2022). For example, a previous study in rats found that the plasma levels of lopinavir were greater than its lung concentrations (Kumar et al., 2004), indicating that the drug may not be reaching the optimal pulmonary concentrations required to effectively eradicate SARS-CoV-2 virus. Yet, studies investigating the spatial distribution of COVID-19 drugs at the primary target cells (Type II alveolar epithelial cells) of SARS-CoV-2 infection within the lung tissues are still lacking.

The lung is heterogeneous, comprising about 40 different cell types with an unequal distribution of drug metabolizing enzymes and membrane transporters (DMETs), which have a lower expression and activity compared to their hepatic counterpart (Enlo-Scott et al., 2021a; 2021b). Alone or in synergy, these DMETs can alter the pulmonary concentration of drugs, rate and extent of their spatial distribution to disease target cells, accumulation in specific cell types and overall pulmonary drug retention, as well as absorption into the systemic circulation resulting in distinct local and systemic pharmacokinetic (PK)/pharmacodynamic (PD) profiles (Gustavsson et al., 2016; Ehrhardt et al., 2017).

Early response pro-inflammatory cytokines such as tumor necrosis factor (TNF)-α, interleukin-6 (IL-6), and IL-1β, are overproduced in a typical hospitalized COVID-19 patient and may be responsible for the acute respiratory distress syndrome, lung injury, and multiple-organ damage seen in some COVID-19 patients at severe stages of the disease (Aziz et al., 2020; Pilla Reddy et al., 2021; Rendeiro et al., 2021; Frisoni et al., 2022). Interestingly, IL-6 and IL-1β have both been implicated in the dysregulation (altering the normal levels) of DMETs (Dunvald et al., 2022), and their presence in COVID-19 pathophysiology warrants a similar investigation. Recent clinical studies have reported altered PK profiles for drugs such as midazolam (Le Carpentier et al., 2022), tacrolimus (Salerno et al., 2021), and lopinavir (Gregoire et al., 2020) in COVID-19 patients. These studies suggests that SARS-CoV-2-associated inflammatory response may be responsible for the altered PK profile. However, the molecular mechanism underlying SARS-CoV-2-mediated alteration of drug PK profile is yet to be demonstrated.

At the molecular level, proinflammatory cytokines may dysregulate the expression of DMETs through xenosensing regulatory proteins including pregnane X receptor (PXR), constitutive androstane receptor (CAR), nuclear factor kappa B (NF-kβ), phosphorylated signal transducer and activator of transcription 3 (pSTAT3) that control transcription (Wu and Lin, 2019; Stanke-Labesque et al., 2020; Dunvald et al., 2022). Also, inflammation-mediated damage of pulmonary cells housing DMETs, as well as recruitment of pulmonary immune cells such as macrophages (which also house DMETs) in response to SARS-CoV-2 infection could also alter local drug PK/PD profile (Nwabufo and Bendayan, 2022). In general, all these effects associated with an immune response to SARS-CoV-2 infection could lead to distinct PK/PD profiles in peripheral tissues and systemic circulation with potential clinical drug safety and efficacy issues for COVID-19 patients, especially those with polypharmacy.

In this present study (Figure 1), we investigated for the first time whether SARS-CoV-2 infection with D614G variant alters the mRNA expression of 9 inflammatory markers, 12 DMETs, in Vero E6 cells compared to mock. The D614G variant of SARS-CoV-2 was the most prevalent form of the virus at the onset of this study and is characterized by a mutation at position 614 in the spike protein which causes a change in amino acid sequence from aspartic acid to glycine (Korber et al., 2020). Several studies have shown that the D614G variant is more infectious than the original strain of the virus with increased spike protein binding to human cells (Korber et al., 2020; Yurkovetskiy et al., 2020; Zhang et al., 2020; Plante et al., 2021). Interestingly, the D614G mutation have been found in several variants of concern (VOI) including alpha (B.1.1.7), beta (B.1.351), delta (B.1.617.2), gamma (P.1), and omicron (BA.1, BA.2, BA.3, BA.4, BA.5) (Ou et al., 2022). Vero E6 cell line is derived from kidney epithelial cells of African green monkey and is one of the most used cell lines for studying SARS-CoV-2 virus because they express high levels of angiotensin-converting enzyme 2 receptor which is essential for cellular entry of the virus (Hoffmann et al., 2020; Rosa et al., 2021). This makes Vero E6 cell a good *in vitro* model for our study. More so, we have not identified any previous study that has examined the full panel of the inflammatory signature associated with SARS-CoV-2 infection or SARS-CoV-2-DMETs interactions in Vero E6 cells. Because the lung is the main organ affected by SARS-CoV-2 infection and may be prone to SARS-CoV-2-mediated dysregulation of DMETs, we further conducted a novel investigation of the cellular localization and changes in protein expression of 2 SARS-CoV-2-associated inflammatory markers, 4 regulatory proteins, and 13 DMETs in postmortem human lung tissues obtained from 10 COVID-19 patients compared to 5 age/sex-matched non-infected controls. We anticipate that any significant dysregulation will adversely affect the concentration of promising COVID-19 drugs in both peripheral tissues and systemic circulation, and may underpin the limited clinical efficacy and safety observed for several COVID-19 drug repurposing programs.

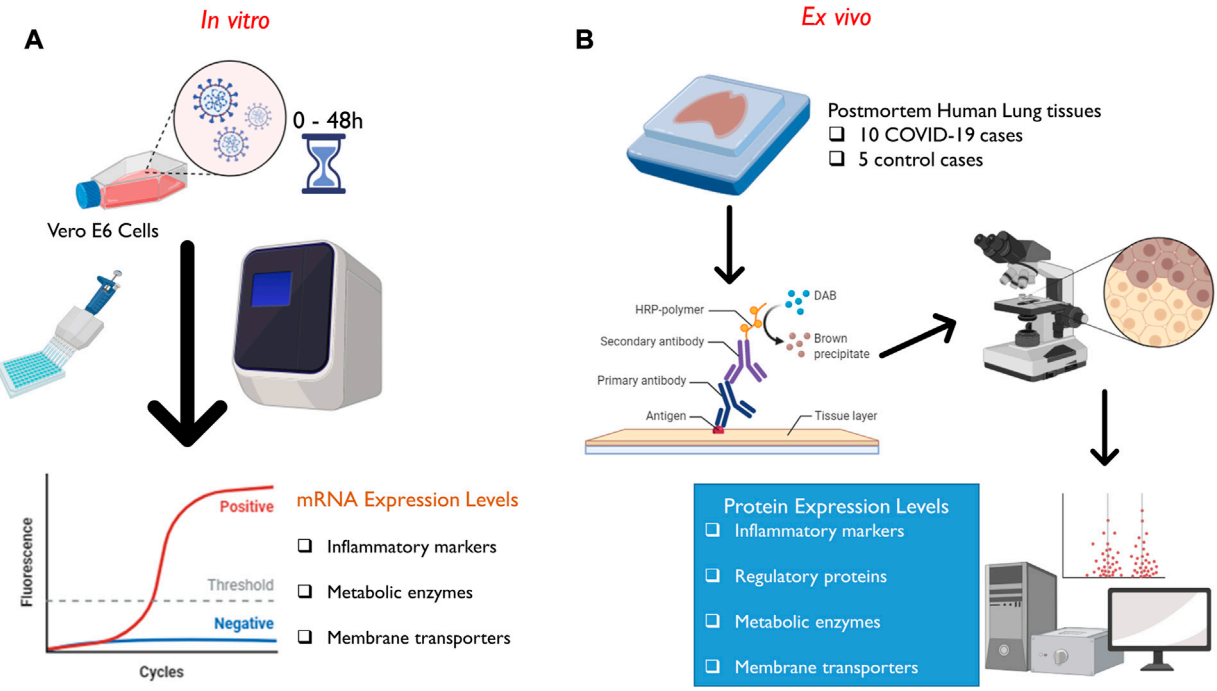

FIGURE 1
Methods deployed for investigation of SARS-CoV-2—DMETs interactions. **(A)** Vero E6 cells were infected with SARS-CoV-2 virus and cell pellets were collected at 0-, 6-, 24-, and 48- hours post-infection. Subsequently, relative mRNA expression of selected clinically relevant inflammatory markers (9), DMETs (12) was determined using qRT-PCR. **(B)** Chromogenic immunohistochemistry was used to localize and compare changes in protein expression of clinically relevant inflammatory markers (2), xenosensing regulatory proteins (4), DMETs (13) between COVID-19 and control postmortem human lung tissues.

Methods

In Vitro SARS-CoV-2—DMETs interactions

SARS-CoV-2 infection in Vero E6 cells and RNA extraction

Vero E6 cells were kindly provided by Dr. Mubareka, Sunnybrook Research Institute, and the SARS-CoV-2 infection was performed in their laboratory. Vero E6 cells were seeded in T75 cm^2 flasks to achieve 95% confluency the next day. Using a multiplicity of infection of 0.001 to avoid over-infection and excessive cell toxicity, cells were inoculated with 1.5 mL of SARS-CoV-2 virus containing the spike-protein D614G mutation. Mock controls were inoculated with DMEM media only. Cells were incubated at 37°C, 5% CO_2 for 45 min and rocked every 10 min before inoculum was removed and topped up with 15 mL DMEM (Wisent #319-005-CL) containing 2% heat-inactivated FBS (Wisent #080450), 100IU penicillin-100 µg/ml streptomycin and 2 mM L-glutamine (Wisent # 450-202-EL). Cell pellets were collected at 0-, 6-, 24-, and 48- hours' post-infection (hpi). Cell pellets were prepared by removing the supernatant, washing with 10 mL cold PBS, and scraping the monolayer with 5 mL fresh PBS. Lifted cells were collected into a tube, and another 5 mL of fresh PBS was added to collect any remaining cells. Cells were spun at 1,000 g for 5 min at 4°C and kept in the −80°C freezer. RNA extraction was performed using the Qiashredder and RNeasy Mini Plus kit (Qiagen). RNA concentrations at an absorbance of 260 nm and purity at an absorbance ratio of 260/280 were quantified using Nanodrop One Spectrophotometer (Thermo Scientific).

Virus stock

The virus (S357_P2_LY) propagated in Vero E6 cells and contains spike-protein D614G mutation. Sequencing revealed that the virus stock has 2 deletions (7% in position 23,598% and 10% in position 23,628) in the polybasic furin cleavage site located on the S gene. Supplementary Table S1 shows a list of other single nucleotide variants and their frequencies.

Real-time quantitative polymerase chain reaction analysis

Real-time quantitative polymerase chain reaction (qRT-PCR) was used to measure the mRNA expression of selected inflammatory markers, and DMETs (Supplementary Table S2). 2 µg isolated RNA was treated with DNase I to remove residual DNA and then reverse transcribed to cDNA using a high-capacity reverse transcription cDNA kit (Applied Biosystems) according to the manufacturer's instructions. Specific monkey TaqMan primers for selected inflammatory markers and DMETs (Supplementary Table S3) obtained from Life Technologies were used with TaqMan quantitative polymerase chain reaction biochemistry. All assays were performed in triplicates with *PPIB* (Peptidylprolyl isomerase B) and *GAPDH* (Glyceraldehyde-3-phosphate dehydrogenase; used for *CRP* and *IL10*) housekeeping genes as an internal control. For each gene, the critical threshold cycle (CT) was normalized to the housekeeping gene using the comparative CT method. Next, the

TABLE 1 Clinical and demographic characteristics for patients included in the immunohistochemistry study.

Sample ID	COVID-19 Status	Age	Gender	Cause of death
1	COVID-19	76	M	COVID-19
2	COVID-19	60	M	COVID-19
3	COVID-19	76	F	COVID-19; Chronic obstructive lung disease; Hypertensive cardiovascular disease
4	COVID-19	48	M	COVID-19
5	COVID-19	53	F	Complications of COVID-19 pneumonia (with saddle pulmonary embolism and deep vein thrombosis
6	COVID-19	37	M	COVID-19 with acute pulmonary thromboembolism
7	COVID-19	83	M	COVID-19; Atherosclerotic and hypertensive heart disease; Pulmonary emphysema
8	COVID-19	66	M	COVID-19; Diabetes mellitus; Essential hypertension
9	COVID-19	56	F	COVID-19
10	COVID-19	32	M	COVID-19
11	Non-COVID-19	32	M	Gammahydroxybutyrate toxicity
12	Non-COVID-19	41	M	Multiple drug toxicity (fentanyl, ethanol, and methamphetamine)
13	Non-COVID-19	59	F	Acute coronary thrombosis; intraplaque hemorrhage and rupture; atherosclerotic coronary artery disease
14	Non-COVID-19	66	M	Atherosclerotic heart disease
15	Non-COVID-19	74	M	Blunt impact head trauma

difference in CT values (ΔCT) between the gene of interest and the housekeeping gene was then normalized to the corresponding ΔCT of the vehicle control (ΔΔCT) and the relative difference in mRNA expression for each gene was represented as $2^{-\Delta\Delta CT}$.

SARS-CoV-2—DMETs interactions in human lung tissues

The studies involving human participants were reviewed and approved by the office of the Chief Coroner at Ontario Forensic Pathology Service (Chief Forensic Pathologist, and Chief Coroner). Written informed consent for participation was not required for this study in accordance with the national legislation and the institutional requirements.

Autopsies and postmortem lung tissue processing

Autopsies were performed as per guidelines provided by the Ontario Forensic Pathology Service with appropriate infection isolation procedures. Histological samples obtained during the autopsy were fixed in 10% neutral buffered formalin for at least 24 h before processing.

Immunohistochemical analysis

Chromogenic immunohistochemistry (IHC) was used to localize and quantify the expression of SARS-CoV-2 virus, inflammatory markers, regulatory proteins, and DMETs (Supplementary Table S4) in postmortem human lung tissues obtained from 10 infected COVID-19 patients and 5 age/sex-matched non-infected controls (Table 1). IHC was performed on 4 µm formalin-fixed paraffin-embedded sections of lung tissues. Primary antibodies for the selected biomarkers (Supplementary Table S5) were detected using a secondary antibody and horseradish peroxidase-conjugated streptavidin (MACH 4 universal HRP kit, Biocare Medical, CA, United States), followed by color development with 3,3′-Diaminobenzidine (DAB; DAKO Cat# K3468). Subsequently, cell morphology and nuclei were visualized by counterstaining with hematoxylin and eosin (H&E). Reagent negative control (Supplementary Figure S1) and positive control (Supplementary Figure S2) were performed to determine specificity. All immunostained slides were imaged with an Aperio AT2 brightfield scanner (Leica Biosystems) at ×20 magnification on a standard slide dimension (1”×3″).

Absolute protein quantitation

HALO software v3.4 (Indica Labs) was used to analyze the entire lung tissue section of each slide across all the investigated biomarkers. The multiplex IHC (v3.1.4) algorithm was used to quantify percentage of DAB positive cells which comprised the total number of DAB positive cells relative to the total number of cells quantified in the images.

Data analysis

All statistical analyses were performed using GraphPad Prism® (version 8.0 for Microsoft Windows, Graph Pad Software, San Diego, CA, United States) with a significant difference defined as a *p*-value of 0.05 or less. All results for mRNA expression and protein quantification were expressed as mean ± standard deviation (SD) and mean ± standard error of the mean (SEM), respectively. An unpaired *t*-test was used to determine significant differences in mRNA expression between the SARS-CoV-2-infected and mock Vero E6 cells. The non-parametric two-tailed Mann-Whitney test was used to assess the differences in protein expression between COVID-19 and control postmortem human lung tissues for absolute quantitative IHC analysis.

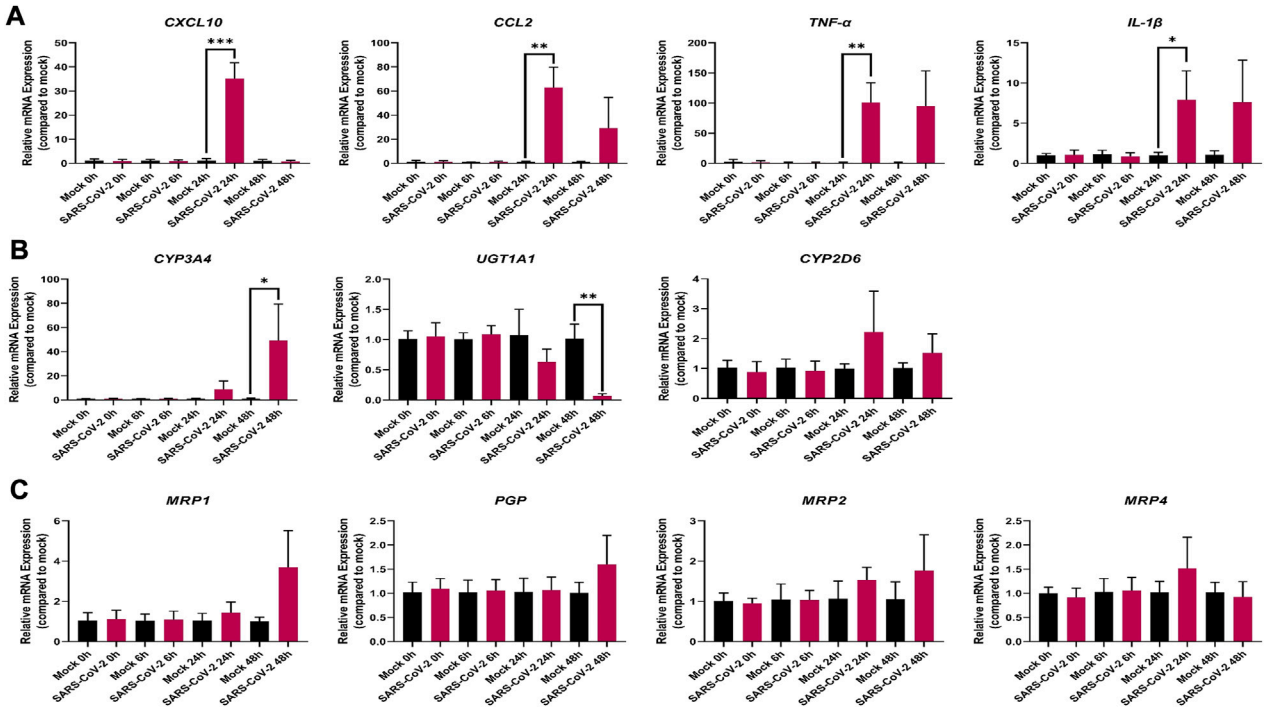

FIGURE 2
Effect of SARS-CoV-2 infection on the mRNA expression of selected **(A)** inflammatory markers; **(B)** drug metabolizing enzymes; and **(C)** membrane-associated drug transporters in Vero E6 cells. Relative mRNA expression was determined using qRT-PCR with normalization to the housekeeping gene and the mock. Results are expressed as mean ± SD from 3 independent experiments, and unpaired *t*-test was used to determine significant differences (*, $p < 0.05$; **, $p < 0.01$; ***, $p < 0.001$).

Results

In Vitro SARS-CoV-2—DMETs interactions

SARS-CoV-2-associated inflammatory response in Vero E6 cells

We observed significant changes in the mRNA expression level of inflammatory markers associated with COVID-19 severity including *IL-1β*, *TNF-α*, *CCL2*, and *CXCL10* in our SARS-CoV-2 infected Vero E6 cells (Figure 2A); suggesting that Vero E6 cells may be used to study the inflammatory events associated with COVID-19 and modelling the severe stage of the disease *in vitro*.

The mRNA expression of the pro-inflammatory cytokines, *IL-1β* and *TNF-α* was markedly upregulated by 7-($p < 0.05$) and 81-($p < 0.01$) fold, respectively, at 24 h (Figure 2A). Similarly, the mRNA expression of the chemokines, *CCL2* and *CXCL10*, was markedly increased by 56-($p < 0.01$) and 29-($p < 0.001$) fold, respectively, at 24 h in the infected SARS-CoV-2 Vero E6 cells (Figure 2A). However, at the 48-h mark, the mRNA expression level of *CXCL10* decreased to baseline in the infected SARS-CoV-2 Vero E6 cells (Figure 2A). No mRNA expression was observed for *CRP* and *IL-10* in both mock and infected Vero E6 cells (data not shown).

It is possible that species differences (humans and monkeys), as well as potential distinctions in the inflammatory events associated with the different variants of SARS-CoV-2 virus may be responsible for the lack of observable significant differences in the mRNA expression of *IL6*, *iNOS*, and *IFN- γ* (Supplementary Figure S3A) in the infected Vero E6 cells.

SARS-CoV-2—DMET interactions in Vero E6 cells

Out of the 7 investigated DMEs, only *CYP3A4* and *UGT1A*1 were significantly dysregulated at the mRNA level in SARS-CoV-2 infected Vero E6 cells (Figure 2B). At 48 h, the mRNA expression of *CYP3A4* was significantly upregulated by 50-fold ($p < 0.05$) in the infected Vero E6 cell (Figure 2B). At the same time point, *UGT1A1* mRNA expression was significantly downregulated by 0.5-fold ($p < 0.001$) in the infected Vero E6 cell (Figure 2B). No significant dysregulation of *CYP2D6* mRNA expression was observed (Figure 2B), and no mRNA expression was detected for *CYP1A2*, *CYP2B6*, *CYP2C8*, and *CYP2C9* in both mock and infected Vero E6 cells (data not shown).

None of the investigated membrane-associated drug transporters (*PGP*, *BCRP*, *MRP1*, *MRP2*, and *MRP4*) showed significant dysregulation in mRNA expression (Figure 2C; Supplementary Figure S3B).

SARS-CoV-2—DMET interactions in human lung tissues

Clinical characteristics and demographic information

Postmortem human lung samples were obtained from 10 and 5 (age/sex-matched) COVID-19 and control patients, respectively

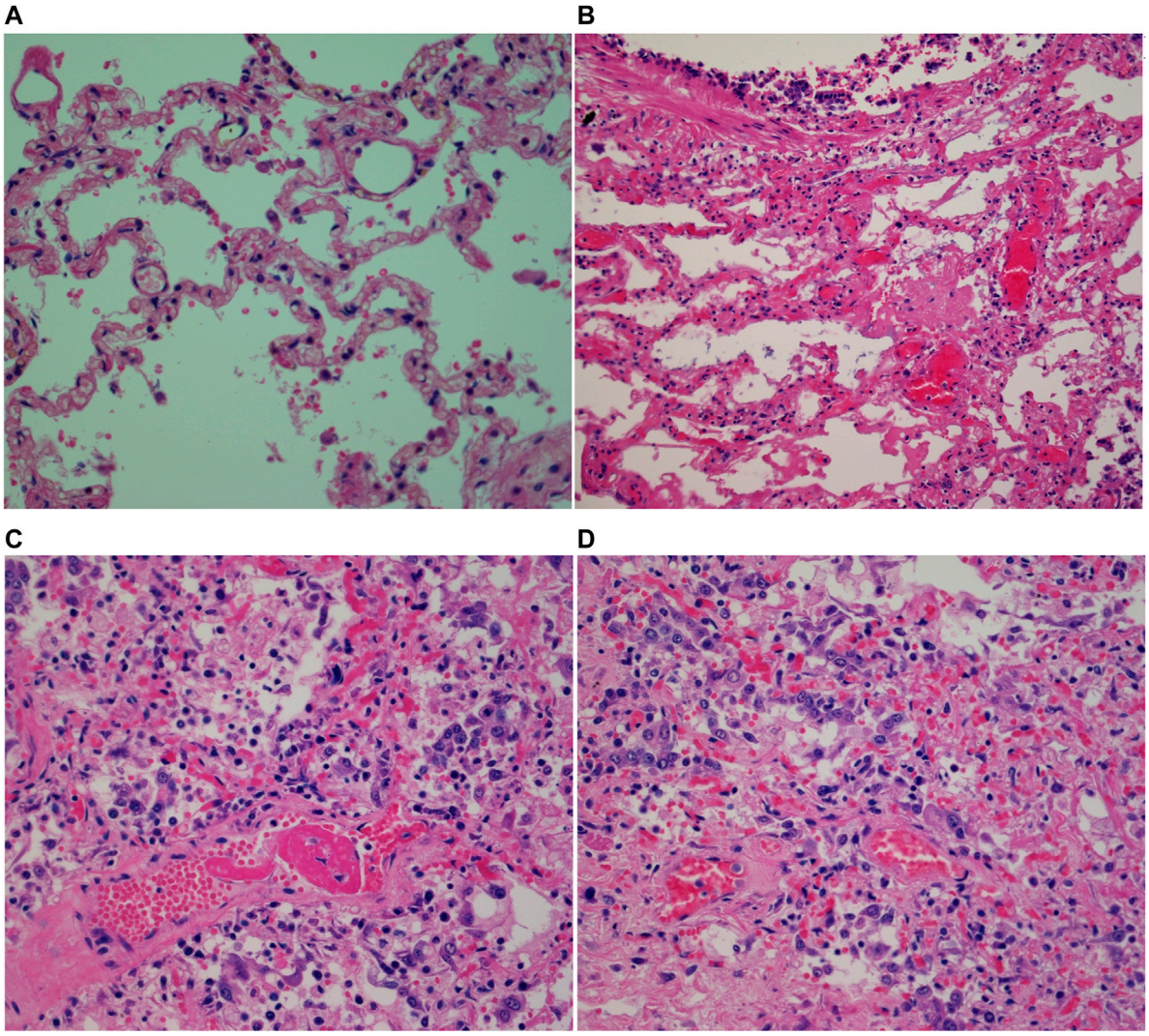

FIGURE 3
Micrographs of H&E stained postmortem human lung tissues (×40 magnification with an Olympus B×43 microscope) showing **(A)** normal human lung; **(B)** hyaline membrane formation; **(C)** perivascular lymphocytes; **(D)** COVID-19 organizing pneumonia.

(Table 1). COVID-19-related pathologies were the primary cause of death reported for the COVID-19 cases while no pulmonary pathologies were reported as the cause of death for the control cases. Comorbidities including pulmonary and cardiovascular diseases, as well as a metabolic disorder (Table 1) was observed in 3 of the COVID-19 cases. No additional information, for example, genetic polymorphisms of DMETs, cytokine panel, and intake of medications, were available for the COVID-19 and control groups.

COVID-19-related histopathological findings

Histological examination of the control cases did not reveal any significant pathologic abnormalities (Figure 3A). In COVID-19 cases, diffuse alveolar damage (DAD) was observed in two cases (Figure 3B). Assessment of preexisting lung disease was obscured by acute pathologies in some cases. For example, one COVID-19 case revealed multiple pathological changes: vascular hyperplasia, pigments in the alveolar spaces, thick alveolar septa, diffuse fibrosis, patchy areas of hyaline membranes, patchy type II pneumocyte hyperplasia, and focal areas of organizing COVID-19 pneumonia (Figures 3C, D). Another COVID-19 case had acute bronchitis, and 6 of the COVID-19 patients had hyaline membrane formation (Figure 3B). Pneumonia, ranging from acute to organizing phase (Figure 3C) was found in 7 COVID-19 cases. Five COVID-19 cases were also found to have inflammatory cells; one case had focal aggregation of chronic inflammatory cells, two cases had more acute and chronic inflammatory cells (Figure 3D), one case had mixed inflammatory infiltrates, and the fifth case had mixed inflammatory cells with more neutrophils. Two of the COVID-19 cases had unique features; one had more expanded air spaces and more diffuse intra-alveolar blood infiltration, while the other case had focal areas of consolidation (data not shown).

Localization of selected biomarkers in postmortem human lung tissues

Figure 4 shows the localization of the selected biomarkers (Supplementary Table S4) in COVID-19 postmortem human

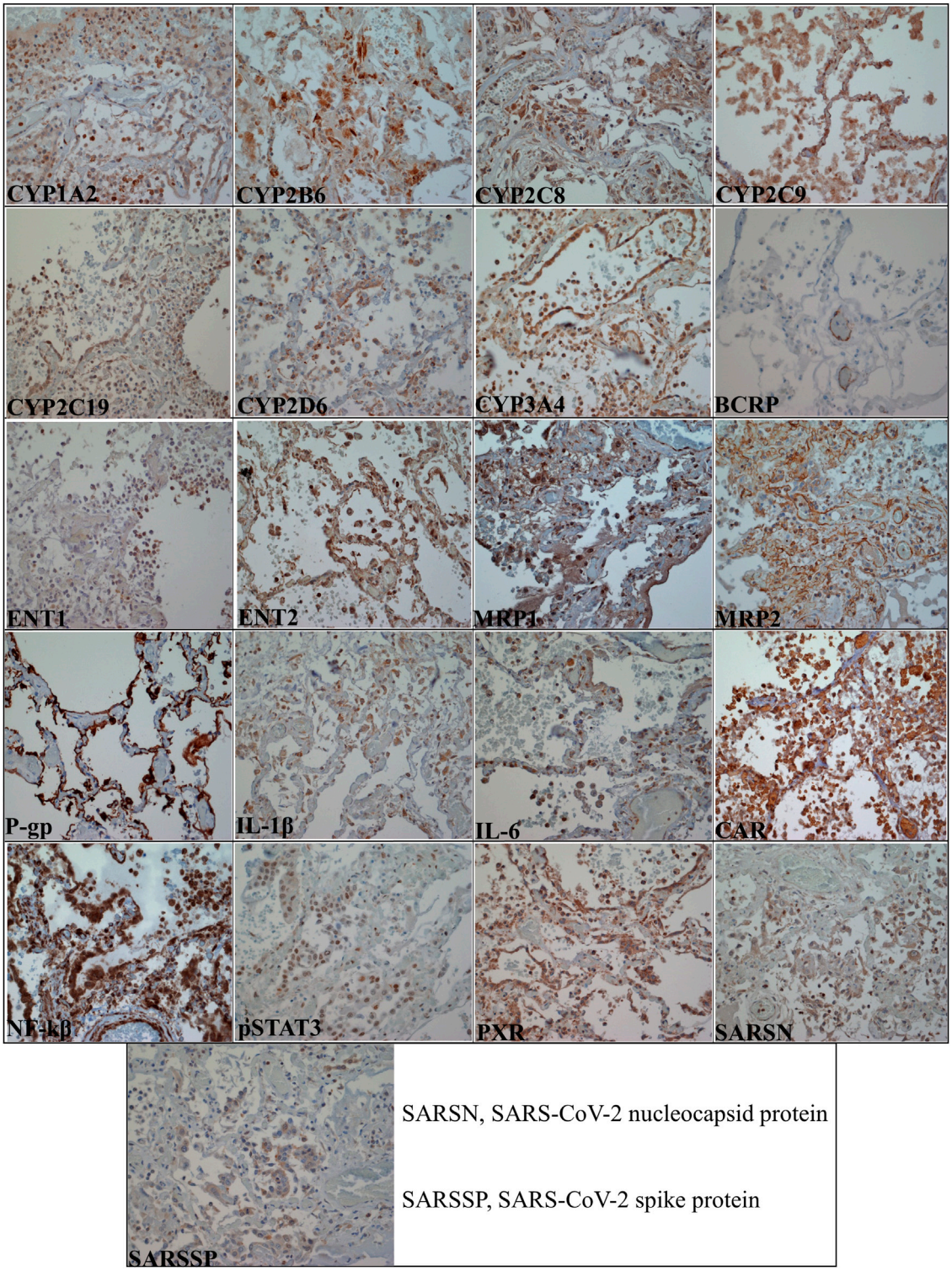

FIGURE 4
Micrographs of COVID-19 postmortem human lung tissue sections (x40 magnification with an Olympus Bx43 microscope) showing positive staining in brown color for all the investigated biomarkers. Table 2 summarizes the pulmonary cellular localization of the investigated biomarkers.

lung tissues while Table 2 summarizes the cellular expression of the biomarkers in each COVID-19 and control postmortem human lung tissues. Supplementary Figures S1, S2 are negative and positive control IHC images showing the good specificity of the antibodies used for the investigated biomarkers. In general, the investigated biomarkers are expressed in different pulmonary cell types with differences in cellular localization between COVID-19 and control cases (Figure 4; Table 2). The distinction in biomarker localization is

TABLE 2 Summary of the cellular localization of investigated biomarkers in postmortem human lung tissues.

Class of biomarkers	Biomarker	Cellular compartment	Pulmonary cells	COVID-19 cases	Control cases
Drug metabolizing enzymes	CYP1A2	Cytoplasm	Intra-alveolar lymphocytes	9/10	2/5
			Alveolar epithelial cells	10/10	5/5
			Macrophages	5/10	1/5
	CYP2B6	Cytoplasm	Alveolar epithelial cells	10/10	4/5
			Macrophages	3/10	3/5
			Lymphocytes	5/10	1/5
			Fibroblast	1/10	ND
		Nucleus	Lymphocytes	4/10	ND
	CYP2C8	Cytoplasm	Lymphocytes	6/10	3/5
			Macrophages	7/10	5/5
			Endothelial cells	8/10	3/5
			Fibroblast	3/10	ND
			Alveolar epithelial cells	8/10	4/5
			Bronchial epithelial cells	1/10	ND
	CYP2C9	Apical membrane	Alveolar epithelial cells	10/10	5/5
		Cytoplasm	Macrophages	9/10	3/5
			Fibroblast	1/10	ND
			Lymphocytes	3/10	ND
	CYP2C19	Cytoplasm	Alveolar epithelial cells	10/10	5/5
			Bronchial epithelial cells	3/10	4/5
			Lymphocytes	5/10	ND
			Macrophages	6/10	3/5
			Fibroblast	2/10	ND
	CYP2D6	Cytoplasm	Bronchial epithelial cells	3/10	3/5
			Lymphocytes	3/10	ND
			Macrophages	3/10	1/5
			Alveolar epithelial cells	8/10	4/5
		Cytoplasmic and circumferential membranous	Macrophages	ND	1/5
			Lymphocytes	1/10	ND
		Apical membrane	Bronchial epithelial cells	1/10	1/5
	CYP3A4	Cytoplasm	Lymphocytes	8/10	1/5
			Macrophages	2/10	3/5
			Alveolar epithelial cells	8/10	4/5
			Bronchial epithelial cells	3/10	1/5
Membrane-associated drug transporters	BCRP	Cytoplasm	Submucosal gland basement membrane	1/10	ND
			Macrophages	ND	1/5
			Endothelial cells	8/10	5/5

(Continued on following page)

TABLE 2 (*Continued*) Summary of the cellular localization of investigated biomarkers in postmortem human lung tissues.

Class of biomarkers	Biomarker	Cellular compartment	Pulmonary cells	COVID-19 cases	Control cases
		Membranous	Macrophages	ND	2/5
	ENT1	Cytoplasm	Macrophages	1/10	2/5
			Subset of lymphocytes	6/10	2/5
		Circumferential membrane	Alveolar epithelial cells	ND	1/5
	ENT2	Apical membrane	Endothelial cells	2/10	ND
			Alveolar epithelial cells	4/10	3/5
		Circumferential membrane	Fibroblast	1/10	ND
		Cytoplasm	Macrophages	6/10	3/5
			Lymphocytes	7/10	1/5
			Alveolar epithelial cells	3/10	1/5
			Endothelial cells	1/10	ND
	MRP1	Cytoplasm	Lymphocytes	6/10	ND
			Macrophages	7/10	3/5
			Bronchial epithelial cells	2/10	1/5
			Alveolar epithelial cells	7/10	4/5
		Nucleus and cytoplasm	Intra-alveolar cells	1/10	ND
		Nucleus	Alveolar epithelial cells	9/10	5/5
	MRP2	Circumferential membrane	Bronchial epithelial cells	1/10	3/5
			Endothelial cells	10/10	4/5
			Macrophages	4/10	ND
			Lymphocytes	3/10	ND
			Alveolar epithelial cells	10/10	5/5
	P-gp	Cytoplasm	Endothelial cells	1/10	ND
		Circumferential membrane	Macrophages	2/10	ND
			Bronchial epithelial cells	4/10	5/5
			Alveolar epithelial cells	5/10	1/5
			Lymphocytes	1/10	4/5
			Submucosal gland epithelium	ND	2/5
		Apical membrane	Alveolar epithelial cells	8/10	4/5
Inflammatory markers	IL-1β	Cytoplasm	Lymphocytes	6/10	ND
			Alveolar epithelial cells	9/10	5/5
			Macrophages	5/10	4/5
			Endothelial cells	1/10	1/5
	IL-6	Cytoplasm	Neutrophils	1/10	ND
			Lymphocytes	9/10	ND
			Smooth muscles of blood vessels	2/10	ND
			Alveolar epithelial cells	8/10	4/5

(Continued on following page)

TABLE 2 (*Continued*) Summary of the cellular localization of investigated biomarkers in postmortem human lung tissues.

Class of biomarkers	Biomarker	Cellular compartment	Pulmonary cells	COVID-19 cases	Control cases
			Bronchial epithelial cells	3/10	3/5
			Macrophages	3/10	3/5
			Scattered intra-vascular lymphocytes	ND	1/5
Regulatory proteins	CAR	Cytoplasm	Macrophages	7/10	4/5
			Lymphocytes	4/10	ND
			Fibroblast	2/10	ND
			Bronchial epithelial cells	ND	1/5
	NF-kβ	Cytoplasm	All the cells except the red blood cells	10/10	5/5
	pSTAT3	Nucleus	Alveolar epithelial cells	10/10	4/5
			Macrophages	4/10	ND
			Intra-alveolar lymphocytes	3/10	ND
			Lymphocytes	2/10	ND
			Endothelial cells	ND	1/5
		Cytoplasm	Macrophages	ND	2/5
	PXR	Cytoplasm	Smooth muscles of blood vessels	10/10	5/5
			Smooth muscles of bronchi	9/10	5/5
			Endothelial cells	10/10	4/5
			Bronchial epithelial cells	4/10	2/5
			Lymphocytes	8/10	ND
			Macrophages	2/10	3/5
Viral proteins	SARS-CoV-2 nucleocapsid protein	Cytoplasm	Lymphocytes	6/10	1/5
			Macrophages	2/10	3/5
			Alveolar epithelial cells	9/10	4/5
			Bronchial epithelial cells	ND	1/5
	SARS-CoV-2 spike protein	Cytoplasm	Lymphocytes	8/10	2/5
			Bronchial epithelial cells	2/10	4/5
			Alveolar epithelial cells	4/10	1/5
			Intra-vascular neutrophils	2/10	3/5
			Macrophages	1/10	3/5
			Intra-vascular lymphocytes	ND	1/5

driven by the infiltration of inflammatory cells such as lymphocytes and macrophages (Figure 4; Table 2). For example, CYP1A2 is predominantly expressed in the cytoplasm of alveolar epithelial cells for both COVID-19 (10/10) and control (5/5) lung tissues; however, it is distinctly expressed in the cytoplasm of intra-alveolar lymphocytes (9/10) and macrophages (5/10) of COVID-19 subjects (Figure 4; Table 2). Furthermore, there is a concordance in the pulmonary cellular localization of SARS-CoV-2 infection, inflammatory response, regulatory proteins, as well as DMETs. For instance, SARS-CoV-2 spike protein, nucleocapsid protein, IL-1β, IL-6, PXR, CAR, CYP2C9, CYP2C19, CYP2D6, and MRP1 are all more distinctly localized in the cytoplasm of lymphocytes in the COVID-19 but not control human lung tissues (Figure 4; Table 2), suggesting that SARS-CoV-2 infection may trigger an

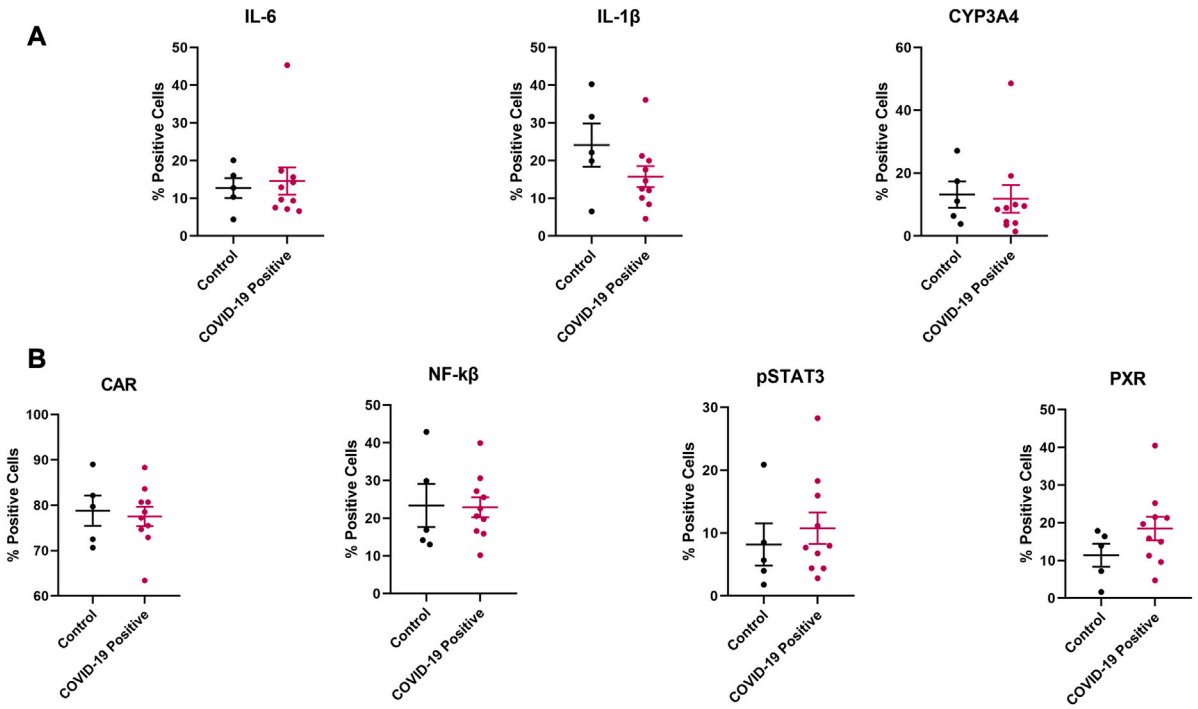

FIGURE 5
Effect of COVID-19 on the protein expression of selected **(A)** inflammatory markers and CYP3A4, **(B)** regulatory proteins in postmortem human lung tissues. Chromogenic images obtained from the immunostained tissue slides from each subject were analyzed using HALO software v3.4 (Indica Labs) for absolute quantitative IHC analysis. Results are expressed as mean ± SEM, and the non-parametric two-tailed Mann-Whitney test was used to determine the differences in protein expression between COVID-19 and control postmortem human lung tissues for absolute quantitative IHC analysis.

inflammation-mediated regulation of the expression of DMETs through regulatory proteins such as PXR and CAR in lymphocytes.

Absolute quantitative analysis of protein expression

Although no significant difference was observed in protein expression for the investigated inflammatory markers and regulatory proteins (Figure 5), the efflux transporters P-gp and MRP1 reached a significant difference in protein expression between the COVID-19 and control groups (Figure 6B). No significant differences in protein expression for the investigated DMEs was observed (Figures 5, 6).

Discussion

In this study, we investigated the effect of SARS-CoV-2 infection in the dysregulation of 25 clinically relevant DMETs at the mRNA and protein levels in Vero E6 cells and postmortem human lung tissues obtained from COVID-19 patients, respectively. In postmortem human lung tissues, we further assessed biomarker localization and the role of SARS-CoV-2-associated inflammatory response and xenosensing regulatory proteins in modulating the dysregulation of DMETs. Our study led to three major outcomes:

SARS-CoV-2-infected Vero E6 cells demonstrated dysregulation of the metabolic enzyme involved in the disposition of commonly prescribed COVID-19 drugs

With the SARS-CoV-2-associated inflammatory response in Vero E6 cells, we observed that at the mRNA level, *CYP3A4* was upregulated while *UGT1A1* was downregulated (Figure 2B). However, none of the investigated transporters were significantly dysregulated (Figure 2C and Supplementary Figure S3B). Several disease-drug interactions associated with SARS-CoV-2 infection have been suggested (Kumar and Trivedi, 2021). For example, CYP3A4 involved in the metabolism of dexamethasone, a corticosteroid drug often administered to hospitalized COVID-19 patients, is known to be dysregulated by inflammation (Kumar and Trivedi, 2021; Dunvald et al., 2022). Also, nirmatrelvir, an antiviral drug used to treat SARS-CoV-2 infection is metabolized by CYP3A4 and is currently coadministered with ritonavir (an inhibitor of CYP3A4) to improve its bioavailability (Nwabufo and Bendayan, 2022). Therefore, it is important to further investigate how SARS-CoV-2-associated inflammatory response will affect the PK profile of nirmatrelvir-ritonavir combination therapy for the treatment of COVID-19. Furthermore, human clinical data suggests that remdesivir is extensively metabolized

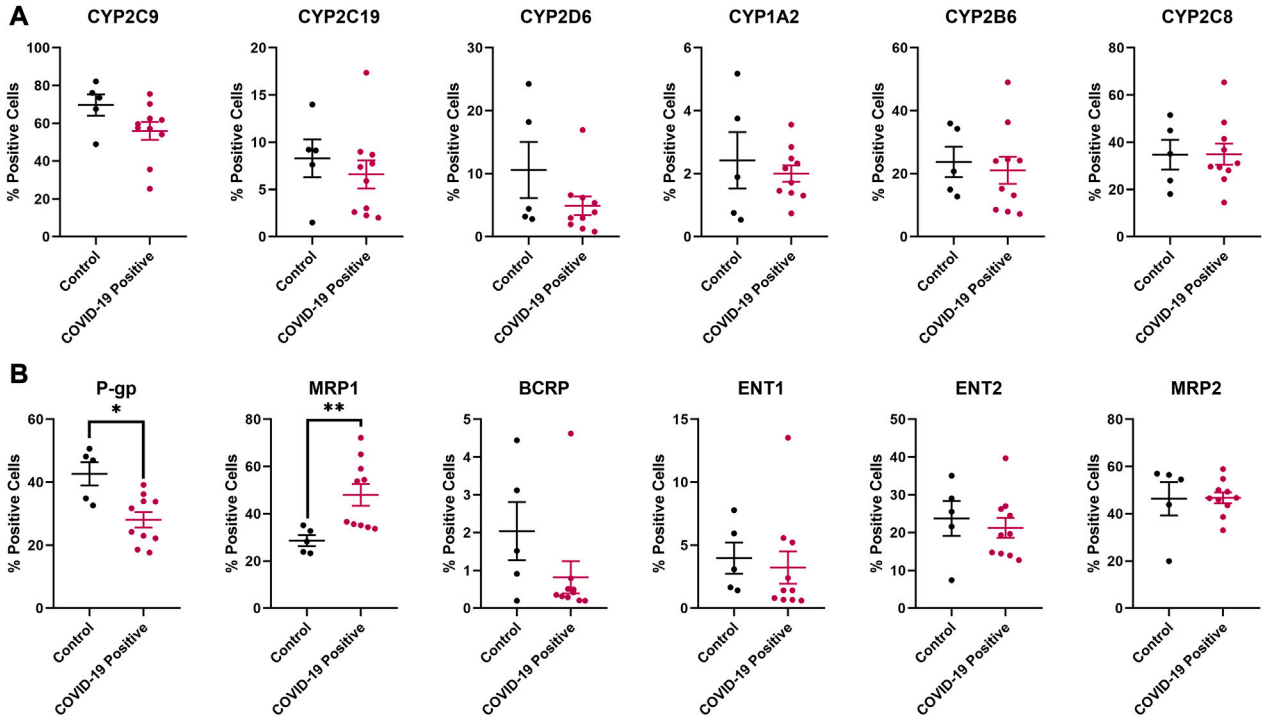

FIGURE 6
Effect of COVID-19 on the protein expression of selected **(A)** drug metabolizing enzymes and **(B)** membrane-associated drug transporters in postmortem human lung tissues. Chromogenic images obtained from the immunostained tissue slides from each subject were analyzed using HALO software v3.4 (Indica Labs) for absolute quantitative IHC analysis. Results are expressed as mean ± SEM, and the non-parametric two-tailed Mann-Whitney test was used to determine the differences in protein expression between COVID-19 and control postmortem human lung tissues for absolute quantitative IHC analysis (*, $p < 0.05$; **, $p < 0.01$).

by CYP2C8, CYP2D6, and CYP3A4 (Yang, 2020) and since studies have shown that these enzymes are dysregulated by inflammation (Dunvald et al., 2022), the PK profile of remdesivir and dexamethasone could be altered by the inflammatory state observed in COVID-19. This may partly explain the variable clinical outcomes observed in several clinical studies that investigated the safety and efficacy of remdesivir (Cascella et al., 2022). In general, remdesivir was primarily approved by the US FDA for administration to COVID-19 patients requiring hospitalization, and proper dosing regimen and treatment course need to be further investigated to achieve the full benefits of remdesivir for patients at different stages of COVID-19. Additionally, caution needs to be taken when administering drugs to COVID-19 patients especially the patient population with comorbidities to mitigate clinically relevant disease–drug interactions. For example, UGT1A1 is highly polymorphic and can impact irinotecan (a prodrug used for small cell lung cancer chemotherapy) metabolite related-toxicity (Bandyopadhyay et al., 2021). Given that *UGT1A1* mRNA expression was significantly downregulated in SARS-CoV-2-infected Vero E6 cells and patients with lung cancer have a greater than 7-fold higher risk of SARS-CoV-2 infection (Rolfo et al., 2022), further investigation is required to determine the effect of prescribing UGT1A1 candidate drugs to COVID-19 patients, especially the UGT1A1 poor metabolizers which accounts for about 10% of North Americans (Dean, 2018).

Dunvald and coworkers recently summarized studies reporting altered mRNA expression of clinically relevant DMETs including *CYP1A2*, *CYP2B6*, *CYP2C8*, *CYP2C9*, *CYP2C19*, *CYP2D6*, *CYP3A4*, *PGP*, *BCRP*, and *MRP2* by proinflammatory cytokines such as IL-6, IL-1β, TNF-α, and IFN-γ in a dose-dependent manner in primary cultures of human hepatocytes (Dunvald et al., 2022). For example, the mRNA expression of the hepatic efflux transporters P-gp, MRP2, and BCRP is typically low, with a maximum downregulation of 2-fold, in response to IL-6, IL-1β, TNF-α, or IFN-γ at doses of 1–100 ng/mL (Ramsden et al., 2015; Moreau et al., 2017; Ning et al., 2017; Dunvald et al., 2022). However, the concentrations of the investigated inflammatory markers in SARS-CoV-2 infected Vero E6 cells are probably more physiologically relevant compared to the artificial stimulation of inflammatory response by the administration of toxins such as lipopolysaccharides, or direct administration of proinflammatory cytokines such as IL-6 and IL-1β—both of which may result in supraphysiological responses. Furthermore, species (human and monkey) and organ (kidney and liver) differences in DMETs expression, may be responsible for the lack of dysregulation of the above-mentioned DMETs. For example, a previous study found that *CYP2C18* mRNA expression is unaffected by cytokine administration due to limited hepatic expression (Aitken and Morgan, 2007).

DMETs are expressed in several human pulmonary cells affected by SARS-CoV-2 infection

We localized for the first time, the cellular expression of uptake transporters—ENT1 and ENT2 in human lung tissues by IHC. We found that both ENT1 and ENT2 were primarily localized in inflammatory cells of lung tissues from COVID-19 patients (Figure 4; Table 2), making them potentially liable to SARS-CoV-2-mediated increases in expression. Interestingly, ENT1 and ENT2 may be prone to downregulation with SARS-CoV-2 infection due to the presence of acute lung injury and hypoxia in some COVID-19 patients (Johnson, 2022). Indeed, previous studies reported a significant downregulation of ENT1 and ENT2 expression in lung epithelial and endothelial cells in both acute lung injury (Morote-Garcia et al., 2013) and hypoxia (Eltzschig et al., 2005). More so, increased extracellular adenosine levels due to acute lung injuries (Eckle et al., 2009) suggest a potential competitive inhibition of ENTs-mediated transport processes. This is clinically important because ENT1 and ENT2 are involved in the uptake of the COVID-19 drugs - remdesivir and molnupiravir, making this uptake pathway potentially liable to dysregulation with SARS-CoV-2 infection and may partly explain the limited and variable clinical efficacy observed for remdesivir (Johnson, 2022).

To the best of our knowledge, our study is the first to reveal the cellular localization of CYP1A2, CYP2C8, CYP2C9, and CYP2D6 by IHC in human lung tissues. Previous studies investigating the expression of DMEs in the human respiratory system, have mostly assessed expression at the mRNA level, used non-intact lung samples such as microsomes and bronchial specimens, or failed to uncover cellular localization (Hukkanen et al., 2002). The human lung tissue is highly heterogeneous, making microsomes, bronchial, and other non-intact lung specimens an inaccurate description of DMETs expression in different pulmonary cell types. For example, the mRNA expression of CYP2C8 was previously found in both bronchial and peripheral lung tissue samples (Macé et al., 1998), but its protein expression and cellular localization were not reported. An IHC study identified CYP2B6 in human Clara cells (Mori et al., 1996) whereas CYP2C19 and CYP3A4 proteins were detected in serous cells of bronchial glands (Yokose et al., 1999) but expression in other pulmonary cell types was not reported. Our study uncovered the pulmonary cellular localization of CYP2B6, CYP2C8, CYP2C19, and CYP3A4 (Figure 4; Table 2).

Efflux transporters such as P-gp and BCRP have previously been identified in human lung tissues (Cordon-Cardo et al., 1990; Van der Valk et al., 1990; Scheffer et al., 2002; Fetsch et al., 2006). In contrast to an earlier study that found BCRP expression only in bronchial epithelial cells and capillaries (Scheffer et al., 2002), later work demonstrated staining of alveolar pneumocytes and negligible staining of the bronchial epithelial cells (Fetsch et al., 2006). These findings are not in agreement with the results of this study. In our study, BCRP was primarily localized in the cytoplasm of endothelial cells in both COVID-19 and control tissues (Figure 4; Table 2). In previous reports, P-gp localization was shown on the luminal surface of bronchial and bronchiolar epithelial cells (Cordon-Cardo et al., 1990; Van der Valk et al., 1990). P-gp was stained in alveolar macrophages whereas staining of alveolar epithelial cells was dependent on the antibody employed (Van der Valk et al., 1990). On the contrary, our findings showed that P-gp is robustly localized in the alveolar epithelial cells (Figure 4; Table 2) of both COVID-19 and control tissues. MRP1 was initially found in the apical membrane of the cytoplasm of bronchial epithelial cells (Flens et al., 1996); however, two later studies confirmed MRP1 localization in the basolateral membrane (Bréchot et al., 1998; Scheffer et al., 2002) which is consistent with its localization in other tissues (Gustavsson et al., 2016). In our study, MRP1 expression in the bronchial epithelium is cytoplasmic (Figure 4; Table 2). Moreover, MRP1 was predominantly localized in the cytoplasm and nucleus of alveolar epithelial cells of both COVID-19 and control postmortem human lung tissues (Figure 4; Table 2). MRP2 positivity was previously found in the apical membrane of the bronchial and bronchiolar epithelial layers (Sandusky et al., 2002; Scheffer et al., 2002). We observed a robust localization in the alveolar epithelial cells of both COVID-19 and control tissues (Table 2). We also found MRP2 expression in bronchial epithelial cells in a higher number for controls (3/5) compared to the COVID-19 (1/10) human lung tissues; however, it was more circumferential not apical membranous compartmentalization (Figure 4; Table 2). Our study demonstrated that circumferential membrane compartmentalization in alveolar epithelial and endothelial cells was the major expression site for MRP2 (Figure 4; Table 2). This circumferential compartmentalization is indicative of potential bidirectional efflux transport processes mediated by MRP2 in human lung tissues compared to the anticipated unidirectional efflux transport.

Typically DMETs are localized in the cytoplasm and cell membrane, however, our study found that some DMETs were localized in atypical cellular compartments (Figure 4; Table 2). For example, our study detected MRP1 in the cytoplasm and nucleus. Although transporters are localized at the cell membrane, they are also present in cytoplasmic organelles such as the Golgi apparatus, rough endoplasmic reticulum, nuclear envelope, and mitochondria. For instance, a previous IHC study found MRP2 expression in both cytoplasm and cell membrane of tumor cells (Yamasaki et al., 2011), and it is anticipated that in the cytoplasm, MRP2 may not function as an efflux pump (Evers et al., 1998). Therefore, further investigation is required to determine whether differences in pulmonary cellular compartmentalization affect the structure and function of the implicated DMETs.

SARS-CoV-2 may dysregulate pulmonary DMETs through inflammatory response and tissue injuries

From the absolute quantitation, we observed significant differences in the expression of P-gp and MRP1 between the COVID-19 and control human lung tissues (Figure 6B). P-gp is involved in the transport of nirmatrelvir, remdesivir, and

dexamethasone while MRP1 transports lopinavir and ritonavir (Nwabufo and Bendayan, 2022)—indicating a potential alteration in pulmonary drug PK/PD profile in COVID-19 patients. The lack of observable significant dysregulation in the protein expression of other DMETs in COVID-19 human lung tissues (Figures 5, 6) could be attributed to the potential variation in the stage of COVID-19 between cases, as well as comorbidities (Table 1), ongoing medications, and genetic polymorphisms in the expression of DMETs for both COVID-19 and control cases. These variables could not be further addressed due to the paucity of premortem clinical information. The small sample size, and other diseases present in the control samples may also have an impact on the expression of inflammatory markers, regulatory proteins, and DMETs, possibly resulting in a negligible dysregulation in their expression between COVID-19 and control tissues. Drug toxicity, cardiovascular diseases, and head trauma are the reported causes of death for the 5 control cases (Table 1), and these disorders can induce inflammatory response and dysregulate the expression of DMETs through regulatory proteins (Wu and Lin, 2019; Stanke-Labesque et al., 2020; Dunvald et al., 2022).

The congruency in the pulmonary cellular localization of SARS-CoV-2 infection, inflammatory markers, regulatory proteins, and DMETs, as well as the several COVID-19-related pulmonary pathologies of the COVID-19 cases suggest a potential dysregulation of pulmonary DMETs which may manifest in regulated clinical studies. We observed that SARS-CoV-2 infection and inflammatory response are distinctly localized to the cytoplasm of lymphocytes in COVID-19 compared to control human lung tissues (Figure 4; Table 2). The detection of SARS-CoV-2 viral protein in the control human lung tissues is indicative of the limited specificity of the antibody; however, clinical testing confirmed the presence of SARS-CoV-2 infection in the COVID-19 cases. Again, underlying diseases in the control cases are probably responsible for the observed inflammatory response. Interestingly, we observed a similar trend in the localization of xenosensing regulatory proteins; for example, the two master xenosensing regulatory proteins - PXR and CAR are both distinctly expressed in the cytoplasm of lymphocytes in COVID-19 human lung tissues but not in the control cases (Figure 4; Table 2). Also, we observed a similar trend in the cellular localization of some DMETs including CYP2C9, CYP2C19, CYP2D6, and MRP1 (Figure 4; Table 2). These observations suggest that SARS-CoV-2 infection could result in an inflammatory response that could activate xenosensing regulatory proteins, which could then dysregulate the expression of DMETs in lymphocytes. However, our study quantified global pulmonary protein expression for the investigated biomarkers to get a better representation of SARS-CoV-2-DMETs interactions. Moreover, it is practically challenging to quantify the investigated biomarkers in the lymphocytes of human lung tissues except when pulmonary lymphocyte isolates are used as specimens for the study.

Furthermore, we observed that the presence of inflammatory cells is a major driving force in the localization of DMETs between COVID-19 and control tissues (Figure 4; Table 2). In general, COVID-19 lung tissues had more inflammatory cells which also expressed DMETs compared to the control lung tissues. Notably, CYP3A4 and ENT2 were strongly localized in lymphocytes in COVID-19 compared to control human lung tissues (Figure 4; Table 2). This suggests a potential SARS-CoV-2-mediated increase in the expression of DMETs through the recruitment of inflammatory cells and may have implications for pulmonary drug PK/PD profiles. For example, CYP3A4 and ENT2 are involved in the disposition of remdesivir (Nwabufo and Bendayan, 2022) and may be susceptible to an altered pulmonary PK/PD profile in the context of SARS-CoV-2 infection. Additionally, the observed COVID-19-related pulmonary pathologies could also reduce the expression of DMETs. For example, DAD could alter the integrity of alveolar epithelial cells—which also house more than 90% of the investigated DMETs including CYP3A4 and P-gp. Our recent paper provides strategies for achieving optimal clinical efficacy and safety amidst SARS-CoV-2-associated inflammatory response (Nwabufo and Bendayan, 2022) and should be considered in the clinical decision-making process for COVID-19 drugs.

In conclusion, our study has shown for the first time that SARS-CoV-2 infection dysregulates clinically relevant DMEs—CYP3A4 and UGT1A1 at the mRNA level, and efflux transporters—P-gp and MRP1 at the protein level in Vero E6 cells and postmortem human lung tissues, respectively. We uncovered the human pulmonary localization of DMETs that are also involved in the disposition of COVID-19 drugs, and showed that inflammatory response is the driving force for the discrepancy in the localization of DMETs between COVID-19 and control human lung tissues. We observed that at the cellular level, DMETs could potentially be dysregulated by SARS-CoV-2-associated inflammatory responses and lung injuries. Further investigation of SARS-CoV-2-mediated dysregulation of human pulmonary DMETs and its potential implication in controlling the safety and efficacy of promising COVID-19 drugs as well as possible unexpected adverse drug reactions in COVID-19 patients on polypharmacy is needed. Further research is required to determine the spatial distribution and disposition of promising COVID-19 drugs at the cellular level in human lung tissues, and mass spectrometry imaging may offer an appealing analytical platform to further investigate this aspects (Nwabufo and Aigbogun, 2022).

Data availability statement

The original contributions presented in the study are included in the article/Supplementary Material, further inquiries can be directed to the corresponding author.

Ethics statement

The studies involving human participants were reviewed and approved by the office of the Chief Coroner at Ontario Forensic Pathology Service (Chief Forensic Pathologist, and Chief Coroner). Written informed consent for participation was not required for this

study in accordance with the national legislation and the institutional requirements.

Author contributions

CN wrote the manuscript; CN and RB designed the research; CN, MTH, LY, and MK performed the research. CN and MTH analyzed the data. MP and SM provided postmortem human lung tissues and Vero E6 cells, respectively. All authors reviewed the manuscript.

Funding

CN is a recipient of the Canadian Institutes of Health Research Doctoral Scholarship, Canadian Institutes of Health Research Doctoral Scholarship—Michael Smith Foreign Study Supplements Award, Ontario Graduate Scholarship, Pfizer Canada Graduate Fellowship, and Leslie Dan Faculty of Pharmacy Dean's Fellowship. This work is supported by grants from the Ontario HIV Treatment Network (fund #506657) and Canadian Institutes of Health Research (fund # 51794) awarded to RB. Biorender was used to create the figures.

Acknowledgments

We thank Kenneth Kodja and other members of the Ontario Forensic Pathology Service, University Health Network - Pathology Research Program Laboratory, Advanced Optical Microscopy Facility, and Centre for Pharmaceutical Oncology, Leslie Dan Faculty of Pharmacy for their contribution.

Conflict of interest

CN was a former employee of Gilead Sciences and was involved in the development of remdesivir. CN was employed by OneDrug. MK and MP were employed by Ontario Forensic Pathology Service.

The remaining authors declare that the research was conducted in the absence of any commercial or financial relationships that could be construed as a potential conflict of interest.

Publisher's note

Supplementary material

The Supplementary Material for this article can be found online at: https://www.frontiersin.org/articles/10.3389/fphar.2023.1124693/full#supplementary-material

References

Aitken, A. E., and Morgan, E. T. (2007). Gene-specific effects of inflammatory cytokines on cytochrome P450 2C, 2B6 and 3A4 mRNA levels in human hepatocytes. *Drug Metabolism Dispos.* 35, 1687–1693. doi:10.1124/dmd.107.015511

Aziz, M., Fatima, R., and Assaly, R. (2020). Elevated interleukin-6 and severe COVID-19: A meta-analysis. *J. Med. Virol.* 92, 2283–2285. doi:10.1002/jmv.25948

Bandyopadhyay, A., Sharma, S., Behera, D., and Singh, N. (2021). *UGT1A1* gene polymorphisms in patients with small cell lung cancer treated with irinotecan-platinum doublet chemotherapy and their association with gastrointestinal toxicity and overall survival. *Oncol.* 26, 701–713. doi:10.1002/onco.13757

Bréchot, J.-M., Hurbain, I., Fajac, A., Daty, N., and Bernaudin, J.-F. (1998). Different pattern of MRP localization in ciliated and basal cells from human bronchial epithelium. *J. Histochem Cytochem* 46, 513–517. doi:10.1177/002215549804600411

Cascella, M., Rajnik, M., Aleem, A., Dulebohn, S. C., and Di Napoli, R. (2022). Features, evaluation, and treatment of coronavirus (COVID-19) *StatPearls* (treasure island (FL): StatPearls publishing), 1–47. Available at: http://www.ncbi.nlm.nih.gov/books/NBK554776/(Accessed September 26, 2022).

Cordon-Cardo, C., O'Brien, J. P., Boccia, J., Casals, D., Bertino, J. R., and Melamed, M. R. (1990). Expression of the multidrug resistance gene product (P-glycoprotein) in human normal and tumor tissues. *J. Histochem Cytochem* 38, 1277–1287. doi:10.1177/38.9.1974900

Dean, L. (2018). "Irinotecan therapy and UGT1A1 genotype," in *Medical genetics summaries*. V. M. Pratt, S. A. Scott, M. Pirmohamed, et al. (Bethesda, MD: National Center for Biotechnology Information).

Dunvald, A.-C. D., Järvinen, E., Mortensen, C., and Stage, T. B. (2022). Clinical and molecular perspectives on inflammation-mediated regulation of drug metabolism and transport. *Clin. Pharmacol. Ther.* 112, 277–290. doi:10.1002/cpt.2432

Eckle, T., Koeppen, M., and Eltzschig, H. K. (2009). Role of extracellular adenosine in acute lung injury. *Physiology* 24, 298–306. doi:10.1152/physiol.00022.2009

Ehrhardt, C., Bäckman, P., Couet, W., Edwards, C., Forbes, B., Fridén, M., et al. (2017). Current progress toward a better understanding of drug disposition within the lungs: Summary proceedings of the first workshop on drug transporters in the lungs. *J. Pharm. Sci.* 106, 2234–2244. doi:10.1016/j.xphs.2017.04.011

Eltzschig, H. K., Abdulla, P., Hoffman, E., Hamilton, K. E., Daniels, D., Schönfeld, C., et al. (2005). HIF-1–dependent repression of equilibrative nucleoside transporter (ENT) in hypoxia. *J. Exp. Med.* 202, 1493–1505. doi:10.1084/jem.20050177

Enlo-Scott, Z., Bäckström, E., Mudway, I., and Forbes, B. (2021a). Drug metabolism in the lungs: Opportunities for optimising inhaled medicines. *Expert Opin. Drug Metab. Toxicol.* 17, 611–625. doi:10.1080/17425255.2021.1908262

Enlo-Scott, Z., Swedrowska, M., and Forbes, B. (2021b). "Epithelial permeability and drug absorption in the lungs," in *Inhaled medicines* (Elsevier), 267–299. doi:10.1016/B978-0-12-814974-4.00004-3

Evers, R., Kool, M., van Deemter, L., Janssen, H., Calafat, J., Oomen, L. C., et al. (1998). Drug export activity of the human canalicular multispecific organic anion transporter in polarized kidney MDCK cells expressing cMOAT (MRP2) cDNA. *J. Clin. Investig.* 101, 1310–1319. doi:10.1172/JCI119886

Fetsch, P. A., Abati, A., Litman, T., Morisaki, K., Honjo, Y., Mittal, K., et al. (2006). Localization of the ABCG2 mitoxantrone resistance-associated protein in normal tissues. *Cancer Lett.* 235, 84–92. doi:10.1016/j.canlet.2005.04.024

Flens, M. J., Zaman, G. J., van der Valk, P., Izquierdo, M. A., Schroeijers, A. B., Scheffer, G. L., et al. (1996). Tissue distribution of the multidrug resistance protein. *Am. J. Pathol.* 148, 1237–1247.

Frisoni, P., Neri, M., D'Errico, S., Alfieri, L., Bonuccelli, D., Cingolani, M., et al. (2022). Cytokine storm and histopathological findings in 60 cases of COVID-19-related death: From viral load research to immunohistochemical quantification of major players IL-1β, IL-6, IL-15 and TNF-α. *Forensic Sci. Med. Pathol.* 18, 4–19. doi:10.1007/s12024-021-00414-9

Garcia-Beltran, W. F., Lam, E. C., St. Denis, K., Nitido, A. D., Garcia, Z. H., Hauser, B. M., et al. (2021). Multiple SARS-CoV-2 variants escape neutralization by vaccine-induced humoral immunity. *Cell.* 184, 2372–2383.e9. doi:10.1016/j.cell.2021.03.013

Gregoire, M., Le Turnier, P., Gaborit, B. J., Veyrac, G., Lecomte, R., Boutoille, D., et al. (2020). Lopinavir pharmacokinetics in COVID-19 patients. *J. Antimicrob. Chemother.* 75, 2702–2704. doi:10.1093/jac/dkaa195

Gustavsson, L., Bosquillon, C., Gumbleton, M., Hegelund-Myrbäck, T., Nakanishi, T., Price, D., et al. (2016). "Drug transporters in the lung: Expression and potential impact on pulmonary drug disposition," in *RSC drug discovery series*. doi:10.1039/9781782623793-00184

Hoffmann, M., Arora, P., Groß, R., Seidel, A., Hörnich, B. F., Hahn, A. S., et al. (2021). SARS-CoV-2 variants B.1.351 and P.1 escape from neutralizing antibodies. *Cell.* 184, 2384–2393.e12. doi:10.1016/j.cell.2021.03.036

Hoffmann, M., Kleine-Weber, H., Schroeder, S., Krüger, N., Herrler, T., Erichsen, S., et al. (2020). SARS-CoV-2 cell entry depends on ACE2 and TMPRSS2 and is blocked by a clinically proven protease inhibitor. *Cell.* 181, 271–280. doi:10.1016/j.cell.2020.02.052

Hukkanen, J., Pelkonen, O., Hakkola, J., and Raunio, H. (2002). Expression and regulation of xenobiotic-metabolizing cytochrome P450 (CYP) enzymes in human lung. *Crit. Rev. Toxicol.* 32, 391–411. doi:10.1080/20024091064273

Johnson, E. K. (2022). A comment on "remdesivir and EIDD-1931 interact with human equilibrative nucleoside transporters 1 and 2: Implications for reaching SARS-CoV-2 viral sanctuary sites. *Mol. Pharmacol.* 101, 120. doi:10.1124/molpharm.121.000425

Korber, B., Fischer, W. M., Gnanakaran, S., Yoon, H., Theiler, J., Abfalterer, W., et al. (2020). Tracking changes in SARS-CoV-2 spike: Evidence that D614G increases infectivity of the COVID-19 virus. *Cell.* 182, 812–827.e19. doi:10.1016/j.cell.2020.06.043

Krammer, F. (2020). SARS-CoV-2 vaccines in development. *Nature* 586, 516–527. doi:10.1038/s41586-020-2798-3

Kumar, D., and Trivedi, N. (2021). Disease-drug and drug-drug interaction in COVID-19: Risk and assessment. *Biomed. Pharmacother.* 139, 111642. doi:10.1016/j.biopha.2021.111642

Kumar, G. N., Jayanti, V. K., Johnson, M. K., Uchic, J., Thomas, S., Lee, R. D., et al. (2004). Metabolism and disposition of the HIV-1 protease inhibitor lopinavir (ABT-378) given in combination with ritonavir in rats, dogs, and humans. *Pharm. Res.* 21, 1622–1630. doi:10.1023/B:PHAM.0000041457.64638.8d

Le Carpentier, E. C., Canet, E., Masson, D., Martin, M., Deslandes, G., Gaultier, A., et al. (2022). Impact of inflammation on midazolam metabolism in severe COVID-19 patients. *Clin. Pharmacol. Ther.* 1, 1033–1039. doi:10.1002/cpt.2698

Macé, K., Bowman, E. D., Vautravers, P., Shields, P. G., Harris, C. C., and Pfeifer, A. M. A. (1998). Characterisation of xenobiotic-metabolising enzyme expression in human bronchial mucosa and peripheral lung tissues. *Eur. J. Cancer* 34, 914–920. doi:10.1016/S0959-8049(98)00034-3

Madhi, S. A., Baillie, V., Cutland, C. L., Voysey, M., Koen, A. L., Fairlie, L., et al. (2021). Efficacy of the ChAdOx1 nCoV-19 covid-19 vaccine against the B.1.351 variant. *N. Engl. J. Med.* 384, 1885–1898. doi:10.1056/NEJMoa2102214

Moreau, A., Le Vée, M., Jouan, E., Denizot, C., Parmentier, Y., and Fardel, O. (2017). Effect of gevokizumab on interleukin-1β-mediated cytochrome P450 3A4 and drug transporter repression in cultured human hepatocytes. *Eur. J. Drug Metab. Pharmacokinet.* 42, 871–878. doi:10.1007/s13318-017-0406-1

Mori, M., Tezuka, F., Chiba, R., Funae, Y., Watanabe, M., Nukiwa, T., et al. (1996). Atypical adenomatous hyperplasia and adenocarcinoma of the human lung: Their heterology in form and analogy in immunohistochemical characteristics. *Cancer* 77, 665–674. doi:10.1002/(sici)1097-0142(19960215)77:4<665::aid-cncr12>3.0.co;2-z

Morote-Garcia, J. C., Köhler, D., Roth, J. M., Mirakaj, V., Eldh, T., Eltzschig, H. K., et al. (2013). Repression of the equilibrative nucleoside transporters dampens inflammatory lung injury. *Am. J. Respir. Cell. Mol. Biol.* 49, 296–305. doi:10.1165/rcmb.2012-0457OC

Ning, R., Zhan, Y., He, S., Hu, J., Zhu, Z., Hu, G., et al. (2017). Interleukin-6 induces DEC1, promotes DEC1 interaction with RXRα and suppresses the expression of PXR, CAR and their target genes. *Front. Pharmacol.* 8, 866. doi:10.3389/fphar.2017.00866

Nwabufo, C. K., and Aigbogun, O. P. (2022). Potential application of mass spectrometry imaging in pharmacokinetic studies. *Xenobiotica* 1–48, 811–827. doi:10.1080/00498254.2022.2119900

Nwabufo, C. K., and Bendayan, R. (2022). Pharmacokinetic considerations to optimize clinical outcomes for COVID-19 drugs. *Trends Pharmacol. Sci.* 43, 1041–1054. S0165614722002012. doi:10.1016/j.tips.2022.09.005

Ou, J., Lan, W., Wu, X., Zhao, T., Duan, B., Yang, P., et al. (2022). Tracking SARS-CoV-2 Omicron diverse spike gene mutations identifies multiple inter-variant recombination events. *Sig Transduct. Target Ther.* 7, 138. doi:10.1038/s41392-022-00992-2

Our World and Data (2021). Coronavirus (COVID-19) vaccinations. *Our World Data*. Available at: https://ourworldindata.org/covid-vaccinations (Accessed July 3, 2021).

Pilla Reddy, V., El-Khateeb, E., Jo, H., Giovino, N., Lythgoe, E., Sharma, S., et al. (2021). Pharmacokinetics under the COVID-19 storm. *Br. J. Clin. Pharmacol.* 89, 158–186. doi:10.1111/bcp.14668

Plante, J. A., Liu, Y., Liu, J., Xia, H., Johnson, B. A., Lokugamage, K. G., et al. (2021). Spike mutation D614G alters SARS-CoV-2 fitness. *Nature* 592, 116–121. doi:10.1038/s41586-020-2895-3

Ramsden, D., Zhou, J., and Tweedie, D. J. (2015). Determination of a degradation constant for CYP3A4 by direct suppression of mRNA in a novel human hepatocyte model, HepatoPac. *Drug Metab. Dispos.* 43, 1307–1315. doi:10.1124/dmd.115.065326

Rendeiro, A. F., Ravichandran, H., Bram, Y., Chandar, V., Kim, J., Meydan, C., et al. (2021). The spatial landscape of lung pathology during COVID-19 progression. *Nature* 593, 564–569. doi:10.1038/s41586-021-03475-6

Rolfo, C., Meshulami, N., Russo, A., Krammer, F., García-Sastre, A., Mack, P. C., et al. (2022). Lung cancer and severe acute respiratory syndrome coronavirus 2 infection: Identifying important knowledge gaps for investigation. *J. Thorac. Oncol.* 17, 214–227. doi:10.1016/j.jtho.2021.11.001

Rosa, R. B., Dantas, W. M., do Nascimento, J. C. F., da Silva, M. V., de Oliveira, R. N., and Pena, L. J. (2021). *In vitro* and *in Vivo* models for studying SARS-CoV-2, the etiological agent responsible for COVID-19 pandemic. *Viruses* 13, 379. doi:10.3390/v13030379

Salerno, D. M., Kovac, D., Corbo, H., Jennings, D. L., Lee, J., Choe, J., et al. (2021). SARS-CoV-2 infection increases tacrolimus concentrations in solid-organ transplant recipients. *Clin. Transpl.* 35, e14193. doi:10.1111/ctr.14193

Sandusky, G. E., Mintze, K. S., Pratt, S. E., and Dantzig, A. H. (2002). Expression of multidrug resistance-associated protein 2 (MRP2) in normal human tissues and carcinomas using tissue microarrays. *Histopathology* 41, 65–74. doi:10.1046/j.1365-2559.2002.01403.x

Scheffer, G. L., Pijnenborg, A. C. L. M., Smit, E. F., Muller, M., Postma, D. S., Timens, W., et al. (2002). Multidrug resistance related molecules in human and murine lung. *J. Clin. Pathology* 55, 332–339. doi:10.1136/jcp.55.5.332

Stanke-Labesque, F., Gautier-Veyret, E., Chhun, S., and Guilhaumou, R.French Society of Pharmacology and Therapeutics (2020). Inflammation is a major regulator of drug metabolizing enzymes and transporters: Consequences for the personalization of drug treatment. *Pharmacol. Ther.* 215, 107627. doi:10.1016/j.pharmthera.2020.107627

Su, F., Patel, G. B., Hu, S., and Chen, W. (2016). Induction of mucosal immunity through systemic immunization: Phantom or reality? *Hum. Vaccines Immunother.* 12, 1070–1079. doi:10.1080/21645515.2015.1114195

Van der Valk, P., van Kalken, C. K., Ketelaars, H., Broxterman, H. J., Scheffer, G., Kuiper, C. M., et al. (1990). Distribution of multi-drug resistance-associated P-glycoprotein in normal and neoplastic human tissues. *Ann. Oncol.* 1, 56–64. doi:10.1093/oxfordjournals.annonc.a057676

World Health organization (2022). WHO coronavirus (COVID-19) dashboard. *WHO*. Available at: https://covid19.who.int/.

Wu, K.-C., and Lin, C.-J. (2019). The regulation of drug-metabolizing enzymes and membrane transporters by inflammation: Evidences in inflammatory diseases and age-related disorders. *J. Food Drug Analysis* 27, 48–59. doi:10.1016/j.jfda.2018.11.005

Yamasaki, M., Makino, T., Masuzawa, T., Kurokawa, Y., Miyata, H., Takiguchi, S., et al. (2011). Role of multidrug resistance protein 2 (MRP2) in chemoresistance and clinical outcome in oesophageal squamous cell carcinoma. *Br. J. Cancer* 104, 707–713. doi:10.1038/sj.bjc.6606071

Yang, K. (2020). What do we know about remdesivir drug interactions? Clin. Transl. Sci. *cts* 13, 842–844. doi:10.1111/cts.12815

Yokose, T., Doy, M., Taniguchi, T., Shimada, T., Kakiki, M., Horie, T., et al. (1999). Immunohistochemical study of cytochrome P450 2C and 3A in human non-neoplastic and neoplastic tissues. *Virchows Arch.* 434, 401–411. doi:10.1007/s004280050359

Yurkovetskiy, L., Wang, X., Pascal, K. E., Tomkins-Tinch, C., Nyalile, T. P., Wang, Y., et al. (2020). Structural and functional analysis of the D614G SARS-CoV-2 spike protein variant. *Cell.* 183, 739–751. doi:10.1016/j.cell.2020.09.032

Zhang, L., Jackson, C. B., Mou, H., Ojha, A., Peng, H., Quinlan, B. D., et al. (2020). SARS-CoV-2 spike-protein D614G mutation increases virion spike density and infectivity. *Nat. Commun.* 11, 6013. doi:10.1038/s41467-020-19808-4

frontiers | Frontiers in Pharmacology

TYPE Original Research
PUBLISHED 04 May 2023
DOI 10.3389/fphar.2023.1174742

OPEN ACCESS

EDITED BY
Ling Ye,
Southern Medical University, China

REVIEWED BY
Rufeng Wang,
Beijing University of Chinese Medicine, China
Jianguo Sun,
China Pharmaceutical University, China
Weifeng Yao,
Nanjing University of Chinese Medicine, China

*CORRESPONDENCE
Yong Zhang,
zhangyong_zhongyao@126.com
Ping Kang,
konnie1984@163.com
Tong Zhang,
zhangtdmj@hotmail.com

†These authors have contributed equally to this work and share first authorship

RECEIVED 27 February 2023
ACCEPTED 14 April 2023
PUBLISHED 04 May 2023

CITATION
Nie W, Yang Y, Li L, Ding Y, Chen X, Li M, He N, Ji G, Zhang Y, Kang P and Zhang T (2023), Comparison of pharmacokinetic profiles of seven major bioactive components in normal and non-alcoholic fatty liver disease (NAFLD) rats after oral administration of Ling-Gui-Zhu-Gan decoction by UPLC-MS/MS. *Front. Pharmacol.* 14:1174742. doi: 10.3389/fphar.2023.1174742

Comparison of pharmacokinetic profiles of seven major bioactive components in normal and non-alcoholic fatty liver disease (NAFLD) rats after oral administration of Ling-Gui-Zhu-Gan decoction by UPLC-MS/MS

Wenlong Nie[1†], Yang Yang[2†], Ling Li[1,3†], Yue Ding[4], Xingmi Chen[2], Ming Li[1], Ning He[3], Guang Ji[5], Yong Zhang[5]*, Ping Kang[1]* and Tong Zhang[1]*

[1]School of Pharmacy, Shanghai University of Traditional Chinese Medicine, Shanghai, China, [2]Experiment Center for Science and Technology, Shanghai University of Traditional Chinese Medicine, Shanghai, China, [3]School of Pharmacy, Anhui University of Chinese Medicine, Hefei, Anhui, China, [4]Experiment Center for Teaching and Learning, Shanghai University of Traditional Chinese Medicine, Shanghai, China, [5]Institute of Digestive Diseases, Longhua Hospital, Shanghai University of Traditional Chinese Medicine, Shanghai, China

A sensitive and rapid ultra-performance liquid chromatography–tandem mass spectrometry (UPLC-MS/MS) method was hereby developed for the determination of seven components, namely, glycyrrhizic acid, glycyrrhetinic acid, dehydrotumulosic acid, isoliquiritin, liquiritin, atractylenolide III, and cinnamic acid, in the plasma of rats after the oral administration of Ling-Gui-Zhu-Gan decoction (LGZGD). Besides, this very method was methodologically validated for specificity, linearity, inter-day and intra-day precision, accuracy, matrix effect, extraction recovery, and stability. It was also successfully used for the first time to compare the pharmacokinetic characteristics of the seven components after oral administration of LGZGD to normal rats and non-alcoholic fatty liver disease (NAFLD) rats. The results indicated significant differences between the pharmacokinetic characteristics of normal and NAFLD rats. To further reveal the different pharmacokinetic behaviors, the expressions of enzymes and transporters in the liver of normal and NAFLD rats were detected using UPLC-MS/MS. In the NAFLD rats, UDP-glucuronosyltransferase 1-1 (UGT1A1) and nine transporters were significantly inhibited and a positive correlation was observed between them and the AUC of the major components. The present results indicate that the pharmacokinetic differences between the normal and NAFLD rats might be attributed to the significant lower expression levels of both the metabolic enzyme UGT1A1 and nine transporter proteins in the NAFLD rats than in the normal rats. Meanwhile, UGT1A1 and the nine transporter proteins might be used as potential biomarkers to assess the ameliorative effect of LGZGD on NAFLD, which could provide useful information to guide the clinical application of LGZGD.

KEYWORDS

NAFLD, UPLC-MS/MS, comparative pharmacokinetics, rat plasma, Ling-Gui-Zhu-Gan decoction

1 Introduction

Non-alcoholic fatty liver disease (NAFLD) is a common chronic liver disease featuring an increasing incidence year after year. The lack of safe and effective drugs for thorough treatment has made related cardiovascular diseases a major problem of chronic diseases (Lou et al., 2020; Gu et al., 2021). To this end, the PubMed/MEDLINE literature covering the epidemiology and progress of NAFLD from 1989 to 2015 has hereby been searched, and the global prevalence of NAFLD estimated to be 25.24% (95% confidence interval: 22.10–28.65) (Younossi et al., 2016). The prevalence is the highest in the Middle East and South America and the lowest in Africa. As the global obesity epidemic intensifies, the clinical and economic burden of NAFLD becomes enormous (Zhou et al., 2019). Given that people with non-alcoholic steatohepatitis are exposed to more severe liver damage than those with steatosis alone, non-alcoholic steatohepatitis leads to further fibrosis of the liver, ultimately leading to liver-related illness and death (Diehl et al., 2017), making it necessarily important to actively prevent and treat NAFLD. However, there is currently no ideal treatment for NAFLD. Although traditional Chinese medicine has become a common treatment for NAFLD in China and its efficacy, specificity, and advantages are gradually being confirmed; however, its specific mechanism still requires further exploration (Li and Hu, 2020). Ling-Gui-Zhu-Gan decoction (LGZGD) is derived from *Treatise on Febrile Diseases* and *Synopsis of the Golden Chamber* drafted by Zhongjing Zhang in the Han dynasty (Commission and C. P., 2020), which is made of four herbs, namely, *Poria cocos* (Schw.) Wolf (Fuling), *Cinnamomum cassia* Presl (Guizhi), *Atractylodes macrocephala* Koidz. (Baizhu), and *Glycyrrhizae Radix et Rhizoma* (Gancao), in the ratio 4:3:3:2 (w/w/w/w) (Gu et al., 2020). LGZGD features an extensive clinical application and a favorable clinical effect. In clinical practice, LGZGD is generally used to treat cardiovascular diseases (Song et al., 2003). In recent years, with the increasing popularity of LGZGD in the treatment of different diseases, such as mental disease, type 2 diabetes, hypertension, and heart failure, the novel applications of LGZGD are constantly discovered (Ding et al., 2005; Chen et al., 2011; Wang and Xiong, 2012; Wang et al., 2020a; Wang et al., 2020b). LGZGD has also been shown to alleviate hepatic steatosis caused by high-fat diets. Yang et al. and Gu et al. found that LGZGD can promote the metabolism of fat and is thus used to prevent and cure NAFLD (Yang et al., 2012; Gu et al., 2020). Besides, LGZGD has also been found capable of regulating the Nrf2/ARE signaling pathway to

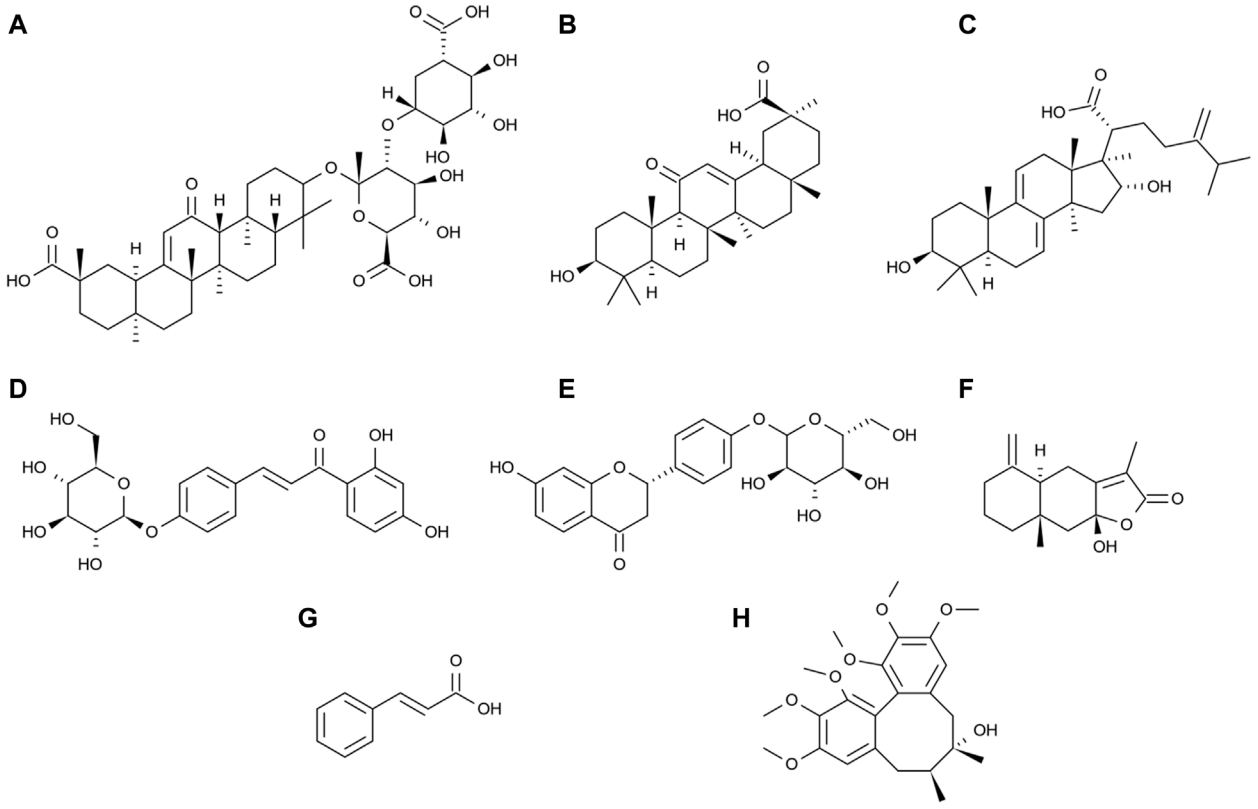

FIGURE 1
Chemical structures of glycyrrhizic acid **(A)**, glycyrrhetinic acid **(B)**, dehydrotumulosic acid **(C)**, isoliquiritin **(D)**, liquiritin **(E)**, atractylenolide III **(F)**, cinnamic acid **(G)**, and schisandrin (IS) **(H)**.

improve NAFLD in rats (Guo et al., 2017), which provides a theoretical basis for the clinical treatment of NAFLD.

Pharmacokinetic studies of drug absorption components can help in understanding the toxicity, safety, and *in vivo* processes of drugs. Previous studies on LGZGD have focused on phytochemistry and pharmacology, but pharmacokinetic studies of LGZGD components in rats have been rarely reported. Pharmacological studies have shown that the main active compounds in *Glycyrrhizae Radix et Rhizoma* include glycyrrhizic acid (Figure 1A), glycyrrhetinic acid (Figure 1B), isoliquiritin (Figure 1D), and liquiritin (Figure 1E). Glycyrrhetinic acid exerts anti-NAFLD effects by regulating the intestinal microbiota. It has been revealed that the function of carbohydrate transport and metabolism is significantly decreased by glycyrrhizic acid. Glycyrrhetinic acid prevents cholestatic liver injury in bile duct–ligated rats, while liquiritin alleviates cyclophosphamide-induced liver sinusoidal endothelial injury and inflammatory injury in mice (Chen M. et al., 2019; Pan et al., 2022; Wang et al., 2022). *Poria cocos* (Schw.) Wolf extracts protect the liver from acute ethanol insult (Yimam et al., 2016). The main active compound in *Poria cocos* (Schw.) Wolf is dehydrotumulosic acid (Figure 1C), which has anti-inflammatory, antitumor, antiviral, and immuno-promoting effects (Ukiya et al., 2002; Akihisa et al., 2007; Xiao et al., 2012). Besides, the main active compound in *Atractylodes macrocephala* Koidz is atractylenolide III (Figure 1F), which has been reported to ameliorate NAFLD by activating the hepatic adiponectin receptor 1–mediated AMPK pathway. After administration, it can significantly reduce the serum levels of alanine aminotransferase and glutamic oxaloacetic transaminase in mice, and alleviate hepatic oxidative stress (Li et al., 2021). Meanwhile, the main active compound in *Cinnamomum cassia* Presl is cinnamic acid (Figure 1G), which can ameliorate NAFLD by suppressing hepatic lipogenesis and promoting fatty acid oxidation (Wu et al., 2021). A high-performance liquid chromatography method for the determination of cinnamic acid and dehydrotumulosic acid in rat plasma was thus developed (Song et al., 2002; Song et al., 2003). The rat plasma samples were acidified with hydrochloric acid and extracted with ethyl acetate. The established method is found to be sensitive and specific, but not fast enough for the rapid determination of a large number of biological samples. The lower limits of quantification (LLOQ) of cinnamic acid and dehydrotumulosic acid by high-performance liquid chromatography are 840 and 200 ng/mL, respectively, which are considered not clinically sensitive. Additionally, the ultraperformance liquid chromatography–tandem mass spectrometry (UPLC-MS/MS) method has been reported to be used in studying the plasma samples of oral LGZGD in rats, and 11 compounds have been successfully analyzed, but the determination time was relatively long (Ji et al., 2018). Therefore, a rapid and sensitive UPLC-MS/MS method is required to determine the components in the plasma after the oral administration of LGZGD.

The pharmacokinetic drug behavior is different in normal and NAFLD rats. The pharmacokinetics of rosiglitazone in normal and high-fat diet–induced NAFLD model rats have hereby been reported (Kulkarni et al., 2016). The results have shown that the pharmacokinetics of rosiglitazone in NAFLD mice changed significantly. Compared with healthy mice, the oral clearance rate of rosiglitazone in NAFLD mice was significantly reduced and the average plasma half-life was significantly prolonged. Actually, NAFLD has been reported to be associated with the regulation of metabolic enzymes and transporters (Fisher et al., 2009). The difference in the pharmacokinetics might be related to changes in the expression of transporters in rats. Therefore, studying the changes of metabolic enzymes and transporters in rat liver is of great significance to reveal the pharmacokinetic process in NAFLD rats. On the basis of the previous research by the present researchers (Yi et al., 2018; Ma et al., 2021), UPLC-MS/MS was used to detect the expression levels of metabolic enzyme UGT1A1 and drug transporters NTCP, OATP1A1, OCT1, MATE1, MRP2, MDR1, BSEP, OATP1A2, and OATP1A4 in the liver of rats in the normal and model groups. Up to now, no comparative pharmacokinetics of these active compounds has been reported in normal and NAFLD rats after LGZGD administration. Therefore, an accurate and reliable UPLC-MS/MS method is hereby proposed for the simultaneous determination of seven components in the plasma of normal and NAFLD rats after LGZGD administration. The results showed significant differences in pharmacokinetic characteristics between the normal and NAFLD groups. The method was fully validated and applied in a comparative pharmacokinetic study. Overall, the results can provide useful information for clinical application.

2 Materials and methods

2.1 Chemicals and reagents

The standards which included glycyrrhizic acid, glycyrrhetinic acid, dehydrotumulosic acid, isoliquiritin, liquiritin, atractylenolide III, cinnamic acid, and schisandrin (≥98% purity) were all procured from Hongyong Biotechnology Co., Ltd. (Shanghai, China). Sulfatase was procured from Helix pomatia (Type H-1, sulfatase ≥10, 000 units/g solid, Sigma, United States). The peptides LTIIPQDPILFSGSLR, GVALPETIEEAENLGR, AAATEDATPAALEK, TFQFPGDIESSK, LLLSGFQEELR, STALQLIQR, NTTGALTTR, EENLGITK, SVQPELK, and TYPVPFQR, as well as stable isotope-labeled internal standards (≥98% purity) were synthesized by Bankpeptide Biological Technology, Co., Ltd. (Hefei, China). The ProteoExtract Native Membrane Protein Extraction Kit was purchased from Merck KGaA (Darmstadt, Germany). The BCA Protein Assay Kit and In-Solution Tryptic Digestion Kit were obtained from Pierce Biotechnology (Rockford, IL, United States). Formic acid dedicated to mass spectrometry (99% purity); ammonium bicarbonate (98% purity); and sodium deoxycholate (98% purity) were purchased from Sinopharm Chemical Reagent Co., Ltd. (Shanghai, China). Acetonitrile and methanol, both MS grades, were obtained from Merck KGaA (Darmstadt, Germany).

2.2 Preparation of LGZGD extract

LGZGD, consisting of Fuling: 120 g, Guizhi: 90 g, Baizhu: 90 g, and Gancao: 60 g, was soaked in 2,880 mL of deionized water (1:8, w/v) for 0.5 h and reflux extracted for 1.5 h. The right amount of

TABLE 1 Multiple reaction monitoring parameters of the mass spectrometer detector.

Component	Signature peptides	Molecular weight	Parent ion	Product ion	Fragmentor (V)	Collision energy (eV)
Glycyrrhizic acid	\	822.93	823.3	453.2	210	34
Glycyrrhetinic acid	\	470.68	471.2	189.1	190	37
Dehydrotumulosic acid	\	484.71	467.2	311.1	165	26
Isoliquiritin	\	418.39	419.0	257.0	115	17
Liquiritin	\	418.39	419.0	137.0	125	24
Atractylenolide III	\	248.32	249.0	231.1	65	7
Cinnamic acid	\	148.16	149.1	103.0	70	23
Schisandrin (IS)	\	432.50	433.0	384.1	80	20
MRP2	LTIIPQDPILFSGSLR	1,770.08	885.7	1,329.9	200	25
OCT1	GVALPETIEEAENLGR	1,697.84	849.7	1,357.8	180	29
NTCP	AAATEDATPAALEK	1,358.42	680	915.5	140	18
IS	AAATEDATPAALE*K**	1,366.42	684	923.0	140	23
OATP1A4	TFQFPGDIESSK	1,355.45	678.6	832.3	160	19
MATE1	LLLSGFQEELR	1,304.48	652.9	965.0	140	24
BSEP	STALQLIQR	1,029.19	515.5	529.5	130	17
MDR1	NTTGALTTR	934.00	467.9	719.4	110	14
OATP1A1	EENLGITK	903.00	452.3	468.1	120	8
OATP1A2	SVQPELK	799.91	400.8	486.3	110	9
UGT1A1	TYPVPFQR	1,336.48	504.5	547.1	140	19

aromatic water was collected for the first time. Then, 2,880 mL of deionized water was added for reflux extraction for another 1.5 h. The extract solutions were mixed and concentrated to an appropriate amount, and LGZGD extract powder was obtained by spray drying. The inlet air temperature of the spray dryer was controlled at 180°C ± 5°C; the outlet air temperature was 90°C–100°C; the dry paste moisture was below 5%; the atomization frequency was 200 Hz; and the extract yield was 17.56%. The aromatic water was taken and β-cyclodextrin inclusion was added to it, and the inclusion compound was mixed with the extract powder. The content of the analyte in the LGZGD extract was determined by the UPLC-MS/MS method. The amount of glycyrrhizic acid, glycyrrhetinic acid, dehydrotumulosic acid, isoliquiritin, liquiritin, atractylenolide III, and cinnamic acid in the content was 5360.3, 16.4, 6.0, 290.5, 6991.5, 141.8, and 739.2 μg/g, respectively.

2.3 Animals handing

Male Sprague–Dawley rats, weighing 200–220 g, SPF grade, were purchased from Shanghai Sippr-BK laboratory animal Co. Ltd. (Shanghai, China) and raised in the Laboratory Animal Center of Shanghai University of Traditional Chinese Medicine. The rats were kept in an environmentally controlled condition: on a 12:12 h light–dark cycle (lights on at 7:00 a.m.) with regulated temperature and humidity, at a temperature of 22°C–24°C and a relative humidity of 60–65%. In the experiment, the rats in the normal group were fed a certified standard rat diet and tap water, while those in the model group were fed a high-fat diet for 8 weeks to construct the NAFLD model (high-fat diet: 2% cholesterol, 10% lard, 0.1% sodium cholate, 10% yolk powder, and 77.9% normal diet). The animal experiment program was approved by the Animal Committee of Shanghai University of Traditional Chinese Medicine (License No.: PZSHUTCM201016001).

2.4 Pharmacokinetic study of LGZGD in normal and NAFLD rat models

2.4.1 Instrumentation and chromatographic conditions

An Agilent 1290 UPLC system was combined with an Agilent 6460 series MS/MS system (Agilent Technologies, Santa Clara, CA, United States) to quantify the analytes in the ESI-positive ionization mode. The mass spectrum conditions were as follows: a capillary voltage of 4,000 V; a gas flow rate of 10 L/min; a nebulizer of 30 psi; a gas temperature of 350°C; and a Delta EMV(+) of 200 V. Five microliters of the samples was injected into an Agilent SB-C_{18} column (2.1 mm × 50 mm, 1.8 μm particles). The analytes were separated using the gradient elution method, and the mobile phase was composed of water (0.05% V/V formic acid) (A) and acetonitrile

(B) at a flow rate of 0.4 mL/min (0–1 min, 10–10% B; 1–5 min, 10–90% B; 5–7 min, 90–90% B; and 7–7.1 min, B 90–10%; rebalance for 2 min). The multiple reaction-monitoring parameters are shown in Table 1.

2.4.2 Sample preparation

A plasma sample of 50 μL was placed in a 1.5 mL centrifuge tube with 10 μL of schisandrin (IS) solution (50 ng/mL) and mixed for 5 min. The samples were successively extracted with 500 μL of ethyl acetate and treated with 250 μL of methanol, which were then mixed for 5 min and centrifuged at 4°C for 10 min (at 18,000 rpm). All the supernatant was absorbed into another 1.5 mL centrifuge tube, dried under a gentle stream of nitrogen at 37°C, and then added with 50 μL of 50% methanol for reconstruction. After being centrifuged at 4°C for 10 min (at 18,000 rpm), 5 μL of the supernatant was extracted and injected into a chromatographic column for analysis, and the chromatograms were recorded.

2.4.3 Method validation

The bioanalytical method was validated based on the current US FDA Bioanalytical Method Validation Guidance for Industry (Gu, 2020), with validation parameters such as specificity, linearity, precision and accuracy, recovery, matrix effect, and stability being involved.

2.4.3.1 Specificity

The specificity of endogenous interference was examined by chromatograms of six batches of blank rat plasma, blank plasma with the seven components and internal standard, and plasma samples after the oral administration of LGZGD for 4 h.

2.4.3.2 Linearity

The calibration curve was obtained by measuring the blank plasma samples with analytes at eight concentration levels and by analyzing the peak area ratio of the components to IS using weighted ($1/x^2$) least squares linear regression. The LLOQ was defined as the lowest quantifiable calibration concentration with an acceptable accuracy within ±20%, which was hereby determined at the lowest concentration with a signal-to-noise ratio (S/N) of 10.

2.4.3.3 Precision and accuracy

The precision and accuracy were evaluated using six duplicated, three (low, medium, and high) quality control samples on the same day and three batches of samples for three consecutive days, respectively. The accuracy was expressed as a relative error percentage (RE, %), while the intra-day and inter-day precisions were evaluated as a relative standard deviation percentage (RSD).

2.4.3.4 Extraction recovery and matrix effect

At three quality control (QC) levels, the extraction recovery was determined by comparing the ratio of the peak area to the internal standard in the blank plasma sample with the analyte added before extraction and after extraction. The matrix effect was measured at three QC levels by comparing the peak areas of the extracted blank plasma samples with the analyte (six batches of rat plasma) and the corresponding pure standard solution.

2.4.3.5 Stability

Stability refers to the ability of the components to retain their chemical properties in the matrix. To analyze the stability of all components in the plasma, six replicates of QC samples at three concentrations were hereby prepared under each condition. The stability of the QC samples at three concentrations was analyzed under different storage conditions: −80°C for 30 days, after three freeze–thaw cycles, and 24 h in an auto sampler at 4°C.

2.5 Application to pharmacokinetic analysis

The rats were randomly divided into the normal group and the model group. According to the preliminary experiment, the dose was adjusted to about eight times the normal dose (Gu, 2020; Li et al., 2023). The normal and NAFLD groups were each orally treated with 23 g/kg of extract (equivalent to LGZGD raw herbs 131 g/kg), and the content of each analyte was determined. The animal research program was approved by the Animal Committee of Shanghai University of Traditional Chinese Medicine. At 0, 0.083, 0.25, 0.5, 0.75, 1, 2, 4, 6, 8, 10, 12, 24, and 48 h after dosing, 150 μL blood samples were collected from the rats' orbital venous plexus into centrifuge tubes containing 10 IU of sodium heparin. After being centrifuged at 5,000 rpm (4°C) for 10 min, the plasma was transferred to 1.5 mL polypropylene tubes and stored at −80°C until the plasma samples were analyzed.

Eight weeks after modeling, the blood samples were collected in the coagulation vessels of the model group and the normal group, which were then centrifuged at 4°C for 10 min (5,000 rpm) to obtain the serum samples. Total cholesterol (TC), triglyceride (TG), high-density lipoprotein cholesterol (HDL-C), and low-density lipoprotein cholesterol (LDL-C) were determined to evaluate the modeling efficiency. Besides, the liver samples were isolated and stored in 4% paraformaldehyde for histological examination. Serum TG, TC, HDL-C, and LDL-C were measured by using a chemical analyzer (Hitachi 7080, Japan). The liver tissue blocks fixed with 4% of formaldehyde solution were embedded in paraffin, sectioned, stained with hematoxylin and eosin (H&E), and observed under an optical microscope.

2.6 Determination of UGT1A1 and nine other transporter proteins in the liver

Herein, a comprehensive study was conducted to detect the expressions of UGT1A1 and nine other transporters in the liver of the NAFLD model group and normal rats, which were successfully determined. Previous methods of protein quantification were immunological, which however require antibodies that are frequently unavailable, and even when available, are often of uncertain specificity. Additionally, the UPLC-MS/MS method was hereby used to detect the expression level of metabolic enzymes, which is provided with advantages in absolute accuracy, stability, operability, and

efficiency when compared with the traditional quantitative methods (Yi et al., 2018).

2.6.1 Instrumentation and chromatographic conditions

The Agilent 1290 series UPLC system and Agilent 6460 series MS/MS system (Agilent Technologies, Santa Clara, CA, United States) were hereby combined to quantify the signature peptides in the ESI-positive ionization mode. The conditions of mass spectrometry were as follows: a capillary voltage of 2,000 V; a gas flow of 8 L/min; a nebulizer of 30 psi; a gas temperature at 300°C; and a Delta EMV(+) of 400 V. Five milliliters of the sample was injected into the column (Agilent SB-C_{18} column, 2.1 mm × 50 mm, 1.8 μm particles) and eluted at 0.4 mL/min with a gradient elution of water (with 0.05% v/v formic acid) (A) and acetonitrile (B) (0–1 min, 5–5% B; 1–4 min, 5–60% B; 4–5 min, 60–5% B; and re-equilibration for 3 min). According to previous experiments by the research group of Yi et al. (2018), the sequences of characteristic peptides corresponding to UGT1A1 and the nine other transporters are listed in Table 1.

2.6.2 Sample preparation

Total membrane proteins were isolated from the liver tissue using the Native Membrane Protein Extraction Kit protocols (three replicates), and the protein concentration was detected by the BCA Protein Assay Kit. The preparation process was based on the previous experiments by the present researchers (Yi et al., 2018; Ma et al., 2021). In simple terms, 10 μL of 5 mg/mL liver cell proteins was cultured with 20 μL of dithiothreitol (100 mM) and 50 μL of ammonium bicarbonate buffer (50 mM, pH = 7.8). After being incubated at 95°C for 5 min, 20 μL of iodoacetamide (20 mM) was added and cultured at 37°C for 20 min away from light. The sample was concentrated, and iced methanol (0.5 mL), chloroform (0.2 mL), and water (0.2 mL) were added, which was then centrifuged at 16,000 *g* for 5 min at 4°C. Afterward, the supernatant was removed, and the sample was washed once with 0.25 mL of cold methanol and recombined with 40 μL of recombination solution (equal volume 3% sodium deoxycholate (w/v) and 5 mM ammonium bicarbonate buffer). Finally, the protein samples were digested with 10 μL of trypsin. The ratio of protein to trypsin was 25:1 (w/w). After incubation at 37°C for 24 h, the digestion reaction was terminated by 60 μL of IS cocktail. The samples were centrifuged at 18,000 *g* for 10 min at 4°C, and 5 μL of the sample was injected in the UPLC-MS/MS system.

2.7 Data processing and statistical analysis

Important pharmacokinetic parameters, which included the maximum plasma concentration (C_{max}), time to maximum concentration (T_{max}), half-life ($t_{1/2}$), area under the curve (AUC_{0-t}), and total area under the curve ($AUC_{0-\infty}$), were hereby calculated using the DAS 3.2.8 software. Meanwhile, the pharmacokinetic data of the normal and model rats were compared using the SPSS software (version 21.0). Besides, Spearman rank bivariate correlation coefficient was used to determine the correlation between AUC values and UGT1A1 and nine other transporters. All the calculated data were expressed as mean ± SD. When $p < 0.05$, the difference was considered significant and statistically significant; and when $p < 0.01$ or <0.001, the difference was considered very significant.

3 Results

3.1 Serum biochemistry and histopathological examination

The weights of the model group rats were significantly increased after being continuously fed a high-fat diet for 8 weeks. The serum biochemical indexes of the NAFLD group were compared with those of the normal group (Figure 2C), and the TC of the model group ($p < 0.05$) and the LDL-C ($p < 0.01$) were significantly increased, but no significant difference was observed between TG and HDL-C. Besides, liver pathological sections were observed under the microscope (Figures 2A, B). The liver cells in the normal group were arranged neatly, with no obvious lesions, were polygonal and with well-defined boundaries, having nuclei located in the center of the cells, with homogeneous and rich cytoplasm, and no fat droplet deposition in the liver cells. In the NAFLD group, the hepatocytes were disordered and the volume of the hepatocytes was significantly enlarged and swollen, which showed diffused steatosis. Lipid vacuoles of different sizes and numbers were observed in the hepatocytes, and the nuclei were displaced and partially dissolved. Similar to the biochemical and pathological aspects of simple NAFLD (Anstee and Goldin, 2006), and in line with the characteristics of NAFLD, the model was successfully prepared.

3.2 Pharmacokinetic study of LGZGD in NAFLD and normal rat models

3.2.1 Method validation

3.2.1.1 Specificity

No endogenous interference was found in the retention time of the analyte and internal standard in the blank plasma of the six different rats, which proved the specificity of this method. Figure 3 presents the typical chromatograms of blank rat plasma, blank samples supplemented with seven compounds and internal standards, and rat plasma samples after the oral administration of LGZGD for 4 h.

3.2.1.2 Linearity

The relationship curve between the peak area ratio (*y*-axis) of each analyte and IS and the corresponding nominal concentration (*x*-axis) of the analyte was plotted by weighted ($1/x^2$) least square linear regression. All standard curves showed a good linearity with the correlation coefficient ($r > 0.9952$). The calibration curves, linear ranges, LLOQ, and correlation coefficients of the seven components are shown in Table 2, where the stablished method can be seen to meet the

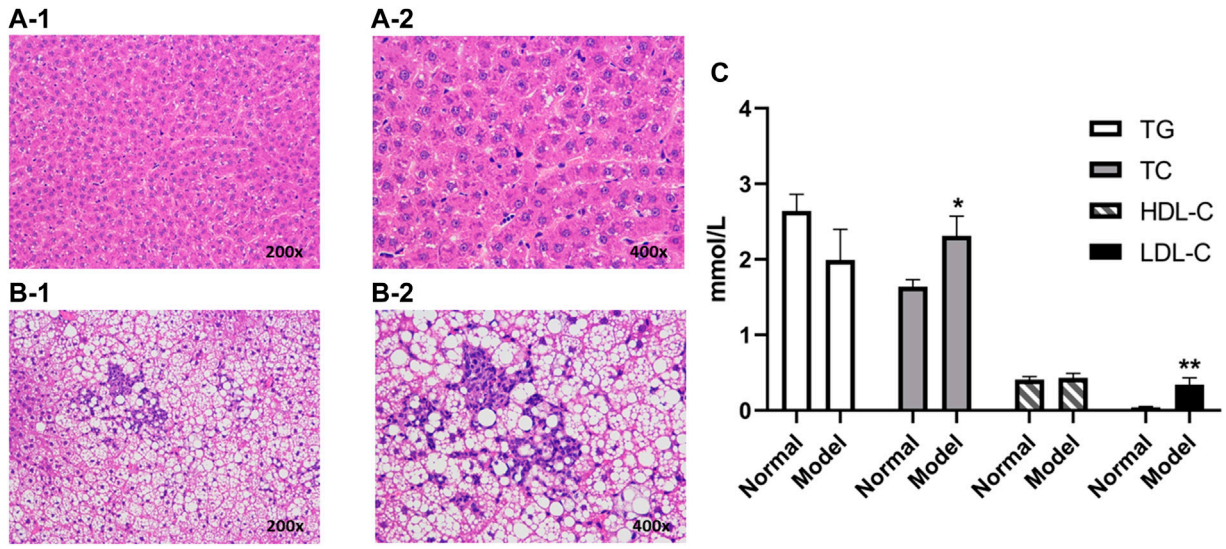

FIGURE 2
Liver histopathology of rats with and without NAFLD. Representative histopathology of liver sections from control (non-NAFLD) rats: **(A-1)** ×200 magnification and **(A-2)** ×400 magnification, and from NAFLD rats: **(B-1)** ×200 magnification and **(B-2)** ×400 magnification. The serum biochemical indexes of the model group were compared with those from the normal group **(C)**. Liver sections were stained with hematoxylin and eosin prior to microscopy (**$p < 0.01$ and *$p < 0.05$, which compared with the control group).

requirements of the quantitative determination of LGZGD in pharmacokinetic studies.

3.2.1.3 Precision and accuracy

The precision and accuracy are summarized in Table 3. The intra-day and inter-day precision (relative standard deviation) was less than 14.9% and the accuracy (relative error) was less than 12.8%. All results were within acceptable standards according to the guidelines for bioassay methods.

3.2.1.4 Extraction recovery and matrix effect

Table 3 summarizes the average extraction recoveries and matrix effects of seven components at three QC levels. The recoveries of the three QC samples of the seven analytes range from 63.8 to 92.0%, while the matrix effect range from 83.4 to 112.6%. These results indicate the acceptable recovery and matrix effect of the liquid–liquid extraction combined with the protein precipitation method in the present study.

3.2.1.5 Stability

The data in Table 4 show that the seven components in the rat plasma are stable in the plasma samples maintained at −80°C for 30 days, during the three freeze–thaw cycles, and in the 24 h in an auto sampler at 4°C—stable and consistent with the analytical criteria during the whole experiment.

3.3 Pharmacokinetic study of LGZGD in normal and NAFLD rat models

The UPLC-MS/MS method was successfully used to compare the pharmacokinetics of the seven components of LGZGD in the normal and NAFLD rats. The glycyrrhizic acid, glycyrrhetinic acid, dehydrotumulosic acid, isoliquiritin, liquiritin, atractylenolide III, and cinnamic acid were detected in the plasma of normal and NAFLD rats. The mean plasma concentration–time curve is shown in Figure 4, and the corresponding pharmacokinetic data are listed in Table 5. The pharmacokinetic behavior of the LGZGD components in the normal group was significantly different from that in NAFLD rats.

By comparing the pharmacokinetic parameters of LGZGD orally taken by NAFLD and normal rats, it was found that isoliquiritin. atractylenolide III, and cinnamic acid were rapidly absorbed in both normal and NAFLD rats, and the T_{max} was not significantly different between the model group and normal rats. The mean $AUC_{0\text{-}t}$ of the model group was significantly lower than that of the normal group. Compared with the normal group, the $MRT_{0\text{-}t}$ of glycyrrhetinic acid, atractylenolide III, and liquiritin was prolonged by 44.4, 31.3, and 31.2%, respectively, while the MRT of dehydrotumulosic acid and isoliquiritin decreased by 27.8 and 21.7%, respectively. The C_{max} value, $AUC_{0\text{-}t}$, and $AUC_{0\text{-}\infty}$ of the NAFLD rats were significantly lower than those of the normal rats. When compared with that in the normal rats, the C_{max} value of glycyrrhizic acid, glycyrrhetinic acid, dehydrotumulosic acid, isoliquiritin, liquiritin, atractylenolide III, and cinnamic acid in NAFLD rats was decreased by 77.4, 65.0, 62.4, 31.1, 63.8, 35.2, and 38.3%, respectively, and the $AUC_{0\text{-}\infty}$ value decreased by 70.8, 50.6, 75.1, 65.8, 53.7, 70.8, and 58.1%, respectively.

The blood concentration of liquiritin in LGZGD was the highest, followed by that of glycyrrhizic acid, glycyrrhetinic acid, cinnamic acid, atractylenolide III, dehydrotumulosic acid, and isoliquiritin. In the NAFLD rats, the clearance rate of

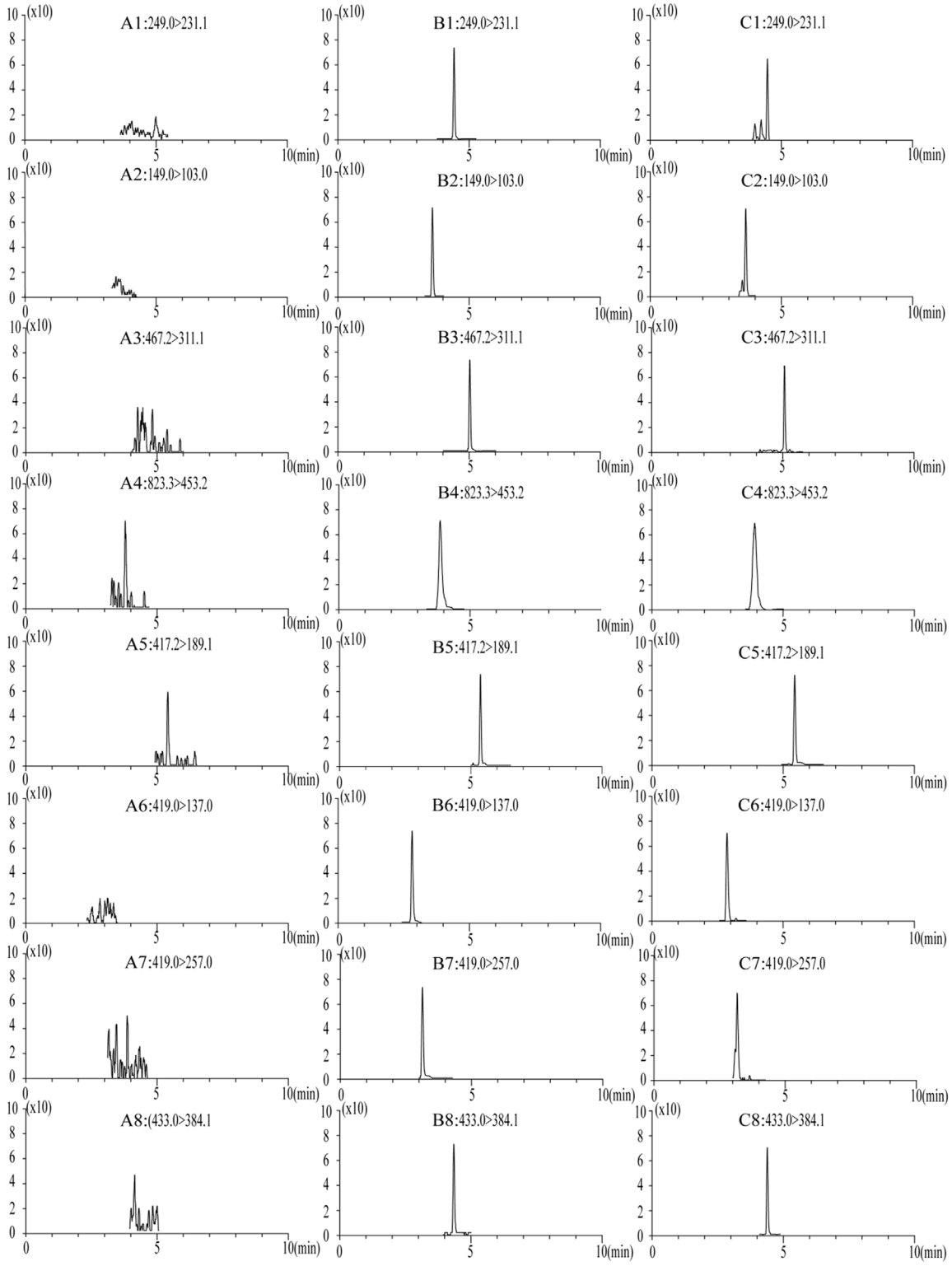

FIGURE 3
MRM chromatograms of blank plasma samples: **(A)** blank spiked with combined standard solutions of the seven analytes and IS, **(B)** rat plasma samples at 4 h after oral administration of LGZGD **(C)**. 1, atractylenolide III; 2, cinnamic acid; 3, dehydrotumulosic acid; 4, glycyrrhizic acid; 5, glycyrrhetinic acid; 6, liquiritin; 7, isoliquiritin; and 8, schisandrin (IS).

glycyrrhizic acid, glycyrrhetinic acid, dehydrotumulosic acid, isoliquiritin, liquiritin, atractylenolide III, and cinnamic acid was significantly higher than that of the normal group. There was also a bimodal phenomenon between glycyrrhetinic acid and isoliquiritin (Xu et al., 2018; Shen et al., 2019), which might have been caused by gastric emptying separation, enterohepatic

TABLE 2 Regression equations, linear range, and LLOQ of the seven components in rat plasma.

Component	Regression equation	Correlation coefficient(r)	Linear range (ng/mL)	LLOQ (ng/mL)
Glycyrrhizic acid	y = 0.0009x + 0.0212	0.9957	2.66–5440	1.97
Glycyrrhetinic acid	y = 0.0137x + 0.1468	0.9952	2.00–8180	1.75
Dehydrotumulosic acid	y = 0.0094x + 0.1236	0.9966	1.23–5050	0.32
Isoliquiritin	y = 0.126x + 0.7072	0.9964	1.18–4850	0.14
Liquiritin	y = 0.0047x + 0.0991	0.9973	4.83–9900	3.99
Atractylenolide III	y = 0.0707x + 0.8165	0.9952	2.63–5390	1.80
Cinnamic acid	y = 0.0321x + 0.4800	0.9982	2.65–5430	0.99

TABLE 3 Summary of accuracy, precision, recovery, and matrix effect of the seven components in rat plasma (n = 6).

Component	Concentration (ng/mL)	Precision and accuracy				Recovery (%)		Matrix effect (%)	
		Intra-day (%)		Inter-day (%)					
		RSD	RE	RSD	RE	Mean	RSD	Mean	RSD
Glycyrrhizic acid	5.31	7.3	−0.1	3.7	−6.6	97.8	4.8	107.2	5.7
	170.0	9.1	−6.1	5.1	−12.8	72.0	2.5	111.2	4.1
	2,720	8.4	−7.6	8.6	2.0	79.6	2.3	112.6	2.4
Glycyrrhetinic acid	3.99	13.4	7.4	13.1	−9.9	67.3	9.7	110.5	3.9
	127.8	8.0	4.4	6.8	−6.3	70.2	7.7	89.9	1.8
	2,045	5.3	−10.2	7.3	2.0	71.1	6.3	91.0	2.5
Dehydrotumulosic acid	4.93	3.9	11.0	10.3	−3.4	71.3	12.1	96.1	4.8
	157.8	6.3	1.5	2.9	−1.7	63.8	9.1	83.4	2.4
	2,525	5.0	3.7	13.0	5.5	67.1	5.6	87.9	12.6
Isoliquiritin	4.74	14.2	−4.0	2.0	−3.0	91.9	7.9	104.2	12.5
	151.6	7.0	−3.0	10.2	3.1	92.0	6.3	100.7	1.8
	2,425	5.3	−11.1	14.9	3.9	90.1	3.1	106.8	1.4
Liquiritin	4.83	11.2	8.5	14.1	−9.0	86.4	2.9	110.3	3.2
	154.7	7.3	−1.8	14.2	−4.6	86.9	6.4	107.2	1.9
	2,475	6.1	0.2	2.4	−0.4	87.2	2.4	105.9	5.4
Atractylenolide III	5.26	12.8	5.7	13.5	−9.4	80.0	2.0	109.2	4.1
	168.4	6.5	4.5	11.8	−10.9	87.1	6.4	102.0	2.4
	2,695	3.8	−3.8	9.8	−0.8	92.0	5.7	101.6	1.2
Cinnamic acid	5.30	9.4	−0.4	6.1	10.6	70.9	3.7	105.4	3.1
	169.7	8.0	−1.3	5.2	8.8	72.2	9.0	104.9	1.8
	2,715	7.5	−1.5	6.2	−0.2	83.8	5.8	112.4	1.5

circulation, and reabsorption (Deng et al., 2008; Zhu et al., 2010). Further research should be carried out to determine the specific mechanism. All these results suggest lower systemic exposure of LGZGD in NAFLD rats, which might provide useful evidence for the pathological changes in NAFLD rats and the clinical application of LGZGD.

3.4 Expression of UGT1A1 and nine other transporter proteins in NAFLD and normal rats' liver

The quantitative results of UGT1A1 and the nine transporters are shown in Figure 5. The expression levels of UGT1A1 and

TABLE 4 Stability of the seven components in rat plasma at three quality control levels (n = 6).

Component	Concentration (ng/mL)	Stability during 24 h at 4°C		Three freeze–thaw cycles		−80°C for 30 days	
		RSD (%)	RE (%)	RSD (%)	RE (%)	RSD (%)	RE (%)
Glycyrrhizic acid	5.31	11.0	−1.6	13.3	−5.9	3.6	−1.0
	170.0	14.6	−5.6	12.6	−3.7	7.1	1.7
	2,720	13.7	−3.3	14.2	9.7	2.7	2.7
Glycyrrhetinic acid	3.99	13.4	5.2	11.4	−0.4	3.6	−5.2
	127.8	2.5	6.7	7.9	−7.7	2.4	−4.9
	2,045	8.7	−8.9	5.6	2.2	5.9	2.6
Dehydrotumulosic acid	4.93	5.0	3.8	14.6	−12.8	6.4	3.2
	157.8	3.6	1.6	2.8	−4.3	8.2	10.2
	2,525	8.1	−2.3	7.6	5.5	3.9	3.0
Isoliquiritin	4.74	5.9	1.3	11.3	−6.8	11.7	−1.1
	151.6	5.6	11.0	8.6	−3.0	7.3	−2.1
	2,425	7.8	−12.7	6.7	3.9	5.5	4.0
Liquiritin	4.83	8.7	1.4	7.2	10.5	5.5	−4.1
	154.7	5.4	5.4	10.6	−1.8	7.4	3.1
	2,475	8.7	−3.0	7.9	4.1	5.6	−1.2
Atractylenolide III	5.26	14.6	6.4	10.4	13.3	10.6	−4.4
	168.4	6.0	5.2	7.4	−9.5	4.4	−3.5
	2,695	7.8	−4.0	8.9	−3.8	7.2	14.1
Cinnamic acid	5.30	14.7	8.4	11.8	−0.4	2.4	−8.0
	169.7	5.4	13.9	4.5	0.7	6.6	3.6
	2,715	14.7	−3.7	7.6	−11.1	5.7	−2.6

NTCP, OATP1A1, OCT1, MATE1, MRP2, MDR1, BSEP, OATP1A2, and OATP1A4 of the nine transporters in the liver of the model group are significantly lower than those of the normal group, which is consistent with the reports of previous studies (Kim et al., 2004; Kirpich et al., 2011). Uridine diphosphate glucuronosyltransferase (UGT) is a common phase II metabolic enzyme that plays an important role in drug binding reactions. Meanwhile, OCT1, NTCP, OATP1A1, OATP1A2, and OATP1A4 are uptake transporters, whereas MRP2, BSEP, MATE1, and MDR1 are efflux transporters (Chen L. et al., 2019). The expressions of UGT1A1 metabolic enzyme and nine transporters are decreased in NAFLD rats, indicating that the metabolism of the drug components absorbed into the blood was inhibited in the model group, and the drug uptake and excretion were also inhibited. When compared with the normal group, UGT1A1, NTCP, OCT1, MATE1, MDR1, BSEP, and OATP1A2 in the NAFLD group are significantly decreased by 24.1, 35.3, 30.8, 38.6, 34.3, 43.7, and 33.8% ($p < 0.05$), respectively.

3.5 Correlation between AUC values and expression levels of metabolic enzyme and transporters

The AUC is an important indicator of drug absorption. In this study, a significant decrease in UGT1A1 and the nine other transporters was observed in the NAFLD rats. In order to further understand the reasons for the pharmacokinetic differences, a correlation analysis between the expression levels of the active ingredients and UGT1A1 and transporters in the model group and the normal group was conducted, and the results are shown in Table 6 and Supplementary Figures S1–S50.

The expression levels of BSEP ($\rho = 0.709$, $\rho = 0.976$, $\rho = 0.903$, $\rho = 0.733$, $\rho = 0.745$, $\rho = 0.855$, and $\rho = 0.891$) ($p < 0.05$) were significantly correlated with the exposure amount of the seven components *in vivo*, respectively, while those of NTCP ($\rho = 0.721$, $\rho = 0.685$, $\rho = 0.661$, $\rho = 0.685$, $\rho = 0.770$, and $\rho = 0.818$) ($p < 0.05$) and OATP1A1 ($\rho = 0.867$, $\rho = 0.733$, $\rho = 0.758$, $\rho = 0.685$, $\rho = 0.867$, and $\rho = 0.939$) ($p < 0.05$) were significantly correlated with the exposure amount of glycyrrhetinic acid,

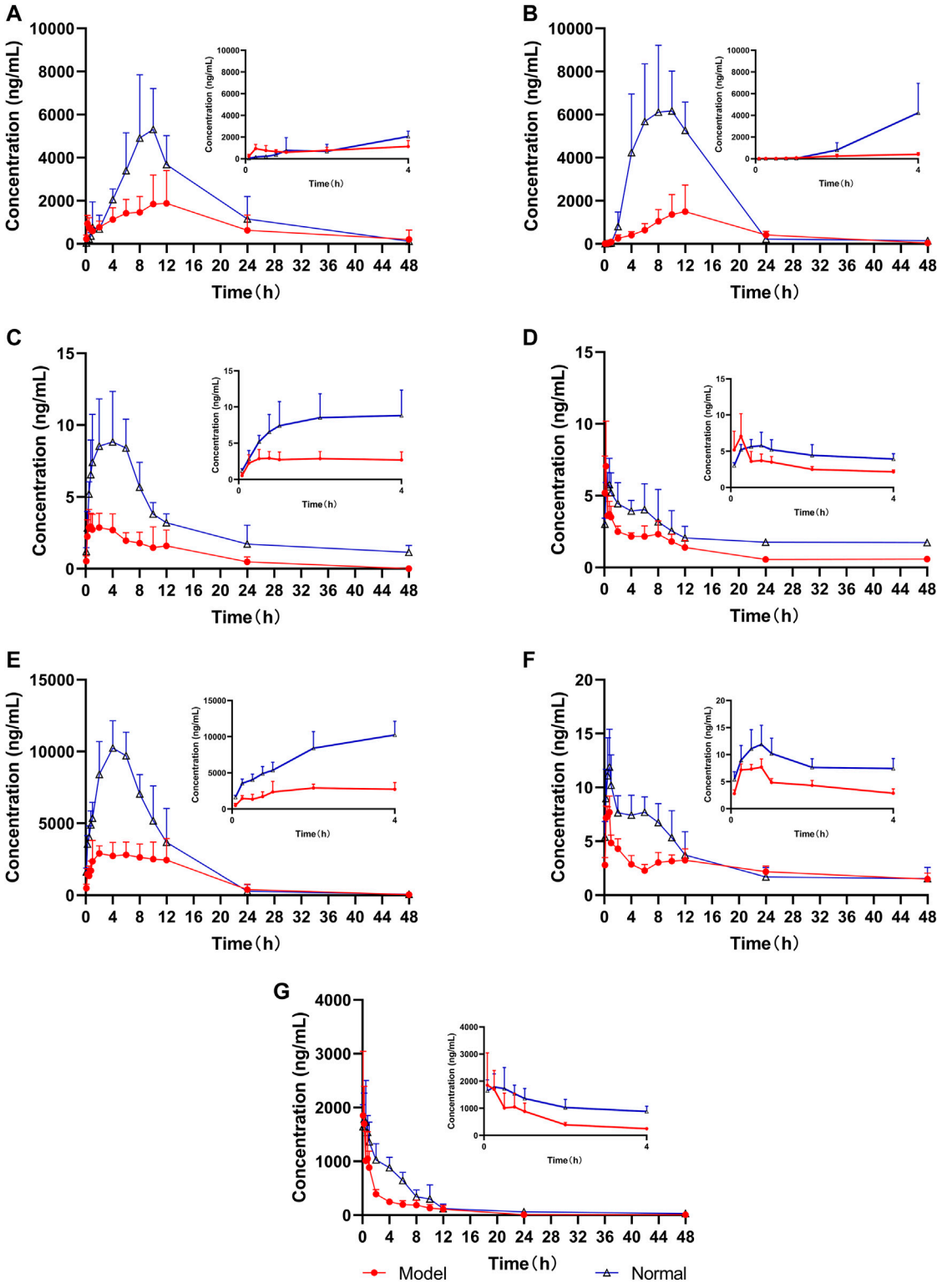

FIGURE 4
Mean concentration–time curves of the seven analytes in rat plasma (n = 6), **(A)** glycyrrhizic acid, **(B)** glycyrrhetinic acid, **(C)** dehydrotumulosic acid, **(D)** isoliquiritin, **(E)** liquiritin, **(F)** atractylenolide III, and **(G)** cinnamic acid.

dehydrotumulosic acid, isoliquiritin, liquiritin, atractylenolide III, and cinnamic acid *in vivo*, respectively, and those of MDR1 were significantly correlated with the AUC values of glycyrrhizic acid ($\rho = 0.681$), glycyrrhetinic acid ($\rho = 0.772$), dehydrotumulosic acid ($\rho = 0.657$), isoliquiritin ($\rho = 0.845$), atractylenolide III ($\rho = 0.802$) ($p < 0.01$), and cinnamic acid

TABLE 5 Pharmacokinetic parameters of the seven components in male SD rats after the oral administration of LGZGD (mean ± SD, n = 6).

Component	Groups	$t_{1/2}$(h)	T_{max}(h)	C_{max} (ug/L)	AUC_{0-t} (ug/L*h)	$AUC_{0-\infty}$(ug/L*h)	CLz/F (L/h/kg)	MRT_{0-t}(h)
Glycyrrhizic acid	Normal	6.3 ± 3.0	10.4 ± 1.7	6415.5 ± 2238.9	81042.3 ± 10475.2	82667.3 ± 10040.9	281.8 ± 36.8	13.7 ± 3.3
	Model	5.4 ± 1.4	8.1 ± 4.9	2243.1 ± 1202.0**	40701.8 ± 25060.3*	40806.7 ± 25026.0**	701.2 ± 305.3*	16.0 ± 8.0
Glycyrrhetinic acid	Normal	6.0 ± 2.1	9.3 ± 1.6	7281.6 ± 2079.1	88249.6 ± 27217.9	89638.0 ± 28611.9	273.6 ± 64.8	10.8 ± 1.1
	Model	8.9 ± 4.5	13.2 ± 6.3	1648.9 ± 1173.3***	25626.1 ± 14778.6**	26152.2 ± 14423.4**	1184.3 ± 716.4*	15.6 ± 2.3**
Dehydrotumulosic acid	Normal	19.0 ± 12.2	4.0 ± 1.8	10.1 ± 3.0	141.6 ± 15.8	174.6 ± 37.2	136156.3 ± 25915.9	14.4 ± 2.7
	Model	5.0 ± 1.8*	1.8 ± 1.6	3.8 ± 0.6**	43.4 ± 12.0***	43.5 ± 12.0***	559085.2 ± 149625.6***	10.4 ± 2.2*
Isoliquiritin	Normal	9.2 ± 4.4	0.6 ± 0.1	6.1 ± 1.8	107.6 ± 21.2	166.5 ± 10.5	82306.9 ± 61479.7	19.8 ± 1.7
	Model	13.1 ± 7.5	0.7 ± 0.2	4.2 ± 0.8*	51.9 ± 7.8***	56.9 ± 10.8***	403580.1 ± 75381.0***	15.5 ± 1.8**
Liquiritin	Normal	5.2 ± 2.5	4.8 ± 1.1	10332.4 ± 1848.3	114704.1 ± 32858.5	115445.5 ± 32941.3	211.0 ± 56.8	7.7 ± 1.6
	Model	6.0 ± 3.4	6.8 ± 4.1	3741.7 ± 991.4***	52772.6 ± 22330.1**	53400.2 ± 22110.2**	491.1 ± 204.8*	10.1 ± 1.3*
Atractylenolide III	Normal	10.2 ± 4.4	0.7 ± 0.1	12.2 ± 3.4	352.5 ± 21.5	568.1 ± 234.7	149538.5 ± 21123.9	14.7 ± 1.5
	Model	18.3 ± 1.3*	0.6 ± 0.1	7.9 ± 1.3*	116.7 ± 16.1***	165.8 ± 45.1**	171606.0 ± 32478.4	19.3 ± 2.9*
Cinnamic acid	Normal	12.8 ± 3.6	0.6 ± 0.1	1930.9 ± 483.9	10094.3 ± 1770.0	10505.6 ± 1902.0	2180.2 ± 440.9	8.2 ± 1.3
	Model	6.6 ± 3.5*	0.6 ± 0.1	1190.4 ± 352.4*	4332.2 ± 1334.7***	4406.4 ± 1420.0***	5187.3 ± 1815.1**	6.2 ± 1.8

ANOVA test was used to calculate the significance of the differences, ***$p < 0.001$, **$p < 0.01$, and *$p < 0.05$, which compared with the normal group. The CLz/F is apparent clearance.

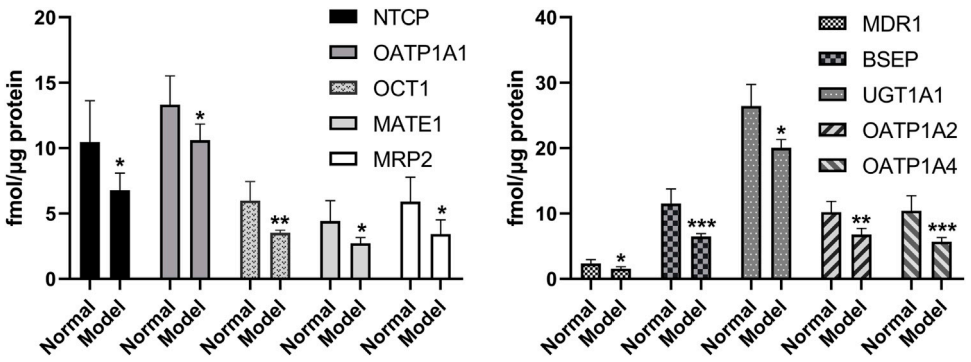

FIGURE 5
Expression levels of metabolic enzyme UGT1A1 and nine transporters in the liver of model group and normal group (*$p < 0.05$, **$p < 0.01$, and ***$p < 0.001$, which compared with the normal group).

(ρ = 0.748) ($p < 0.05$). In addition, the expression levels of NTCP and OATP1A1 were significantly correlated with the AUC values of glycyrrhetinic acid (ρ = 0.721 and ρ = 0.867), dehydrotumulosic acid (ρ = 0.685 and ρ = 0.733), isoliquiritin (ρ = 0.661 and ρ = 0.758), liquiritin (ρ = 0.685 and ρ = 0.685), atractylenolide III (ρ = 0.770 and ρ = 0.867) ($p < 0.01$), and cinnamic acid (ρ = 0.818 and ρ = 0.939) ($p < 0.01$). The expression levels of OCT1, MATE1, and MRP2 were found related to the AUC values of glycyrrhetinic acid (ρ = 0.830, ρ = 0.745, and ρ = 0.903), dehydrotumulosic acid (ρ = 0.758, ρ = 0.648, and ρ = −0.794), isoliquiritin (ρ = 0.782, ρ = 0.770, and ρ = 0.673), atractylenolide III (ρ = 0.733, ρ = 0.867, and ρ = 0.733), and cinnamic acid (ρ = 0.661, ρ = 0.721, and ρ = 0.709) ($p < 0.05$).

Besides, the expression levels of OATP1A4 were significantly correlated with the AUC values of glycyrrhetinic acid (ρ = 0.855) ($p < 0.01$), dehydrotumulosic acid (ρ = 0.794) ($p < 0.01$), atractylenolide III (ρ = 0.685) ($p < 0.05$), and cinnamic acid (ρ = 0.673) ($p < 0.05$), while those of OATP1A2 were significantly correlated with the AUC values of glycyrrhetinic acid (ρ = 0.733) ($p < 0.05$), dehydrotumulosic acid (ρ = 0.697) ($p < 0.05$), and cinnamic acid (ρ = 0.733) ($p < 0.05$).

TABLE 6 Correlation results of AUC values with metabolic enzymes and transporters ($p < 0.01$ and *$p < 0.05$).**

Component	Correlation coefficient ρ									
	UGT1A1	NTCP	OATP1A1	OCT1	MATE1	MRP2	MDR1	BSEP	OATP1A2	OATP1A4
Glycyrrhizic acid	0.515	0.455	0.600	0.624	0.491	0.612	0.681*	0.709*	0.552	0.539
Glycyrrhetinic acid	0.576	0.721*	0.867**	0.830**	0.745*	0.903**	0.772**	0.976**	0.733*	0.855**
Dehydrotumulosic acid	0.564	0.685*	0.733*	0.758*	0.648*	0.794**	0.657*	0.903**	0.697*	0.794**
Isoliquiritin	0.770**	0.661*	0.758*	0.782**	0.770**	0.673*	0.845**	0.733*	0.600	0.612
Liquiritin	0.588	0.685*	0.685*	0.527	0.539	0.527	0.547	0.745*	0.564	0.564
Atractylenolide III	0.697*	0.770**	0.867**	0.733*	0.867**	0.733*	0.802**	0.855**	0.612	0.685*
Cinnamic acid	0.733*	0.818**	0.939**	0.661*	0.721*	0.709*	0.748*	0.891**	0.733*	0.673*

4 Discussion

As mentioned previously, NAFLD is a common chronic liver disease (Parlati et al., 2021) and the lack of safe and effective drugs for its thorough treatment has made related cardiovascular diseases a major problem of chronic diseases (Lou et al., 2020; Gu et al., 2021). Herein, the animal models were divided into the genetic model, diet model, and combination model of genetic and diet factors (Takahashi et al., 2012). High-fat diets were found more closely related to the pathogenesis of human patients, and this method was more widely used in the manufacture of animal models of NAFLD. The NAFLD model of rats was established by high-fat diets. Under the microscope, the liver cells in the model group appeared disordered, the volume of liver cells had increased significantly, lipid vacuoles of different sizes were observed in the cells, and the nucleus was displaced and partially dissolved. In terms of biochemistry and pathology, the TC and HDL-C of the model rats were significantly different from those of the normal rats, similar to those of NAFLD alone (Anstee and Goldin, 2006), in line with the characteristics of NAFLD. Thus, the model was successfully prepared and used in pharmacokinetic research.

Liquid–liquid extraction can effectively reduce the endogenous effect. In the early stage of the experiment, organic reagents were used to precipitate protein, but the recoveries of dehydrotumulosic acid and glycyrrhizic acid were not higher than 50%. Methanol, ethyl acetate, and methanol combined with ethyl acetate were subsequently investigated, and the recovery of glycyrrhizic acid and dehydrotumulosic acid was found to be the highest when the samples were extracted with 500 μL ethyl acetate and treated with 250 μL methanol successively. The pharmacokinetics of seven LGZGD components in the normal and NAFLD rats were successfully compared by using the UPLC-MS/MS method. The pharmacokinetic behavior of the seven components was significantly different between the normal group and the fatty liver model rats. The $AUC_{0-\infty}$ and C_{max} of glycyrrhizic acid, glycyrrhetinic acid, dehydrotumulosic acid, isoliquiritin, liquiritin, atractylenolide III, and cinnamic acid in the plasma of NAFLD rats were significantly lower than those of normal rats. This is basically the same trend in the normal group and the NAFLD rats. The mean residence time of atractylenolide III, glycyrrhizic acid, glycyrrhetinic acid, and liquiritin was increased in the NAFLD group when compared with the normal group. The mean retention time of isoliquiritin and dehydrotumulosic acid was decreased. In the rat model of NAFLD, the scavenging rates of seven analytes were increased when compared with the normal group, while the *in vivo* absorption of atractylenolide III, dehydrotumulosic acid, and glycyrrhetinic acid was enhanced. The absorption of glycyrrhizic acid, liquiritin, and isoliquiritin was inhibited when compared with that in the normal group. The pharmacokinetics of the main bioactive components of *Ilex hainanensis* extract after oral administration to normal and NAFLD rats were also studied (Yang et al., 2013). The AUC and C_{max} of chlorogenic acid, kaempferol 7-O-β-D-glucoside, and ilexgenin A was decreased significantly under the plasma concentration–time curve. Kaempferol 7-O-β-D-glucoside and ilexgenin A increased the MRT in NAFLD rats. This pharmacokinetic feature is similar to the hereby observed phenomenon.

Changes of enzymes and transporters in the rat liver directly affect drug absorption and metabolism (Fisher et al., 2009; Li et al., 2011; Müller and Fromm, 2011). Studies have shown that protein transporters such as MDR1, NTCP, OATP1A2, OCT1, and MATE1 matter considerably in the metabolism of the components in the liver (Niemela et al., 2000; Nies et al., 2011; Koepsell, 2013; König et al., 2013). Most components of LGZGD are similar to the metabolic process of bilirubin (Wang et al., 2015; Yi et al., 2018), and its structure contains hydroxyl groups, where UGT1A1-mediated glucuronic acid coupling reaction can occur. The results of UGT1A1 and the nine other transporters in the NAFLD rats showed that the metabolism of drug components absorbed into the blood, and drug uptake and excretion were inhibited in the model group. The OCT1, NTCP, OATP1A1, OATP1A2, and OATP1A4 promoted the drug uptake transporter (Kim et al., 2004), the NAFLD model was reduced, and the drug absorption was restrained. The exposure characteristics of LGZGD active components were correlated with the expression levels of UGT1A1 and the nine transporters, with glycyrrhetinic acid, dehydrotumulosic acid, isoliquiritin, atractylenolide III, and

cinnamic acid being correlated the most. The AUC values of glycyrrhetinic acid, dehydrotumulosic acid, isoliquiritin, atractylenolide III, and cinnamic acid were compared with those of NTCP, OCT1, MATE1, MRP2, MDR1, and BSEP, which were found positively correlated, indicating an increase in the excretion levels of glycyrrhetinic acid, dehydrotumulosic acid, isoliquiritin, atractylenolide III, and cinnamic acid when the expression levels of NTCP, OCT1, MATE1, MRP2, MDR1, and BSEP were inhibited. The contents of glycyrrhetinic acid, dehydrotumulosic acid, isoliquiritin, atractylenolide III, and cinnamic acid in the blood were decreased. The metabolism of LGZGD active components in the NAFLD rats require further studies.

It has also been shown that hepatic cytochrome P450 expression is significantly higher in NAFLD rats than in normal rats, which led to faster metabolism of the drug in the liver of NAFLD rats, (Prompila et al., 2008; Li et al., 2011), consistent with the pharmacokinetic behavior we observed in the model group of rats. Besides, it has been confirmed by literature reports (Lickteig et al., 2007; Kolodziejczyk et al., 2019) that the upregulated expressions of hepatic efflux transporters MRP3, MRP4, and BCRP in NAFLD rats might accelerate the excretion of drugs into the blood of NAFLD rats, resulting in reduced drug exposure in model group rats, which is consistent with the observed enhancement of the elimination rate in the model group. Further exploration should be carried out on whether the pharmacokinetic difference between the NAFLD group and the normal group after oral administration of LGZGD is related to the levels of liver phase II metabolic enzymes and transporters. The composition and function of gut microbiota are influenced by a variety of host and environmental factors, which include the diet. Additionally, the study showed that NAFLD rats had different microbiome compositions when compared with those fed on a controlled diet, and changes in the intestinal microbiome were related to metabolic parameters. The changes in intestinal flora in the model group might affect drug absorption of rats, resulting in significantly lower AUC in the NAFLD group than in the normal group. These differences might be attributed to the changes in the absorption mechanism of these components caused by the altered pathological status. The expression levels of metabolic enzymes UGT1A1 and the nine transporter proteins, that is, NTCP, OATP1A1, OCT1, MATE1, MRP2, MDR1, BSEP, OATP1A2, and OATP1A4, were significantly lower in NAFLD rats than in normal rats. The results suggest the potential application of UGT1A1 and the nine transporter proteins as biological markers for the evaluation of the ameliorative effect of LGZGD on NAFLD. However, the mechanism of the decreased absorption of the seven analytes after the oral administration of LGZGD in NAFLD rats require further studying.

5 Conclusion

An efficient and stable UPLC-MS/MS method was used to simultaneously determine seven components in rat plasma, which were successfully applied to study the pharmacokinetics of LGZGD in normal rats and NAFLD rats. It is also the first time to compare the pharmacokinetic characteristics of the seven components between normal and NAFLD rats after LGZGD administration. After LGZGD administration, the pharmacokinetic profiles of the seven compounds were significantly altered in NAFLD rats when compared to normal rats, which might be attributed to the decreased expression of UGT1A1 metabolizing enzymes and the nine transporters in NAFLD rats. The results indicate the applicability of UGT1A1 and the nine other transporters as potential biological markers for evaluating the ameliorative effects of LGZGD in NAFLD. Additionally, it is suggested that in hepatic pathological states, attention should be paid to the effects of abnormal drug metabolism on hepatic drug enzymes to avoid hepatotoxicity. Overall, the hereby obtained information can provide a meaningful basis for the clinical development of a dosing regimen for the treatment of NAFLD.

Data availability statement

The original contributions presented in the study are included in the article/Supplementary Material. Further inquiries can be directed to the corresponding authors.

Ethics statement

The animal study was reviewed and approved by Animal Committee of Shanghai University of Traditional Chinese Medicine.

Author contributions

TZ and YZ formulated the study concept and design of this paper and guided the critical revision of the manuscript. WN, LL, and YY performed the research, acquired and analyzed the data, and drafted the manuscript. WN, LL, and YY have contributed equally to this work and share first authorship. XC and GJ helped in executing part of research. NH and YD provided important intellectual content and improved the manuscript. All the authors have reviewed the manuscript, agreed to all the contents, and agreed the submission.

Funding

The authors gratefully acknowledge the financial support by programs of the National Natural Science Foundation of China [grant number 81872981, 81973554] and The Key project of Shanghai 3-year plan [grant number ZY (2021-2023)-0215]; Program of Shanghai Academic/Technology Research Leader [grant number 22XD1423000]; Shanghai Science and technology innovation project [grant number 19401901800].

Conflict of interest

The authors declare that the research was conducted in the absence of any commercial or financial relationships that could be construed as a potential conflict of interest.

Publisher's note

All claims expressed in this article are solely those of the authors and do not necessarily represent those of their affiliated organizations, or those of the publisher, the editors, and the reviewers. Any product that may be evaluated in this article, or claim that may be made by its manufacturer, is not guaranteed or endorsed by the publisher.

Supplementary material

The Supplementary Material for this article can be found online at: https://www.frontiersin.org/articles/10.3389/fphar.2023.1174742/full#supplementary-material

References

Akihisa, T., Nakamura, Y., Tokuda, H., Uchiyama, E., Suzuki, T., Kimura, Y., et al. (2007). Triterpene acids fromPoria cocos and their anti-tumor-promoting effects. *J. Nat. Prod.* 70 (6), 948–953. doi:10.1021/np0780001

Anstee, Q. M., and Goldin, R. D. (2006). Mouse models in non-alcoholic fatty liver disease and steatohepatitis research. *Int. J. Exp. Pathol.* 87 (1), 1–16. doi:10.1111/j.0959-9673.2006.00465.x

Chen, D. S., Ke, B., Huang, Y. J., Meng, J., Zhang, J. J., Chen, Z. X., et al. (2011). Effects of the modified linggui zhugan decoction (see text) combined with short-term very low calorie diets on glycemic control in newly diagnosed type 2 diabetics. *J. Tradit. Chin. Med.* 31 (3), 185–188. doi:10.1016/s0254-6272(11)60038-1

Chen, L., Liao, L., Zhai, T., Huang, X., and Chen, Y. (2019). Influence of orally administered borneol on the expression of hepatic transporters in rats. *Eur. J. Drug Metab. Ph.* 44 (1), 103–109. doi:10.1007/s13318-018-0499-1

Chen, M., Zhang, C., Zhang, J., Kai, G., Lu, B., Huang, Z., et al. (2019). The involvement of DAMPs-mediated inflammation in cyclophosphamide-induced liver injury and the protection of liquiritigenin and liquiritin. *Eur. J. Pharmacol.* 856, 172421. doi:10.1016/j.ejphar.2019.172421

Commission, C. P. (2020). *Pharmacopoeia of the people's Republic of China*.

Deng, Y., Liao, Q., Li, S., Bi, K., Pan, B., and Xie, Z. (2008). Simultaneous determination of berberine, palmatine and jatrorrhizine by liquid chromatography–tandem mass spectrometry in rat plasma and its application in a pharmacokinetic study after oral administration of coptis–evodia herb couple. *J. Chromatogr. B* 863 (2), 195–205. doi:10.1016/j.jchromb.2007.12.028

Diehl, A. M., Day, C., and Longo, D. L. (2017). Cause, pathogenesis, and treatment of nonalcoholic steatohepatitis. *N. Engl. J. Med.* 377 (21), 2063–2072. doi:10.1056/NEJMra1503519

Ding, G., Yu, G., Zhang, J., Liang, S., Li, L., Huang, P., et al. (2005). The therapeutic effects of ling gui Zhu Gan tang mixture in 50 psychotic patients with obesity induced by the psychoactive drugs. *J. Tradit. Chin. Med.* 25 (1), 25–28.

Fisher, C. D., Lickteig, A. J., Augustine, L. M., Oude Elferink, R. P. J., Besselsen, D. G., Erickson, R. P., et al. (2009). Experimental non-alcoholic fatty liver disease results in decreased hepatic uptake transporter expression and function in rats. *Eur. J. Pharmacol.* 613 (1-3), 119–127. doi:10.1016/j.ejphar.2009.04.002

Gu, D., Yi, H., Jiang, K., Fakhar, S. H., Shi, J., He, Y., et al. (2021). Transcriptome analysis reveals the efficacy of ginsenoside-Rg1 in the treatment of nonalcoholic fatty liver disease. *Life Sci.* 267, 118986. doi:10.1016/j.lfs.2020.118986

Gu, S. (2020). *History evolution on the classical famous prescription of Linggui Zhugan Decoction*. China: China Medical Herald. doi:10.27320/d.cnki.gszyu.2020.000638

Gu, S., Zhang, W., Wang, B., Ji, G., Wu, W., Li, L., et al. (2020). History evolution on the classical famous prescription of Linggui Zhugan Decoction. *Chin. J. Med.* 17 (21), 145–148.

Guo, Y., Li, J., Wang, Y., Mao, T., Chen, C., Xie, T., et al. (2017). Yinchen linggui zhugan decoction ameliorates nonalcoholic fatty liver disease in rats by regulating the Nrf2/ARE signaling pathway. *Evid.-based Compl. Alt.* 2017, 6178358. doi:10.1155/2017/6178358

Ji, B., Zhao, Y., Yu, P., Yang, B., Zhou, C., and Yu, Z. (2018). LC-ESI-MS/MS method for simultaneous determination of eleven bioactive compounds in rat plasma after oral administration of Ling-Gui-Zhu-Gan Decoction and its application to a pharmacokinetics study. *Talanta* 190, 450–459. doi:10.1016/j.talanta.2018.08.020

Kim, M., Wang, S., Shen, Z., Kochansky, C. J., Strauss, J. R., Franklin, R. B., et al. (2004). Differences in the pharmacokinetics of peroxisome proliferator-activated receptor agonists in genetically obese zucker and sprague-dawley rats: Implications of decreased glucuronidation in obese zucker rats. *Drug metabolism Dispos. Biol. fate Chem.* 32 (9), 909–914.

Kirpich, I. A., Gobejishvili, L. N., Homme, M. B., Waigel, S., Cave, M., Arteel, G., et al. (2011). Integrated hepatic transcriptome and proteome analysis of mice with high-fat diet-induced nonalcoholic fatty liver disease. *J. Nutr. Biochem.* 22 (1), 38–45. doi:10.1016/j.jnutbio.2009.11.009

Koepsell, H. (2013). The SLC22 family with transporters of organic cations, anions and zwitterions. *Mol. Asp. Med.* 34 (2-3), 413–435. doi:10.1016/j.mam.2012.10.010

Kolodziejczyk, A. A., Zheng, D., Shibolet, O., and Elinav, E. (2019). The role of the microbiome in NAFLD and NASH. *EMBO Mol. Med.* 11 (2), e9302. doi:10.15252/emmm.201809302

König, J., Müller, F., and Fromm, M. F. (2013). Transporters and drug-drug interactions: Important determinants of drug disposition and effects. *Pharmacol. Rev.* 65 (3), 944–966. doi:10.1124/pr.113.007518

Kulkarni, N. M., Malampati, S., Mahat, M. Y. A., Chandrasekaran, S., Raghul, J., Khan, A. A., et al. (2016). Altered pharmacokinetics of rosiglitazone in a mouse model of non-alcoholic fatty liver disease. *Drug Metabolism Personalized Ther.* 31 (3), 165–171. doi:10.1515/dmpt-2016-0008

Li, H., and Hu, Y. (2020). Intestinal microecology: An important target for Chinese medicine treatment of non-alcoholic fatty liver disease. *Chin. J. Integr. Med.* 26 (10), 723–728. doi:10.1007/s11655-020-3268-3

Li, L., Gi, G., Zhang, T., Xiao, W., and Yang, Z. (2023). Clinical effect of 'Fast-track Management' guided by ERAS concept under the multi-disciplinary cooperation mode of femoral intertrochanteric fracture in the elderly. *Chin. Tradit. Pat. Med.*, 1–16. doi:10.1080/02648725.2023.2199541

Li, P., Robertson, T. A., Thorling, C. A., Zhang, Q., Fletcher, L. M., Crawford, D. H. G., et al. (2011). Hepatic pharmacokinetics of cationic drugs in a high-fat emulsion-induced rat model of nonalcoholic steatohepatitis. *Drug Metab. Dispos.* 39 (4), 571–579. doi:10.1124/dmd.110.036806

Li, Q., Tan, J. X., He, Y., Bai, F., Li, S. W., Hou, Y. W., et al. (2021). Atractylenolide III ameliorates non-alcoholic fatty liver disease by activating hepatic adiponectin receptor 1-mediated AMPK pathway. *Int. J. Biol. Sci.* 18(4):1594–1611. doi:10.7150/ijbs.68873

Lickteig, A. J., Fisher, C. D., Augustine, L. M., Aleksunes, L. M., Besselsen, D. G., Slitt, A. L., et al. (2007). Efflux transporter expression and acetaminophen metabolite excretion are altered in rodent models of nonalcoholic fatty liver disease. *Drug Metab. Dispos.* 35 (10), 1970–1978. doi:10.1124/dmd.107.015107

Lou, J., Yan, G., Huang, Z., Yuan, H., and Lu, Y. (2020). Progress in the study on innate immunity and non-alcohol fatty liver disease. *Zhong Nan Da Xue Xue Bao Yi Xue Ban.* 45 (12), 1464–1468. doi:10.11817/j.issn.1672-7347.2020.190359

Ma, N., Zhang, Y., Sun, L., Zhao, Y., Ding, Y., and Zhang, T. (2021). Comparative studies on multi-component pharmacokinetics of polygonum multiflorum thunb extract after oral administration in different rat models. *Front. Pharmacol.* 12, 655332. doi:10.3389/fphar.2021.655332

Müller, F., and Fromm, M. F. (2011). Transporter-mediated drug–drug interactions. *Pharmacogenomics* 12 (7), 1017–1037. doi:10.2217/pgs.11.44

Niemela, O., Parkkila, S., Juvonen, R., Viitala, K., Gelboin, H. V., and Pasanen, M. (2000). Cytochromes P450 2A6, 2E1, and 3A and production of protein-aldehyde adducts in the liver of patients with alcoholic and non-alcoholic liver diseases. *J. Hepatol.* 33 (6), 893–901. doi:10.1016/s0168-8278(00)80120-8

Nies, A. T., Koepsell, H., Damme, K., and Schwab, M. (2011). "Organic cation transporters (OCTs, MATEs)," *in Vitroand* in vivo *evidence for the importance in drug therapy*, 105–167. doi:10.1007/978-3-642-14541-4_3

Pan, P., Wang, Y., Lin, S., Liao, S., Chen, Y., Huang, W. C ., et al. (2022). 18β-Glycyrrhetinic acid protects against cholestatic liver injury in bile duct-ligated rats. *Antioxidants (Basel)* 11 (5), 961. doi:10.3390/antiox11050961

Parlati, L., Régnier, M., Guillou, H., and Postic, C. (2021). New targets for NAFLD. *JHEP Rep. innovation hepatology* 3 (6), 100346. doi:10.1016/j.jhepr.2021.100346

Prompila, N., Wittayalertpanya, S., and Komolmit, P. (2008). Hepatic cytochrome P450 2E1 activity in nonalcoholic fatty liver disease. *J. Med. Assoc. Thail.* 91 (5), 733–738.

Shen, Y., Cui, X., Jiang, S., Qian, D. W., and Duan, J. A. (2019). Comparative pharmacokinetics of nine major bioactive components in normal and ulcerative colitis rats after oral administration of Lizhong decoction extracts by UPLC–TQ–MS/MS. *Biomed. Chromatogr.* 33 (7), e4521. doi:10.1002/bmc.4521

Song, Z., Bi, K., and Luo, X. (2002). An HPLC method for the determination and pharmacokinetic study of cinnamic acid in the plasma of rats having taken the traditional Chinese medicinal preparation Ling-Gui-Zhu-Gan decoction. *J. Chromatogr. Sci.* 40 (4), 198–200. doi:10.1093/chromsci/40.4.198

Song, Z., Bi, K., and Luo, X. (2003). High-performance liquid chromatographic method for the determination and pharmacokinetic study of dehydrotumulosic acid in the plasma of rats having taken the traditional Chinese medicinal preparation Ling-Gui-Zhu-Gan decoction. *J. Chromatogr. B* 788 (2), 387–391. doi:10.1016/S1570-0232(02)00411-7

Takahashi, Y., Soejima, Y., and Fukusato, T. (2012). Animal models of nonalcoholic fatty liver disease/nonalcoholic steatohepatitis. *World J. gastroentero.* 18 (19), 2300–2308. doi:10.3748/wjg.v18.i19.2300

Ukiya, M., Akihisa, T., Tokuda, H., Hirano, M., Oshikubo, M., Nobukuni, Y., et al. (2002). Inhibition of tumor-promoting effects by poricoic acids G and H and other lanostane-type triterpenes and cytotoxic activity of poricoic acids A and G fromPoria cocos. *J. Nat. Prod.* 65 (4), 462–465. doi:10.1021/np0103721

Wang, J., and Xiong, X. (2012). Control strategy on hypertension in Chinese medicine. *Evid.-based Compl. Alt.* 2012, 284847. doi:10.1155/2012/284847

Wang, L., Prasad, B., Salphati, L., Chu, X., Gupta, A., Hop, C. E., et al. (2015). Interspecies variability in expression of hepatobiliary transporters across human, dog, monkey, and rat as determined by quantitative proteomics. *Drug Metab. Dispos.* 43, 367–374. doi:10.1124/dmd.114.061580

Wang, S., Li, X., Ji, H., and Shen, L. (2022). Modulation of gut microbiota by glycyrrhizic acid may contribute to its anti-NAFLD effect in rats fed a high-fat diet. *Life Sci.* 310, 121110. doi:10.1016/j.lfs.2022.121110

Wang, X., Gao, Y., Tian, Y., Liu, X., Zhang, G., Wang, Q., et al. (2020a). Integrative serum metabolomics and network analysis on mechanisms exploration of Ling-Gui-Zhu-Gan Decoction on doxorubicin-induced heart failure mice. *J. Ethnopharmacol.* 250, 112397. doi:10.1016/j.jep.2019.112397

Wang, X., Tang, T., Zhai, M., Ge, R., Wang, L., Huang, J., et al. (2020b). Ling-Gui-Zhu-Gan decoction protects H9c2 cells against H2O2-induced oxidative injury via regulation of the nrf2/keap1/HO-1 signaling pathway. *Evid.-based Compl. Alt.* 2020, 8860603–8860611. doi:10.1155/2020/8860603

Wu, Y., Wang, M., Yang, T., Qin, L., Hu, Y., Zhao, D., et al. (2021). Cinnamic acid ameliorates nonalcoholic fatty liver disease by suppressing hepatic lipogenesis and promoting fatty acid oxidation. *Evid. Based Complement. Altern. Med.* 2021, 9561613. doi:10.1155/2021/9561613

Xiao, F., Li, Q., Liang, K., Zhao, L., He, B., Ji, W., et al. (2012). Comparative pharmacokinetics of three triterpene acids in rat plasma after oral administration of Poria extract and its formulated herbal preparation: GuiZhi-FuLing capsule. *Fitoterapia* 83 (1), 117–124. doi:10.1016/j.fitote.2011.10.001

Xu, M., Xu, Z., Xu, Q., Zhang, H., Liu, M., Geng, F., et al. (2018). UPLC-MS/MS method for the determination of 14 compounds in rat plasma and its application in a pharmacokinetic study of orally administered xiaoyao powder. *Molecules* 23 (10), 2514. doi:10.3390/molecules23102514

Yang, J., Lv, F., Chen, X., Cui, W., Chen, L., Wen, X., et al. (2013). Pharmacokinetic study of major bioactive components in rats after oral administration of extract of Ilex hainanensis by high-performance liquid chromatography/electrospray ionization mass spectrometry. *J. Pharm. Biomed.* 77, 21–28. doi:10.1016/j.jpba.2013.01.011

Yang, L., Zhang, L., Song, H., Li, D., and Ji, G. (2012). Comparative study on the effects of different therapeutic methods in preventing and treating nonalcoholic fatty liver in rats. *J. Chin. Integr. Med.* 10 (10), 1120–1126. doi:10.3736/jcim20121008

Yi, Y., Ding, Y., Zhang, Y., Ma, N., Shi, F., Kang, P., et al. (2018). Yinchenhao decoction ameliorates alpha-naphthylisothiocyanate induced intrahepatic cholestasis in rats by regulating phase II metabolic enzymes and transporters. *Front. Pharmacol.* 9, 510. doi:10.3389/fphar.2018.00510

Yimam, M., Jiao, P., Hong, M., and Jia, Q. (2016). A standardized composition from extracts of myristica fragrans, Astragalus membranaceus, and Poria cocos protects liver from acute ethanol insult. *J. Med. Food* 19 (8), 780–788. doi:10.1089/jmf.2016.0023

Younossi, Z. M., Koenig, A. B., Abdelatif, D., Fazel, Y., Henry, L., and Wymer, M. (2016). Global epidemiology of nonalcoholic fatty liver disease-Meta-analytic assessment of prevalence, incidence, and outcomes. *Hepatology* 64 (1), 73–84. doi:10.1002/hep.28431

Zhou, F., Zhou, J., Wang, W., Zhang, X., Ji, Y., Zhang, P., et al. (2019). Unexpected rapid increase in the burden of NAFLD in China from 2008 to 2018: A systematic review and meta-analysis. *Hepatology* 70 (4), 1119–1133. doi:10.1002/hep.30702

Zhu, Z., Zhao, L., Liu, X., Chen, J., Zhang, H., Zhang, G., et al. (2010). Comparative pharmacokinetics of baicalin and wogonoside by liquid chromatography–mass spectrometry after oral administration of Xiaochaihu Tang and Radix scutellariae extract to rats. *J. Chromatogr. B* 878 (24), 2184–2190. doi:10.1016/j.jchromb.2010.06.021

frontiers | Frontiers in Pharmacology

TYPE Original Research
PUBLISHED 22 May 2023
DOI 10.3389/fphar.2023.1196137

OPEN ACCESS

EDITED BY
Zipeng Gong,
Guizhou Medical University, China

REVIEWED BY
Mahdi Moridi Farimani,
Shahid Beheshti University, Iran
Xi-Tao Yan,
Northwest A&F University, China
Jinming Zhang,
Chengdu University of Traditional Chinese Medicine, China
Jiabo Wang,
Capital Medical University, China

*CORRESPONDENCE
Pengfei Yue,
1053438076@qq.com
Ming Yang,
ypfpharm@126.com

RECEIVED 29 March 2023
ACCEPTED 12 May 2023
PUBLISHED 22 May 2023

CITATION
Liu Y, Wang F, Guo H, Zhang D, Zhang X, Wu Z, Li H, Xian Y, Yue P and Yang M (2023), Effect of molecular distillation on the anti-inflammatory activity and neurotoxicity of *Asarum* essential oil. *Front. Pharmacol.* 14:1196137. doi: 10.3389/fphar.2023.1196137

Effect of molecular distillation on the anti-inflammatory activity and neurotoxicity of *Asarum* essential oil

Yang Liu[1], Fang Wang[1], HuiWen Guo[2], Dingkun Zhang[3], Xiaofei Zhang[4], Zhenfeng Wu[1], Huiting Li[1], Yang Xian[5], Pengfei Yue[1]* and Ming Yang[1]*

[1]Key Laboratory of Modern Preparation of TCM, Ministry of Education, Jiangxi University of Chinese Medicine, Nanchang, China, [2]College of Chinese Medicine, Jiangxi University of Chinese Medicine, Nanchang, China, [3]Chengdu University of Traditional Chinese Medicine, Chengdu, China, [4]Shanxi University of Chinese Medicine, Xian, China, [5]College of Continuing Education, Jiangxi University of Chinese Medicine, Nanchang, China

Asarum essential oil (AEO) has been shown to have good pharmacological activities for the anti-inflammatory and analgesic effects, but increasing the dose may cause toxicity. Therefore, we studied the toxic and pharmacodynamic components of AEO by molecular distillation (MD). Anti-inflammatory activity was assessed using RAW264.7 cells. Neurotoxicity was assessed in PC12 cells and the overall toxicity of AEO was evaluated in the mouse acute toxicity assay. The results showed that AEO is primarily composed of safrole, methyl eugenol, and 3,5-dimethoxytoluene. After MD, three fractions were obtained and contained different proportions of volatile compounds relative to the original oil. The heavy fraction had high concentrations of safrole and methyl eugenol, while the light fraction contained high concentrations of α-pinene and β- pinene. The original oil and all three fractions exhibited anti-inflammatory effects, but the light fraction demonstrated more excellent anti-inflammatory activity than the other fractions. *Asarum* virgin oil and MD products are all neurotoxic. The exposure of PC12 cells to high concentrations of AEO resulted in abnormal nuclei, an increased number of apoptotic cells, increased ROS formation, and decreased SOD levels. Moreover, the results of acute toxicity tests in mice revealed that the light fractions were less toxic than virgin oils and other fractions. In summary, the data suggest that the MD technology enables the enrichment and separation of essential oil components and contributes to the selection of safe concentrations of AEO.

KEYWORDS

***Asarum* essential oil, molecular distillation, anti-inflammatory activity, neurotoxicity, reducing toxicity and increasing efficacy**

1 Introduction

The "Chinese Pharmacopoeia" records that *Asarum* can dispel wind and cold, relieve pain through the orifice, and warm the lungs (National Pharmacopoeia Commission, 2020). It is used for wind chills and colds, headaches, toothache, nasal congestion, rheumatism and pain, phlegm, asthma, and cough. *Asarum* essential oil (AEO) is isolated from the dry rhizome of the Chinese

herb *Asarum* [*Asarum heterotropoides Fr. Schmidt var. mandshuricum* (*Maxim.*)*Kitag.*] (Yang et al., 2021), the main components of which are methyl eugenol, safrole, and 3,5-Dimethoxytoluene (Liu et al., 2020). AEO is known for its antipyretic, analgesic, anti-inflammatory, and bacteriostatic properties (Liu et al., 2023). It has been developed into various products which are widely used in clinical medical supplies, pesticides of plant origin, construction materials, and other fields (Maseehullah et al., 2022) (Wu et al., 2020) (Akhlaq et al., 2022).

Multiple studies have documented that AEO exhibits a significant anti-inflammatory effect both *in vivo* and *in vitro* (Choi et al., 2021) (Zhang et al., 2021) (Liu et al., 2022; Liu et al., 2022), which indicates that it is helpful for relieving cough and asthma, relieving bronchospasm, and reducing inflammation in the lungs (Han et al., 2022). Network pharmacological analysis of AEO components showed that methyl eugenol and safrole could act on the inflammatory genes COX-1 and LAT4H (Liu and Wang, 2022). The aforementioned data suggested that methyl eugenol and safrole are the active components of AEO and are may responsible for their anti-inflammatory effects (Fan et al., 2021).

The use of *Asarum* has been documented in "Ben Cao Bie Shuo", an ancient Chinese pharmacology book written in the Song Dynasty. According to this book, the use of *Asarum* alone should not exceed a dosageof one qian (which is equivalent to 3.72 g). Overdosaging may lead to Qi stuffiness and congestion, ultimately causing death (Hu et al., 2019). Pharmacological studies have confirmed that *Asarum* exhibits a certain degree of toxicity, primarily in the respiratory and nervous systems (Hou et al., 2023). It should be noted that the toxicity of AEO is closely related to the content of volatile oil. The safety of *Asarum* was often ensured through dosage, preparation form, the processing of medicinals, and combination in Chinese medicine. Therefore, a widely used method is to prepare *Asarum* as a decoction, which can reduce its toxicity by prolonging cooking time and decreasing the amount of the volatile oil. However, this limits the medicinal effects of AEO. Furthermore, according to modern drug toxicology studies, the toxicity of *Asarum* mainly originates from aristolochic acid and volatile oil (Antsyshkina et al., 2020). Safrole in volatile oil is the primary toxic component, which can paralyze animal respiratory centers, damage the human nervous system, circulatory system, and respiratory system, and exhibit a carcinogenic effect (Cao et al., 2020) (Kemprai et al., 2020) (Yao et al., 2020). To retain the pharmacological activity of AEO, some researchers separated and removed safrole from the volatile oil by liquid phase preparation, silica gel column chromatography, and adsorption using high-efficiency adsorbent (Nie et al., 2022). However, these methods are costly and, therefore, economically unfeasible for large-scale development and application. Moreover, prior evidence has demonstrated that the toxicity of the whole AEO is higher than that of the enriched safrole oil and methyl eugenol (Liu et al., 2021). The aforementioned results suggest that the combined toxicity of the individual components is less than that of the whole volatile oil, but the underlying reasons for the reduction in toxicity after enrichment remain poorly understood. Hence, further investigation into the components causing toxicity of AEO and the associated mechanisms is necessary to promote safer and more effective market application.

Molecular distillation (MD) is a unique liquid-liquid separation technology that can separate different substances based on their molecular characteristics, such as the mean free path of different molecules under high vacuum conditions (Mahrous and Farag, 2022) (Reza Shirzad Kebria and Rahimpour, 2020). MD can achieve the "refinement" of the main components of volatile oils, "enrichment and enhancement" of the active ingredients, "toxicity reduction" of the toxic components, and "aroma intensification " (Dantas et al., 2020). In this study, AEO was enriched by MD. The primary components of AEO causing its anti-inflammatory activity, and toxicity were identified and further research was conducted on its toxic/effective components.

2 Materials and methods

2.1 Reagents and chemicals

n-Hexane (F2124114GC > 99%) was obtained from Aladdin Biotechnology (Shanghai, China). Butyl acetate (RH269812GC ≥ 97.7%) was obtained from Shanghai Yien Chemical Technology Co., Ltd. (Shanghai, China). Anhydrous sodium sulfate (1804081) was procured from Xilong Scientific (Guangdong, China).

Lipopolysaccharide (LPS), dimethyl sulfoxide (DMSO), and dexamethasone (Dex) were purchased from Sigma-Aldrich (St. Louis, MO, United States). Cell culture medium RPMI 1640, DMEM, phosphate buffer saline solution (PBS), and trypsin were obtained from Solarbio Life Sciences (Beijing, China). Fetal bovine serum (FBS) was obtained from Gibco BRL Life Technology (Gibco BRL, Gaithersburg, MD). A cell counting kit 8 (CCK-8) was obtained from Meilunbio (Dalian, China). Interleukin-6 (IL-6) and tumor necrosis factor-α (TNF-α) kits were purchased from Meimian Biotechnology (Jiangsu, China). Superoxide dismutase (SOD) assay kits were procured from Nanjing Jiancheng Bioengineering Institute (Nanjing, China). 4′,6-Diamidino-2-phenylindole dihydrochloride (DAPI) was purchased from Solarbio Life Sciences (Beijing, China). Annexin V-FITC apoptosis detection kit, mitochondrial membrane potential assay kit, and reactive oxygen species (ROS) assay kit were obtained from Beyotime Biotechnology (Shanghai, China).

2.2 Plant materials and extraction of AEO

Asarum (jk20220118008) was purchased from Chengdu and authenticated as genuine Chinese herbal medicine by Professor Zhang Puzhao of the School of Pharmacy, Jiangxi University of Chinese Medicine. AEO was obtained by steam distillation (*Asarum* was cut into 1 cm, 12 times the amount of water was added, and extracted for 5 h), with an oil yield of approximately 1%. The volatile oil was stored in a refrigerated cabinet at 4°C.

2.3 Three-stage molecular distillation of volatile oil

AEO was spread on a thin film on a heated surface to ensure even heating and improve evaporation efficiency and shorten the distillation time. The feed flow rate and scraping speed had a relatively minor impact on the separation results, unlike the evaporation temperature and vacuum degree, which significantly affected the degree of evaporation (Wang et al., 2023). The optimum experimental conditions were determined by pre-experimentation using a short-path MD (F417-9078, UIC GmbH Company, Germany). The

optimized conditions were as follows: evaporation temperature of 50°C, vacuum of 8 mbar, primary condensation temperature of 15°C, and secondary condensation temperature of −15°C. Finally, the crude oil (C) was separated, and the fractions were obtained as a heavy fraction (H), a middle fraction (M), and a light fraction (L).

2.4 Gas chromatograph-mass spectrometry (GC-MS) analysis of the volatile oil

2.4.1 Preparation of internal standard solution

To a 10-mL volumetric flask, 1,000 μL of butyl acetate was added and the flask was accurately weighed on an analytical balance. The solution was then diluted to 10 mL with n-Hexane and allowed to mix well.

2.4.2 Preparation of sample solution

Asarum crude oil was dried with anhydrous Na_2SO_4. Next, 50 μL of crude oil and 50 μL of each distillate were pipetted into four 10-mL volumetric flasks. Then, 50 μL of the internal standard solution was added to each flask and diluted to 10 mL with n-hexane. The mixture was evenly mixed and thereafter filtered with a 0.22-μm microporous membrane to obtain the GC sample.

2.4.3 GC conditions

Gas phase conditions: A gas chromatograph-mass spectrometer (7890B-5977A, Agilent Technologies, Inc., United States) and HP-5MS columns were used. The carrier gas was He, the flow rate was 1.0 mL/min, and the split ratio was 10:1. The inlet temperature was 250°C. The heating conditions are shown in Supplementary Table S1.

MS conditions: Electrospray ionization (ESI) was performed. The electron energy was 70 eV, the ion source temperature was 230°C, and the quadrupole temperature was 150°C. Then, the scan range was defined as m/z 30–650 amu, and the injection volume was 0.3 μL. The results were searched with the NIST14. L database in combination with related literature.

2.5 Cell lines and treatment

PC12 (Rat adrenal pheochromocytoma) cells were purchased from Shanghai Zhong Qiao Xin Zhou Biotechnology Co., Ltd. (ZQ 0150, Shanghai, China). The cells were cultured in RPMI 1,640 medium containing 1% penicillin/streptomycin and 10% FBS in a 5% CO_2 incubator at 37°C. The cells were harvested using 0.25% trypsin/EDTA when they reached 80%–90% confluency. The cells were treated with different concentrations of the previously obtained four distillates for the following experiments.

RAW264.7 murine macrophage cells were kindly given by the Research and Experiment Center, College of Traditional Chinese Medicine, Jiangxi University of Chinese Medicine. The cell medium was prepared with DMEM (containing 1% penicillin/streptomycin) and 10% FBS and was cultured in a humidified 5% CO_2 incubator at 37°C. After the cells reached 80%–90% confluency, they were collected using 0.25% trypsin/EDTA for the subsequent experiments. Then, the cells were treated with 0.5, 0.25, 0.125, and 0.0625 μL/mL concentrations of each of the four distillates.

LPS was diluted to 1 mg/mL in sterile PBS stored at −20°C and then diluted to 100 μg/mL in DMEM medium. Dex was diluted to 4 μg/mL in PBS. LPS and Dex were used in the anti-inflammatory experiment with RAW264.7 cells.

2.6 Cell viability assay

PC12 and RAW264.7 cells were harvested by centrifugation and seeded in 96-well plates at 1×10^4 per well. Then, the cells were treated with eight different concentrations (2, 1, 0.5, 0.25, 0.125, 0.0625, 0.03125, and 0.015625 μL/mL) of four distillates (C, H, M, and L) in an incubator for 24 h. According to the kit instructions, RPMI 1,640 containing 10% CCK-8 reagent was added to each well. After incubation at 37°C for 2 h, the optical density (OD) value of each well was measured at 450 nm using a microplate reader (Multiskan GO, Thermo Fisher Scientific, United States).

2.7 Measurement of anti-inflammatory activity

A total of 4×10^4 RAW264.7 cells per well were cultured in 24-well plates. Four concentrations (0.5, 0.25, 0.125, and 0.0625 μL/mL) of distillates C, H, M, and L were added for intervention on the second day. After 2 h of incubation, the cells were induced by LPS (100 μg/mL). The untreated RAW264.7 cells served as the control group, the cells induced by LPS without dosing were used as the model group, and dexamethasone was added for the Dex group. After 24 h of incubation, cell supernatants were collected for further experiments with commercial IL-6 and TNF-α kits. Then, after rinsing the plate five times, the kit reagents were added to the reaction plate and incubated at 37°C for 30 min. After washing the samples five times, reagents were added following the manufacturer's instructions and reacted for 10 min. The OD values of the wells were detected at 450 nm via a microplate reader, and the anti-inflammatory activity of the cells was calculated.

2.8 Measurement of the oxidative enzyme system

PC12 cells were collected by trypsin and seeded in 6-well plates with 4×10^5 cells per well. The cells were cultured overnight and exposed to 1, 0.5, 0.25, and 0.125 μL/mL of the four distillates (C, H, M, and L). Then, the cells were incubated in an incubator for 24 h. The cells and cell supernatants were centrifuged and collected in 2 mL EP tubes. Thereafter, the cells were broken using a cell disruptor and stored at −80°C for subsequent assays for the determination of oxidative enzymes. The SOD levels in PC12 cells were measured using the 96-well plates in the commercial assay kits with five replicate wells per sample. The OD values were measured via a microplate reader.

2.9 DAPI and annexin V-fluorescein isothiocyanate (FITC)/propidium iodide (PI) staining

DAPI and Annexin V-FITC were used to detect the apoptosis of PC12 cells. For DAPI staining, 4×10^5 PC12 cells were cultured in

each well of the 6-well plates. Four different concentrations (1, 0.5, 0.25, and 0.125 μL/mL) of distillates C, H, M, and L were separately added to the cells and incubated for 24 h. After incubation, the cell supernatants were discarded. The cells were washed twice in PBS, and fixed with 4% paraformaldehyde (PFA) (DF0135, Leagene Biotechnology, China) for 15 min. Thereafter, the DAPI reagent was added for 5–10 min at room temperature (RT), followed by washing with PBS twice. The stained cells were observed under a fluorescence microscope (Nikon, Japan).

Annexin V-FITC assay was performed according to the manufacturer's instructions. PC12 cells were collected after trypsin digestion and centrifuged (1,000 rpm, 5 min). After resuspending with PBS, the cells were centrifuged again, and the supernatants were discarded. Next, 195 μL Annexin V-FITC binding reagent was added. The cells were resuspended and 5 μL of Annexin V-FITC and 10 μL of PI staining solution were added. The samples were incubated for 10–20 min at RT under a dark condition. A flow cytometer (Becton, Dickinson, and Company, United States) was used to analyze the stained cells.

2.10 Measurement of ROS levels

The ROS levels in PC12 cells were determined using the fluorescent probe DCFH-DA. Approximately 4×10^5 cells were seeded in each well of a 6-well plate, and the ROS level was measured after treatment with the distillates (C, H, M, and L) for 24 h. To each well, 2 mL of DCFH-DA was added, followed by incubation at 37°C for 20 min. Thereafter, the cells were rinsed thrice with serum-free RPMI 1,640 medium. The cells were then studied using a flow cytometer with an excitation wavelength of 488 nm and an emission wavelength of 525 nm.

2.11 Measurement of mitochondrial membrane potential

JC-1 was used as a fluorescent probe in the Mitochondrial Membrane Potential Assay Kit (JC-1) for early apoptosis detection. PC12 cells (4×10^5 per well) were seeded in 6-well plates and incubated with four concentrations (1, 0.5, 0.25, and 0.125 μL/mL) of the four distillates (C, H, M, and L) for dosing intervention. After 24 h of intervention, the experiment was performed according to the manufacturer's instructions. JC-1 staining solution was added to the cells and cultured at 37°C for 20 min. A fluorescence microscope was used to observe the fluorescence of the cells.

2.12 Effect of AEO on acute toxicity in mice

A total of 90 SPF KM mice (6–8 weeks old; 18–22 g each), half male and half female, were obtained from the Experimental Animal Center of the Jiangxi University of Chinese Medicine. This experiment was approved by the Animal Ethics Committee of the university (Animal Ethics Number: 20220306029) and strictly followed the Guidelines for the Management and Use of Laboratory Animals. The acute toxicity test was performed to assess the toxicity of AEO, and the LD_{50} value was used as the assessment index. The mice were divided into 22 groups: blank (saline), control (20% Tween-80), and 20 experimental groups (four distillates, five dose groups for each distillate, six mice in each group, half male and half female). According to the pre-experimental results, the doses of both crude oil and H distillate were 1.0792, 1.3489, 1.6862, 2.1077, and 2.6347 g/Kg; the concentrations of M were 2.1077, 2.6347, 3.2865, 4.1080, 5.1349 g/Kg, and the administration concentrations of L distillate were 2.6347, 3.2865, 4.1080, 5.1349, 6.4185 g/Kg. The mice fasted without water for 12 h before the experiment. After 12 h, the four distillates were administered by gavage at 0.2 mL/10 g per mouse.

2.13 Statistics and analysis

Data were processed using SPSS 21.0 (IBM, New York, NY, United States) for plotting and statistical analysis. Graphs were constructed using GraphPad Prism 9.0 (GraphPad Software, CA, United States) and SIMCA 14.1 (Umetrics, Sweden). Data were expressed as mean ± standard deviation ($\bar{X} \pm SD$) and compared using one-way analysis of variance (ANOVA). $p < 0.05$ was considered statistically significant.

3 Results

3.1 GC-MS analysis of different distillates

Asarum volatile crude oil (C) was divided into three distillates, heavy oil (H), medium oil (M), and light oil (L) via MD. A total of 34 components were identified and isolated from the *Asarum* crude oil, among which methyl eugenol had the highest content (24.02%), and the others were mainly safrole (17.08%), 3,5-dimethoxytoluene (10.62%), myristyl ether (8.20%), 3,4,5-trimethoxytoluene (7.04%), 3-carene (4.77%), β-pinene (4.51%), eugenolone (3.00%), lobenol (1.21%), and levulinic-limonene (1.05%) (Figure 1, S4). The primary components of medium oil and light oil were also analyzed through distillation. The results showed that the main components of distillates M and L were (1S) -(−)-alpha-Pinene (10.64%, 19.84%), β-pinenelaevo (12.51%, 19.69%), and (1S) -(+)-3-Carene (13.96%, 19.63%). Unlike the light fraction, the M fraction contained safrole (12.55%) and 3,5-dimethoxytoluene (7.93%). The main components of the heavy fraction were methyleugenol (31.36%), safrole (19.42%), and 3,5-dimethoxytoluene (12.01%). From the aforementioned results, it is evident that the components in different distillates have significant differences in mass fraction. Therefore, by using MD, the separation and enrichment of AEO was achieved (Table 1).

From these results, the contents of monoterpenes in crude oil, H, M, and L were 13.58, 1.31, 53.72, and 77.25%, respectively, whereas the contents of ethers in C, H, M, and L were 69.44, 86.21, 27.86, and 5.83%, respectively. The monoterpenes, with boiling points generally in the range of 140°C–180°C, exhibit analgesic, antibacterial, detoxification, and diuretic effects. For example, the boiling point of β-pinenelaevo is 155°C–156°C, and (+) -3-caren has a boiling point of 168°C–169°C. However, the ethers in AEO had higher boiling points, such as safrole 232°C–234°C and methyl eugenol 254°C–255°C. These ether components exhibited neuroleptic effects

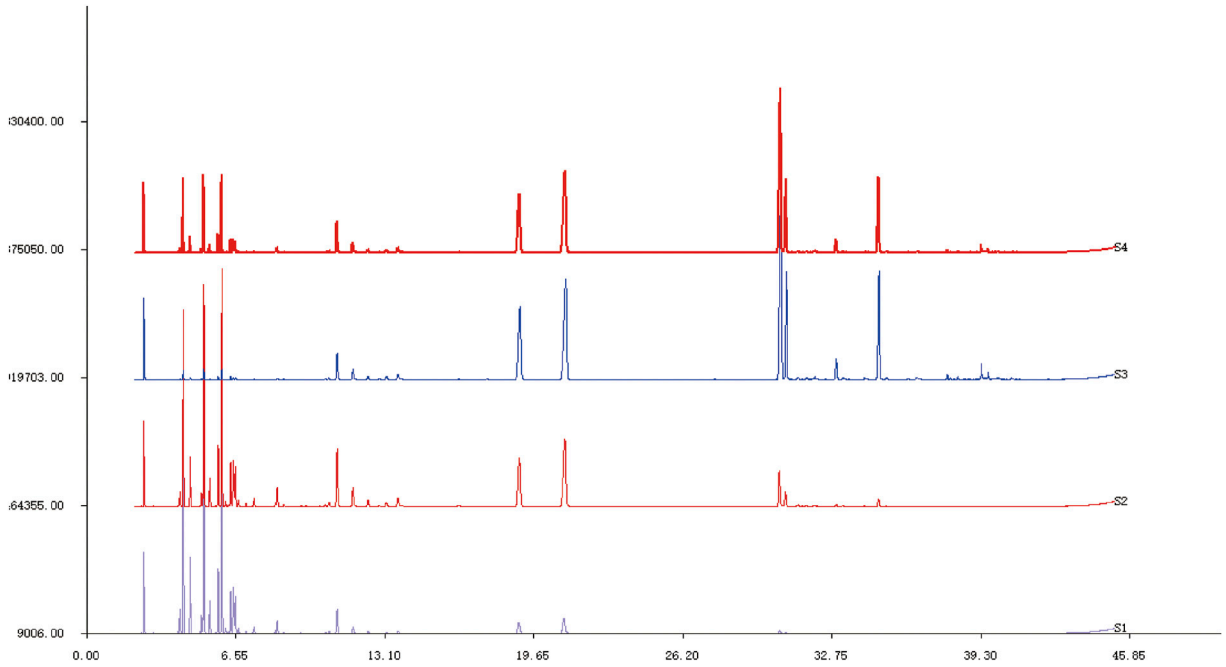

FIGURE 1
GC-MS spectra of *Asarum* volatile crude oil and each distillate after molecular distillation S1: Light distillate (L). S2: Medium distillate (M). S3: Heavy distillate (H). S4: *Asarum* volatile crude oil (C).

and were also the primary toxic components of AEO. From these results, it can be concluded that the light distillate is enriched in low-boiling-point components, while the heavy distillate is enriched in high-boiling-point components.

3.2 Cell viability of RAW264.7 cells and PC12 cells

To investigate the safety concentrations of the four distillates C, H, M, and L on RAW264.7 cells and PC12 cells, eight different concentrations (2, 1, 0.5, 0.25, 0.125, 0.0625, 0.03125, and 0.015625 μL/mL) of these distillates were added to the RAW264.7 cells and PC12 cells to detect cell viability for 24 h.

The cell viability results of RAW264.7 cells showed that the survival rate was close to 0 at a concentration of 2 μL/mL. However, the survival rates increased with the decrease in the distillate concentration for all the distillates. Especially at 1 μL/mL concentrations, the cell viability with heavy, medium, and light distillates was significantly higher than that with crude oil. Meanwhile, when the concentrations of crude oil, heavy distillate, medium distillate, and light distillate were all less than or equal to 0.5 μL/mL, the cell viability of RAW264.7 cells was greater than 85%. Therefore, four concentrations (0.5, 0.25, 0.125, and 0.0625 μL/mL) of C, H, M, and L were selected for the following experiments on RAW264.7 cells (Figure 2A).

Furthermore, the cell viability results from PC12 cells showed an increase in survival rate with the decrease of concentrations of C, H, M, and L. At 2 μL/mL concentration of the four distillates, the survival rates of PC12 cells were almost 0, while at a concentration of 1 μL/mL of C, H, M, and L, the cell viability of the C group was lower than that of the H, M, and L groups. Notably, the survival rates of PC12 cells were greater than 85% at a concentration of 0.5 μL/mL for all four distillates. This indicates that 0.5 μL/mL was a safe distillate concentration for PC12 cells (Figure 2B).

3.3 IL-6 levels in RAW264.7 cells after treatment with AEO and its different distillates

The IL-6 level in RAW264.7 cells was determined via the commercial ELISA kit after treatment with AEO and its different distillates. First, the IL-6 levels at different concentrations (0.5, 0.25, 0.125, and 0.0625 μL/mL) of crude oil, heavy distillate, medium distillate, and light distillate were compared. The results showed that compared with the LPS-induced model group, there were decreasing trends in IL-6 levels in the Dex groups and four concentration groups of H, M, and L. Furthermore, the IL-6 levels in 0.5 and 0.25 μL/mL groups of C were decreased ($p < 0.05$, vs. model group). These results indicated that distillates H, M, and L, obtained from AEP by MD, could reduce the contents of pro-inflammatory cytokine IL-6 compared with that of the model group (Figures 3A–D).

Then, the levels of IL-6 in C, H, M, and L were analyzed at the concentration (0.5, 0.25, 0.125, and 0.0625 μL/mL)of distillates. Compared with the C group, the IL-6 levels were significantly lower in M and L groups for 0.5 L/mL distillate concentration ($p < 0.05$). When the concentrations were 0.25, 0.12,5, and 0.0625 μL/mL, the IL-6 levels IL-6 in H, M, and L groups were

TABLE 1 Chemical composition and content of each distillate after molecular distillation.

No.	RT	CAS	Common name	Quality fraction (%)			
				C	H	M	L
1	2.4974	000123-86-4	Butyl acetate	3.8947	4.0919	4.5102	4.9352
2	4.0801	002867-05-2	alpha-Thujene	0.2791	—	—	1.4746
3	4.2314	007785-26-4	(1S)-(−)-alpha-Pinene	4.183	0.465	10.6367	19.8361
4	4.5339	000079-92-5	Camphene	0.9851	—	2.6924	4.7972
5	5.0363	028634-89-1	Bicyclo [3.1.0]hex-2-ene,4-	0.2417	—	0.7651	—
6	5.1281	000127-91-3	beta-Pinene	4.5104	0.5572	12.505	19.6851
7	5.3982	000123-35-3	Myrcene	0.5025	—	1.6231	2.1255
8	5.771	000099-83-2	α-Phellandrene	1.1322	0.1483	3.522	4.3413
9	5.9276	000498-15-7	(1S)-(+)-3-Carene	4.7743	0.6086	13.9615	19.6277
10	6.3111	000527-84-4	o-Cymene	0.8599	0.1629	0.1143	2.9636
11	6.4354	000138-86-3	(1S)-Limonene	1.0493	—	3.3502	3.9054
12	6.5164	000470-82-6	1,8-Cineole	0.791	0.1553	2.4182	2.6329
13	6.6677	003779-61-1	trans-β-Ocimene	0.1107	—	0.3678	0.3693
14	7.3483	000099-85-4	gamma-Terpinene	0.17	—	0.5435	0.3142
15	8.3585	000586-62-9	Terpinolene	0.4575	—	1.4383	0.2107
16	10.6327	000076-22-2	(+/−)-Camphor	0.2077	—	—	—
17	10.9893	000503-93-5	Eucarvone	3.001	2.3242	5.3055	2.4981
18	11.6807	000507-70-0	Borneol	1.2083	1.0079	—	0.7308
19	12.3506	000562-74-3	4-Carvomenthenol	0.3645	—	0.6204	0.3645
20	13.1609	000098-55-5	α-Terpineol	0.407	—	—	—
21	13.6632	000140-67-0	Estragole	0.6339	0.5721	0.9396	0.3029
22	19.0166	004179-19-5	3,5-Dimethoxytoluene	10.6157	12.0113	7.9303	1.9804
23	21.0207	000094-59-7	Safrole	17.0851	19.4187	12.5543	3.15
24	30.4796	000093-15-2	Methyleugenol	24.0203	31.3644	4.0635	0.3947
25	30.7227	006443-69-2	3,4,5-Trimethoxytoluene	7.0425	9.1769	1.3602	—
26	31.2629	017334-55-3	Calarene	0.2472	0.2764	0.2097	—
27	31.9867	036577-33-0	(−)-Guaia-6,9-Diene	0.1855	0.4505	—	—
28	32.9321	000607-91-0	Myristicin	1.5114	2.0284	0.2217	—
29	33.2292	054274-73-6	1-Epibicyclosequiphellandren	0.1409	—	—	—
30	34.7957	000607-91-0	Myristicin	8.1986	11.1031	0.7939	—
31	37.81	000487-11-6	Elemicin	0.2202	0.3604	—	—
32	38.2746	005353-15-1	γ-Asarone	0.1092	0.1725	—	—
33	39.3064	018607-90-4	Kakuol	0.5873	0.792	—	—
34	39.6035	005986-55-0	patchouli alcohol	0.2721	0.3147	—	—
Monoterpene hydrocarbons				13.5813	1.3141	53.7151	77.2481
Sesquiterpene hydrocarbons				0.4327	1.2153	0.2097	—
Monoterpenoids				1.9798	1.0079	0.6204	1.0953

(Continued on following page)

TABLE 1 (*Continued*) **Chemical composition and content of each distillate after molecular distillation.**

No.	RT	CAS	Common name	Quality fraction (%)			
				C	H	M	L
Monoterpene ketone				3.5883	3.5136	5.7304	2.7235
Ether				69.4369	86.2078	27.8635	5.828
% Identified of total peaks area				89.019	93.2587	88.1391	86.8949

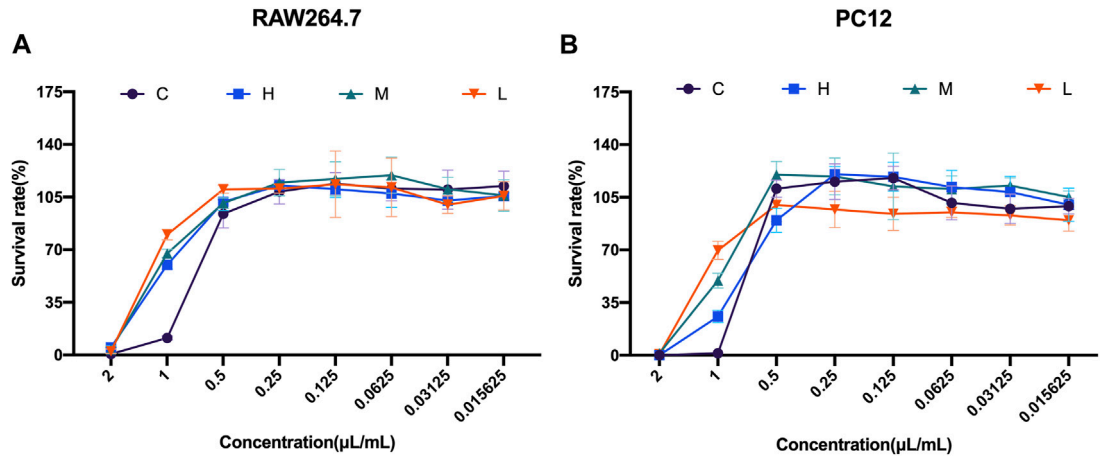

FIGURE 2
Cell viability studies of *Asarum* volatile oil and its distillates with RAW264.7 cells and PC12 cells **(A)** Cell viability on RAW264.7 cells, with eight concentrations (2, 1, 0.5, 0.25, 0.125, 0.0625, 0.03125, and 0.015625 μL/mL) of C (*Asarum* volatile crude oil), H (heavy distillate), M (medium distillate), and L (light distillate). **(B)** PC12 cells were treated with eight concentrations (2, 1, 0.5, 0.25, 0.125, 0.0625, 0.03125, and 0.015625 μL/mL) of C (*Asarum* volatile crude oil), H (heavy distillate), M (medium distillate), and L (light distillate) to measure cell viability.

clearly decreased ($p < 0.05$, vs. C group). This indicated that distillates H, M, and L showed a relative decrease in the content of pro-inflammatory cytokine IL-6 at the same concentrations compared to crude oil in a dose-dependent manner (Figures 3E–H).

3.4 TNF-α levels in RAW264.7 cells after treatment with AEO and its different distillates

AEO also exhibits pro-inflammatory effects. Therefore, we investigated the TNF-α levels in RAW264.7 cells after AEO, and H, M, and L intervention. Similarly, the TNF-α levels in the four concentrations of C, H, M, and L were measured first. Compared with the LPS-induced model group, the TNF-α levels in the Dex groups and four concentrations (0.5, 0.25, 0.125, and 0.0625 μL/mL) of the H, M, and L groups showed a decreasing trend ($p < 0.05$) (Figures 4A–D). Further, the TNF-α levels in C, H, M, and L at the same concentration were compared. The results showed that at 0.5, 0.125, and 0.0625 μL/mL, the TNF-α levels in H, M, and L were notably lower than that of C group. Only the TNF-α level in the L group was decreased ($p < 0.05$, vs. C group) when the concentration was 0.25 μL/mL (Figures 4E–H). These results illustrated that the three distillates (H, M, and L) could reduce the release of TNF-α in RAW264.7 cells and exert anti-inflammatory effects compared with crude oil.

3.5 Orthogonal partial least squares-discriminant analysis (OPLS-DA) of the anti-inflammatory activity of AEO

Principal component analysis was used to analyze the relationship between AEO and the IL-6 and TNF-α levels via SIMCA14.1software. The results are shown in Figure 5. The data were downscaled and simplified by OPLS analysis, with Q2 (cum) of the TNF-α model being 0.832 and that of (cum) Q2 (cum) of the IL-6 model being 0.586, which showed good overall predictive ability. Further correlation analysis was performed on the two data sets to screen for compounds (Figure 6).

The correlation analysis between anti-inflammatory activity and components of AEO revealed that the anti-inflammatory activity was primarily associated with methyl eugenol, α-pinene, β-pinene, α-phellandrene, 1,8 eucalyptol, camphorene, and β-laurelene. Therefore, the strong anti-inflammatory activity of L may be related to the high relative percentage content of α-pinene and β-pinene.

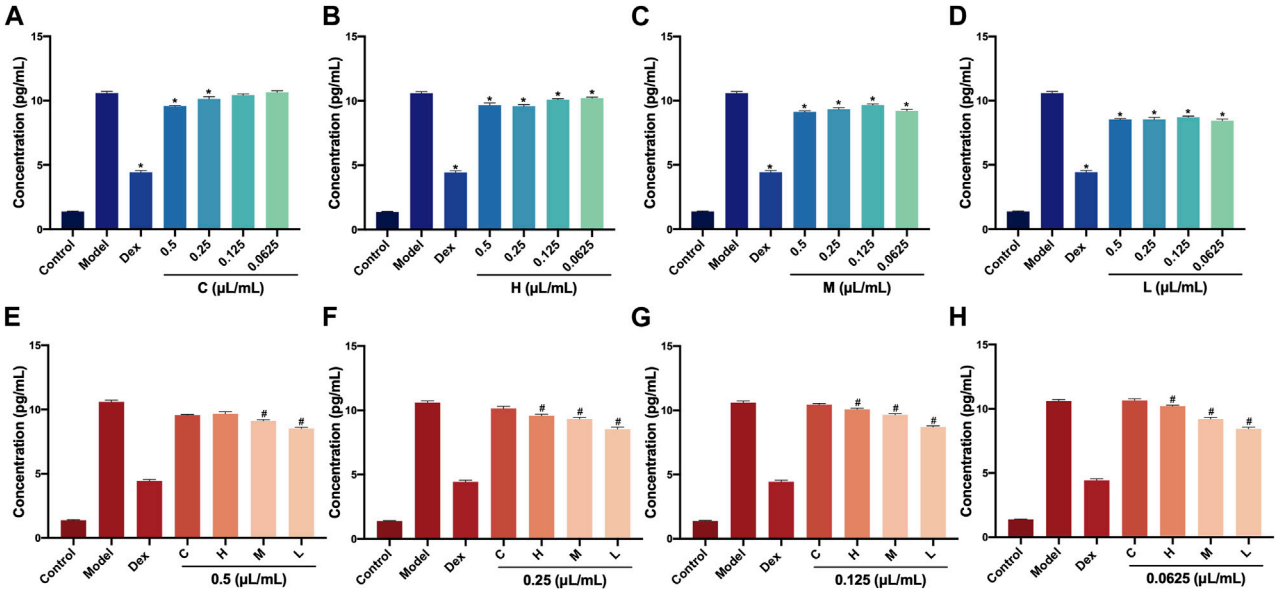

FIGURE 3
Levels of IL-6 in RAW264.7 cells after treatment with *Asarum* volatile crude oil and different distillates **(A)** Concentrations of IL-6 in RAW264.7 cells with 0.5, 0.25, 0.125, and 0.0625 μL/mL of **(C)**. **(B)** Concentrations of IL-6 in RAW264.7 cells with 0.5, 0.25, 0.125, and 0.0625 μL/mL of **(H)**. **(C)** Concentrations of IL-6 in RAW264.7 cells with 0.5, 0.25, 0.125, and 0.0625 μL/mL of M. **(D)** Concentrations of IL-6 in RAW264.7 cells with 0.5, 0.25, 0.125, and 0.0625 μL/mL) of L. **(E)** Concentrations of IL-6 in RAW264.7 cells after treatment at 0.5 μL/mL of C, H, M, and L. **(F)** Concentrations of IL-6 in RAW264.7 cells after treatment at 0.25 μL/mL of C, H, M, and L. **(G)** Concentrations of IL-6 in RAW264.7 cells after treatment at 0.125 μL/mL of C, H, M, and L. **(H)** Concentrations of IL-6 in RAW264.7 cells after treatment at 0.0625 μL/mL of C, H, M, and L. C (*Asarum* volatile crude oil), H (heavy distillate), M (medium distillate), L (light distillate).*$p < 0.05$, compared with model group, #$p < 0.05$, compared with the C group.

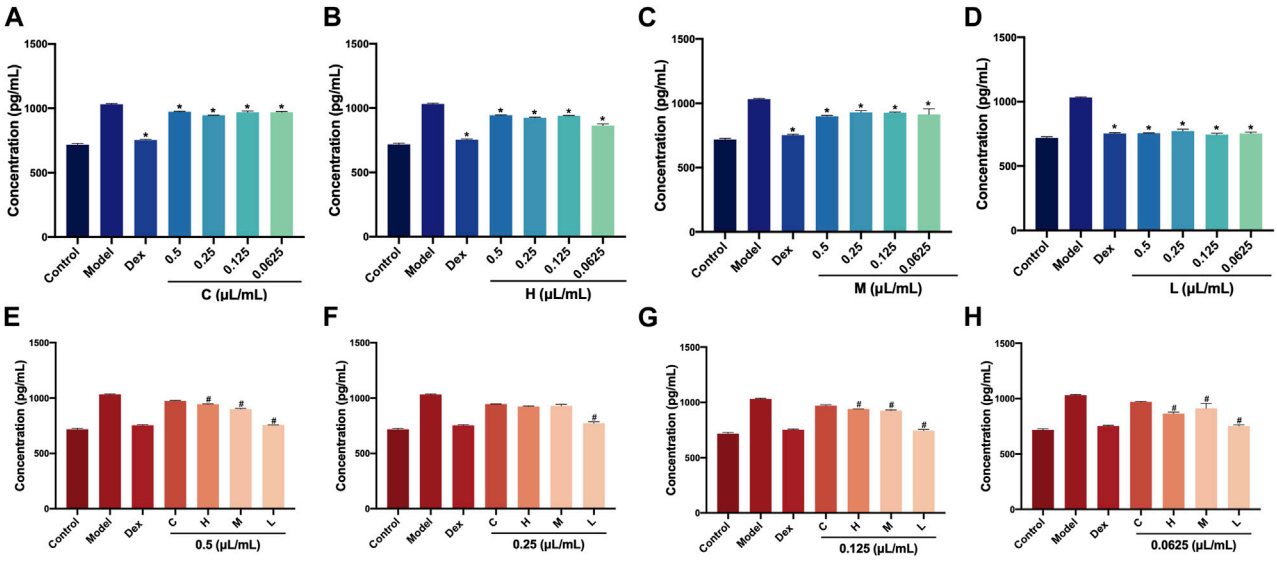

FIGURE 4
Levels of TNF-α in RAW264.7 cells after treatment with *Asarum* volatile crude oil and different distillates **(A)** Concentrations of TNF-α in RAW264.7 cells with 0.5, 0.25, 0.125, and 0.0625 μL/mL of **(C)**. **(B)** Concentrations of TNF-α in RAW264.7 cells with 0.5, 0.25, 0.125, and 0.0625 μL/mL of **(H)**. **(C)** Concentrations of TNF-α in RAW264.7 cells with 0.5, 0.25, 0.125, and 0.0625 μL/mL of M. **(D)** Concentrations of TNF-α in RAW264.7 cells with 0.5, 0.25, 0.125, and 0.0625 μL/mL) of L. **(E)** Concentrations of TNF-α in RAW264.7 cells after treatment at 0.5 μL/mL of C, H, M, and L. **(F)** Concentrations of TNF-α in RAW264.7 cells after treatment at 0.25 μL/mL of C, H, M, and L. **(G)** Concentrations of TNF-α in RAW264.7 cells after treatment at 0.125 μL/mL of C, H, M, and L. **(H)** Concentrations of TNF-α in RAW264.7 cells after treatment at 0.0625 μL/mL of C, H, M, and L. C (*Asarum* volatile crude oil), H (heavy distillate), M (medium distillate), L (light distillate).*$p < 0.05$, compared with model group, #$p < 0.05$, compared with C group.

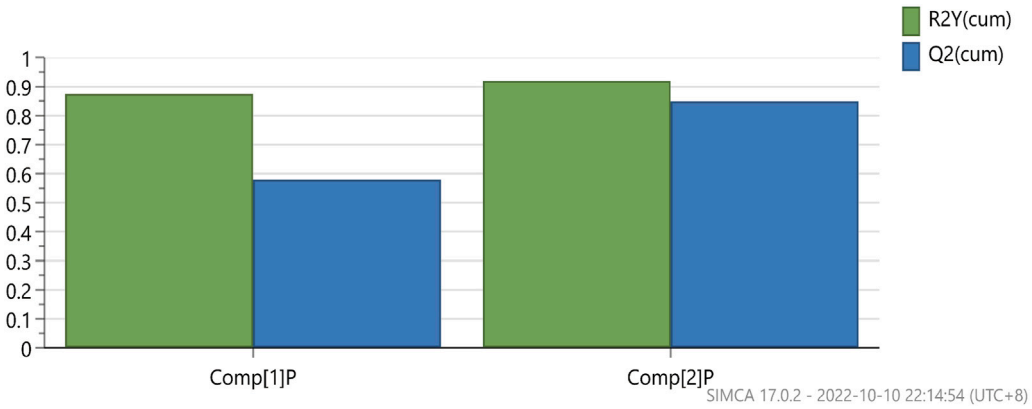

FIGURE 5
Principal component analysis of each fraction of *Asarum* essential oil.

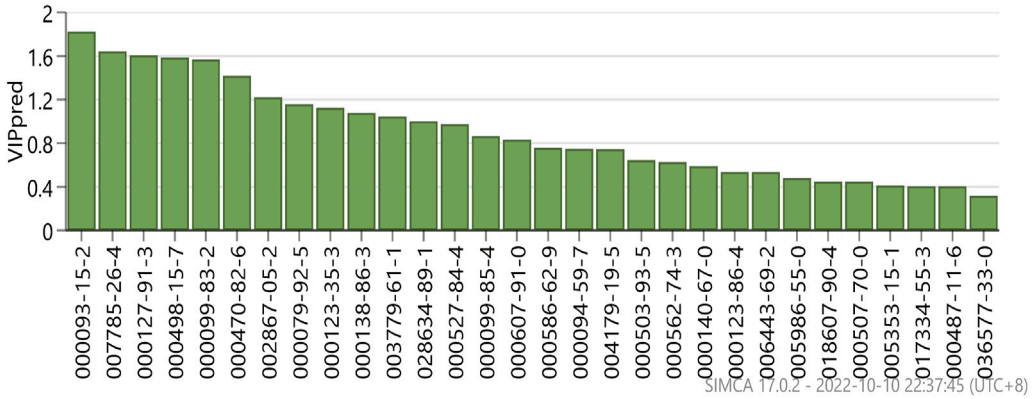

FIGURE 6
VIP values for the individual distillate compounds of *Asarum* essential oil.

3.6 ROS levels in PC12 cells after treatment with AEO and its different distillates

Next, the effect of crude oil and its distillates on intracellular ROS in PC12 cells was investigated via flow cytometry. A1 to A4 were ROS level expressions under C stimulation, B1 to B4 were under H, C1 to C4 were under M, and D1 to D4 were under L intervention. These findings from this experiment demonstrated that both the intracellular ROS levels and fluorescence intensity significantly changed after C, H, M, and L intervention compared to those of the normal group (blank group). Moreover, the fluorescence intensity tended to be normal as the drug concentration decreased. In addition, the statistical results showed that under C intervention, the fluorescence intensities of A2 (0.5 μL/mL), A3 (0.25 μL/mL), and A4 (0.125 μL/mL) were significantly changed compared with that of the normal group ($p < 0.01$). Fluorescence intensities corresponding to all four concentrations of H were statistically significant, while only C4 (0.125 μL/mL) had a significant change in M distillate ($p < 0.01$). Finally, all four concentrations (1, 0.5, 0.25, and 0.125 μL/mL) of H distillate caused significant changes in the cellular oxidative stress levels compared to the normal group ($p < 0.01$) (Figure 7).

3.7 Cell apoptosis of PC12 cells after treatment with AEO and its different distillates

The Annexin V-FITC assay kits were used to investigate the cell apoptosis rates of crude oil and distillates with PC12 cells. The results of this study showed that the high concentration (1 μL/mL) of these distillates (H, M, L) obtained after MD exhibited a higher apoptosis rates compared to the normal group (blank group). Furthermore, the apoptosis rate varied in a concentration-dependent manner. Lower concentration resulted in lower cell apoptosis rate. In addition, the statistical findings revealed that A2 (0.5 μL/mL) in distillate C and B1 (1 μL/mL) in distillate H exhibited a significant increase in apoptosis rate ($p < 0.01$, compared with that with the normal group). In M groups, the apoptosis rates of 1, 0.5, and 0.25 μL/mL were significantly different from those of the normal group. In distillate L groups, the apoptosis

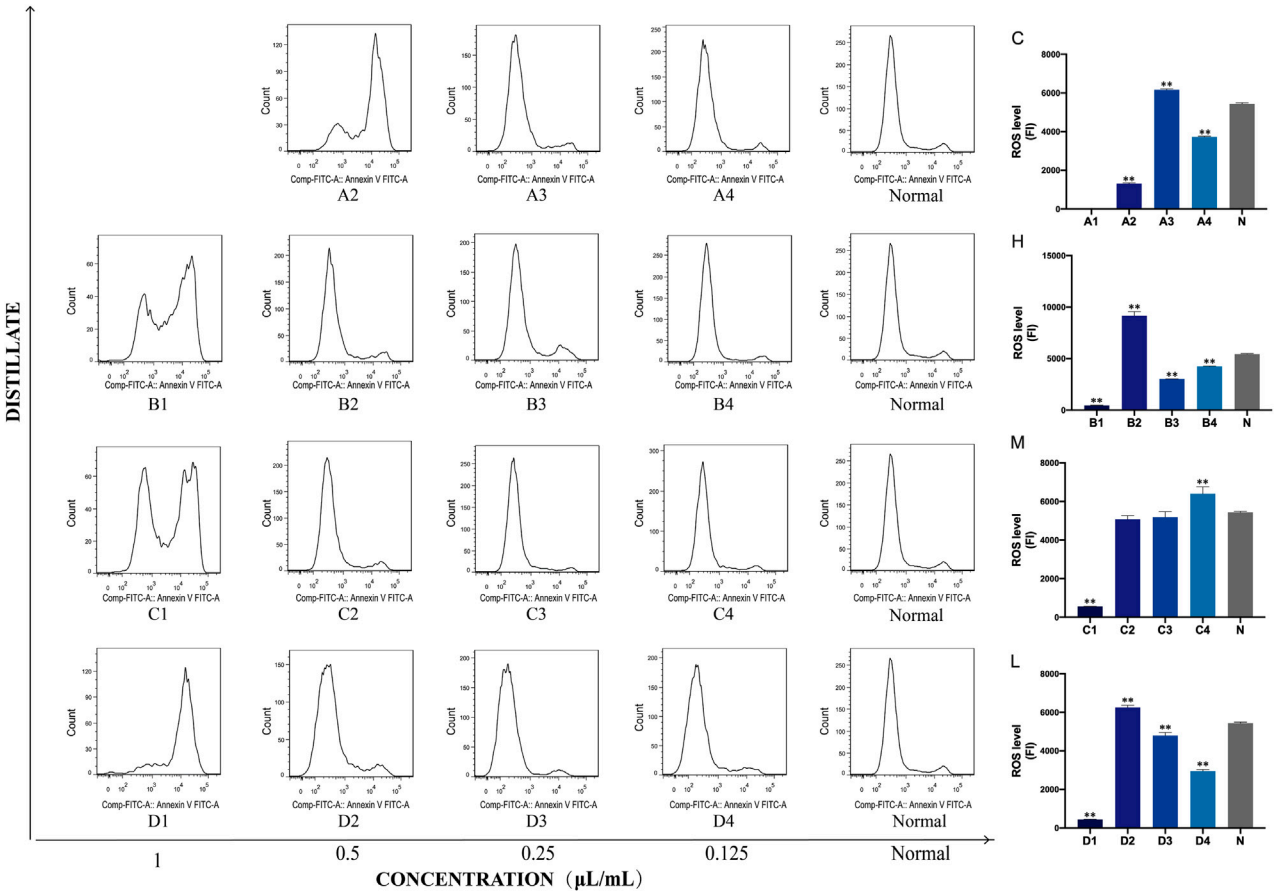

FIGURE 7
Concentrations of ROS in PC12 cells after treatment with Asarum volatile crude oil and different distillates. Concentrations of ROS in PC12 cells after treatment with 1, 0.5, 0.25, and 0.125 μL/mL of *Asarum* volatile crude oil **(C)**, heavy distillate **(H)**, medium distillate **(M)**, and light distillate **(L)**. **(A2–A4)** represent ROS levels in PC12 cells after treatment with C (**A2**: 0.5 μL/mL, **A3**: 0.25 μL/mL, **A4**: 0.125 μL/mL). **(B1–B4)** represent ROS levels in PC12 cells after treatment with H (**B1**: 1 μL/mL, **B2**: 0.5 μL/mL, **B3**: 0.25 μL/mL, **B4**: 0.125 μL/mL). **(C1–C4)** represent ROS levels in PC12 cells after treatment with M (**C1**: 1 μL/mL, **C2**: 0.5 μL/mL, **C3**: 0.25 μL/mL, **C4**: 0.125 μL/mL). **(D1–D4)** represent ROS levels in PC12 cells after treatment with L (**D1**: 1 μL/mL, **D2**: 0.5 μL/mL, **D3**: 0.25 μL/mL, **D4**: 0.125 μL/mL). The ROS levels of the **(C–L)** groups are shown on the right side, ** $p < 0.01$, compared with the normal group (N).

rates were significantly changed for the concentrations of 1, 0.25, and 0.125 μL/mL ($p < 0.05$, compared with the normal group) (Figure 8).

3.8 Cell morphology of PC12 cellsafter treatment with AEO and its different distillates

The effects of *Asarum* volatile crude oil and the different distillates on PC12 cell morphology by DAPI staining were observed. Cells in 1 μL/mL of each of C, H, M, and L (A1, B1, C1, and D1) groups demonstrated significant morphological changes with abnormal nuclei and increased apoptotic cells. However, as the concentration of the added distillate decreased, the morphology of cells in C, H, M, and L (A4, B4, C4, and D4) groups at 0.12 5 μL/mL of C, H, M, and L cells demonstrated similar morphology to that of the normal group (blank group), with intact nuclei and significantly more viable cells. These results suggested thatthat the survival rates of PC12 cells is concentration-responsively changed following treatment with AEO and its different distillates. (Figure 9).

3.9 Effect of AEO on the oxidase system

Oxidative damage can induce apoptosis. The expression levels of superoxide dismutase (SOD) in the different distillates of AEO at different concentrations are shown in. The SOD levels were significantly decreased at high concentrations of AEO, suggesting that AEO affects the oxidative stress system at high concentrations. Notably, the SOD expression of H was significantly lower than that of the other three groups (B2 < A2, C2, D2) when the concentration was 0.25 μL/mL, which may be related to the higher safrole content in H (Figure 10).

3.10 Effect of AEO on acute toxicity in mice

Acute toxicity experiments on mice were performed to investigate the toxicity of AEO and three AEO distillates. Mice mortality was investigated and determined after AEO administration. The results showed that the LD_{50} of C, H, and M was 1.8852, 1.9566, and 3.6741 g/Kg, respectively, and the toxicity of the M group was lower than that of the other two groups. The mortality rate of mice was only 16.67% when the

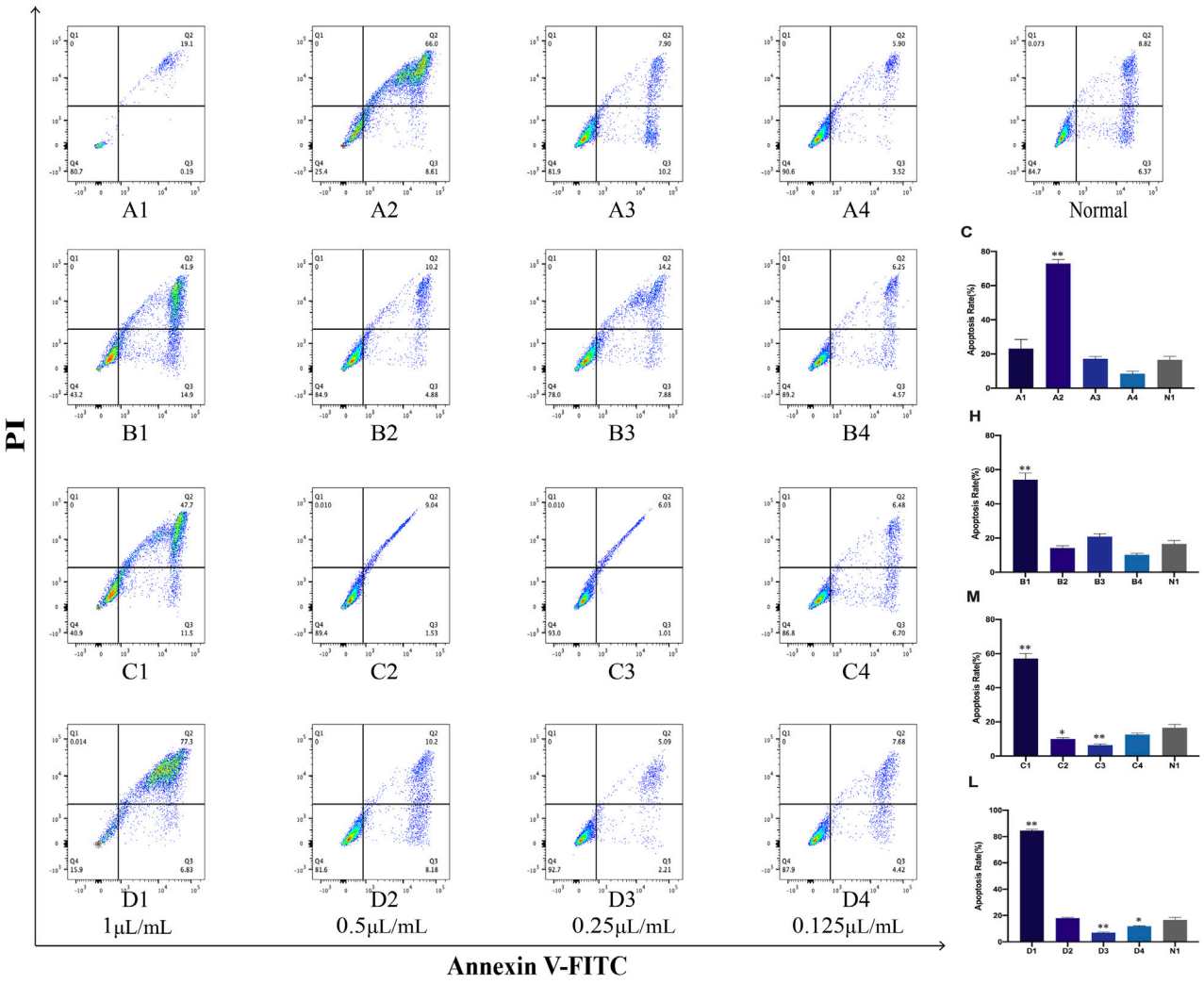

FIGURE 8
Apoptosis in PC12 cells after treatment with *Asarum* volatile crude oil and different distillates Apoptosis rates in PC12 cells were measured by flow cytometry after treatment with 1, 0.5, 0.25, and 0.125 μL/mL of *Asarum* volatile crude oil (C), heavy distillate (H), medium distillate (M), and light distillate (L). **(A1–A4)** represent apoptosis in PC12 cells after treatment with **(C)**. **(B1–B4)** represent apoptosis in PC12 cells after treatment with **(H)**. **(C1–C4)** represent apoptosis in PC12 cells after treatment with **(M)**. **(D1–D4)** represent apoptosis in PC12 cells after treatment with **(L)**. Figure on the top right represents normal PC12 cells. The lower right is the apoptosis rate in PC12 cells of the **(C, H, M, and L)** groups, *$p < 0.05$, **$p < 0.01$, compared with the normal group (N1).

administration concentration of L was 6.4185 g/Kg, indicating that the toxicity of L was significantly lower than the other distillates (Table 2).

4 Discussion

As the primary active component of *Asarum*, the volatile oil has pharmacological effects on the nervous, immune, and cardiovascular systems (Fung et al., 2021). Despite prior research on the chemical composition and pharmacological action of AEO, notable disagreements persist regarding its main components, such as methyl eugenol, safrole, and 3,5-dimethyltoluene (Hue et al., 2022; Gu et al., 2023). Therefore, MD was used to facilitate the enrichment and separation of AEO components. Furthermore, further research was conducted to establish the relationship between toxicity, pharmacodynamics, and the main components of AEO. The results from these investigations will help elucidate the specifically effective or toxic component of the AEO and provide references for more rational and effective clinical applications of *Asarum* in the future.

Using MD, the enrichment and separation of AEO were achieved. Compared with crude oil, the content of olefin components with lower boiling points in the heavy distillate was significantly reduced, while methyl eugenol increased from 24.0203 (C) to 31.3644% (H). However, the olefin components in the middle and light distillates achieved enrichment. The ratios of α-pinene and β-pinene contents in crude oil, heavy distillate, middle distillate, and light distillate are 1:0.1:2.5:4.7 and 1:0.1:2.8:4.4, respectively, and the total amount of α-pinene and β-pinene accounts for 39.5% of the light oil distillate, which is five times more than that of crude oil. Furthermore, significant differences in the relative contents of methyl eugenol, safrole, and 3,5-dimethyl

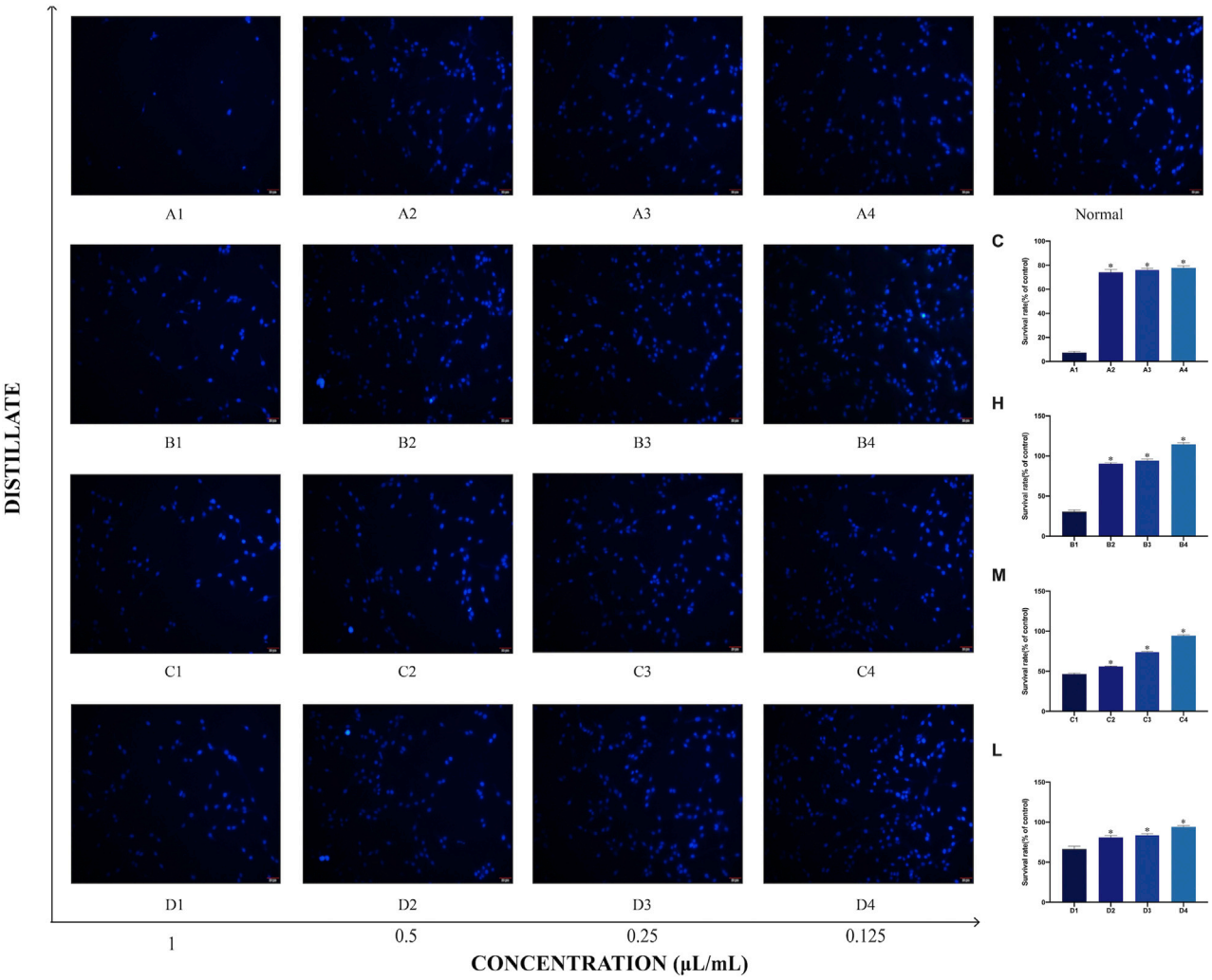

FIGURE 9
Morphology of PC12 cells after treatment with *Asarum* volatile crude oil and different distillates. The morphology of PC12 cells was measured by the DAPI staining method, scale bar: 20 μm. **(A1–A4)** represent the PC12 cells to which were added 1, 0.5, 0.25, and 0.125 μL/mL of *Asarum* volatile crude oil **(C)**, heavy distillate **(H)**, medium distillate **(M)**, and light distillate **(L)**, respectively. The top right corner shows normal PC12 cells. The survival rates of PC12 cells under different distillates are shown on the right side.

methylbenzene were observed in each distillate, with 3,5-dimethyl methylbenzene in C, H, M, and L in the ratio 1:1.1:0.8:0.2 and safrole in C, H, M, and L in the ratio 1:1.1:0.7:0.2. The ratio of methyl eugenol in C, H, M, and L was 1:1.3:0.2:0.02. The methyl eugenol content was significantly reduced in the light fraction, and the safrole content was only 18.44% of the crude oil. The difference in the composition of each distillate was influenced by the different boiling points of the components, providing a basis for further toxicological investigation.

Numerous experiments have shown that the AEO exhibits a significant anti-inflammatory effect both *in vivo* and *in vitro* (Zhang et al., 2021) (Antsyshkina et al., 2020). During inflammation, activated inflammatory cells secrete large amounts of pro-inflammatory cytokines IL-1β, IL-6, and TNF-α (Siouti and Andreakos, 2019) (Choudhury et al., 2021). Therefore, in the current study, the anti-inflammatory activity of the essential oil was chosen as the index for the evaluation of the efficacy of the essential oil. In the LPS-induced RAW264.7 cell model, LPS caused an increase in IL-6 and TNF-α levels. AEO and its fractions significantly reduced the elevation of TNF-α and IL-6 and decreased the production and release of the pro-inflammatory cytokines TNF-α and IL-6, resulting in anti-inflammatory effects. Principal component analysis showed that the monoterpene component had better anti-inflammatory activity than other components. The relative percentage of monoterpenes was higher in the light fraction than in the other fractions, so it had a better anti-inflammatory activity.

A previous study by our group demonstrated that AEO at a dose of 1.8852 g/kg inhibited the normal functioning of the central nervous system of KM mice and impaired their balance and coordination, with clinical manifestations including an intoxicated state, abnormal gait, limping, slowed movement, and the loss of appetite. These results are consistent with the reported adverse events of *Asarum*, including hepatotoxicity, nephrotoxicity, and neurologic reactions (Zhang et al., 2019). According to clinical reports, AEO could cause respiratory excitation at low doses and respiratory depression at high doses (Yan, 2022). Because of the two-way

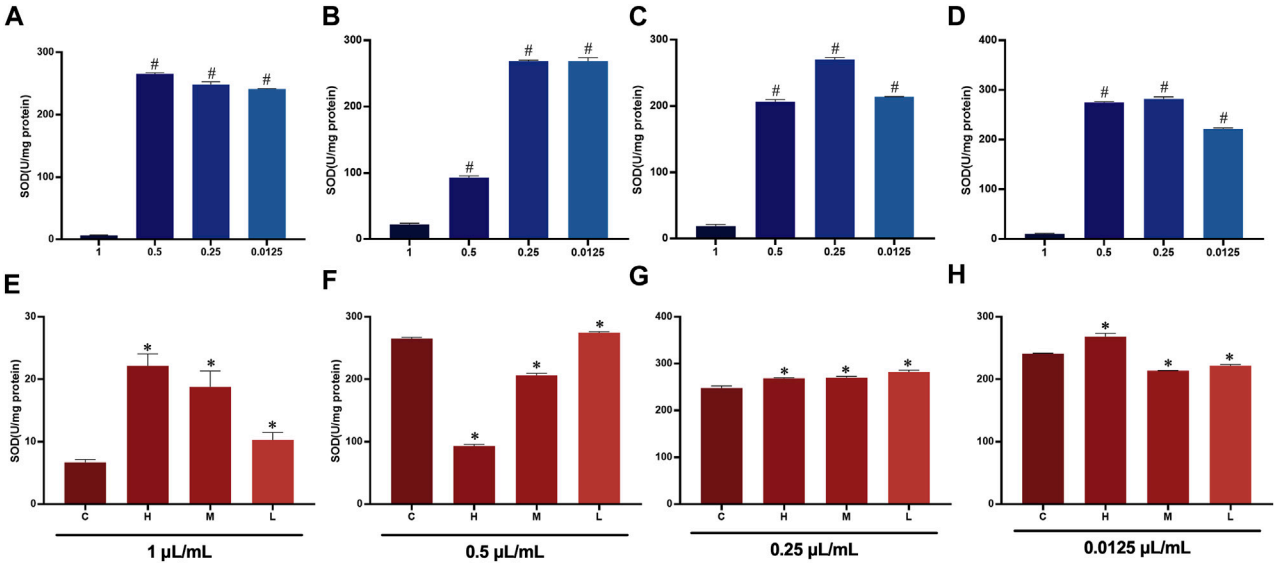

FIGURE 10
SOD expression in PC 12 cells after essential oil intervention **(A)** Expression of SOD in PC 12 cells with 0.5, 0.25, 0.125, and 0.0625 μL/mL of **(C)**. **(B)** Expression of SOD in PC 12 cells with 0.5, 0.25, 0.125, and 0.0625 μL/mL of **(H)**. **(C)** Expression of SOD in PC 12 cells with 0.5, 0.25, 0.125, and 0.0625 μL/mL of M. **(D)** Expression of SOD in PC 12 cells with 0.5, 0.25, 0.125, and 0.0625 μL/mL) of L. **(E)** Expression of SOD in PC 12 cells after treatment at 0.5 μL/mL of C, H, M, and L. **(F)** Expression of SOD in PC 12 cells after treatment at 0.25 μL/mL of C, H, M, and L. **(G)** Expression of SOD in PC 12 cells after treatment at 0.125 μL/mL of C, H, M, and L. **(H)** Expression of SOD in PC 12 cells after treatment at 0.0625 μL/mL of C, H, M, and L.

TABLE 2 LD_{50} value of AEO in mice.

Groups	Dose (g/Kg)	Total (N)	Deaths (x)	Mortality (x/N, %)	LD_{50} (g/Kg)
C	1.0792	6	0	0	1.8852
	1.3489	6	0	0	
	1.6862	6	3	50	
	2.1077	6	3	50	
	2.6347	6	6	100	
H	1.0792	6	0	0	1.9566
	1.3489	6	1	16.67	
	1.6862	6	1	16.67	
	2.1077	6	3	50	
	2.6347	6	6	100	
M	2.1077	6	0	0	3.6741
	2.6347	6	1	16.67	
	3.2865	6	2	33.33	
	4.1080	6	3	50	
	5.1349	6	6	100	
L	2.6347	6	0	0	/
	3.2865	6	0	0	
	4.1080	6	0	0	
	5.1349	6	0	0	
	6.4185	6	1	16.67	

modulation of the nervous system by AEO, it is vital and significant to find the threshold between the therapeutic effect and toxicity and determine a safe therapeutic window. The acute toxicity test in mice indicated that the LD_{50} assessment confirmed that the toxicity of the crude oil was similar to that of the heavy distillate. In contrast, the toxicities of the middle and light distillates were remarkably reduced. A comparison of the components revealed that the reduction in toxicity was associated with a reduction in the contents of safrole, methyl eugenol, and 3,5-dimethyl methylbenzene.

Only a few studies are available on the mechanism of neurotoxic effects of AEO, which mainly focus on cell apoptosis, oxidative stress, and the inhibition of neuraxial growth (Hue et al., 2022). Prior evidence has indicated that mitochondrial dysfunction is a major pathogenesis of neurological diseases (Reiss et al., 2022) (Calvo-Rodriguez and Bacskai, 2021). Hence, it was investigated whether the mechanism of toxicity was related to the induction of apoptosis by the mitochondrial pathway involving ROS. PC12 cells, which are extensively applied to study neurotoxicity, are derived from the sympathetic nervous system that has stopped dividing and grows neurons when induced by nerve growth factors (Kagan et al., 2022; Xie et al., 2023). Therefore, PC12 cells were chosen to establish an *in vitro* model to explore AEO neurotoxicity in this study. According to the flow cytometric detection, biochemical methods, and the DAPI staining, it was demonstrated that AEO administration induced oxidative damage and dysfunction in the mitochondria of PC 12 cells, with significant changes in cell morphology, abnormal nuclei, and an increase in apoptotic cells. Moreover, we also noted that the apoptosis rate of PC12 cells was increased after AEO treatment, indicating that AEO could induce apoptosis in PC12 cells. In summary, the enrichment of the AEO by MD confirmed that the primary anti-inflammatory components in the AEO were methyl eugenol, α-pinene, β-pinene, α-phellandrene, 1,8 eucalyptol, camphorene, and β-myrcene, and the main toxic components were safrole, methyl eugenol and, 3,5-Dimethoxytoluene. This finding is consistent with previous literature reports. Methyl eugenol and myristicin in AEO have been reported to have hepatorenal toxicity and genotoxicity (Cao et al., 2020) (Akhlaq et al., 2022) (Carvalho et al., 2022). A study has found that safrole oxide can cause apoptosis in mouse neuronal cells by regulating the activity of ROS (Su et al., 2007a). In the meantime, safrole oxide could affect the activity of VECs, thereby inhibiting the differentiation of NSCs and inducing their apoptosis (Su et al., 2007b).

The *in vitro* findings were also validated by *in vivo* experiments. The experimental results in mice demonstrated that the light distillates of AEO exhibited low toxicity. However, the characteristic components of AEO were safrole, methyl-eugenol, and 3,5-Dimethoxytoluene, and the light distillates contained relatively low levels of the characteristic components and were not representative of AEO. Therefore, further investigations are needed to apply the MD technique to enrich the distillates containing the characteristic constituents of AEO and identify a safety window for clinical applications by studying the varying proportions of the constituents.

5 Conclusion

In summary, the MD technique can effectively enrich and separate essential oils. AEO exhibits good anti-inflammatory activity and considerable toxicity. The potential mechanism of neurotoxicity is related to oxidative stress and apoptosis. Most of the current methods of reducing the toxicity of *Asarum* are based on increasing the decoction time and reducing the essential oil content. However, studies have indicated that the essential oil of *Asarum* exhibits a significant anti-inflammatory effect, and reducing the essential oil content also reduces its effectiveness. Therefore, determining the safety window is essential for the clinical applications of AEO, both to exploit its medicinal properties and avoid the toxicity of the essential oil. In the current study, the MD technique was used to enrich and separate the *Asarum* essential oil and provide methods and ideas for future experiments.

Based on our previous studies, AEO has anti-inflammatory, antibacterial and analgesic effects. Through molecular distillation technology to reduce its toxicity, it is expected to be developed as a spray gel for treating oral ulcers.

Data availability statement

The raw data supporting the conclusion of this article will be made available by the authors, without undue reservation.

Ethics statement

The animal study was reviewed and approved by Laboratory Animal Ethics Committee of Jiangxi University of Traditional Chinese Medicine.

Author contributions

YL, prepared the first draft. FW, rewrote the discussion section. HG, rewrote the methodology. DZ, ZW, helped to design the experimental orientation. XZ, HL, teaching data analysis. YX, article format modification. PY, revised the whole manuscript and rewrote the introduction and abstract section. MY, conceptualized the study. All authors listed have made a substantial, direct, and intellectual contribution to the work and approved it for publication.

Funding

This work was financially supported by the National Natural Science Foundation of China (No. 82074026).

Acknowledgments

We would like to thank the participants for their contribution to this study.

Conflict of interest

The authors declare that the research was conducted in the absence of any commercial or financial relationships that could be construed as a potential conflict of interest.

The reviewer JZ declared a shared affiliation with the author DZ to the handling editor at the time of review.

Publisher's note

All claims expressed in this article are solely those of the authors and do not necessarily represent those of their affiliated organizations, or those of the publisher, the editors and the reviewers. Any product that may be evaluated in this article, or claim that may be made by its manufacturer, is not guaranteed or endorsed by the publisher.

Supplementary material

The Supplementary Material for this article can be found online at: https://www.frontiersin.org/articles/10.3389/fphar.2023.1196137/full#supplementary-material

References

Akhlaq, S., Ara, S. A., Fazil, M., Ahmad, B., Akram, U., Haque, M., et al. (2022). Ethno pharmacology, phytochemical analysis, safety profile, prophylactic aspects, and therapeutic potential of Asarum europaeum L. in Unani medicine: An evidence-based appraisal. *Phytomedicine Plus* 2, 100226. doi:10.1016/j.phyplu.2022.100226

Antsyshkina, A. M., Ars, Yu.V., Bokov, D. O., Pozdnyakova, N. A., Prostodusheva, T. V., and Zaichikova, S. G. (2020). The genus asarum L.: A phytochemical and ethnopharmacological review. *Syst. Rev. Pharm.* 11 (5), 472–502. doi:10.31838/srp.2020.5.66

Calvo-Rodriguez, M., and Bacskai, B. J. (2021). Mitochondria and calcium in alzheimer's disease: From cell signaling to neuronal cell death. *Trends Neurosci.* 44, 136–151. doi:10.1016/j.tins.2020.10.004

Cao, S., Han, L., Li, Y., Yao, S., Hou, S., Ma, S., et al. (2020). Integrative transcriptomics and metabolomics analyses provide hepatotoxicity mechanisms of asarum. *Exp. Ther. Med.* 20, 1359–1370. doi:10.3892/etm.2020.8811

Carvalho, R. P. R., Ribeiro, F. C. D., Lima, T. I., Ervilha, L. O. G., de Oliveira, E. L., de Oliveira Faustino, A., et al. (2022). High doses of eugenol cause structural and functional damage to the rat liver. *Life Sci.* 304, 120696. doi:10.1016/j.lfs.2022.120696

Choi, S., Jung, M. A., Hwang, Y. H., Pyun, B. J., Lee, J. Y., Jung, D. H., et al. (2021). Anti-allergic effects of Asarum heterotropoides on an ovalbumin-induced allergic rhinitis murine model. *Biomed. Pharmacother.* 141, 111944. doi:10.1016/j.biopha.2021.111944

Choudhury, C., Mazumder, R., Biswas, R., and Sengupta, M. (2021). Cadmium exposure induces inflammation through the canonical NF-κB pathway in monocytes/macrophages of Channa punctatus Bloch. *Fish Shellfish Immunol.* 110, 116–126. doi:10.1016/j.fsi.2021.01.002

Dantas, T. N. C., Cabral, T. J. O., Dantas Neto, A. A., and Moura, M. C. P. A. (2020). Enrichmnent of patchoulol extracted from patchouli (Pogostemon cablin) oil by molecular distillation using response surface and artificial neural network models. *J. Industrial Eng. Chem.* 81, 219–227. doi:10.1016/j.jiec.2019.09.011

Fan, Y., Yang, D., Huang, X., Yao, G., Wang, W., Gao, M., et al. (2021). Pharmacokinetic study of safrole and methyl eugenol after oral administration of the essential oil extracts of asarum in rats by GC-MS. *BioMed Res. Int.* 2021, 6699033–6699038. doi:10.1155/2021/6699033

Fung, T. K. H., Lau, B. W. M., Ngai, S. P. C., and Tsang, H. W. H. (2021). Therapeutic effect and mechanisms of essential oils in mood disorders: Interaction between the nervous and respiratory systems. *IJMS* 22, 4844. doi:10.3390/ijms22094844

Gu, E. Y., Jung, J., Back, S. M., Lim, K. H., Kim, W., Min, B. S., et al. (2023). Evaluation of genotoxicity and 13-week subchronic toxicity of root of Asarum heterotropoides var. seoulense (Nakai) Kitag. *J. Ethnopharmacol.* 305, 116012. doi:10.1016/j.jep.2022.116012

Han, J. M., Kim, M. H., Choi, L. Y., Kim, G., and Yang, W. M. (2022). Exploring the potential effects and mechanisms of asarum sieboldii radix essential oil for treatment of asthma. *Pharmaceutics* 14, 558. doi:10.3390/pharmaceutics14030558

Hou, H., Li, Y., Xu, Z., Yu, Z., Peng, B., Wang, C., et al. (2023). Applications and research progress of Traditional Chinese medicine delivered via nasal administration. *Biomed. Pharmacother.* 157, 113933. doi:10.1016/j.biopha.2022.113933

Hu, Z. X., Yu, Z., and Peng, B. (2019). A literature study on the clinical dosage of foxglove before Ben Cao Zai. *Jiangsu Tradit. Chin. Med.* 51 (04), 69–71.

Hue, H. T. T., Ky, L. D., and Hoang, N. H. (2022). Analysis of DNA markers from Vietnamese asarum L. Species. *VNU J. Sci. Nat. Sci. Technol.* 38, 4. doi:10.25073/2588-1140/vnunst.5499

Kagan, T., Stoyanova, G., Lockshin, R. A., and Zakeri, Z. (2022). Ceramide from sphingomyelin hydrolysis induces neuronal differentiation, whereas de novo ceramide synthesis and sphingomyelin hydrolysis initiate apoptosis after NGF withdrawal in PC12 Cells. *Cell. Commun. Signal* 20, 15. doi:10.1186/s12964-021-00767-2

Kemprai, P., Protim Mahanta, B., Sut, D., Barman, R., Banik, D., Lal, M., et al. (2020). Review on safrole: Identity shift of the 'candy shop' aroma to a carcinogen and deforester. *Flavour Fragr. J.* 35, 5–23. doi:10.1002/ffj.3521

Liu, F., Ali, T., and Liu, Z. (2021). Comparative transcriptomic analysis reveals the effects of drought on the biosynthesis of methyleugenol in asarum sieboldii miq. *Biomolecules* 11, 1233. doi:10.3390/biom11081233

Liu, G. X., Xu, F., Shang, M. Y., Wang, X., and Cai, S. Q. (2020). The Relative Content and Distribution of Absorbed Volatile Organic Compounds in Rats Administered Asari Radix et Rhizoma Are Different between Powder- and Decoction-Treated Groups. *Molecules* 25, 4441. doi:10.3390/molecules25194441

Liu, H., Li, S., Huan, X., Xie, Y., Xie, Z., Sun, Y., et al. (2022a). The antinociceptive and anti-inflammatory potential and pharmacokinetic study of significant alkamides ingredients from Asarum Linn. *J. Ethnopharmacol.* 297, 115569. doi:10.1016/j.jep.2022.115569

Liu, H., and Wang, C. (2022). The genus asarum: A review on phytochemistry, ethnopharmacology, toxicology and pharmacokinetics. *J. Ethnopharmacol.* 282, 114642. doi:10.1016/j.jep.2021.114642

Liu, M. T., Chen, X., and Zhang, W. (2023). Advances in the chemical composition, pharmacology and toxicology of Asarum. *Chin. J. Exp. Formulation* 1, 18. doi:10.13422/j.cnki.syfjx.20230828

Liu, Y., Jiang, P., Chen, X., Zhang, W., and Shi, J. (2022b). Efficacy and safety of rupatadine fumarate combined with acupoint application in allergic rhinitis complicated with diabetes. *Comput. Intell. Neurosci.* 2022, 6935758–6935766. doi:10.1155/2022/6935758

Mahrous, E. A., and Farag, M. A. (2022). Trends and applications of molecular distillation in pharmaceutical and food industries. *Sep. Purif. Rev.* 51, 300–317. doi:10.1080/15422119.2021.1924205

Maseehullah, M., Zakir, M., Anas, M., and Kazmi, M. H. (2022). Ethno-pharmacology of asaroon (*Asarum europaeum* L) with special reference to unani system of medicine. *J. Complementary Integr. Med.* 19, 181–192. doi:10.1515/jcim-2021-0021

National Pharmacopoeia Commission (2020). *Pharmacopoeia of the people 's Republic of China (volume one)*. China: China Pharmaceutical Science and Technology Press.

Nie, Y., Luo, Y., Luo, S., Cao, X., Song, G., and Deng, C. (2022). Amphiphilic copolymers grafted on monodisperse magnetic microspheres as an efficient adsorbent for the extraction of safrole in the plasma. *J. Chromatogr. A* 1662, 462733. doi:10.1016/j.chroma.2021.462733

Reiss, A. B., Ahmed, S., Dayaramani, C., Glass, A. D., Gomolin, I. H., Pinkhasov, A., et al. (2022). The role of mitochondrial dysfunction in alzheimer's disease: A potential pathway to treatment. *Exp. Gerontol.* 164, 111828. doi:10.1016/j.exger.2022.111828

Reza Shirzad Kebria, M., and Rahimpour, A. (2020). "Membrane distillation: Basics, advances, and applications," in *Advances in membrane Technologies*. Editor A. Abdelrasoul (London, United Kingdom: Intechopen Limited). doi:10.5772/intechopen.86952

Siouti, E., and Andreakos, E. (2019). The many facets of macrophages in rheumatoid arthritis. *Biochem. Pharmacol.* 165, 152–169. doi:10.1016/j.bcp.2019.03.029

Su, L., Zhao, B., Lv, X., Wang, N., Zhao, J., Zhang, S., et al. (2007a). Safrole oxide induces neuronal apoptosis through inhibition of integrin beta4/SOD activity and elevation of ROS/NADPH oxidase activity. *Life Sci.* 80 (11), 999–1006. doi:10.1016/j.lfs.2006.11.041

Su, L., Zhao, B., Lv, X., Zhao, J., Zhang, S., and Miao, J. (2007b). Safrole oxide is a useful tool for investigating the effect of apoptosis in vascular endothelial cells on neural stem cell survival and differentiation *in vitro*. *Bioorg. Med. Chem. Lett.* 17 (11), 3167–3171. doi:10.1016/j.bmcl.2007.03.032

Wang, J., Zheng, S., Gao, Y., Shi, J., Zhou, Z., and Ren, Z. (2023). Enrichment of high-purity nervonic acid ethyl ester from *Acer truncatum* B unge seed oil by combination

method of urea inclusion and molecular distillation. Can. J. Chem. Eng. *cjce* 2023, 24875. doi:10.1002/cjce.24875

Wu, M., Xiong, Y., Han, R., Dong, W., and Xiao, C. (2020). Fumigant Toxicity and Oviposition Deterrent Activity of Volatile Constituents from Asari Radix et Rhizoma against *Phthorimaea operculella* (Lepidoptera: Gelechiidae). *J. Insect Sci.* 20, 32. doi:10.1093/jisesa/ieaa133

Xie, D., Deng, T., Zhai, Z., Sun, T., and Xu, Y. (2023). The cellular model for alzheimer's disease research: PC12 cells. *Front. Mol. Neurosci.* 15, 1016559. doi:10.3389/fnmol.2022.1016559

Yan, X. Q. (2022). Study on the concoction process and quality evaluation of Hosin. [dissertation/master's thesis]. Jilin: Jilin Agricultural University.

Yang, Q., Shen, F., Zhang, F., Bai, X., Zhang, Y., and Zhang, H. (2021). The combination of two natural medicines, chuanxiong and asarum: A review of the chemical constituents and pharmacological activities. *J. Chem. Res.* 45, 957–976. doi:10.1177/17475198211039130

Yao, G., Ma, W., Huang, X., Jia, Q., Shen, J., Chang, Y., et al. (2020). Identification and quality evaluation of raw and processed *asarum* species using microscopy, DNA barcoding, and gas chromatography-mass spectrometry. *J. Anal. Methods Chem.* 2020, 2690238–2690312. doi:10.1155/2020/2690238

Zhang, H. M., Zhao, X. H., Sun, Z. H., Li, G. C., Liu, G. C., Sun, L. R., et al. (2019). Recognition of the toxicity of aristolochic acid. *J. Clin. Pharm. Ther.* 44, 157–162. doi:10.1111/jcpt.12789

Zhang, Y., Li, S., Liang, Y., Liu, R., Lv, X., Zhang, Q., et al. (2021). A systematic strategy for uncovering quality marker of Asari Radix et Rhizoma on alleviating inflammation based chemometrics analysis of components. *J. Chromatogr. A* 1642, 461960. doi:10.1016/j.chroma.2021.461960

frontiers | Frontiers in Pharmacology

TYPE Original Research
PUBLISHED 07 July 2023
DOI 10.3389/fphar.2023.1216985

OPEN ACCESS

EDITED BY
Zipeng Gong,
Guizhou Medical University, China

REVIEWED BY
Rufeng Wang,
Beijing University of Chinese Medicine, China
Runbin Sun,
Nanjing Drum Tower Hospital, China
Shan Xiong,
Shandong First Medical University and Shandong Academy of Medical Sciences, China

*CORRESPONDENCE
Zuqiang Wu,
lywuzq@scut.edu.cn

RECEIVED 04 May 2023
ACCEPTED 28 June 2023
PUBLISHED 07 July 2023

CITATION
Ye L, Cheng L, Deng Y, Wang S, Wu X, Ou S, Chang Q, Zhao X, Zhou W, Yu J and Wu Z (2023), Absorption, tissue distribution, and excretion of glycycoumarin, a major bioactive coumarin from Chinese licorice (*Glycyrrhiza uralensis* Fisch). *Front. Pharmacol.* 14:1216985. doi: 10.3389/fphar.2023.1216985

Absorption, tissue distribution, and excretion of glycycoumarin, a major bioactive coumarin from Chinese licorice (*Glycyrrhiza uralensis* Fisch)

Linhu Ye[1,2,3], Lei Cheng[2], Yan Deng[2], Sen Wang[3], Xinyu Wu[2], Shuiping Ou[3], Qi Chang[4], Xinqian Zhao[2], Wen Zhou[1], Jinghua Yu[1] and Zuqiang Wu[1]*

[1]The Sixth Affiliated Hospital, School of Medicine, South China University of Technology, Nanhai District People's Hospital of Foshan, Foshan, China, [2]Bijie City First People's Hospital, Bijie, China, [3]School of Pharmacy, Zunyi Medicinal University, Zunyi, China, [4]Institute of Medicinal Plant Development, Chinese Academy of Medical Sciences and Peking Union Medical College, Beijing, China

Licorice (*Glycyrrhiza uralensis* Fisch) is a natural plant resource widely used as a food and herbal medication in China. Glycycoumarin (GCM) is a major coumarin in licorice that possesses several biological activities. However, little is known about its pharmacokinetic profile. The present study aimed to describe the oral absorption, tissue distribution, and excretion of GCM in rats. Free (parent drug) and/or total (parent drug plus the glucuronidated metabolite) GCM in biological samples was quantified before and after the hydrolysis reaction with β-glucuronidase using a reliable LC-MS/MS method. The results indicated that GCM was rapidly absorbed and transformed into its conjugated metabolites after administration. Free GCM plasma concentrations after *i. v.* (10 mg/kg) administration quickly decreased with an average $t_{1/2,\lambda z}$ of 0.71 h, whereas the total GCM concentration reduced slowly with a $t_{1/2,\lambda z}$ of 2.46 h. The area under the curve of glucuronidated metabolites was approximately four-times higher than that of free GCM. Presumably, because of hepatic and/or intestinal tract first-pass metabolism, GCM exhibited a poor bioavailability of 9.22%, as estimated from its total plasma concentration. Additionally, GCM was distributed rapidly and widely in various tissues except the brain. The liver had the highest concentration; further, GCM was promptly eliminated from test tissues after intraperitoneal (20 mg/kg) administration, but only a small amount of GCM was excreted via bile and urine. Overall, GCM is absorbed and rapidly transformed into its conjugated metabolites with low bioavailability; further, it is distributed in various tissues, except the brain. These pharmacokinetic results are helpful for better understanding the characteristics and pharmacological effects of GCM.

KEYWORDS

glycycoumarin, pharmacokinetics, bioavailability, tissue distribution, LC-MS/MS

1 Introduction

Licorice (*Glycyrrhiza uralensis* Fisch), known as Gan Cao in traditional Chinese medicine, is one of the best-known herbal medicines throughout Asia and is widely used as a medicine and food in China. Licorice appears in the pharmacopoeia of the People's Republic of China, where its applications include detoxification and treatment of spleen and stomach disorders, palpitations and shortness of breath, coughs, influenza infection, and liver disease. Pharmacological studies have demonstrated that licorice exhibits various biological activities, including antioxidant, anti-inflammatory, antidiabetic, anticancer, and skin-whitening effects (Asl and Hosseinzadeh, 2008; Fu et al., 2013; Fukuchi et al., 2016). Phytochemical studies have shown that licorice is rich in triterpenes and their glycosides, flavonoids, and coumarins (Ji et al., 2016).

Glycycoumarin (GCM, Figure 1) is a major coumarin in licorice, accounting for 0.81 mg/g in the crude roots and rhizomes of licorice (Qiao et al., 2014b). The reported biological activities of GCM include antioxidant, anti-inflammatory and anti-hepatitis C virus activities (Adianti et al., 2014). More recently, additional beneficial effects of GCM have been described. For example, GCM exerts anti-hepatoma effects by binding to and inactivating the oncogenic kinase TOPK and activating the p53 pathway (Song et al., 2016). It also improves the efficacy of BH3 mimetic ABT-737 against liver cancer and attenuates the platelet toxicity of ABT-737 (Zhang et al., 2018). Moreover, GCM can ameliorate alcohol-induced hepatic injury by activating Nrf2 and autophagy (Song et al., 2015) and protect against acetaminophen-induced liver injury by activating sustained autophagy (Yan et al., 2018). The major metabolic pathways of GCM *in vivo* are glucuronidation and hydroxylation; three metabolites are formed in the glucuronidation reaction, and the binding sites may include its three hydroxyl groups (Wang et al., 2014).

Despite increasing studies on the biological activities of GCM and its underlying metabolic pathways, little is known about its pharmacokinetic profile. In this study, we performed a rapid and reliable liquid chromatography coupled with mass spectrometry (LC-MS/MS) method for determining GCM abundance. This method was successfully used to assess the pharmacokinetic properties of GCM and its tissue distribution in rats. To our knowledge, this study is the first to report the pharmacokinetics of purified GCM, including its oral absorption, bioavailability, tissue distribution, and excretion, after oral, intravenous (*i.v.*), and intraperitoneal administration in rats for exploring its disposal in the body and further understand its *in vivo* pharmacological activities.

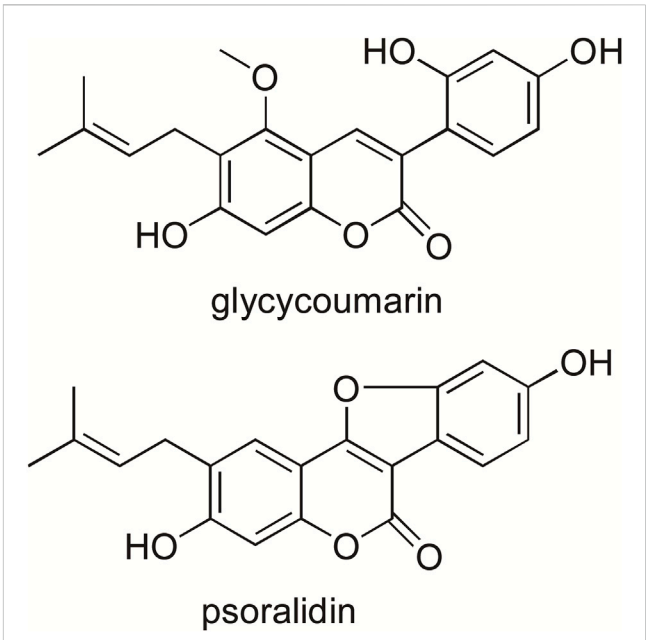

FIGURE 1
Chemical structure of glycycoumarin and psoralidin (internal standard).

2 Materials and methods

2.1 Chemicals and reagents

Glycycoumarin (purity>98%, Cat# DSTDG010801) was used as a reference compound and was purchased from Lemeitian Medical Technology Co., Ltd. (Chengdu, China). Psoralidin (Cat# 180526), used as an internal standard (IS), was obtained from Ronghe Pharmaceutical Sciences (Shanghai, China). β-Glucuronidase (Type H-1, Cat# SLCH4420) was obtained from Sigma (St. Louis, MO, United States). Solutol HS-15 (Cat# 159186) was obtained from MedChemExpress LLC (Shanghai, China). Anhydrous sodium acetate (Cat# C12095781) was purchased from Macklin Biochemical Technology Co., Ltd. (Shanghai, China). HPLC-grade acetonitrile and methanol were purchased from Fisher Scientific (Emerson, IA, United States). MCI GEL was purchased from Mitsubishi Chemical (Tokyo, Japan). Silica gel was obtained from Qingdao Haiyang Chemical Co., Ltd. (Qingdao, China). Analytical-grade ethyl acetate, methanol, and dichloromethane were obtained from Fuyu Fine Chemical Co., Ltd. (Tianjin, China).

2.2 Plant material

The roots and rhizomes of licorice (*G. uralensis* Fisch.) were obtained from the Institute of Medicinal Plant Development, Chinese Academy of Medical Sciences, and Peking Union Medical College in November 2018 in Beijing. It was identified by Associate Professor Cha Qin from the Institute of Chinese Materia Medica of Bijie City. A voucher specimen (No. 2018-1101) was deposited at the Key Laboratory of Pharmacy of Bijie City First People's Hospital, Guizhou, China.

2.3 Extraction and isolation of glycycoumarin

Licorice (21 kg) was powdered and extracted thrice with 90% (v/v) ethanol for 2 h under reflux. The extracts were pooled and filtered, concentrated *in vacuo* to remove ethanol, and free-dried to obtain a dry licorice alcohol extract (3.6 kg). The licorice extract was dissolved in distilled water and extracted using ethyl acetate. The

resulting ethyl acetate extract (860 g) was applied to a silica gel column and successively eluted with 0, 5, 10, 30, 50, and 100% (v/v) methanol in dichloromethane. The eluents from the 5% methanol application were collected and subjected to MCI GEL column chromatography for decolorization. The extracted compounds were then separated by repeated column chromatography and preparative high-performance liquid chromatography (HPLC) to isolate GCM. The chemical structure of the isolated GCM was identified by comparing the mass and fragmentation profiles obtained by electrospray ionization mass spectrometry (ESI-MS), as well as nuclear magnetic resonance (^{1}H- and ^{13}C-NMR) spectra (Bruker AV-600, Fällanden, Switzerland) with those available in the literature. We also compared the GCM HPLC retention times and online UV spectra with those of the reference compound. The purity of GCM was assessed using HPLC-UV analysis.

2.4 Animals

Male Sprague-Dawley rats (200 ± 20 g) were obtained from SJA Laboratory Animal Co. Ltd. (Hunan, China). All animals were kept under standard conditions of light, humidity, and temperature, and were allowed free access to a standard diet and water. All animal experiments were approved by the Animal Ethics Committee of Bijie City First People's Hospital (BY[2019]-02-198). On the day before GCM administration, rats were subjected to a minor surgical procedure. Briefly, a polyurethane catheter (0.59 mm ID, 0.94 mm OD; Skillsmodel Limited, Beijing, China) was cannulated into the right jugular vein while under anesthesia induced using an intraperitoneal dose of chloral hydrate at 350 mg/kg. After surgery, the rats were individually placed in metabolism cages to allow recovery for at least 24 h. The rats were fasted overnight with free access to water before GCM administration.

2.5 Preparation of standards and quality control samples

GCM (2.0 mg) and IS (2.0 mg) were accurately weighed and then dissolved in methanol to prepare respective stock solutions with a concentration of 2 mg/mL each. After dilution with methanol, the stock solution was prepared as a series of standard working solutions. The working solutions were used to spike the plasma, bile, urine, or tissue homogenates to obtain final GCM concentrations of 1, 2, 5, 10, 20, 50, 100, 200, 500, 1000, and 2000 ng/mL for the standard curve of all samples. The final concentration of IS used in the plasma, bile, urine, and tissue homogenates was 100 ng/mL. Four concentrations (5, 15, 150, and 1500 ng/mL) of quality control (QC) samples were freshly prepared for method validation.

2.6 Drug administration and sample collection

2.6.1 Drug administration

All GCM dosing drugs were freshly prepared at a concentration of 10 mg/mL prior to the experiments. Briefly, GCM was dissolved in normal saline containing 5% (v/v) Solutol HS 15. The animals were randomly divided into three groups. The *i. v.* administration group was treated intravenously with 10 mg/mL GCM by quick injection through the cannulated catheter, and approximately 0.2 mL saline with 20 units of heparin was injected to flush the catheter and prevent blood coagulation. The oral administration group was treated with 20 mg/mL GCM in a single gastric gavage dose, and the intraperitoneal injection group received 20 mg/kg GCM through intraperitoneal injection.

2.6.2 Plasma sample collection

Approximately 0.3 mL blood samples were collected via the cannula and placed into heparinized micro centrifuge (Eppendorf) tubes at multiple time-points (0.08, 0.25, 0.50, 1, 2, 3, 4, 5, 6, 7, 8, 10, 12, and 24 h) after GCM administration. The samples were centrifuged at 3000 × *g* for 5 min at 4°C for plasma separation; a 0.1 mL aliquot of each separated plasma sample was harvested and stored at −40°C until assessed.

2.6.3 Tissue sample collection

Twenty-five rats were randomly divided into five groups and administered 20 mg/kg GCM intraperitoneally. Samples of various tissues (heart, liver, spleen, lung, kidney, and brain) of a certain weight were collected from the rats at 0.5, 1, 2, 4, and 6 h following GCM administration. All tissues were then rinsed with normal saline to clean the blood, blotted with filter paper, and stored at −40°C until use. Blood samples were collected *via* the carotid artery at the specified time points, and plasma samples were harvested as described above.

2.6.4 Bile sample collection

Rats (n = 6) underwent bile fistula cannulation under anesthesia prior to bile sample collection. Bile samples from rats following *i. v.* GCM administration (10 mg/kg) were collected *via* cannula every 2 h over an 8 h collection period. Samples were collected from the catheter and delivered into acidified (0.1% HCl) centrifuge tubes. The rats were placed on thermostatic plates and kept under mild anesthesia throughout the experiment. The bile samples were diluted with saline and stored at −40°C until assayed.

2.6.5 Urine sample collection

Six rats were individually placed in metabolic cages and administered 10 mg/kg GCM by *i. v.* injection. Urine samples were collected over 24 h after administration in a urine reservoir containing 2 mL 0.1% HCl to avoid GCM degradation. Each urine reservoir was rinsed with 5 mL normal saline after collection. Every urine sample was diluted to 20 mL with normal saline and then stored at −40°C until assayed.

2.7 Determination of GCM levels in biological samples

Free (parent drug) and/or total (including parent and glucuronidated metabolites) GCM concentrations in rat plasma, tissues, urine, and bile were quantitatively assayed using LC-MS/MS before and after hydrolytic treatment with β-glucuronidase.

2.7.1 Preparation of plasma samples

Aliquots (100 μL) of plasma samples were divided into two equal fractions for determining the free and total GCM concentrations, as previously described (Chang et al., 2012). Briefly, two aliquots of 50 μL plasma were incubated at 37°C with or without β-glucuronidase at a concentration of 1,200 units for total and free GCM, respectively. After 40 min of incubation, 10 μL of IS (1,000 ng/mL) was added to the mixtures followed by extraction with ethyl acetate. After centrifugation, the clear ethyl acetate layer was transferred and concentrated using a freeze-dry concentration method at 4°C. Subsequently, the remaining material was reconstituted in 200 μL of 90% (v/v) methanol. A 10 μL aliquot of the supernatant was injected into the LC-MS/MS system for analysis.

2.7.2 Preparation of tissue samples

Tissue samples were accurately weighed and homogenized in ice-cold saline (1:4, w/v) using a glass tissue homogenizer. Homogenized organs were centrifuged at 12,000 × *g* for 10 min to obtain clear supernatants; the supernatant was then transferred to a clean test tube kept at −40°C until assayed.

2.7.3 Preparation of gastrointestinal tract solutions

The gastrointestinal tract solutions were collected as described previously (Kong et al., 2013). Briefly, rats were fasted overnight and sacrificed; the entire stomach, small intestine, and colon of each rat were removed, and their contents were rapidly collected on ice. Each of the contents was suspended in buffer solutions at pH 1.2, 6.8, and 7.4. Following mixing and centrifugation, the protein content of the gastrointestinal tract solutions was assayed using the BCA protein assay kit from Solarbio (Beijing, China) and then adjusted to 12 mg/mL for further study.

2.7.4 Preparation of bile and urine samples

Two aliquots of 50 μL prepared bile or urine samples were spiked with or without β-glucuronidase to determine the total or free GCM concentrations, as described above. The mixtures were incubated at 37°C for 40 min, and the mixtures were then spiked with 120 μL of ice-cold methanol containing IS to stop incubation. A 10 μL supernatant of each sample was used for the analysis.

2.8 Analysis of GCM stability in the gastrointestinal tract

The stability of GCM in the gastrointestinal tract, including chemical stability and enzymatic stability, was assessed using an *in vitro* method as described previously (Kong et al., 2013). Briefly, GCM was spiked into different pH (1.2, 6.8, and 7.4) buffers and gastrointestinal content solutions containing the GCM at a final concentration of 0.8 μg/mL. The solutions were then mixed and incubated at 37°C. Aliquots of 200 μL samples were collected at 0.5, 1, 2, and 4 h, and 200 μL ice-cold methanol containing 200 ng/mL IS was added to stop the incubation. After centrifugation, 10 μL of the supernatant was used for analysis. Each experiment was performed in triplicate.

2.9 LC-MS/MS conditions

An LC-MS/MS system comprising an Agilent 1260 HPLC system (Palo Alto, CA, United States) and an Applied Biosystems 4500 Q-Trap mass spectrometer equipped with an electrospray ionization source (Foster City, CA, United States) was used. Chromatographic separation was performed on a C18 column (100 × 4.6 mm, 3 μm, Thermo Fisher Scientific, Waltham, MA, United States) maintained at 30°C. The mobile phases comprised 0.1% (v/v) formic acid in water (A) and acetonitrile (B) at a flow rate of 0.4 mL/min. Phase B was linearly increased from 40% to 90% over a period of 0.1 min, maintained at 90% for 2 min, and then decreased to 40% for re-equilibration. The total run time was 4 min. For mass spectrometry detection, the positive ion mode was used and the ion spray voltage was set at 5,500 V. The operating conditions were as follows: ion source temperature, 450°C; curtain gas, 20 psi; collision gas, medium. Ion source gases 1 and 2 were both at 60 psi. The collision energies were 37 and 42 V, and the declustering potentials for GCM and IS were 110 and 136 V, respectively. Quantification was performed by multiple reaction monitoring (MRM) of molecular ions and product ions at *m/z* 369.3 and 284.7 for GCM and 337.0 and 280.9 for IS (Supplementary Figure S1). Analyst® software (Version 1.6.3) was used for data acquisition and peak integration.

2.10 Pharmacokinetic data analysis

Pharmacokinetic parameters were calculated based on changes in the plasma drug concentration *versus* the time profile of each rat using a non-compartmental model using WinNonlin software (Pharsight Corporation, Mountain View, CA, United States, Version 6.1). Plasma maximum concentration (Cmax) and the time of Cmax (Tmax); initial plasma concentration (C_0) for *i. v.* administration; terminal elimination half-life ($t_{1/2,\ \lambda z}$); area under the plasma concentration *versus* time curve from time zero to the last sample collection time point (AUC_{0-t}) and to infinity ($AUC_{0-\infty}$); total body clearance (CL); and volume of distribution ($V_{d,\ \lambda z}$). Absolute bioavailability (F) was calculated based on the $AUC_{0-\infty,\ oral}/AUC_{0-\infty,\ i.\ v.}$ at equivalent doses.

3 Results and discussion

3.1 Isolation and identification of glycycoumarin

After several purification steps (silica gel column, MCI GEL™ column, and reverse-phase HPLC), pure GCM was isolated. Its chemical structure was characterized based on the high-resolution ESI-MS (HRESI-MS), ^{1}H-NMR, and ^{13}C-NMR spectra (Supplementary Figures S2–S5, Supplementary Material) in accordance with the literature (Ji et al., 2016). Furthermore, the HPLC retention time and online UV spectrum of the isolated GCM were the same as those of the reference standard. The purity of the isolated GCM was determined to be 97.4% using HPLC-UV analysis.

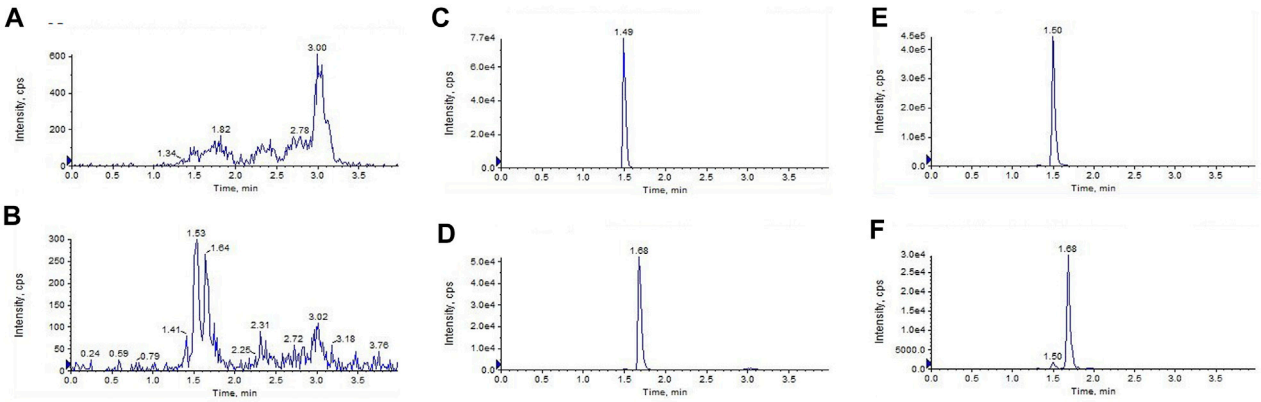

FIGURE 2
Liquid chromatography tandem-mass spectrometry chromatograms of **(A,B)**blank plasma **(C,D)** blank plasma spiked with glycycoumarin and the internal standard(IS) both at 100 ng/mL, and **(E,F)** the plasma sample 1 h after *i. v.* administration of glycycoumarin at a single dose of 10 mg/kg and spiked with IS.

3.2 Method validation

Before the pharmacokinetic studies, a LC-MS/MS method was established and validated for the quantitative analysis of free and total GCM concentrations in rat plasma, urine, bile, and tissues.

3.2.1 Specificity

Figure 2 shows the representative LC-MS/MS chromatograms of the blank plasma (Figures 2A, B), quality control plasma samples (blank plasma supplemented with GCM and IS at 100 ng/mL, respectively. Figures 2C, D), and plasma samples collected 1 h after *i. v.* dosing (10 mg/kg) of GCM (Figures 2E, F). The retention times of GCM and IS were 1.49 and 1.68 min, respectively. Supplementary Figure S6 shows the typical MRM chromatograms of pooled blank urine and bile samples spiked with GCM and IS; these were eluted at 1.49 and 1.68 min, respectively. The typical chromatograms of blank tissue homogenates spiked with GCM and IS were obtained under the same conditions (Supplementary Figure S7). This revealed that GCM and IS were completely separated, and that there was no interference to influence GCM quantification in the biological sample.

3.2.2 Linearity, LLOD, and LLOQ

The standard calibration curves for rat plasma, urine, and bile containing GCM exhibited good linearity (R^2 > 0.99) over a concentration range of 2–2,000 ng/mL. The LLOD was 1 ng/mL, and the LLOQ was 2 ng/mL. Linear responses of GCM were observed at 5–2,000 ng/mL in the tissue samples. The LLOD was 1 ng/mL, and the LLOQ was 5 ng/mL. The results of the linear regression analyses are listed in Supplementary Table S1.

3.2.3 Extraction recovery and matrix effect

The average extraction recovery of the QC samples ranged from 85.47% to 111.54% for GCM in all biological samples. The internal standard normalized matrix factor (ISNMF), which was evaluated by the matrix factor of the analyte *versus* the internal standard matrix factor, was recommended for evaluating the matrix effects (De Nicolò et al., 2017). The RSD of ISNMFs ranged from 1.75% to 14.14%, indicating that the influence of co-eluted substances could be corrected by using the IS.

3.2.4 Stability, precision, and accuracy

Stability studies were carried out by analyzing different concentrations for QC after biological sample preparation at 4°C for 24 h and storage at −40°C for 7 days, respectively. As shown in Supplementary Table S2, their accuracies ranged from 85.53% to 114.13%, and all RSDs were within 14%.The intra-day and inter-day precision and accuracy for GCM are shown in Supplementary Table S3. The intra-day and inter-day precision of GCM determinations were <15%, and their accuracy ranged from 85.69% to 118.42% at 5, 15, 150, and 1,500 ng/mL.

3.2.5 Dilution

The accuracy of dilution for 10,000 ng/mL GCM (n = 5) ranged from 86.24% to 112.28% in the plasma, heart, liver, and spleen. These values correspond to the Food and Drug Administration (FDA) criteria for bioanalytical validation methods.

3.3 Pharmacokinetics

To better understand the oral absorption and disposal process of GCM in the body, free and total plasma GCM concentrations (the parent form and glucuronidated metabolites) were determined. The plasma concentration *versus* time profiles of free and/or total GCM in rats after receiving an *i. v.* dose (10 mg/kg) or oral administration (20 mg/kg) are shown in Figure 3. The pharmacokinetic parameters of the free and/or total GCM are presented in Table 1. After *i. v.* dosing, only a minor quantity of parent GCM was detected in plasma samples after the first 6 h post-administration; it was almost undetectable in plasma collected after 6 h. It might be transformed into its glucuronidated metabolites because relatively high GCM concentrations were detected in the plasma after enzymatic

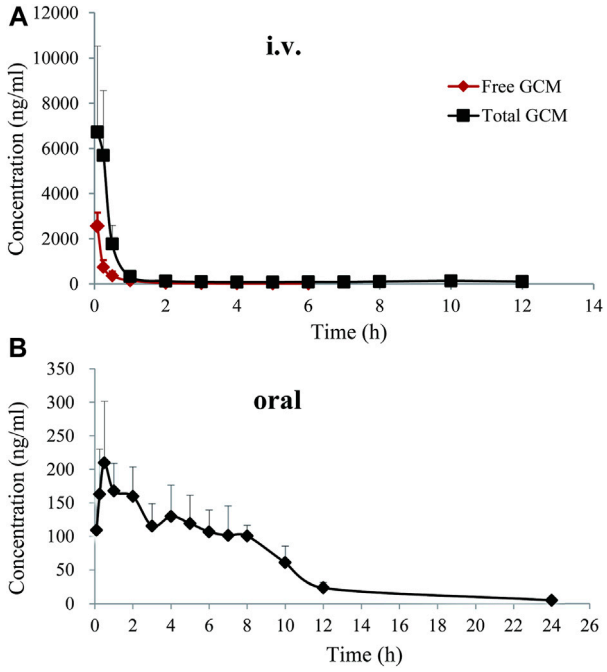

FIGURE 3
Free and total plasma concentration-time profiles of glycycoumarin in rats after single intravenous (*i.v.*, 10 mg/kg)or oral administration (20 mg/kg). Each pointrepresentsthe mean ± standard deviation (n = 6).

treatment with *β*-glucuronidase. The results showed that the $AUC_{0-\infty}$ of conjugated GCM was approximately four times higher than that of free GCM. This implies that glucuronidated metabolites are the major form of GCM in rats. The glucuronidated metabolites were eliminated slowly from the body, with average $t_{1/2,\lambda z}$ values of 2.46 h after *i. v.* administration, more than 3 folds those of free GCM.

After oral administration of 20 mg/kg, free GCM was almost undetectable in the plasma after 2 h. However, after treatment with *β*-glucuronidase, GCM was detected in the plasma over 24 h after dosing. Total GCM reached a C_{max} of 232.18 ng/mL at a T_{max} of 0.79 h, and was eliminated from the body with a $t_{1/2,\lambda z}$ of 4.75 h; the $AUC_{0-\infty}$ was 1,017.85 ng h/mL.The absolute bioavailability of GCM was not determined because the concentration of free GCM after oral administration was too low to be detected at most time points. The bioavailability of total GCM was estimated to be 9.22%, which was calculated by an $AUC_{0-\infty}$ of total GCM. This result suggested that a certain amount of GCM could be absorbed into the body and then quickly metabolized into glucuronidated metabolites *via* intestinal and/or hepatic first-pass effects.

GCM is reported to be rapidly absorbed into circulation and is involved in Phase I and Phase II biotransformation; further, GCM glucuronidation and hydroxylation are the main metabolic pathways involved (Wang et al., 2014). The isoprenyl methyl group is the major metabolic participant in hydroxylation reactions. The glucuronidation products include the parent GCM and its hydroxyl metabolites conjugated to glucuronic acid. However, in this study, our developed method could only monitor GCM but not detect other metabolites. Cytochrome P450 enzymes are also reported to be involved in GCM metabolism because many GCM metabolites have been demonstrated to be catalyzed in rat liver microsomes (Wang et al., 2014). Thus, the most likely reason for the low oral bioavailability of GCM might be related to its extensive first-pass effect when transiting the liver and/or intestine, which deserves further study.

3.4 *In vitro* stability of GCM

In addition to hepatic metabolism, chemical stability, and drug metabolism in the intestine are considered important factors for low oral bioavailability (Crozier et al., 2009; Stalmach et al., 2012). To further explore whether the low bioavailability of GCM was related to intestinal metabolism, GCM was investigated *in vitro* using different pH buffer solutions and in gastrointestinal content samples. The results indicated that GCM was relatively stable in these tested solutions (pH 1.2, 6.8, and 7.4) and in stomach content solutions after 4 h of incubation at 37°C, but was unstable in the small intestine and colon content solutions (Figure 4). This result is consistent with reports on polyphones, which undergo rapid and extensive first-pass effects via conjugation in the intestinal tract and are poorly bioavailable (Stalmach et al., 2012; Ma et al., 2014; Wang et al., 2014; Wang et al., 2015). Thus, these results indicate the intestinal tract and hepatic first-pass metabolism are the main reasons for low GCM bioavailability.

3.5 Tissue distribution

The tissue distribution profile of drugs or compounds *in vivo* is closely related to their pharmacological effects, which determine the strength and duration of these effects. Further, understanding the characteristics of tissue distribution of drugs or compounds is helpful to further understand the sites and extent of their accumulation *in vivo* (Yuan et al., 2015). This will be beneficial in predicting adverse drug reactions, which are significant for providing guidance, especially for certain drugs or compounds metabolized in the body.

Our previous studies have shown that intraperitoneal injection of GCM exerts strong hepatoprotective and anti-liver cancer activity (Yan et al., 2018; Zhang et al., 2018). We thus questioned whether GCM is well-distributed in the liver tissue. Combining previous modes of drug administration (Song et al., 2015; Song et al., 2016; Yan et al., 2018), reducing the influence of individual absorption differences in animals, and directly observing the distribution of GCM in rats, intraperitoneal administration was used in the experiments reported here. After intraperitoneal administration of 20 mg/kg, GCM was widely distributed in all tissues, except the brain, as shown in Figure 5. Despite being a lipophilic polyhydroxy compound, GCM was not detected in brain samples. These results indicate that GCM cannot cross the blood-brain barrier. The highest GCM concentration was observed in the liver, followed by that in the spleen, lung, heart, and kidney; the concentration in the liver increased during 0.5–1 h, and then decreased. However, the GCM levels significantly

TABLE 1 Pharmacokinetic parameters of glycycoumarin (GCM) after a single intravenous (i.v., 10 mg/kg) or oral (20 mg/kg) administration to rats. All data are expressed as the mean ± standard deviation (n = 6).

Parameters	i.v. (10 mg/kg)		Oral (20 mg/kg)
	Free GCM	Total GCM	Total GCM
C_{max} (ng/mL)	-	-	232.18 ± 78.30
T_{max} (h)	0	0	0.79 ± 0.64
C_0 (ng/mL)	5686.95 ± 1362.90	9727.38 ± 5068.72	-
$t_{1/2}$, λz (h)	0.71 ± 0.11	2.46 ± 0.61	4.75 ± 0.46
AUC_{0-t} (ng h/mL)	1163.66 ± 283.73	5033.80 ± 1840.97	983.23 ± 217.32
$AUC_{0-\infty}$(ng h/mL)	1169.64 ± 283.36	5521.77 ± 2112.90	1017.85 ± 238.94
CL/F (L/h/kg)	8.95 ± 2.0	-	-
$V_{d,\ \lambda z}$/F	9.25 ± 3.13	-	-
F (%)	-	-	9.22
Urine recovery (% of dose)			
0–12 h	0.28 ± 0.25	0.74 ± 0.46	
12–24 h	0.11 ± 0.10	0.23 ± 0.22	
Bile recovery (% of dose)			
0–2 h	0.20 ± 0.12	1.97 ± 0.59	
2–4 h	0.08 ± 0.06	1.71 ± 0.55	
4–6 h	0.05 ± 0.04	1.51 ± 0.38	
6–8 h	nd	1.33 ± 0.96	

"–" not applicable; "nd" not detectable.

decreased to undetectable levels by 6 h after dosing in most tissues. The highest concentration detected in the liver implied that the liver may be the main binding site for GCM, and that hepatic clearance may represent the primary route for GCM elimination. This may also help explain the hepatic first-pass effect of GCM. The concentration of GCM in plasma decreased rapidly after 0.5 h, which is in agreement with the results of the pharmacokinetic studies. Compared with the plasma concentrations, GCM can be quantified in various tissue samples, meaning that it has a relatively high degree of tissue distribution. Overall, these results provide an important material basis for the pharmacological effects of GCM.

3.6 Urinary and biliary excretion of GCM

The total amount of a drug in the circulatory system can be calculated after *i. v.* administration, which can yield the precise excretion rate of a parent drug in bile and urine. However, oral administration cannot result in this because of individual differences in drug absorption. Therefore, we performed *i. v.* administration to explore the excretion rate of GCM. The urinary and biliary recoveries of free and total GCM after *i. v.* administration are displayed in Table 1. The results indicated that a small amount of GCM was excreted as glucuronidated metabolites from bile with approximately 1.97%, 1.71%, 1.51%, and 1.33% of the dose administered over the periods of 0–2, 2–4, 4–6 and 6–8 h post-dosing, respectively. Furthermore, very low amounts of GCM in the parent form were excreted from bile: <1% of the delivered dose over 0–8 h. The urinary recovery of GCM over 24 h after dosing was 0. 39% and 0.97% of the administered dose for free and total GCM, respectively. In the study of another polyphenol compound, a large number of sulfonated metabolites can also be excreted through bile and urine in addition to glucuronidated metabolites (Chang et al., 2012). This suggests that biliary and urinary excretion represent minor pathways for glucuronidated GCM metabolites.

The liver is rich in a large number of phase I and II metabolic enzymes, including CYP450, UDP-glucuronosyltransferases (UGTs), and sulfotransferases, which are the main sites of drug metabolism (Zhang et al., 2020). Our results show that a large amount of GCM is distributed in the liver and further metabolized in the liver. In addition to phase I metabolism, parent GCM and its phase I metabolites can undergo glucuronidation reactions by UGT enzymes because there is an abundance of UGT enzymes including UGT1A1, UGT1A3, UGT1A4, UGT1A6, UGT1A9, UGT1A19, and UGT2B7 in the liver (Wang et al., 2014). More recently, GCM was found to strongly inhibit P450 family members, including CYP1A2, CYP2B6, CYP2C8, CYP2C9, and CYP2C19, as well as UGT1A19 in human liver microsomes (Li et al., 2017; Kuang et al., 2021). Furthermore, GCM also significantly inhibits CYP2D6 activity, which mediates the metabolism of approximately 30% of the

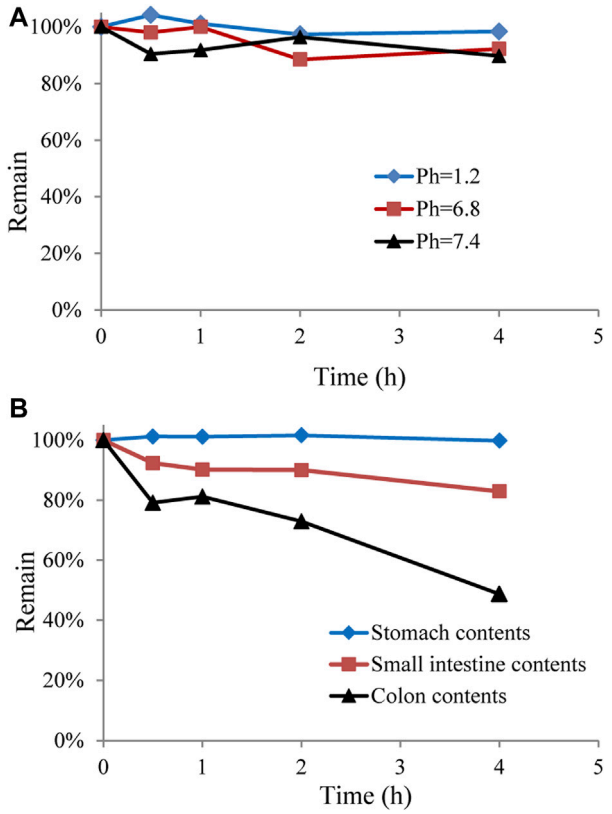

FIGURE 4
Stability of glycycoumarin in different pH buffer solutions and in gastrointestinal content solutions. Each point represents the mean ± standard deviation (n = 3).

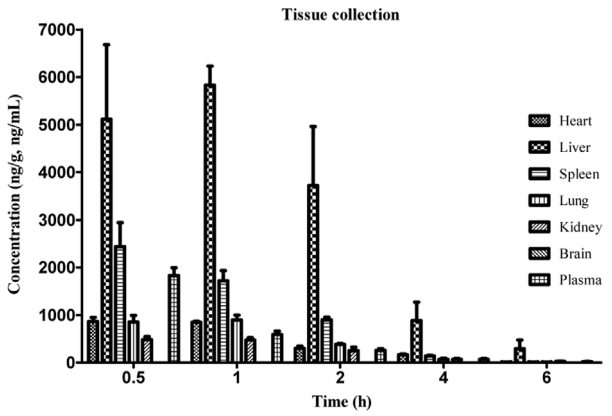

FIGURE 5
Concentration of glycycoumarin (GCM) in various tissues at the indicated time points after intraperitoneal administration at a single dose of 20 mg/kg to rats. Each point represents the mean ± standard deviation (n = 5).

drugs on the market (Qiao et al., 2014a). Glycyrol, with a similar structure to that of GCM, is another major bioactive coumarin in licorice, as well as being a metabolite of GCM, and is not absorbed into the blood after oral administration (Wang et al., 2015). However, glycyrol also displays competitive inhibitory effects on CYP1A1 and CYP2C9 in human liver microsomes(Kim et al., 2016). In summary, the above results suggest that GCM may cause potential drug interactions when co-administered with agents metabolized by such enzymes. Therefore, as a lead compound with developmental value, the mechanisms of GCM absorption and its inhibitory effects on P450 should be investigated further.

4 Conclusion

A simple and reliable LC-MS/MS method for quantifying GCM concentrations in plasma, urine, bile, and tissue samples was developed and validated. To the best of our knowledge, this is the first systematic report regarding the pharmacokinetic and tissue distribution profiles of GCM in rats. The obtained pharmacokinetic and tissue distribution data indicate that GCM can be absorbed by the body with low bioavailability, which is then rapidly converted to conjugated GCM metabolites, and that only a small amount is removed from the body *via* biliary and urinary excretion. Furthermore, GCM is distributed rapidly and widely in various tissues, with the liver representing the major distribution site, whereas GCM does not cross the blood-brain barrier. These results can help us better understand the pharmacological effects of GCM in the body.

Data availability statement

The original contributions presented in the study are included in the article/Supplementary Material, further inquiries can be directed to the corresponding author.

Ethics statement

The animal study was reviewed and approved by All animal experiments were approved by the Animal Ethics Committee at the Bijie City First People's Hospital.

Author contributions

LY, QC, XZ, and ZW participated in the research design. LY, LC, YD, XW, SO, and WZ conducted the experiments. LC, JY, and SW analyzed the data. LY and QC wrote the manuscript. All authors contributed to the article and approved the submitted version.

Funding

This study was financially supported by the Science and Technology Support Program of Guizhou province ([2020] 4Y118) and (ZK[2023]561), and Foshan "Fourteen Five" Key Medical Specialty Construction Project.

Conflict of interest

The authors declare that the research was conducted in the absence of any commercial or financial relationships that could be construed as a potential conflict of interest.

Publisher's note

All claims expressed in this article are solely those of the authors and do not necessarily represent those of their affiliated organizations, or those of the publisher, the editors and the reviewers. Any product that may be evaluated in this article, or claim that may be made by its manufacturer, is not guaranteed or endorsed by the publisher.

Supplementary material

The Supplementary Material for this article can be found online at: https://www.frontiersin.org/articles/10.3389/fphar.2023.1216985/full#supplementary-material

References

Adianti, M., Aoki, C., Komoto, M., Deng, L., Shoji, I., Wahyuni, T. S., et al. (2014). Anti-hepatitis C virus compounds obtained from Glycyrrhiza uralensis and other Glycyrrhiza species. *Microbiol. Immunol.* 58, 180–187. doi:10.1111/1348-0421.12127

Asl, M. N., and Hosseinzadeh, H. (2008). Review of pharmacological effects of Glycyrrhiza sp. and its bioactive compounds. *Phytother. Res.* 22, 709–724. doi:10.1002/ptr.2362

Chang, Q., Wang, G. N., Li, Y., Zhang, L., You, C., and Zheng, Y. (2012). Oral absorption and excretion of icaritin, an aglycone and also active metabolite of prenylflavonoids from the Chinese medicine Herba Epimedii in rats. *Phytomedicine* 19, 1024–1028. doi:10.1016/j.phymed.2012.05.017

Crozier, A., Jaganath, I. B., and Clifford, M. N. (2009). Dietary phenolics: Chemistry, bioavailability and effects on health. *Nat. Prod. Rep.* 26, 1001–1043. doi:10.1039/b802662a

De Nicolò, A., Cantù, M., and D'avolio, A. (2017). Matrix effect management in liquid chromatography mass spectrometry: The internal standard normalized matrix effect. *Bioanalysis* 9, 1093–1105. doi:10.4155/bio-2017-0059

Fu, Y., Chen, J., Li, Y. J., Zheng, Y. F., and Li, P. (2013). Antioxidant and anti-inflammatory activities of six flavonoids separated from licorice. *Food Chem.* 141, 1063–1071. doi:10.1016/j.foodchem.2013.03.089

Fukuchi, K., Okudaira, N., Adachi, K., Odai-Ide, R., Watanabe, S., Ohno, H., et al. (2016). Antiviral and antitumor activity of licorice root extracts. *Vivo* 30, 777–785. doi:10.21873/invivo.10994

Ji, S., Li, Z., Song, W., Wang, Y., Liang, W., Li, K., et al. (2016). Bioactive constituents of Glycyrrhiza uralensis (licorice): Discovery of the effective components of a traditional herbal medicine. *J. Nat. Prod.* 79, 281–292. doi:10.1021/acs.jnatprod.5b00877

Kim, S. J., Kim, S. J., Hong, M., Choi, H. G., Kim, J. A., and Lee, S. (2016). Investigation of selective inhibitory effects of glycyrol on human CYP 1A1 and 2C9. *Xenobiotica* 46, 857–861. doi:10.3109/00498254.2015.1131345

Kong, L. T., Wang, Q., Xiao, B. X., Liao, Y. H., He, X. X., Ye, L. H., et al. (2013). Different pharmacokinetics of the two structurally similar dammarane sapogenins, protopanaxatriol and protopanaxadiol, in rats. *Fitoterapia* 86, 48–53. doi:10.1016/j.fitote.2013.01.019

Kuang, Y., Chai, Y., Xu, L., Wang, Z., Liang, L., Qiao, X., et al. (2021). Glabrone as a specific UGT1A9 probe substrate and its application in discovering the inhibitor glycycoumarin. *Eur. J. Pharm. Sci.* 161, 105786. doi:10.1016/j.ejps.2021.105786

Li, G., Simmler, C., Chen, L., Nikolic, D., Chen, S. N., Pauli, G. F., et al. (2017). Cytochrome P450 inhibition by three licorice species and fourteen licorice constituents. *Eur. J. Pharm. Sci.* 109, 182–190. doi:10.1016/j.ejps.2017.07.034

Ma, Y., Zeng, M., Sun, R., and Hu, M. (2014). Disposition of flavonoids impacts their efficacy and safety. *Curr. Drug Metab.* 15, 841–864. doi:10.2174/1389200216666150206123719

Qiao, X., Ji, S., Yu, S. W., Lin, X. H., Jin, H. W., Duan, Y. K., et al. (2014a). Identification of key licorice constituents which interact with cytochrome P450: Evaluation by LC/MS/MS cocktail assay and metabolic profiling. *AAPS J.* 16, 101–113. doi:10.1208/s12248-013-9544-9

Qiao, X., Liu, C. F., Ji, S., Lin, X. H., Guo, D. A., and Ye, M. (2014b). Simultaneous determination of five minor coumarins and flavonoids in Glycyrrhiza uralensis by solid-phase extraction and high-performance liquid chromatography/electrospray ionization tandem mass spectrometry. *Planta Med.* 80, 237–242. doi:10.1055/s-0033-1360272

Song, X., Yin, S., Huo, Y., Liang, M., Fan, L., Ye, M., et al. (2015). Glycycoumarin ameliorates alcohol-induced hepatotoxicity via activation of Nrf2 and autophagy. *Free Radic. Biol. Med.* 89, 135–146. doi:10.1016/j.freeradbiomed.2015.07.006

Song, X., Yin, S., Zhang, E., Fan, L., Ye, M., Zhang, Y., et al. (2016). Glycycoumarin exerts anti-liver cancer activity by directly targeting T-LAK cell-originated protein kinase. *Oncotarget* 7, 65732–65743. doi:10.18632/oncotarget.11610

Stalmach, A., Edwards, C. A., Wightman, J. D., and Crozier, A. (2012). Gastrointestinal stability and bioavailability of (poly)phenolic compounds following ingestion of Concord grape juice by humans. *Mol. Nutr. Food Res.* 56, 497–509. doi:10.1002/mnfr.201100566

Wang, Q., Qiao, X., Liu, C. F., Ji, S., Feng, L. M., Qian, Y., et al. (2014). Metabolites identification of glycycoumarin, a major bioactive coumarin from licorice in rats. *J. Pharm. Biomed. Anal.* 98, 287–295. doi:10.1016/j.jpba.2014.06.001

Wang, Q., Qiao, X., Qian, Y., Liu, C. F., Yang, Y. F., Ji, S., et al. (2015). Metabolites identification of glycyrin and glycyrol, bioactive coumarins from licorice. *J. Chromatogr. B Anal. Technol. Biomed. Life Sci.* 983-984, 39–46. doi:10.1016/j.jchromb.2014.12.028

Yan, M., Ye, L., Yin, S., Lu, X., Liu, X., Lu, S., et al. (2018). Glycycoumarin protects mice against acetaminophen-induced liver injury predominantly via activating sustained autophagy. *Br. J. Pharmacol.* 175, 3747–3757. doi:10.1111/bph.14444

Yuan, T. T., Xu, H. T., Zhao, L., Lv, L., He, Y. J., Zhang, N. D., et al. (2015). Pharmacokinetic and tissue distribution profile of curculigoside after oral and intravenously injection administration in rats by liquid chromatography-mass spectrometry. *Fitoterapia* 101, 64–72. doi:10.1016/j.fitote.2014.12.012

Zhang, E., Yin, S., Lu, X., Ye, L., Fan, L., and Hu, H. (2018). Glycycoumarin sensitizes liver cancer cells to ABT-737 by targeting de novo lipogenesis and TOPK-survivin Axis. *Nutrients* 10, 353. doi:10.3390/nu10030353

Zhang, Y., Peng, Y., Guangji, W., and Sun, J. (2020). Advances in study of phase II metabolic enzyme expression and activity under diseases status. *Chin. J. Clin. Pharmacol. Ther.* 25, 686–700. doi:10.12092/j.issn.1009-2501.2020.06.012

frontiers | Frontiers in Pharmacology

TYPE Original Research
PUBLISHED 20 July 2023
DOI 10.3389/fphar.2023.1200828

OPEN ACCESS

EDITED BY
Guo Ma,
Fudan University, China

REVIEWED BY
Karen Rowland-Yeo,
Simcyp, United Kingdom
Yue Ding,
Shanghai University of Traditional Chinese Medicine, China

*CORRESPONDENCE
Faleh Alqahtani,
afaleh@ksu.edu.sa

RECEIVED 05 April 2023
ACCEPTED 04 July 2023
PUBLISHED 20 July 2023

CITATION
Alasmari F, Alasmari MS, Muwainea HM, Alomar HA, Alasmari AF, Alsanea S, Alshamsan A, Rasool MF and Alqahtani F (2023), Physiologically-based pharmacokinetic modeling for single and multiple dosing regimens of ceftriaxone in healthy and chronic kidney disease populations: a tool for model-informed precision dosing.
Front. Pharmacol. 14:1200828.
doi: 10.3389/fphar.2023.1200828

Physiologically-based pharmacokinetic modeling for single and multiple dosing regimens of ceftriaxone in healthy and chronic kidney disease populations: a tool for model-informed precision dosing

Fawaz Alasmari[1], Mohammed S. Alasmari[1], Hussa Mubarak Muwainea[1], Hatun A. Alomar[1], Abdullah F. Alasmari[1], Sary Alsanea[1], Aws Alshamsan[2], Muhammad F. Rasool[3] and Faleh Alqahtani[1]*

[1]Department of Pharmacology and Toxicology, College of Pharmacy, King Saud University, Riyadh, Saudi Arabia, [2]Department of Pharmaceutics, College of Pharmacy, King Saud University, Riyadh, Saudi Arabia, [3]Department of Pharmacy Practice, Faculty of Pharmacy, Bahauddin Zakariya University, Multan, Pakistan

Introduction: Ceftriaxone is one of commonly prescribed beta-lactam antibiotics with several label and off-label clinical indications. A high fraction of administered dose of ceftriaxone is excreted renally in an unchanged form, and it may accumulate significantly in patients with impaired renal functions, which may lead to toxicity.

Methods: In this study, we employed a physiologically-based pharmacokinetic (PBPK) modeling, as a tool for precision dosing, to predict the biological exposure of ceftriaxone in a virtually-constructed healthy and chronic kidney disease patient populations, with subsequent dosing optimizations. We started developing the model by integrating the physicochemical properties of the drug with biological system information in a PBPK software platform. A PBPK model in an adult healthy population was developed and evaluated visually and numerically with respect to experimental pharmacokinetic data. The model performance was evaluated based on the fold error criteria of the predicted and reported values for different pharmacokinetic parameters. Then, the model was applied to predict drug exposure in CKD patient populations with various degrees of severity.

Results: The developed PBPK model was able to precisely describe the pharmacokinetic behavior of ceftriaxone in adult healthy population and in mild, moderate, and severe CKD patient populations. Decreasing the dose by approximately 25% in mild and 50% in moderate to severe renal disease provided a comparable exposure to the healthy population. Based on the simulation of multiple dosing regimens in severe CKD population, it has been found that accumulation of 2 g every 24 h is lower than the accumulation of 1 g every 12 h dosing regimen.

Discussion: In this study, the observed concentration time profiles and pharmacokinetic parameters for ceftriaxone were successfully reproduced by

the developed PBPK model and it has been shown that PBPK modeling can be used as a tool for precision dosing to suggest treatment regimens in population with renal impairment.

KEYWORDS

PBPK, Pk-sim®, CKD, ceftriaxone, PK parameters

1 Introduction

Ceftriaxone is a third-generation cephalosporin antibiotic with a broad-spectrum activity against a wide range of microbial infections. Mechanistically, ceftriaxone acts as a bactericidal agent by inactivating penicillin-binding proteins in the outer cytoplasmic membrane and inhibiting bacterial cell wall synthesis (Fontana et al., 1998; Kocaoglu and Carlson, 2015). Due to its physicochemical characteristics, ceftriaxone can cross different biological barriers and penetrate deep into other systemic tissues, including the blood-brain barrier. Thus, it has been approved to treat infections that affect various body organs, including the central nervous system, lung tissue, skin and soft tissue, bone and joints, and urinary tract infections. (Steele, 1984; Le Turnier et al., 2019). It is well tolerated and exhibits a good safety profile at the standard doses with a predictable pharmacokinetic behavior. Clinically, ceftriaxone can be used as empirical therapy before the culture susceptibility is available, and then treatment protocol can be converted to a pathogen-specific therapy. According to the literature, 33%–67% of ceftriaxone is eliminated in unchanged form through the kidney, while the remaining fraction is excreted through the biliary system (Patel and Kaplan, 1984). The protein bound fraction of ceftriaxone in the plasma was estimated to be 60%–95% (Popick et al., 1987). Given that ceftriaxone exhibits very low bioavailability after oral administration (<1%), it is only administered parenterally as intravenous or intramuscular injections (Nau et al., 2010).

One of the most determinants of drug kinetic behavior is the kidney's functional status, and pharmacokinetic parameters are highly affected in patients with chronic kidney disease (CKD) (Rowland Yeo et al., 2011; Velenosi and Urquhart, 2014). Therefore, patients with CKD should be closely monitored, especially for renally excreted drugs (Tan et al., 2018). Appropriate dose selection according to the functional status of the kidneys is necessary to avoid drug build-up in the body, which may increase the risk of toxicity (Trotman et al., 2005; Patel et al., 2010; Morales-Alvarez, 2020). According to recently published data (Lacroix et al., 2021), severe adverse reactions, including deaths, convulsions, hallucinations, and other brain toxicities, were seen in patients treated with ceftriaxone. It has been mentioned that these toxic events were attributed to ceftriaxone. A recommendation has been given to clinicians to avoid this danger, especially in patients with renal impairment. Notably, the plasma level of ceftriaxone was found to be above the toxic limits in many patients. Therefore, proper administration of ceftriaxone is necessary to achieve the optimal benefit and prevent potential toxicities by maintaining ceftriaxone plasm levels within therapeutic ranges and avoiding any accumulation (Aloy et al., 2020; Chahine, 2022).

Physiologically-based pharmacokinetic (PBPK) models are mathematical and quantitative in nature, and they are developed to predict drug absorption, distribution, metabolism, and excretion (ADME). Modeling and simulation are now standard practices in the drug development process with the ultimate goal of improving the efficacy and safety of drugs (Li et al., 2017; Taskar et al., 2020; Verscheijden et al., 2020; Wang et al., 2021). In early clinical trials, several patient populations are inaccessible, either ethically or for other reasons, and they cannot be included in clinical studies, such as pediatrics, pregnant women, or patients with chronic renal and hepatic diseases. PBPK models are one of the alternative approaches that are authenticated to predict drug exposure in those populations with subsequent dosing suggestions based on individualized physiological needs. PBPK models have been used in various fields, such as human health risk assessment, environmental risk assessment, and drug discovery and development. They are considered a powerful approach for detecting the concentration of xenobiotics in tissues of interest, and they facilitate the *in vitro* to *in vivo* extrapolation. Accurate parametrization of the models is very important for the extrapolation and application of the PBPK model (Thiel et al., 2015).

According to clinical indications, ceftriaxone has been recommended to be given in doses of 250 mg, 500 mg, 1 g, or 2 g daily or two times a day for a specific period of time. A previous study demonstrated alterations in the PK parameters of ceftriaxone in patients with mild, moderate, and severe renal impairment (Patel et al., 1984). Except for patients on dialysis, the study did not recommend dosing modification as long as no more than 2 g/day was prescribed. However, the recently published data about ceftriaxone-induced toxicity mentioned that the median dose that intoxicated patients administered was 1.7 g/day (Lacroix et al., 2021). Therefore, using the PBPK method is highly suitable in the current situation to provide a quick overview of drug exposure in the CKD population and validate the PK information of ceftriaxone that might be required to avoid the potential of adverse events. Thus, the current study was performed to evaluate the need for ceftriaxone dosage adjustment in patients at different stages of renal insufficiency.

2 Materials and methods

2.1 PBPK software

PK-Sim software (version 9; Open System Pharmacology [OSP] Suite (https://www.open-systems-pharmacology.org) was used to simulate ceftriaxone concentrations over time in the plasma. The simulation was created based on the interplay between physicochemical, physiological, and biochemical factors (Cole et al., 2020). The PK-Sim platform was designed to be consisting of several building blocks while taking into account several external and internal factors that may influence the PK of the drugs (Farhan

TABLE 1 Clinical studies that were used for development and evaluation of the ceftriaxone PBPK model.

Dose	Inf. Time	N	Female (n)	Age (year)	Weight (kg)	Reference
Single dosing regimens of ceftriaxone in adult healthy population						
500 mg	20 min	10	5	29.5 (22–43)	65.2 (49–75)	Borner et al. (1985)
2000 mg	20 min	10	5	29.5 (22–43)	65.2 (49–75)	Borner et al. (1985)
500 mg	30 min	12	2	36 (21–47)	74.1 (53–94.8)	Patel et al. (1981)
1,000 mg	30 min	12	2	36 (21–47)	74.1 (53–94.8)	Patel et al. (1981)
2000 mg	30 min	12	2	36 (21–47)	74.1 (53–94.8)	Patel et al. (1981)
1,000 mg	30 min	30	5	34.5 (18–65)	79.3 ± 11.3	Harb et al. (2010)
500 mg	3 min	6	0	(21–37)	78.2	Seddon et al. (1980),[a]
500 mg	Bolus	6	N/A	N/A	N/A	Stoeckel (1981),[a]
1,500 mg	Bolus	6	N/A	N/A	N/A	Stoeckel (1981),[a]
3,000 mg	Bolus	6	0	(23–29)	N/A	McNamara et al. (1982),[a]
Multiple dosing regimens of ceftriaxone in adult healthy population						
500 mg q12 h	30 min	12	N/A	29 (19–45)	70 (57–99)	Pollock et al. (1982)
1,000 mg q12 h	30 min	12	N/A	31 (21–51)	73 (56–99)	Pollock et al. (1982)
2000 mg q12 h	30 min	12	N/A	33 (20–51)	74 (54.5–113.5)	Pollock et al. (1982)
2000 mg q24 h	30 min	8	N/A	28.3 (21–46)	71.8 (62.5–75.2)	Pollock et al. (1982)
Single dosing regimen of ceftriaxone in CKD patient population with various degree of severity						
1,000 mg	15 min	30	N/A	52.6 (21–75)	65.9 (51.8–103)	Patel et al. (1984)

[a]Data from these studies were used as external test dataset.

TABLE 2 Parameters that were used for developing the ceftriaxone PBPK model.

	Unit	Input value	Reported value	Reference of reported value
Physicochemical properties				
Molecular weight	g/mol	554.58	554.58	Wishart et al. (2018b)
Lipophilicity	Log	− 1.7	− 1.7	Wishart et al. (2018b)
pKa (acid)		2.7	2.7	Wishart et al. (2018a)
Distribution				
Partition coefficient model	Poulin/Theil model			PK-Sim
Cellular permeability model	PK-Sim standard model			
Fraction unbound	%	12.5[a]	5–40	Popick et al. (1987)
Elimination				
Biliary clearance	mL/min	3.67[a]	1–13	Arvidsson et al. (1982)
Renal clearance	L/hour	0.657[a]	0.32–0.73	Kim et al. (2021)

[a]Value has been identified using parameter identification feature supplied with the PK-Sim software.

et al., 2022). Structurally, the model is represented by several biological compartments correlated to each other utilizing arterial and venous blood circulations. The observed data of ceftriaxone plasma concentration *versus* time was digitized using Get-Data Graph Digitizer® (version 2.26), according to a previous study (Wojtyniak et al., 2020).

2.2 Literature search

A literature search was conducted through different electronic databases, including MEDLINE, EMBASE, and Google Scholar, to retrieve clinical PK studies to be used for the PBPK model development process. We included studies that evaluated

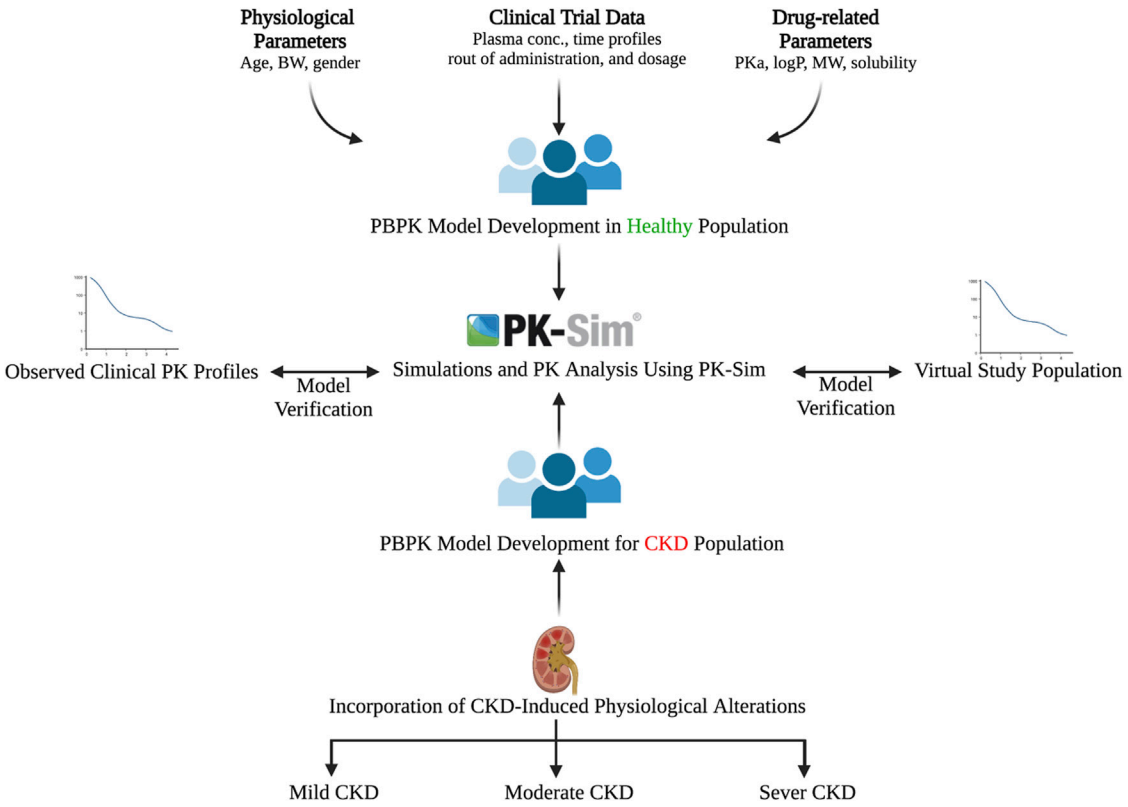

FIGURE 1
Workflow for developing the ceftriaxone PBPK model. The figure was created with BioRender.com with agreement number HZ250T3MDL.

intravenous administration of ceftriaxone in adult healthy and CKD patient populations. In order to use clinical PK data in the development and verification processes of PBPK models, concentration *versus* time profiles have to be available and described with rich-sampling scheme and uniform sampling times, which typically conducted in early phase of drug development. Clinical PK studies used for developing and evaluating the ceftriaxone PBPK model are shown in Table 1. The physicochemical properties of ceftriaxone (Table 2) that were used for developing this model were obtained from PubChem (Kim et al., 2021), DrugBank (Wishart et al., 2018a), and the Human Metabolome Database (Wishart et al., 2018b).

2.3 Designing PBPK models for adult healthy and CKD patient populations

The general guideline of the European Medicines Agency was followed for PBPK model development and evaluation (Luzon et al., 2017). Previous preliminary PBPK models for several renally cleared drugs, including ceftriaxone in Chinese pregnant women, were identified and reviewed to have better initial estimates for the model parameters (Song et al., 2020). A general schematic workflow for the overall process of developing the ceftriaxone PBPK model is depicted in Figure 1, and model parameters are defined in Table 2. We started the modeling by integrating drug-specific parameters (e.g., MW. logP, pKa), and trial design-specific parameters (e.g., administration protocol, route of administration, dose, and dosing frequency) with the predefined biological system-specific parameters in the PK-Sim. The fraction of drug unbound in plasma was used in conjunction with the physicochemical characteristics to quantify tissue partitioning, membrane permeation, and other biological passive processes. Given that ceftriaxone is administered parenterally, the model was established after intravenous administration, and thus, only information on distribution and elimination properties were gathered. The distribution phase was modeled by taking into account partition coefficients and cellular permeability. The partition coefficient was calculated automatically using Poulin/Theil method, whereas cellular permeability was calculated using the PK-Sim standard method. Renal clearance was modeled by choosing renal plasma clearance as a process type in the PK-Sim software. When choosing this process type, the PK-Sim software automatically calculates the renal clearance by taking into account the experimental value for kidney plasma clearance and fraction unbound of the drug (fu) in plasma. Biliary clearance was added to the model based on the experimental values as illustrated in Table 2. Once the model was developed and evaluated based on adult healthy population demographics and data, the model was used to predict the exposure in CKD patients by taking into account the accompanying pathophysiological alterations of CKD with various degrees of severity based on the previous findings, as identified in Table 3. The physiological parameters that have been modified in the CKD are creatinine clearance, kidney

TABLE 3 Pathophysiological changes associated with the severity of the CKD according to Malik et al., 2020 (Malik et al., 2020).

Parameter	Stage of CKD		
	Mild 30–60 mL/min/1.73 m^2	Moderate 15–30 mL/min/1.73 m^2	Severe <15 mL/min/1.73 m^2
Creatinine clearance	41–74	18–30	5–14
Kidney volume	132 mL	92 mL	76 mL
Renal perfusion	176 mL/min/100 g	97 mL/min/100 g	75.35 mL/min/100 g
Hematocrit	0.44	0.40	0.34
Correction factor[a]	1.45	2.20	2.50

[a]Correction factor for the effect of the CKD, on the content of plasma proteins as described by Malik and colleagues (Malik et al., 2020).

volume, renal perfusion, and hematocrit (Malik et al., 2020). These parameters directly impact renal clearance. The effect of the CKD on the fraction unbound was accounted for by using a plasma protein scaling factor that is provided with the PK-Sim software. This scalar is recommended to be used if the changes in plasma protein concentrations and, as a result, plasma protein binding are expected due to pathological conditions such as renal failure. For biliary clearance, no parameter was accounted for in the CKD modeling. Thus, it is assumed that CKD patients have intact biliary system.

2.4 Evaluation of the PBPK model and predictability assessment

The PBPK model was evaluated according to previously published guidelines (Kuepfer et al., 2016). The model's performance was evaluated visually and considered successful when the simulated and experimental PK findings fell within the 5th and 95th percentiles. A numerical evaluation according to the mean fold error (MFE) and mean square root of error (RMSE) was used as indicators to examine how much the predicted values deviated from the observed values (Eqs 2, 3). As described in many previous constructed models, the acceptable error range for the predicted to observed values was determined to be within a two-fold range.

$$Ratio = \frac{Predicted\ value\ of\ PK\ parameter}{Observed\ value\ of\ PK\ parameter} \quad (1)$$

$$MFE = \frac{Mean\ of\ Predicted\ Values}{Mean\ of\ Observed\ Values} \quad (2)$$

$$RMSE = \sqrt{\frac{\sum_1^N (Observed\ value - Predicted\ value)^2}{N}} \quad (3)$$

3 Results

3.1 Development of a PBPK model in adult healthy population after single and multiple dosing regimens

The clinical PK studies used for the model development and evaluation are summarized in Table 1. Data from three studies were used as external test dataset (Seddon et al., 1980; Stoeckel, 1981; McNamara et al., 1982) and they were only used for the visual verification of the model. Using a virtual human population of 100 healthy individuals, we developed a population PBPK model after intravenous administration for a wide range of single and multiple dosing regimens of ceftriaxone with subsequent model validation processes with respect to the observed data from the clinical PK studies. The model's performance was evaluated visually as demonstrated in Figures 2–4, where most of the observed time points were included within the 5th to 95th prediction interval. For single dosing regimens, the developed model was further evaluated by comparing the ratio of predicted-to-observed values for the PK parameters, including AUC, Cmax, T½, and clearance (CL). All the calculated predicted-to-observed PK data were within the predefined acceptable two-fold range as demonstrated in Table 4. The MFE of the AUC, Cmax, T½, and CL were 1.01, 0.90, 1.20, and 0.98, respectively. Because that peak and trough concentrations are very important PK parameters in the dosing adjustment for antibiotics, the PBPK model for multiple dosing regimens was evaluated based on the ability of the model to reproduce the maximum and minimum concentrations after the first dose and at steady state. Four days were required for ceftriaxone to reach steady state concentration which is in the line with the reported values (Pollock et al., 1982). We evaluated the ability of the model to capture the peak (Cmax) and trough concentrations (Cmin) at the first day and at the steady state visually (Figure 4) and numerically by comparing the ratio of predicted-to-observed values for the corresponding parameters. All the calculated predicted-to-observed values were within the predefined acceptable two-fold range as demonstrated in Table 5.

3.2 Development of the PBPK model in different stages of CKD after ceftriaxone intravenous administration

Pathophysiological changes associated with the CKD severity stages were obtained from a previous study (Malik et al., 2020). They included creatinine clearance, kidney volume, renal perfusion, and hematocrit. The altered values were incorporated into the PK-Sim to predict drug concentration in the CKD patient population with varying degrees of severity. A previous clinical PK study investigated the effects of CKD on PK parameters of 1 g ceftriaxone after

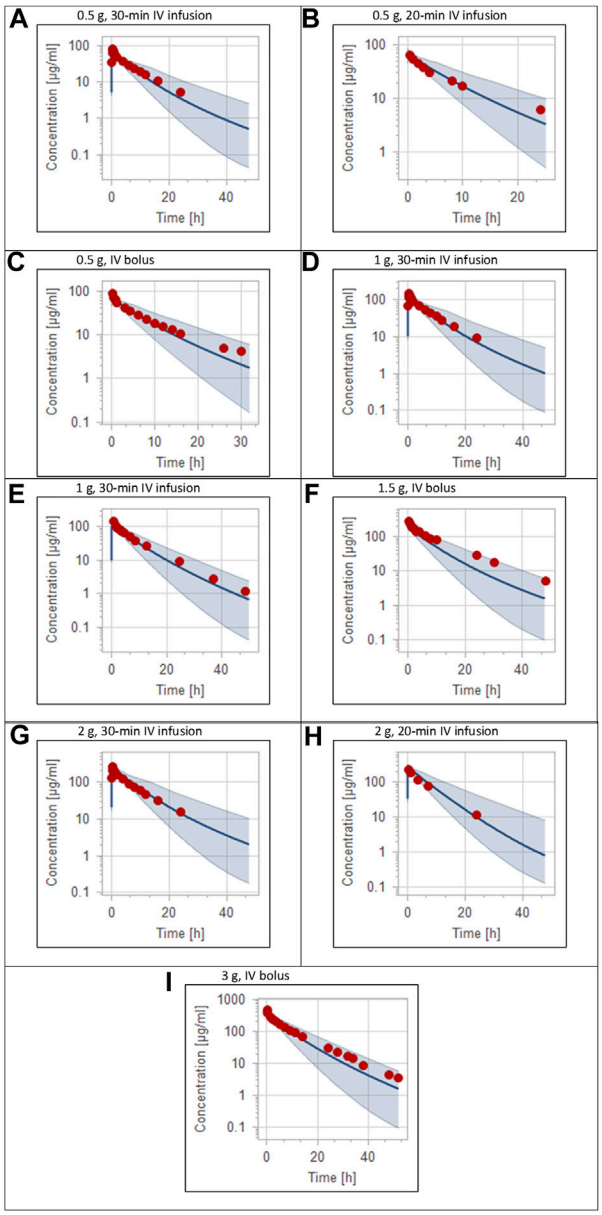

FIGURE 2
Plasma concentration-time profiles for intravenous administration of ceftriaxone in adult healthy population. **(A)** 0.5 g (Patel et al., 1981), **(B)** 0.5 g (Borner et al., 1985), **(C)** 0.5 g (Seddon et al., 1980), **(D)** 1 g (Patel et al., 1981), **(E)** 1 g (Harb et al., 2010), **(F)** 1.5 g (Stoeckel, 1981), **(G)** 2 g (Patel et al., 1981), **(H)** 2 g (Borner et al., 1985), **(I)** 3 g (McNamara et al., 1982). The 5th to 95th percentile prediction range is shown as a shaded area, and observed data points are indicated as red circles; simulated means are indicated as solid lines.

intravenous administration, and it was used for the CKD PBPK model evaluation (Patel et al., 1984). After generating a virtual CKD population with different degrees of severity based on the previously mentioned CKD-specific physiological alterations, the model was used to predict PK parameters of ceftriaxone in case of mild, moderate, and severe renal impairment. The model successfully captured the observed data, as represented graphically in Figure 5. Moreover, the model was verified according to the predicted-to-observed ratios of the PK parameters (AUC, T½, and CL). The fold errors of all PK parameters of ceftriaxone in the healthy model and the mild, moderate, and severe renal impairment disease models were within the predefined acceptable two-fold error range (Table 6). Based on the simulation of multiple dosing regimens in severe CKD population (supplementary, Figure 1S), it has been found that accumulation of 2 g every 24 h (factor of 1.50) is lower than the accumulation of 1 g every 12 h (factor of 2.30) dosing regimen (Table 7). This may be an indicator of the applicability of the high-dose extended-interval protocol in patient with deterioration in renal function, in comparison to low-dose multiple interval treatment protocol.

3.3 Dosing adjustment of ceftriaxone in subjects with different stages of CKD

Box-whisker plots for the AUC of 1 g intravenous ceftriaxone in patients with various degrees of CKD compared to healthy individuals as a reference are shown in Figure 6. It has been shown that the exposure increased as CKD progressed. In gradual dosing reduction simulation trials, we found that 750 mg (25% reduction in the initial dose) and 450 mg (55% reduction in the initial dose) are comparable in exposure to the reference healthy simulated population for mild CKD population, and for moderate to severe CKD population, respectively (Figure 6 B, C, and D).

4 Discussion

Ceftriaxone is a highly effective antimicrobial agent used to treat various infections (Epstein et al., 1982; Cleeland and Squires, 1984). The PK of ceftriaxone has been extensively studied in human and animal models (Patel et al., 1981; Rebuelto et al., 2003; Buragohain et al., 2021); however, the literature is still incomplete in many key areas, including special populations such as CKD patients. Clinically, it has been demonstrated that ceftriaxone clearance is decreased severely in patients with creatinine clearance lower than 5 mL/min/1.73 m^2 (Patel et al., 1984). Although ceftriaxone is prescribed with caution in patients with CKD, specific dosing recommendations based on renal function have not been provided (Munar et al., 2007). In this study, we aimed to explore the effects of renal failure on the pharmacokinetic parameters of ceftriaxone in a virtual human population using modeling and simulation. To the best of our knowledge, this is the first study that used the PBPK modeling and simulation to predict ceftriaxone exposure in the CKD patient population based on the degree of severity and physiological needs. The performance of the developed ceftriaxone PBPK model was verified visually, where the observed data contained within the constructed 5th to 95th predictive interval, and statistically according to values of the predicted-to-observed ratio, and all values fell within the predefined error range.

There has been widespread debate on the pharmacokinetics and appropriate dosing regimens of ceftriaxone in critically ill patients and those with various degrees of renal impairment. In a

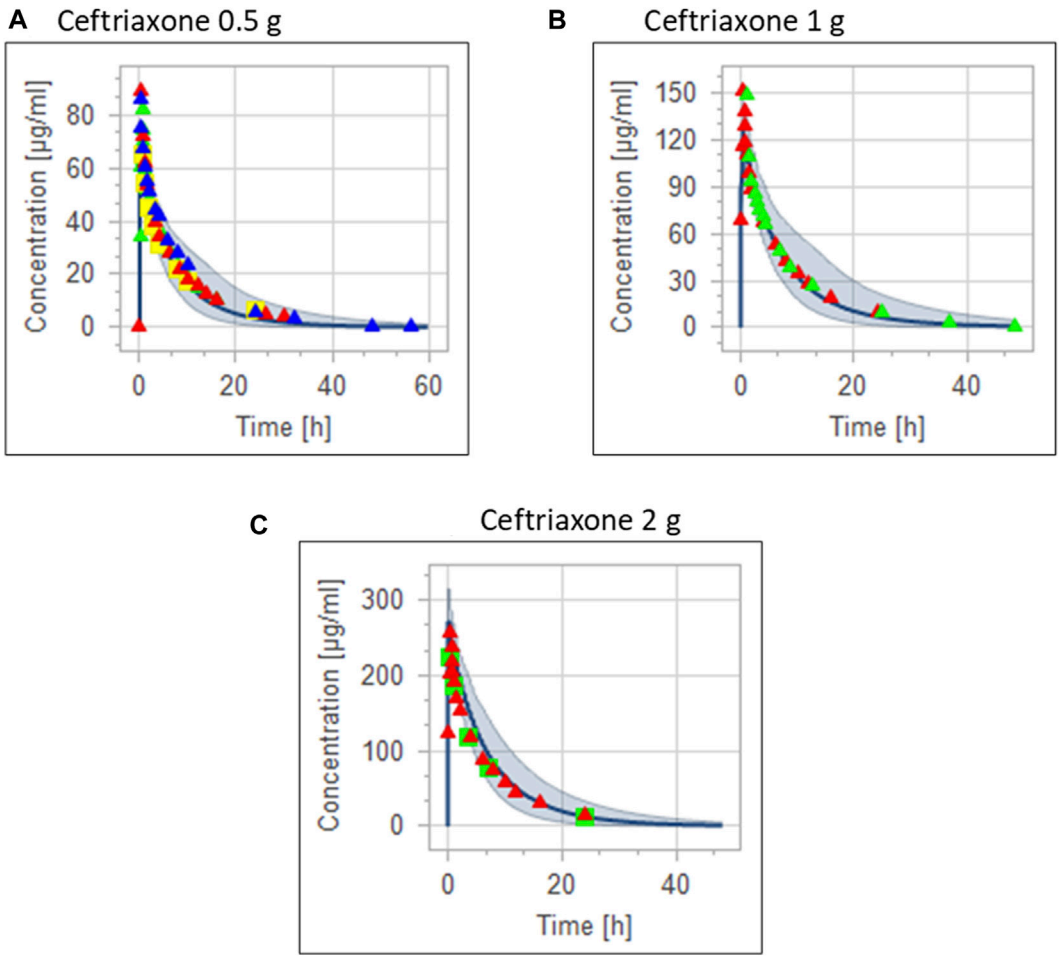

FIGURE 3
Combining the same doses of ceftriaxone from different studies for visual verification of the PBPK model in adult healthy population. Observed data are depicted as colored shapes, while solid line and shaded areas representing the prediction mean and 5th to 95th prediction range, respectively. **(A)** after administering 0.5 g ceftriaxone. **(B)** after administering 1 g ceftriaxone. **(C)** after administering 2 g ceftriaxone.

pharmacokinetic analysis of data obtained from critically ill patients infused with 2 g ceftriaxone once daily over 30 min, Joynt et al. (2001) concluded that ceftriaxone may be accumulated in patients with renal failure in comparison to those with intact renal function. It has been found that elimination half-life was 3-fold higher in patients with moderate or severe renal failure, and there was 50% reduction in clearance (Joynt et al., 2001). Moreover, another two pharmacokinetic studies demonstrated the accumulation of ceftriaxone in critically ill patients with moderate to severe renal failure (Heinemeyer et al., 1990; Van Dalen and Vree, 1990). The results from our PBPK modeling and simulation confirm what the abovementioned studies found in relation to the accumulation of ceftriaxone in patients with moderate and severe renal failure. In addition, we simulated the plasma concentration of 2 g intravenous ceftriaxone as being taken once daily (2 g every 24 h) or in a divided dosing scheme (1 g every 12 h). We found that the divided dosing scheme accumulated even more than single dosing regimen, illustrating the appropriateness of the single dose regimen. This finding is comparable to that found by TI et al. (1984). The investigators concluded that in patients with severe renal impairment, a once daily dosage regimen is feasible in compare to the 12-h dosage regimen (Ti et al., 1984). Furthermore, Stoeckel and Koup. (1984) found that a large single dose of ceftriaxone is favored rather than divided dose in case of renal insufficiency, despite no major accumulation was found in the patients (Stoeckel and Koup, 1984).

It has been argued that no dose adjustment was needed for ceftriaxone in case of renal failure due to the assumption that biliary clearance could make a balance on the total ceftriaxone clearance (Stoeckel and Koup, 1984). However, the contribution of biliary system into the overall clearance of ceftriaxone was not found to compensate the impairment of renal function (Heinemeyer et al., 1990; Grégoire et al., 2019). Moreover, the functional status of kidney was found to be one of the most important covariates that significantly impact the pharmacokinetic of ceftriaxone, and it has been recommended to be considered for the purpose of dosing adjustment (Bos et al., 2018; Grégoire et al., 2019).

In a recently published pharmacokinetic analysis of data obtained from three independently conducted studies, Heffernan

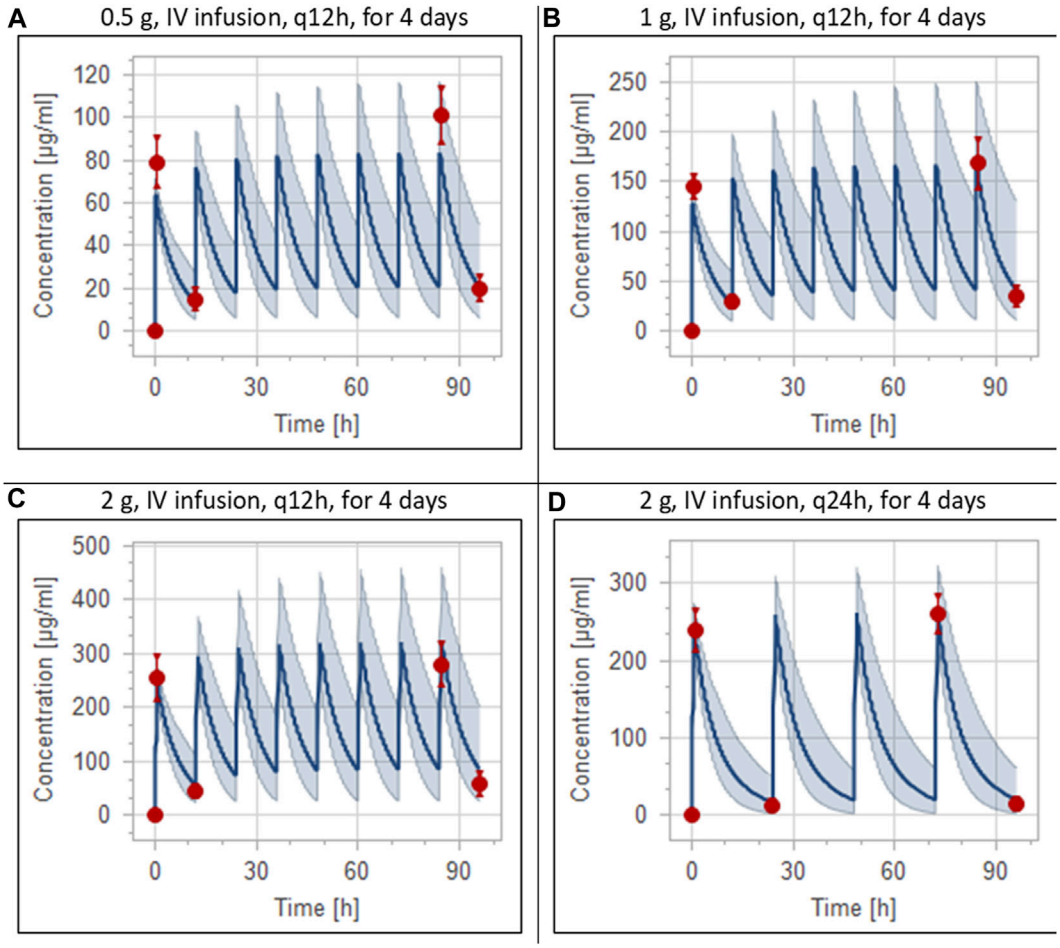

FIGURE 4
Simulation of concentration *versus* time profiles of multiple dosing regimens of ceftriaxone in adult healthy populations. Observed peak and trough concentrations (Pollock et al., 1982) are depicted as colored circles, while solid lines and shaded areas representing the prediction mean and 5th to 95th prediction interval, respectively. **(A)** after administering 0.5 g ceftriaxone intravenous infusion every 12 h for 4 days. **(B)** after administering 1 g ceftriaxone intravenous infusion every 12 h for 4 days. **(C)** after administering 2 g ceftriaxone intravenous infusion every 12 h for 4 days. **(D)** after administering 2 g ceftriaxone intravenous infusion every 24 h for 4 days.

et al. (2022) empirically described ceftriaxone pharmacokinetic parameters with taking into account both free and total concentration, and accordingly, optimized dosing regimens (Heffernan et al., 2022). The researchers mentioned that the dose of ceftriaxone should be adjusted based on renal function, albumin concentration, and minimum inhibitory concentration of the isolated pathogens. They recommended that ceftriaxone 1 g twice daily is generally suitable regimen for providing therapeutic exposure in patients with a normal renal function (creatinine clearance is around 100 mL/min), assuming that minimum inhibitory concentration is ≤0.25 mg/L. Importantly, because that patients' overall clinical context (e.g., impaired renal function) should be taken into account, they mentioned that lower dose (1 g once daily) of ceftriaxone might be suitable for isolates with low minimum inhibitory concentration (≤0.125 mg/L). Furthermore, in critically ill patients with augmented renal clearance with or without hypoalbuminemia, the investigators recognized that there is a need for higher doses of ceftriaxone to achieve the therapeutic target exposure. In contrast to the empirical approach that they used, we described the ceftriaxone exposure using physiologically meaningful approach with more biologically relevant parameters and then we applied the model to predict exposure in patients with various degrees of CKD. We mainly focused on the applicability of the PBPK modeling in predicting ceftriaxone exposure in patients with renal impairment and subsequently determining the appropriate dose reduction that result in an exposure comparable to normal subjects.

The developed PBPK model precisely described an observed data obtained from a PK study conducted on both healthy and renal failure patients (Patel et al., 1984). Patel et al. (1984) examined the effects of renal failure on the pharmacokinetic of 1 g ceftriaxone infused over 15 min. They noted two-fold increase in half-life, and more than 50% decrease in plasma clearance, in comparison to young healthy population with intact renal function at the same dose. We tested our PBPK model for reproducing the results from this trial that was

TABLE 4 Predicted-to-observed ratios of PK parameters of ceftriaxone in the adult healthy population.

PK parameter	Predicted	Observed	Ratio
0.5 g I.V. infusion (Patel et al., 1981)			
AUC [μg/mL*h]	490.1	551 (462–737)	0.89
Cmax [μg/mL]	63.5	82	0.77
T½ [h]	8.34	6.30 (5.45–7.75)	1.32
CL [mL/min]	17.04	15.48 (11.3–19.83)	1.10
0.5 g I.V. infusion (Borner et al., 1985)			
AUC [μg/mL*h]	490.1	551 (462–737)	0.89
Cmax [μg/mL]	63.5	82	0.77
T½ [h]	8.34	6.30 (5.45–7.75)	1.32
CL [mL/min]	17.04	15.48 (11.3–19.83)	1.10
0.5 g I.V. infusion (Borner et al., 1985)			
AUC [μg/mL*h]	517.3	549 ± 125	0.94
Cmax [μg/mL]	74.23	83.8 ± 40.1	0.89
T½ [h]	7.20	9.87 ± 2.22	0.73
CL [mL/min]	16.11	16 ± 4.3	1.01
1 g I.V. infusion (Patel et al., 1981)			
AUC [μg/mL*h]	988	1,006 (764–1,238)	0.98
Cmax [μg/mL]	127	150.7	0.84
T½ [h]	8.37	6.13 (5.0–7.24)	1.37
CL [mL/min]	17.03	16.78 (13.47–21.82)	1.01
1 g I.V. infusion (Harb et al., 2010)			
AUC [μg/mL*h]	933	1,085.8 ± 187.5	0.86
Cmax [μg/mL]	120.86	150 ± 19.9	0.81
T½ [h]	8.89	8.25 (6.03–10.4)	1.08
CL [mL/min]	17.87	15.86	1.13
2 g I.V. infusion (Patel et al., 1981)			
AUC [μg/mL*h]	1974.5	1,703 (1,308–2,055)	1.16
Cmax [μg/mL]	254	256.9	0.99
T½ [h]	8.86	5.82 (4.73–6.84)	1.68
CL [mL/min]	16.90	19.83 (16.22–25.48)	0.85
2 g I.V. infusion (Borner et al., 1985)			
AUC [μg/mL*h]	1,908.44	1,565 ± 328	1.22
C_max [μg/mL]	278	258 ± 38.4	1.08
T½ [h]	6.58	6.4 ± 1.07	1.03
CL [mL/min]	17.47	22.1 ± 5.0	0.79
Predictability assessment			
	AUC	C_max	T½	CL
MFE	1.01	0.90	1.20	0.98
RMSE	191.5	19.4	2.08	2.47

(Continued in next column)

TABLE 4 (*Continued*) Predicted-to-observed ratios of PK parameters of ceftriaxone in the adult healthy population.

conducted on CKD patients with various degrees of severity. After stratifying the CKD patients by the exposure, we simulated the drug concentration after gradually reducing the dose that has been used in the clinical trial (1 g daily) to get a comparable exposure to healthy subjects. We found that 450–500 mg ceftriaxone in patients with moderate to severe renal failure resulted in a biological exposure that is comparable to the 1,000 mg that was given to healthy subjects in this trial. Thus, we concluded that 50% decrease in the dose for moderate to severe CKD is likely to provide the same exposure as seen in healthy individuals. In comparison to Heffernan et al. (2022) where the researchers depended on the minimum inhibitory concentration in the dosing recommendation, we provided our recommendation based on the comparability of total biological exposure in renally impaired patients to healthy individuals. It is important to note that while Heffernan et al. (2022) took into account both free and total concentration in their empirical model, our PBPK model is already accounting for this effect by incorporating the fraction of drug unbound as a drug-related parameter; Heffernan et al. (2022) generally recommended higher doses of ceftriaxone because the patients were critically ill, who are usually infected with more resistant bacteria and have lower albumin concentration (Heffernan et al., 2022). In contrast, Patel et al. (1984) recruited renally impaired patients otherwise free of clinical illness and they were not critically ill. The study was conducted to only characterize ceftriaxone kinetically in renally impaired patients, which is very important to understand the general trend in pharmacokinetic of ceftriaxone in renally impaired patients (Patel et al., 1984).

Patients with renal diseases are at a high risk of developing bacterial infections with increased resistance to many antibiotics (Berns and Tokars, 2002; Su et al., 2018; Wang et al., 2019). Simultaneously, there is a limited choice of antibiotics for treating these infections owing to their toxicity profiles. Ceftriaxone is commonly prescribed to patients with CKD at doses of 2 g/day or less, even though the median dose in patients diagnosed with ceftriaxone-induced toxicity was 1.7 g/day (Lacroix et al., 2021). A case report documented an association between a high therapeutic dose of ceftriaxone (2 g/12 h for 7 days) and the development of neurotoxicity in patients with End Stage Renal Disease (ESRD) (Hagiya et al., 2017). These adverse effects are present in the form of altered mental status, choreoathetosis, and myoclonus, and these adverse events disappear following drug withdrawal (Hagiya et al., 2017).

Other studies have demonstrated the influence of the kidney functional state on toxicity and how ceftriaxone led to side effects (Kim et al., 2012; Safadi et al., 2014; Tan and Tun, 2019; Yamada

TABLE 5 Comparison of predicted and observed (Pollock et al., 1982) peak and trough concentrations of ceftriaxone after multiple dosing regimens.

	Peak concentration[a]			Trough concentration[a]		
	Simulated	Observed	FE	Simulated	Observed	FE
0.5 g intravenous ceftriaxone q12 h in healthy population						
Day 1	64 (57–71)	79 (64–102)	1.23	14 (6–28)	15 (8.6–24)	1.07
Day 4	84 (66–117)	101 (77–117)	1.20	21 (7–50)	20 (14–28)	1.05
0.5 g intravenous ceftriaxone q12h in severe CKD population						
Day 1	63 (43–127)			31 (20–57)		
Day 4	130 (80–240)			68 (36–146)		
1 g intravenous ceftriaxone q12h in healthy population						
Day 1	128 (113–143)	145 (130–160)	1.13	28 (12–56)	30 (23–42)	1.07
Day 4	167 (133–234)	168 (132–213)	1.01	42 (13–101)	35 (23–58)	1.2
1 g intravenous ceftriaxone q12h in severe CKD population						
Day 1	136 (85–259)			66 (40–113)		
Day 4	279 (160–480)			149 (73–295)		
2 g intravenous ceftriaxone q12h in healthy population						
Day 1	244 (216–273)	255 (184–338)	1.04	58 (24–114)	45 (29–64)	1.30
Day 4	322 (252–459)	280 (214–346)	1.15	87 (28–205)	59 (37–111)	1.5
2 g intravenous ceftriaxone q12h in severe CKD population						
Day 1	263 (166–494)			135 (81–230)		
Day 4	546 (315–945)			301 (146–590)		
2 g intravenous ceftriaxone q24h in healthy population						
Day 1	244 (212–270)	239 (198–278)	1.02	17 (3–50)	13 (7–23)	1.31
Day 4	263 (222–323)	260 (216–281)	1.01	21 (3–63)	15 (7–27)	1.40
2 g intravenous ceftriaxone q24h in severe CKD population						
Day 1	263 (167–487)			72 (36–130)		
Day 4	361 (215–631)			107 (46–225)		

[a]The simulated and observed values (Pollock et al., 1982) represent the mean and the values between parentheses is the range. FE: fold error, CKD: chronic kidney disease.

et al., 2020; Oyama et al., 2021). For instance, a case series reported that ceftriaxone treatment for a long period at high dosages was associated with the development of pseudolithiasis in patients with severe renal impairment who received dialysis (Oyama et al., 2021). In addition to pseudolithiasis, choreoathetosis was associated with ceftriaxone treatment (2 g/day) in ESRD patients (Tan and Tun, 2019). Moreover, a patient with CKD developed nonconvulsive status epilepticus after treatment with ceftriaxone (2 g/day) (Kim et al., 2012). Further, acute cholangitis and large pseudostones are produced in humans after kidney transplantation and are treated with ceftriaxone (Yamada et al., 2020). Other studies have found that ceftriaxone treatment at 2 g/day for 3 days causes encephalopathy in patients with ESRD (Safadi et al., 2014). Taken together, toxicity may develop in patients with ESRD treated with 2 g/day of ceftriaxone.

The variability in plasma concentration, protein binding, and other PK properties among individuals who received ceftriaxone (Patel and Kaplan, 1984; Popick et al., 1987; Schleibinger et al., 2015) play crucial roles in PBPK model system. A high percentage of ceftriaxone excreted renally in unchanged form, indicating that renal clearance is the rate-limiting step of ceftriaxone accumulation in patients with kidney diseases. Thus, PBPK can provide preliminary data regarding the expected ceftriaxone exposure in CKD patients. Extensive protein binding affects the kinetic behavior of ceftriaxone. This hypothesis was confirmed in a previous study demonstrating increased free ceftriaxone concentrations in the blood of patients with iatrogenic hypoalbuminemia (Mimoz et al., 2000). A different study found that ceftriaxone treatment at 1g/day resulted in values of 100% above the minimum inhibitory

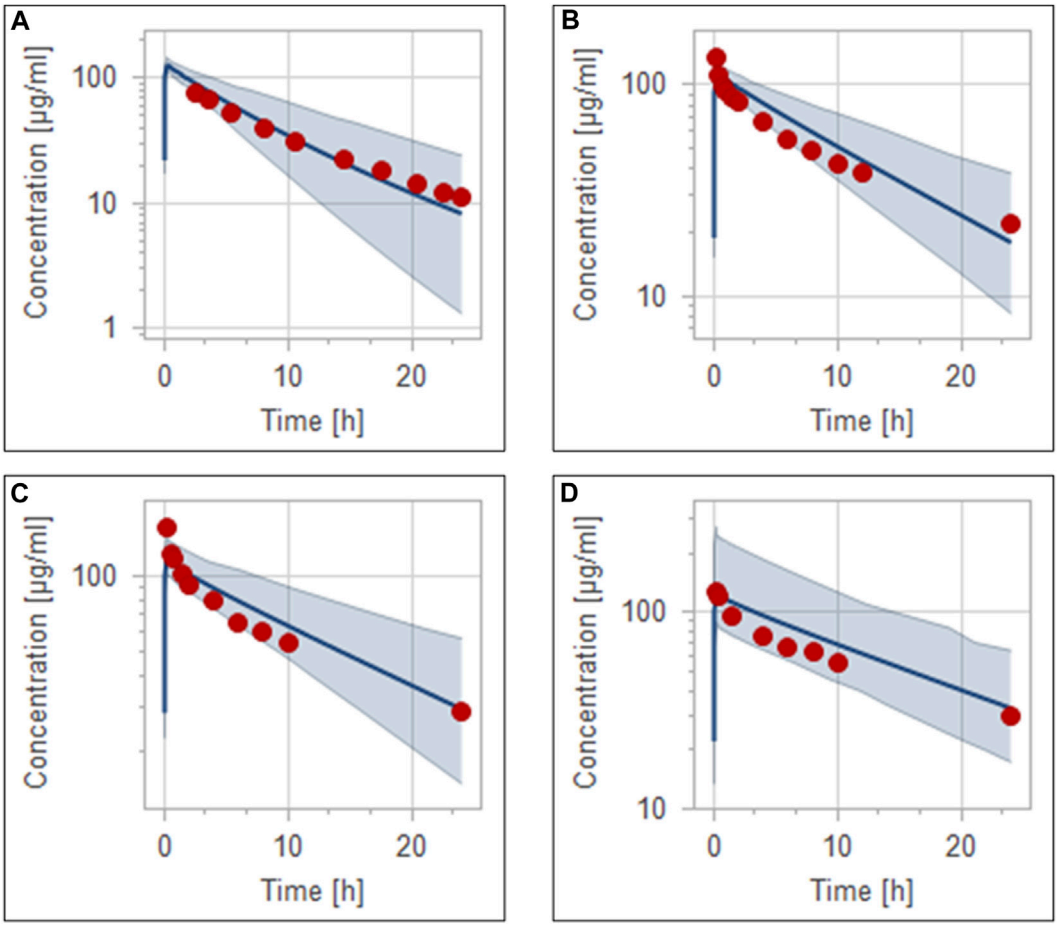

FIGURE 5
Simulation of concentration *versus* time profiles of 1 g intravenous infusion of ceftriaxone in healthy population **(A)**, mild renal impairment population **(B)**, moderate renal impairment population **(C)**, and severe renal impairment population **(D)**. Observed data are depicted as colored circles, while solid line and shaded areas representing the prediction mean and 5th to 95th prediction range, respectively.

TABLE 6 PK analysis of time profiles for CKD patients.

PK parameter	Data type	Healthy	CKD		
			Mild	Moderate	Severe
AUC [µg/mL*h]	Predicted	1,037	1,454.63	2,011.93	2,211.58
	Observed	894.77	1,558.10	1,970.87	2,025.89
	Fold error	1.16	1.07	1.02	1.09
T½ [h]	Predicted	7.67	9.40	12.88	13.08
	Observed	8.96	14.69	15.30	15.42
	Fold error	1.17	1.56	1.19	1.18
Clearance [mL/min]	Predicted	16.10	11.45	8.30	7.54
	Observed	20.05 ± 3.15	11.75 ± 4.20	8.82 ± 1.62	10.05 ± 2.95
	Fold error	1.25	1.03	1.06	1.33

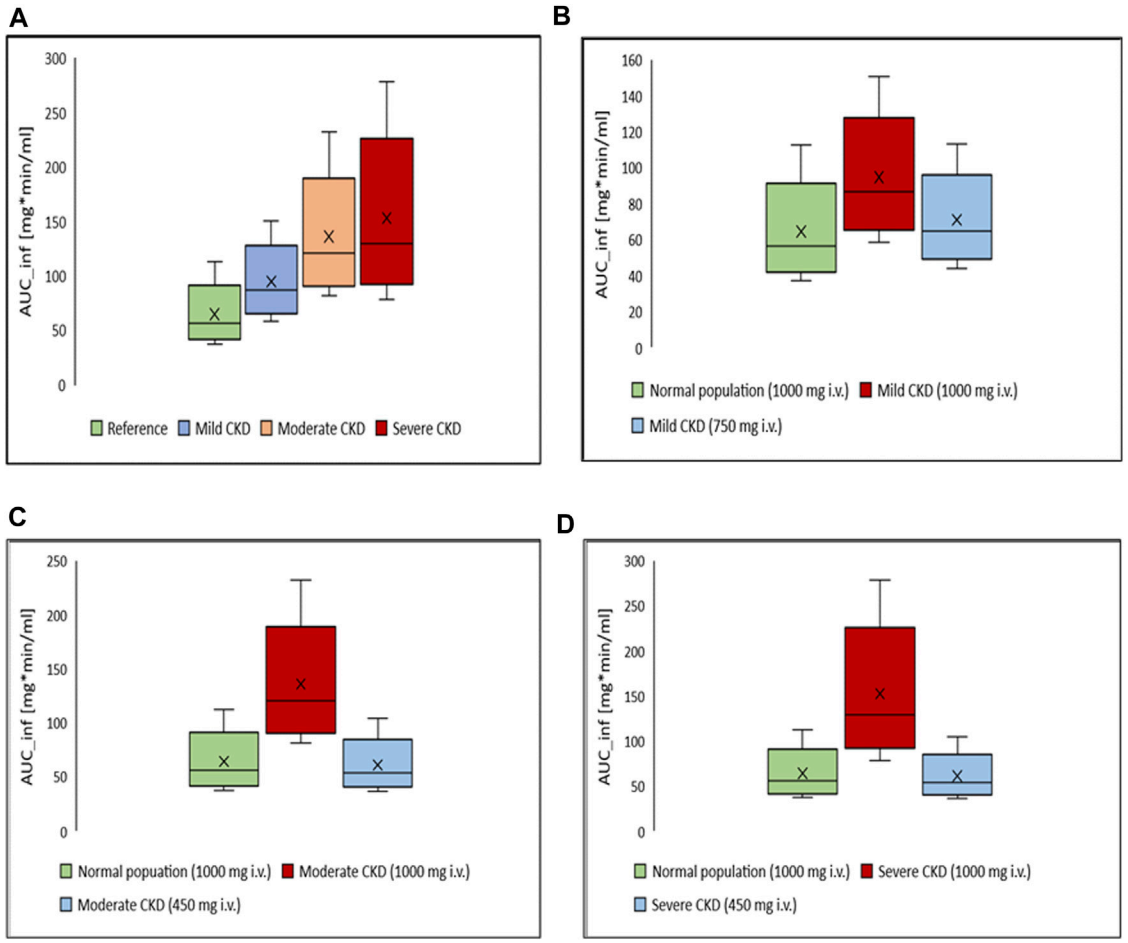

FIGURE 6
Box-whisker plots for the effect of various degrees of CKD on the exposure of ceftriaxone in comparison to healthy individuals, with subsequent dosing optimizations. **(A)** Comparison, in term of AUC, between healthy (reference) and CKD populations with various degrees of severity after administration of 1,000 mg intravenous ceftriaxone. **(B)** AUC of ceftriaxone after the dose was decreased to 750 mg in mild CKD, in comparison to healthy subjects administered 1,000 mg ceftriaxone. **(C)** AUC after the dose was decreased to 450 mg in moderate CKD, in comparison to normal subjects administered 1,000 mg ceftriaxone. **(D)** AUC after the dose was decreased to 450 mg in severe CKD, in comparison to normal subjects administered 1,000 mg ceftriaxone.

TABLE 7 Ratio of trough concentrations at steady state to the trough concentrations after the first application, as estimation of accumulation index.

Regimen	Healthy		CKD
	Simulated	Observed	Simulated
0.5 g, q12h, for 4 days	1.50	1.33	2.20
1 g, q12h, for 4 days	1.50	1.20	2.30
2 g, q12h, for 4 days	1.50	1.31	2.23
2 g, q24h, for 4 days	1.24	1.20	1.50

concentrations in patients with hypoalbuminemia and septic shock (Ulldemolins et al., 2021).

In summary, the kinetic properties of ceftriaxone after intravenous administration in healthy individuals and at various stages of CKD were successfully described using the current ceftriaxone PBPK model. Based on the generated AUC data, the model was used to suggest dosages for various CKD stages comparable to those in the healthy population. Clinicians should be aware about the increase in ceftriaxone exposure in patients with severe renal impairment, especially for diseases requiring high dosages of ceftriaxone. We outlined the current state-of-the-art of PBPK in drug investigations and provided guidance for future applications. In addition, we demonstrated that applying PBPK can help identify novel safety concerns and optimize dose regimens when conducting clinical trials with ceftriaxone in patients. Future PBPK studies are warranted to simulate further the antimicrobial compounds accumulations in the blood of patients with CKD and to recommend updated dosage regimens.

Data availability statement

The original contributions presented in the study are included in the article/Supplementary Material, further inquiries can be directed to the corresponding author.

Author contributions

Conceptualization, FwA, MA, FlA, and MR; methodology, FwA, MA, FlA, MR; software, FwA, MA, FlA, and MR; validation, FwA, MA, FlA, MR, AA, and HM; formal analysis, FwA, MA, FlA, MR, AA, HM, and HA; investigation, FwA, MA, FlA, MR, AA, HM, and HA; resources, FwA, FlA, and MR; data curation, FwA, MA, FlA, and MR; writing—original draft preparation, FwA, MA, FlA, and HM; writing—review and editing, MR, AA, SA, AA, and HA visualization, FwA, MA, FlA, SA, AA, and MR; supervision, FlA and MR; project administration, FlA, MR; funding acquisition, FlA. All authors contributed to the article and approved the submitted version.

Funding

This research was funded by The Deputyship for Research and Innovation "Ministry of Education" in Saudi Arabia, grant number "IFKSUDR_H193".

Conflict of interest

The authors declare that the research was conducted in the absence of any commercial or financial relationships that could be construed as a potential conflict of interest.

Publisher's note

All claims expressed in this article are solely those of the authors and do not necessarily represent those of their affiliated organizations, or those of the publisher, the editors and the reviewers. Any product that may be evaluated in this article, or claim that may be made by its manufacturer, is not guaranteed or endorsed by the publisher.

Supplementary material

The Supplementary Material for this article can be found online at: https://www.frontiersin.org/articles/10.3389/fphar.2023.1200828/full#supplementary-material

References

Aloy, B., Launay-Vacher, V., Bleibtreu, A., Bortolotti, P., Faure, E., Filali, A., et al. (2020). Antibiotics and chronic kidney disease: Dose adjustment update for infectious disease clinical practice. *Med. maladies Infect.* 50, 323–331. doi:10.1016/j.medmal.2019.06.010

Arvidsson, A., Alván, G., Angelin, B., Borgå, O., and Nord, C. E. (1982). Ceftriaxone: Renal and biliary excretion and effect on the colon microflora. *J. Antimicrob. Chemother.* 10, 207–215. doi:10.1093/jac/10.3.207

Berns, J. S., and Tokars, J. I. (2002). Preventing bacterial infections and antimicrobial resistance in dialysis patients. *Am. J. kidney Dis.* 40, 886–898. doi:10.1053/ajkd.2002.36332

Borner, K., Lode, H., Hampel, B., Pfeuffer, M., and Koeppe, P. (1985). Comparative pharmacokinetics of ceftriaxone after subcutaneous and intravenous administration. *Chemotherapy* 31, 237–245. doi:10.1159/000238342

Bos, J. C., Prins, J. M., Mistício, M. C., Nunguiane, G., Lang, C. N., Beirão, J. C., et al. (2018). Pharmacokinetics and pharmacodynamic target attainment of ceftriaxone in adult severely ill sub-saharan african patients: A population pharmacokinetic modelling study. *J. Antimicrob. Chemother.* 73, 1620–1629. doi:10.1093/jac/dky071

Buragohain, R., Sar, T. K., Biswas, U., Samanta, I., and Mandal, T. K. (2021). Pharmacokinetics and efficacy of ceftriaxone in staphylococcal mastitis in crossbred cows following single intravenous administration. *Curr. Drug Metab.* 22, 383–390. doi:10.2174/1389200222666210210113641

Chahine, B. (2022). Antibiotic dosing adjustments in hospitalized patients with chronic kidney disease: A retrospective chart review. *Int. Urology Nephrol.* 54, 157–163. doi:10.1007/s11255-021-02834-6

Cleeland, R., and Squires, E. (1984). Antimicrobial activity of ceftriaxone: A review. *Am. J. Med.* 77, 3–11.

Cole, S., Kerwash, E., and Andersson, A. (2020). A summary of the current drug interaction guidance from the European Medicines Agency and considerations of future updates. *Drug Metabolism Pharmacokinet.* 35, 2–11. doi:10.1016/j.dmpk.2019.11.005

Epstein, J., Hasselquist, S. M., and Simon, G. L. (1982). Efficacy of ceftriaxone in serious bacterial infections. *Antimicrob. Agents Chemother.* 21, 402–406. doi:10.1128/AAC.21.3.402

Farhan, M., Rani, P., Moledina, F., George, T., Tummala, H. P., and Mallayasamy, S. (2022). Application of physiologically based pharmacokinetic modeling of lamotrigine using PK-sim in predicting the impact of drug interactions and dosage adjustment. *J. Pharmacol. Pharmacother.* 13, 160–166. doi:10.1177/0976500x221111455

Fontana, R., Aldegheri, M., Ligozzi, M., Lo Cascio, G., and Cornaglia, G. (1998). Interaction of ceftriaxone with penicillin-binding proteins of *Escherichia coli* in the presence of human serum albumin. *J. Antimicrob. Chemother.* 42, 95–98. doi:10.1093/jac/42.1.95

Grégoire, M., Dailly, E., Le Turnier, P., Garot, D., Guimard, T., Bernard, L., et al. (2019). High-dose ceftriaxone for bacterial meningitis and optimization of administration scheme based on nomogram. *Antimicrob. Agents Chemother.* 63, e00634-19. doi:10.1128/AAC.00634-19

Hagiya, H., Miyawaki, K., Yamamoto, N., Yoshida, H., Kitagawa, A., Asaoka, T., et al. (2017). Ceftriaxone-induced neurotoxicity in a patient after pancreas-kidney transplantation. *Intern. Med.* 56, 3103–3107. doi:10.2169/internalmedicine.8774-16

Harb, G., Lebel, F., Battikha, J., and Thackara, J. W. (2010). Safety and pharmacokinetics of subcutaneous ceftriaxone administered with or without recombinant human hyaluronidase (rHuPH20) versus intravenous ceftriaxone administration in adult volunteers. *Curr. Med. Res. Opin.* 26, 279–288. doi:10.1185/03007990903432900

Heffernan, A. J., Sime, F. B., Kumta, N., Wallis, S. C., Mcwhinney, B., Ungerer, J., et al. (2022). Multicenter population pharmacokinetic study of unbound ceftriaxone in critically ill patients. *Antimicrob. Agents Chemother.* 66, e0218921. doi:10.1128/aac.02189-21

Heinemeyer, G., Link, J., Weber, W., Meschede, V., and Roots, I. (1990). Clearance of ceftriaxone in critical care patients with acute renal failure. *Intensive care Med.* 16, 448–453. doi:10.1007/BF01711224

Joynt, G., Lipman, J., Gomersall, C., Young, R., Wong, E., and Gin, T. (2001). The pharmacokinetics of once-daily dosing of ceftriaxone in critically ill patients. *J. Antimicrob. Chemother.* 47, 421–429. doi:10.1093/jac/47.4.421

Kim, K. B., Kim, S. M., Park, W., Kim, J. S., Kwon, S. K., and Kim, H.-Y. (2012). Ceftriaxone-induced neurotoxicity: Case report, pharmacokinetic considerations, and literature review. *J. Korean Med. Sci.* 27, 1120–1123. doi:10.3346/jkms.2012.27.9.1120

Kim, S., Chen, J., Cheng, T., Gindulyte, A., He, J., He, S., et al. (2021). PubChem in 2021: New data content and improved web interfaces. *Nucleic acids Res.* 49, D1388–D1395. doi:10.1093/nar/gkaa971

Kocaoglu, O., and Carlson, E. E. (2015). Profiling of β-lactam selectivity for penicillin-binding proteins in *Escherichia coli* strain DC2. *Antimicrob. Agents Chemother.* 59, 2785–2790. doi:10.1128/AAC.04552-14

Kuepfer, L., Niederalt, C., Wendl, T., Schlender, J. F., Willmann, S., Lippert, J., et al. (2016). Applied concepts in PBPK modeling: How to build a PBPK/PD model. *CPT pharmacometrics Syst. Pharmacol.* 5, 516–531. doi:10.1002/psp4.12134

Lacroix, C., Bera-Jonville, A.-P., Montastruc, F., Velly, L., Micallef, J., and Guilhaumou, R. (2021). Serious neurological adverse events of ceftriaxone. *Antibiotics* 10, 540. doi:10.3390/antibiotics10050540

Le Turnier, P., Navas, D., Garot, D., Guimard, T., Bernard, L., Tattevin, P., et al. (2019). Tolerability of high-dose ceftriaxone in CNS infections: A prospective multicentre cohort study. *J. Antimicrob. Chemother.* 74, 1078–1085. doi:10.1093/jac/dky553

Li, M., Zou, P., Tyner, K., and Lee, S. (2017). Physiologically based pharmacokinetic (PBPK) modeling of pharmaceutical nanoparticles. *AAPS J.* 19, 26–42. doi:10.1208/s12248-016-0010-3

Luzon, E., Blake, K., Cole, S., Nordmark, A., Versantvoort, C., and Berglund, E. G. (2017). Physiologically based pharmacokinetic modeling in regulatory decision-making at the European Medicines Agency. *Clin. Pharmacol. Ther.* 102, 98–105. doi:10.1002/cpt.539

Malik, P. R., Yeung, C. H., Ismaeil, S., Advani, U., Djie, S., and Edginton, A. N. (2020). A physiological approach to pharmacokinetics in chronic kidney disease. *J. Clin. Pharmacol.* 60, S52–S62. doi:10.1002/jcph.1713

Mcnamara, P., Stoeckel, K., and Ziegler, W. (1982). Pharmacokinetics of ceftriaxone following intravenous administration of a 3 g dose. *Eur. J. Clin. Pharmacol.* 22, 71–75. doi:10.1007/BF00606428

Mimoz, O., Soreda, S., Padoin, C., Tod, M., Petitjean, O., and Benhamou, D. (2000). Ceftriaxone pharmacokinetics during iatrogenic hydroxyethyl starch-induced hypoalbuminemia: A model to explore the effects of decreased protein binding capacity on highly bound drugs. *J. Am. Soc. Anesthesiol.* 93, 735–739. doi:10.1093/bja/85.5.735

Morales-Alvarez, M. C. (2020). Nephrotoxicity of antimicrobials and antibiotics. *Adv. chronic kidney Dis.* 27, 31–37. doi:10.1053/j.ackd.2019.08.001

Munar, M. Y., Munar, M. Y., and Signh, H. (2007). Drug dosing adjustments in patients with chronic kidney disease. *Am. Fam. physician* 75, 1487–1496.

Nau, R., Sorgel, F., and Eiffert, H. (2010). Penetration of drugs through the blood-cerebrospinal fluid/blood-brain barrier for treatment of central nervous system infections. *Clin. Microbiol. Rev.* 23, 858–883. doi:10.1128/CMR.00007-10

Oyama, Y., Iwafuchi, Y., and Narita, I. (2021). Ceftriaxone-associated pseudolithiasis in hemodialysis patients: A case series study. *Ren. Replace. Ther.* 7, 6–8. doi:10.1186/s41100-021-00320-4

Patel, I., Chen, S., Parsonnet, M., Hackman, M., Brooks, M., Konikoff, J., et al. (1981). Pharmacokinetics of ceftriaxone in humans. *Antimicrob. Agents Chemother.* 20, 634–641. doi:10.1128/AAC.20.5.634

Patel, I., Kaplan, S., and Van Brummelen, P. (1984). Role of alpha adrenoceptors in hypertension and in anti hypertensive drug treatment. *Am. J. Med.* 77, 17–25. doi:10.1016/s0002-9343(84)80033-9

Patel, I., Sugihara, J., Weinfeld, R., Wong, E., Siemsen, A., and Berman, S. (1984). Ceftriaxone pharmacokinetics in patients with various degrees of renal impairment. *Antimicrob. agents Chemother.* 25, 438–442. doi:10.1128/AAC.25.4.438

Patel, N., Scheetz, M. H., Drusano, G. L., and Lodise, T. P. (2010). Determination of antibiotic dosage adjustments in patients with renal impairment: Elements for success. *J. Antimicrob. Chemother.* 65, 2285–2290. doi:10.1093/jac/dkq323

Pollock, A. A., Tee, P., Patel, I., Spicehandler, J., Simberkoff, M., and Rahal, J., Jr (1982). Pharmacokinetic characteristics of intravenous ceftriaxone in normal adults. *Antimicrob. Agents Chemother.* 22, 816–823. doi:10.1128/AAC.22.5.816

Popick, A., Crouthamel, W., and Bekersky, I. (1987). Plasma protein binding of ceftriaxone. *Xenobiotica* 17, 1139–1145. doi:10.3109/00498258709167406

Rebuelto, M., Ambros, L., and Rubio, M. (2003). Daily variations in ceftriaxone pharmacokinetics in rats. *Antimicrob. agents Chemother.* 47, 809–812. doi:10.1128/AAC.47.2.809-812.2003

Rowland Yeo, K., Aarabi, M., Jamei, M., and Rostami-Hodjegan, A. (2011). Modeling and predicting drug pharmacokinetics in patients with renal impairment. *Expert Rev. Clin. Pharmacol.* 4, 261–274. doi:10.1586/ecp.10.143

Safadi, S., Mao, M., and Dillon, J. J. (2014). Ceftriaxone-induced acute encephalopathy in a peritoneal dialysis patient. *Case Rep. Nephrol.* 2014, 108185. doi:10.1155/2014/108185

Schleibinger, M., Steinbach, C. L., Töpper, C., Kratzer, A., Liebchen, U., Kees, F., et al. (2015). Protein binding characteristics and pharmacokinetics of ceftriaxone in intensive care unit patients. *Br. J. Clin. Pharmacol.* 80, 525–533. doi:10.1111/bcp.12636

Seddon, M., Wise, R., Gillett, A., and Livingston, R. (1980). Pharmacokinetics of Ro 13-9904, a broad-spectrum cephalosporin. *Antimicrob. Agents Chemother.* 18, 240–242. doi:10.1128/AAC.18.2.240

Song, L., Yu, Z., Xu, Y., Li, X., Liu, X., Liu, D., et al. (2020). Preliminary physiologically based pharmacokinetic modeling of renally cleared drugs in Chinese pregnant women. *Biopharm. Drug Dispos.* 41, 248–267. doi:10.1002/bdd.2243

Steele, R. (1984). Ceftriaxone therapy of meningitis and serious infections. *Am. J. Med.* 77, 50–53.

Stoeckel, K., and Koup, J. (1984). Pharmacokinetics of ceftriaxone in patients with renal and liver insufficiency and correlations with a physiologic nonlinear protein binding model. *Am. J. Med.* 77, 26–32.

Stoeckel, K. (1981). Pharmacokinetics of Rocephin®, a highly active new cephalosporin with an exceptionally long biological half-life. *Chemotherapy* 27, 42–46. doi:10.1159/000238028

Su, G., Xu, H., Riggi, E., He, Z., Lu, L., Lindholm, B., et al. (2018). Association of kidney function with infections by multidrug-resistant organisms: An electronic medical record analysis. *Sci. Rep.* 8, 13372–13379. doi:10.1038/s41598-018-31612-1

Tan, M. L., Yoshida, K., Zhao, P., Zhang, L., Nolin, T. D., Piquette-Miller, M., et al. (2018). Effect of chronic kidney disease on nonrenal elimination pathways: A systematic assessment of CYP1A2, CYP2C8, CYP2C9, CYP2C19, and OATP. *Clin. Pharmacol. Ther.* 103, 854–867. doi:10.1002/cpt.807

Tan, M. L., and Tun, W. W. W. (2019). Reversible choreoathetosis in a patient with end-stage renal disease from administration of ceftriaxone. *Cureus* 11, e5764. doi:10.7759/cureus.5764

Taskar, K. S., Pilla Reddy, V., Burt, H., Posada, M. M., Varma, M., Zheng, M., et al. (2020). Physiologically-based pharmacokinetic models for evaluating membrane transporter mediated drug–drug interactions: Current capabilities, case studies, future opportunities, and recommendations. *Clin. Pharmacol. Ther.* 107, 1082–1115. doi:10.1002/cpt.1693

Thiel, C., Schneckener, S., Krauss, M., Ghallab, A., Hofmann, U., Kanacher, T., et al. (2015). A systematic evaluation of the use of physiologically based pharmacokinetic modeling for cross-species extrapolation. *J. Pharm. Sci.* 104, 191–206. doi:10.1002/jps.24214

Ti, T.-Y., Fortin, L., Kreeft, J., East, D., Ogilvie, R., and Somerville, P. (1984). Kinetic disposition of intravenous ceftriaxone in normal subjects and patients with renal failure on hemodialysis or peritoneal dialysis. *Antimicrob. agents Chemother.* 25, 83–87. doi:10.1128/AAC.25.1.83

Trotman, R. L., Williamson, J. C., Shoemaker, D. M., and Salzer, W. L. (2005). Antibiotic dosing in critically ill adult patients receiving continuous renal replacement therapy. *Clin. Infect. Dis.* 41, 1159–1166. doi:10.1086/444500

Ulldemolins, M., Bastida, C., Llauradó-Serra, M., Csajka, C., Rodríguez, A., Badia, J. R., et al. (2021). Once-daily 1 g ceftriaxone optimizes exposure in patients with septic shock and hypoalbuminemia receiving continuous veno-venous hemodiafiltration. *Eur. J. Clin. Pharmacol.* 77, 1169–1180. doi:10.1007/s00228-021-03100-5

Van Dalen, R., and Vree, T. (1990). Pharmacokinetics of antibiotics in critically ill patients. *Intensive Care Med.* 16, S235–S238. doi:10.1007/BF01709707

Velenosi, T. J., and Urquhart, B. L. (2014). Pharmacokinetic considerations in chronic kidney disease and patients requiring dialysis. *Expert Opin. drug metabolism Toxicol.* 10, 1131–1143. doi:10.1517/17425255.2014.931371

Verscheijden, L. F., Koenderink, J. B., Johnson, T. N., De Wildt, S. N., and Russel, F. G. (2020). Physiologically-based pharmacokinetic models for children: Starting to reach maturation? *Pharmacol. Ther.* 211, 107541. doi:10.1016/j.pharmthera.2020.107541

Wang, K., Yao, X., Zhang, M., Liu, D., Gao, Y., Sahasranaman, S., et al. (2021). Interaction between gender and post resuscitation interventions on neurological outcome in an asphyxial rat model of cardiac arrest. *CPT pharmacometrics Syst. Pharmacol.* 10, 441–454. doi:10.1186/s12872-021-02262-5

Wang, T. Z., Kodiyanplakkal, R. P. L., and Calfee, D. P. (2019). Antimicrobial resistance in nephrology. *Nat. Rev. Nephrol.* 15, 463–481. doi:10.1038/s41581-019-0150-7

Wishart, D. S., Feunang, Y. D., Guo, A. C., Lo, E. J., Marcu, A., Grant, J. R., et al. (2018a). DrugBank 5.0: A major update to the DrugBank database for 2018. *Nucleic acids Res.* 46, D1074–D1082. doi:10.1093/nar/gkx1037

Wishart, D. S., Feunang, Y. D., Marcu, A., Guo, A. C., Liang, K., Vázquez-Fresno, R., et al. (2018b). Hmdb 4.0: The human metabolome database for 2018. *Nucleic acids Res.* 46, D608–D617. doi:10.1093/nar/gkx1089

Wojtyniak, J. G., Britz, H., Selzer, D., Schwab, M., and Lehr, T. (2020). Data digitizing: Accurate and precise data extraction for quantitative systems pharmacology and physiologically-based pharmacokinetic modeling. *CPT Pharmacometrics Syst. Pharmacol.* 9, 322–331. doi:10.1002/psp4.12511

Yamada, S., Takesako, M., Nakano, T., Tsuruya, K., and Kitazono, T. (2020). Rapid formation of large pseudostones and acute cholangitis caused by ceftriaxone treatment for bacterial pneumonia in a patient on kidney transplantation: Potential risk of ceftriaxone use in patients with decreased kidney function. *Cen. case Rep.* 9, 87–88. doi:10.1007/s13730-019-00418-z

frontiers | Frontiers in Pharmacology

TYPE Original Research
PUBLISHED 09 August 2023
DOI 10.3389/fphar.2023.1227354

OPEN ACCESS

EDITED BY
Ling Ye,
Southern Medical University, China

REVIEWED BY
Andrei Medvedovici,
University of Bucharest, Romania
Florentin Tache,
University of Bucharest, Romania

*CORRESPONDENCE
Bo Zhang,
zhangbopumch@163.com
Ying Peng,
ypeng@imm.ac.cn

RECEIVED 23 May 2023
ACCEPTED 28 July 2023
PUBLISHED 09 August 2023

CITATION
Sun Z, Liu X, Zuo W, Fu Q, Xu T, Cui L, Zhang B and Peng Y (2023), Development of a robust UPLC-MS/MS method for the quantification of riluzole in human plasma and its application in pharmacokinetics.
Front. Pharmacol. 14:1227354.
doi: 10.3389/fphar.2023.1227354

Development of a robust UPLC-MS/MS method for the quantification of riluzole in human plasma and its application in pharmacokinetics

Zhuo Sun[1,2,3], Xin Liu[1,2], Wei Zuo[1,2], Qiang Fu[1,2], Tingting Xu[1,2], Liying Cui[4,5], Bo Zhang[1,2]* and Ying Peng[3]*

[1]Department of Pharmacy, Peking Union Medical College Hospital, Chinese Academy of Medical Sciences and Peking Union Medical College, Beijing, China, [2]State Key Laboratory of Complex Severe and Rare Diseases, Peking Union Medical College Hospital, Beijing, China, [3]State Key Laboratory of Bioactive Substances and Functions of Natural Medicines, Institute of Materia Medica, Chinese Academy of Medical Sciences and Peking Union Medical College, Beijing, China, [4]Department of Neurology, Peking Union Medical College Hospital, Chinese Academy of Medical Sciences and Peking Union Medical College, Beijing, China, [5]Neuroscience Center, Chinese Academy of Medical Sciences and Peking Union Medical College, Beijing, China

Introduction: The aim of the present study was to establish a simple method for the determination of riluzole in human plasma by ultraperformance liquid chromatography-tandem mass spectrometry (UPLC-MS/MS) and apply it for the determination of riluzole in amyotrophic lateral sclerosis (ALS) patients.

Methods: Samples were prepared by protein precipitation and were then gradient-eluted on a column of ACQUITY UPLC® HSS T3 by using 0.1% formic acid acetonitrile and 0.1% formic acid water as the mobile phase. Detection was performed on a Xevo TQ-S tandem mass spectrometer in the multiple-reaction monitoring mode using positive electrospray ionization. Validation was performed in the range of 5–800 ng/mL.

Results and discussion: Three batches of precision accuracy, selectivity, matrix effects, extraction recovery, and stability were also verified and met the requirements. The results showed that the method was reliable and successfully applied to the pharmacokinetics study of riluzole in Chinese amyotrophic lateral sclerosis patients. Meanwhile, in comparison with other prior published methods, our method has the advantages of simple sample preparation, relatively short running time, and small plasma sample consumption, which represented a high-throughput sample determination potential.

KEYWORDS

riluzole, clobazam, amyotrophic lateral sclerosis, ultraperformance liquid chromatography-tandem mass spectrometry, pharmacokinetics

1 Introduction

Riluzole is an anti-glutamate drug that has been used to treat amyotrophic lateral sclerosis (ALS) since it was approved by the United States Food and Drug Administration in 1996 (RILUTEK®, tablets) (Fehlings et al., 2021). ALS is a rare disease in which patients typically have a survival of only 3–5 years, due to respiratory failure (Grad et al., 2017). In addition, riluzole is the the only oral drug for ALS treatment in China that can prolong the survival of patients by approximately 3 months (Miller et al., 2012). However, the pharmacokinetic characteristics of riluzole in Chinese ALS patients are unknown. Therefore, the goal is to establish a simple method for determining riluzole in humans, which is convenient for the subsequent construction of population pharmacokinetics (popPK) models of Chinese ALS patients to describe their pharmacokinetics characteristics (Bruno et al., 1997).

So far, several methods have been reported for quantitative determination of riluzole in plasma (Sarkar et al., 2017; Chandu et al., 2010; Chow et al., 2012; Le Liboux et al., 1997; van Kan et al., 2004). These methods used either high-performance liquid chromatography (HPLC) with UV detection or ultraperformance liquid chromatography-tandem mass spectrometry (UPLC-MS/MS). The lower limits of quantification (LLOQ) of the HPLC-UV methods described by Le Liboux, van Kan HJ, and Chow DS were 10 ng/mL, 20 ng/mL, and 20 ng/mL, respectively, and all required large amounts of human plasma (1 mL, 500 μL, and 200 μL) (Chow et al., 2012; Le Liboux et al., 1997; van Kan et al., 2004). More recently, Mahua Sarkar and Chandu BR developed the UPLC-MS/MS method for the riluzole assay in human plasma with an LLOQ of 0.5 ng/mL, but all required 200 μL human plasma (Chandu et al., 2010; Sarkar et al., 2017). In addition, the pre-treatment processes for these methods were all liquid–liquid extraction or solid-phase extraction (SPE), which were considered complex.

In this paper, a novel UPLC-MS/MS method was developed. The plasma sample was prepared using protein precipitation, which was simpler than liquid–liquid extraction or SPE, the analytes were highly efficient in a relatively short time on the T3 column, and the volume of the plasma sample used was small. The combination of the three features resulted in a robust and high-throughput analysis method. In addition, the validated analytical method was successfully applied to the quantitative determination of riluzole in Chinese ALS patients.

2 Materials and method

2.1 Chemicals and regents

Riluzole (Figure 1) was purchased from MedChemExpress (New Jersey, United States). The internal standard (IS) clobazam (Figure 1) (solution in methanol, 100 μg/mL, expiry date 2024.2.23) was purchased from Tianjin Alta Technology Co., Ltd. (Tianjin, China). Methanol, acetonitrile, and water (HPLC-grade) were purchased from Honeywell Burdick and Jackson (Ulsan, Korea). Formic acid (analytical grade) was purchased from Thermo Fisher Scientific CN Co., Ltd. (Shanghai, China).

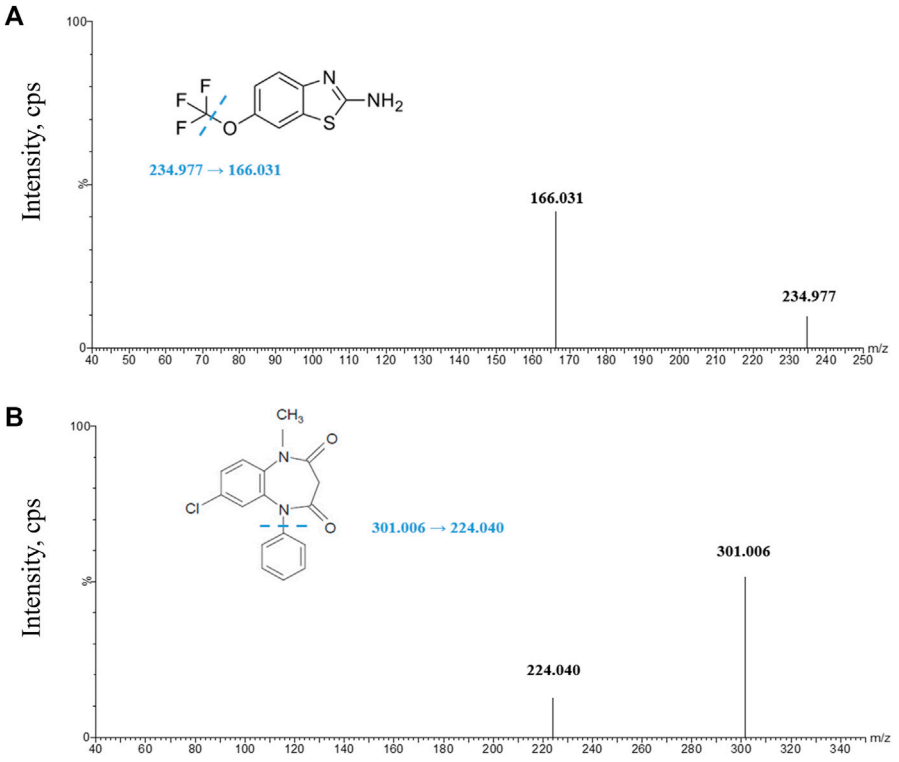

FIGUR 1
Product ion spectra of analytes. **(A)** Riluzole parent ion and daughter ion scan; **(B)** clobazam parent ion and daughter ion scan. The illustrations in Figures **(A)** and **(B)** give the structures of riluzole and clobazam, respectively, and the location of the possible break.

2.2 UPLC conditions

Chromatographic separation was performed on an ACQUITY UPLC I-Class System (Waters, Milford, United States). The analytical column was an ACQUITY UPLC® HSS T3 (2.1 × 50 mm, 1.8 μm, Waters, Milford, United States). The column temperature was set to 40°C. The mobile phase consisted of 0.1% formic acid in acetonitrile and 0.1% formic acid in water. The gradient elution procedure started with 95% formic acid in water maintained for 0.5 min, then the gradient was decreased to 40% formic acid in water within 0.5 min. In addition, the proportion of formic acid in water was continuously decreased to 5% within 2 min and held for 1 min. Finally, the proportion of formic acid in water was switched back to 95% in 0.5 min and held for 0.5 min before the next run. The flow rate was fixed at 0.3 mL/min. In addition, riluzole and clobazam were gradient-eluted at 1.9 min and 2.12 min, respectively. The injection volume was 5 μL, and the total running time was set to 5 min.

2.3 Mass spectrometer conditions

Mass spectrometry was performed using a Xevo TQ-S mass spectrometer (Waters, Milford, United States) equipped with a positive-mode electrospray ionization source (ESI). The test was operated in a multiple-reaction monitoring (MRM) mode with a dwell time of 0.043 s per conversion. Due to time and price constraints, we chose clobazam, which was already available in the laboratory and has similar UPLC conditions to those of riluzole, as the internal standard. The transitions monitored were m/z 234.977→166.031 for riluzole and m/z 301.006→224.040 for clobazam. Ultrahigh-pressure nitrogen was used as the desolvation gas (1000 L/h) and the cone gas (150 L/h). The desolvation temperature was 500°C. The collision energy of riluzole and IS was 28 V and 32 V, respectively. In addition, the capillary voltages of riluzole and IS were both 3 kv.

2.4 Calibration standards and quality control samples

In order to save the drug-free human plasma, we first dilute the stock solution into the working standard solutions and QC solutions with reagents and then dilute the working solutions and QC solutions into the standards and QC samples with the drug-free plasma. The working standard solutions were prepared at concentrations of 0.5, 1, 2, 4, 10, 20, 40, and 80 μg/mL by diluting the stock solution (1 mg/mL) with water–acetonitrile (v: v = 95:5). A standard curve of final concentrations of 5, 10, 20, 40, 100, 200, 400, and 800 ng/mL was obtained by diluting the working standard solution with drug-free human plasma. Similarly, QC solutions at concentrations of 1.5, 6, and 60 μg/mL were also obtained by diluting the stock solution with water–acetonitrile (v: v = 95:5). Quality control samples (QCs) at concentrations of 15, 60, and 600 ng/mL were also obtained by dilution of blank human plasma. All solutions, standards, and QCs were stored frozen at −80°C.

2.5 Sample preparation

A 50 μL volume of the plasma sample was first added to a 1.5 mL Eppendorf tube, and then 200 μL protein precipitation solution (acetonitrile) containing IS (5 ng/mL) was added. The mixture was thoroughly vortexed for 2 min. The supernatant (50 μL) was collected by centrifugation at 12,000 rpm for 10 min. Then, 450 μL of water–acetonitrile (v: v = 95:5) was added and mixed well. The plasma volume used (50 μL) is much lower than that of the published studies (200 μL–1 mL) (Sarkar et al., 2017; Chandu et al., 2010; Chow et al., 2012; Le Liboux et al., 1997; van Kan et al., 2004).

2.6 Data acquisition and analysis

All data were collected and processed using MassLynx software (version 4.1 SCN810). A weighted least-squares linear regression model (weighted 1/x2) was used to establish the relationship between the concentration and the peak area ratio of the analyte to IS. The concentrations of the QC samples and the unknown clinical sample were calculated by interpolation of the equation. For QC samples and calibration standards, except for LLOQ samples (bias <20%), the remaining sample bias should be <15%. In addition, in each analysis run, more than 75% of the QC samples should meet the aforementioned criteria, and the correlation coefficient (r) should be >0.99.

2.7 Method validation

The method was validated in accordance with the FDA (2018) bioanalytical method validation guidance for industry and the European Medicines Agency (2011) guideline on bioanalytical method validation including precision and accuracy, LLOQ, linearity, and stability of the analyte under various conditions, such as carry-over, extraction recovery, and matrix effect.

Three independent and continuous batches of LLOQ, low-, medium-, and high-QC samples were evaluated in at least 2 days to assess the precision and accuracy. In each analysis batch, the QC assessment for each concentration level was repeated six times. Relative standard deviation (RSD) and relative error (RE) were used to indicate precision and accuracy, respectively. In addition to LLOQ, the other three concentration levels of QCs' intra-batch and inter-batch RSD should be ≤ *15%* and RE should be within ±*15%*, while LLOQs' inter-batch and intra-batch RSD should be <*20%* and RE should be within ±*20%*.

The linearity response of riluzole was assessed over calibration ranges. The calibration curve was performed with eight concentrations, and the requirements were the same as those given in Section 2.6.

Stability assessment of the riluzole in a stock solution included long-term stability and short-term stability. However, according to the certificate of analysis (COA) of riluzole, the riluzole solution can be stored for up to 6 months at −80°C, and the short-term stability was evaluated by keeping it at room temperature for 5 h. The IS was diluted when it would be used.

Stability assessment of the analyte in plasma and whole blood included short-term stability, autosampler stability, freeze–thaw stability, whole blood stability, and long-term stability. Short-term stability was evaluated by measuring QCs maintained at room temperature for 4 h. Autosampler stability was achieved by analyzing the processed QCs that had been held in the autosampler (10°C) for 24 h. The freeze–thaw stability was evaluated after seven freeze (−80°C) and thawing (room temperature) cycles before QC sample preparation. Whole blood QCs were kept at room temperature for 4 h to assess the whole blood stability. Long-term stability was assessed by analyzing QCs after storage for 26 days at −80°C.

Extraction recovery was evaluated by comparing the peak areas of the analyte extracted from the three-level QC samples with those of post-extraction spiked QC samples at the same concentrations. The RSD of the extraction should be ≤ *15%*; the RE should be within ±*15%*.

Matrix effects were assessed using low-, medium-, and high-level QCs from six individuals. Matrix factors were evaluated by calculating the peak area's ratio of the presence of the matrix (measured by analyzing the blank matrix spiked with the analyte after extraction) to the absence of the matrix (pure solution of the analyte). The RSD of the matrix effect should be ≤ *15%*.

2.8 Application

The validated analytical method was applied to determine the concentration of riluzole in patient plasma after oral administration of riluzole. The clinical study was approved by the Ethics Committee of Peking Union Medical College Hospital and was in line with good clinical practice. All subjects signed informed consent prior to the study. The criteria for inclusion of ALS patients taking riluzole in our hospital were as follows: 1) age ≥18 years; 2) the treatment course of oral riluzole was ≥2 weeks, indicating that riluzole reached homeostasis in the patient. Exclusion criteria: 1) the duration of medication could not be determined; 2) elderly patients (≥80 years of age) with poor basic condition and many influencing factors are difficult to evaluate; 3) had taken clobazam within 1 month. Since riluzole reached a steady state in enrolled patients, a blood sample was collected from each patient at a random time point, and the last time of medication before blood collection, the time of blood collection, and demographic information about the patients were accurately recorded. All blood samples were centrifuged at 3000 rpm for 10 min to obtain plasma samples, which were stored at −80°C prior to analysis.

3 Results and discussion

3.1 Method development and optimization

3.1.1 Optimization of mass spectrometric parameters

Filtering and optimizing mass spectrometry conditions by systematic methods. We tried atmospheric pressure chemical ionization (APCI) and ESI source in positive and negative ionization modes. Usually, positive ionization is the preferred ionization mode for the detection of neutral or basic analytes. The results show that the ESI source has higher ionization efficiency in the positive ionization mode, which may be related to the presence of the amine group in the molecular structure of riluzole.

An apposite MRM transition of riluzole and IS was selected based on the ion spectrum of the analyte product. In addition, the voltage and gas parameters were adjusted to obtain the most suitable ionization and fragmentation conditions.

3.1.2 Optimization of chromatographic conditions

In order to improve the response and peak shape and reduce the carryover of riluzole, the organic phase and aqueous phase of formic acid with different proportions were tested. Finally, it was found that when the mobile phase was 0.1% formic acid in acetonitrile and 0.1% formic acid in water, and the flow rate of the system was 0.3 mL/min, the best effect was obtained. In addition, under the chromatographic conditions described herein, effective chromatographic separation guaranteed the accurate determination of riluzole within a running time of 5 min.

3.1.3 Optimization of sample preparation

Protein precipitation, liquid–liquid extraction, and SPE are the most common sample pre-treatment methods. Previously reported pre-treatment methods of riluzole samples were liquid–liquid extraction or SPE, which were considered too complicated. Therefore, our study explored the selection of plasma volume, the proportion of the precipitant to plasma, and whether to dilute the supernatant. The results showed that the response of riluzole was appropriate when the volume of the plasma sample was 50 μL, the acetonitrile-to-plasma ratio was 4:1, and 50 μL of the supernatant was diluted with 450 μL solution. If the supernatant was not diluted, the response of the ULOQ sample (800 ng/mL) will exceed the highest response of the machine. In the process of exploration, in order to save clinical samples, we tried to take only 5 μL plasma and added 20 μL acetonitrile in the ratio of 1: 4 for protein precipitation, but the standards and QCs' bias did not meet the requirements. In addition, the dilution of the supernatant with different proportions of water–acetonitrile and whether to add 0.1% formic acid were studied. The response of riluzole was appropriate when water–acetonitrile (v: v = 95:5) was chosen as a diluent, and there was no effect on the results irrespective of adding 0.1% formic acid in water–acetonitrile (v: v = 95:5), so we chose the simpler water–acetonitrile (v: v = 95:5) as a diluent.

In addition, we tried different collision energies, and each analyte obtained three different daughter ions, namely, m/z 234.977→166.031 (28 V), 234.977→149.764 (30 V), and 234.977→138.053 (34 V) for riluzole and m/z 301.006→224.04 (32 V), 301.006→153.064 (36 V), and 301.006→105.110 (34 V) for clobazam. We compared their response, peak shape, and carryover after sample preparation under the corresponding chromatographic conditions. Finally, the product ion spectra were obtained (Figure 1) to select the transitions of the analyte (riluzole, 234.977→166.031) and the IS (clobazam, m/z 301.006→224.040).

All in all, the time and effort required to prepare samples using protein precipitation is significantly reduced compared to that taken by liquid–liquid extraction or SPE reported so far. In addition, the relatively short running time of the method (5 min) and the plasma

TABLE 1 Back-calculated concentrations of calibration standards for riluzole (linear-weighted 1/x2).

Item	S1 (n = 15)	S2 (n = 15)	S3 (n = 15)	S4 (n = 13)	S5 (n = 16)	S6 (n = 13)	S7 (n = 16)	S8 (n = 16)	R^2	Slope	Intercept	Regression equation
Nominal Concentration	5.00 ng/mL	10.0 ng/mL	20.0 ng/mL	40.0 ng/mL	100 ng/mL	200 ng/mL	400 ng/mL	800 ng/mL				
Mean[a]	4.95	9.55	19.3	42.8	94.7	215.9	426.2	765.3	0.996	0.972	5.994	y = 0.972x + 5.994
RE (%)[b]	−0.9	−4.5	−3.7	7.0	−5.3	7.9	6.5	−4.3				
RSD (%)[c]	3.8	3.4	4.7	5.6	3.2	4.2	3.2	2.5				

[a]Concentration is to three significant figures.

[b]Expressed as [(mean observed concentration − nominal concentration)/(nominal concentration)] × 100 (to one decimal place).

[c]Relative standard deviation: standard deviation/mean × 100 (to one decimal place).

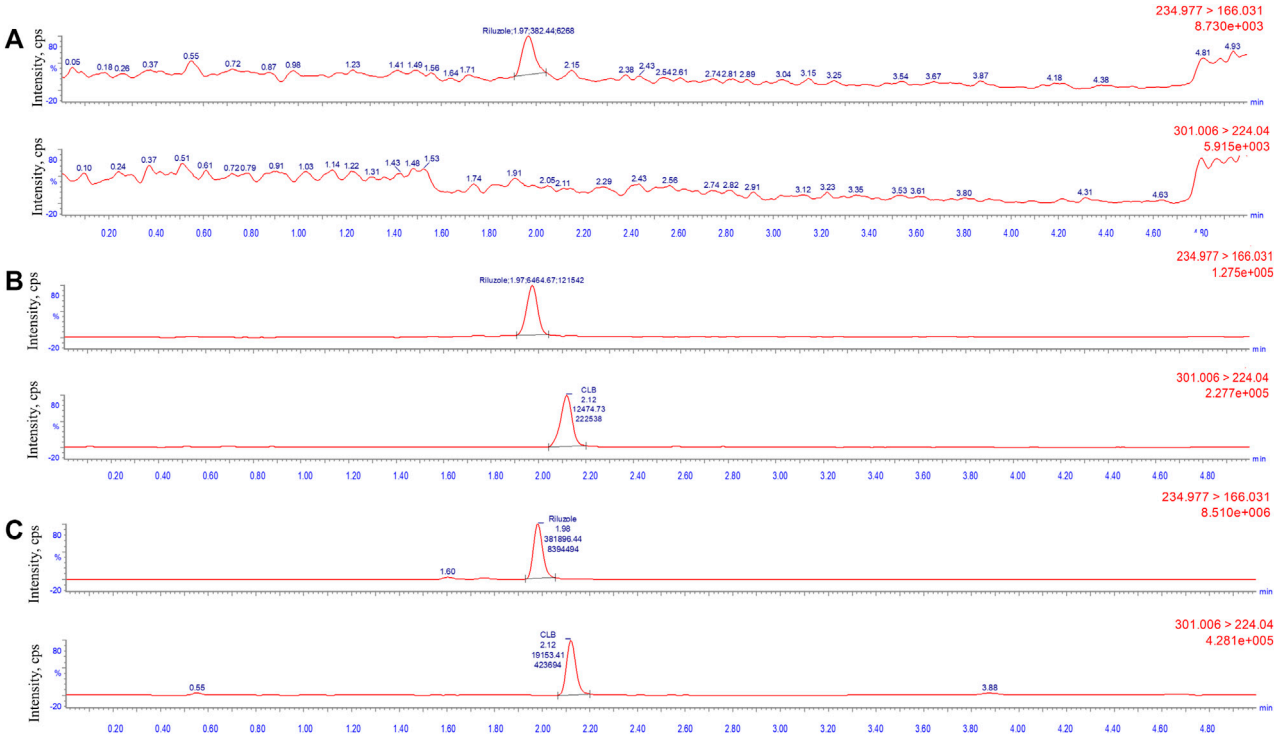

FIGURE 2
Typical multiple-reaction monitoring chromatograms of riluzole and clobazam: **(A)** blank plasma sample; **(B)** plasma spiked with the analytes at LLOQ level (5 ng/mL) and internal standard; and **(C)** real clinical samples (137.2 ng/mL).

volume used (50 μL) is much smaller than that of the published works (200 μL–1 mL), making it ideal for drug analysis in the clinical setting (Sarkar et al., 2017; Chandu et al., 2010; Chow et al., 2012; Le Liboux et al., 1997; van Kan et al., 2004).

3.2 Method validation

3.2.1 Linearity, carryover, and selectivity

Eight calibration standards were analyzed per batch, and the calibration curve showed good linearity in the range of 5–800 ng/mL. The regression coefficients of all standard curves were >0.99 and the back-calculated concentrations were within *85%–115%* of their nominal values (Table 1). Carryover was investigated by testing the blank sample after the upper limit of quantitation (ULOQ). The peak area of carryover was within *20%* of the peak area at LLOQ in every analytical batch. As a result, the peak area of carryover was approximately *10%* of the peak area at LLOQ throughout method validation, which met the requirements.

The concentration of LLOQ was 5 ng/mL. Figure 2 shows a typical chromatogram of the analyte and IS in blank plasma samples spiked with the analyte at the LLOQ level and IS (5 ng/mL). The results indicated that the method had satisfactory selectivity for riluzole and IS.

TABLE 2 Intra- and inter-day precision and accuracy of quality control samples of riluzole.

Batch	Item	LLOQ	Low QC	Medium QC	High QC
	Nominal concentration	5.00 ng/mL	15.0 ng/mL	60.0 ng/mL	600 ng/mL
1 (n = 6)	Mean[a]	5.1	15.5	55.6	632
1 (n = 6)	RE (%)[b]	2.0	3.4	−7.4	5.3
1 (n = 6)	RSD (%)[c]	2.5	1.9	1.4	2.9
2 (n = 6)[d]	Mean[a]	5.1	15.8	54.6	629
2 (n = 6)[d]	RE (%)[b]	2.3	5.0	−8.9	4.9
2 (n = 6)[d]	RSD (%)[c]	2.9	2.7	0.8	0.7
3 (n = 6)	Mean[a]	4.5	15.4	63.1	660
3 (n = 6)	RE (%)[b]	−11.0	2.6	5.2	10.0
3 (n = 6)	RSD (%)[c]	1.9	1.7	2.0	1.6
Inter-day (n = 17)	Mean[a]	4.9	15.6	58.0	640
Inter-day (n = 17)	RE (%)[b]	−2.2	3.7	−3.4	6.7
Inter-day (n = 17)	RSD (%)[c]	6.9	2.3	6.9	2.9

[a]Concentration is to three significant figures.
[b]Expressed as [(mean observed concentration − nominal concentration)/(nominal concentration)] × 100 (to one decimal place).
[c]Relative standard deviation: standard deviation/mean × 100 (to one decimal place).
[d]For batch 2, the number of Q2 was 5.

TABLE 3 Matrix effect (n = 6) and extraction recovery (n = 6) of riluzole in plasma.

	Spiked concentration (ng/mL)	Extraction recovery (%)		Matrix effect (%)	
		Mean ± SD	RSD	Mean ± SD	RSD
Riluzole	15.0	93.0 ± 3.9	4.2	103.8 ± 3.6	3.5
	60.0	100.1 ± 1.8	1.8	102.4 ± 0.7	0.7
	600	98.5 ± 1.4	1.4	105.2 ± 0.6	0.6
Clobazam	5.00	109.6 ± 4.7	4.3	103.7 ± 2.9	2.8

[a]Concentration is to three significant figures.
[b]Expressed as [(mean observed concentration − nominal concentration)/(nominal concentration)] × 100 (to one decimal place).
[c]Relative standard deviation: standard deviation/mean × 100 (to one decimal place).

3.2.2 LLOQ, precision, and accuracy

Table 2 summarizes the intra- and inter-assay precision and accuracy of riluzole measured by LLOQ and three QC levels. Compared with the nominal concentration, the RE of LLOQ samples ranged from *-12.3% to 5.9%*, the RE of other QC samples ranged from *-10.1% to 13.1%*, and the RSD level for each concentration was also *<15%*. The results showed that the precision and accuracy were within an acceptable range. The method was reliable and reproducible and can be used for the determination of riluzole concentration in human plasma.

3.2.3 Matrix effect and extraction recovery

The results of matrix effect and extraction recovery are shown in Table 3. The matrix effect of riluzole was between *99.1% and 107.6%*; therefore, the matrix did not significantly affect the determination of drug concentration. The overall average extraction recovery of riluzole at three different concentrations was *97.2%*.

3.2.4 Stability

The results showed that the riluzole stock solution can be kept at room temperature for 4 h. The stability results of riluzole in plasma and in whole blood are shown in Table 4. The riluzole plasma samples could be stably placed at room temperature for 4 h, remained stable after seven freeze–thaw cycles (−80°C to room temperature), and could be stably stored at −80°C for at least 26 days. In addition, the processed samples remained stable after being placed in the autosampler for 24 h, and the riluzole whole blood samples were stable for 4 h at room temperature, providing a time window for clinical sample processing. At the same time, according to the concentrations measured after the preparation of the whole blood QCs, it can be inferred that riluzole may

TABLE 4 Stability assessments for riluzole in plasma, processed, and whole blood samples (n = 6).

Stability type	Nominal concentration (ng/mL)	Mean[a]	RE (%)[b]	RSD (%)[c]
Short-term	15.0	14.8	−1.3	1.5
(plasma samples, room temperature for 4 h)	60.0	62.3	3.8	1.6
	600	630.8	5.1	1.4
Freeze–thaw	15.0	15.3	1.9	1.3
(plasma samples, seven cycles)	60.0	61.8	3.0	1.0
	600	635.3	5.9	1.6
Long-term	15.0	16.8	11.9	1.3
(plasma samples, −80°C for 26 days)	60.0	66.4	10.6	0.9
	600	677.9	13.0	1.6
Autosampler	15.0	17.2	14.8	1.9
(processed samples, 10°C for 24 h)	60.0	66.9	11.6	1.2
	600	685.4	14.2	1.7
Whole blood[a]	7.1	7.0	−0.9	1.6
(room temperature for 4 h)	29.3	25.6	−12.6	1.2
	279	275	−1.5	1.3

[a]Concentration is to three significant figures.
[b]Expressed as [(mean observed concentration − nominal concentration)/(nominal concentration)] × 100 (to one decimal place).
[c]Relative standard deviation: standard deviation/mean × 100 (to one decimal place).
*When configuring whole blood stable QC samples, assuming that riluzole is not distributed in blood cells, the volume of plasma centrifuged is about half of the volume of whole blood, so the configured final concentrations of whole blood QC samples were 7.5, 30, and 300 ng/mL.

TABLE 5 Concentration of riluzole in ALS patients after multiple oral doses (50 mg bid).

Patient	The time of the last dosing before the blood collection (h)	Concentration (ng/mL)	Patient	C_{trough} (ng/mL)
1	4.5	37	2	20.6
3	4	76.6	4	37
5	8.5	71.7	10	16
6	2.5	137.2	11	37.4
7	5.25	90.8	13	58

Note: Steady-state trough concentrations were collected for patients 2, 4, 8, 9, and 10.

be distributed in the whole blood cells, but further experimental verification is needed.

3.2.5 Application

The UPLC-MS/MS method was successfully applied to determine the steady-state concentration of riluzole in ALS patients treated with riluzole for at least 1 month. So far, 10 plasma samples from 10 ALS patients have been successfully analyzed, and no notable problems have occurred during the whole analysis, such as changes in retention time and interference. Table 5 shows the concentrations of 10 subjects who received riluzole. At present, steady-state trough concentrations were collected for patients 2, 4, 8, 9, and 10, and the collection time points for other patients were in the elimination phase. According to (Bruno et al. 1997), the steady-state trough concentration of patients with SCI after taking riluzole ranged from 11.17 to 147.55 ng/mL. The concentrations of the five samples that had reached the steady state in our experiments were 20.6, 37, 16, 37.4, and 58 ng/mL, respectively, which were consistent with the range of SCI patients. Of course, further verification of large samples was needed. Therefore, based on the current results, 5 ng/mL was a suitable LLOQ. At the same time, considering the range of steady-state peak concentration of riluzole reported in foreign patients with SCI (Bruno et al., 1997), the ULOQ is also appropriate in order to continue the determination of subsequent collected samples, including those with around peak concentration. In general, the range of the standard curve in our method was suitable for the clinical setting. We will further establish popPK of riluzole in Chinese ALS patients after measuring the samples collected later and compare its pharmacokinetic characteristics with those of foreign patients with ALS or SCI (Bruno et al., 1997).

In addition, as the disease progresses, swallowing difficulties may gradually appear in ALS patients, resulting in an inability to take oral riluzole tablets. Therefore, in recent years, researchers have

devoted themselves to the development of new dosage forms of riluzole, such as suspension and oral films (Wymer et al., 2023). The simple method was established for the determination of riluzole concentration, which was convenient for other groups to refer to, and can be applied in the study of pharmacokinetics and bioavailability of new forms of riluzole.

4 Conclusion

A robust UPLC-MS/MS method has been developed and validated for the determination of riluzole in human plasma, and the feasibility of this method was further verified by the determination of the riluzole concentration in clinical samples. Compared with other reported analytical methods, our method has the advantages of simple sample preparation, relatively short running time, and small plasma sample volume. Considering the high-throughput potential of our method, it can be easy to analyze patient samples in the clinical setting or clinical trials. At the same time, this was the first published method used to determine the riluzole concentration of Chinese ALS patients, and the first to report the stability data of riluzole in whole blood, which is conducive to the development of subsequent studies related to the pharmacokinetics of riluzole.

Data availability statement

The raw data supporting the conclusion of this article will be made available by the authors, without undue reservation.

Ethics statement

The studies involving human participants were reviewed and approved by Peking Union Medical College Hospital. The patients/participants provided their written informed consent to participate in this study.

Author contributions

ZS designed, performed, and interpreted the experiments and wrote the manuscript. XL, WZ, QF, TX, and LC supported the collection of the samples and experiment execution. BZ and YP conceived the study, supervised the participants, interpreted the experiments, and modified the manuscript. All authors contributed to the article and approved the submitted version.

Funding

The study was supported by National High Level Hospital Clinical Research Funding (2022-PUMCH-B-059), CAMS Innovation Fund for Medical Sciences (CIFMS 2021-I2M-1-003), the Fundamental Research Funds for the Central Universities (3332021003, 2021-RW310-001), the Youth Research Fund of Peking Union Medical College Hospital (201911755), and the Research Fund of Chinese Research Hospital Association (Y2021FH-YWPJ01-106).

Conflict of interest

The authors declare that the research was conducted in the absence of any commercial or financial relationships that could be construed as a potential conflict of interest.

Publisher's note

All claims expressed in this article are solely those of the authors and do not necessarily represent those of their affiliated organizations, or those of the publisher, the editors, and the reviewers. Any product that may be evaluated in this article, or claim that may be made by its manufacturer, is not guaranteed or endorsed by the publisher.

References

Bruno, R., Vivier, N., Montay, G., Le Liboux, A., Powe, L. K., Delumeau, J. C., et al. (1997). Population pharmacokinetics of riluzole in patients with amyotrophic lateral sclerosis. *Clin. Pharmacol. Ther.* 62 (5), 518–526. doi:10.1016/S0009-9236(97)90047-3

Chandu, B. R., Nama, S., Kanala, K., Challa, B. R., Shaik, R. P., and Khagga, M. (2010). Quantitative estimation of riluzole in human plasma by LC-ESI-MS/MS and its application to a bioequivalence study. *Anal. Bioanal. Chem.* 398 (3), 1367–1374. doi:10.1007/s00216-010-4034-8

Chow, D. S., Teng, Y., Toups, E. G., Aarabi, B., Harrop, J. S., Shaffrey, C. I., et al. (2012). Pharmacology of riluzole in acute spinal cord injury. *J. Neurosurg. Spine* 17 (1), 129–140. doi:10.3171/2012.5.AOSPINE12112

Fehlings, M. G., Badhiwala, J. H., Ahn, H., Farhadi, H. F., Shaffrey, C. I., Nassr, A., et al. (2021). Safety and efficacy of riluzole in patients undergoing decompressive surgery for degenerative cervical myelopathy (CSM-Protect): A multicentre, double-blind, placebo-controlled, randomised, phase 3 trial. *Lancet Neurol.* 20 (2), 98–106. doi:10.1016/S1474-4422(20)30407-5

Grad, L. I., Rouleau, G. A., Ravits, J., and Cashman, N. R. (2017). Clinical spectrum of amyotrophic lateral sclerosis (ALS). *Cold Spring Harb. Perspect. Med.* 7 (8), a024117. doi:10.1101/cshperspect.a024117

Le Liboux, A., Lefebvre, P., Le Roux, Y., Truffinet, P., Aubeneau, M., Kirkesseli, S., et al. (1997). Single- and multiple-dose pharmacokinetics of riluzole in white subjects. *J. Clin. Pharmacol.* 37 (9), 820–827. doi:10.1002/j.1552-4604.1997.tb05630.x

Miller, R. G., Mitchell, J. D., and Moore, D. H. (2012). Riluzole for amyotrophic lateral sclerosis (ALS)/motor neuron disease (MND). *Cochrane Database Syst. Rev.* 2012 (3), CD001447. doi:10.1002/14651858.CD001447.pub3

Sarkar, M., Grossman, R. G., Toups, E. G., and Chow, D. S. (2017). UPLC-MS/MS assay of riluzole in human plasma and cerebrospinal fluid (CSF): Application in samples from spinal cord injured patients. *J. Pharm. Biomed. Anal.* 146, 334–340. doi:10.1016/j.jpba.2017.08.045

van Kan, H. J., Spieksma, M., Groeneveld, G. J., Toraño, J. S., van den Berg, L. H., and Guchelaar, H. J. (2004). A validated HPLC assay to monitor riluzole plasma or serum concentrations in patients with amyotrophic lateral sclerosis. *Biomed. Chromatogr.* 18 (9), 723–726. doi:10.1002/bmc.384

Wymer, J., Apple, S., Harrison, A., and Hill, B. A. (2023). Pharmacokinetics, bioavailability, and swallowing safety with riluzole oral film. *Clin. Pharmacol. Drug Dev.* 12 (1), 57–64. doi:10.1002/cpdd.1168

frontiers | Frontiers in Pharmacology

TYPE Original Research
PUBLISHED 18 September 2023
DOI 10.3389/fphar.2023.1199548

OPEN ACCESS

EDITED BY
Ling Ye,
Southern Medical University, China

REVIEWED BY
Przemyslaw Jan Danek,
Polish Academy of Sciences, Poland
Jiangeng Huang,
Huazhong University of Science and Technology, China

*CORRESPONDENCE
Jingjing Nie,
niejingjing413@126.com
Jingjing Lin,
75114292@qq.com

†These authors have contributed equally to this work

RECEIVED 03 April 2023
ACCEPTED 16 August 2023
PUBLISHED 18 September 2023

CITATION
Zhan Y, Wang A, Yu Y, Chen J, Xu X, Nie J and Lin J (2023), Inhibitory mechanism of vortioxetine on CYP450 enzymes in human and rat liver microsomes. *Front. Pharmacol.* 14:1199548. doi: 10.3389/fphar.2023.1199548

Inhibitory mechanism of vortioxetine on CYP450 enzymes in human and rat liver microsomes

Yunyun Zhan[1†], Anzhou Wang[2,3†], Yige Yu[3], Jie Chen[3], Xinhao Xu[3], Jingjing Nie[2*] and Jingjing Lin[3*]

[1]Department of Pharmacy, The Affiliated Lihuili Hospital, Ningbo University, Ningbo, Zhejiang, China, [2]Department of Pharmacy, The Third Affiliated Hospital of Wenzhou Medical University, Wenzhou, Zhejiang, China, [3]Department of Pharmacy, The First Affiliated Hospital of Wenzhou Medical University, Wenzhou, Zhejiang, China

Vortioxetine is a novel anti-major depression disorder drug with a high safety profile compared with other similar drugs. However, little research has been done on drug-drug interactions (DDI) about vortioxetine. In this paper, the inhibitory effect of vortioxetine on cytochrome P450 (CYP450) and the type of inhibitory mechanism were investigated in human and rat liver microsomes. We set up an *in vitro* incubation system of 200 μL to measure the metabolism of probe substrates at the present of vortioxetine at 37°C. The concentrations of the metabolites of probe substrates were all measured by ultra-performance liquid chromatography tandem mass spectrometry (UPLC-MS/MS) method. It was found no time-dependent inhibition (TDI) of vortioxetine through determination of half-maximal inhibitory concentration (IC_{50}) shift values. The enzymes and metabolites involved in this experiment in human and rats were as follows: CYP3A4/CYP3A (midazolam); CYP2B6/CYP2B (bupropion); CYP2D6/CYP2D (dextromethorphan); CYP2C8/CYP2C-1 (amodiaquine); CYP2C9/CYP2C-2 (losartan); and CYP2C19/CYP2C-3 (mephenytoin). We found that vortioxetine competitively inhibited CYP2C19 and CYP2D6 in human liver microsomes (HLMs) with inhibition constant (K_i) values of 2.17 μM and 9.37 μM, respectively. It was noncompetitive inhibition for CYP3A4 and CYP2C8, and its K_i values were 7.26 μM and 6.96 μM, respectively. For CYP2B6 and CYP2C9, vortioxetine exhibited the mixed inhibition with K_i values were 8.55 μM and 4.17 μM, respectively. In RLMs, the type of vortioxetine inhibition was uncompetitive for CYP3A and CYP2D (K_i = 4.41 and 100.9 μM). The inhibition type was competitive inhibition, including CYP2B and CYP2C-2 (K_i = 2.87 and 0.12 μM). The inhibition types of CYP2C-1 and CYP2C-3 (K_i = 39.91 and 4.23 μM) were mixed inhibition and noncompetitive inhibition, respectively. The study of the above mechanism will provide guidance for the safe clinical use of vortioxetine so that the occurrence of DDI can be avoided.

KEYWORDS

vortioxetine, inhibition mechanism, drug-drug interaction, CYP450, UPLC-MS/MS

1 Introduction

With the rapid development of the times and fast-paced life, the number of people suffering from depression is increasing year by year (Lam et al., 2014). The cognitive function of the brain will be greatly damaged after suffering from major depressive disorder, which will greatly affect people's daily life and work (Pehrson and Sanchez, 2014). Vortioxetine, as a

TABLE 1 Analytical parameters for the metabolites and internal standard (IS).

Analytes	Ionization mode	Parent (*m/z*)	Daughter (*m/z*)	Cone (V)	Collision (V)
Hydroxy bupropion	ESI $^+$	256.0	238.0	20	10
4-hydroxy mephenytoin	ESI $^+$	235.1	150.0	15	20
Dextrorphan	ESI $^+$	258.0	157.0	55	40
E-3174	ESI $^+$	437.2	235.0	20	15
N-desethyl amodiaquine	ESI $^+$	328.0	282.8	20	15
1-Hydroxymidazolam	ESI $^+$	341.9	324.0	50	20
Diazepam (IS)	ESI $^+$	285.0	154.0	10	30

TABLE 2 The IC_{50} values on CYP450 in (−) NADPH or (+) NADPH with IC_{50} fold shift and inhibitory effects of vortioxetine on CYP450 in HLMs and RLMs.

	CYP isoform	IC_{50}	IC_{50} values (μM)		IC_{50} fold shift	Inhibition type			
			(−) NADPH	(+) NADPH			Ki (μM)	αKi (μM)	α
HLMs	CYP3A4	9.31	15.52	13.65	1.14	Noncompetitive	7.26	6.82	0.94
	CYP2B6	8.94	5.38	6.69	0.80	Mixed	8.55	23.04	2.70
	CYP2C8	15.00	18.21	18.70	0.97	Noncompetitive	6.96	13.48	1.94
	CYP2C9	23.03	18.57	16.66	1.11	Mixed	4.17	66.5	15.94
	CYP2C19	2.40	5.88	2.83	2.08	Competitive	2.17	-	-
	CYP2D6	17.93	19.37	18.35	1.06	Competitive	9.37	-	-
RLMs	CYP3A	16.37	20.94	16.41	1.28	Uncompetitive	4.41	-	-
	CYP2B	8.89	10.11	5.30	1.91	Competitive	2.87	-	-
	CYP2C-1	22.17	19.78	9.97	1.98	Mixed	39.91	56.73	1.42
	CYP2C-2	0.37	8.97	37.47	0.24	Competitive	0.12	-	-
	CYP2C-3	20.28	24.63	5.21	4.72	Noncompetitive	4.23	12.54	2.97
	CYP2D	15.67	3.35	7.38	0.45	Uncompetitive	100.9	-	-

Note: IC_{50} fold shift value is the ratio of the IC_{50} value of (−) NADPH, to the IC_{50} value of (+) NADPH.

novel anti-major depressive disorder drug, may have two mechanisms at present: one is to inhibit serotonin transporter, and the other is to modulate the effects of several serotonin (5-HT) receptors (Pehrson and Sanchez, 2014). Based on the above mechanism of action, vortioxetine has certain therapeutic effects on cognitive impairment repair, sleep disturbance and chronic neuropathic pain (Frampton, 2016; Adamo et al., 2021). Clinical data show that vortioxetine does not need to adjust the therapeutic dose for these influencing factors such as gender and age, which means that the drug has greater clinical safety (Chen et al., 2018).

In addition to paying attention to the pharmacodynamics of the drug, we should also pay attention to its pharmacokinetics, such as what happens to vortioxetine in the body's metabolism. Drug's metabolism through the liver, gastrointestinal tract, lungs, skin, kidneys, etc., of which 90% of the drugs are metabolized by the liver (Arora et al., 2015). The reason is that there are a lot of cytochrome P450 (CYP450) enzymes in the liver, and these enzyme proteins are mainly used for the oxidation reaction of substances in the human body. In human, vortioxetine has been shown to be involved in the metabolism of CYP450 enzymes, including CYP2A6, CYP3A4/5, and CYP2C9, CYP2C19, and CYP2D6 (Hvenegaard et al., 2012). Its main metabolic enzyme was CYP2D6, followed by others (Hvenegaard et al., 2012). According to the current statistics, there is no significant difference about using vortioxetine between Chinese people and non-Chinese people whether they were strong metabolizers or poor metabolizers (Miao et al., 2019). But whether drug-drug interactions (DDI) affect its metabolism is now poorly understood.

Here we explored the type of mechanism of inhibition by vortioxetine on CYP3A4/3A, CYP2B6/2B, CYP2C8/2C-1, CYP2C9/2C-2, CYP2C19/2C-3, and CYP2D6/2D in human liver microsomes (HLMs) and rat liver microsomes (RLMs), in which the substrates corresponding to each enzyme were midazolam, bupropion, amodiaquine, losartan, mephenytoin, and detromethorphan. We used an ultra-performance liquid chromatography tandem mass spectrometry (UPLC-MS/MS) as the analytical instrument to assess the specific mechanism of inhibition of vortioxetine on CYP450 enzymes. However, no related results have been reported before.

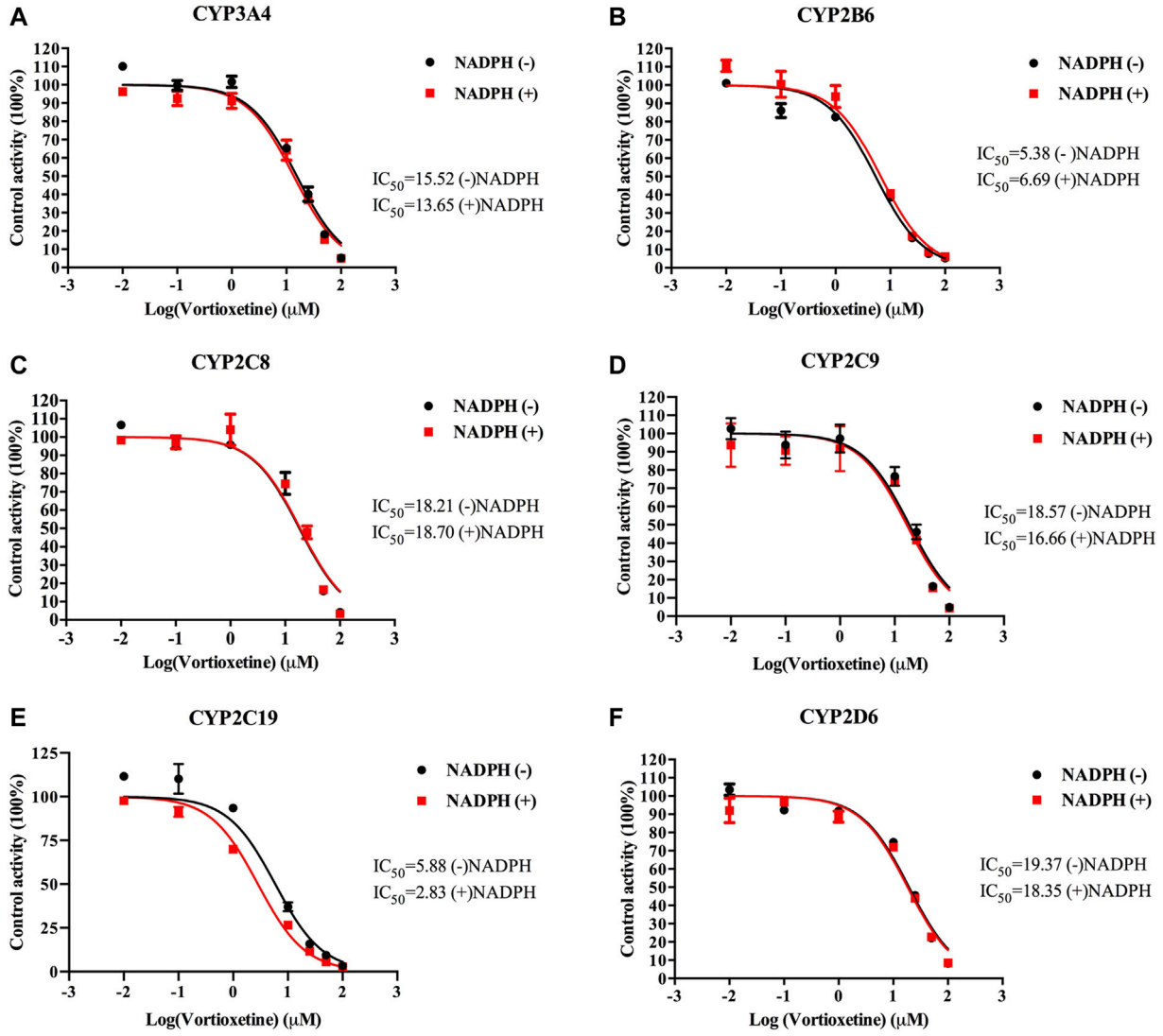

FIGURE 1
The IC_{50} shift curves of vortioxetine on the **(A)** CYP3A4, **(B)** CYP2B6, **(C)** CYP2C8, **(D)** CYP2C9, **(E)** CYP2C19 and **(F)** CYP2D6 activities in HLMs. The concentrations of vortioxetine were 0.01–100 μM. Values are expressed as mean ± SD of three samples.

2 Materials and methods

2.1 Materials and regents

HLMs and RLMs all were purchased from iPhase Pharmaceutical Services Co., Ltd. (Beijing, China). Metabolic probe substrates and their metabolites including midazolam, 1-hydroxymidazolam, bupropion, hydroxy bupropion, amodiaquine, N-desethyl amodiaquine, losartan, E-3174, mephenytoin, 4-hydroxy mephenytoin, dextromethorphan, and dextrorphan were purchased from Shanghai Canspec Scientific Instruments Co., Ltd. (Shanghai, China). The internal standard diazepam and vortioxetine were purchased from Beijing Sunflower Technology Development Co., Ltd. (Beijing, China). The reduced nicotinamide adenine dinucleotide phosphate (NADPH) used in the incubation system was purchased from Roche Pharmaceutical Ltd. (Basel, Switzerland). Methanol and acetonitrile used for UPLC-MS/MS were purchased from Merck (Darmstadt, Germany). Ultrapure water was obtained from Millipore (Bedford, MA, United States) by using a Milli-Q A10 purification system.

2.2 Microsomal incubation procedure

To study the inhibitory effect of vortioxetine on specific enzymes, *in vitro* incubation system of 200 μL was established, and the incubation temperature was 37°C. The components of the incubation system were as follows: 0.20 mg/mL HLMs or 0.20 mg/mL RLMs, 0.1 M Tris-HCl, vortioxetine, and the probe substrates of each enzyme. In the study of K_m's (Michaelis–Menten constant) experiment, midazolam (1, 2, 5, 10, 20, 50 and 100 μM in HLMs and RLMs) corresponded to CYP3A4/3A; bupropion (10, 20, 50, 100, 200, 500, 1,000 and 2000 μM in HLMs; 1, 2, 5, 10, 20, 50, 100 and

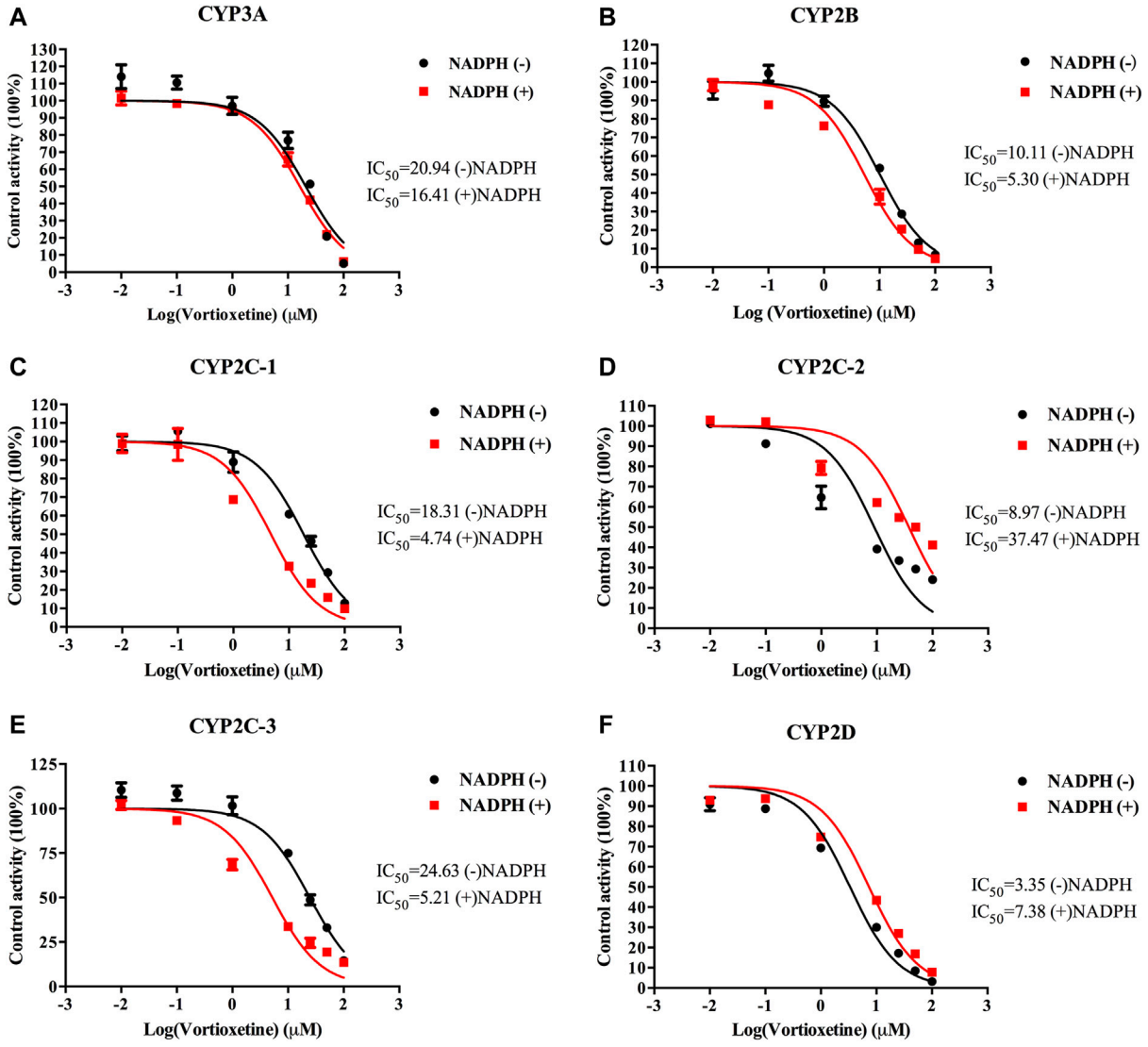

FIGURE 2
The IC_{50} shift curves of vortioxetine on the **(A)** CYP3A, **(B)** CYP2B, **(C)** CYP2C-1, **(D)** CYP2C-2, **(E)** CYP2C-3 and **(F)** CYP2D activities in RLMs. The concentrations of vortioxetine were 0.01–100 μM. Values are expressed as mean ± SD of three samples.

200 μM in RLMs) corresponded to CYP2B6/2B; amodiaquine (5, 10, 20, 50, 100 and 200 μM in HLMs; 10, 20, 50, 100, 200, 500 μM in RLMs) corresponded to CYP2C8/CYP2C-1; losartan (1, 2, 5, 10, 20, 50, 100, 200 μM in HLMs; 10, 20, 50, 100, 200, 500 and 1,000 μM in RLMs) corresponded to CYP2C9/CYP2C-2; mephenytoin (20, 50, 100, 200, 500 and 1,000 μM in HLMs; 5, 10, 20, 50, 100, 200, 500 and 1,000 μM in RLMs) corresponded to CYP2C19/CYP2C-3; and dextromethorphan (1, 2, 5, 10, 20, 50 and 100 μM in HLMs and RLMs) corresponded to CYP2D6/CYP2D. After 5.0 min of preincubation in the shaking water bath, the reaction was started with the addition of 1.0 mM NADPH. The incubated temperature at 37°C for 30 min. After the incubation, the enzyme reaction was stopped by cooling at −80°C, and 200 μL of acetonitrile and 20 μL of internal standard diazepam (200 ng/mL) were added for protein precipitation. The solution was fully vortexed and centrifuged at 13,000 × rpm for 10 min, and the supernatant was collected for data analysis by UPLC-MS/MS.

The significance of half-maximal inhibitory concentration (IC_{50}) was the concentration of the inhibitor to cause 50% inhibition of original enzyme activity. To explore the IC_{50}, the concentrations of the inhibitor vortioxetine were all 0.01, 0.1, 1, 10, 25 and 50 μM, while individual substrate was set according to its corresponding K_m value.

2.3 IC_{50}-shift experiments of vortioxetine

IC_{50}-shift was used to investigate whether the drug produced time-dependent inhibition (TDI) of the enzyme. This inhibitory property belongs to the category of irreversible inhibition among the types of enzyme inhibition. The IC_{50}-shift experiment was performed by preincubating vortioxetine with HLMs or RLMs for 30 min at 37°C in the absence and presence of 1.0 mM

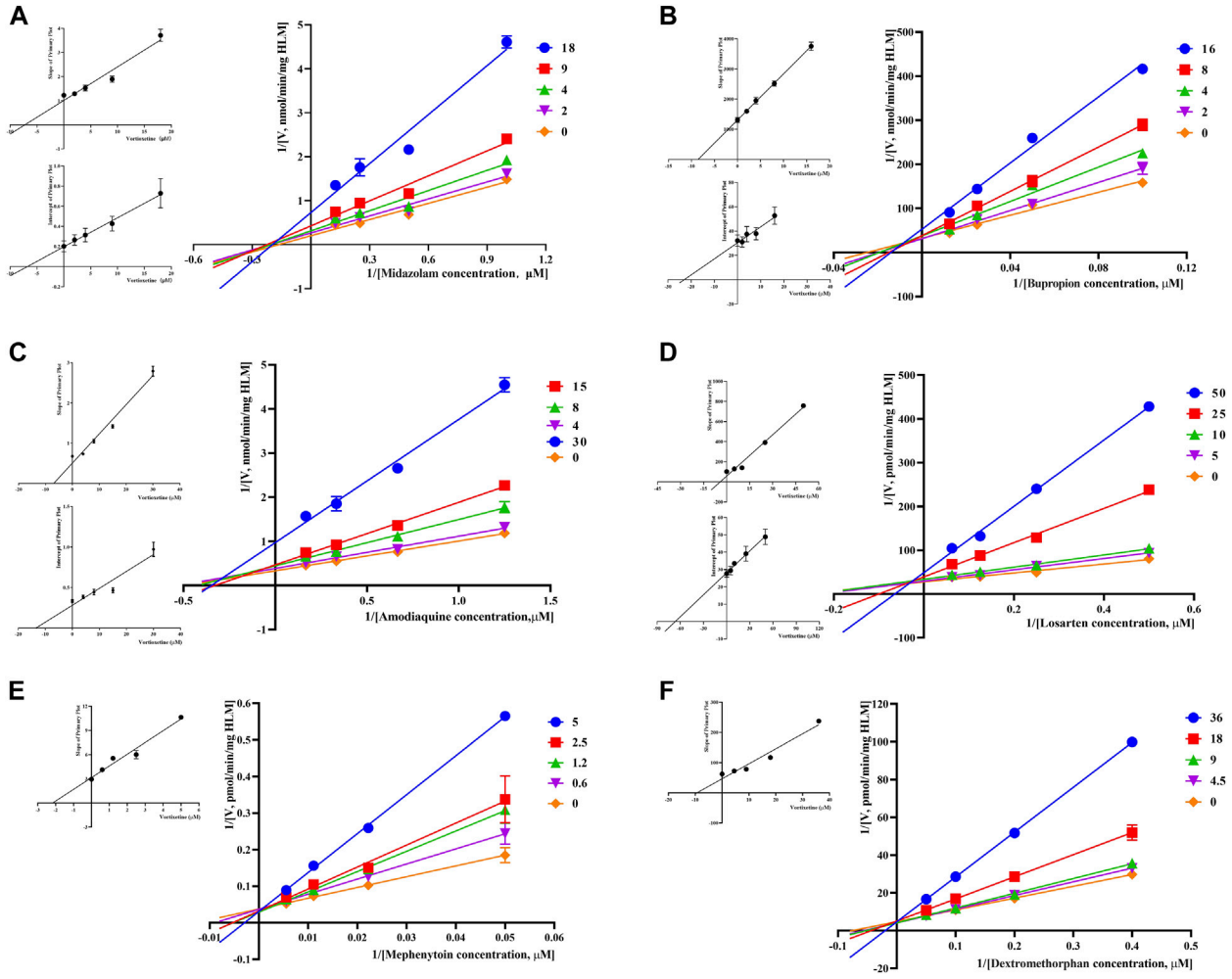

FIGURE 3
Primary Lineweaver–Burk plot, the secondary plot for K_i and the secondary plot for αK_i in the inhibition of CYP-mediated probe metabolism by various concentrations of vortioxetine in HLMs. **(A)** Midazolam was used at concentration of 2, 4, 9 and 18 μM; **(B)** bupropion was used at concentration of 2, 4, 8 and 16 μM; **(C)** amodiaquine was used at concentration of 4, 8, 15 and 30 μM; **(D)** losartan was used at concentration of 5, 10, 25 and 50 μM; **(E)** mephenytoin was used at concentrations of 0.6, 1.2, 2.5 and 5 μM; **(F)** dextromethorphan was used at concentrations of 4.5, 9, 18 and 36 μM. Each data point represents the mean of three samples.

NADPH. The above mixture was then incubated for another 30 min. During the experiment, the individual substrates midazolam (4 μM), bupropion (40 μM), amodiaquine (3 μM), losartan (8 μM), mephenytoin (90 μM), and dextromethorphan (10 μM) were determined with vortioxetine IC_{50}-shift in HLMs. In RLMs, the substrates midazolam (3.5 μM), bupropion (20 μM), amodiaquine (20 μM), losartan (15 μM), mephenytoin (400 μM), and dextromethorphan (20 μM) were determined with vortioxetine IC_{50}-shift, which based on its K_m value. Other experimental conditions were the same as above.

2.4 Reversible inhibition of vortioxetine on CYP450

The inhibitory effect of the drug on different enzymes was different. The inhibitory mechanism of the inhibitor on the enzyme was generally used by different concentrations of the inhibitor against different concentrations of the probe substrate. The concentrations of the inhibitor and the concentrations of probe substrates in the experiment were estimated based on IC_{50} and K_m values, respectively.

In HLMs, the concentrations of the substrates midazolam, bupropion, amodiaquine, losartan, mephenytoin, and dextromethorphan were 1, 2, 4, 8 μM; 10, 20, 40, 80 μM; 0.8, 1.5, 3, 6 μM; 2, 4, 8, 16 μM; 20, 45, 90, 180 μM; 2.5, 5, 10, 20 μM, respectively. Corresponding to the concentration of vortioxetine were 2, 4, 9, 18 μM; 2, 4, 8, 16 μM; 4, 8, 15, 30 μM; 5, 10, 25, 50 μM; 0.6, 1.2, 2.5, 5 μM; 4.5, 9, 18, 36 μM, respectively.

In RLMs, the concentrations of the substrates midazolam and dextromethorphan were 0.8, 1.6, 3.5, 7 μM and 5, 10, 20, 40 μM, respectively, vortioxetine concentrations were 4, 8, 16, 32 μM. The concentrations of mephenytoin and amodiaquine were 100, 200, 400, 800 μM and 5, 10, 20, 40 μM, respectively, vortioxetine

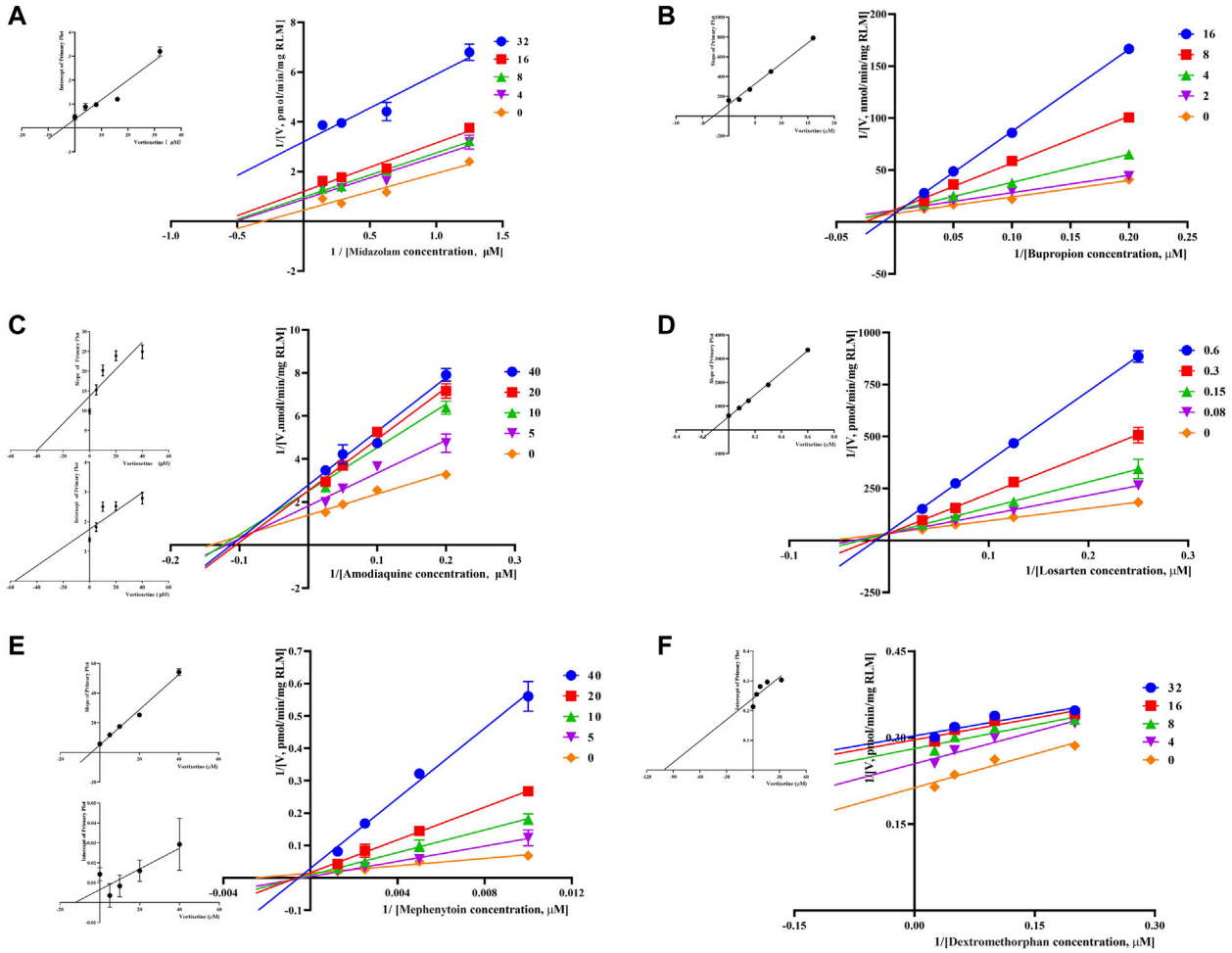

FIGURE 4
Primary Lineweaver–Burk plot, the secondary plot for Ki and the secondary plot for αKi in the inhibition of CYP-mediated probe metabolism by various concentrations of vortioxetine in RLMs. **(A)** Midazolam and dextromethorphan were both used at concentration of 4, 8, 16 and 32 μM; **(B)** bupropion was used at concentration of 2, 4, 8 and 16 μM; **(C)** amodiaquine and mephenytoin were both used at concentration of 5, 10, 20 and 40 μM; **(D)** losartan was used at concentration of 0.08, 0.15, 0.3 and 0.6 μM; **(E)** Mephenytoin was used at concentration of 5, 10, 20 and 40 μM; **(F)** Dextromethorphan was used at concentration of 4, 8, 16 and 32 μM. Each data point represents the mean of three samples.

concentrations were 5, 10, 20, 40 μM. The losartan concentrations were 4, 8, 15, 30 μM, corresponding to vortioxetine concentrations of 0.08, 0.15, 0.3, 0.6 μM. Bupropion concentrations were 5, 10, 20, 40 μM, corresponding to vortioxetine concentrations of 2, 4, 8, 16 μM. The experimental conditions were the same as above.

2.5 UPLC-MS/MS conditions

All experiments results were detected by UPLC-MS/MS, which equipped with a Waters Acquity UPLC system (Milford, MA, United States) and a Waters Xevo TQ-S triple quadrupole tandem mass spectrometer with an electrospray ionization source (Milford, MA, United States). The chromatographic separation was performed on a Waters ACQUITY UPLC BEH C18 column (2.1 × 50 mm, 1.7 μm, Waters Corp.) at 40°C. The mobile phase was consisted of acetonitrile (A) and 0.1% formic acid in water (B). The gradient elution at a flow rate of 0.4 mL/min was conducted as follows: 0–0.5 min, 10% A; 0.5–1.0 min, 10%–90% A; 1.0–2.0 min, 90% A; 2.0–2.1 min, 90%–10% A, and 2.1–3.0 min, 10% A. The relevant analysis parameters were shown in Table 1.

2.6 Statistical analysis

IC_{50} values and enzyme kinetic parameters were calculated by Graphpad Prism 6.0 (GraphPad software Inc., CA, United States). Lineweaver-Burk Plot was used to determine inhibitor patterns. Dixon plots of K_i values were obtained from the slope of the nonlinear regression line in the Lineweaver-Burk plot as a function of different inhibitor concentrations, while secondary plots for αK_i were obtained from the y-intercept of the nonlinear regression line in Lineweaver-Burk Plot versus concentration of different inhibitors. Data for each experiment were expressed as mean ± SD (n = 3).

3 Results

3.1 IC_{50}-shift assay in HLMs and RLMs

According to the results in Table 2, vortioxetine was a potential inhibitor of CYP450. It was found that vortioxetine had medium inhibitory efficiency on CYP3A4, CYP2B6, and CYP2C19 in HLMs. In RLMs, vortioxetine had medium inhibitory efficiency on CYP2B, and strong inhibitory effect on CYP2C-2.

The value of IC_{50}-shift was used to assess whether there was a TDI in the process of enzyme inhibition. As previously reported, when IC_{50}-shift >10, there will be obvious TDI. According to the results, we found no TDI for CYP450 by vortioxetine (Table 2; Figures 1, 2). Particularly, the activity of CYP2C19 was significantly reduced with the NADPH in HLMs. Conversely, the activity of CYP2C-2 was significantly increased with the NADPH in RLMs.

3.2 Enzyme kinetic analysis of vortioxetine

Through the value of IC_{50}-shift, we can preliminarily determine whether there was a TDI of vortioxetine on CYP450 enzymes. To further investigate the inhibitory mechanism of vortioxetine on the CYP450 enzymes, we used a series of concentrations of vortioxetine to react with the probe substrates and determine their metabolisms in HLMs and RLMs. In HLMs (Figure 3), the type of inhibition mechanism of vortioxetine on CYP3A4 and CYP2C8 was noncompetitive, with K_i values of 7.26 μM and 2.96 μM, respectively. The type of inhibition mechanism of vortioxetine on CYP2B6 and CYP2C9 was mixed, with K_i values of 8.55 μM and 4.17 μM, respectively. The inhibition mechanism of CYP2C19 and CYP2D6 was competitive, with K_i values of 2.17 μM and 9.37 μM, respectively. In RLMs (Figure 4), the type of inhibitory mechanism of vortioxetine on CYP3A and CYP2D was uncompetitive, with K_i values of 4.41 μM and 100.9 μM, respectively. The type of inhibitory mechanism of vortioxetine on CYP2B and CYP2C-2 was competitive, with K_i values of 2.87 μM and 0.12 μM, respectively. The inhibition mechanism type was mixed to CYP2C-1 with the K_i value of 39.91 μM and the inhibition mechanism type was noncompetitive to CYP2C-3 with the K_i value of 4.23 μM.

4 Discussion

Although current clinical data suggested that vortioxetine was a higher safety profile compared with other anti-major depressive disorder drug, polypharmacy cannot be avoided in most patients (Yee et al., 2018). DDI still cannot be ignored. Most of DDI occurred because a drug affected the activity of liver enzymes, resulting in toxic reactions caused by changed in the rate of metabolism of other drugs (Fowler and Zhang, 2008). Though we found that propafenone showed the inhibitory effect on vortioxetine metabolism in previous study (Xu et al., 2021), the mechanism of action of vortioxetine on liver drug enzymes has never been reported before. Here we firstly explored the mechanism of vortioxetine's inhibition on CYP450 enzymes in HLMs and RLMs.

Judging the inhibitory strength of a drug on an enzyme was usually judged by the value of the IC_{50}. According to the general standard, IC_{50} < 1 μM suggested strong inhibitory effect, 1 μM < IC_{50} < 10 μM suggested medium inhibitory effect, and IC_{50} > 10 μM suggested weak inhibitory effect (Jin et al., 2015). The results (Table 2) showed that vortioxetine was medium inhibitory effect on CYP3A4, CYP2B6 and CYP2C19 in HLMs, and medium inhibitory effect on CYP2B and strong inhibitory effect on CYP2C-2 in RLMs. As for other CYP450 enzymes, there were also weak inhibitory effects. Therefore, vortioxetine can be determined as a potential liver drug enzyme inhibitor. The mechanism of drug inhibition on CYP450 enzymes can be divided into reversible inhibition and irreversible inhibition (Lou et al., 2019). Reversible mechanisms are divided into competitive inhibition, noncompetitive inhibition, uncompetitive inhibition and mixed inhibition.

All the competition mode calculations in this experiment were obtained by Lineweaver-Burk. TDI in irreversible inhibition is the most commonly explored mode of inhibition today. Nowadays, there is no accurate conclusion about whether drugs have TDI in CYP450 enzymes, and the IC_{50}-shift value is often used to determine whether there is TDI (Bao et al., 2018). It has been reported in the literature that TDI is a positive reaction when IC_{50}-shift >10 (Grimm et al., 2009). The result of our experiment was that there was no significant change in IC_{50}-shift detected after 30 min pre-incubation with NADPH or not. It can be concluded that vortioxetine has no TDI on the above six CYP450 isoforms.

Based on the above judgments, the inhibitory effects of vortioxetine on CYP450 enzymes studied in this paper were all reversible inhibition. We found that CYP2C19 and CYP2D6 were competitive inhibition, CYP3A4 and CYP2C8 were noncompetitive inhibition, and CYP2B6 and CYP2C9 were mixed inhibition in HLMs. Based on the above-mentioned inhibitory mechanism, it is of great help for the guidance of multiple drugs in clinical practice. Thus, in the clinic, the combination of vortioxetine and CYP450 substrate drugs should be avoided or monitored, even when these drugs are administered in therapeutic doses. For example, common gastric ulcer patients used proton pump inhibitors such as omeprazole or H_2 receptor inhibitor cimetidine, which are inhibitors of CYP2C19 and CYP2C9, respectively (Miner et al., 2003; Burt et al., 2016). When these drugs were taken concurrently with vortioxetine, the patient's blood concentration should be monitored or the dosage should be adjusted appropriately to avoid adverse reactions. The differences in IC_{50} value and inhibitory mechanism between HLMs and RLMs may also be caused by differences between species (Shimada et al., 1997; Komura and Iwaki, 2008; Nishimuta et al., 2013).

More studies are needed to interpret the role of vortioxetine in altering the response of drug-metabolizing CYP450 enzymes. The structural information may yield insights into the loss of activities of CYP450 enzymes and the differences in the inhibitory mechanisms, which provide further aids in understanding how vortioxetine influences protein function in biologic systems (Parikh et al., 2020). Previously, Pallan et al. team had obtained a crystal structure of human P450 21A2 in complex with progesterone, a substrate in adrenal 21-hydroxylation, and the structure of the human P450 21A2-substrate complex provides direct insight into mechanistic effects of genetic variants (Pallan et al., 2015b). Similar paper could also be found that several minor structural differences of

x-ray crystal structures of zebrafish P450s 17A1 and 17A2, as well as with human P450 17A1, may be critical in understanding the basis of lyase function (Pallan et al., 2015a). Moreover, serotonin levels are controlled beside reuptake by the enzyme monoamine oxidase A (MAO-A) and that impaired MAO A leads to pathology that cannot be treated pharmacologically (Prah et al., 2020; Prah et al., 2022).

Vortioxetine at a single oral dose of 10 mg was clinically used in 14 healthy subjects with a C_{max} of 4.60 ng/mL and an $AUC_{(0-t)}$ of 254.72 ngh/mL (Chen et al., 2018). Another study found that patients with severe liver impairment taking a single oral dose of 10 mg of vortioxetine, $AUC_{(0-t)}$ was 10% higher and C_{max} 24% lower than healthy subjects, but it is not considered to adjust the clinical dose (2022). However, the plasma protein of vortioxetine was as high as 99%, and no serious adverse reactions caused by other drugs competing with vortioxetine for plasma proteins have been found, which should be paid attention to together with vortioxetine's inhibition of CYP450 enzymes *in vivo*. Other antipsychotic drugs inhibited CYP450 enzymes as well. For example, the novel atypical antipsychotic drug asenapine is mainly metabolized in the body by CYP1A2, CYP2D6 and CYP3A4. *In vitro*, it was found that asenapine significantly inhibited CYP1A2, CYP2D6, CYP3A4, and the data of CYP1A2 and CYP2D6 were likely to speculate that the same reaction will occur *in vivo* (Wójcikowski et al., 2020). If inhibitors of the corresponding enzymes or metabolites of enzymes are taken together in the body, it is likely to cause adverse reactions by DDI. In another study, the interaction relationship between iloperidone and lurasidone *in vitro* was found, and it is very likely that it can occur *in vivo* (Danek et al., 2020).

In this paper, the studies we did were *in vitro* on the inhibitory effect of vortioxetine on CYP450. Based on the inhibition mechanism discussed above, it is helpful to treat different conditions encountered by different patients, and it also provides an indispensable basis for the research of *in vivo*.

5 Conclusion

In summary, we investigated the inhibitory mechanism and Ki values of vortioxetine on CYP3A4/3A, CYP2B6/CYP2B, CYP2C8/CYP2C-1, CYP2C9/CYP2C-2, CYP2C19/CYP2C-3, CYP2D6/CYP2D and found no TDI effect of vortioxetine on CYP450. In HLMs, CYP3A4 and CYP2C8 were noncompetitive inhibition, CYP2B6 and CYP2C9 were mixed inhibition, and CYP2C19 and CYP2D6 were competitive inhibition. In RLMs, CYP2C-3 was noncompetitive inhibition, CYP2C-1 was mixed inhibition, CYP2B and CYP2C-2 were competitive inhibition, and CYP3A and CYP2D were uncompetitive inhibition. All data need to be supported by future *in vivo* experimental data and provide guidance for the safe use of vortioxetine in clinical practice.

Data availability statement

The original contributions presented in the study are included in the article/Supplementary material, further inquiries can be directed to the corresponding authors.

Author contributions

YZ and AW: writing—original draft; conceptualization; data curation; formal analysis; YY: investigation; methodology; JC: investigation; methodology; XX: investigation; methodology; JN: project administration; resources; software; supervision; writing—review and editing; validation. JL: project administration; resources; software; supervision; writing—review and editing; validation. All authors contributed to the article and approved the submitted version.

Acknowledgments

The authors thank Ren-ai Xu for his advice and assistance.

Conflict of interest

The authors declare that the research was conducted in the absence of any commercial or financial relationships that could be construed as a potential conflict of interest.

Publisher's note

References

Adamo, D., Calabria, E., Coppola, N., Pecoraro, G., and Mignogna, M. (2021). Vortioxetine as a new frontier in the treatment of chronic neuropathic pain: a review and update. *Ther. Adv. Psychopharmacol.* 11, 20451253211034320. doi:10.1177/20451253211034320

Arora, S., Taneja, I., Challagundla, M., Raju, K., Singh, S., and Wahajuddin, M. (2015). *In vivo* prediction of CYP-mediated metabolic interaction potential of formononetin and biochanin A using *in vitro* human and rat CYP450 inhibition data. *Toxicol. Lett.* 239, 1–8. doi:10.1016/j.toxlet.2015.08.202

Bao, S., Wen, J., Zheng, X., Zhou, Q., Qu, G., Chen, M., et al. (2018). Evaluation of the inhibition effects of apatinib on human and rat cytochrome P450. *Toxicol. Lett.* 297, 1–7. doi:10.1016/j.toxlet.2018.08.010

Burt, H., Neuhoff, S., Almond, L., Gaohua, L., Harwood, M., Jamei, M., et al. (2016). Metformin and cimetidine: physiologically based pharmacokinetic modelling to investigate transporter mediated drug-drug interactions. *Eur. J. Pharm. Sci.* 88, 70–82. doi:10.1016/j.ejps.2016.03.020

Chen, G., Højer, A., Areberg, J., and Nomikos, G. (2018). Vortioxetine: clinical pharmacokinetics and drug interactions. *Clin. Pharmacokinet. Drug Interact.* 57, 673–686. doi:10.1007/s40262-017-0612-7

Danek, P., Wójcikowski, J., and Daniel, W. (2020). The atypical neuroleptics iloperidone and lurasidone inhibit human cytochrome P450 enzymes *in vitro*. Evaluation of potential metabolic interactions. *Eval. potential metabolic Interact.* 72, 1685–1694. doi:10.1007/s43440-020-00102-5

Fowler, S., and Zhang, H. (2008). *In vitro* evaluation of reversible and irreversible cytochrome P450 inhibition: current status on methodologies and their utility for predicting drug-drug interactions. *AAPS J.* 10, 410–424. doi:10.1208/s12248-008-9042-7

Frampton, J. (2016). Vortioxetine: A review in cognitive dysfunction in depression. *Drugs* 76, 1675–1682. doi:10.1007/s40265-016-0655-3

Grimm, S., Einolf, H., Hall, S., He, K., Lim, H., Ling, K., et al. (2009). The conduct of *in vitro* studies to address time-dependent inhibition of drug-metabolizing enzymes: a perspective of the pharmaceutical research and manufacturers of America. *Drug Metab. Dispos.* 37, 1355–1370. doi:10.1124/dmd.109.026716

Hvenegaard, M., Bang-Andersen, B., Pedersen, H., Jørgensen, M., Püschl, A., and Dalgaard, L. (2012). Identification of the cytochrome P450 and other enzymes involved in the *in vitro* oxidative metabolism of a novel antidepressant, Lu AA21004. *Drug Metab. Dispos.* 40, 1357–1365. doi:10.1124/dmd.112.044610

Jin, C., He, X., Zhang, F., He, L., Chen, J., Wang, L., et al. (2015). Inhibitory mechanisms of celastrol on human liver cytochrome P450 1A2, 2C19, 2D6, 2E1 and 3A4. *Xenobiotica.* 45, 571–577. doi:10.3109/00498254.2014.1003113

Komura, H., and Iwaki, M. (2008). Species differences in *in vitro* and *in vivo* small intestinal metabolism of CYP3A substrates. *J. Pharm. Sci.* 97, 1775–1800. doi:10.1002/jps.21121

Lam, R., Kennedy, S., Mclntyre, R., and Khullar, A. (2014). Cognitive dysfunction in major depressive disorder: effects on psychosocial functioning and implications for treatment. *Can. J. Psychiatry* 59, 649–654. doi:10.1177/070674371405901206

Lou, D., Bao, S. S., Li, Y. H., Lin, Q. M., Yang, S. F., and He, J. Y. (2019). Inhibitory mechanisms of myricetin on human and rat liver cytochrome P450 enzymes. *Eur. J. Drug Metab. Pharmacokinet.* 44, 611–618. doi:10.1007/s13318-019-00546-y

Miao, J., Wang, G., Hou, J., Areberg, J., Zhao, Y., Højer, A., et al. (2019). Pharmacokinetics and safety of vortioxetine in the Chinese population. *Adv. Ther.* 36, 3134–3146. doi:10.1007/s12325-019-01092-4

Miner, P., Katz, P., Chen, Y., and Sostek, M. (2003). Gastric acid control with esomeprazole, lansoprazole, omeprazole, pantoprazole, and rabeprazole: a five-way crossover study. *Am. J. Gastroenterol.* 98, 2616–2620. doi:10.1111/j.1572-0241.2003.08783.x

Nishimuta, H., Nakagawa, T., Nomura, N., and Yabuki, M. (2013). Species differences in hepatic and intestinal metabolic activities for 43 human cytochrome P450 substrates between humans and rats or dogs. *Xenobiotica* 43, 948–955. doi:10.3109/00498254.2013.787155

Pallan, P., Nagy, L., Lei, L., Gonzalez, E., Kramlinger, V., Azumaya, C., et al. (2015a). Structural and kinetic basis of steroid 17α,20-lyase activity in teleost fish cytochrome P450 17A1 and its absence in cytochrome P450 17A2. *J. Biol. Chem.* 290, 3248–3268. doi:10.1074/jbc.M114.627265

Pallan, P., Wang, C., Lei, L., Yoshimoto, F., Auchus, R., Waterman, M., et al. (2015b). Human cytochrome P450 21A2, the major steroid 21-hydroxylase: structure of the ENZYME·PROGESTERONE substrate complex and rate-limiting C-H bond cleavage. *J. Biol. Chem.* 290, 13128–13143. doi:10.1074/jbc.M115.646307

Parikh, S., Evans, C., Obi, J., Zhang, Q., Maekawa, K., Glass, K., et al. (2020). Structure of cytochrome P450 2C9*2 in complex with losartan: insights into the effect of genetic polymorphism. *Mol. Pharmacol.* 98, 529–539. doi:10.1124/molpharm.120.000042

Pehrson, A., and Sanchez, C. (2014). Serotonergic modulation of glutamate neurotransmission as a strategy for treating depression and cognitive dysfunction. *CNS Spectr.* 19, 121–133. doi:10.1017/S1092852913000540

Prah, A., Pregeljc, D., Stare, J., and Mavri, J. (2022). Brunner syndrome caused by point mutation explained by multiscale simulation of enzyme reaction. *Sci. Rep.* 12, 21889. doi:10.1038/s41598-022-26296-7

Prah, A., Purg, M., Stare, J., Vianello, R., and Mavri, J. (2020). How monoamine oxidase A decomposes serotonin: an empirical valence bond simulation of the reactive step. *J. Phys. Chem. B* 124, 8259–8265. doi:10.1021/acs.jpcb.0c06502

Shimada, T., Mimura, M., Inoue, K., Nakamura, S., Oda, H., Ohmori, S., et al. (1997). Cytochrome P450-dependent drug oxidation activities in liver microsomes of various animal species including rats, Guinea pigs, dogs, monkeys, and humans. *Arch. Toxicol.* 71, 401–408. doi:10.1007/s002040050403

Wójcikowski, J., Danek, P., Basińska-Ziobroń, A., Pukło, R., and Daniel, W. J. P. R. P. (2020). *In vitro* inhibition of human cytochrome P450 enzymes by the novel atypical antipsychotic drug asenapine: a prediction of possible drug-drug interactions. *Pharmacol. Rep.* 72, 612–621. doi:10.1007/s43440-020-00089-z

Xu, R.-A., Luo, S., Lin, Q., Shao, Y., Chen, C., and Ye, X. (2021). Inhibitory effect of propafenone on vortioxetine metabolism *in vitro* and *in vivo*. *Arabian J. Chem.* 14, 103136. doi:10.1016/j.arabjc.2021.103136

Yee, A., Ng, C., and Seng, L. J. C. D. T. (2018). Vortioxetine treatment for anxiety disorder: A meta-analysis study. *A Meta-Analysis Study* 19, 1412–1423. doi:10.2174/1389450118666171117131151

frontiers | Frontiers in Pharmacology

TYPE Original Research
PUBLISHED 10 November 2023
DOI 10.3389/fphar.2023.1265252

OPEN ACCESS

EDITED BY
Ling Ye,
Southern Medical University, China

REVIEWED BY
Vinay S. Sharma,
Gujarat University, India
Malgorzata Szafarz,
Jagiellonian University, Poland

*CORRESPONDENCE
Gexin Dai,
daigexin@wmu.edu.cn
Guanyang Lin,
13867702133@163.com,
Ren-Ai Xu,
xra@wmu.edu.cn

†These authors have contributed equally to this work

RECEIVED 22 July 2023
ACCEPTED 30 October 2023
PUBLISHED 10 November 2023

CITATION
Chen J, Shen Y, Xia H, Chen X, Xu R-A, Lin G and Dai G (2023), Development of a UPLC-MS/MS method for the determination of lacosamide and its metabolite and its application to drug-drug interaction.
Front. Pharmacol. 14:1265252.
doi: 10.3389/fphar.2023.1265252

Development of a UPLC-MS/MS method for the determination of lacosamide and its metabolite and its application to drug-drug interaction

Jie Chen[1,2†], Yuxin Shen[3†], Hailun Xia[1], Xiaohai Chen[1], Ren-Ai Xu[1*], Guanyang Lin[1,2*] and Gexin Dai[1*]

[1]Department of Pharmacy, The First Affiliated Hospital of Wenzhou Medical University, Wenzhou, Zhejiang, China, [2]School of Pharmaceutical Sciences, Wenzhou Medical University, Wenzhou, Zhejiang, China, [3]Key Laboratory of Diagnosis and Treatment of Severe Hepato-Pancreatic Diseases of Zhejiang Province, The First Affiliated Hospital of Wenzhou Medical University, Wenzhou, Zhejiang, China

Lacosamide, a third-generation novel antiepileptic drug, was first approved in 2008 as an adjunct to partial seizures. In 2014, the U.S. Food and Drug Administration (FDA) approved it as a single agent for partial seizures. Since epilepsy is a chronic condition, most patients need long-term antiepileptic medicinal products, so it is even more important to consider the drug-drug interactions (DDIs). For the purpose of this experiment, an ultra performance liquid chromatography tandem mass spectrometry (UPLC-MS/MS) assay with accuracy and simplicity was optimized and fully validated for the simultaneous quantitative determination of lacosamide and O-Desmethyl-lacosamide (ODL), and DDIs between lacosamide and nisoldipine *in vivo* and *in vitro* was researched. The protein was precipitated with acetonitrile, the analytes were eluted with acetonitrile and a 0.1% formic acid solution in a gradient program, and lacosamide, ODL, and lamotrigine (Internal Standard, IS) were successfully separated by chromatography. The findings of the biological analysis revealed that the lower limit of quantification (LLOQ) for lacosamide in samples was 2 ng/mL and the linearity ranged from 2 to 10000 ng/mL. The LLOQ for ODL was 1 ng/mL, while the linearity range for this substance was 1–1,000 ng/mL. In rat liver microsomes (RLM), the LLOQ of ODL was 80 ng/mL and the linear range was 80–40000 ng/mL. The selectivity, stability, matrix effect and recovery rate were all satisfied with the need of quantitative analysis of samples. Then, the UPLC-MS/MS assay was employed successfully on the interactions of lacosamide and nisoldipine *in vivo* and *in vitro*. The half-maximal inhibitory concentration (IC_{50}) was 3.412 μM in RLM, where nisoldipine inhibited the metabolism of lacosamide with a mixture of inhibition mechanism. In rat pharmacokinetic experiments, it was found that nisoldipine could significantly change the pharmacokinetic characteristics of lacosamide, including $AUC_{(0-t)}$, $AUC_{(0-\infty)}$, T_{max}, $CL_{z/F}$ and C_{max}, but had no significant effect on ODL. In summary, the UPLC-MS/MS method could accurately and sensitively quantify lacosamide and ODL, and could be used for the interaction between nisoldipine and lacosamide *in vivo* and *in vitro*.

KEYWORDS

methodological verification, lacosamide, UPLC-MS/MS, interaction, pharmacokinetic

Introduction

Approximately 70 million individuals globally are suffering from epilepsy, among the most prevalent brain disorders. It is distinguished by a propensity to repeatedly cause spontaneous seizures, which have a variety of neurobiological, cognitive, and psychosocial effects (Thijs et al., 2019). The first generation of antiepileptic drugs had more adverse reactions, mainly in cognitive aspects, and were rarely used in clinical practice (Nanau and Neuman, 2013; Steinhoff and Staack, 2019). The second generation of antiepileptic drugs had relatively fewer side effects than the first generation and were slightly better at controlling seizures (Perucca et al., 2020).

Lacosamide (Figure 1A), as a third-generation novel antiepileptic drug, stands out for its good efficacy and safety, with better pharmacokinetic characteristics and tolerability compared to the first and second generation (Carona et al., 2021). It is used adjunctively for the treatment of adults with or without secondary systemic partial seizures, with a low incidence of adverse effects, and is now available for the treatment of primary generalized tonic-clonic seizures or generalized epilepsy, in addition to being shown to be therapeutic as adjunctive therapy for focal epilepsy (Kim et al., 2012; Ahn et al., 2022).

Antiepileptic drugs often require other drugs in combination with multiple therapies to control the occurrence of seizures and thus promote the development of drug-drug interactions (DDIs). Therefore, their co-administration with lacosamide may affect their pharmacokinetic and pharmacological effects. In a clinical study, when lacosamide was used in combination with an enzyme inducer of anticonvulsants such as carbamazepine, phenobarbital, or phenytoin, the concentration of lacosamide was lower than when used alone (Markoula et al., 2014). Lacosamide is metabolized by several cytochrome P450 (CYP) enzymes (CYP2C19, CYP2C9, and CYP3A4) (Cawello et al., 2014; Ahn et al., 2022), the main metabolite of which is O-Desmethyl-lacosamide (ODL) (Figure 1B). The first-generation anti-epileptic drug carbamazepine induces CYP3A4, CYP1A2, CYP2C19, so carbamazepine can alter the pharmacokinetic profile of lacosamide (Lakehal et al., 2002). Lacosamide can cause arrhythmias, and patients with diabetic peripheral neuropathy and cardiovascular disease are prone to atrial arrhythmias (DeGiorgio et al., 2013; Malissin et al., 2013). Digoxin is primarily used to treat heart failure and atrial fibrillation because it has a limited range of therapeutic targets. It is used in combination with lacosamide, and has no significant effect on the absorption of lacosamide and the elimination of metabolites (Cawello and Bonn, 2012).

In addition, as global life expectancy increases, the number of elderly epilepsy patients is increasing. Elderly patients with epilepsy are at great risk of cardiovascular disease, and many epilepsy patients with cardiovascular and cerebrovascular diseases in the treatment of the primary disease at the same time to take cardiovascular drugs to control the disease (Husein et al., 2021). Due to the chronic nature of epilepsy, most patients need to take anti-epileptic drugs for a long period of time, so it is more important to take into account drug interactions in order to alleviate the patient's condition (Cawello, 2015). In order to improve the effectiveness and safety of clinical drugs, a rapid and accurate method for the determination of drug concentration is needed. The main methods reported for the determination of lacosamide included gas chromatography-mass spectrometer (GC-MS) (Nikolaou et al., 2015; Mouskeftara et al., 2020), high performance liquid chromatography (HPLC) (Kestelyn et al., 2011; Shah et al., 2012), and liquid chromatography tandem mass spectrometry (LC-MS/MS) (Kim et al., 2012; Payto et al., 2014; Korman et al., 2015; Bharwad et al., 2020; Qiu et al., 2022). The significant features of these methods and the detection methods in this experiment are compared in Table 1.

However, to the best of our knowledge, only one analytical method for the simultaneous measurement of lacosamide and its metabolite ODL in biological matrices by LC-MS/MS has been reported. In this investigation, the LC-MS/MS method for the measurement of lacosamide and ODL had long analysis run time (6.5 min) and low sensitivity (0.95 μg/mL) (Payto et al., 2014). Thus, in this study, we firstly established a simple, quick and sensitive ultra performance liquid chromatography tandem mass spectrometry (UPLC-MS/MS) method for the measurement of the concentrations of lacosamide and ODL in plasma and rat liver microsomes (RLM) using lamotrigine as internal standard (IS). In addition, the effect of nisoldipine on lacosamide in RLM and its mechanism were investigated. Moreover, since our *in vitro* results suggested that nisoldipine had a significant inhibitory effect on lacosamide in RLM, we performed *in vivo* drug interaction experiments in the presence or absence of nisoldipine in rats,

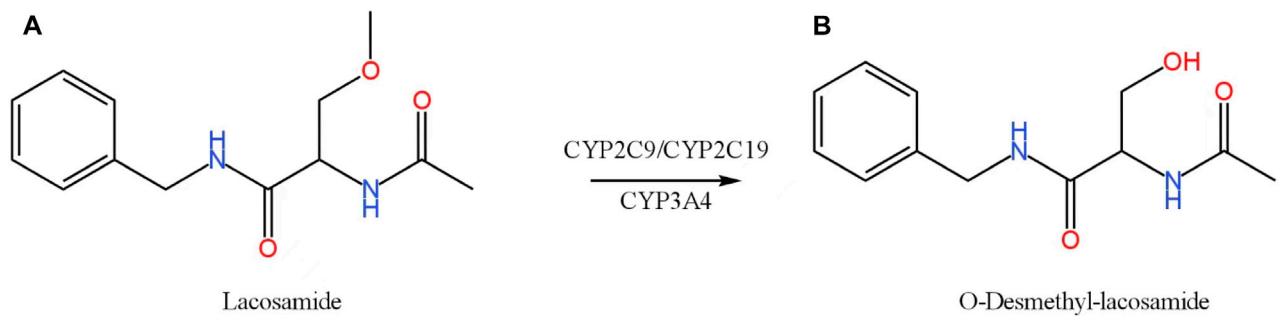

FIGURE 1
Chemical structures and biotransformation pathway of lacosamide **(A)** and O-Desmethyl-lacosamide **(B)**.

TABLE 1 Summary of methods for the measurement of lacosamide in the literatures.

Sample preparation	Metabolite	IS	Run time (min)	Methodology	LLOQ (μg/mL)	HLOQ (μg/mL)	Ref
Rat plasma (100 μL) plus IS (10 μL) protein precipitation with acetonitrile	O-desmethyl lacosamide	lamotrigine	2.0	UPLC-MS/MS	0.002	10	Our method
Human plasma (25 μL) plus methanol precipitated solution (150 μL) containing IS (5 μg/mL)	O-desmethyl lacosamide	lacosamide-13C	6.5	LC–MS/MS	0.95	30.29	Payto et al. (2014)
Human plasma (500 μL) plus IS (25 μL) extracted with ethyl acetate	None	moclobemide	7.0	GC-MS	2	100	Mouskeftara et al. (2020)
Human plasma (200 μL) plus IS (20 μL) derivatized by silylation	None	levetiracetam-d6	11.5	GC-MS	0.2	20	Nikolaou et al. (2015)
Human plasma (100 μL) plus IS (25 μL) protein precipitation with methanol	None	AC-Phe-Nhme	25	HPLC-UV	0.5	12.5	Kestelyn et al. (2011)
Rat plasma (200 μL) plus IS (10 μL) extracted with ethyl acetate	None	nevirapine	17	HPLC	0.025	10	Shah et al. (2012)
Human plasma (50 μL) plus methanol precipitated solution (200 μL) containing IS (1 μg/mL)	None	lacosamide-13C	0.2	SPE-MS/MS	0.5	50	Korman et al. (2015)
Rat plasma (50 μL) plus IS (100 μL) protein precipitation with acetonitrile	None	LCD001	4.5	LC-MS/MS	0.0003	1	Kim et al. (2012)
Rat plasma (50 μL) plus acetonitrile precipitated solution (150 μL) containing IS (50 ng/mL)	None	midazolam	6.5	UPLC-MS/MS	0.5	5	Qiu et al. (2022)
Human plasma (150 μL) plus IS (50 μL) protein precipitation with methanol and acetonitrile	None	lacosamide-13C	2.2	UPLC-MS/MS	0.02	20	Bharwad et al. (2020)

and evaluated the changes of pharmacokinetic parameters of lacosamide and ODL.

Materials and methods

Chemicals and reagents

Lacosamide (purity, 98%), lamotrigine (purity, 98%, used as internal standard, IS), and ODL, were supplied from Beijing Sunflower Technology Development Co., Ltd (Beijing, China). Nisoldipine (purity, 99%), Lercanidipine (purity, 99%), Nitrendipine (purity, 98%), Nimodipine (purity, 98%), Lacidipine (purity, 98%), Felodipine (purity, 98%) and Nicardipine (purity, 98%) were provided by Shanghai Canspec Scientific Instruments Co., Ltd. (Shanghai, China). Acetonitrile (HPLC grade) and methanol (HPLC grade), were produced by Merck Company (Darmstadt, Germany). Ultra-pure water was prepared by a Milli-Q water purification system manufactured by Milli-Q (Millipore, Bedford, USA). All other chemicals and biologicals were of analytical grade or above.

Liquid chromatographic and mass spectrometric conditions

A Waters UPLC-MS/MS System comprised of a Waters Xevo TQ-S triple quadrupole tandem mass spectrometer (Milford, MA, USA) and a Waters Acquity UPLC I-Class system (Milford, MA, USA) was used for chromatographic analysis using an Acquity BEH C18 chromatography column (2.1 mm × 50 mm, 1.7 μm) at a flow rate of 0.40 mL/min. In addition, other conditions were set as follows: injection volume of 6.0 μL, autosampler temperature of 10°C, column temperature of 40°C. 0.1% formic acid in water (solution A) and acetonitrile (solution B) was used to form the mobile phase with a gradient elution as below: 0–0.5 min, 90% A; 0.5–1.0 min 90%–10% A; 1.0–1.4 min, 10% A; and 1.4–1.5 min, 10%–90% A. 90% A was then maintained at 1.5–2.0 min to reach equilibrium. The entire run time was 2.0 min.

A Waters Xevo TQ-S triple quadrupole tandem mass spectrometer was combined with electrospray ionization (ESI) in positive ion mode for mass spectrometry. Measurements were conducted by multiple reaction monitoring (MRM). The quantitative ion pairs and related parameters of lacosamide, its metabolite ODL, and IS are listed in Table 2. The Masslynx 4.1 software (Waters Corp, Milford, MA, USA) was used to collect, process, and control the apparatus.

Rat liver microsomes

Six blank rat livers were weighed and homogenized with 0.01 mM cold PBS buffer containing 0.25 mM sucrose solution (stored at 4°C). For 15 min, the homogenate was centrifuged at 11,000 rpm. After that, discard the precipitation, and the supernatant was transferred to a fresh

TABLE 2 The Quantitative Ion Pairs and Related Parameters of lacosamide, Its Metabolite ODL, and IS.

Compound	Parent (*m/z*)	Daughter (*m/z*)	Cone (V)	Collision (eV)
Lacosamide	251.1	108.2	20	25
ODL	237.1	108.2	20	10
IS	256.0	145.0	10	20

tube and centrifuged once again for 15 min at 11,000 rpm. Supernatant was then spun at 100,000 ×*g* for 1 h. Finally, the supernatant was discarded and the microsomal microspheres were frozen in a 0.01 mM PBS suspension and kept at −80°C. The Bradford Protein Assay Kit (Thermo Scientific, Waltham, MA, USA) was used to measure the protein concentration (Wang et al., 2015).

Preparation of standard curve and quality control (QC) samples

A certain amount of lacosamide was accurately weighed, and diluent (methanol) was added into the EP tube to dissolve. After shaking, 1.00 mg/mL lacosamide reserve solution was obtained. A series of standard working solutions with concentration gradients of 20, 100, 500, 1,000, 5,000, 10,000, 50,000 and 100,000 ng/mL were obtained by dilution with methanol. According to the same method, ODL were prepared and a series of concentration gradients were obtained: 10, 20, 50, 100, 500, 1,000, 5,000 and 10,000 ng/mL. From the prepared standard working solution, 10 μL lacosamide and 10 μL ODL were added to 80 μL blank matrix to prepare calibration standards with concentrations of 2, 10, 50, 100, 500, 1,000, 5,000 and 10,000 ng/mL for lacosamide, and 1, 2, 5, 10, 50, 100, 500 and 1,000 ng/mL for ODL, and these standard curves were determined. Lower limit of quantification (LLOQ) and three Quality Control (QC) samples were obtained by the same method. The LLOQ of lacosamide and ODL were 2 ng/mL and 1 ng/mL, respectively, and the three QC samples of lacosamide and ODL were 5, 4,000 and 8,000 ng/mL, and 2, 400 and 800 ng/mL, respectively. All chemicals and solutions were stored at - 80°C for further use.

Calibration curves (80–40000 ng/mL) in RLM were established by preparing calibration products according to the above method. The three QC concentrations were 200, 16,000 and 32,000 ng/mL, respectively, and the LLOQ was 80 ng/mL.

Pre-treatment of samples

Protein precipitation was used to remove proteins from plasma and extract the test materials. 100 μL plasma sample was mixed with 10 μL IS working solution (1 μg/mL) and 300 μL acetonitrile, and centrifuged at 13,000 rpm for 10 min at 4 °C. The supernatant was obtained and aspirated into a sample bottle. Finally, 6.0 μL of sample was injected for analysis.

Method validation

The parameters of this test, which was conducted according to with the FDA bioassay, included selectivity, calibration curve, LLOQ, accuracy and precision, matrix effect, recovery, and stability (US Food and Drug Administration, 2018).

Different batches of matrix-match samples were treated to examine the selectivity of the UPLC-MS/MS method. Analysis of blank matrix samples (neither analyte nor IS), and real sample is done to determine whether endogenous chemicals interfere with the retentions of the analytes and IS.

The concentrations of lacosamide and ODL in matrix were taken as the horizontal coordinate, and the ratio of the two to the IS peak area was taken as the vertical coordinate. The weighted least square method was used to perform regression operations, and the calibration curves of lacosamide and ODL were obtained respectively. LLOQ is the minimum concentration of the calibration curve and should be accurate and precise in the range of ±20%.

To achieve inter-day and intra-day precision and accuracy, QC samples were analyzed in five batches over three consecutive days. Separate calibration is performed on each verification day. Relative standard deviation (RSD%) is used to indicate accuracy, and relative error (RE%) is used to indicate accuracy. Accuracy of ±15% or less, precision of 15% or less is considered acceptable.

Lacosamide and ODL standard solutions were added to the treated various blank matrices to prepare three QC concentrations. The peak areas obtained were compared with those obtained from three QC levels of pure standard solutions, that is, matrix effect. The recovery was obtained by comparing the peak area before extraction of lacosamide and ODL with the peak area after extraction at the three QC levels.

Three concentrations of QC matrix-match samples were placed in various conditions to test the stability of lacosamide and ODL for short-term, long-term, three freeze-thaw cycles, and at autosampler. Sample storage at room temperature for at least 3 h was used to test the short-term stability. After 21 days of storage at −80°C, samples were tested to establish their long-term stability. By assessing the stability of three freeze-thaw cycles from freezing (−80°C) to thawing (room temperature) three times, the stability of the samples was assessed. Additionally, the stability of the produced samples was assessed after 4 h of storage in an autosampler at 10°C.

Enzyme reaction of lacosamide using RLM

The range of 20–2000 μM of lacosamide had been dissolved in DMSO to comply with the K_m (Michaelis-Menten constant) sequence concentrations. Incubation system of 200 μL was made up of 100 mM of PBS buffer, 0.2 mg/mL of RLM, 1 mM of NADPH, and 20–2000 μM of lacosamide. In addition to NADPH, the solution was mixed and pre-incubated at 37°C for 5 min prior to the addition of 1 mM NADPH, followed by incubation for 50 min and placed at -80°C to discontinue the reaction. After complete completion of the

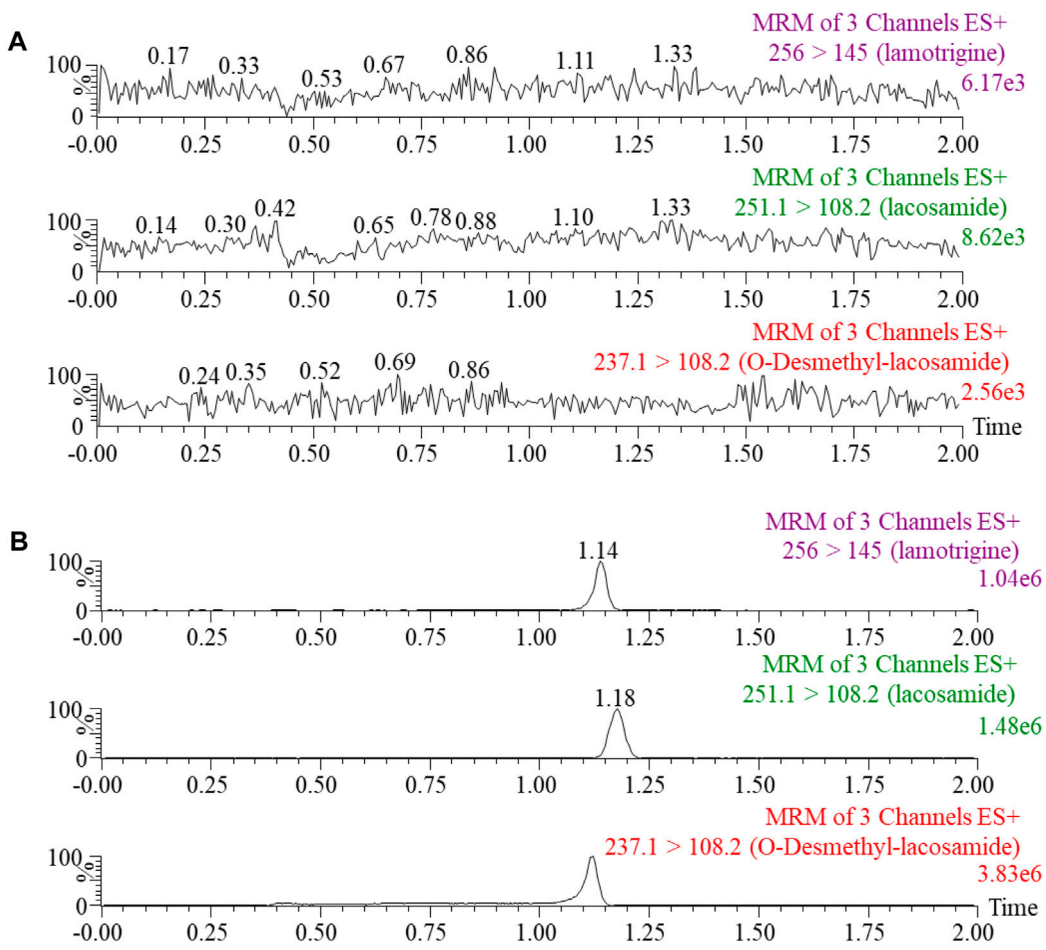

FIGURE 2
Blank rat plasma samples **(A)**: no analyte, no IS). Typical MRM chromatograms of lacosamide, O-Desmethyl-lacosamide and lamotrigine (IS) in rat plasma **(B)**.

enzyme reaction, the mixture was added 10 μL of 200 ng/mL IS solution and 300 μL of acetonitrile (protein precipitant). The mixture was then swirled for 2 min and centrifuged at 13,000 rpm for an additional 10 min, and the supernatant of 100 μL was placed in an injector for the quantification by UPLC-MS/MS.

Effect of cardiovascular drugs on the metabolism of lacosamide in RLM

In the RLM incubation system, the K_m of lacosamide was 1,016 μM. In order to investigate the potential DDIs of lacosamide, the 200 μL system remained unchanged, and using K_m as the concentration of lacosamide in the RLM system, 7 cardiovascular drugs (nitrendipine, lercanidipine, nisoldipine, lacidipine, felodipine, nimodipine, nicardipine, 100 μM of each drug as the inhibitor) were tested for inhibition on the metabolism of lacosamide. The following reaction procedure was identical to the above-mentioned enzyme reaction. The experiment had to be redone with an inhibition rate of 80% or higher.

The half maximal inhibitory concentration (IC_{50}) of inhibitors (nisoldipine, lacidipine, felodipine, nimodipine, nicardipine) against lacosamide was determined in RLM. The cardiovascular drugs was dissolved in DMSO and diluted with DMSO at a concentration gradient of the IC_{50} was 0, 0.01, 0.1, 1, 10, 25, 50 and 100 μM, and the concentration of lacosamide was 1,016 μM in RLM. The subsequent processing steps were the same as above to obtain the IC_{50} values of inhibitors in RLM. To identify the mechanisms underlying the inhibitory effect of nisoldipine on lacosamide, 0, 1.7, 3.4 and 6.8 μM of nisoldipine (based on the IC_{50} value), and 254, 508, 1,016, and 2032 μM of lacosamide (according to the K_m value) in the RLM system, were selected. The subsequent reaction and treatment process were the same as the described above.

In vivo pharmacokinetic study

18 Sprague-Dawley (SD) male rats (200 ± 10 g) were bought from the Animal Experimental Center of the First Affiliated Hospital of Wenzhou Medical University and were randomly assigned to three groups (n = 6): group A (control group) and group B, C (experimental group). The animals fasted for 12 h

TABLE 3 Evaluation of the Intra-Day and Inter-Day Precision and Accuracy by the Proposed UPLC-MS/MS Method for Determination of lacosamide and ODL in various matrices (n = 5).

Matrix	Analytes	Concentration (ng/mL)	Intra-Day		Inter-Day	
			Precision (RSD %)	Accuracy (RE %)	Precision (RSD %)	Accuracy (RE %)
Plasma	Lacosamide	2	19.9	−3.5	18.7	7.6
		5	2.4	−1.0	3.2	2.5
		4,000	4.8	11.2	3.6	11.5
		8,000	3.3	−3.4	2.9	3.6
	ODL	1	10.7	−0.9	8.9	3.1
		2	9.2	2.0	6.9	0.1
		400	2.6	2.0	3.7	0.7
		800	6.4	5.5	5.3	5.0
RLM	ODL	80	12.3	0.0	11.6	3.0
		200	4.5	3.5	6.0	5.0
		16,000	3.7	5.5	7.6	11.8
		32,000	6.7	2.5	6.4	4.3

TABLE 4 Matrix effect and recovery rate of lacosamide and ODL in various matrices (n = 5).

Matrix	Analytes	Concentration (ng/mL)	Recovery rate (%)		Matrix effect (%)	
			Mean ± SD	RSD%	Mean ± SD	RSD%
Plasma	Lacosamide	5	104.8 ± 12.9	12.3	111.6 ± 4.5	4.0
		4,000	110.4 ± 3.7	3.3	89.8 ± 5.8	6.5
		8,000	99.0 ± 7.9	8.0	92.8 ± 7.7	8.3
	ODL	2	92.5 ± 4.6	5.0	96.0 ± 3.6	3.8
		400	89.9 ± 5.0	5.6	95.7 ± 6.8	7.1
		800	102.3 ± 3.6	3.6	112.5 ± 2.6	2.3
RLM	ODL	200	102.8 ± 5.6	5.4	99.6 ± 11.8	11.9
		16,000	99.4 ± 4.6	4.6	109.2 ± 6.9	6.3
		32,000	104.9 ± 8.2	7.8	105.3 ± 4.3	4.1

before the experiment, with no restricted water intake. Lacosamide, felodipine, and nisoldipine were prepared with suspension of 0.5% sodium carboxymethyl cellulose (CMC-Na) solution and administered orally. Groups B and C were given felodipine (1 mg/kg), and nisoldipine (1 mg/kg) by gavage, respectively, and the same amount of CMC-Na solution was administered to group A. After 30 min, all rats were received 10 mg/kg of lacosamide by gavage. Tail venous blood was collected at 0.333, 0.667, 1, 1.5, 2, 3, 4, 6, 8, 12, 24 and 48 h after dosing. The blood sample (0.3 mL) was centrifuged at 8,000 rpm for 5 min 100 μL of plasma was obtained and frozen at - 80°C for further processing. The subsequent treatment was carried out according to the chapter of Pre-treatment of samples.

Data analysis

The GraphPad Prism 9.0 software was used to generate the K_m, IC_{50}, the Lineweaver-Burk plot, and the mean plasma concentration-time curve. Drug and Statistics (DAS) software (version 3.0 software, Mathematical Pharmacology Professional Committee of China, Shanghai, China) with non-compartment model analyses was used to obtain the pharmacokinetic parameters of lacosamide and ODL in rats. The comparison of the pharmacokinetic parameters among three groups in rats was performed with SPSS (version 26.0; SPSS Inc., Chicago, IL, USA), with one-way ANOVA, and the p-value <0.05 was regarded as statistically significant.

TABLE 5 Stability Results of lacosamide and ODL in various matrices Under Different Conditions (n = 5).

Matrix	Analytes	Concentration (ng/mL)	Room temperature (3 h)		10°C (4 h)		Three freeze-thaw		21 days	
			RSD (%)	RE (%)	RSD (%)	RE (%)	RSD (%)	RE (%)	RSD (%)	RE (%)
Plasma	Lacosamide	5	2.4	10.0	9.5	−1.7	4.0	7.3	12.7	1.0
		4,000	3.9	5.8	2.6	12.7	3.4	1.5	1.0	−4.6
		8,000	0.7	−10.4	4.7	−1.9	2.2	−14.4	1.5	−2.4
	ODL	2	3.4	4.4	5.8	−0.3	12.3	−1.6	5.0	9.3
		400	4.1	0.0	2.3	−7.4	4.6	1.6	2.5	−5.1
		800	4.4	0.6	2.8	−7.4	2.9	4.1	5.8	0.0
RLM	ODL	200	9.5	−4.3	5.2	9.9	4.8	−10.4	10.9	−9.7
		16,000	2.9	−0.2	3.2	10.4	2.8	−0.9	3.5	1.1
		32,000	1.6	1.9	7.3	2.6	3.4	−1.0	2.2	3.9

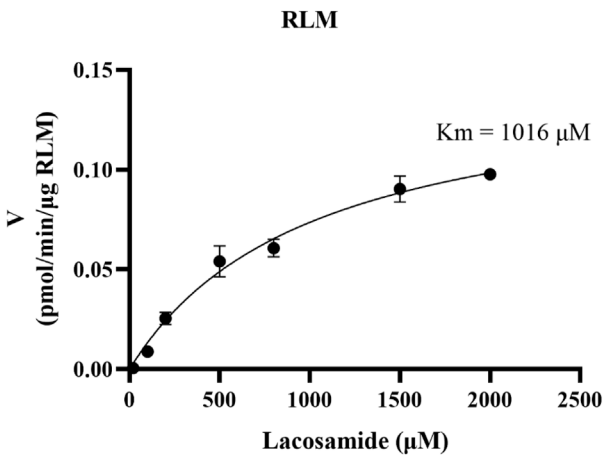

FIGURE 3
Michaelis–Menten kinetics of lacosamide in RLM.

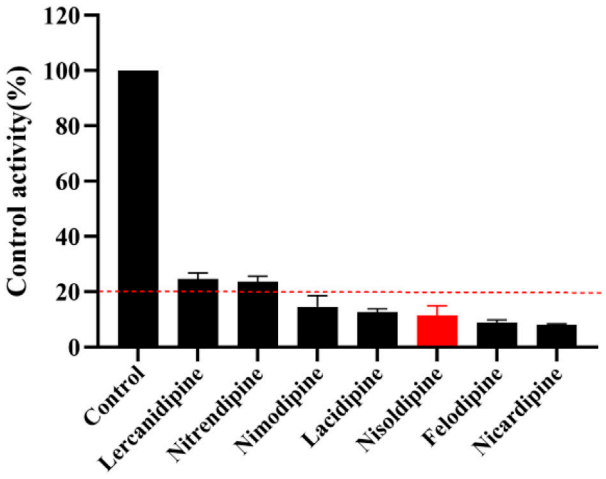

FIGURE 4
Comparison of the inhibitory effects of 7 cardiovascular drugs on lacosamide in RLM.

Results

Method validation

The method for the quantification of lacosamide and ODL had been successfully established, as illustrated in Figure 2, with no interference peaks. In this study, the regression equation of calibration standard curve was constructed as follows: lacosamide, y= (0.000764*x + 0.001259, r^2 = 0.996); ODL in plasma, y= (0.005327*x + 0.003107, r^2 = 0.999); ODL in RLM, y= (0.004099*x + 0.000403, r^2 = 0.998). The calibration standard curves illustrated excellent linearity at a concentration range of 2–10000 ng/mL for lacosamide and that of 1–1,000 ng/mL for ODL in plasma, also 80–40000 ng/mL for ODL in RLM.

Four concentration levels of each analyte have been employed to measure the precision and accuracy. Lacosamide and ODL have intra-day and inter-day precision of less than 15% and accuracy of ±15% at three QC levels. As for LLOQ, the precision was below 20% and the accuracy was within ±20%. All the results in various matrices are presented in Table 3.

Three QC levels were used to study the recovery and matrix effects. As shown in Table 4, the recovery rates of lacosamide and ODL in rat plasma ranged from 99.0% to 110.4% and 89.9%–102.3%, respectively. The matrix effect of lacosamide and ODL were calculated to be within the acceptable range (89.8%–111.6% and 95.7%–112.5%). The recovery and matrix effect in RLM also met the requirements of the guidelines on bioanalytical method validation. Thus, matrix effect had little influence on the ionization of the analytes, nor did it influence the precision of UPLC-MS/MS optimization.

The stability of lacosamide and ODL in various matrices was determined by the stability test, and were expressed in Table 5.

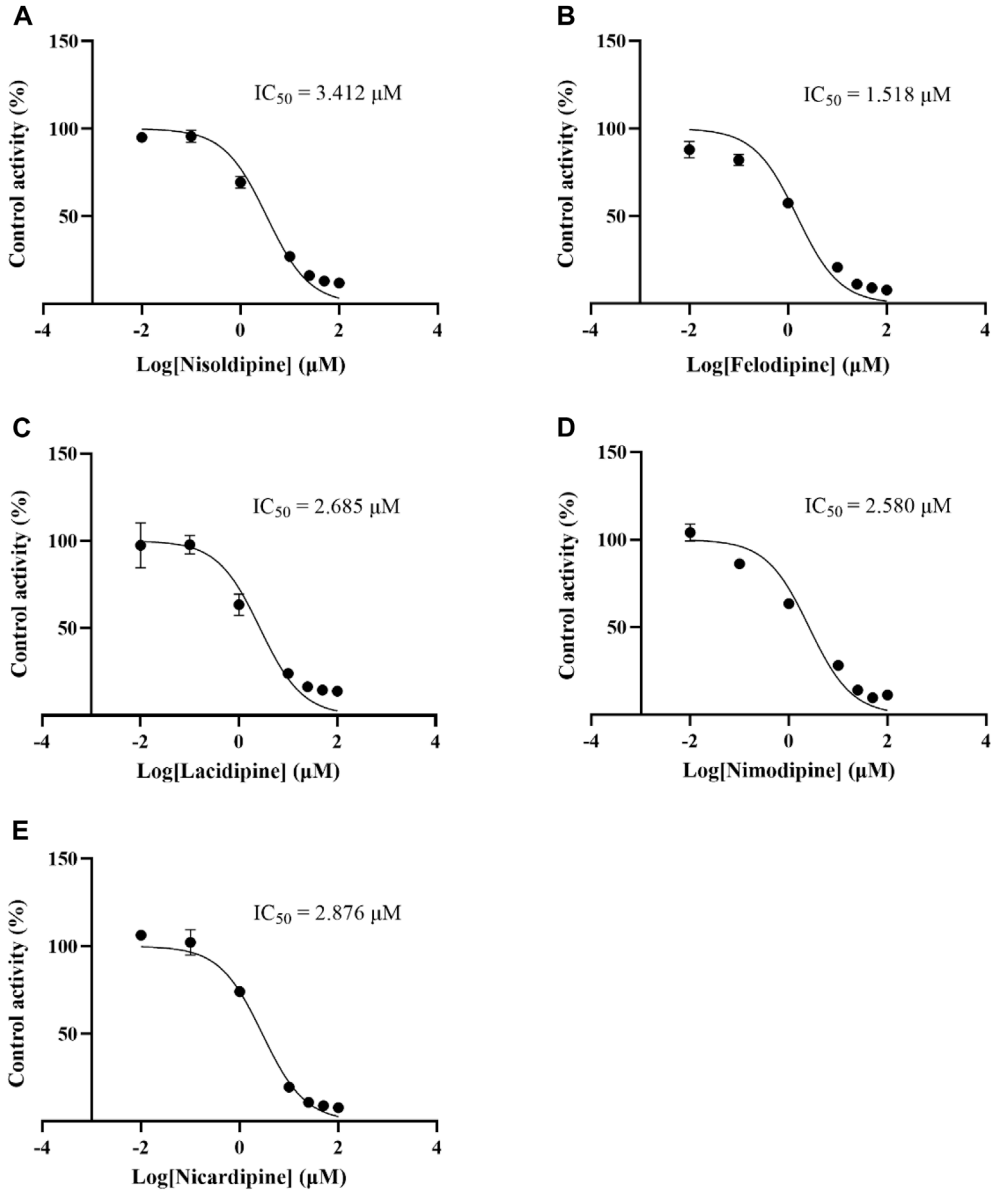

FIGURE 5
IC_{50} curves of 5 cardiovascular drugs on lacosamide metabolism in RLM. Nisoldipine **(A)**, Felodipine **(B)**, Lacidipine **(C)**, Nimodipine **(D)**, Nicardipine **(E)**.

The results showed that lacosamide and ODL in matrix-match samples were stable after analysis under four different conditions: room temperature for 3 h, 10°C for 4 h, three complete freezing (−80°C)/thawing (RT) cycles, or storage at −80°C for 21 days. The stability test results were in the range of error (±15%).

Screening drugs with potential interactions in combination with lacosamide

The K_m value for lacosamide was determined by non-linear regression of the rate of reaction to the concentration of the substrate (Figure 3). The K_m values of lacosamide was 1,016 μM in RLM. In this study, 7 cardiovascular drugs that may be used in combination with lacosamide were selected, and it was found that 5 drugs (nisoldipine, felodipine, lacidipine, nimodipine, and nicardipine) with inhibition rates greater than 80% were screened out (Figure 4).

Effect of nisoldipine on the enzyme kinetics of lacosamide *in vitro*

The IC_{50} curves of 5 cardiovascular drugs on lacosamide metabolism in RLM are displayed in Figure 5. The assessment of inhibition revealed that nisoldipine, felodipine, lacidipine,

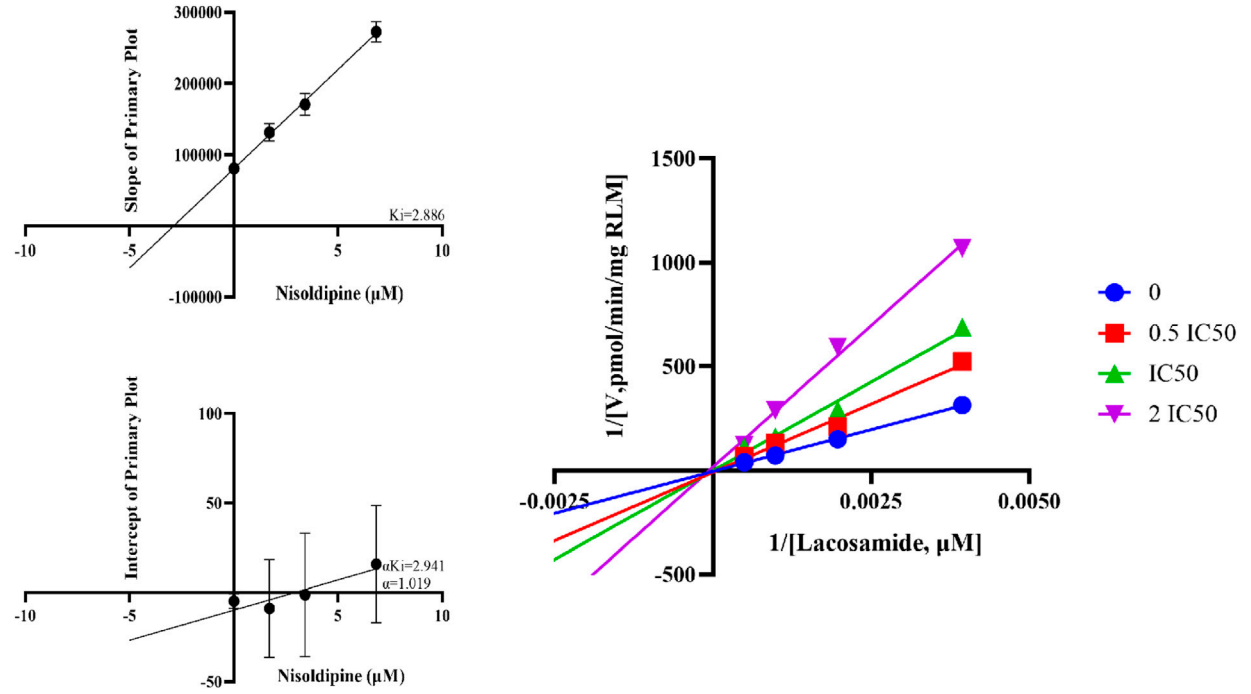

FIGURE 6
Linewever-burk plot, secondary diagram of Ki and secondary diagram of αKi inhibiting lacosamide metabolism at different concentrations of nisoldipine in RLM.

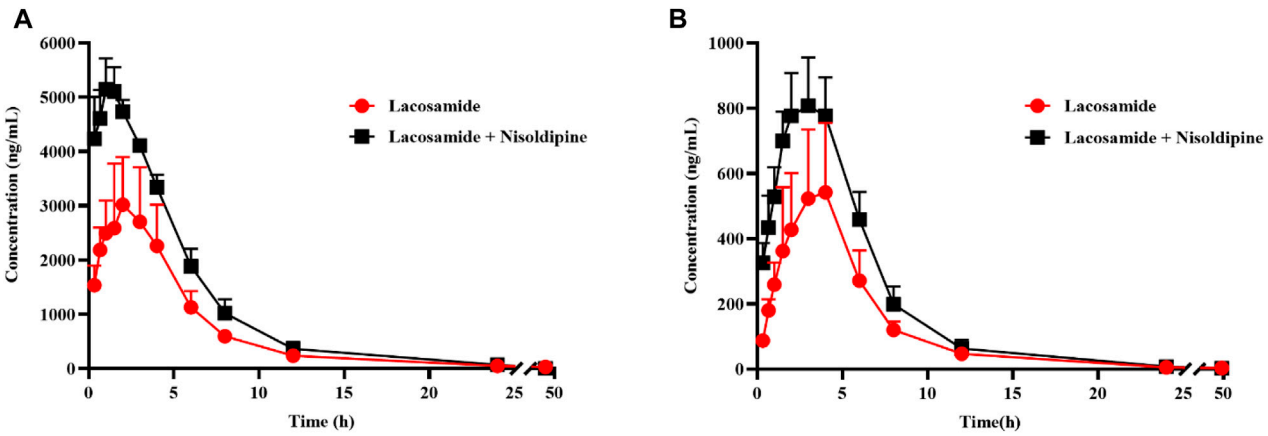

FIGURE 7
Mean concentration-time curve of lacosamide **(A)**, and ODL **(B)** in rats. Data are presented as the means ± SD, n = 6.

nimodipine, and nicardipine could significantly decrease the concentration of ODL (IC_{50} were 3.412, 1.518, 2.685, 2.580 and 2.876 μM, respectively). The IC_{50} was below 10 μM, suggesting a modest inhibition of the metabolism of lacosamide *in vitro*. The inhibitory mechanisms of nisoldipine on lacosamide in RLM were further investigated, and it inhibited the metabolism of lacosamide with a Ki of 2.886 and αKi of 2.941, by a mixed inhibition mechanism, involving un-competitive as well as non-competitive inhibition, in accordance with the Lineweaver-Burk plots (Figure 6).

Effect of nisoldipine on the pharmacokinetics of lacosamide *in vivo*

The average concentration-time curves of lacosamide and ODL in rats are shown in Figure 7; Tables 6, 7 show the main pharmacokinetic results obtained from non-compartment model analyses in rats with or without nisoldipine. The results indicated that the combination of nisoldipine and lacosamide was the most effective. The $AUC_{(0-t)}$, $AUC_{(0-\infty)}$ and C_{max} of lacosamide were significantly increased when nisoldipine was administered in

TABLE 6 The Pharmacokinetic Parameters of Lacosamide in the Presence and Absence of nisoldipine (n = 6).

Parameters	Lacosamide	Lacosamide + nisoldipine
$AUC_{(0-t)}$ (ng/mL*h)	18,734.31 ± 4,192.44	31,364.27 ± 3251.79***
$AUC_{(0-\infty)}$ (ng/mL*h)	18,742.60 ± 4,200.86	31,367.45 ± 3255.93***
$MRT_{(0-t)}$ (h)	6.54 ± 2.31	5.07 ± 0.92
$MRT_{(0-\infty)}$ (h)	7.01 ± 3.14	5.11 ± 0.92
$t_{1/2z}$ (h)	3.49 ± 1.03	3.26 ± 0.71
T_{max} (h)	2.08 ± 0.49	1.42 ± 0.38*
$CL_{z/F}$ (L/h/kg)	0.60 ± 0.13	0.32 ± 0.00**
$V_{z/F}$ (L/kg)	2.72 ± 0.58	1.49 ± 0.19***
C_{max} (ng/mL)	3164.24 ± 1,070.20	5,297.66 ± 466.35***

AUC, area under the plasma concentration-time curve, $t_{1/2z}$ elimination half time, T_{max} peak time, $CL_{z/F}$ plasma clearance, C_{max} maximum blood concentration *$p < 0.05$, **$p < 0.01$, ***$p < 0.001$, compared with the group A.

TABLE 7 The Pharmacokinetic Parameters of ODL in the Presence and Absence of nisoldipine (n = 6).

Parameters	Lacosamide	Lacosamide + nisoldipine
$AUC_{(0-t)}$ (ng/mL*h)	3422.11 ± 1,059.19	5,482.80 ± 807.91**
$AUC_{(0-\infty)}$ (ng/mL*h)	3423.38 ± 1,061.55	5,495.81 ± 817.99**
$MRT_{(0-t)}$ (h)	6.01 ± 0.64	5.30 ± 0.39*
$MRT_{(0-\infty)}$ (h)	6.28 ± 0.74	5.44 ± 0.40*
$t_{1/2z}$ (h)	3.26 ± 0.54	3.11 ± 0.21
T_{max} (h)	3.50 ± 0.55	2.83 ± 0.75
$CL_{z/F}$ (L/h/kg)	3.11 ± 0.77	1.86 ± 0.32**
$V_{z/F}$ (L/kg)	14.99 ± 5.04	8.38 ± 1.71*
C_{max} (ng/mL)	558.05 ± 220.49	829.00 ± 128.67*

AUC, area under the plasma concentration-time curve, $t_{1/2z}$ elimination half time, T_{max} peak time, $CL_{z/F}$ plasma clearance, C_{max} maximum blood concentration *$p < 0.05$, **$p < 0.01$, compared with the group A.

combination with lacosamide in rats, while $CL_{z/F}$, T_{max}, and, $V_{z/F}$ were significantly decreased. And, there was no significant change in $MRT_{(0-t)}$, $MRT_{(0-\infty)}$ and $t_{1/2z}$. These results suggested that nisoldipine could increase the plasma exposure of lacosamide in SD rats, demonstrating that nisoldipine might be a potential interaction drug with lacosamide. With respect to ODL, the $AUC_{(0-t)}$, $AUC_{(0-\infty)}$ and C_{max} increased significantly, the $MRT_{(0-t)}$, $MRT_{(0-\infty)}$, $CL_{z/F}$ and $V_{z/F}$ decreased significantly, and $t_{1/2z}$ and T_{max} had no significant difference when nisoldipine was administered. As for felodipine, it did not change the exposure of lacosamide and ODL in rats.

Discussion

People with epilepsy often have complications or underlying conditions that may be combined with cardiovascular medications (Cawello, 2015). Depending on the drug's dose as well as its specific metabolic path, DDIs may result in negative reactions to drugs. Lacosamide is metabolized by multiple cytochrome P450 enzymes, including CYP3A4, CYP2C9, and CYP2C19, producing the primary inactive O-demethylated metabolite.

To better analyze lacosamide, ODL, and IS and produce more precise analytical results, the MS settings were improved in this experiment. Lacosamide, ODL, and IS have good peak and separation effects following the optimized gradient elution process with 0.1% formic acid in water and acetonitrile as mobile phase, and the retention time is 1.18 min, 1.12 min and 1.14 min, respectively. The quantitative fragment ions of lacosamide, ODL and IS were *m/z* 251.1→108.2,*m/z* 237.1→108.2 and *m/z* 256.0→145.0, respectively. Samples need to be processed before UPLC-MS/MS detection, and we used acetonitrile one-step precipitation extraction to reduce interference from endogenous substances, especially proteins, and to obtain permitted recovery and matrix effects.

Many cardiovascular drugs are substrates for CYP3A4, CYP2C19, and CYP2C9, or inhibitors of these enzymes (Yuan et al., 2014; Zhou et al., 2014; Fuhr et al., 2022). In this study, after screening 7 potential cardiovascular drugs before the *in vivo*

study, 5 drugs with higher inhibitory rates were selected for their IC_{50} values, all of which were less than 10 μM, and 2 drugs (felodipine, and nisoldipine) were selected for *in vivo* pharmacokinetic experiments in rats. All two cardiovascular drugs are calcium channel blockers that are widely used in the treatment of cardiovascular disease and are clinically approved for the treatment of hypertension (Wei et al., 2012; Wu et al., 2015).

As far as we know, nisoldipine is a substrate of CYP3A4, but its inhibitory effect on CYP450 has not been reported. In this study, we firstly studied the inhibitory mechanism of nisoldipine on lacosamide in RLM through the production of ODL *in vitro*. The results showed that nisoldipine could significantly inhibit the formation of ODL and showed moderate inhibition on lacosamide, and its inhibitory effect occurred through a mixed inhibitory mechanism (non-competitive inhibition and un-competitive inhibition). These results suggested that nisoldipine may exhibit mixed inhibition through multiple pathways.

Previously reported $t_{1/2z}$, $CL_{z/F}$ and $V_{z/F}$ of lacosamide alone in rats were similar to those in our study, with slight differences in C_{max} and T_{max}, such differences may have resulted from individual variances between rats. The values of $AUC_{(0-t)}$ and $MRT_{(0-t)}$ are roughly half of those in this study, which are 9270.3 ± 3231.7 ng/mL*h and 3.6 ± 0.5 h respectively (Qiu et al., 2022), while the values of these two parameters in this experiment are 18,734.3 ± 4,192.4 ng/mL*h and 6.54 ± 2.31 h respectively. The reason may be that the oral dose in the literature (5 mg/kg) is half of the dose in this experiment (10 mg/kg). The pharmacokinetic parameters of ODL in rats have not been reported despite in healthy subjects, where the previously reported value of C_{max} (0.459 μg/mL) in healthy subjects was consistent with our study of C_{max} (558.0 ± 220.5 ng/mL) (Cawello et al., 2014).

The results of pharmacokinetic experiments in rats showed that in the present of nisoldipine, AUC and C_{max} were increased significantly, and $CL_{z/F}$ were decreased by about 50%, so the metabolism of lacosamide were slowed down and/or drug absorption were increased. Nisoldipine had no significant effect on the final $t_{1/2z}$ of lacosamide, indicating that nisoldipine had a moderate effect on lacosamide clearance, and the effect on the final $t_{1/2z}$ was not as significant as that on AUC. The AUC, C_{max}, and $CL_{z/F}$ values for ODL were consistent with the prototype in the presence of nisoldipine, according to the pharmacokinetic data of the metabolite. This result could be explained by lacosamide's higher bioavailability in the presence of nisoldipine, which suggests that greater amounts of lacosamide has the potential to be transformed into ODL. However, *in vivo* studies in rats cannot properly predict the situation in people since the role of the CYP450 enzymes for substrate metabolism in humans and rats differ, and additional research is required to confirm this in clinical investigations.

Conclusion

All in all, this study assessed the impact of DDIs on the metabolism of lacosamide. Through sample pre-treatment and complete methodology verification, the method was characterized by simple operation, high recovery, high sensitivity and specificity. When co-administered with lacosamide in rats, nisoldipine could significantly alter lacosamide and ODL pharmacokinetic parameters. In addition, we found that the inhibition of nisoldipine on lacosamide was consistent *in vivo* and *in vitro*. Due to the wide range of clinical applications of lacosamide and nisoldipine, we could provide basis for the appropriate and rational combination of lacosamide and nisoldipine, offer evidence for the joint development of antiepileptic drugs and cardiovascular drugs, and furnish support for personalized clinical medication.

Data availability statement

The raw data supporting the conclusion of this article will be made available by the authors, without undue reservation.

Ethics statement

The animal studies were approved by the Animal Experimental Center of the First Affiliated Hospital of Wenzhou Medical University. The studies were conducted in accordance with the local legislation and institutional requirements. Written informed consent was obtained from the owners for the participation of their animals in this study.

Author contributions

JC: Data curation, Visualization, Writing–original draft. YS: Validation, Writing–original draft. HX: Investigation, Writing–original draft. XC: Data curation, Writing–original draft. R-AX: Conceptualization, Supervision, Writing–review and editing. GL: Supervision, Validation, Writing–review and editing. GD: Project administration, Validation, Writing–review and editing.

Funding

The author(s) declare that financial support was received for the research, authorship, and/or publication of this article. This work was supported by the National Natural Science Foundation of China (82104297).

Conflict of interest

The authors declare that the research was conducted in the absence of any commercial or financial relationships that could be construed as a potential conflict of interest.

Publisher's note

References

Ahn, S. J., Oh, J., Kim, D. Y., Son, H., Hwang, S., Shin, H. R., et al. (2022). Effects of CYP2C19 genetic polymorphisms on the pharmacokinetics of lacosamide in Korean patients with epilepsy. *Epilepsia* 63 (11), 2958–2969. doi:10.1111/epi.17399

Bharwad, K. D., Shah, P. A., Shrivastav, P. S., and Sharma, V. S. (2020). Selective quantification of lacosamide in human plasma using UPLC-MS/MS: application to pharmacokinetic study in healthy subjects with different doses. *Biomed. Chromatogr.* 34 (11), e4928. doi:10.1002/bmc.4928

Carona, A., Bicker, J., Silva, R., Fonseca, C., Falcao, A., and Fortuna, A. (2021). Pharmacology of lacosamide: from its molecular mechanisms and pharmacokinetics to future therapeutic applications. *Life Sci.* 275, 119342. doi:10.1016/j.lfs.2021.119342

Cawello, W. (2015). Clinical pharmacokinetic and pharmacodynamic profile of lacosamide. *Clin. Pharmacokinet.* 54 (9), 901–914. doi:10.1007/s40262-015-0276-0

Cawello, W., and Bonn, R. (2012). No pharmacokinetic interaction between lacosamide and valproic acid in healthy volunteers. *J. Clin. Pharmacol.* 52 (11), 1739–1748. doi:10.1177/0091270011426875

Cawello, W., Mueller-Voessing, C., and Fichtner, A. (2014). Pharmacokinetics of lacosamide and omeprazole coadministration in healthy volunteers: results from a phase I, randomized, crossover trial. *Clin. Drug Investig.* 34 (5), 317–325. doi:10.1007/s40261-014-0177-2

DeGiorgio, A. C., Desso, T. E., Lee, L., and DeGiorgio, C. M. (2013). Ventricular tachycardia associated with lacosamide co-medication in drug-resistant epilepsy. *Epilepsy Behav. Case Rep.* 1, 26–28. doi:10.1016/j.ebcr.2012.10.001

Fuhr, L. M., Marok, F. Z., Mees, M., Mahfoud, F., Selzer, D., and Lehr, T. (2022). A physiologically based pharmacokinetic and pharmacodynamic model of the CYP3A4 substrate felodipine for drug-drug interaction modeling. *Pharmaceutics* 14 (7), 1474. doi:10.3390/pharmaceutics14071474

Husein, N., Josephson, C. B., and Keezer, M. R. (2021). Understanding cardiovascular disease in older adults with epilepsy. *Epilepsia* 62 (9), 2060–2071. doi:10.1111/epi.16991

Kestelyn, C., Lastelle, M., Higuet, N., Dell'Aiera, S., Staelens, L., Boulanger, P., et al. (2011). A simple HPLC-UV method for the determination of lacosamide in human plasma. *Bioanalysis* 3 (22), 2515–2522. doi:10.4155/bio.11.261

Kim, S. J., Koo, T. S., Ha, D. J., Baek, M., Lee, S. K., Shin, D. S., et al. (2012). Liquid chromatography-tandem mass spectrometry for quantification of lacosamide, an antiepileptic drug, in rat plasma and its application to pharmacokinetic study. *Biomed. Chromatogr.* 26 (3), 371–376. doi:10.1002/bmc.1668

Korman, E., Langman, L. J., and Jannetto, P. J. (2015). High-throughput method for the quantification of lacosamide in serum using ultrafast SPE-MS/MS. *Ther. Drug Monit.* 37 (1), 126–131. doi:10.1097/FTD.0000000000000115

Lakehal, F., Wurden, C. J., Kalhorn, T. F., and Levy, R. H. (2002). Carbamazepine and oxcarbazepine decrease phenytoin metabolism through inhibition of CYP2C19. *Epilepsy Res.* 52 (2), 79–83. doi:10.1016/s0920-1211(02)00188-2

Malissin, I., Baud, F. J., Deveaux, M., Champion, S., Deye, N., and Megarbane, B. (2013). Fatal lacosamide poisoning in relation to cardiac conduction impairment and cardiovascular failure. *Clin. Toxicol. (Phila).* 51 (4), 381–382. doi:10.3109/15563650.2013.778993

Markoula, S., Teotonio, R., Ratnaraj, N., Duncan, J. S., Sander, J. W., and Patsalos, P. N. (2014). Lacosamide serum concentrations in adult patients with epilepsy: the influence of gender, age, dose, and concomitant antiepileptic drugs. *Ther. Drug Monit.* 36 (4), 494–498. doi:10.1097/FTD.0000000000000051

Mouskeftara, T., Alexandridou, A., Krokos, A., Gika, H., Mastrogianni, O., Orfanidis, A., et al. (2020). A simple method for the determination of lacosamide in blood by GC-MS. *J. Forensic Sci.* 65 (1), 288–294. doi:10.1111/1556-4029.14151

Nanau, R. M., and Neuman, M. G. (2013). Adverse drug reactions induced by valproic acid. *Clin. Biochem.* 46 (15), 1323–1338. doi:10.1016/j.clinbiochem.2013.06.012

Nikolaou, P., Papoutsis, I., Spiliopoulou, C., Voudris, C., and Athanaselis, S. (2015). A fully validated method for the determination of lacosamide in human plasma using gas chromatography with mass spectrometry: application for therapeutic drug monitoring. *J. Sep. Sci.* 38 (2), 260–266. doi:10.1002/jssc.201400858

Payto, D., Foldvary-Schaefer, N., So, N., Bruton, M., and Wang, S. (2014). A sensitive and rapid method for quantification of lacosamide and desmethyl lacosamide by LC-MS/MS. *Bioanalysis* 6 (23), 3161–3168. doi:10.4155/bio.14.158

Perucca, E., Brodie, M. J., Kwan, P., and Tomson, T. (2020). 30 years of second-generation antiseizure medications: impact and future perspectives. *Lancet Neurol.* 19 (6), 544–556. doi:10.1016/S1474-4422(20)30035-1

Qiu, E., Yu, L., Liang, Q., and Wen, C. (2022). Simultaneous determination of lamotrigine, oxcarbazepine, lacosamide, and topiramate in rat plasma by ultra-performance liquid chromatography-tandem mass spectrometry. *Int. J. Anal. Chem.* 2022, 1838645. doi:10.1155/2022/1838645

Shah, S., Vasantharaju, S. G., Arumugam, K., Muddukrishna, B. S., and Desai, N. (2012). Development of a sensitive bioanalytical method for the quantification of lacosamide in rat plasma. Application to preclinical pharmacokinetics studies in rats. *Arzneimittelforschung* 62 (5), 243–246. doi:10.1055/s-0032-1301911

Steinhoff, B. J., and Staack, A. M. (2019). Levetiracetam and brivaracetam: a review of evidence from clinical trials and clinical experience. *Ther. Adv. Neurol. Disord.* 12, 1756286419873518. doi:10.1177/1756286419873518

Thijs, R. D., Surges, R., O'Brien, T. J., and Sander, J. W. (2019). Epilepsy in adults. *Lancet* 393 (10172), 689–701. doi:10.1016/S0140-6736(18)32596-0

US Food and Drug Administraton (2018). Center for Drug Evaluation and Research (CDER), Center for Veterinary Medicine (CVM), Bioanalytical Method Validation Guidance for Industry, Center for Drug Evaluation and Research. Available at: https://www.fda.gov/regulatory-information/search-fda-guidance-documents/bioanalytical-method-validation-guidance-industry.

Wang, Z., Sun, W., Huang, C. K., Wang, L., Xia, M. M., Cui, X., et al. (2015). Inhibitory effects of curcumin on activity of cytochrome P450 2C9 enzyme in human and 2C11 in rat liver microsomes. *Drug Dev. Ind. Pharm.* 41 (4), 613–616. doi:10.3109/03639045.2014.886697

Wei, D., He, W. Y., and Lv, Q. Z. (2012). Effect of nisoldipine and olmesartan on endothelium-dependent vasodilation in essential hypertensive patients. *CNS Neurosci. Ther.* 18 (5), 400–405. doi:10.1111/j.1755-5949.2012.00304.x

Wu, Y., Xu, M., Wang, H., Xu, X., Zhao, S., Zhang, M., et al. (2015). Lercanidipine hydrochloride versus felodipine sustained-release for mild-to-moderate hypertension: a multi-center, randomized clinical trial. *Curr. Med. Res. Opin.* 31 (1), 171–176. doi:10.1185/03007995.2014.960073

Yuan, L., Jia, P., Sun, Y., Zhao, C., Zhi, X., Sheng, N., et al. (2014). Study of *in vitro* metabolism of m-nisoldipine in human liver microsomes and recombinant cytochrome P450 enzymes by liquid chromatography-mass spectrometry. *J. Pharm. Biomed. Anal.* 97, 65–71. doi:10.1016/j.jpba.2014.03.030

Zhou, Y. T., Yu, L. S., Zeng, S., Huang, Y. W., Xu, H. M., and Zhou, Q. (2014). Pharmacokinetic drug-drug interactions between 1,4-dihydropyridine calcium channel blockers and statins: factors determining interaction strength and relevant clinical risk management. *Ther. Clin. Risk Manag.* 10, 17–26. doi:10.2147/TCRM.S55512

frontiers | Frontiers in Pharmacology

TYPE Clinical Trial
PUBLISHED 23 November 2023
DOI 10.3389/fphar.2023.1260599

OPEN ACCESS

EDITED BY
Guo Ma,
Fudan University, China

REVIEWED BY
Sojeong Yi,
United States Food and Drug Administration, United States
Melanie Felmlee,
The University of the Pacific, United States

*CORRESPONDENCE
Dongwei Liu,
liu-dongwei@126.com
Xin Tian,
tianx@zzu.edu.cn

†These authors have contributed equally to this work and share first authorship

RECEIVED 18 July 2023
ACCEPTED 03 November 2023
PUBLISHED 23 November 2023

CITATION
Tao J, Liu S, Zhao YY, Qi L, Yan P, Wu N, Liu X, Liu D and Tian X (2023), Pharmacokinetics, pharmacodynamics, and safety of ciprofol emulsion in Chinese subjects with normal or impaired renal function.
Front. Pharmacol. 14:1260599.
doi: 10.3389/fphar.2023.1260599

Pharmacokinetics, pharmacodynamics, and safety of ciprofol emulsion in Chinese subjects with normal or impaired renal function

Jun Tao[1,2†], Shuaibing Liu[1,2†], Ying Ying Zhao[3], Lei Qi[1], Pangke Yan[4], Nan Wu[4], Xiao Liu[4], Dongwei Liu[5]* and Xin Tian[1,2]*

[1]Department of Pharmacy, The First Affiliated Hospital of Zhengzhou University, Zhengzhou, China, [2]Henan Provincial Key Laboratory of Precision Clinical Pharmacy, Zhengzhou University, Zhengzhou, China, [3]Department of Anesthesiology, Pain and Perioperative Medicine, The First Affiliated Hospital of Zhengzhou University, Zhengzhou, China, [4]Sichuan Haisco Pharmaceutical Group Co., Ltd., Chengdu, China, [5]Department of Nephrology, The First Affiliated Hospital of Zhengzhou University, Zhengzhou, China

Background: Ciprofol, a novel sedative–hypnotic drug, has been approved for its use in inducing and maintaining general anesthesia, as well as for providing sedation.

Methods: In this phase I, single-center, parallel, controlled, open-label clinical trial, our objective was to analyze the pharmacokinetics (PK), pharmacodynamics (PD), and safety of ciprofol emulsion in 24 participants with mild and moderate renal impairment (n = 8 per group) and matched healthy participants (n = 8). An initial loading infusion of ciprofol was administered at 0.4 mg/kg for 1 min, followed by a maintenance infusion at a rate of 0.4 mg/kg/h for 30 min. We collected plasma and urine samples from the participants to assess the PK of ciprofol and its metabolite M4. The evaluation of PD involved using a modified observer's alertness/sedation scale (MOAA/S) in combination with bispectral index (BIS) monitoring. Safety assessments were conducted throughout the trial process.

Results: The plasma concentration–time curve of ciprofol in participants with renal impairment was similar to that in participants with normal kidney function. The area under the curve (AUC) and maximum concentration (C_{max}) of total and unbound ciprofol in plasma for participants with renal impairment were only slightly higher (0.7–1.2-fold) than those in participants with normal renal function. In contrast, for the metabolite M4, AUC values were 1.3- and 2.1-fold greater in participants with mild and moderate renal impairment, respectively, than in healthy controls. However, renal impairment had no significant impact on the PD parameters. The study found that ciprofol was well-tolerated, with all adverse events (AEs) reported being mild or moderate in severity.

Conclusion: Based on these findings, we can conclude that no dosage adjustment of ciprofol is necessary for patients with mild–moderate renal impairment who receive the injection.

Clinical Trial Registration: https://clinicaltrials.gov, identifier NCT04142970.

KEYWORDS

pharmacokinetics, pharmacodynamics, safety, ciprofol, anesthetic, renal impairment

1 Introduction

Ciprofol (HSK3486) is a sedative–hypnotic compound approved in 2020 for use in inducing and maintaining sedation, as well as providing general anesthesia. The primary mechanism of action of ciprofol is to enhance the activity of the ion channel mediated by gamma–aminobutyric acid type A ($GABA_A$) receptors, resulting in an influx of chloride ions (Qin et al., 2017). This leads to suppression of the central nervous system. This channel is also the primary target of propofol, a commonly used intravenous anesthetic with rapid onset and a short duration of action (Sahinovic et al., 2018). However, propofol has limitations, including injection pain, hemodynamic issues, and the risk of a potentially fatal condition known as propofol infusion syndrome (PIS) (Mahmoud and Mason, 2018). To address these limitations and improve the pharmacological and physicochemical properties of drug–receptor binding, propofol was optimized into ciprofol by incorporating a cyclopropyl group (Qin et al., 2017). Ciprofol has been shown to be highly effective, causing significant reductions in pain and improved hemodynamic stability (Qin et al., 2017; Li et al., 2022; Liu et al., 2022; Wang et al., 2022).

Ciprofol exhibits wide tissue distribution, with approximately 95% of the drug binding to plasma proteins (Lu et al., 2023). It is primarily metabolized in the liver by phase II glucuronosyltransferases (UGTs), and UGT1A9 is the main enzyme responsible for converting ciprofol into its major metabolite, M4. Subsequently, M4 is excreted through the renal route (84.59%) (Bian et al., 2021). The M4 metabolite does not exhibit any toxic or hypnotic properties, and it may not be necessary to evaluate the function of the kidney in removing this metabolite (Bian et al., 2021). It is well-established that renal impairment can have a notable effect on the renal excretion of drugs, as well as their metabolism and transport in the kidney, liver, and intestine. Additionally, it can impact the protein binding of drugs, resulting in substantial changes in both pharmacokinetics (PK) and pharmacodynamics (PD) (Boucher et al., 2006; Dixon et al., 2014; Celestin and Musteata, 2021). Thus, regulatory agencies recommend that studies be conducted to evaluate the potential effects of renal impairment on the PK and PD of any drug that may be used in patients with renal impairment, even if the kidneys are not primarily the elimination route for small molecules of drugs or their active metabolites (European Medicines Agency, 2015; U.S. Food and Drug Administration, 2020). Previous investigations have explored the PK, PD, and safety of ciprofol in a few special populations, including patients with hepatic impairment, the elderly (ages 65–73) vs. younger adults (ages 21–44), and male vs. female subgroups (Li et al., 2021; Teng et al., 2021; Hu et al., 2022). However, there were limited data to determine whether dose adjustment of ciprofol is necessary in patients with renal impairment.

In the current study, our objectives were to explore the PK profiles of total ciprofol, unbound ciprofol, and its major metabolite M4 and to evaluate the PD of ciprofol and its safety profile in patients with mild-to-moderate renal impairment, as well as in healthy controls. These results may provide essential information for recommending appropriate dosage adjustments of ciprofol for patients with varying stages of renal impairment.

2 Materials and methods

2.1 Subjects

The study, conducted at the First Affiliated Hospital of Zhengzhou University in China between November 2019 and August 2020, received approval from an independent Ethics Committee. All participants provided written informed consent. This clinical trial (NCT04142970, principal investigator: Zhangsuo Liu, date of registration: October 2019, https://clinicaltrials.gov/) adhered to ethical guidelines, such as the Declaration of Helsinki principles and Good Clinical Practice rules.

Participants eligible for the trial were males and females aged between 18 and 65, with a body weight ≥45 kg and a body mass index (BMI) ranging from 18 to 28 kg/m^2. Exclusion criteria included individuals with any clinically significant medical conditions (except for renal impairment or its underlying causes); medical instability; including psychiatric or neurological disorders; cardiovascular, endocrine, pulmonary, hepatic, gastrointestinal, or metabolic illnesses; or any other condition that could interfere with the assessment of the PK of the investigational drug or the completion of the trial. Potential participants underwent a pre-study screening, which involved reviewing their medical history, physical examinations, a 12-lead ECG, and monitoring of vital signs (blood pressure, oxygen saturation, and respiratory and cardiac rates). Laboratory examinations, including coagulation, hematology, clinical chemistry, and urinalysis, were conducted 14 days prior to the study.

2.2 Study design and procedures

In this phase I, single-center, parallel, controlled, open-label clinical trial, the participants were admitted to the clinic the day before receiving medication. They fasted for at least 8 h and abstained from drinking water for at least 2 h prior to drug administration. On the subsequent morning, the participants were administered a 0.4 mg/kg dose of ciprofol as a 1-min bolus, followed by a continuous infusion of 0.4 mg/kg/h for 30 min using a pump in a fully equipped operating room. To calculate the rate of ciprofol administration, the following formulas were used: dosing rate of the loading dose (mL/h) = 0.4 mg/kg × subject's baseline weight (kg) ÷ 2.5 mg/mL × 60 h^{-1} and administration rate of the maintenance dose (mL/h) = 0.4 mg/kg/h × baseline weight (kg) ÷ 2.5 mg/mL. The degree of anesthesia or sedation experienced by participants was evaluated using two methods: the modified observer's alertness/sedation scale (MOAA/S) and bispectral index (BIS) monitoring. Vital signs, electrocardiograms, and other indicators were monitored using an electrocardiogram monitor. These observations continued until the participants were fully awakened and achieved an MOAA/S score of 5 for three consecutive assessments. MOAA/S scores (Yamada et al., 2022) (Supplementary Table S1) were evaluated at various time points, including 5 min before drug administration, 1 min after the start of the loading dose, every 5 min during the continuous maintenance infusion, and every 2 min until the end of the infusion. BIS values were recorded 5 min before and 60 min after drug administration. Each subject received 100% oxygen via a mask until they were fully awake. Food and water were provided to the

participants after they had fully awakened following medication administration.

Arterial blood samples (3 mL in volume) were collected at specific time intervals, including 30 min before administration; 1 min after the completion of the loading infusion; and at 5, 10, 20, and 30 min after the start of the maintenance infusion, as well as at 1, 2, 4, 8, 15, 30 min, and 1 h after the end of the infusion. Venous blood samples (3 mL in volume) were collected at 2, 3, 4, 6, 8, 12, 24, and 48 h after drug administration. In addition, each 5 mL of arterial blood was sampled to estimate the protein binding rate, 1 min after the start of administration and 1 min after the end of the infusion. Blood samples were collected in K_2EDTA-containing tubes and centrifuged for 10 min at 4°C and 1,700 × g, and the plasma was separated and stored at−80°C.

Urine samples were collected over a 24-h period before ciprofol administration and at specific time intervals after administration: 0–4, 4–8, 8–12, 12–24, and 24–48 h. The urine samples (3 mL) were aliquoted into polypropylene tubes and cryopreserved at −80°C for future analysis.

Once the final PK samples were collected and safety evaluations were completed, the participants were allowed to leave the clinical site on the third day.

2.3 Assay of ciprofol and M4

The concentrations of ciprofol and its metabolite M4 in plasma, as well as the concentration of M4 in urine, were evaluated using established high-performance liquid chromatography-tandem mass spectrometry (HPLC-MS/MS) techniques. The analytical instrument used for the analysis was an LC-30 AD system (Shimadzu), coupled to a Triple Quad 6500$^+$ mass spectrometer and Analyst™ 1.6.3 software (both AB Sciex). Protein precipitation was performed as a pretreatment step for human plasma and urine samples. To monitor ciprofol and M4, multi-reaction monitoring was performed in negative mode. The compound HSK23287 served as the internal standard for assessing ciprofol, while nimesulide was used as the internal standard for M4. A quadratic regression analysis was conducted to determine the best-fit line for the calibration standards, with a weighing factor set to $1/x^2$. The linear range of ciprofol and M4 in plasma was 5–5,000 ng/mL, and in urine, it was 10–10,000 ng/mL.

2.4 Pharmacokinetic and pharmacodynamic analyses

PK parameters were computed using a noncompartmental approach with the Phoenix WinNonlin 8.3.1 (Certara, L.P., Princeton, NJ, United States). The maximum plasma concentration (C_{max}) was directly obtained from the plasma concentration–time plot. The peak time (T_{max}) was defined as the time at which C_{max} was obtained. The area under the plasma concentration–time curve (AUC) from 0 to t (AUC_{0-t}) was computed using the linear trapezoidal rule. AUC_{0-inf} was calculated as follows: $AUC_{0-inf} = AUC_{0-t} + C_t/k_e$, where C_t is the final determined concentration and k_e is estimated by linear regression of the log-linear part of the plasma concentration–time curve. The terminal elimination half-life ($t_{1/2}$) was calculated as ln2/ke, the total clearance (CL) as Dose/AUC_{0-inf}, and the distribution volume (V_d) as Dose/(AUC_{0-inf}* k_e). Protein binding (PB) was measured with equilibrium dialysis. For each participant, the protein binding was calculated as the average following the loading infusion and 1 min after the infusion was discontinued. The fraction unbound (Fu) was calculated as follows: Fu (%) = 100%—PB (%). Unbound concentration was estimated using the measured total concentration at each time point multiplied by Fu, assumed to be constant. The unbound C_{max} ($C_{max,u}$) of ciprofol was calculated as C_{max} × Fu(%), and unbound AUC_{0-inf} ($AUC_{0-inf,u}$) of ciprofol was calculated using the linear trapezoidal rule, as previously described, from the unbound ciprofol concentrations.

The PK parameters of urine were as follows: cumulative excretion (Ae_{0-48}) and renal clearance (CL_R) of M4. Ae_{0-48} was determined by summing the quantity of M4 excreted in urine between 0 and 48 h following dosing. CL_R was computed as Ae_{0-48}/AUC_{0-t}.

PD parameters were calculated using Adopt SAS® 9.4 (SAS Institute, Cary, North Carolina, United States). The PD parameters included the following: minimum BIS value (BIS_{peak}), the time to reach BIS_{peak} ($T_{BISpeak}$), and BIS AUC_{0-t}.

2.5 Safety

For safety assessment, the alterations in vital signs, ECG signals, laboratory findings, physical examinations, and assessments of injection pain were surveilled. Particular attention was given to adverse reactions associated with sedation, such as bradycardia, apnea, hypoxia, and hypotension.

2.6 Statistics analysis

Continuous variables were expressed as medians (maximum and minimum) or means (standard deviations). Adopt SAS® 9.4 (SAS Institute, Cary, North Carolina, United States) was used to statistically assess the PK and PD data. The impact of renal impairment versus the control group was investigated using analysis of variance (ANOVA), which included renal function as a fixed effect, and the corresponding 90% confidence intervals (CIs) around the geometric least-squares mean (GLSM) ratio of C_{max}, AUC_{0-inf}, $C_{max,u}$, and $AUC_{0-inf,u}$ were calculated. Multiple regression analysis was conducted to assess the correlation between clinical variables (age, sex, weight, and eGFR) and PK parameters (C_{max}, AUC_{0-inf}, CL, $C_{max,u}$, $AUC_{0-inf,u}$, CL_u, and CL_R). The correlation was determined by multiple regression analysis, using PK parameters as the dependent variable and clinical variables as independent variables.

3 Results

3.1 Subject demographics

A total of 24 participants with varying degrees of renal function, i.e., mildly impaired function (eGFR: 60–89 mL/min/1.73 m^2), moderately impaired function (eGFR: 30–59 mL/min/1.73 m^2),

and normal kidney function (eGFR: ≥90 mL/min/1.73 m^2) ($n = 8$ for each group), were enrolled in the study (Figure 1). The categorization of renal function was established by assessing the estimated glomerular filtration rate (eGFR) through the modification of diet in renal disease (MDRD) equation (Levey et al., 2006): eGFR (mL/min/1.73 m^2) = 175 × (Scr, std)$^{-1.234}$ × (age)$^{-0.179}$ × (0.79 for females). The demographic attributes of the normal control participants closely resembled those of the participants with renal impairment (Table 1).

3.2 Pharmacokinetics

The mean plasma concentration–time graphs of ciprofol and its metabolite M4 are shown in Figure 2. In Figure 2A, it is evident that the plasma concentration–time curve of ciprofol is similar across the three groups. The C_{max} of ciprofol was achieved 1 min after administration. Following the cessation of administration, the plasma concentration of ciprofol measured 352 ng/mL in the mild renal impairment group, 314 ng/mL in the moderate renal impairment group, and 297 ng/mL in the normal kidney function control group. The concentration of ciprofol in plasma decreased to the lowest limit of quantitation (5 ng/mL) approximately 8–12 h after the administration was stopped.

The primary PK parameters of ciprofol are presented in Table 2. The results showed that compared to the healthy control participants, the individuals with mild renal impairment exhibited an 8.56% decrease in C_{max} and a 15.67% increase in $AUC_{0\text{-inf}}$ of ciprofol. On the other hand, the individuals with moderate renal impairment showed a decline of 15.15% and 1.80% in C_{max} and $AUC_{0\text{-inf}}$ of ciprofol, respectively (Table 2, 3). The C_{max} values in the participants with mild and moderate renal impairment showed significant inter-individual variability, with coefficient of variation (CV%) values amounting to 138.15% and 42.72%, respectively.

The results of the protein binding assay indicated that ciprofol exhibits a high degree of binding to plasma proteins. The mean protein binding (%) for ciprofol was 99.10%, 99.15%, and 99.24% among the normal, mild renal impairment, and moderate renal impairment groups, respectively. The Fu (%) was 0.9%, 0.85%, and 0.76% for healthy participants and patients with mild and moderate renal impairment, respectively. As renal function worsened, decreased Fu was noted.

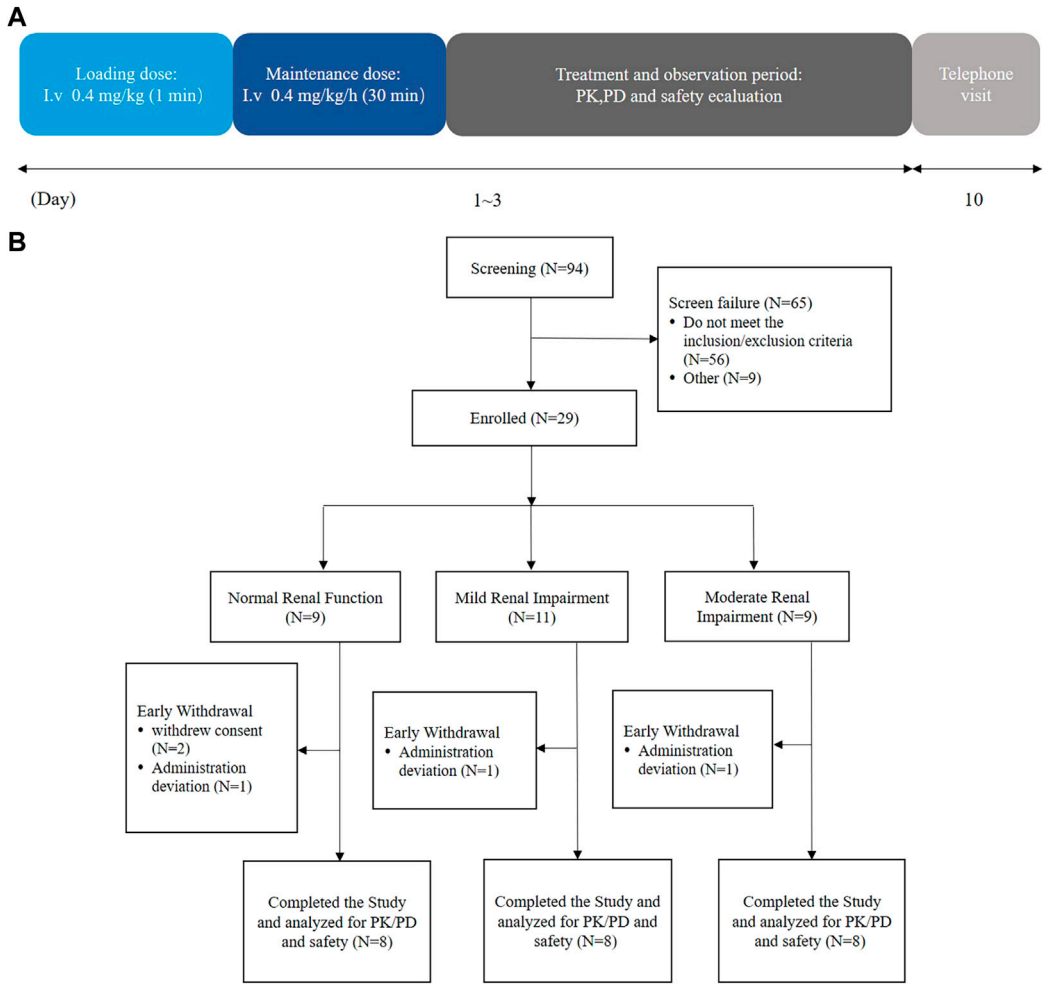

FIGURE 1
Flow diagrams of the current trial. **(A)** Schematic of the trial duration and **(B)** schematic of the trial participants.

10.3389/fphar.2023.1260599

TABLE 1 Demographic and baseline characteristics.

Parameter	Renal function group		
	Normal (n = 8)	Mild (n = 8)	Moderate (n = 8)
Sex [M/F (n)]	6/2	7/1	6/2
Age (years)	44.1 (1.2)	41.4 (8.0)	47.8 (11.0)
Weight (kg)	63.9 (4.7)	71.0 (8.4)	60.7 (8.2)
BMI (kg/m^2)	23.7 (1.5)	25.7 (1.5)	23.5 (2.5)
eGFR (mL/min/1.73 m^2)	128.6 (20.7)	72.7 (7.5)	43.0 (10.6)

Unless otherwise specified, all data are reported as means (SDs). The body mass index (BMI) is formulated as [weight in kg ÷ (height in m)^2]. The modification of diet in renal disease (MDRD) equation is used to compute the estimated glomerular filtration rate (eGFR).

TABLE 2 Pharmacokinetic (pk) parameters in plasma and urine collected from participants with normal and impaired renal function.

Parameter	Renal function group		
	Normal (n = 8)	Mild (n = 8)	Moderate (n = 8)
Plasma ciprofol			
C_{max} (ng/mL)	5,941.25 (1,478.36)	5,432.50 (3,314.53)	5,041.25 (1,945.57)
T_{max} (h)	0.02 (0.02, 0.02)	0.02 (0.02, 0.10)	0.02 (0.02, 0.02)
AUC_{0-t} (ng•h/mL)	521.99 (77.30)	596.24 (167.44)	517.71 (98.52)
AUC_{0-inf} (ng•h/mL)	549.18 (87.17)	635.26 (174.15)	539.31 (99.40)
CL (L/h)	70.60 (10.58)	69.54 (14.21)	68.52 (11.40)
V_d (L)	272.41 (99.04)	378.12 (182.56)	212.49 (95.90)
$t_{1/2}$ (h)	2.82 (1.39)	4.02 (2.58)	2.13 (0.71)
Plasma unbound ciprofol			
$C_{max,\ u}$ (ng/mL)	52.74 (11.39)	46.97 (29.51)	37.55 (12.79)
$AUC_{0-t,u}$ (ng•h/mL)	4.67 (0.71)	5.09 (1.56)	3.91 (0.61)
$AUC_{0-inf,u}$ (ng•h/mL)	4.91 (0.76)	5.42 (1.62)	4.07 (0.61)
CL_u (L/h)	7,841.62 (778.60)	8,297.30 (2,093.28)	9,023.51 (1,470.86)
$V_{d,u}$ (L)	31,321.77 (14,232.70)	44,791.11 (20,668.31)	27,957.51 (12,240.64)
Plasma metabolite M4			
C_{max} (ng/mL)	1,371.75 (345.81)	1,250.63 (249.83)	1,455.50 (768.97)
T_{max} (h)	0.55 (0.53, 0.65)	0.62 (0.50, 1.57)	0.62 (0.53, 2.52)
AUC_{0-t} (ng•h/mL)	7,285.16 (3,010.77)	9,721.68 (2,322.06)	15,377.32 (9,426.84)
AUC_{0-inf} (ng•h/mL)	7,538.73 (3,111.54)	10,058.72 (2,438.99)	16,029.21 (9,662.07)
$t_{1/2}$ (h)	11.71 (4.20)	9.01 (1.55)	11.04 (1.75)
Urine metabolite M4			
Ae_{0-t} (mg)	23.85 (6.92)	23.83 (4.18)	16.76 (5.18)
CL_R	3.50 (0.84)	2.61 (0.90)	1.23 (0.39)

Data are means (SDs) for all, except time to maximum concentration (T_{max}), which is the median (range).
C_{max}, maximum observed concentration; AUC_{0-t}, area under the curve from 0 to 48 h after the end of administration; AUC_{0-inf}, area under the curve from 0 to infinity time; CL, total clearance; V_d, distribution volume; $t_{1/2}$, terminal elimination half-life; u, free fraction; Ae, accumulative urine excretion; CL_R, renal clearance.

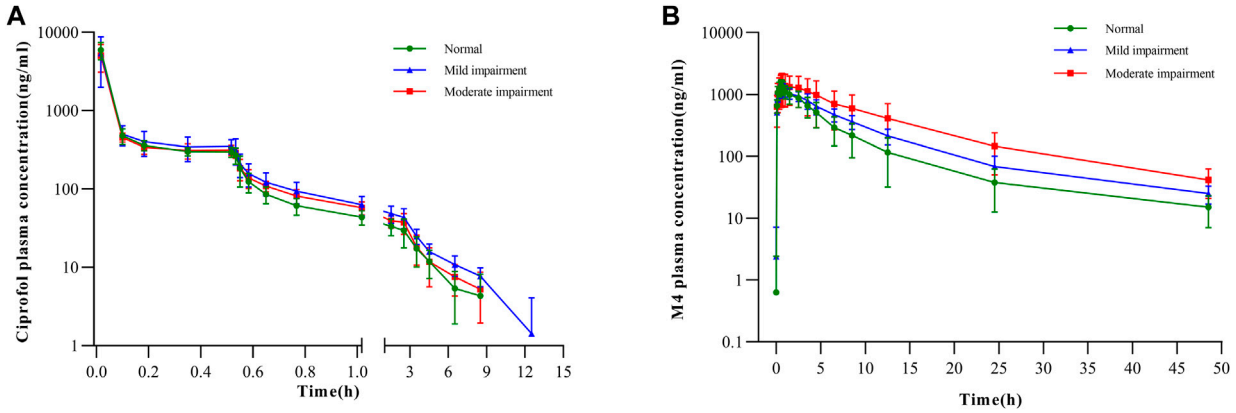

FIGURE 2
Plasma concentration–time curves for **(A)** ciprofol in semi-log scale and **(B)** M4 in semi-log scale.

TABLE 3 Statistical summaries of PK parameters for participants with mild and moderate renal impairment in comparison to the normal renal function controls.

Parameter	GLSM		Ratio (%)	90% CI of ratio (%)
	Renal impairment	Normal renal function		
Mild renal impairment vs. normal renal function				
C_{max}	3,933.47	5,770.81	68.16	(38.65, 120.20)
$AUC_{0\text{-}inf}$	614.90	543.24	113.19	(94.36, 135.77)
$C_{max,u}$	33.32	51.63	64.55	(36.52, 114.07)
$AUC_{0\text{-}inf,u}$	5.20	4.86	107.19	(89.22, 128.79)
Moderate renal impairment vs. normal renal function				
C_{max}	4,699.23	5,770.81	81.43	(46.18, 143.60)
$AUC_{0\text{-}inf}$	531.21	543.24	97.78	(81.52, 117.29)
$C_{max,u}$	35.65	51.63	69.05	(39.07, 122.03)
$AUC_{0\text{-}inf,u}$	4.03	4.86	82.92	(69.01, 99.62)

Natural log-transformed parameters were subjected to analysis of variance, where groups served as the fixed effect and subjects as the random effect. For the parameters, the geometric least-squares mean (GLSM) difference and its 90% confidence interval (CI) are obtained. The inverse logarithm is used in the aforementioned findings to obtain the point estimation and 90% CI for the GLSM ratio of the parameters between the two groups.

In comparison to participants with normal renal function, those with mild renal impairment demonstrated a 10.94% decrease in $C_{max,\ u}$ and a 10.39% increase in $AUC_{0\text{-}inf,\ u}$ for unbound ciprofol (Table 2). On the other hand, participants with moderate renal impairment exhibited 28.80% and 17.11% reductions in $C_{max,\ u}$ and $AUC_{0\text{-}inf,\ u}$, respectively, in contrast with individuals with normal renal function (Table 2, 3). Similarly, there was substantial variability in $C_{max,\ u}$ within the mildly and moderately impaired groups, with CV% values amounting to 146.04% and 36.02%, respectively.

There was no apparent trend observed in C_{max}, and $t_{1/2}$ of M4 among the three groups with respect to the aggravation of renal function damage (Table 2). Nonetheless, there was an observed increase in $AUC_{0\text{-}inf}$ with increase in the degree of kidney impairment (Figure 2B). The mean $AUC_{0\text{-}inf}$ increased by 33.43% and 112.62% in the mildly and moderately impaired groups, respectively (Table 2). In contrast to those with normal renal function, those with moderate impairment showed a 29.73% decrease in $Ae_{0\text{-}t}$ (Table 2). However, there was no clear difference in $Ae_{0\text{-}t}$ between the mild renal impairment and normal function groups.

Based on the findings from the multiple regression analysis conducted on PK parameters and clinical variables (age, sex, weight, and eGFR) among the examined groups, it was identified that the eGFR exhibited a significant correlation with CL_R for metabolite M4 (Supplementary Table S2; Figure 3). In the case of total and unbound ciprofol, $C_{max,u}$ appeared to be linearly associated with sex, while $AUC_{0\text{-}inf}$ or $AUC_{0\text{-}inf,u}$ was significantly associated with weight, as indicated in Supplementary Table S2.

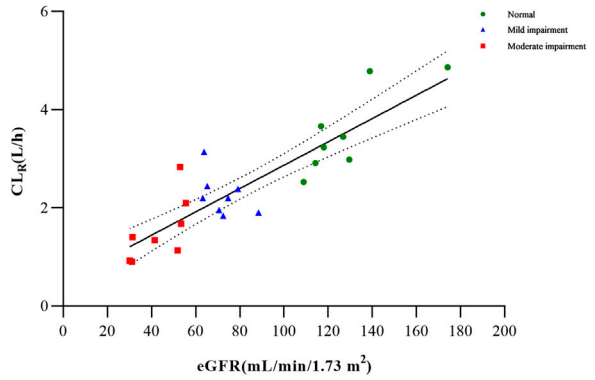

FIGURE 3
Correlation between CL_R and eGFR across the renal function groups ($p < 0.0001$).

3.3 Pharmacodynamics

The results revealed that the MOAA/S score–time curves were similar across the three groups, consistent with the PK profiles (Figure 4A). All three groups experienced deep sedation (MOAA/S 0–1) 6 min after infusion and regained consciousness immediately after infusion (Pastis et al., 2022). The median recovery time for the normal renal function group was 0.00 min, that for the mild renal impairment group was 1.08 min, and that for the moderate renal impairment group was 0.00 min, suggesting that the fluctuations in the recovery time were not significant.

Mean BIS–time profiles and parameters are shown in Figure 4B; Table 4, respectively. The BIS values decreased rapidly following the start of the infusion and reached their lowest levels (ranging from 41.13 to 47.63) at median times of 4.00, 3.48, and 3.00 min post-infusion for the normal function, mild renal impairment, and moderate renal impairment groups, respectively. The mean BIS corresponding to a 3–4 MOAA/S score, the desired sedation depth (Yamada et al., 2022), was 69. BIS_{peak} and BIS $AUC_{0\text{-}t}$ were similar across the three groups.

3.4 Safety

In the current study, 14 participants (58.3%) encountered a total of 19 AEs, as detailed in Table 5. The trial documented four cases of respiratory adverse events, with one occurring in the mild impairment group and three in the moderate impairment group. This suggests that there may be a potential association between the severity of renal injury and the increased incidence of adverse respiratory reactions. Throughout the entire duration of the trial, no occurrences of participant withdrawal due to adverse effects, severe adverse reactions, or fatalities were documented.

Vital signs, which included diastolic and systolic blood pressures, mean arterial pressure, oxygen saturation, and respiratory and cardiac rates, exhibited a consistent pattern of change (Figure 5), with fluctuations remaining within a 20% range. These observations suggest that ciprofol had minimal impact on hemodynamic stability, signifying its favorable safety profile.

4 Discussion

This study is the first to investigate the impact of varying degrees of renal impairment on the PK, PD, and safety of ciprofol,

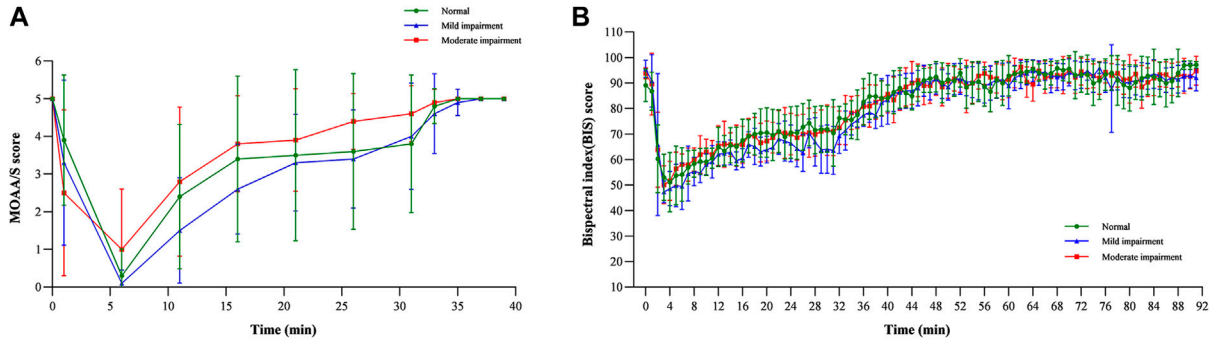

FIGURE 4
Pharmacodynamic parameter curves for **(A)** MOAA/S score–time and **(B)** BIS value–time.

TABLE 4 Bispectral index (BIS) parameters in participants with normal and impaired renal function.

Parameter	Renal function group		
	Normal (n = 8)	Mild (n = 8)	Moderate (n = 8)
BIS_{peak}	47.63 (10.183)	41.13 (5.515)	47.63 (6.323)
BIS $AUC_{0\text{-}t}$	7,445.44 (303.404)	7,270.08 (323.113)	7,448.91 (302.779)
$T_{BISpeak(min)}$	4.00 (2.00, 31.00)	3.48 (1.98, 7.00)	3.00 (2.00, 4.02)

Data are means (SD) for all except $T_{BISpeak}$, which is the median (range).
BIS_{peak}, BIS peak value (the lowest BIS value); BIS $AUC_{0\text{-}t}$, area under the BIS curve from zero to 1 h after the end of administration; $T_{BISpeak}$, time to BIS peak.

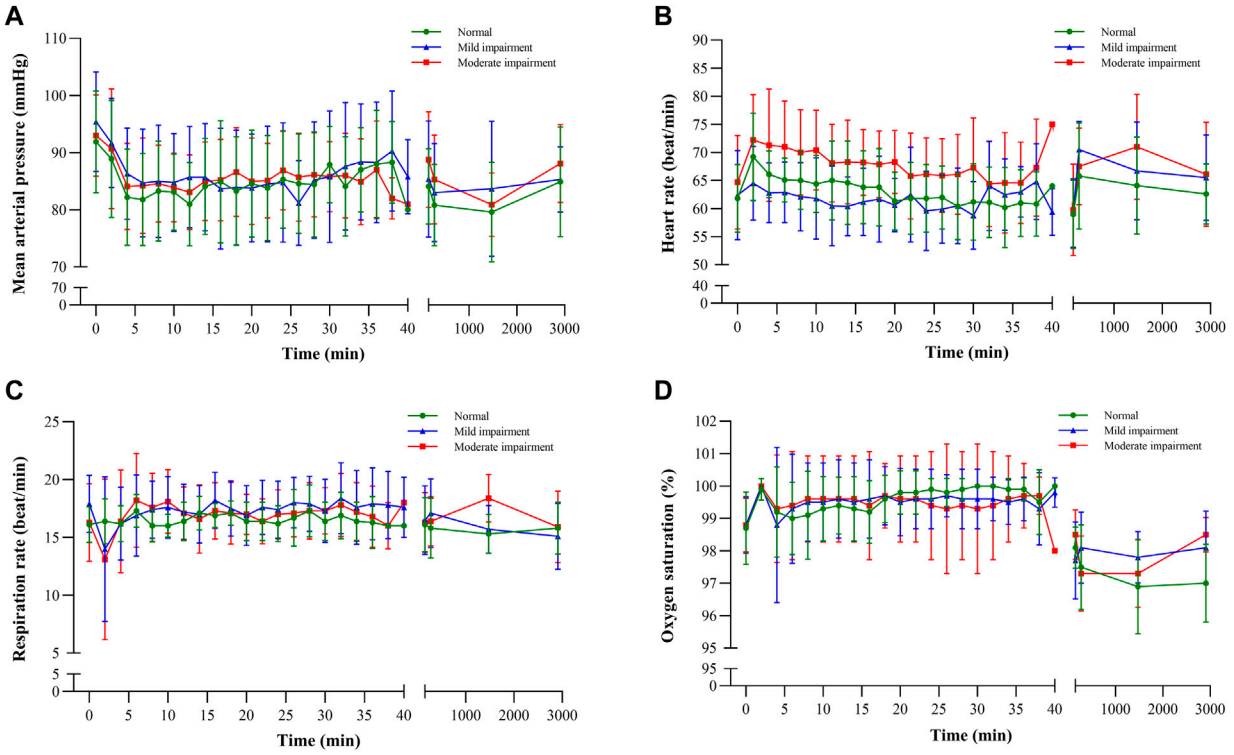

FIGURE 5
Vital sign–time curves: **(A)** mean arterial pressure, **(B)** heart rate, **(C)** respiration rate, and **(D)** oxygen saturation.

aiming to provide insights for dose adjustment in patients with mild–moderate kidney function impairment. The AUCs and C_{max} of total and unbound ciprofol in plasma for participants with renal impairment were only slightly higher (0.7–1.2-fold) than those in participants with normal renal function. Linear regression analysis revealed that PK parameters for ciprofol did not exhibit a significant correlation with the eGFR. However, given the relatively small sample size and larger variability (geometric % coefficient of variation), the reason behind the observed difference should be further investigated. It is crucial to acknowledge that the variation in C_{max} and AUC between healthy individuals and patients with renal impairment may be influenced by differences in infusion rates or distribution volume. Additionally, variations in $C_{max,u}$ and AUC_u could also be linked to variances in protein binding (Celestin and Musteata, 2021). Ciprofol is a drug with a substantial affinity for binding to proteins, primarily associating with serum albumin. It has been documented that the level of albumin tends to decrease in various types of renal diseases (Garrido et al., 1994). However, our study found that with the decrease in renal function, protein binding increased. This indicates that other proteins, including lipoproteins, may have a role in the protein binding of ciprofol (Zamacona et al., 1997; Zamacona et al., 1998).

The $AUC_{0\text{-}inf}$ of M4 showed a 1.3–2.1-fold higher concentration in participants with mild and moderate kidney impairment, respectively, compared to participants with normal renal function. The increase in $AUC_{0\text{-}inf}$ with the severity of renal impairment is consistent with its renal clearance. This is not surprising as M4 is primarily eliminated by kidneys. However, as M4 has been shown to have no excitatory effects on GABAA receptor-mediated cellular currents (Bian et al., 2021), it may not have a clinically relevant effect on the PD of ciprofol.

UGT1A9 serves as the principal enzyme responsible for the conversion of ciprofol into M4 and is acknowledged to exhibit polymorphic characteristics. Genetic polymorphisms within the UGT1A9 gene have been documented in association with the PK and/or toxicity of various pharmaceutical agents, including propofol, fluoroquinolone, and mycophenolic acid (Lévesque et al., 2007; Kansaku et al., 2011; Annisa et al., 2022). Nevertheless, no investigations to date have explored the potential correlations between UGT1A9 genetic polymorphisms and the PK and/or PD of ciprofol. Consequently, further investigations are imperative to ascertain the plausible impact of these genetic variations on ciprofol's PK and/or PD.

The temporal profiles of the MOAA/S score and BIS value for PD were similar among the various renal impairment groups, indicating that adjusting ciprofol dosages based on renal function may not be warranted. A significant correlation between ciprofol exposure and parameters such as recovery time, BIS $AUC_{0\text{-}t}$, BIS_{peak}, and $T_{BISpeak}$ has been observed, suggesting the potential utility of ciprofol exposure as a predictor of therapeutic efficacy. Concerning safety, there was an increased incidence of respiratory adverse reactions in the renal function impaired group, relative to the normal renal function group. Such adverse events are well-recognized in the context of anesthesia

TABLE 5 Statistics of adverse events and adverse drug reactions.

System organ class preferred term	Renal function group [N (%), E]		
	Normal (n = 8)	Mild (n = 8)	Moderate (n = 8)
Overall AEs	4 (50%), 5	5 (62.5%), 6	5 (62.5%), 8
Injection site pain	0 (0), 0	1 (12.5%), 1	1 (12.5%), 1
Bradycardia	1 (12.5%), 1	1 (12.5%), 1	0 (0), 0
Electrocardiogram abnormal	0 (0), 0	2 (25%), 2	0 (0), 0
Apnea	0 (0), 0	1 (12.5%), 1	2 (25%), 2
Respiratory depression	0 (0), 0	0 (0), 0	1 (12.5%), 1
Dizziness	0 (0), 0	0 (0), 0	1 (12.5%), 1
Blood pressure increased	1 (12.5%), 1	1 (12.5%), 1	0 (0), 0
Hypotension	1 (12.5%), 1	0 (0), 0	0 (0), 0
Protein present in urine	1 (12.5%), 1	0 (0), 0	0 (0), 0
Facial paralysis	1 (12.5%), 1	0 (0), 0	0 (0), 0
Puncture site swelling	0 (0), 0	0 (0), 0	1 (12.5%), 1
Vessel puncture site ecchymosis	0 (0), 0	0 (0), 0	2 (25%), 2
Drug-related AEs	3 (37.5%), 3	2 (25%), 3	5 (62.5%), 5
Injection site pain	0 (0), 0	1 (12.5%), 1	1 (12.5%), 1
Bradycardia	1 (12.5%), 1	1 (12.5%), 1	0 (0), 0
Apnea	0 (0), 0	1 (12.5%), 1	2 (25%), 2
Respiratory depression	0 (0), 0	0 (0), 0	1 (12.5%), 1
Dizziness	0 (0), 0	0 (0), 0	1 (12.5%), 1
Hypotension	1 (12.5%), 1	0 (0), 0	0 (0), 0
Facial paralysis	1 (12.5%), 1	0 (0), 0	0 (0), 0

E, number of AEs; N, number of subjects with AEs.

administration (Gan, 2006). Diligent monitoring by airway management experts is essential to ensure patient safety (Dinis-Oliveira, 2018). Overall, ciprofol demonstrated favorable tolerability, an acceptable safety profile, and stable patient hemodynamics.

Regrettably, this study did not include patients with severe renal impairment (eGFR: 15–29 mL/min/1.73 m^2), individuals with end-stage renal disease (ESRD) (eGFR<15 mL/min/1.73 m^2), or those undergoing dialysis. Notably, ESRD patients may experience gastrointestinal absorption alterations, changes in distribution volumes, shifts in protein binding, and variations in drug metabolic clearance. Patients with ERSD may require higher propofol induction doses (Goyal et al., 2002). The possible causes of high propofol doses in individuals with renal dysfunction include hyperdynamic circulation brought on by anemia. de Gasperi et al. (1996) also found lower plasma propofol concentrations in patients with severe renal impairment, attributed to increased phenol-induced glucuronosyltransferase activity, enhanced glucuronic acid binding, and accelerated hepatic biotransformation in patients with renal dysfunction patients. Nonetheless, clinical data on ciprofol in patients with severe renal impairment and ESRD receiving ciprofol remain unexplored, thus warranting cautious usage in this patient subgroup.

5 Conclusion

In summary, patients with mild (eGFR: 60–89 mL/min/1.73 m^2) to moderate (eGFR: 30–59 mL/min/1.73 m^2) renal function impairment displayed no clinically significant alterations in the PK and PD of ciprofol. Moreover, ciprofol exhibited favorable tolerance and an acceptable safety profile across all renal function groups. Consequently, the adjustment of ciprofol dosages is deemed unnecessary for individuals with mild to moderately impaired renal function based on the aforementioned findings.

Data availability statement

The original contributions presented in the study are included in the article/Supplementary Material; further inquiries can be directed to the corresponding authors.

Ethics statement

The studies involving human participants were reviewed and approved by the Ethics Committee for Scientific Research and Clinical Trials of the First Affiliated Hospital of Zhengzhou University. The Ethics Committee is affiliated with the First Affiliated Hospital of Zhengzhou University. The patients/participants provided their written informed consent to participate in this study.

Author contributions

JT: Conceptualization, Data curation, Formal Analysis, Validation, Writing–original draft, and Writing–review and editing. SL: Data curation, Formal Analysis, Validation, Writing–original draft, and Writing–review and editing. YZ: Data curation and Writing–review and editing. LQ: Data curation and Writing–review and editing. PY: Methodology, Project administration, and Writing–review and editing. NW: Methodology, Project administration, and Writing–review and editing. XL: Methodology, Project administration, and Writing–review and editing. DL: Conceptualization, Supervision, and Writing–review and editing. XT: Conceptualization, Supervision, and Writing–review and editing.

Funding

The author(s) declare financial support was received for the research, authorship, and/or publication of this article. This work was funded by Sichuan Haisco Pharmaceutical Group Co., Ltd.

Conflict of interest

Authors PY, NW, and XiL were employed by Sichuan Haisco Pharmaceutical Group Co., Ltd.

The authors declare that this study received funding from Sichuan Haisco Pharmaceutical Group Co., Ltd. The funder had the following involvement with the study: study design, analysis and and the decision to submit it for publication.

Publisher's note

All claims expressed in this article are solely those of the authors and do not necessarily represent those of their affiliated organizations, or those of the publisher, the editors, and the reviewers. Any product that may be evaluated in this article, or claim that may be made by its manufacturer, is not guaranteed or endorsed by the publisher.

Supplementary material

The Supplementary Material for this article can be found online at: https://www.frontiersin.org/articles/10.3389/fphar.2023.1260599/full#supplementary-material

References

Annisa, N., Barliana, M. I., Santoso, P., and Ruslami, R. (2022). Transporter and metabolizer gene polymorphisms affect fluoroquinolone pharmacokinetic parameters. *Front. Pharmacol.* 13, 1063413. doi:10.3389/fphar.2022.1063413

Bian, Y., Zhang, H., Ma, S., Jiao, Y., Yan, P., Liu, X., et al. (2021). Mass balance, pharmacokinetics and pharmacodynamics of intravenous HSK3486, a novel anaesthetic, administered to healthy subjects. *Br. J. Clin. Pharmacol.* 87 (1), 93–105. doi:10.1111/bcp.14363

Boucher, B. A., Wood, G. C., and Swanson, J. M. (2006). Pharmacokinetic changes in critical illness. *Crit. Care Clin.* 22 (2), 255–271. doi:10.1016/j.ccc.2006.02.011

Celestin, M. N., and Musteata, F. M. (2021). Impact of changes in free concentrations and drug-protein binding on drug dosing regimens in special populations and disease States. *J. Pharm. Sci.* 110 (10), 3331–3344. doi:10.1016/j.xphs.2021.05.018

de Gasperi, A., Mazza, E., Noe, L., Corti, A., Cristalli, A., Prosperi, M., et al. (1996). Pharmacokinetic profile of the induction dose of propofol in chronic renal failure patients undergoing renal transplantation. *Minerva Anestesiol.* 62 (1-2), 25–31.

Dinis-Oliveira, R. J. (2018). Metabolic profiles of propofol and fospropofol: clinical and forensic interpretative aspects. *Biomed. Res. Int.* 2018, 6852857. doi:10.1155/2018/6852857

Dixon, J., Lane, K., Macphee, I., and Philips, B. (2014). Xenobiotic metabolism: the effect of acute kidney injury on non-renal drug clearance and hepatic drug metabolism. *Int. J. Mol. Sci.* 15 (2), 2538–2553. doi:10.3390/ijms15022538

European Medicines Agency (2015). *Guideline on the evaluation of the pharmacokinetics of medicinal products in patients with decreased renal function*. Amsterdam, Netherlands: European Medicines Agency. Available at: https://www.ema.europa.eu/en/documents/scientific-guideline/guideline-evaluation-pharmacokinetics-medicinal-products-patients-decreased-renal-function_en.pdf.

Gan, T. J. (2006). Pharmacokinetic and pharmacodynamic characteristics of medications used for moderate sedation. *Clin. Pharmacokinet.* 45 (9), 855–869. doi:10.2165/00003088-200645090-00001

Garrido, M. J., Jimenez, R. M., Rodriguez-Sasiain, J. M., Aguirre, C., Aguilera, L., and Calvo, R. (1994). Characterization of propofol binding to plasma proteins and possible interactions. *Rev. Esp. Anestesiol. Reanim.* 41 (6), 308–312.

Goyal, P., Puri, G. D., Pandey, C. K., and Srivastva, S. (2002). Evaluation of induction doses of propofol: comparison between endstage renal disease and normal renal function patients. *Anaesth. Intensive Care* 30 (5), 584–587. doi:10.1177/0310057X0203000506

Hu, Y., Li, X., Liu, J., Chen, H., Zheng, W., Zhang, H., et al. (2022). Safety, pharmacokinetics and pharmacodynamics of a novel γ-aminobutyric acid (GABA) receptor potentiator, HSK3486, in Chinese patients with hepatic impairment. *Ann. Med.* 54 (1), 2769–2780. doi:10.1080/07853890.2022.2129433

Kansaku, F., Kumai, T., Sasaki, K., Yokozuka, M., Shimizu, M., Tateda, T., et al. (2011). Individual differences in pharmacokinetics and pharmacodynamics of anesthetic agent propofol with regard to CYP2B6 and UGT1A9 genotype and patient age. *Drug Metabolism Pharmacokinet.* 26 (5), 532–537. doi:10.2133/dmpk.DMPK-11-RG-039

Lévesque, E., Delage, R., Benoit-Biancamano, M. O., Caron, P., Bernard, O., Couture, F., et al. (2007). The impact of UGT1A8, UGT1A9, and UGT2B7 genetic polymorphisms on the pharmacokinetic profile of mycophenolic acid after a single oral dose in healthy volunteers. *Clin. Pharmacol. Ther.* 81 (3), 392–400. doi:10.1038/sj.clpt.6100073

Levey, A. S., Coresh, J., Greene, T., Stevens, L. A., Zhang, Y. P., Hendriksen, S., et al. (2006). Using standardized serum creatinine values in the modification of diet in renal disease study equation for estimating glomerular filtration rate. *Ann. Intern. Med.* 145 (4), 247–254. doi:10.7326/0003-4819-145-4-200608150-00004

Li, J., Wang, X., Liu, J., Wang, X., Li, X., Wang, Y., et al. (2022). Comparison of ciprofol (HSK3486) versus propofol for the induction of deep sedation during gastroscopy and colonoscopy procedures: a multi-centre, non-inferiority, randomized, controlled phase 3 clinical trial. *Basic Clin. Pharmacol. Toxicol.* 131 (2), 138–148. doi:10.1111/bcpt.13761

Li, X., Yang, D., Li, Q., Wang, H., Wang, M., Yan, P., et al. (2021). Safety, pharmacokinetics, and pharmacodynamics of a single bolus of the gamma-aminobutyric acid (GABA) receptor potentiator HSK3486 in healthy Chinese elderly and non-elderly. *Front. Pharmacol.* 12, 735700. doi:10.3389/fphar.2021.735700

Liu, Y., Yu, X., Zhu, D., Zeng, J., Lin, Q., Zang, B., et al. (2022). Safety and efficacy of ciprofol vs. propofol for sedation in intensive care unit patients with mechanical ventilation: a multi-center, open label, randomized, phase 2 trial. *Chin. Med. J. Engl.* 135 (9), 1043–1051. doi:10.1097/CM9.0000000000001912

Lu, M., Liu, J., Wu, X., and Zhang, Z. (2023). Ciprofol: a novel alternative to propofol in clinical intravenous anesthesia? *Biomed. Res. Int.* 2023, 7443226. doi:10.1155/2023/7443226

Mahmoud, M., and Mason, K. P. (2018). Recent advances in intravenous anesthesia and anesthetics. *F1000Res* 7, F1000 Faculty Rev-470. doi:10.12688/f1000research.13357.1

Pastis, N. J., Hill, N. T., Yarmus, L. B., Schippers, F., Imre, M., Sohngen, W., et al. (2022). Correlation of vital signs and depth of sedation by modified observer's assessment of alertness and sedation (MOAA/S) scale in bronchoscopy. *J. Bronchology Interv. Pulmonol.* 29 (1), 54–61. doi:10.1097/LBR.0000000000000784

Qin, L., Ren, L., Wan, S., Liu, G., Luo, X., Liu, Z., et al. (2017). Design, synthesis, and evaluation of novel 2,6-disubstituted phenol derivatives as general anesthetics. *J. Med. Chem.* 60 (9), 3606–3617. doi:10.1021/acs.jmedchem.7b00254

Sahinovic, M. M., Struys, M., and Absalom, A. R. (2018). Clinical pharmacokinetics and pharmacodynamics of propofol. *Clin. Pharmacokinet.* 57 (12), 1539–1558. doi:10.1007/s40262-018-0672-3

Teng, Y., Ou, M. C., Wang, X., Zhang, W. S., Liu, X., Liang, Y., et al. (2021). Pharmacokinetic and pharmacodynamic properties of ciprofol emulsion in Chinese subjects: a single center, open-label, single-arm dose-escalation phase 1 study. *Am. J. Transl. Res.* 13 (12), 13791–13802. Available at: https://www.ncbi.nlm.nih.gov/pubmed/35035718.

U.S. Food and Drug Administration (2020). *Pharmacokinetics in patients with impaired renal function – study design, data analysis, and impact on dosing*. White Oak, Maryland: U.S. Food and Drug Administration. https://www.fda.gov/media/78573/download.

Wang, X., Wang, X., Liu, J., Zuo, Y. X., Zhu, Q. M., Wei, X. C., et al. (2022). Effects of ciprofol for the induction of general anesthesia in patients scheduled for elective surgery compared to propofol: a phase 3, multicenter, randomized, double-blind, comparative study. *Eur. Rev. Med. Pharmacol. Sci.* 26 (5), 1607–1617. doi:10.26355/eurrev_202203_28228

Yamada, J., Hazama, D., Tachihara, M., Kawanami, Y., Kawaguchi, A., Yatani, A., et al. (2022). The utility of bispectral index monitoring in flexible bronchoscopy: a single-center, retrospective observational study. *Thorac. Cancer* 13 (21), 3052–3057. doi:10.1111/1759-7714.14658

Zamacona, M. K., Suarez, E., Aguilera, L., Rodriguez, S., Aguirre, C., and Calvo, R. (1997). Serum protein binding of propofol in critically ill patients. *Acta Anaesthesiol. Scand.* 41 (10), 1267–1272. doi:10.1111/j.1399-6576.1997.tb04643.x

Zamacona, M. K., Suarez, E., Garcia, E., Aguirre, C., and Calvo, R. (1998). The significance of lipoproteins in serum binding variations of propofol. *Anesth. Analg.* 87 (5), 1147–1151. doi:10.1097/00000539-199811000-00032

frontiers | Frontiers in Pharmacology

TYPE Original Research
PUBLISHED 22 May 2024
DOI 10.3389/fphar.2024.1293464

OPEN ACCESS

EDITED BY
Ling Ye,
Southern Medical University, China

REVIEWED BY
Xie-an Yu,
Shenzhen Institute For Drug Control, China
Beatriz Garcia Mendes,
Federal University of Santa Catarina, Brazil

*CORRESPONDENCE
Jun He,
hejun673@163.com

†These authors have contributed equally to this work

RECEIVED 13 September 2023
ACCEPTED 06 May 2024
PUBLISHED 22 May 2024

CITATION
Zhu Y, Ouyang H, Lv Z, Yao G, Ge M, Cao X, Chang Y and He J (2024), Simultaneous determination of multiple components in rat plasma by UPLC-MS/MS for pharmacokinetic studies after oral administration of *Pogostemon cablin* extract.
Front. Pharmacol. 15:1293464.
doi: 10.3389/fphar.2024.1293464

Simultaneous determination of multiple components in rat plasma by UPLC-MS/MS for pharmacokinetic studies after oral administration of *Pogostemon cablin* extract

Yameng Zhu[1,2†], Huizi Ouyang[1,2†], Zhenguo Lv[3], Guangzhe Yao[3], Minglei Ge[3], Xiunan Cao[3], Yanxu Chang[3] and Jun He[3*]

[1]First Teaching Hospital of Tianjin University of Traditional Chinese Medicine, Tianjin, China, [2]National Clinical Research Center for Chinese Medicine Acupuncture and Moxibustion, Tianjin, China, [3]State Key Laboratory of Component-Based Chinese Medicine, Tianjin University of Traditional Chinese Medicine, Tianjin, China

Introduction: *Pogostemon cablin* (PC) is used in traditional Chinese medicine and food, as it exerts pharmacological effects, such as immune-modulatory, antibacterial, antioxidant, antitumor, and antiviral. Currently, the pharmacokinetics (PK) studies of PC mainly focus on individual components. However, research on these individual components cannot reflect the actual PK characteristics of PC after administration. Therefore, the simultaneous determination of multiple components in rat plasma using UPLC-MS/MS was used for the pharmacokinetic study after oral administration of PC extract in this study, providing reference value for the clinical application of PC.

Methods: In the present study, a reliable and sensitive ultra-high performance liquid chromatography/tandem mass spectrometry (UPLC-MS/MS) method was developed and validated for the simultaneous determination of 15 prototype components (vanillic acid, vitexin, verbascoside, isoacteoside, hyperoside, cosmosiin, apigenin, β-rhamnocitrin, acacetin, ombuin, pogostone, pachypodol, vicenin-2, retusin, and diosmetin-7-O-β-D-glucopyranoside) in rat plasma after oral administration of the PC extract. Plasma samples were prepared via protein precipitation using acetonitrile, and icariin was used as the internal standard (IS).

Results: The intra-day and inter-day accuracies ranged from –12.0 to 14.3%, and the precision of the analytes was less than 11.3%. The extraction recovery rate of the analytes ranged from 70.6–104.5%, and the matrix effects ranged from 67.4–104.8%. Stability studies proved that the analytes were stable under the tested conditions, with a relative standard deviation lower than 14.1%.

Abbreviations: PC, *P. cablin*; TCM, traditional Chinese medicine; IS, internal standard; ME, methanol; ACN, acetonitrile; FA, formic acid; UPLC-MS/MS, ultra-high performance liquid chromatography/tandem mass spectrometry; MRM, multiple reaction monitoring; RE, relative error; RSD, relative standard deviation; LLOQ, lower limits of quantitation; QC, quality control; T_{max}, concentration maximum; $T_{1/2}$, plasma half-life; C_{max}, concentration maximum; AUC, area-under-the-curve.

Conclusion: The developed method can be applied to evaluate the PK of 15 prototype components in PC extracts of rats after oral administration using UPLC-MS/MS, providing valuable information for the development and clinical safe, effective, and rational use of PC.

KEYWORDS

***Pogostemon cablin* extract, prototype components, pharmacokinetic, rat plasma, UPLC-MS/MS**

1 Introduction

Medicinal plants are natural resources with crucial medicinal value, not only for the treatment of diseases but also for the enhancement of immunity and prevention of diseases. Therefore, an in-depth study of medicinal plants is of great significance (Zhu et al., 2022; Lai et al., 2023). *Pogostemon cablin* (Blanco) Benth., is a plant of the Lamiaceae family, commonly called patchouli, or "Guanghuoxiang." *Pogostemon cablin* (PC), is extensively distributed in the tropical and subtropical areas of Asia, and widely cultivated in the Philippines, India, and southern and southwestern China (Su et al., 2017; Chen et al., 2020). As a traditional herbal medicine, PC was used as a stomach tonic to remove dampness, improve indigestion, and relieve vomiting and diarrhea. It was also used to treat the common cold, headache, nausea, fever, and so on (Zhang et al., 2019; Chinese Pharmacopoeia Committee, 2020; Li et al., 2023). There are a number of components in PC, such as monoterpenoids, triterpenoids, sesquiterpenoids, phytosterols, and flavonoids. Studies have suggested that PC has immune-modulatory, antibacterial, antioxidant, antitumor, and antiviral bioactivities due to its multi-component properties (Kiyohara et al., 2012; Kim et al., 2015; Liu et al., 2015; Junren et al., 2021). PC is one of the ingredients in the formulations of many famous traditional Chinese patent medicines, including Huoxiang Zhengqi Oral Liquid and Huodan Wan (Pills). It can be used to treat gastrointestinal disorders with Huoxiang Zhengqi Oral Liquid, and Huodan Wan can be used for cold rhinitis and nasal congestion caused by dampness-heat in clinical (Lan and Yuan, 2018; Zhao et al., 2019). In addition to the traditional use of herbal medicine, PC also has high edible value and health benefits due to its various nutrients, including amino acids, proteins, vitamins, and minerals (Zhang, 2004). The leaves or stems of fresh PC can be stir-fried, fried, dipped in sauce, cold mixed, pickled, cooked in soup or congee, and it is mainly used as side dishes and stews to taste because of its properties of fishiness-eliminating and flavor-enhancing. Huoxiang jam is considered a food with higher health value. Meanwhile, PC is combined with *Mentha haplocalyx, Glycyrrhiza uralensis, Perilla frutescens, Ophiopogonis Radix, Chrysanthemum morifolium*, and other raw materials, which can form a variety of medicinal teas with fitness, beauty, and disease treatment effects. Moreover, PC can be used as a fixing agent for various perfumes, and as a raw material for cosmetics and oral hygiene products (Huo et al., 2007; Zhang J. et al., 2016; Sandes et al., 2016).

Pharmacokinetics (PK) is the study of the absorption, distribution, metabolism, and excretion of drugs *in vivo*, which plays an important role in the determination of the drug's kinetics and bioavailability. Notably, PK is very important for evaluating the absorption properties of different active components of traditional Chinese medicine (TCM). Moreover, the development of sensitive and reliable biological sample analysis technology to simultaneously determine multiple active ingredients *in vivo* is a hotspot in the PK research of TCM extracts, due to the complex composition and significant differences in the content (Cao et al., 2021). Therefore, an accurate and selective bioanalytical method is urgently required for the simultaneous determination of multiple biological components in plasma to understand the characteristics and diversity of the PK properties of PC.

In this study, a method for the simultaneous detection of 15 compounds (vanillic acid, vitexin, verbascoside, isoacteoside, hyperoside, cosmosiin, apigenin, β-rhamnocitrin, acacetin, ombuin, pogostone, pachypodol, diosmetin-7-O-β-D-glucopyranoside, vicenin-2, and retusin) in rat plasma was established and validated using ultra-high-performance liquid chromatography/tandem mass spectrometry (UPLC-MS/MS), which provided a reference for the clinical safe, effective and rational use of PC.

2 Materials and methods

2.1 Chemicals and reagents

Standard compound including vanillic acid, vitexin, verbascoside, isoacteoside, hyperoside, cosmosiin, apigenin, β-rhamnocitrin, acacetin, ombuin, pogostone, pachypodol, diosmetin-7-O-β-D-glucopyranoside, vicenin-2, and retusin (purity ≥98%) were purchased from Chengdu Desite Bio-Technology Co., Ltd. (Chengdu, China). Icariin [internal standard (IS)] was provided by Tianjin Yifang Zhongkang Pharmaceutical Technology Co., Ltd. (Tianjin, China). Fisher Scientific (Fair Lawn, NJ, United States) supplied the chromatographic grade methanol (ME) and acetonitrile (ACN). The chromatographic grade of formic acid (FA) was provided by ROE (St Louis, MO, United States). PC was purchased from Guangdong province (China).

2.2 Chromatography and mass spectrometry (MS)

The analyte was separated and detected through the utilization of a UPLC-MS/MS system, consisting primarily of the Agilent-1290 high-performance liquid chromatography system (Agilent, United States) and the Agilent-6470 triple quadrupole tandem mass spectrometer (Agilent, United States).

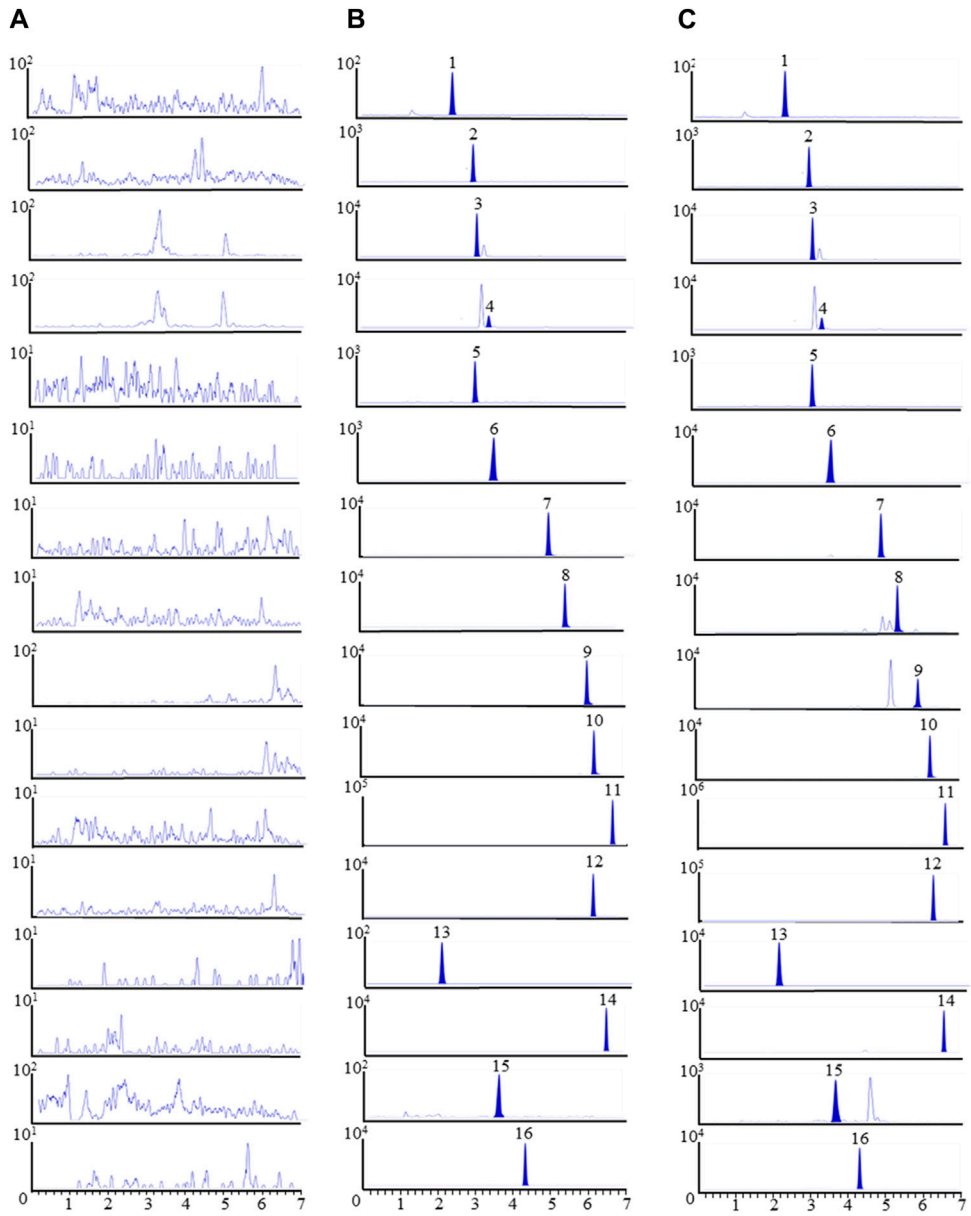

FIGURE 1
The MRM chromatograms of 15 components and IS in rat plasma samples. **(A)** Plasma samples without any added analytes, **(B)** plasma samples combined with the 15 compounds and IS, **(C)** post-dosing plasma samples from rats following oral ingestion of PC. 1. Vanillic acid, 2. Vitexin, 3. Verbascoside, 4. Isoacteoside, 5. Hyperoside, 6. Cosmosiin, 7. Apigenin, 8. β-Rhamnocitrin, 9. Acacetin, 10. Ombuin, 11. Pogostone, 12. Pachypodol, 13. Vicenin-2, 14. Retusin 15. Diosmetin-7-O-β-D-glucopyranoside 16. Icariin (IS).

The components were separated using an ACQUITY UPLC®BEH C18 column (2.1 × 100 mm, 1.7 μm) maintained at a temperature of 25°C. 0.1% FA-water and ACN were used as mobile phases A and B. The gradient elution conditions were as follows: 0–4 min, 14%–53% B; 4–5 min, 53%–100% B; and 5–7 min, 100%–100% B. A flow rate of 0.3 mL/min and an injection volume of 5 μL were used.

Mass spectrometry analysis was conducted in the multiple reaction monitoring (MRM) mode with both positive and negative ionization (Zhu et al., 2022). The parameters for the mass spectrometer included drying gas (N_2) temperature, gas flow rate, atomizer pressure, and capillary voltage of 320°C, 7 L/min, 35 psi, and 3500 V, respectively. The detailed MRM parameters can be found in Supplementary Table S1.

2.3 PC extract preparation

PC (0.5 kg) was accurately weighed and extracted with 10-fold ethanol (85%, *v/v*) under heated reflux conditions twice for 1.5 h. Next, the solutions for extraction underwent filtration and were subsequently combined. The ensuing mixture underwent

TABLE 1 Standard curve regression equation, linear range and LLOQ of 15 components.

Compound	Calibration curve	Linear range (ng/mL)	Correlation coefficients (r)	LLOQ (ng/mL)
Vanillic acid	$Y = 0.0023X - 2.3543^{E-004}$	20–8,000	0.998	20.0
Vitexin	$Y = 0.0919X + 1.3292^{E-004}$	0.5–200	0.998	0.5
Verbascoside	$Y = 0.0335X + 0.0024$	10–4,000	0.999	10.0
Isoacteoside	$Y = 0.0490X + 0.0015$	2–800	0.997	2.0
Hyperoside	$Y = 0.0687X - 1.3570^{E-004}$	0.3–120	0.998	0.3
Cosmosiin	$Y = 0.0.1527X + 0.0031$	0.5–200	0.998	0.5
Apigenin	$Y = 0.0805X + 0.0013$	1.5–600	0.999	1.5
β-rhamnocitrin	$Y = 0.2143X + 0.0057$	0.3–120	0.999	0.3
Acacetin	$Y = 0.4803X + 0.0023$	0.3–120	0.998	0.3
Ombuin	$Y = 0.0472X + 0.0015$	0.5–200	0.996	0.5
Pogostone	$Y = 0.0056X + 0.1677$	125–50000	0.999	30.0
Pachypodol	$Y = 0.2386X + 0.0209$	1–400	0.999	1.0
Vicenin-2	$Y = 0.0112X - 0.0013$	20–8,000	0.997	20.0
Retusin	$Y = 0.0989X + 0.0070$	0.2–80	0.996	0.2
Diosmetin-7-O-β-D-glucopyranoside	$Y = 0.2742X - 4.2961^{E-004}$	0.3–120	0.999	0.3

concentration through evaporation under decreased pressure. Ultimately, the dried PC extract was stored in a dry environment for further analysis. The levels of vanillic acid, vitexin, verbascoside, isoacteoside, hyperoside, cosmosiin, apigenin, β-rhamnocitrin, acacetin, ombuin, pogostone, pachypodol, vicenin-2, retusin, and diosmetin-7-O-β-D-glucopyranoside in the PC extract are displayed in Supplementary Table S2.

2.4 Preparation of standard solutions, calibration standards, and quality control (QC) samples

Vanillic acid, vitexin, verbascoside, isoacteoside, hyperoside, cosmosiin, apigenin, β-rhamnocitrin, acacetin, ombuin, pogostone, pachypodol, vicenin-2, retusin, diosmetin-7-O-β-D-glucopyranoside, and icariin (IS) were individually weighed and mixed with ME to prepare standard stock solution (1 mg/mL). To obtain the subsequent working solutions, the standard stock solutions were diluted using ME.

To prepare the calibration solutions, 20 μL of a mixture of working solution and IS was added to blank rat plasma (100 μL), resulting in concentrations: 20, 50, 100, 200, 400, 1,000, 2000, 4,000, and 8,000 ng/mL for vanillic acid and vicenin-2; 0.5, 1.25, 2.5, 5, 10, 25, 50, 100, and 200 ng/mL for vitexin, cosmosiin, and ombuin; 0.3, 0.75, 1.5, 3, 6, 15, 30, 60, and 120 ng/mL for hyperoside, β-rhamnocitrin, acacetin, and diosmetin-7-O-β-D-glucopyranoside; 10, 25, 50, 100, 200, 500, 1,000, 2000, and 4,000 ng/mL for verbascoside; 2, 5, 10, 20, 40, 100, 200, 400, and 800 ng/mL for isoacteoside; 1.5, 3.75, 7.5, 15, 30, 75, 150, 300, and 600 ng/mL for apigenin; 1, 2.5, 5, 10, 20, 50, 100, 200, and 400 ng/mL for pachypodol; 0.2, 0.5, 1, 2, 4, 10, 20, 40, and 80 ng/mL for retusin; 125, 312.5, 635, 1,250, 2,500, 6,250, 12,500, 25,000, and 50,000 ng/mL for pogostone. QC samples at three concentrations (low, medium, and high) were obtained similarly. Prior to analysis, all solutions were stored in an environment of 4°C.

2.5 Preparation of plasma sample

The 100 μL plasma sample was combined with 20 μL of ME, 20 μL of IS (500 ng/mL), and 2.5 μL of FA, followed by vortexing for 1 min. This mixture underwent extraction with 600 μL ACN through vortexing at room temperature for 3 min. Subsequent to centrifugation at 14,000 rpm for a period of 10 min, the resulting supernatant was moved to another tube and dried under a stream of nitrogen. The dried residue was dissolved in 100 μL ME-ACN (50:50 *v/v*), followed by vortexing for 5 min, and subsequent centrifugation at 14,000 rpm for 10 min. Finally, 20 μL of the supernatant was used for analysis.

2.6 Method validation

2.6.1 Specificity

In order to assess specificity, chromatograms of rat plasma samples without any added analytes, plasma with added analytes, and post-dosing plasma samples from rats following oral ingestion of PC were analyzed.

2.6.2 Linearity and LLOQ

By graphing the correlation between the peak area ratios of each component to IS versus the concentration of those particular analytes to obtain calibration curves. The regression association was depicted utilizing a linear formula with a weighting factor of 1/

TABLE 2 Accuracy and precision of 15 components in rat plasma (n = 6).

Compound	Spiked concent-ration (ng/mL)	Intra-day			Inter-day		
		Measured (ng/mL)	RE (%)	RSD (%)	Measured (ng/mL)	RE (%)	RSD (%)
Vanillic acid	20	22.3 ± 0.5	11.5	2.4	22.1 ± 0.6	10.6	2.5
	400	401.0 ± 6.1	0.3	1.5	395.5 ± 15.4	−1.1	3.9
	6,400	6,544.7 ± 92.7	2.3	1.4	6,203.9 ± 375.4	−3.1	6.1
Vitexin	0.5	0.6 ± 0.1	12.0	10.5	0.6 ± 0.1	11.5	8.5
	10	9.8 ± 0.5	−1.7	5.1	10.3 ± 0.3	2.7	3.1
	160	153.7 ± 3.9	−3.9	2.5	168.3 ± 11.7	5.2	7.0
Verbascoside	10	11.4 ± 1.2	14.3	10.6	11.1 ± 0.3	10.8	2.8
	200	193.8 ± 15.8	−3.1	8.2	193.4 ± 13.1	−3.3	6.7
	3200	3147.6 ± 156.6	−1.6	5.0	3498.1 ± 208.3	9.3	6.0
Isoacteoside	2	2.3 ± 0.2	12.4	7.6	2.2 ± 0.2	9.8	7.4
	40	43.9 ± 2.1	9.8	4.7	43.7 ± 2.1	9.3	4.8
	640	657.2 ± 27.8	2.7	4.2	661.9 ± 21.4	3.4	3.2
Hyperoside	0.3	0.3 ± 0.1	12.1	10.9	0.3 ± 0.0	3.9	2.3
	6	6.1 ± 0.3	1.2	5.5	6.1 ± 0.2	1.9	3.6
	96	96.4 ± 2.0	0.4	2.1	104.6 ± 6.5	9.0	6.2
Cosmosiin	0.5	0.5 ± 0.0	3.2	2.0	0.5 ± 0.0	3.3	2.5
	10	10.0 ± 0.4	0.3	3.6	10.2 ± 0.3	2.4	2.5
	160	168.8 ± 5.5	5.5	3.3	164.8 ± 4.4	3.0	2.6
Apigenin	1.5	1.7 ± 0.2	13.4	9.3	1.7 ± 0.2	12.1	9.9
	30	29.4 ± 1.6	−1.9	5.4	31.8 ± 1.5	6.0	4.8
	480	484.8 ± 8.7	1.0	1.8	487.8 ± 5.0	1.6	1.0
β-rhamnocitrin	0.3	0.3 ± 0.1	14.0	9.2	0.3 ± 0.1	12.6	9.3
	6	5.3 ± 0.5	−12.0	8.5	6.1 ± 0.2	0.8	3.4
	96	87.2 ± 9.3	−9.2	10.6	100.8 ± 4.0	5.0	4.0
Acacetin	0.3	0.3 ± 0.0	10.8	11.3	0.3 ± 0.1	9.2	10.2
	6	5.6 ± 0.2	−6.6	3.8	5.9 ± 0.5	−1.0	8.0
	96	95.2 ± 2.7	−0.9	2.8	97.6 ± 2.7	1.7	2.8
Ombuin	0.5	0.5 ± 0.0	6.3	6.0	0.5 ± 0.1	7.5	11.2
	10	9.8 ± 0.5	−2.3	5.0	9.5 ± 0.6	−5.1	5.9
	160	151.4 ± 4.7	−5.4	3.1	153.5 ± 1.9	−4.0	1.2
Pogostone	125	132.5 ± 7.3	6.0	5.5	131.7 ± 3.6	5.4	2.7
	2,500	2,611.9 ± 125.9	4.5	4.8	2,535.6 ± 75.2	1.4	3.0
	40,000	37,526.9 ± 1,130.5	−6.2	3.0	37,411.8 ± 1754.1	−6.5	4.7
Pachypodol	1	1.1 ± 0.1	9.5	4.9	1.1 ± 0.1	7.2	7.8
	20	22.2 ± 0.8	10.7	3.6	21.0 ± 1.1	4.8	5.4
	320	346.8 ± 13.8	8.4	4.0	317.9 ± 24.5	−0.7	7.7
Vicenin-2	20	22.7 ± 0.8	13.5	3.5	22.7 ± 1.2	13.2	5.3

(Continued on following page)

TABLE 2 (*Continued*) Accuracy and precision of 15 components in rat plasma (n = 6).

Compound	Spiked concent-ration (ng/mL)	Intra-day			Inter-day		
		Measured (ng/mL)	RE (%)	RSD (%)	Measured (ng/mL)	RE (%)	RSD (%)
	400	369.3 ± 16.7	−7.7	4.5	407.5 ± 21.8	1.9	5.3
	6,400	6,403.5 ± 115.5	0.1	1.8	6,480.6 ± 158.8	1.3	2.5
Retusin	0.2	0.2 ± 0.0	10.6	6.1	0.2 ± 0.0	6.6	4.2
	4	4.4 ± 0.1	9.5	2.9	4.2 ± 0.1	5.9	2.7
	64	64.6 ± 4.1	0.9	6.3	64.2 ± 4.2	0.3	6.5
Diosmetin-7-O-β-D-glucopyranoside	0.3	0.3 ± 0.0	13.6	5.6	0.3 ± 0.0	12.2	5.8
	6	6.19 ± 0.2	3.1	3.8	6.0 ± 0.4	−0.9	5.9
	96	102.7 ± 4.9	7.0	4.7	99.3 ± 4.3	3.4	4.3

x^2. The determination of LLOQ relied on the baseline noise, ensuring a signal-to-noise ratio of around ten.

2.6.3 Precision and accuracy

QC samples three concentrations (20, 400, and 6,400 ng/mL for vanillic acid and vicenin-2; 0.5, 10, and 160 ng/mL for vitexin, cosmosiin, and ombuin; 0.3, 6, and 96 ng/mL for hyperoside, β-rhamnocitrin, acacetin and diosmetin-7-O-β-D-glucopyranoside; 10, 200, and 3200 ng/mL for verbascoside; 2, 40, and 640 ng/mL for isoacteoside; 1.5, 30, and 480 ng/mL for apigenin; 1, 20, and 320 ng/mL for pachypodol; 0.2, 4, and 64 ng/mL for retusin; 125, 2,500, and 40,000 ng/mL for pogostone) were analyzed six repetitions over one or three consecutive days to assess the precision and accuracy. Relative error (RE) was used to determine accuracy, while the precisions were expressed as the relative standard deviation (RSD).

2.6.4 Extraction recovery and matrix effect

Analyzing the peak areas of QC samples and the peak areas of the post-extraction mixed samples to measure the extraction recovery rates at three concentrations. Matrix effects were determined by comparing the peak areas of QC samples in post-extracted mixed samples to those in standard solutions, calculating the ratio for evaluation.

2.6.5 Stability

Plasma samples were retained for 12 h in an auto-sampler, exposed to room temperature for 4 h, undergoing three freeze-thaw cycles, and stored at −80°C for a period of 1 week to assess the stability of all compounds.

2.7 PK study

Six male rats (220 ± 10 g) were utilized in this experiment and were not restricted from drinking water but fasted for 12 h before the investigation. A concentration of 0.5 g/mL of PC extract was obtained by dissolving in 0.5% CMC-Na aqueous solution. The PC suspension of the 4.0 g/kg dose was given to rats by single oral administration. Samples of blood (300 μL) were obtained from the orbital venous plexus prior to and following oral dosing at 0, 0.03, 0.08, 0.25, 0.5, 0.75, 1, 2, 6, 10, 12, 24, 36, and 48 h. Subsequently, the plasma collected underwent centrifugation at a speed of 7000 rpm for a duration of 10 min. It was then moved to clean tubes and kept at a temperature of −80°C.

2.8 Data analysis

Data in this study was presented as the mean ± standard deviation (SD). The MassHunter Workstation software (version B.09.00, Agilent, United States) was utilized for determining the plasma levels of the 15 analytes. Additionally, PK parameters were analyzed using DAS 3.0 Software (Medical College of Wannan, China).

3 Result and discussion

3.1 Optimization of chromatography and MS

To improve the separation of the 15 compounds, an investigation was conducted on the impact of different columns, including ACQUITY UPLC BEH C18 (2.1 × 100 mm, 1.7 μm) and ACQUITY UPLC HSS T3 (2.1 × 100 mm, 1.8 μm), on the chromatographic peaks and retention times. The findings revealed that the ACQUITY UPLC BEH C18 (2.1 × 100 mm, 1.7 μm) column provided superior separation capability for the 15 compounds. Different mobile phases were also evaluated, such as 0.1% FA/water-ACN, 0.1% FA/water-ME, water-ME, and water-ACN, to optimize the separation of all compounds. The findings demonstrated that the 0.1% FA/water-ACN proved to be superior in improving the separation and peak profiles of the compounds. All 15 components and IS were eluted successfully within a 7-min, and with no observed interference peaks.

Optimizing the primary parameters of the MS was crucial in enhancing the response of compounds. In positive ion mode, the

10.3389/fphar.2024.1293464

TABLE 3 Extraction recovery and matrix effects of 15 components in rat plasma (n = 6).

Compound	Spiked concentration (ng/mL)	Extraction recovery (%)	RSD (%)	Matrix effect (%)	RSD (%)
Vanillic acid	20	90.2 ± 8.0	8.8	89.3 ± 7.0	7.9
	400	97.1 ± 6.8	7.0	93.1 ± 8.1	8.7
	6,400	92.1 ± 4.5	4.9	86.5 ± 8.3	9.6
Vitexin	0.5	88.1 ± 9.1	10.3	83.7 ± 6.7	7.9
	10	89.2 ± 10.3	11.5	85.1 ± 8.1	9.5
	160	76.20 ± 5.9	7.7	75.2 ± 7.4	9.8
Verbascoside	10	89.0 ± 5.4	6.0	81.2 ± 6.8	8.4
	200	92.3 ± 9.1	9.9	82.4 ± 5.78	7.0
	3200	84.9 ± 4.9	5.8	85.2 ± 7.3	8.6
Isoacteoside	2	83.1 ± 6.5	7.8	80.3 ± 8.4	10.4
	40	86.7 ± 6.8	7.9	81.8 ± 9.2	11.2
	640	91.7 ± 10.4	11.4	86.9 ± 9.3	10.7
Hyperoside	0.3	79.4 ± 6.6	8.3	88.2 ± 9.4	10.6
	6	77.3 ± 4.3	5.6	85.7 ± 7.3	8.5
	96	78.4 ± 4.4	5.6	70.7 ± 3.5	5.0
Cosmosiin	0.5	82.4 ± 7.7	9.3	91.9 ± 8.5	9.3
	10	81.0 ± 7.5	9.3	97.0 ± 6.2	6.3
	160	87.2 ± 11.2	12.8	83.1 ± 3.5	4.3
Apigenin	1.5	95.3 ± 6.9	7.3	103.3 ± 2.8	2.7
	30	81.8 ± 1.6	1.9	100.5 ± 3.0	3.0
	480	90.4 ± 4.9	5.4	83.8 ± 3.4	4.1
β-rhamnocitrin	0.3	96.0 ± 6.5	6.8	80.4 ± 4.2	5.3
	6	84.0 ± 5.5	6.6	97.8 ± 7.6	7.7
	96	86.2 ± 4.2	4.9	93.9 ± 4.3	4.6
Acacetin	0.3	94.3 ± 7.6	8.0	72.2 ± 4.8	6.7
	6	90.1 ± 7.7	8.5	92.5 ± 10.2	11.0
	96	89.0 ± 11.3	12.7	71.2 ± 9.1	12.8
Ombuin	0.5	70.6 ± 7.0	9.9	79.4 ± 9.3	11.7
	10	79.4 ± 3.0	3.8	79.1 ± 10.9	13.8
	160	88.4 ± 8.0	9.0	83.4 ± 4.7	5.6
Pogostone	125	87.4 ± 11.3	13.0	98.5 ± 12.2	12.4
	2,500	87.8 ± 5.4	6.2	99.1 ± 4.1	4.1
	40,000	78.5 ± 7.0	8.9	87.1 ± 9.7	11.1
Pachypodol	1	89.4 ± 10.5	11.7	69.3 ± 6.1	8.7
	20	104.5 ± 9.6	9.2	78.1 ± 7.0	9.0
	320	96.3 ± 9.1	9.5	82.1 ± 10.6	12.9
Vicenin-2	20	93.4 ± 5.1	5.4	89.5 ± 10.4	11.7
	400	71.1 ± 3.4	4.8	104.8 ± 13.2	12.6

(Continued on following page)

TABLE 3 (*Continued*) Extraction recovery and matrix effects of 15 components in rat plasma (n = 6).

Compound	Spiked concentration (ng/mL)	Extraction recovery (%)	RSD (%)	Matrix effect (%)	RSD (%)
	6,400	79.2 ± 10.2	12.9	76.9 ± 6.6	8.6
Retusin	0.2	95.2 ± 8.1	8.5	70.9 ± 6.3	8.9
	4	89.1 ± 11.5	12.9	69.9 ± 7.4	10.5
	64	71.6 ± 9.3	13.0	67.4 ± 6.9	10.3
Diosmetin-7-O-β-D-glucopyranoside	0.3	85.5 ± 7.0	8.1	75.8 ± 9.7	12.7
	6	89.7 ± 7.1	7.9	68.7 ± 3.9	5.7
	96	93.5 ± 5.7	6.1	72.8 ± 6.6	9.0
Icariin (IS)	500	86.2 ± 2.4	2.8	87.5 ± 2.1	2.5

compounds retusin, diosmetin-7-O-β-D-glucopyranoside, and IS were examined, while others were assessed in negative ion mode.

3.2 Sample preparation

The study evaluated four different extraction methods to determine the most effective method for preparing plasma samples, including protein precipitation using ME or ACN, ethyl acetate liquid-liquid extraction, and extraction using a mixture of ME and ACN (v/v = 1:4). The findings indicated that the protein precipitation using ACN showed higher extraction recovery rates for the 15 analytes tested. Additionally, different volumes (400, 600, 800, and 1,000 μL) of precipitated solvent were used to assess the extraction recovery and matrix effect. The outcomes demonstrated that the extraction recovery and matrix effects of the ACN-protein precipitation using 600 μL satisfied the criteria for analyzing biological specimens, with no interference from endogenous compounds. Additionally, the impacts of various reconstitution solvents such as ME, ACN, 50% ME, and ME-ACN (v/v = 1:1, 1:4, and 4:1) were assessed. The results indicated that the redissolution effectiveness was optimal with a ME-ACN mixture of (v/v = 1:1).

3.3 Method validation

3.3.1 Specificity

The MRM chromatograms in Figure 1 displayed the rat plasma samples without any added analytes (A), plasma samples combined with the 15 compounds and IS (B), and post-dosing plasma samples from rats following oral ingestion of PC (C). The results suggested no noticeable interference peaks were noted at the retention time of the 15 compounds and IS.

3.3.2 Linearity and LLOQ

The calibration curves, linear ranges, correlation coefficients, and LLOQ for 15 compounds are shown in Table 1. Within their respective concentration ranges, the calibration profiles of these 15 compounds exhibited excellent linearity (r > 0.996). The LLOQ of vanillic acid, vitexin, verbascoside, isoacteoside, hyperoside, cosmosiin, apigenin, β-rhamnocitrin, acacetin, ombuin, pogostone, pachypodol, diosmetin-7-O-β-D-glucopyranoside, vicenin-2, and retusin and were 20.0, 0.5, 10.0, 2.0, 0.3, 0.5, 1.5, 0.3, 0.3, 0.5, 30.0, 1.0, 0.3, 20.0, and 0.2 ng/mL, respectively.

3.3.3 Precision and accuracy

The precision and accuracy of QC samples at three concentrations are provided in Table 2. The RSD of intra- and inter-day were below 11.3%, the RE of intra-day ranged from −12.0%–14.3%, and the inter-day ranged from −6.5%–13.2%. These findings indicated that is accurate and precise to a satisfactory degree.

3.3.4 Extraction recovery and matrix effect

As listed in Table 3, the 15 analytes and the IS displayed extraction recovery and matrix effects within the ranges of 70.6%–104.5%, and 67.4%–104.8%, respectively. These findings revealed that the method's extraction recovery and matrix effects were accurate and satisfactory.

3.3.5 Stability

As shown in Table 4, the RSD values for the stability of all analytes tested were less than 14.1%, indicating that they were adequately stable across different conditions. This further suggested that the established UPLC-MS/MS method could effectively measure the 15 components in rat plasma.

3.4 PK study

Following oral administration of the PC extract, 15 plasma constituents were analyzed using the validated method. Unfortunately, certain analytes such as vitexin, hyperoside, acacetin, and diosmetin-7-O-β-D-glucopyranoside were only detected in the initial plasma samples, leading to difficulties in obtaining a complete PK profile. As a result, these analytes were not included in our analysis. The mean plasma concentration-

TABLE 4 Stability of 15 components in rat plasma (n = 6).

Compound	Spiked concentration (ng/mL)	Room temperature for 4 h		Autosampler for 12 h		Three freeze-thaw cycles		−80 °C for 7 days	
		Measured (ng/mL)	RSD (%)	Measured (ng/mL)	RSD (%)	Measured (ng/mL)	RSD (%)	Measured (ng/mL)	RSD (%)
Vanillic acid	20	22.0 ± 0.4	2.0	22.7 ± 1.0	4.3	22.7 ± 0.5	2.1	23.1 ± 0.8	3.4
	400	405.6 ± 17.8	4.4	396.6 ± 8.7	2.2	374.6 ± 10.2	2.7	392.0 ± 8.5	2.2
	6,400	5821.2 ± 241.2	4.1	6,602.7 ± 196.9	3.0	6,149.2 ± 382.8	6.2	5892.7 ± 220.9	3.7
Vitexin	0.5	0.5 ± 0.0	2.0	0.5 ± 0.1	7.0	0.5 ± 0.0	3.0	0.6 ± 0.1	7.1
	10	9.7 ± 0.2	2.2	9.9 ± 0.4	4.2	9.3 ± 0.4	4.8	9.0 ± 0.4	4.0
	160	153.8 ± 6.7	4.4	166.2 ± 6.9	4.1	154.6 ± 8.7	5.6	147.4 ± 10.7	7.2
Verbascoside	10	11.3 ± 0.7	5.9	11.7 ± 1.0	8.1	11.3 ± 0.7	6.3	11.6 ± 0.8	6.9
	200	188.8 ± 4.7	2.5	197.3 ± 14.2	7.2	178.9 ± 9.6	5.4	180.0 ± 4.9	2.7
	3200	3280.8 ± 140.4	4.3	3327.3 ± 190.1	5.7	3240.3 ± 93.8	2.9	3114.3 ± 67.0	2.2
Isoacteoside	2	2.2 ± 0.1	5.7	2.2 ± 0.1	5.0	2.2 ± 0.1	3.9	2.2 ± 0.1	4.0
	40	41.6 ± 1.3	3.2	43.8 ± 1.4	3.3	43.0 ± 1.2	2.8	42.2 ± 0.9	2.2
	640	657.1 ± 21.8	3.3	666.7 ± 12.2	1.8	667.9 ± 11.3	1.7	654.5 ± 18.0	2.8
Hyperoside	0.3	0.3 ± 0.1	10.9	0.3 ± 0.0	6.5	0.3 ± 0.0	5.9	0.3 ± 0.0	2.7
	6	5.5 ± 0.4	7.6	6.0 ± 0.2	3.8	5.9 ± 0.4	6.1	5.9 ± 0.2	3.5
	96	94.9 ± 5.8	6.2	99.1 ± 4.5	4.6	95.8 ± 3.3	3.5	93.3 ± 5.3	5.6
Cosmosiin	0.5	0.5 ± 0.0	6.9	0.5 ± 0.0	3.7	0.6 ± 0.1	7.4	0.5 ± 0.0	4.2
	10	9.2 ± 0.5	5.5	10.2 ± 0.3	2.7	10.1 ± 0.5	4.5	9.6 ± 0.5	5.3
	160	163.7 ± 5.5	3.4	175.3 ± 5.9	3.4	168.0 ± 6.0	3.6	156.0 ± 2.3	1.5
Apigenin	1.5	1.6 ± 0.1	4.6	1.7 ± 0.2	9.1	1.6 ± 0.0	1.1	1.8 ± 0.1	3.7
	30	28.3 ± 0.9	3.1	31.6 ± 1.0	3.1	28.8 ± 1.2	4.3	29.0 ± 0.7	2.5
	480	478.3 ± 18.4	3.8	494.4 ± 11.3	2.3	461.1 ± 23.0	5.0	440.2 ± 27.4	6.2
β-rhamnocitrin	0.3	0.3 ± 0.0	2.5	0.3 ± 0.0	5.0	0.3 ± 0.0	4.6	0.3 ± 0.0	6.8
	6	6.0 ± 0.1	2.0	6.2 ± 0.1	1.7	5.5 ± 0.3	6.0	5.9 ± 0.2	3.4
	96	102.6 ± 4.6	4.5	103.9 ± 4.2	4.0	97.0 ± 3.3	3.4	96.2 ± 4.4	4.6
Acacetin	0.3	0.4 ± 0.1	10.5	0.3 ± 0.0	8.9	0.3 ± 0.0	5.1	0.3 ± 0.0	2.4
	6	5.4 ± 0.4	7.3	5.8 ± 0.5	8.5	5.6 ± 0.3	4.9	5.8 ± 0.2	2.7
	96	94.4 ± 1.3	1.4	96.5 ± 4.2	4.3	94.3 ± 1.4	1.5	93.5 ± 1.8	1.9
Ombuin	0.5	0.5 ± 0.0	2.6	0.5 ± 0.0	2.6	0.6 ± 0.0	7.7	0.5 ± 0.0	5.6
	10	9.9 ± 0.3	2.7	9.6 ± 0.2	2.5	9.0 ± 0.2	2.6	9.3 ± 0.4	4.5
	160	151.0 ± 5.3	3.5	155.3 ± 4.2	2.7	154.7 ± 7.3	4.7	154.9 ± 4.8	3.1
Pogostone	125	132.6 ± 8.9	6.7	131.4 ± 5.9	4.5	132.1 ± 7.6	5.7	132.8 ± 10.2	7.7
	2,500	2,756.7 ± 171.1	6.2	2,482.5 ± 168.7	6.8	2,618.0 ± 112.1	4.3	2,618.0 ± 112.1	4.3
	40,000	38,298.2 ± 647.9	1.7	37047.4 ± 2,580.0	7.0	36825.8 ± 1555.6	4.2	38116.7 ± 1,540.2	4.0
Pachypodol	1	1.1 ± 0.1	10.0	1.1 ± 0.1	4.5	1.18 ± 0.12	10.4	1.1 ± 0.1	8.3
	20	21.4 ± 2.0	9.1	18.7 ± 0.8	4.5	20.6 ± 1.7	8.3	20.8 ± 1.8	8.9

(Continued on following page)

TABLE 4 (*Continued*) Stability of 15 components in rat plasma (n = 6).

Compound	Spiked concentration (ng/mL)	Room temperature for 4 h		Autosampler for 12 h		Three freeze-thaw cycles		−80 °C for 7 days	
		Measured (ng/mL)	RSD (%)	Measured (ng/mL)	RSD (%)	Measured (ng/mL)	RSD (%)	Measured (ng/mL)	RSD (%)
	320	337.2 ± 12.6	3.7	334.8 ± 21.1	6.3	345.1 ± 7.2	2.1	330.2 ± 21.4	6.5
Vicenin-2	20	22.4 ± 0.4	1.9	23.2 ± 0.6	2.7	23.0 ± 1.1	4.9	22.7 ± 0.3	1.2
	400	399.2 ± 2.7	0.7	409.4 ± 12.1	3.0	389.6 ± 17.1	4.4	400.1 ± 5.7	1.4
	6,400	6,476.6 ± 162.3	2.5	6,139.7 ± 284.7	4.6	6,473.2 ± 140.7	2.2	6,317.8 ± 84.9	1.3
Retusin	0.2	0.2 ± 0.0	6.8	0.2 ± 0.0	12.9	0.2 ± 0.0	7.1	0.3 ± 0.1	14.1
	4	4.1 ± 0.2	4.6	3.7 ± 0.3	9.2	4.1 ± 0.1	3.0	3.9 ± 0.4	10.2
	64	61.2 ± 1.6	2.6	69.4 ± 6.4	9.2	63.5 ± 1.8	2.8	63.3 ± 5.3	8.4
Diosmetin-7-O-β-D-glucopyranoside	0.3	0.3 ± 0.0	3.3	0.3 ± 0.0	6.4	0.3 ± 0.0	5.4	0.4 ± 0.1	10.2
	6	6.5 ± 0.2	2.9	6.3 ± 0.2	3.8	6.6 ± 0.4	5.7	6.6 ± 0.6	8.8
	96	98.0 ± 1.7	1.7	99.4 ± 4.7	4.8	103.3 ± 2.9	2.8	102.2 ± 3.6	3.5

time curves for the remaining 11 analytes are displayed in Figure 2, with corresponding PK parameters detailed in Table 5.

The concentration maximum (T_{max}) of vanillic acid, verbascoside, isoacteoside, cosmosiin, apigenin, β-rhamnocitrin, ombuin, pogostone, pachypodol, vicenin-2, and retusin were 1.4, 0.4, 0.5, 0.5, 0.3, 0.5, 0.6, 1.9, 0.8, 0.3 and 0.9 h, respectively. The T_{max} of all components was within 2 h, indicating that the absorption of these compounds happened quickly. Pogostone was rapidly absorbed in rats after oral administration, potentially attributed to its low polarity profile and small molecule size (Liu et al., 2012; Chen et al., 2013). Verbascoside and isoacteoside could be rapidly absorbed *in vivo*, which might be related to their relatively large polarity, and previous research has shown comparable PK characteristics. (Zheng et al., 2015). The plasma half-life ($T_{1/2}$) of pogostone was 0.8 ± 0.5 h, which was relatively short compared to other compounds. It is speculated that this might be due to its distribution and elimination rapidly in rats (Zheng et al., 2015). The area-under-the-curve (AUC) for pogostone significantly exceeded that of the other constituents, suggesting that pogostone exhibited a higher plasma exposure level, correlating with its abundant PC content. Additionally, the concentration maximum (C_{max}) of pogostone was 37204.0 ± 10,901.0 ng/mL, coupled with its substantial exposure *in vivo*, suggesting that pogostone may be the mian active component in the PC extract (Li et al., 2021). Furthermore, the maximum concentration (Cmax) of pogostone was measured at 37204.0 ± 10,901.0 ng/mL.

The apigenin, *β*-rhamnocitrin, and pachypodol have a double-peak phenomenon in Figure 2, which is likely due to enterohepatic circulation (Wang et al., 2014). Additionally, the absorption of drugs in the gastrointestinal tract is a complex process that is influenced by many physical, chemical, and physiological factors. There are multiple absorption sites in different parts of the gastrointestinal tract, but due to the different permeability of the inner membrane of the cavity to drugs at different sites, the absorption rates and times differ following oral administration. Consequently, absorbed drugs overlap in the blood, creating a bimodal phenomenon (Zhou, 2003).

PK is an indispensable strategy for understanding the behavior *in vivo* after drug administration, which is of great significance in elucidating the mechanism of action, reducing toxic and side effects, optimizing the drug administration program, and guiding the clinical application of drugs (Jin et al., 2019; Liu et al., 2021). Currently, the PK studies of PC mainly focus on a few components, such as pogostone and verbascoside (Li et al., 2012; Chen et al., 2013; Huo et al., 2016). However, research on these individual components cannot reflect the actual PK characteristics of PC after administration. Therefore, in this study, the simultaneous determination of multiple components in rat plasma and PK study by UPLC-MS/MS, which is crucial in elucidating the pharmacological substance basis, mechanism of action, and optimal dosing regimen of PC, and may provide a reference for the clinical application of PC.

Notably, most of the current PK studies are in normal animals, and there are fewer in model animals. Numerous studies have shown that disease states may cause significant alterations in PK parameters (Chen et al., 2022; Liu et al., 2022; Xiong et al., 2023). Since the drugs are mainly used in the pathological state of the body, it is more meaningful to study the PK of TCM in pathological states (Luo et al., 2014). Moreover, PK and pharmacodynamics (PD) are two important interrelated and inseparable aspects in the field of pharmacological research of TCM. PK/PD modeling is extensively utilized in both preclinical and clinical drug research, which aids in gaining a comprehensive and precise

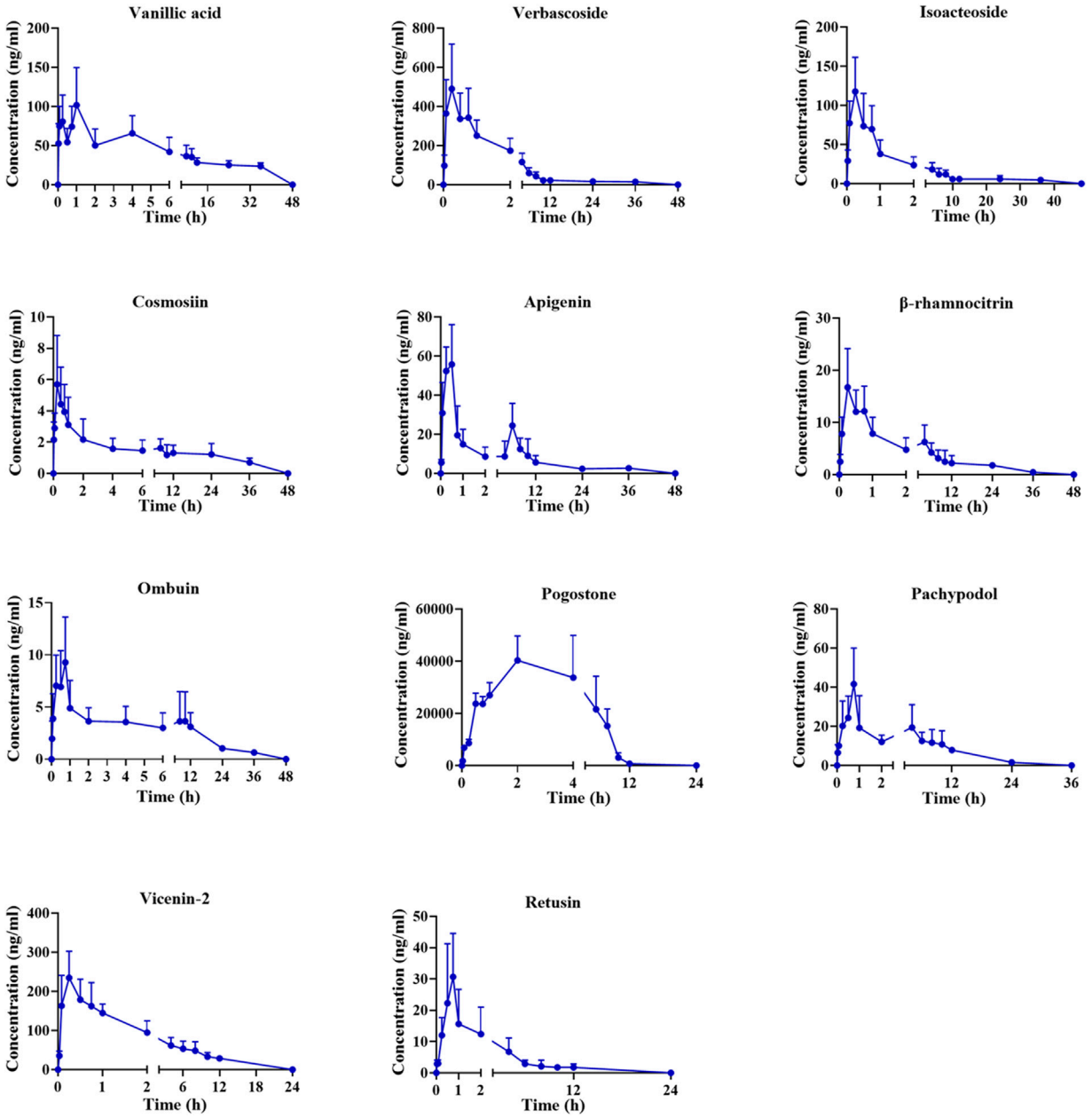

FIGURE 2
Mean plasma concentration-time profiles in rats after oral administration of PC extract.

understanding of drug effectiveness over time and plasma concentration. Additionally, it provides a valuable reference for optimizing clinical dosage, improving efficacy, and minimizing adverse effects. Therefore, it is vital to explore the ideas and methods of PK-PD modeling of TCM to elucidate the nature and laws (Zhang Z. et al., 2016; Zhu et al., 2023). Only normal rats were investigated in this study, while the PK of PC in model animals was lacking. In the future, The PK research of PC should focus on studies in disease states and develop PK-PD models to elucidate the pharmacodynamic basis and mechanism of action of PC.

4 Conclusion

In this study, a UPLC-MS/MS method was developed to simultaneously measure 15 components in rat plasma following the oral administration of PC extract. The method has the benefits of uncomplicated sample preparation and the simultaneous analysis of multiple components within a brief timeframe. Furthermore, the method is specific, stable, and reliable. Moreover, PK results are crucial in elucidating the pharmacodynamic material basis, mechanism of action, and optimal dosing regimen of PC, and may provide guidance for the future advancement and clinical application of PC.

TABLE 5 Pharmacokinetic parameters of 11 components in rats (n = 6).

Compound	T_{max}	C_{max}	$T_{1/2z}$	AUC $_{(0-tn)}$	AUC $_{(0-\infty)}$
	(h)	(μg/L)	(h)	(μg/L*h)	(μg/L*h)
Vanillic acid	1.4 ± 1.4	115.8 ± 36.8	2.5 ± 0.1	1,314.1 ± 172.4	1,314.1 ± 172.4
Verbascoside	0.4 ± 0.3	553.9 ± 159.4	2.6 ± 0.21	1702.2 ± 394.5	1702.2 ± 394.5
Isoacteoside	0.5 ± 0.3	109.3 ± 41.5	2.9 ± 0.3	383.8 ± 93.8	383.8 ± 93.8
Cosmosiin	0.5 ± 0.3	6.2 ± 2.5	3.7 ± 0.6	50.1 ± 10.2	50.1 ± 10.2
Apigenin	0.3 ± 0.2	64.2 ± 15.8	2.7 ± 0.6	254.7 ± 65.5	254.7 ± 65.5
β-rhamnocitrin	0.5 ± 0.3	17.4 ± 4.5	4.8 ± 2.6	111.9 ± 37.7	112.7 ± 38.4
Ombuin	0.6 ± 0.2	11.2 ± 1.5	3.8 ± 1.8	95.1 ± 28.1	95.4 ± 28.4
Pogostone	1.9 ± 1.3	37204.0 ± 10,901.0	0.8 ± 0.5	258294.0 ± 93,104.7	258320.9 ± 93120.6
Pachypodol	0.8 ± 0.2	47.8 ± 15.9	2.0 ± 0.1	243.4 ± 63.5	243.4 ± 63.5
Vicenin-2	0.3 ± 0.1	249.4 ± 50.8	1.2 ± 0.6	968.0 ± 131.9	968.8 ± 132.9
Retusin	0.9 ± 0.6	33.0 ± 14.6	1.5 ± 0.2	92.2 ± 33.0	92.2 ± 33.0

Data availability statement

The original contributions presented in the study are included in the article/Supplementary Material, further inquiries can be directed to the corresponding author.

Ethics statement

The animal study was approved by The animal experiments were performed strictly in accordance with the Principles of Animal Care and Use approved by The Animal Ethic Review Committee of Tianjin University of Traditional Chinese Medicine (TCM-LAEC2023059). The study was conducted in accordance with the local legislation and institutional requirements.

Author contributions

YZ: Data curation, Formal Analysis, Investigation, Writing–original draft. ZL: Data curation, Formal Analysis, Writing–original draft. GY: Data curation, Formal Analysis, Writing–original draft. MG: Data curation, Formal Analysis, Methodology, Writing–original draft. XC: Data curation, Formal Analysis, Investigation, Writing–original draft. YC: Data curation, Formal Analysis, Investigation, Writing–original draft. HO: Data curation, Formal Analysis, Investigation, Writing–original draft. JH: Conceptualization, Funding acquisition, Resources, Supervision, Writing–review and editing.

Funding

The author(s) declare that financial support was received for the research, authorship, and/or publication of this article. This study was supported by Tianjin Committee of Science and Technology, China (23ZYJDSS00010).

Conflict of interest

The authors declare that the research was conducted in the absence of any commercial or financial relationships that could be construed as a potential conflict of interest.

Publisher's note

All claims expressed in this article are solely those of the authors and do not necessarily represent those of their affiliated organizations, or those of the publisher, the editors and the reviewers. Any product that may be evaluated in this article, or claim that may be made by its manufacturer, is not guaranteed or endorsed by the publisher.

Supplementary material

The Supplementary Material for this article can be found online at: https://www.frontiersin.org/articles/10.3389/fphar.2024.1293464/full#supplementary-material

References

Cao, L., Zhan, S., Ji, X., Zheng, B., Ye, C., Chen, Z., et al. (2021). Research advance in multi-component pharmacokinetics of Chinese herbal extracts in recent five years. *China J. Chin. Materia Medica* 46, 3270–3287. doi:10.19540/j.cnki.cjcmm.20210310.601

Chen, H., Li, Y., Wu, X., Li, C., Li, Q., Qin, Z., et al. (2013). LC-MS/MS determination of pogostone in rat plasma and its application in pharmacokinetic studies. *Biomed. Chromatogr. BMC* 27, 1092–1099. doi:10.1002/bmc.2897

Chen, H., Luo, Y., Liu, J., Chen, J., Chen, Y., and Li, X. (2022). Comparative pharmacokinetic study of six lignans in normal and diabetic rats after oral administration of Saururus chinensis extract by LC-MS/MS. *Biomed. Chromatogr. BMC* 36, e5253. doi:10.1002/bmc.5253

Chen, Y., Luo, Q., Li, S., Li, C., Liao, S., Yang, X., et al. (2020). Antiviral activity against porcine epidemic diarrhea virus of Pogostemon cablin polysaccharide. *J. Ethnopharmacol.* 259, 113009. doi:10.1016/j.jep.2020.113009

Chinese Pharmacopoeia Committee (2020) *Pharmacopoeia of the people's Republic of China*. Beijing: China Medical Science Press.

Huo, F., Sun, J., Shen, J., and Hu, Y. (2007). Study on the combination condiment for stewing fish by raw material of northeast Agastache rugosa. *China Condiment*, 60–62.

Huo, S., Li, J., Gao, L., Peng, X., Chen, X., Wen, Y., et al. (2016). Absorption, distribution and excretion of acteoside in rats. *Chin. J. Hosp. Pharm.* 36, 450–454. doi:10.13286/j.cnki.chinhosppharmacyj.2016.06.07

Jin, J., Xue, H., Sun, X., Zan, B., Li, Y., Wang, T., et al. (2019). Simultaneous determination of multiple compounds of Da-Huang-Xiao-Shi decoction in rat plasma by LC-MS/MS and its application in a pharmacokinetic study. *J. Pharm. Biomed. analysis* 174, 8–18. doi:10.1016/j.jpba.2019.05.050

Junren, C., Xie, X., Li, M., Xiong, Q., Li, G., Zhang, H., et al. (2021). Pharmacological activities and mechanisms of action of Pogostemon cablin Benth: a review. *Chin. Med.* 16, 5. doi:10.1186/s13020-020-00413-y

Kim, K. H., Beemelmanns, C., Clardy, J., and Cao, S. (2015). A new antibacterial octaketide and cytotoxic phenylethanoid glycosides from Pogostemon cablin (Blanco) Benth. *Bioorg. Med. Chem. Lett.* 25, 2834–2836. doi:10.1016/j.bmcl.2015.04.094

Kiyohara, H., Ichino, C., Kawamura, Y., Nagai, T., Sato, N., and Yamada, H. (2012). Patchouli alcohol: *in vitro* direct anti-influenza virus sesquiterpene in Pogostemon cablin Benth. *J. Nat. Med.* 66, 55–61. doi:10.1007/s11418-011-0550-x

Lai, K., Xiao, J., Wang, H., Qiu, J., Wan, X., Yan, B., et al. (2023). Mechanism and application prospects of microbial fertilizers in regulating quality formation of medicinal plants. *China J. Chin. Materia Medica*, 1–14. doi:10.19540/j.cnki.cjcmm.20230921.101

Lan, H., and Yuan, H. (2018). Treating cold rhinitis with huodan wan. *Clin. J. Chin. Med.* 10, 124–125.

Li, M., Chen, S., Wang, X., Li, L., Xu, Y., and Di, L. (2021). UPLC fingerprint of Pogostemonis Herbal and prediction of its potential quality markers based on network pharmacology. *Chin. Traditional Herb. Drugs* 52, 2665–2677.

Li, S., Feng, Y., Zhou, Y., Liao, C., Su, L., Liu, D., et al. (2023). Pogocablenes A-O, fifteen undescribed sesquiterpenoids with structural diversity from Pogostemon cablin. *Phytochemistry* 214, 113829. doi:10.1016/j.phytochem.2023.113829

Li, Y., Liang, H., Chen, H., Tan, L., Yi, Y., Qin, Z., et al. (2012). Anti-Candida albicans activity and pharmacokinetics of pogostone isolated from Pogostemonis Herba. *Phytomedicine Int. J. phytotherapy Phytopharm.* 20, 77–83. doi:10.1016/j.phymed.2012.08.008

Liu, F., Zeng, Y., Dai, P., Huang, K., Zhang, K., Tao, T., et al. (2022). Comparative pharmacokinetics of three bioactive diterpenoids of rabdosia serra extract in normal and con A-induced liver injury rats using UPLC-MS/MS. *Front. Pharmacol.* 13, 944949. doi:10.3389/fphar.2022.944949

Liu, J., Li, X., Peng, C., Lin, D., Wang, Y., Yang, Y., et al. (2015). 4-nor-β-Patchoulene sesquiterpenoids from the essential oil of Pogostemon cablin. *Phytochem. Lett.* 12, 27–30. doi:10.1016/j.phytol.2015.02.016

Liu, L., Liu, K., Wen, Y., Zhang, H., Lu, Y., and Yin, Z. (2012). Development of a fully automated on-line solid phase extraction and high-performance liquid chromatography with diode array detection method for the pharmacokinetic evaluation of bavachinin: a study on absolute bioavailability and dose proportionality. *J. Chromatogr. B, Anal. Technol. Biomed. life Sci.* 893, 21–28. doi:10.1016/j.jchromb.2012.02.020

Liu, X., Zhang, Y., Yang, X., Xu, W., Liu, L., Zhang, P., et al. (2021). Simultaneous determination of twenty-five compounds with anti-inflammatory activity in Spatholobi Caulis by using an optimized UFLC-MS/MS method: an application to pharmacokinetic study. *J. Pharm. Biomed. analysis* 204, 114267. doi:10.1016/j.jpba.2021.114267

Luo, T., Li, J., and Tong, R. (2014). Application status and prospect of the PK-PD model in Chinese medicine research. *China J. Traditional Chin. Med. Pharm.* 29, 332–335.

Sandes, S., Zucchi, M., Pinheiro, J., Bajay, M., Batista, C., Brito, F., et al. (2016). Molecular characterization of patchouli (Pogostemon spp) germplasm. *Genet. Mol. Res. GMR* 15 (1). doi:10.4238/gmr.15017458

Su, J., He, J., Su, Z., Zhou, L., Zeng, Y., Lai, X., et al. (2017). T cell inhibition by pogostone from Pogostemon cablin (Blanco) Benth: *in vitro* and *in vivo* immunosuppressive analysis. *Mol. Med. Rep.* 16, 4511–4520. doi:10.3892/mmr.2017.7147

Wang, Y., Yang, G., Guo, C., Pei, Q., Zhang, R., and Huang, L. (2014). Plasma double-peak phenomenon following oral administration. *Chin. J. Clin. Pharmacol. Ther.* 19, 341–345.

Xiong, S., Li, X., Chu, H., Deng, Z., Sun, L., Liu, J., et al. (2023). Comparative pharmacokinetics of four major compounds after oral administration of Mori Cortex total flavonoid extract in normal and diabetic rats. *Front. Pharmacol.* 14, 1148332. doi:10.3389/fphar.2023.1148332

Zhang, C., Liu, T., Yuan, X., Huang, H., Yao, G., Mo, X., et al. (2019). The plastid genome and its implications in barcoding specific-chemotypes of the medicinal herb Pogostemon cablin in China. *PloS one* 14, e0215512. doi:10.1371/journal.pone.0215512

Zhang, J., Wang, Y., Piao, C., Yu, H., Liu, J., Jiang, L., et al. (2016a). Application and prospect of agastache rugosa in food. *Food Res. Dev.* 37, 208–211.

Zhang, Q. (2004). Resources of Agastache Rugosa's development and utilization. *Ginseng Res.*, 10–12. doi:10.19403/j.cnki.1671-1521.2004.03.004

Zhang, Z., Qin, L., Peng, L., Zhang, Q., Wang, Q., Lu, Z., et al. (2016b). Pharmacokinetic-pharmacodynamic modeling to study the antipyretic effect of qingkailing injection on pyrexia model rats. *Molecules* 21, 317. doi:10.3390/molecules21030317

Zhao, M., Chen, Y., Wang, C., Xiao, W., Chen, S., Zhang, S., et al. (2019). Systems pharmacology dissection of multi-scale mechanisms of action of Huo-Xiang-Zheng-Qi formula for the treatment of gastrointestinal diseases. *Front. Pharmacol.* 9, 1448. doi:10.3389/fphar.2018.01448

Zheng, D., Chen, W., Ma, S., Shao, J., Wang, J., and Luo, Y. (2015). Simultaneous determination of three phenolic giycosides in Callicarpa nudiflora by UHPLC-MS methods and analysis of their pharmacokinetics in plasma of rats. *Chin. Traditional Herb. Drugs* 46, 3533–3538. doi:10.7501/j.issn.0253-2670.2015.23.015

Zhou, H. (2003). Pharmacokinetic strategies in deciphering atypical drug absorption profiles. *J. Clin. Pharmacol.* 43, 211–227. doi:10.1177/0091270002250613

Zhu, Y., Fan, Y., Cao, X., Wei, S., Zhang, M., Chang, Y., et al. (2023). Pharmacokinetic-pharmacodynamic (PK/PD) modeling to study the hepatoprotective effect of Perilla Folium on the acute hepatic injury rats. *J. Ethnopharmacol.* 313, 116589. doi:10.1016/j.jep.2023.116589

Zhu, Y., Wei, S., Cao, X., Wang, S., Chang, Y., Ouyang, H., et al. (2022). Multi-component pharmacokinetic study of prunus mume fructus extract after oral administration in rats using UPLC-MS/MS. *Front. Pharmacol.* 13, 954692. doi:10.3389/fphar.2022.954692

Frontiers in Pharmacology

Explores the interactions between chemicals and living beings

The most cited journal in its field, which advances access to pharmacological discoveries to prevent and treat human disease.

Discover the latest Research Topics

See more →

Frontiers

Avenue du Tribunal-Fédéral 34
1005 Lausanne, Switzerland
frontiersin.org

Contact us

+41 (0)21 510 17 00
frontiersin.org/about/contact